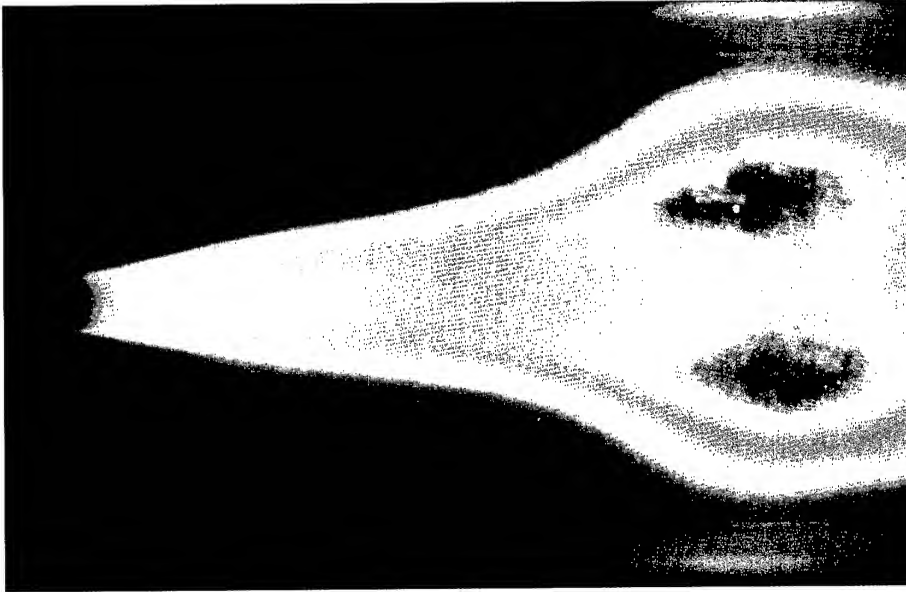


PROCEEDINGS

INTERNATIONAL WORKSHOP ON
RESEARCH STATUS AND PERSPECTIVES
IN LIQUID ROCKET COMBUSTION CHAMBER FLOW DYNAMICS



GDR Research Group Mascotte Bench
OH Emission (P = 60 bar) - (EM2C/CNRS-ONERA)



DISTRIBUTION STATEMENT A
Approved for Public Release
Distribution Unlimited

19990719 063

DTIC QUALITY INSPECTED 4

PARIS France
May 27-28, 1999

REPORT DOCUMENTATION PAGE

Form Approved OMB No. 0704-0188

Public reporting burden for this collection of information is estimated to average 1 hour per response, including the time for reviewing instructions, searching existing data sources, gathering and maintaining the data needed, and completing and reviewing the collection of information. Send comments regarding this burden estimate or any other aspect of this collection of information, including suggestions for reducing this burden to Washington Headquarters Services, Directorate for Information Operations and Reports, 1215 Jefferson Davis Highway, Suite 1204, Arlington, VA 22202-4302, and to the Office of Management and Budget, Paperwork Reduction Project (0704-0188), Washington, DC 20503.

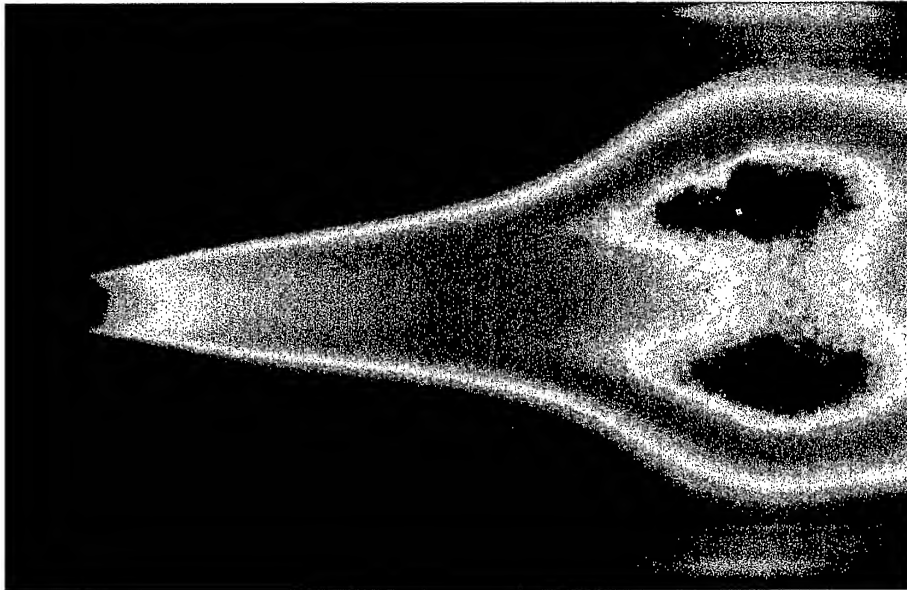
1. AGENCY USE ONLY (Leave blank)		2. REPORT DATE 1999	3. REPORT TYPE AND DATES COVERED Conference Proceedings	
4. TITLE AND SUBTITLE International Workshop on Research Status of Perspectives in Liquid Rocket Chamber Dynamics			5. FUNDING NUMBERS F61775-99-WF043	
6. AUTHOR(S) Conference Committee				
7. PERFORMING ORGANIZATION NAME(S) AND ADDRESS(ES) ONERA Direction de l'Energetique B.P.72 Chatillon 92322 France			8. PERFORMING ORGANIZATION REPORT NUMBER N/A	
9. SPONSORING/MONITORING AGENCY NAME(S) AND ADDRESS(ES) EOARD PSC 802 BOX 14 FPO 09499-0200			10. SPONSORING/MONITORING AGENCY REPORT NUMBER CSP 99-5043	
11. SUPPLEMENTARY NOTES				
12a. DISTRIBUTION/AVAILABILITY STATEMENT Approved for public release; distribution is unlimited.			12b. DISTRIBUTION CODE A	
13. ABSTRACT (Maximum 200 words) The Final Proceedings for International Workshop on Research Status of Perspectives in Liquid Rocket Chamber Dynamics, 27 May 1999 - 28 May 1999 This is an interdisciplinary conference. Topics will focus on liquid rocket combustion issues, including: Injection and Atomization (experimental and analysis aspects), Spray combustion in liquid rocket chambers, Experimental Methods and Diagnostics, Modeling and Analysis, Heat Transfer in combustion chamber, Liquid Rocket Combustion Instability, Low Cost Technology				
14. SUBJECT TERMS EOARD, Combustion, Rocket Engines			15. NUMBER OF PAGES 575	
			16. PRICE CODE N/A	
17. SECURITY CLASSIFICATION OF REPORT UNCLASSIFIED	18. SECURITY CLASSIFICATION OF THIS PAGE UNCLASSIFIED	19. SECURITY CLASSIFICATION OF ABSTRACT UNCLASSIFIED	20. LIMITATION OF ABSTRACT UL	

NSN 7540-01-280-5500

Standard Form 298 (Rev. 2-89)
Prescribed by ANSI Std. Z39-18
298-102

PROCEEDINGS

INTERNATIONAL WORKSHOP ON
RESEARCH STATUS AND PERSPECTIVES
IN LIQUID ROCKET COMBUSTION CHAMBER FLOW DYNAMICS



GDR Research Group Mascotte Bench
OH Emission (P = 60 bar) - (EM2C/CNRS-ONERA)



PARIS France
May 27-28, 1999

AQ F99-10-1832

Acknowledgments

We wish to thank the following organizations for their contribution to the success of this conference :

- European Office of Aerospace Research and Development,
- Air Force Office of Scientific Research,
- United States Air Force Research Laboratory,
- Centre National d'Etudes Spatiales,
- Centre National de la Recherche Scientifique,
- SNECMA Division SEP,
- Deutsches Zentrum für Luft-Und Raumfahrt,
- Office National d'Etudes et de Recherches Aérospatiales.

Organizing Committee
International Workshop on Research Status and Perspectives
in Liquid Rocket Combustion Chamber Flow Dynamics

Objectives of the workshop

The workshop is aimed at gathering international experts in liquid rocket propulsion in order to :

- Provide an instantaneous picture of current international research activities in liquid rocket propulsion and planned efforts for the next few years.
- Identify fields of common interest and importance in liquid rocket combustion chamber flow dynamics research activity.
- Establish networks and enhance international scientific cooperation in the liquid rocket propulsion area.

Topics

- Injection and Atomization : Experimental and Analysis Aspects
- Spray Combustion in Liquid Rocket Combustion Chambers : Experimental Aspects and Diagnostics
- Spray Combustion in Liquid Rocket Combustion Chambers : Aspects of Modeling and Analysis
- Heat Transfer in Combustion Chambers
- Liquid Rocket Combustion Instability
- Low Cost Technology

Organizing Committee

France : Paul Kuentzmann, Mohammed Habiballah (ONERA)
Michel Pons, Patrick Vuillermoz, Eric Robert (CNES)

Germany : Wolfgang Koschel, Oskar Haidn (DLR)

USA : Mitat Birkan (AFOSR), Jay Levine (Air Force Research Laboratory), Vigor Yang
(Penn State University)

Local Committee

Fabienne Debruyère, Victor Burnley, Gérard Ordonneau, Yves Mauriot,
Mohammed Habiballah (ONERA)

Contents

Acknowledgments

Objectives of the workshop – Topics - Committees

The status of the United States Air Force liquid propulsion basic research program <i>M. Birkan (AFOSR)</i>	1
Ten years of research on H₂-O₂ injection in France <i>V. Duthoit, M. René-Corail, M. Sion, S. Zurbach (SNECMA SEP division), R. Borghi, G. Searby (IRPHE), M. Pons, P. Vuillermoz (CNES)</i>	27
Comparative study of swirl-coaxial and non-swirl-coaxial injectors <i>H. Tamura (NAL)</i>	43
Experimental investigations of cryogenic sprays in combustion <i>P. Gicquel, L. Vingert (ONERA)</i>	55
Quantitative density measurements in supercritical LN₂-sprays using Raman scattering <i>M. Oschwald, A. Schik, U.E. Mayer, W. Stricker (DLR)</i>	63
Studies on the break-up regimes of LOx droplets <i>I. Gökalp, C. Chauveau, B. Vieille (University of Orléans-CNRS) B. Gelfand (Russian Academy of Science)</i>	85
Modeling of supercritical droplet and spray combustion <i>V. Yang (Penn State University)</i>	113
Cryogenic combustion modeling <i>B. Barbeau, F. Lacas, G. Rymer, S. Candel (ECP-EM2C)</i>	183
Thin film dynamics and the physics of atomization <i>D. Meinköhn (DLR)</i>	207
Computation of spray combustion using PDF-equation approach <i>P. Durand, M. Gorokhowski (CORIA), R. Borghi (IRPHE)</i>	225
Rocket injector challenges : performance, stability and reliability at low cost <i>R. Santoro (Penn State University)</i>	243
Recent studies on preburner injector characteristics for the hydrogen-oxygen engine <i>J. Wang, S.Q. Cheng, L.Z. Song, P.X. Hu (11th Research Institute of China Aerospace Corporation)</i>	267
Numerical simulation of reactive flow within the MASCOTTE combustor <i>M. Pourouchottamane, V. Burnley, F. Dupoirieux, G. Deuchst, I. Dubois, P. Gilbank (ONERA)</i>	279
Basic research in liquid rocket combustion at the Air Force Research Laboratory <i>D. Talley (United States Air Force Research Laboratory)</i>	309
The structure of cryogenic jet flames inferred from experiments <i>A. Tripathi, M. Juniper, P. Scoufflaire, D. Durox, C. Rolon, S. Candel (ECP-EM2C) L. Vingert, M. Habiballah (ONERA)</i>	325

Coherent anti-Stokes Raman scattering (CARS) measurements in a shear-coaxial cryogenic jet flame <i>F. Grisch, P. Bouchardy (ONERA) - W. Clauss (DLR)</i>	345
Statistical investigations of the turbulent flame geometrical structures in a liquid oxygen/gaseous hydrogen shear-coaxial jet <i>A. Cessou, P. Colin, D. Stepowski (CORIA)</i>	357
Some possible consequences of bifurcations in combustor <i>F. Culick (CALTECH)</i>	369
Some aspects of non-reproductibility of self-oscillation excitation in combustion chamber of liquid rocket engine <i>K.P. Denisov, V.N. Ivanov, V.P. Pikalov (Research Institute of Chemical Machine Building)</i>	435
Fundamental combustion instability research at Glenn Research Center in the 90's <i>K. Breisacher (NASA Glenn Research Center)</i>	465
Current and planned collaborative research activities related to the chemical propulsion at the Technical University of Istanbul, Faculty of Mechanical Engineering <i>NiLufer A.Egrican (Istanbul Technical University)</i>	509



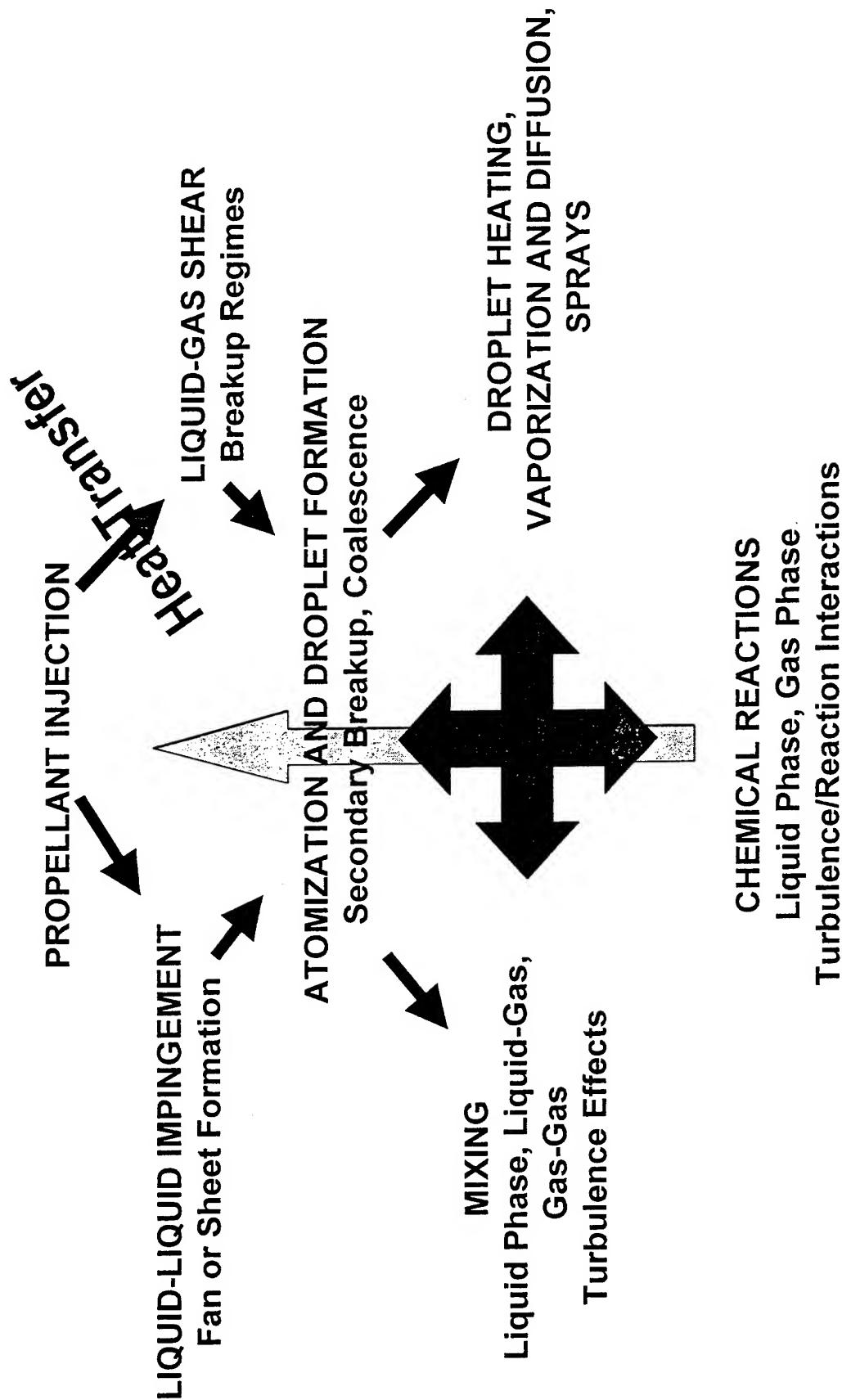
The Status of the United States Air Force Liquid Propulsion Basic Research Program

*International Workshop on Research Status and Perspectives in
Liquid Rocket Combustion Chamber Flow Dynamics*
27 May 1999

Mitat A. Birkan
Air Force Office of Scientific Research

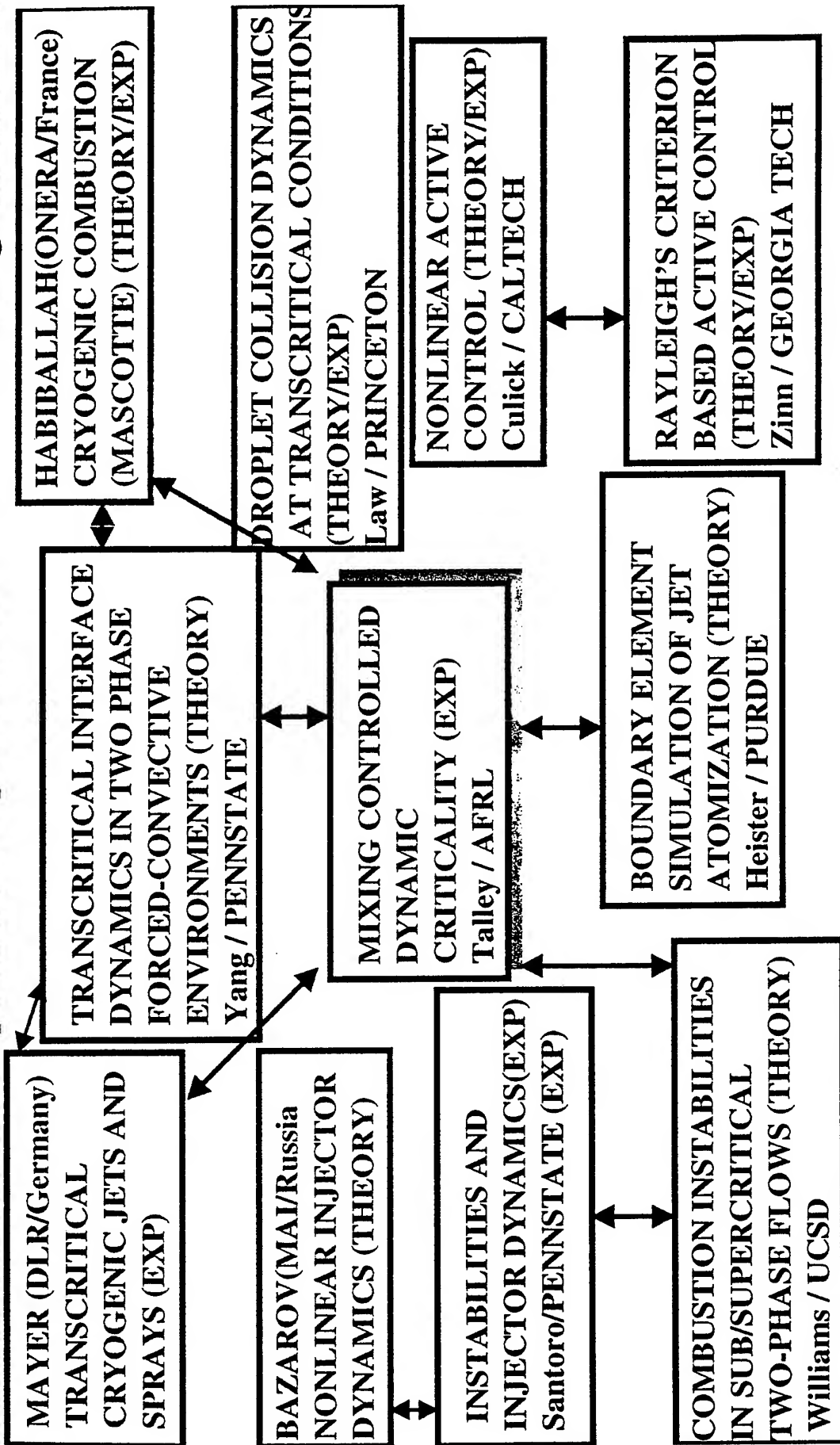


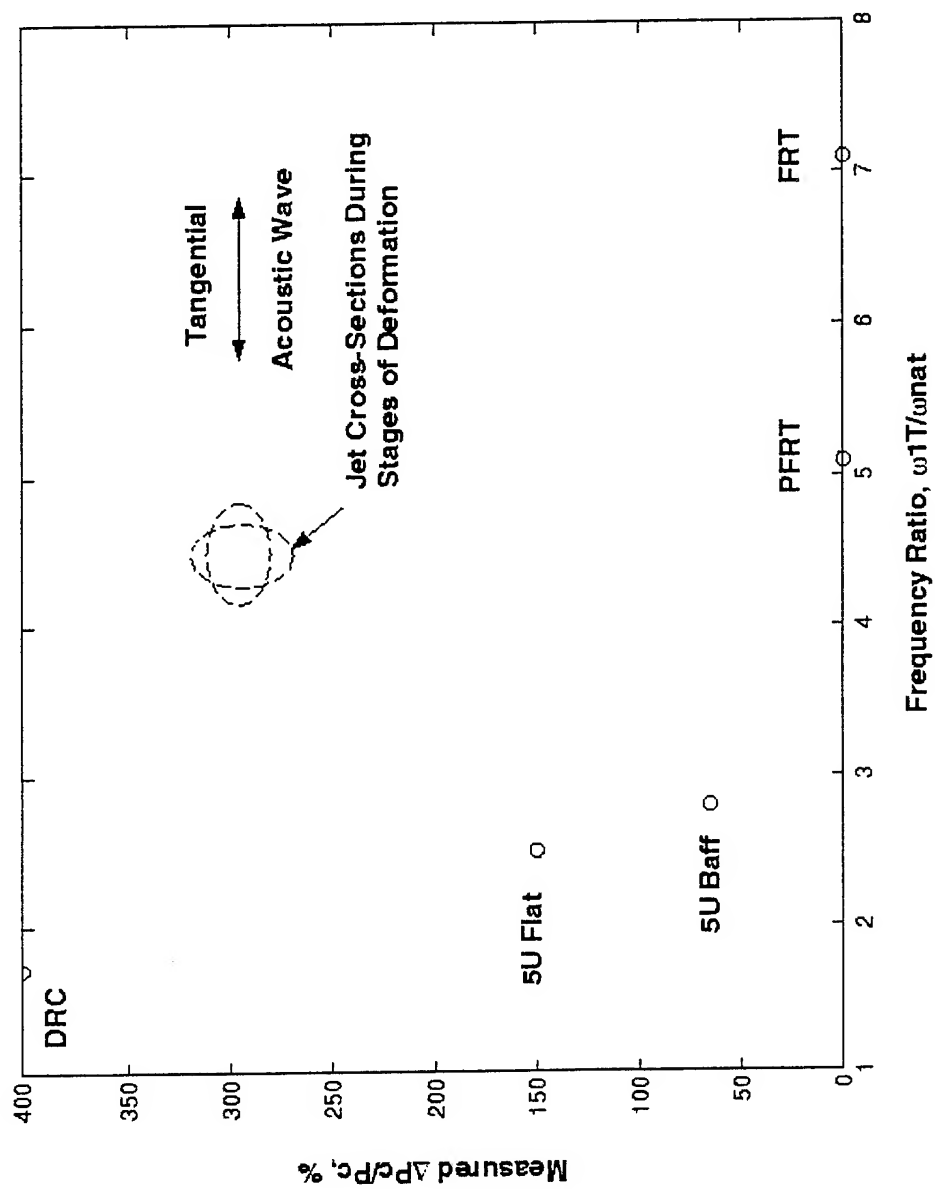
Physicochemical Allied Processes in Liquid Engines

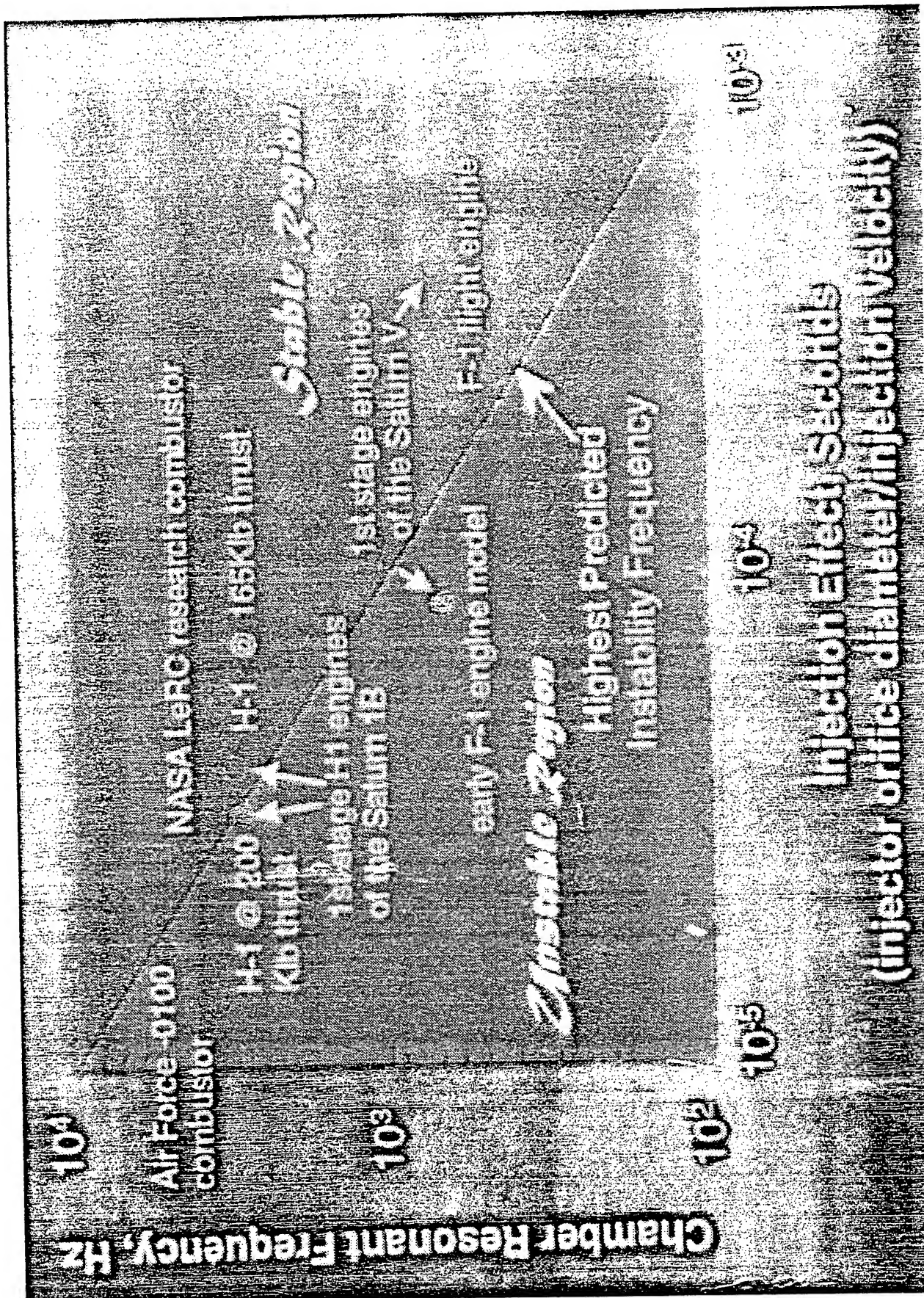




Transcritical Jets and Instability Control in Liquid Propellant Rocket Engines





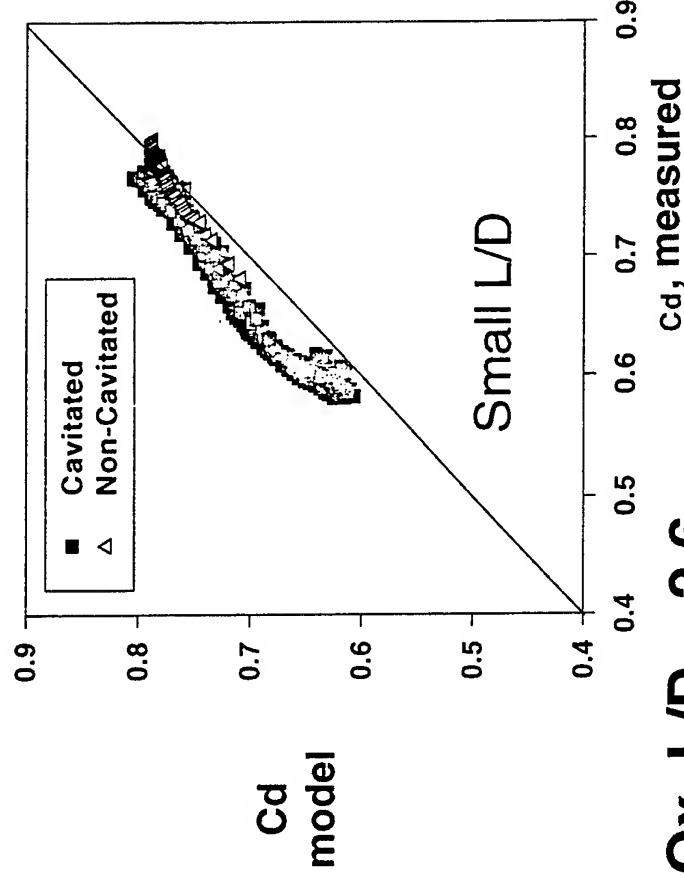
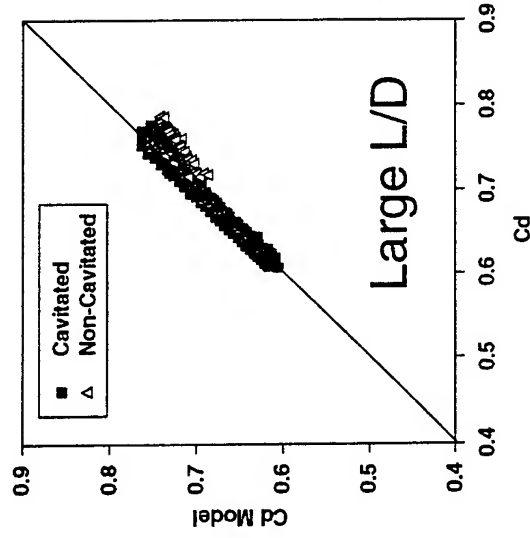




Liquid Rocket Engine Instability Injector Orifice Dynamics

- Can effect combustion efficiency by as much as 5%.
- SSME Specific Impulse Error +/- 0.5 sec, \$3M loss per launch.

AFRL empirical model
(Talley, AFRL/PRSA)



•X-34 Fastrac engine Ox $L/D = 2.6$

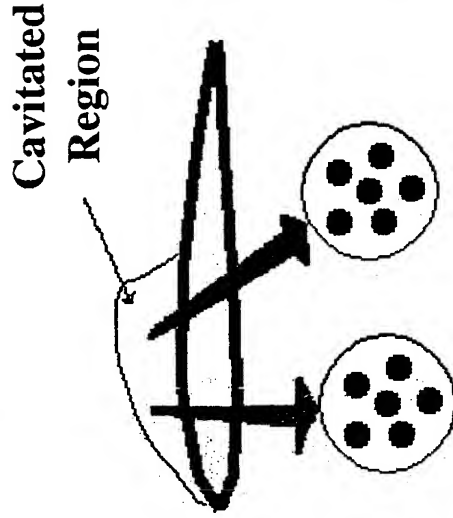
•Improved CFD required to resolve flow losses at short L/D .



Innovative Approach:

Pseudo-Density Formulation in 2-Phase Flows

Kubota *et al.* (1992)



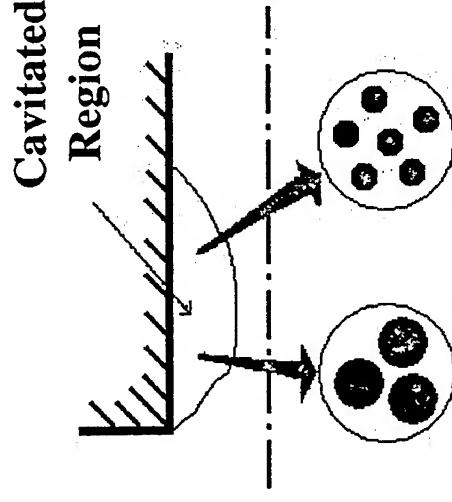
Fixed # Bubbles

Per Unit Mass

$$\frac{D\rho}{Dt} = f(\rho, P, \vec{v})$$

- Assumes Constant Number of Bubbles Per Unit Volume

Heister *et al.* (1998)



- Permits Bubble Number Density to Continually Change

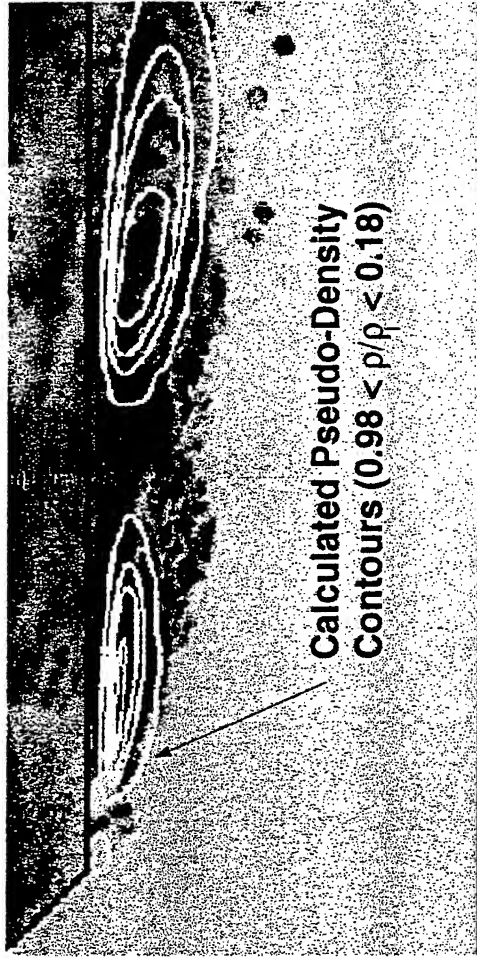
• Integral Averaging of Rayleigh-Plesset Bubble Dynamics for 3D Codes

AFOSR/NA 3-Dec-98

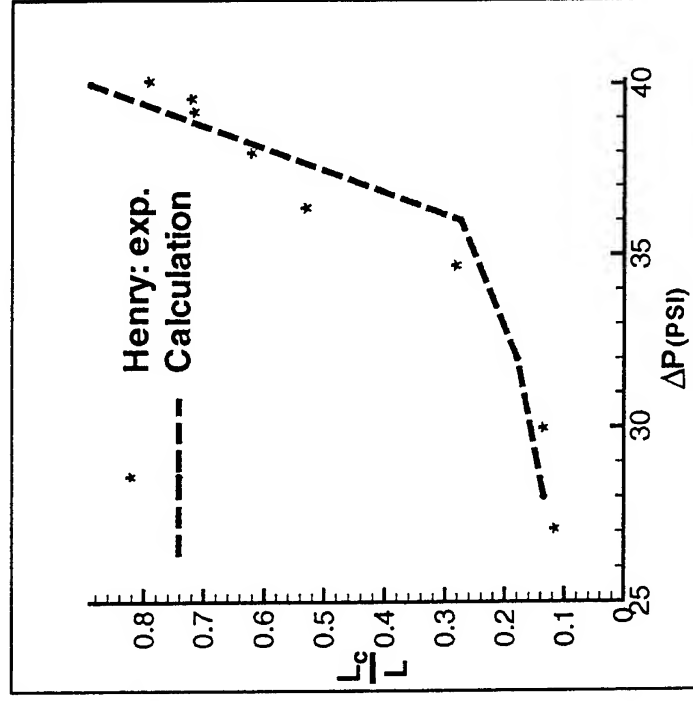
Aerospace and Materials Sciences, 98 PR SAB



Pseudo-Density Code Accurately Predicts Unsteady Cavitating Slot Flow



Cavitation Length Slot Length

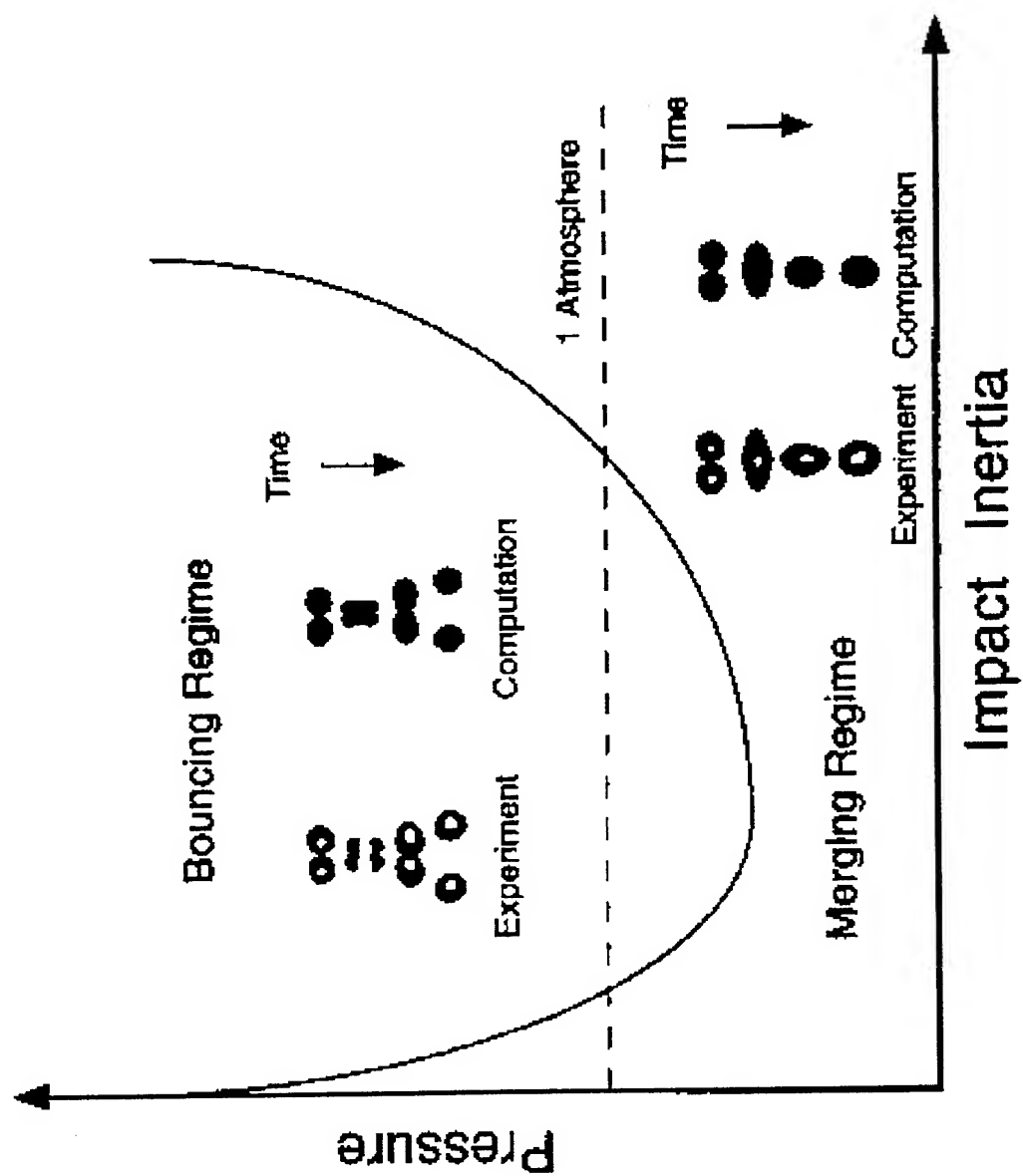


Theory:

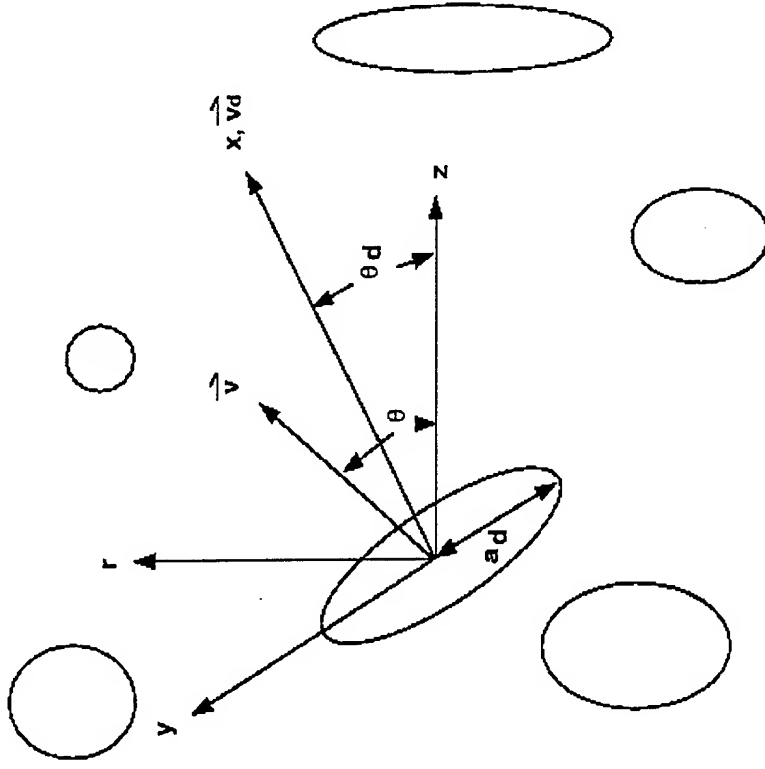
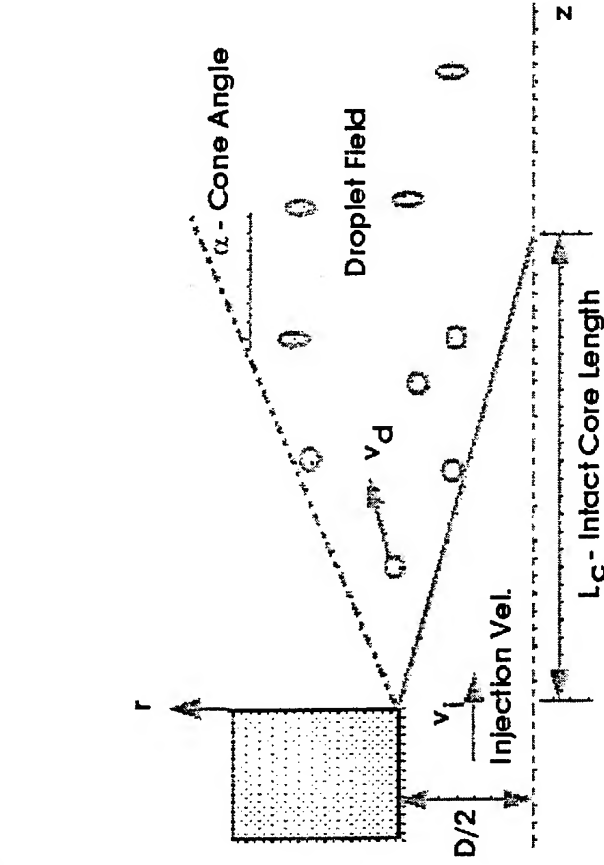
Heister / Purdue
Sponsored by AFOSR
and Cummins Engine Co.

Experiments:

Henry & Collicott / Purdue
Sponsored by NSF and
Cummins Engine Co.



Elements of Model to Investigate Fully Coupled Dense Sprays Including Deforming Droplets

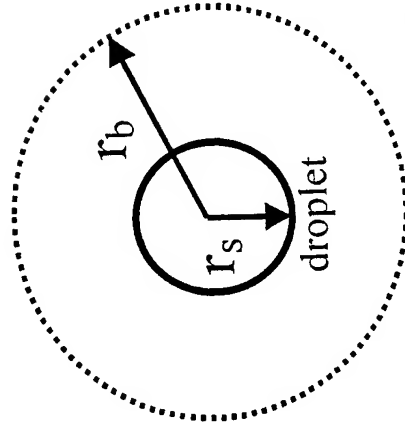


Spray Attributes Evolve Naturally from Simulation

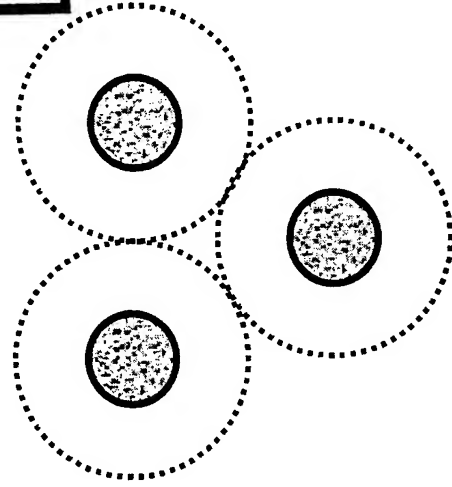
Droplet Atomization, Collisions, and Coalescence are all Modeled



Steady-State Vaporization Theory of Interacting Droplets



bubble



$$\beta = \left(\frac{r_s}{r_b} \right)_0 \Delta = \frac{\ln \{ 1 + B_{\text{interactive}} \}}{\ln \{ 1 + B \}}$$

$$B_{\text{interactive}} = (Y_{Fb} - Y_{Fs}) / (Y_{Fs} - 1) \quad \tau = t_{sd} / t$$

$$3 (4 - d_s^2) - 2\beta (8 - d_s^3) = (12\Delta / \tau)$$

$$\tau_{\text{interactive droplet lifetime}} = \frac{\Delta}{1 - (4/3) \beta}$$



Unsteady Vaporization Theory of Interacting Droplets

Mass conservation:

$$\frac{d}{dt} \iiint \rho dV + \iint \rho (\vec{v} - \vec{w}) \cdot \vec{n} dA = 0$$

Momentum conservation:

$$\nabla p = 0$$

Energy conservation:

$$\frac{d}{dt} \iiint \rho e dV + \iint \rho (\vec{v} - \vec{w}) \cdot \vec{e} n dA = - \iint_e \vec{q} \cdot \vec{n} dA - \iint \vec{p} \cdot \vec{v} \cdot \vec{n} dA$$

Species conservation:

$$\frac{d}{dt} \iiint \rho Y_i dV + \iint \rho Y_i (\vec{v} - \vec{w}) \cdot \vec{n} dA = - \iint \vec{q}_i \cdot \vec{n} dA$$

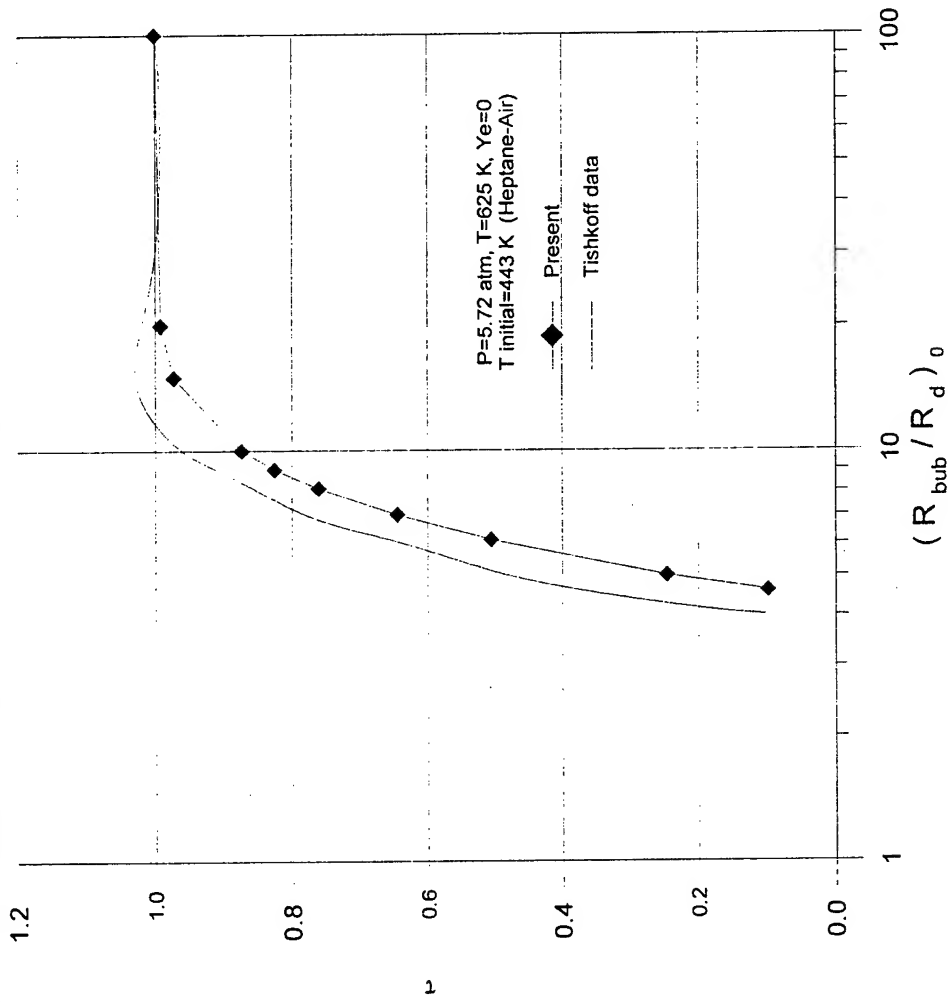
Soave-Redlich-Kwong equation of state:

$$p = \frac{\rho R T}{(W - b\rho)} + \frac{a \alpha \rho^2}{W(W + b\rho)}$$



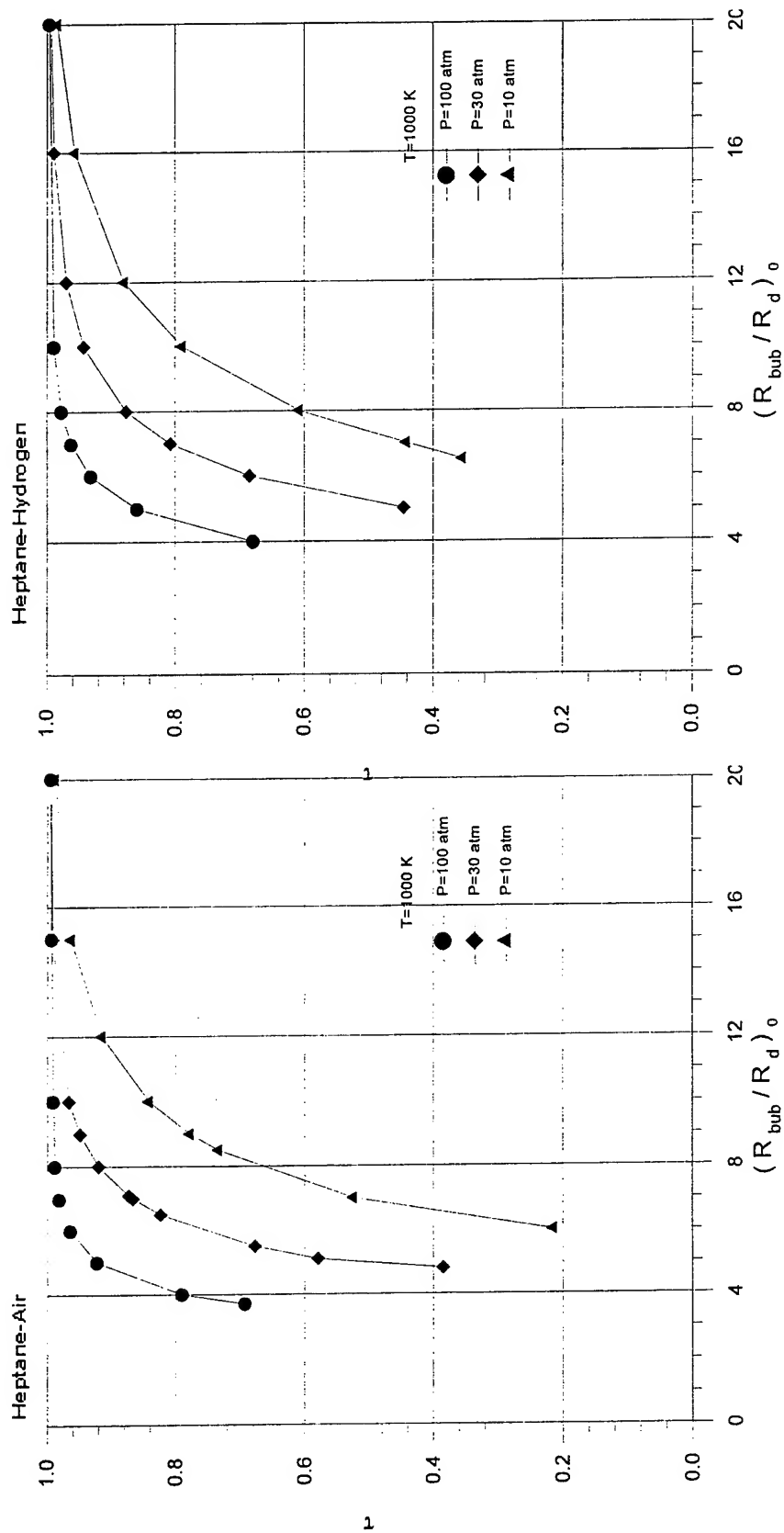
Unsteady vs. Steady Models at Subcritical Pressures

Example: Heptane Droplet Vaporizing in 625 K Air at 5.72 atm
Initial droplet temperature = 443 K



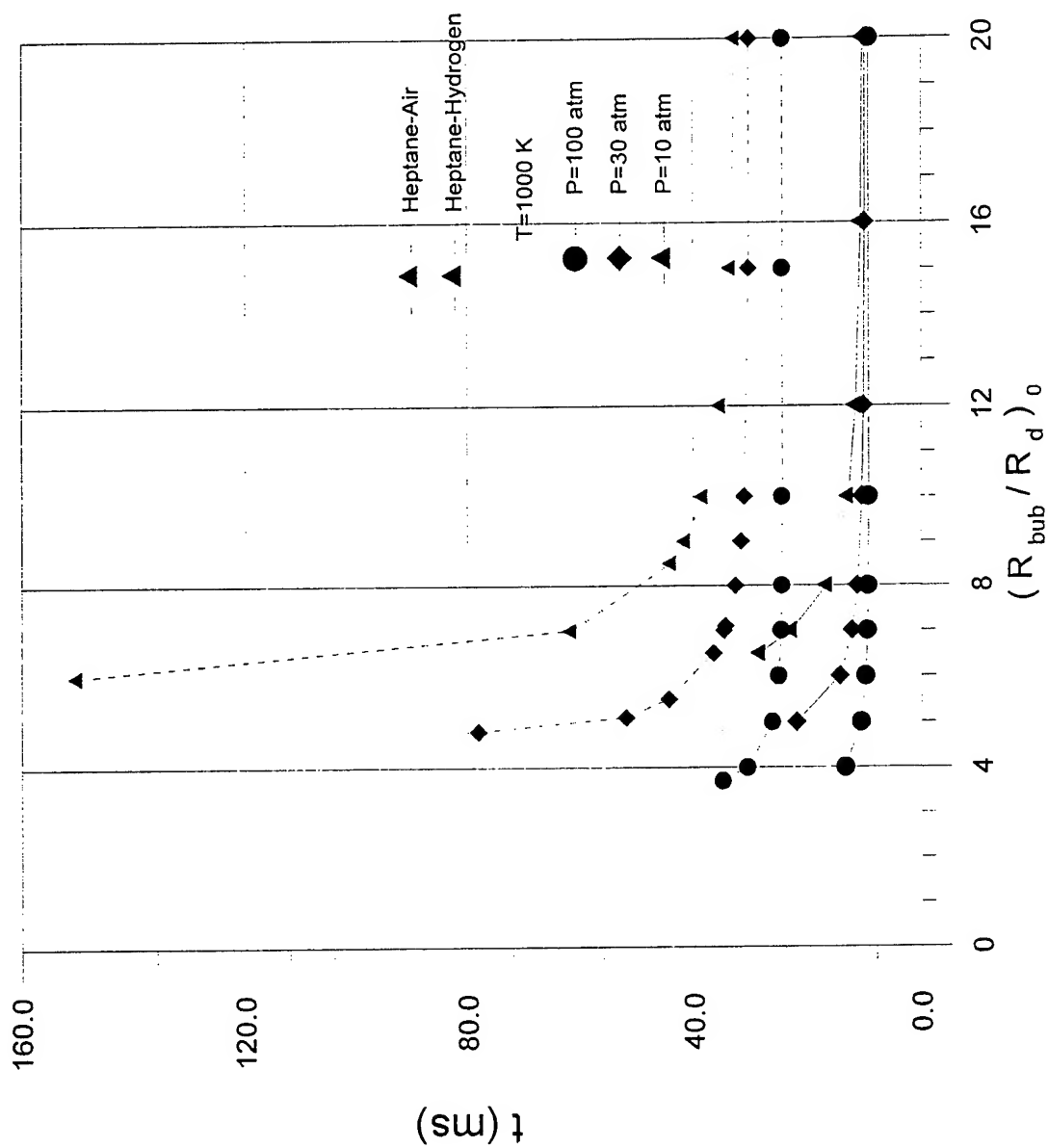


Effect of Droplet Interaction on Heptane Vaporization in 1000 K Air and Hydrogen Environments





Effect of Droplet Interaction on Heptane Vaporization in 1000 K Air and Hydrogen Environments





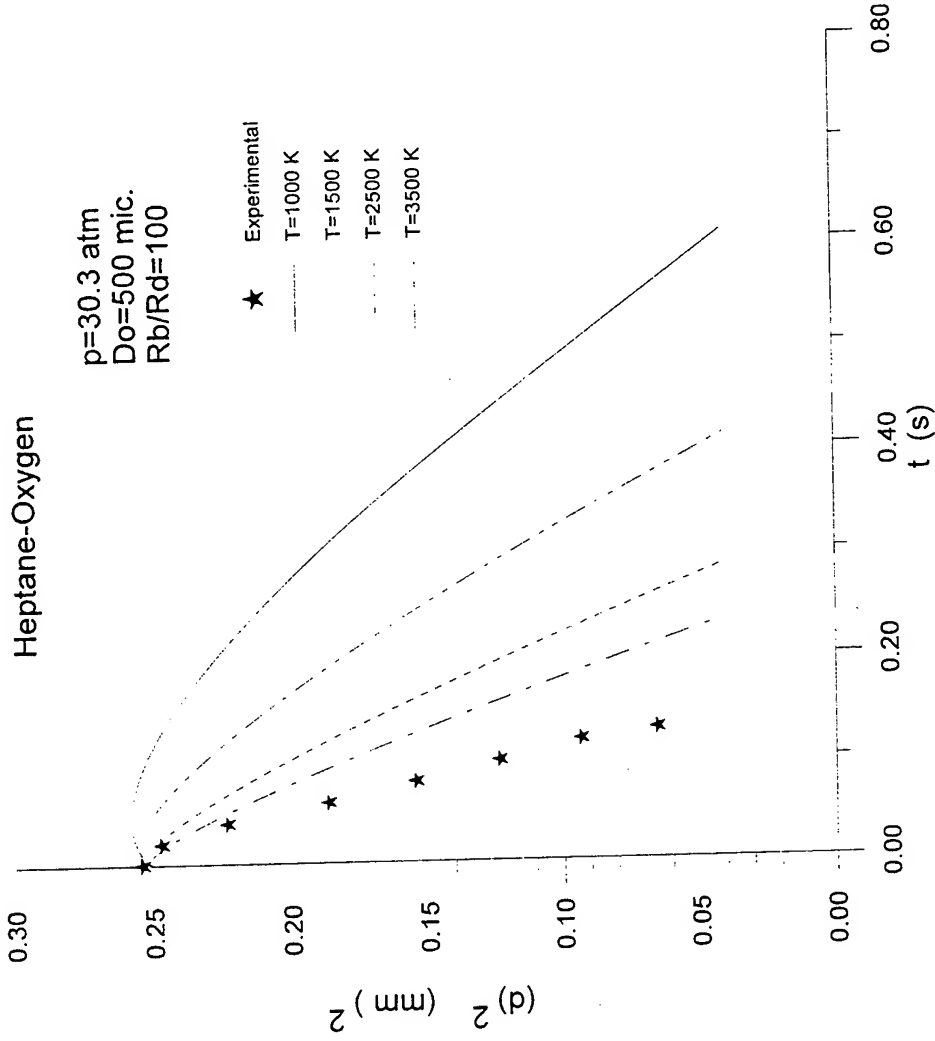
Experimental Data vs Numerical Results

Heptane / Oxygen

Initial Droplet
Diameter: 500 micron

Calculated Regression
Rate: $0.6 \text{ mm}^2/\text{sec}$

Measured Regression
Rate: $1.58 \text{ mm}^2/\text{sec}$
(Clemons et al)



•Experiments conducted with RP-1 in a Convective Combustion Environment



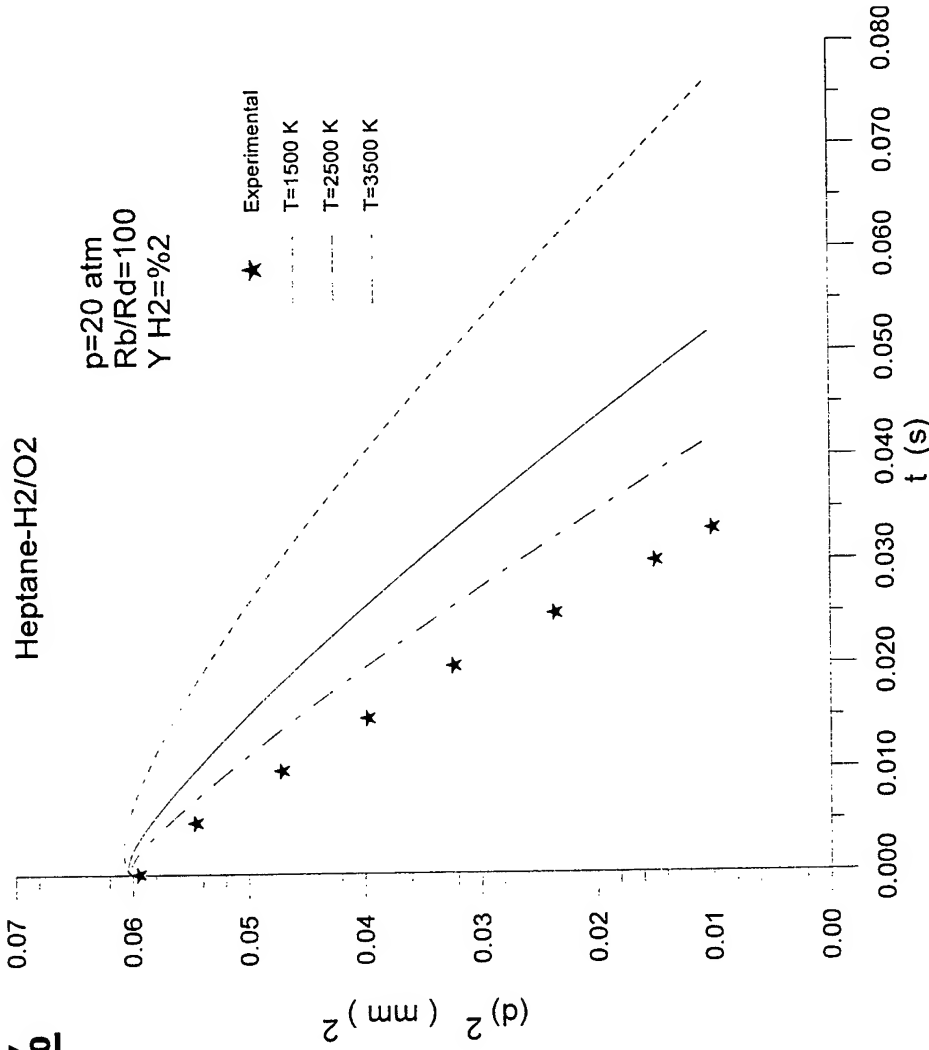
Experimental Data vs Numerical Results

Heptane / Oxygen / $Y_{H_2}=2\%$

Initial Droplet
Diameter: 245 micron

Calculated Regression
Rate: $0.8 \text{ mm}^2/\text{sec}$

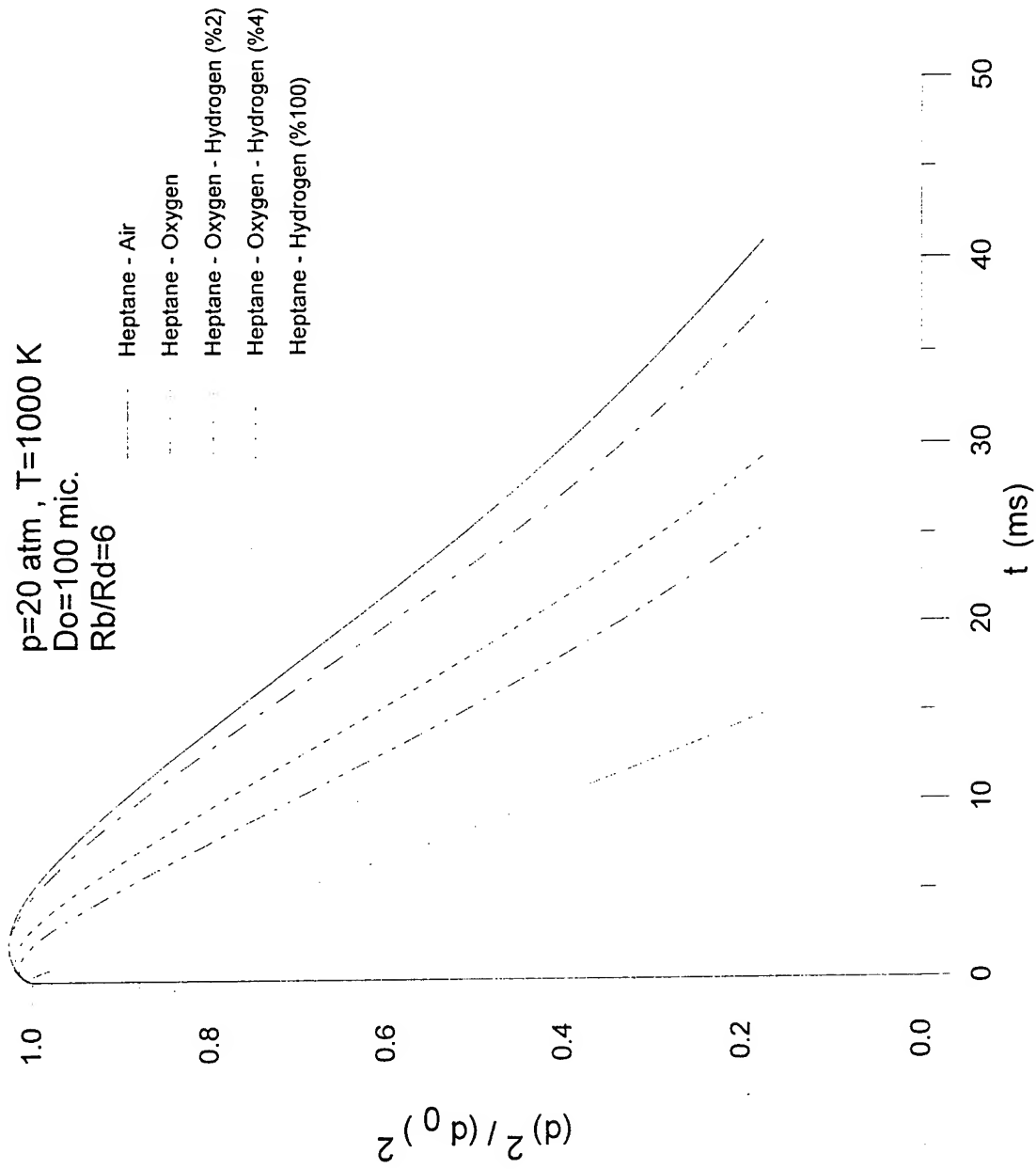
Measured Regression
Rate: $1.66 \text{ mm}^2/\text{sec}$
(Clemons *et al*)



•Experiments conducted with RP-1 in a Convective Combustion Environment

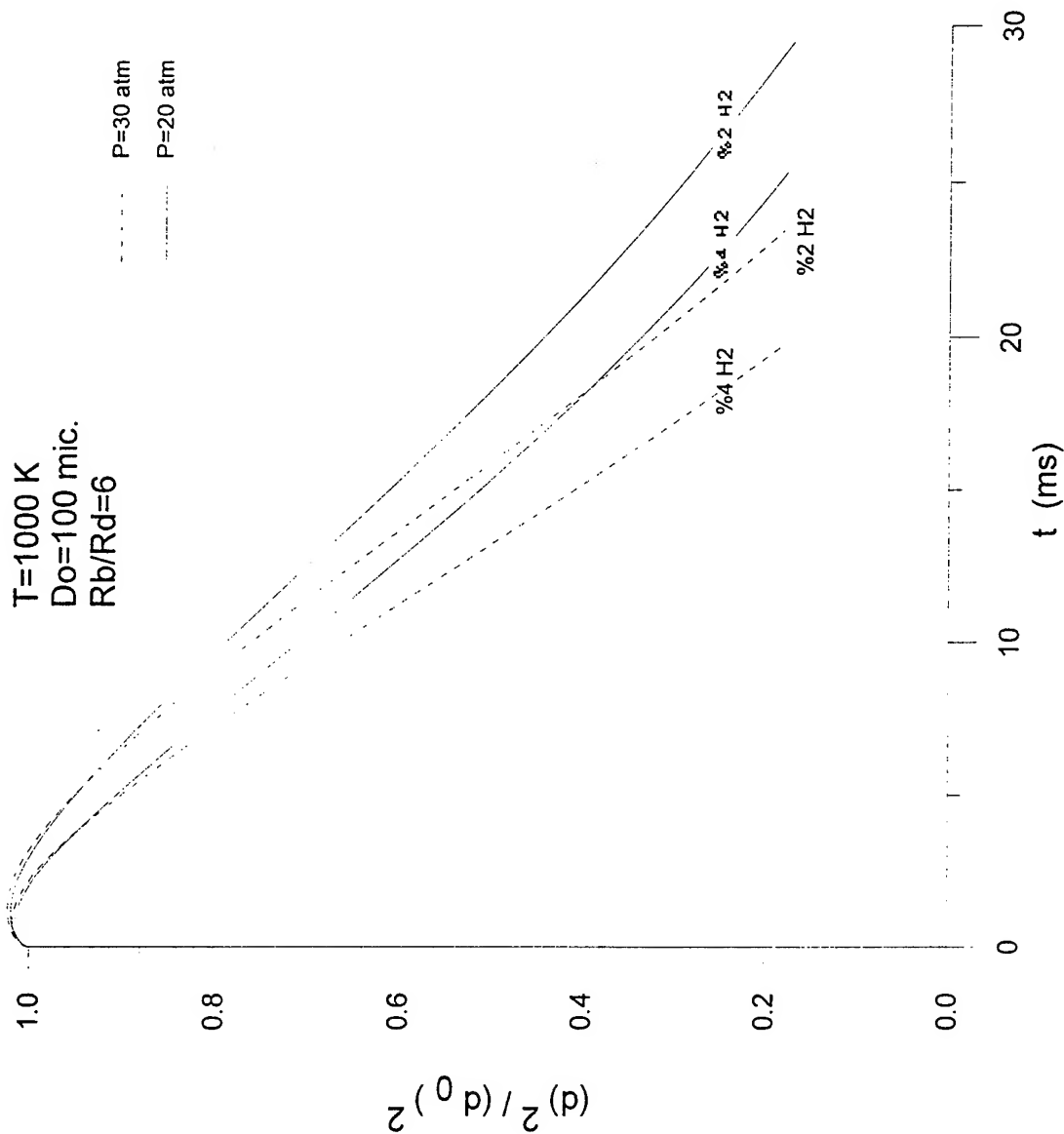


Droplet Lifetimes for Various Interacting Heptane Droplets in Various Gaseous Environments





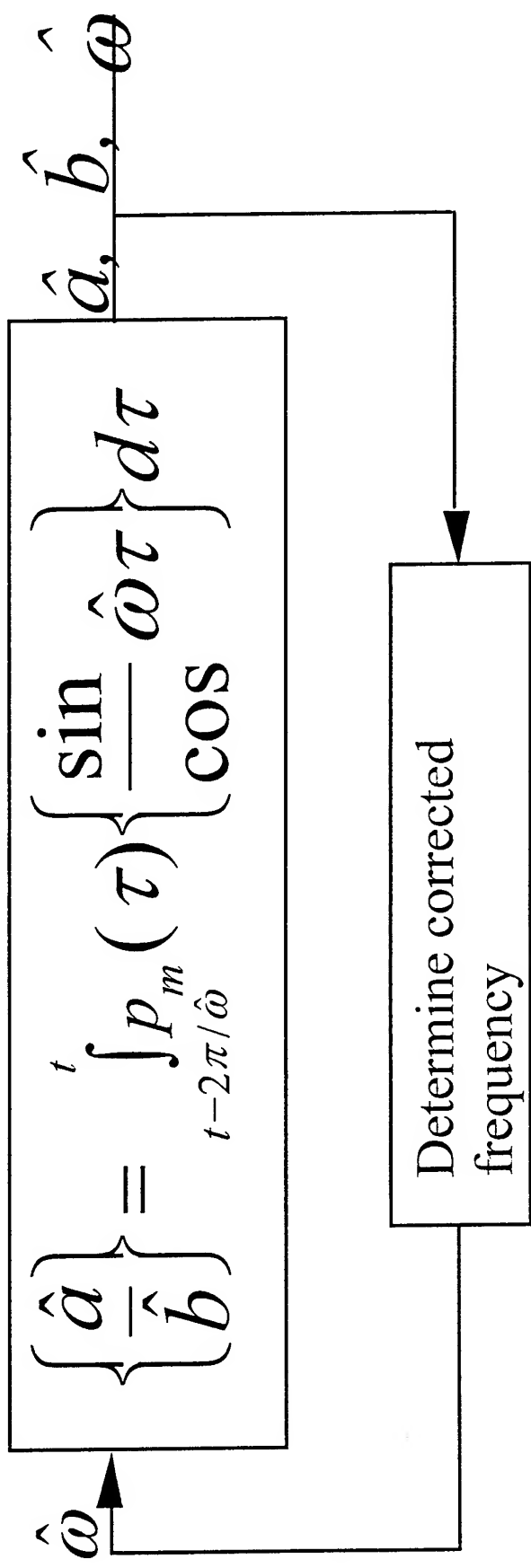
Droplet Lifetimes for Various Interacting Heptane Droplets in Various Gaseous Environments

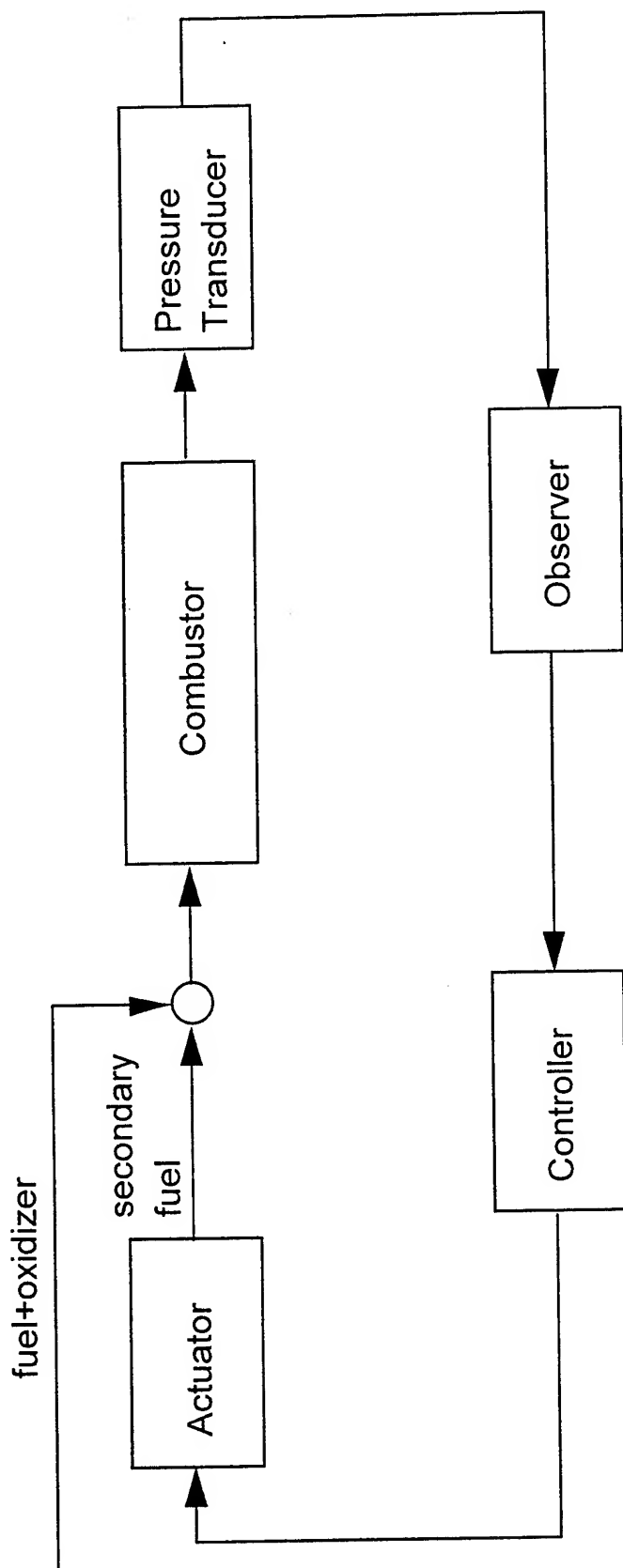


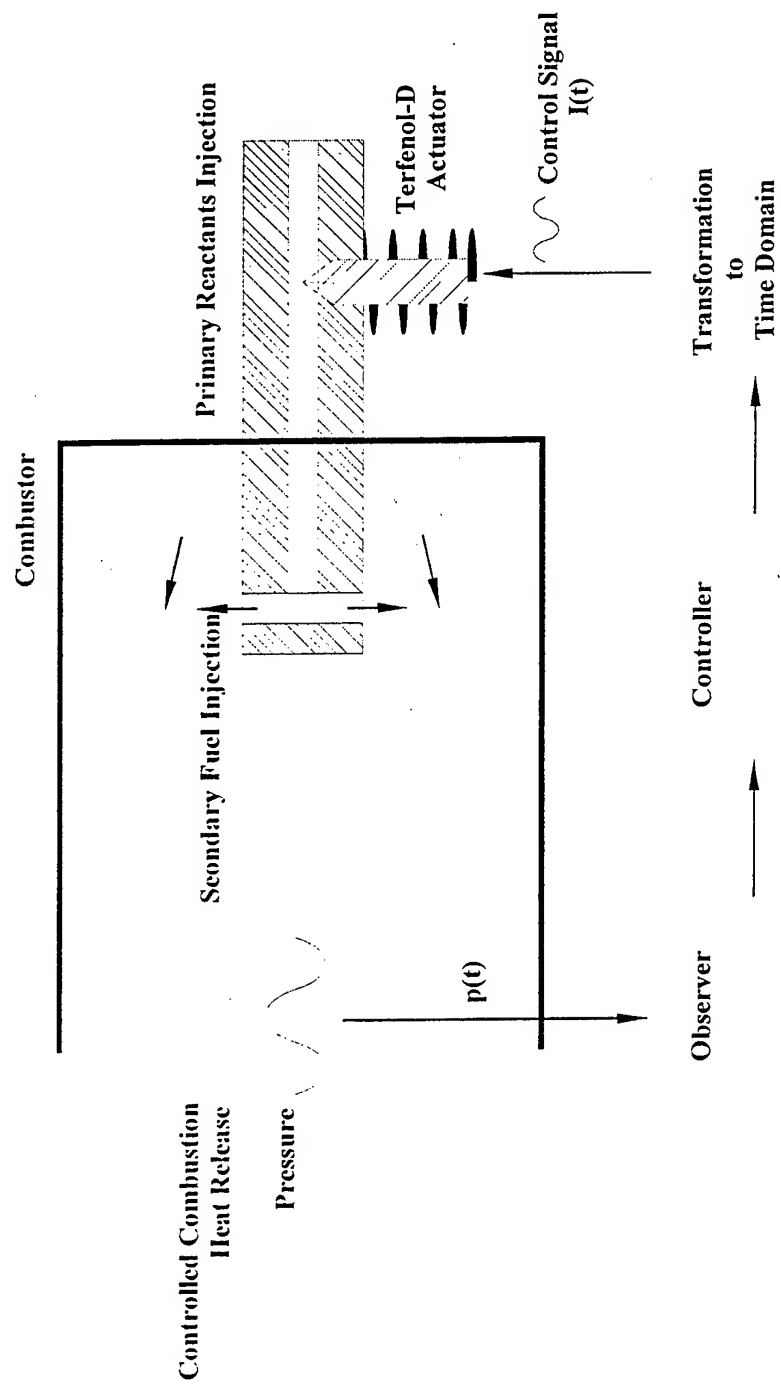
Observation of Unstable Modes

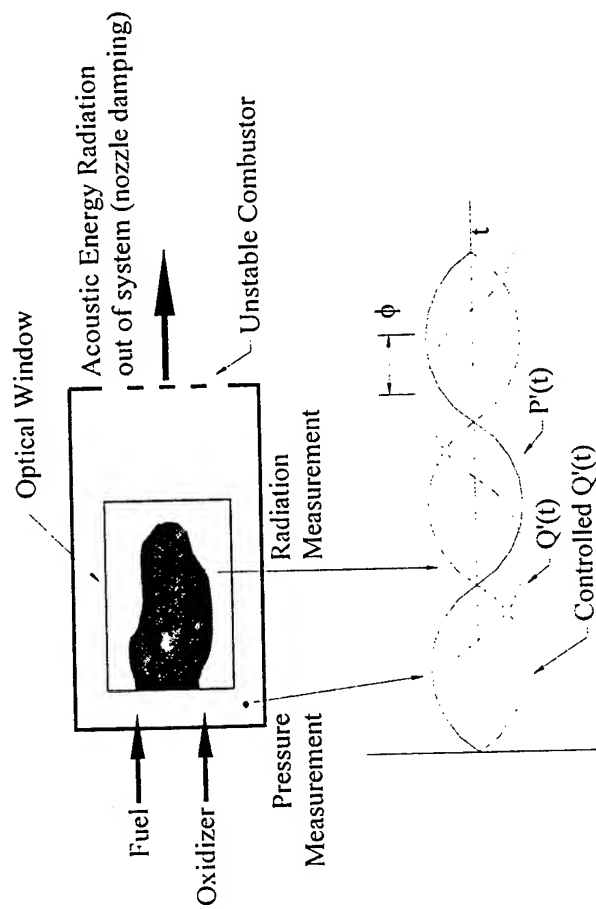
Measured Pressure p_m is expressed as:

$$p_m(t) = \sum_{n=1}^N [a_n \sin(\omega_n t) + b_n \cos(\omega_n t)]$$









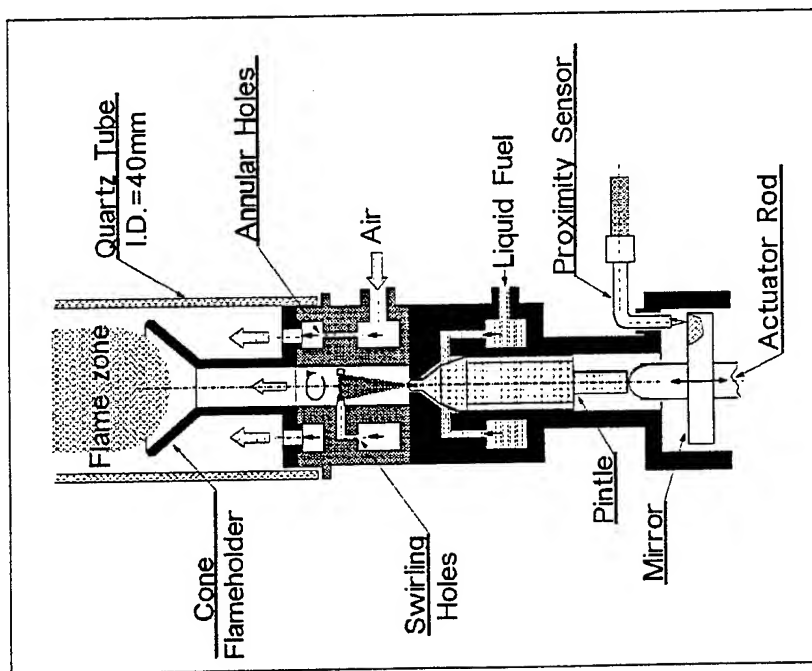
Oscillating Liquid Spray Combustion for Control of Combustion Instabilities

• Objective:

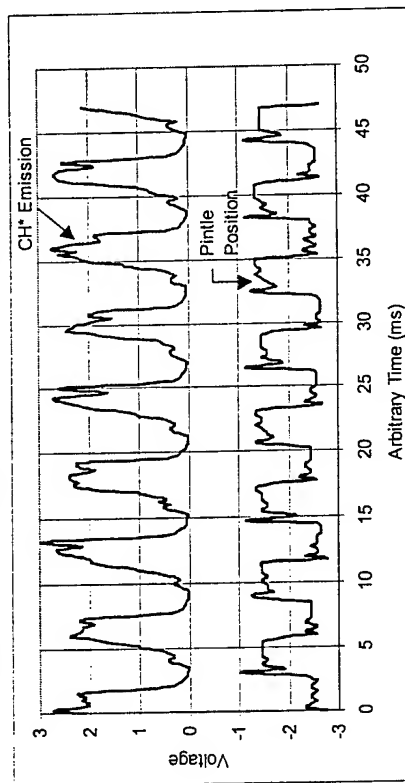
Maximize the effectiveness of actuators that use liquid fuels to damp combustion instabilities

• Goals of Controlled Combustion Process:

- Flame length much shorter than the acoustic wavelength.
- Burn most of the fuel in a modulated form.
- Release energy in a narrow phase domain.



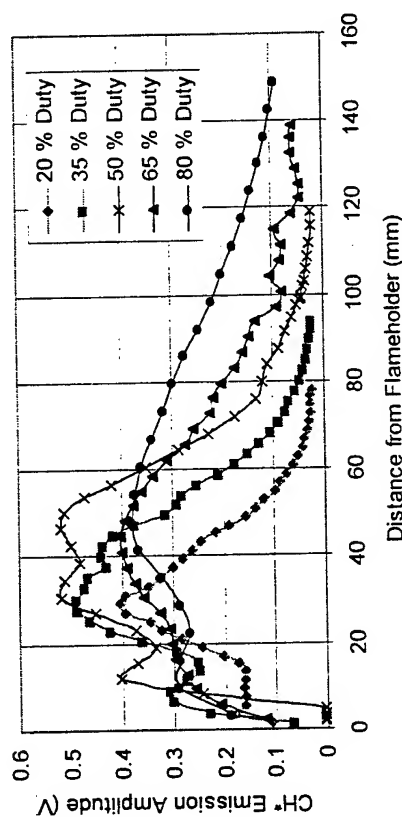
A Schematic of the Investigated Combustor Setup



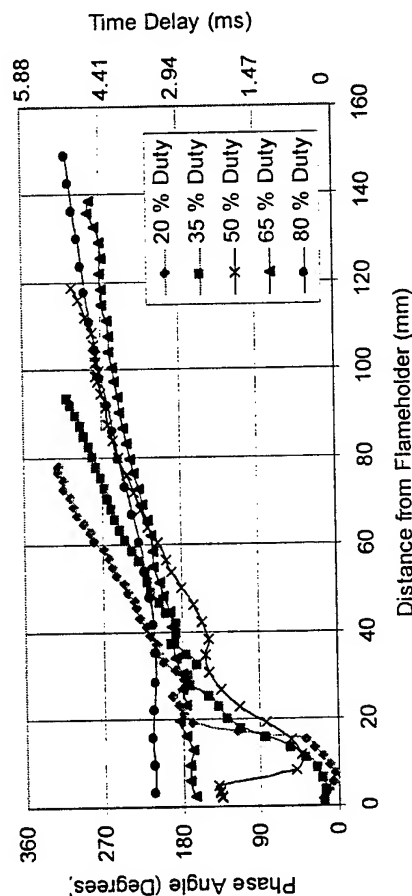
Measured CH* Emission and Pintle Displacement at 170 Hz demonstrated excellent flame response.



Oscillating Liquid Spray Combustion (continued)



Axial dependence of CH* Emissions Amplitude at 170 Hz



Axial dependence of CH* Emissions Phase at 170 Hz

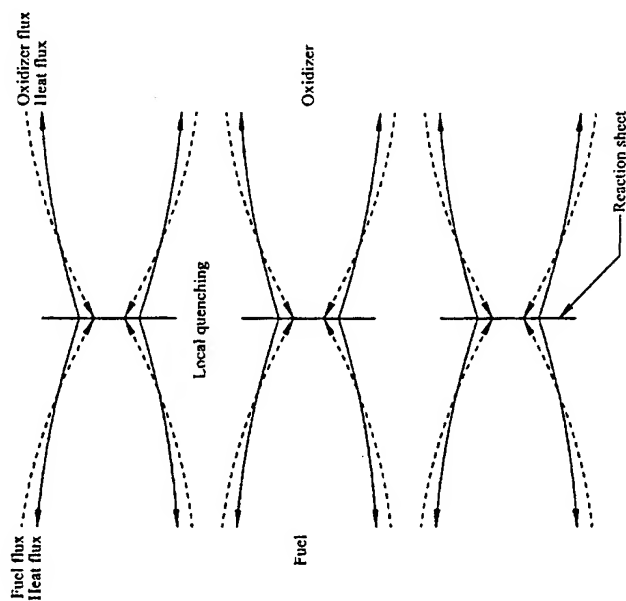
Preliminary Results:

- High Effectiveness of the developed liquid fuel actuator demonstrated in the frequency range 150-800 Hz.
- The Amplitude and Phase of oscillations depend on the droplet size and velocity and are modified by variation of the control signal.
- Closed loop control of an unstable combustor was successfully demonstrated with the developed liquid fuel actuator.

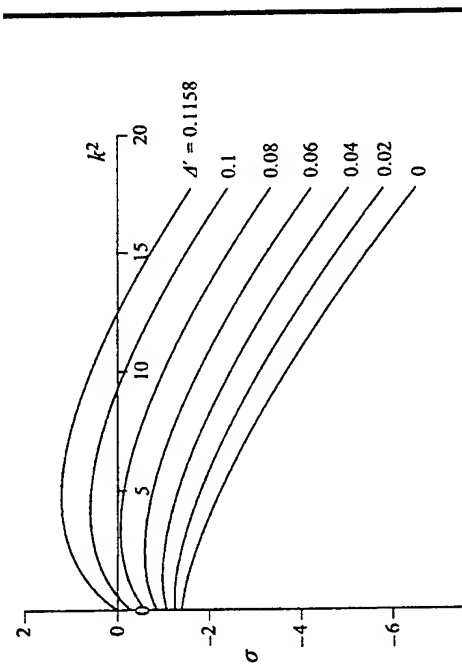


Intrinsic Instabilities Identified for Diffusion Flames

- Relevant to Nonlinear Phenomena in Liquid-Propellant Rocket Instability
- Activation-Energy Asymptotics Applied to Derive Dispersion Relations
- Lewis-Number Effects are Important; Related to Cellular Flames
- Rate-Ratio Asymptotic Analyses are Needed in Future Work



Physical Mechanism



Dispersion Relation



TEN YEARS OF RESEARCH ON H₂-O₂ INJECTION

Vianney DUTHOIT

Michel RENE-CORAIL

Martin SION

Stéphan ZURBACH

Roland BORGHI

Geoffrey SEARBY

Patrick VUILLERMOZ

Michel PONS

SNECMA SEP Division,
Vernon, France

IRPHE Laboratory
Marseilles, France

CNES
Evry, France



sneema



TEN YEARS OF RESEARCH ON H_2-O_2 INJECTION

- 1 Research Group**
Organization
Partners
- 2 Research Themes**
Atomization
Single droplet
Mixing
Turbulent multiphase combustion
- 3 Industrial interest**
Phenomena comprehension
Model elaboration
- 4 Perspectives & lessons**

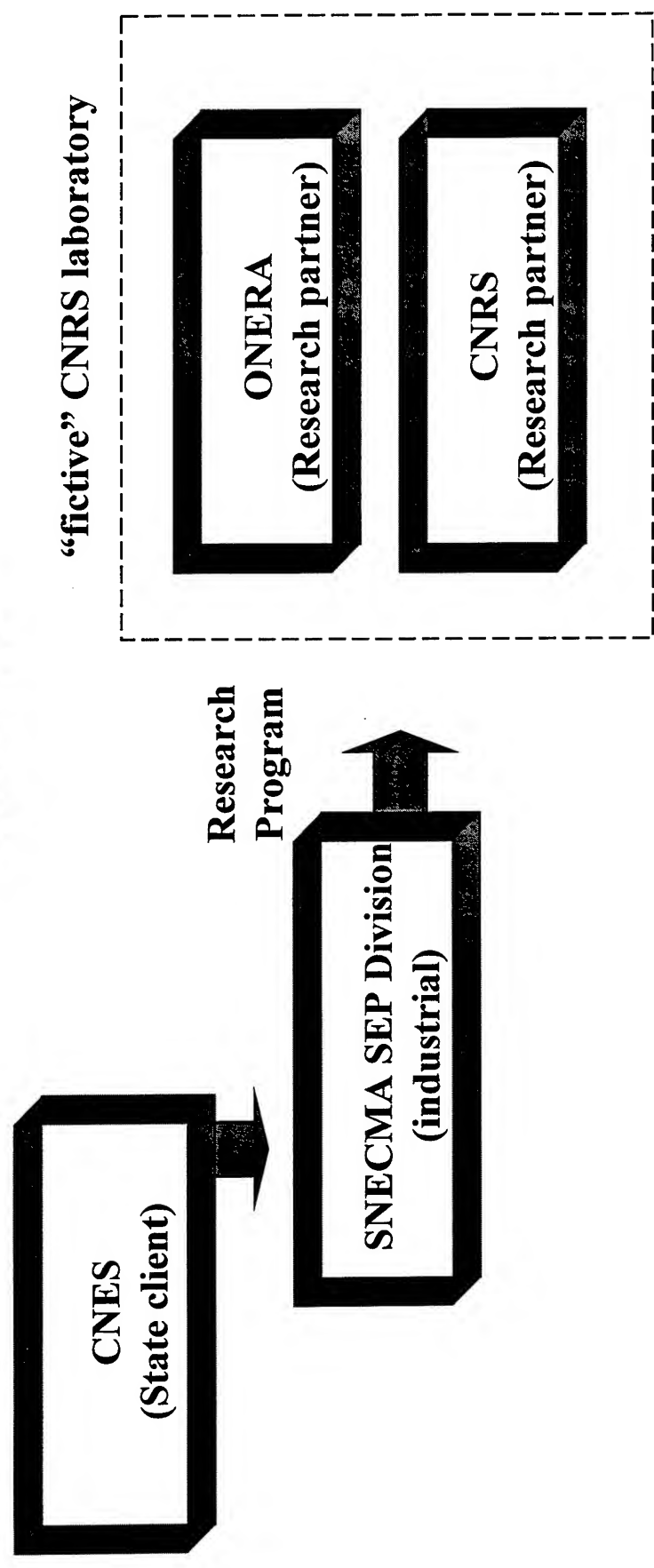




TEN YEARS OF RESEARCH ON H₂-O₂ INJECTION

1 “Research Group”

- Organization -



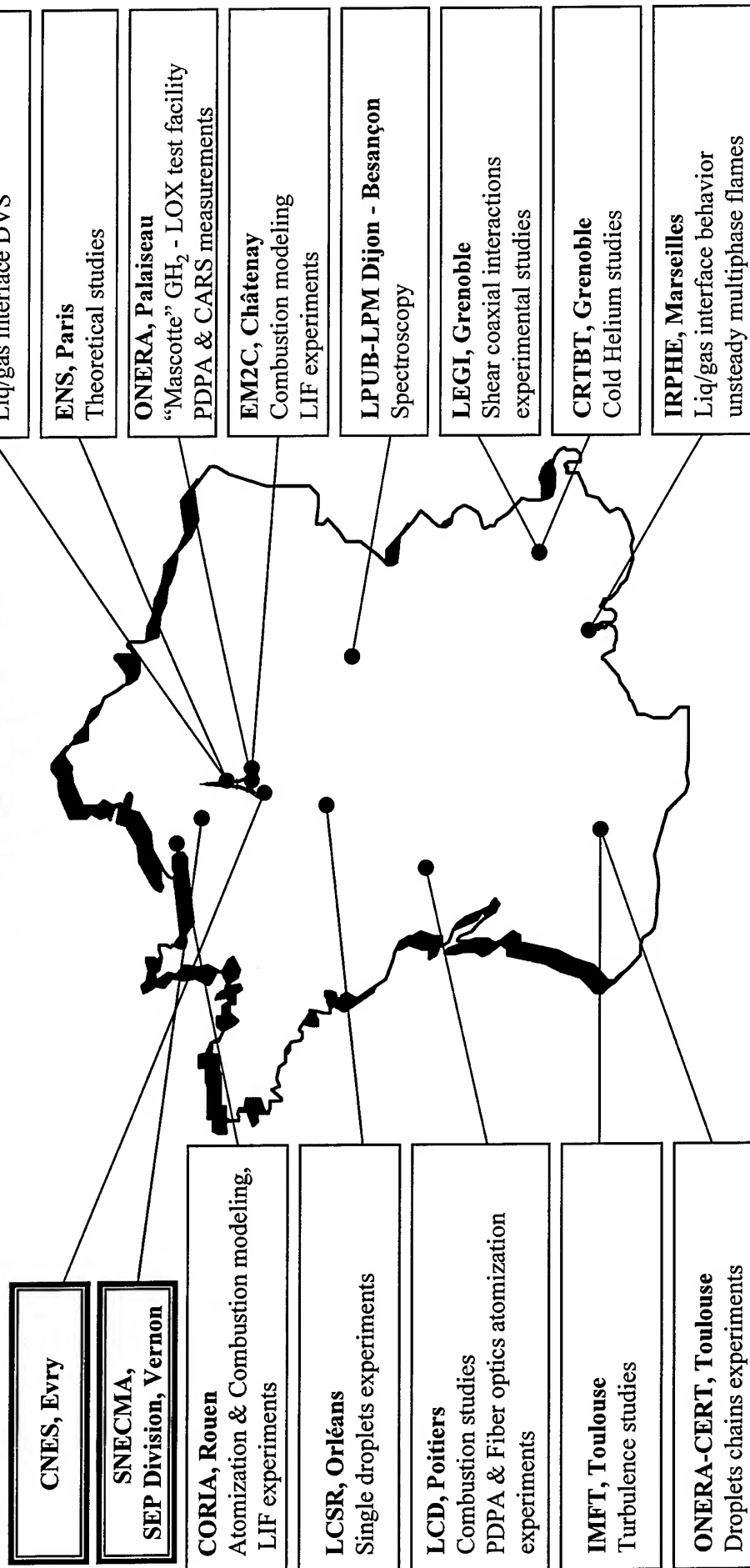
SCIENTIFIC COMMITTEE involving all four partners
deciding upon studies (Scientific / industrial relevance,
continuation, evaluation).



TEN YEARS OF RESEARCH ON H_2-O_2 INJECTION

1 "Research Group"

- Partners -



FLTC 384/99



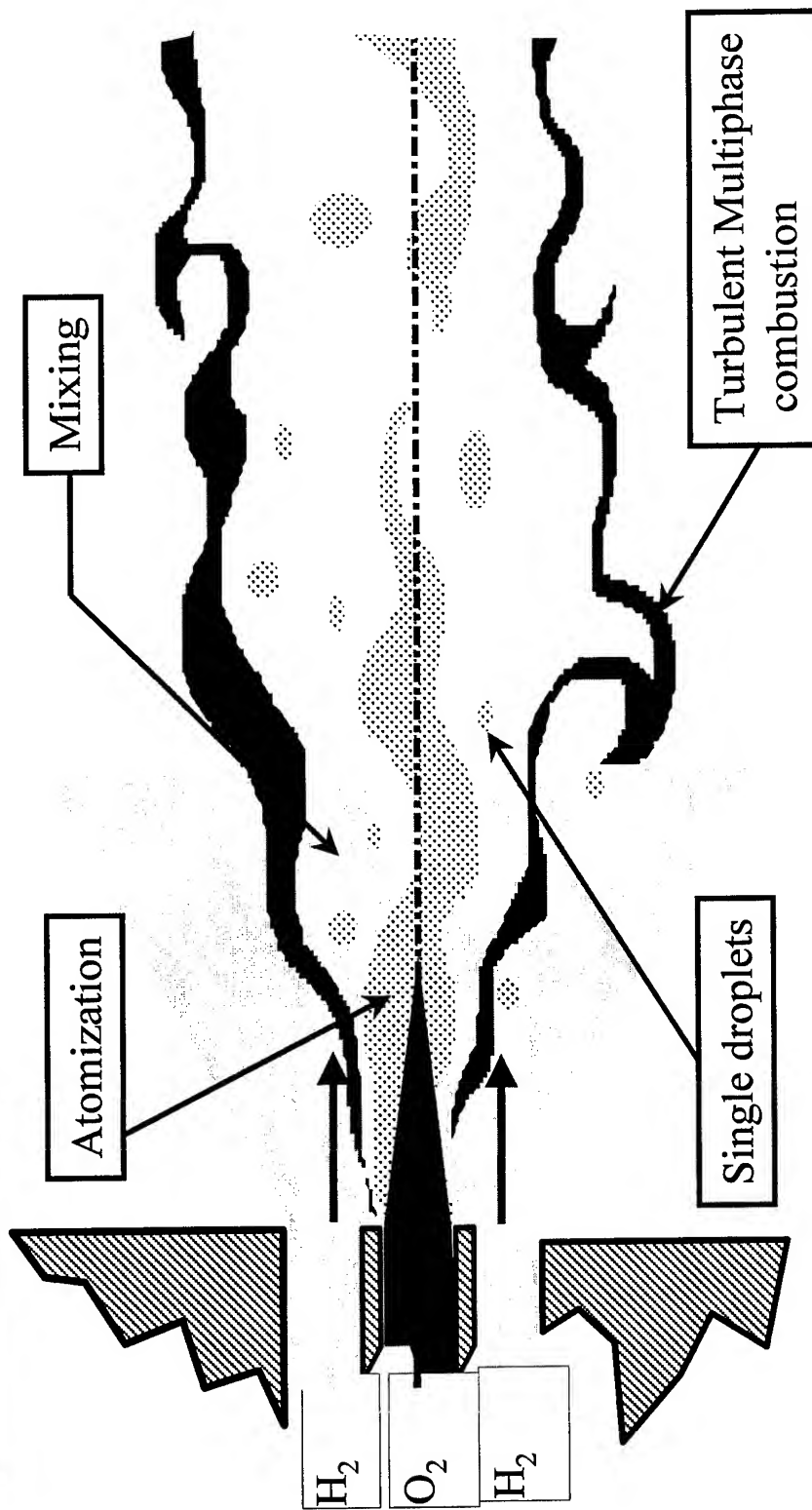
SNECMA

Division SEP



TEN YEARS OF RESEARCH ON H_2 - O_2 INJECTION

2 “Research Themes”



sne cma

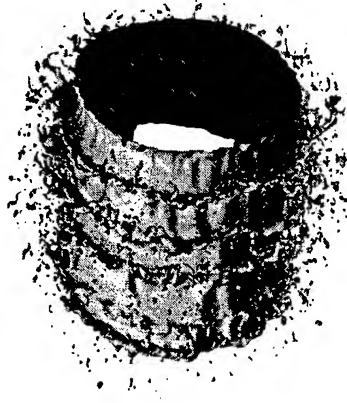
Division SEP



TEN YEARS OF RESEARCH ON H₂-O₂ INJECTION

2 “Research Themes”

- Atomization -



Parameters of interest :

➤ Liquid core length

Water-air experiments

Fiber optics & ombroscopy
measurements

Laser sheet tomography & fluorescence

➤ Resulting granulometry

PDPA measurements on H₂/O₂ 10 bars

Dependency on momentum ratio

$$J = \frac{\delta_G U_G^2}{\delta_L U_L}$$

Dependency on Weber number

$$We = \frac{\delta_G U_G^2 D_L}{\tau}$$





TEN YEARS OF RESEARCH ON H_2-O_2 INJECTION

2 “Research Themes”

- Single droplets -

Parameters of interest :

- Thermodynamical behavior of liquid gas interface at high p/pc ratio
- Droplet break-up type and length

No ‘trivial’ behavior (persistence or collapse) of liquid-gas interface

Result in We-Oh plane available for CFD models





TEN YEARS OF RESEARCH ON H_2-O_2 INJECTION

2 “Research Themes”

- Mixing -

Parameters of interest :

Mass fraction of propellants

Water-water experiments

High density gradients DNS

➤ Size of structures

Statistical maxwellian experiment analysis

High density gradient turbulence studies

Relevance of a turbulence based liquid-gas mixing approach : High density gradient turbulence model, liquid-gas surface density transport equations





TEN YEARS OF RESEARCH ON H_2-O_2 INJECTION

2 “Research Themes”

Turbulent multiphase combustion -

Parameters of interest :

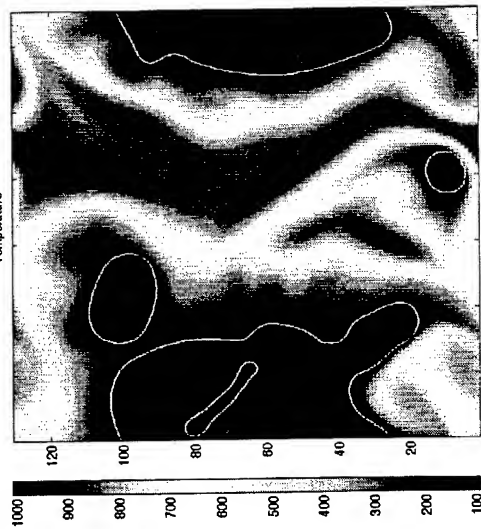
➤ Basic chemical kinetics and flame structure

➤ Interaction with liquid phase

Influence of droplet size and supercritical conditions

Adaptation of PdF shapes to liquid presence

Adaptation of flame velocity evaluation



‘simple’ chemistry for H_2/O_2
‘Thin’ flame

Both families (flamelet & PdF) of models adapted





TEN YEARS OF RESEARCH ON H_2 - O_2 INJECTION

3 Industrial interest

- Phenomena comprehension -

- Confirmation of the key role of momentum ratio and LOX post diameter on liquid core (and flame) length (and efficiency).
- Flame anchoring very near LOX post lips
- Data on droplet sizes (\Rightarrow inlet multiphase boundary conditions)
- Data on global flow structure (\Rightarrow code calibration, thermal fluxes evaluation)
- Direct use for injector transfer function evaluation (“low frequency” instabilities)





TEN YEARS OF RESEARCH ON H_2-O_2 INJECTION

3 Industrial interest

- Model elaboration and validation -

Atomization :

➤ “High- $\nabla\rho$ ” turbulence k- ϵ model

+ liquid-gas interface density transport equations

Closure laws Criteria and delays for fragmentation and vaporization

Single LOX droplet studies (LCSR)

DNS high- $\nabla\rho$ (CORIA), liquid-gas interface (LMM)

Validation coaxial experimental setups :

Water-air + laser, fiber optics and ombroscopy (CORIA, LCD, LEGI)

Liquid-gaseous Helium + thermography (CRTBT)

Mascotte LOX-Hydrogen + laser tomography and PDPA (ONERA)
fiber optics (LCD)





TEN YEARS OF RESEARCH ON H_2 - O_2 INJECTION

3 Industrial interest

Turbulent multiphase combustion :

- “PdF” based approach (CORIA)
- “Flamelet” based approach (EM2C)

Closure laws Two phase flame velocity Single droplet (LCSR)

Droplet chain (ONERA-CERT)	
Counter-flow flame	}
DNS	
	EM2C

Validation base Metranol-air flame + statistical study (CORIA)

Mascotte LOX- H_2 flame + LIF OH (EM2C)

(1, 10, 60 bar)

LIF O_2 (CORIA)

CARS (ONERA)



TEN YEARS OF RESEARCH ON H₂-O₂ INJECTION

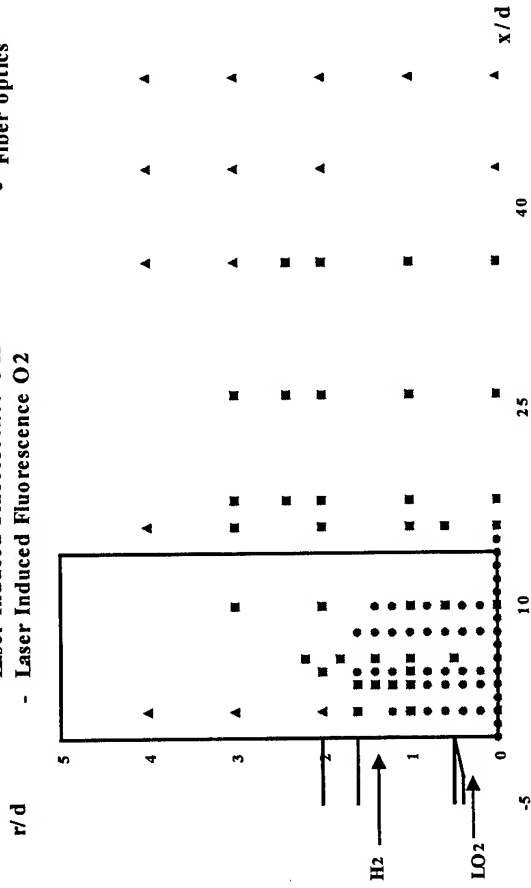
3 Industrial

Mascotte test facility :

- LOX, 90 K, 40 => 400 g/s
- GH₂, 100 => 300 K, 5 => 70 g/s
- Test duration from 10 s (60 bar) to 20 s (1 bar)

Visualizations :
 - OH Emission ,
 - Laser Induced Fluorescence OH
 - Laser Induced Fluorescence O₂

Measurements :
 ■ PDPA
 ▲ CARS
 • Fiber optics





TEN YEARS OF RESEARCH ON H₂-O₂ INJECTION

3 Industrial interest

Simulation tool :

➤ Allow to accumulate research results usable for technology and hardware developments

⇨ Types of calculations :

Feasibility studies to “explore” new code possibilities

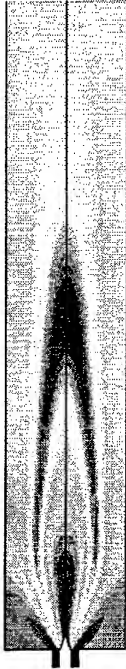
Design studies allowing parametric investigation

Simulation studies at the end of a design loop

Cost	Manpower	CPU	Complexity
High	High	Medium	High
Low	Low	Low	Low
High	High	High	Medium



Temperature field prediction of the Mascotte configuration at 1 bar



Temperature field prediction of the Mascotte configuration at 10 bar



TEN YEARS OF RESEARCH ON H₂-O₂ INJECTION

4 Perspectives & Lessons

- Model implementation to finalize
- Future research directions
 - Technological features
 - swirl
 - recess
 - wide operating range
 - Combustion instabilities
 - low frequency
 - high frequency
- Complementary between basic research / exp. validation / simulation tool
- Complementary between state / industrial / research partners :
long term commitment and financial involvement of everyone.



Comparative Study of Swirl-coaxial and Non-swirl-coaxial Injectors

Hiroshi TAMURA

National Aerospace Laboratory, KRC

1-Koganesawa, Kakuda, Miyagi 981-1522, Japan

email: tamura@kakuda-splab.go.jp

ABSTRACT

In connection with cost reduction and improvement of combustion efficiency of LOX/Hydrogen or LOX/Methane engines, employment of swirl-coaxial injectors seem to be wise, because with swirl-coaxial injectors, even employing large injection elements, which are easy to manufacture and thus can decrease production cost, high combustion efficiency may be expected. To establish the design methodology of swirl-coaxial injectors, a comparative study of swirl-coaxial injectors and shear-coaxial injectors has been conducted.^{1,2)} Steady state combustion characteristics were examined with multi-element injectors with a nominal thrust of 10 kN and a 14 kN, and a chamber pressure of 3.5 MPa. Combustion characteristics were evaluated in relation to chamber pressure distributions, wall temperature distributions, and η_c^* s.

The main findings on the steady state characteristics were as follows:

1) Shear-coaxial injectors require a longer chamber to complete vaporization as compared with those of swirl injectors; therefore, the η_c^* of shear-coaxial injectors is apt to be limited by vaporization efficiency. 2) Combustion with swirl injectors starts near the injector face and ends within a short chamber length. The η_c^* of swirl injectors is, therefore, apt to be limited by mixing efficiency. 3) Injection velocity of fuel affects secondary atomization of LOX spray. That is, the higher the fuel injection velocity, the finer the size of LOX droplets. Fine atomization promotes combustion near the injector face.

Because of the remarkable differences of steady state combustion characteristics, combustion stability characteristics are also expected to be significantly different from each other. Stability characteristics were examined by introducing a bomb disturbance during steady state combustion.³⁾ LOX/hydrogen and LOX/methane were used to see the effect of fuel density on the stability characteristics. Although

all tests were judged to be stable, the differences of stability characteristics of shear-coaxial and swirl-coaxial injectors were evaluated based on amplitudes and frequencies of the induced pressure disturbances.

The main findings on the stability characteristics were as follows.

1) The magnitudes of the induced maximum pressure disturbances, P'_{max}/P_c , decrease with an increase of injection velocity ratio, V_f/V_o , for both injector types. 2) The magnitudes of P'_{max}/P_c with swirl-coaxial injectors were shown to be smaller than those with coaxial injectors at the same V_f/V_o . 3) The correlations between P'_{max}/P_c and V_f/V_o were grouped in a single curve regardless of the difference of propellant combinations for coaxial injectors and for swirl-coaxial injectors, respectively. 4) A plausible reason for the observed trends is the interaction between the shock wave induced by a bomb and LOX droplets.

A cooperative study between NAL and DLR is now on going to see the combustive flame during unstable combustion. The rectangular chamber whose acoustic frequency is the same order with a typical large rocket engine will be designed. The chamber has 12 injection-elements with glass windows which allows optical observation. Bomb disturbance is planned to be introduced.

REFERENCE

- [1] Sasaki, M. et al., "Comparative Study of Recessed and Non-recessed Swirl Coaxial Injectors," AIAA 97-2907, 1997.
- [2] Tamura, H. et al., "LOX/LH2 Subscale Swirl Coaxial Injector Testing," AIAA 97-2906, 1997.
- [3] Sasaki, M. et al., "Experimental Study on Stability Characteristics of Non-swirl and Swirl Coaxial Injectors," AIAA 98-3438, 1998.

International Workshop on Research Status and Perspectives in Liquid
Rocket Combustion Chamber Flow Dynamics

Paris-France
Dates: May 27-28, 1999

Comparative Study of Swirl-coaxial and Non-swirl-coaxial Injectors

Hiroshi TAMURA
National Aerospace Laboratory, KRC
1-Koganesawa, Kakuda, Miyagi 981-1522, Japan
email: tamura@kakuda-splab.go.jp

PARIS-France May 27-28, 1999

Purpose of the Study and Method of Approach

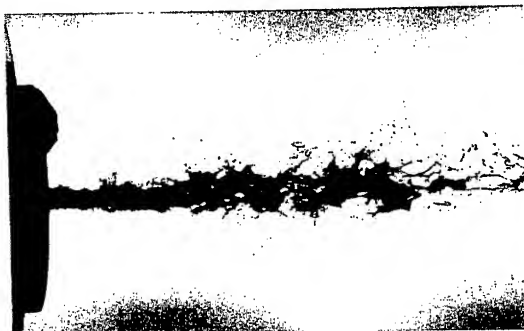
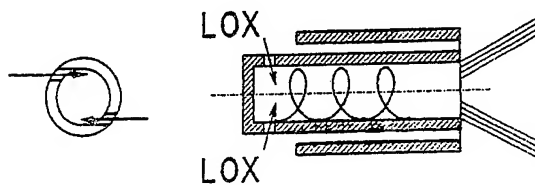
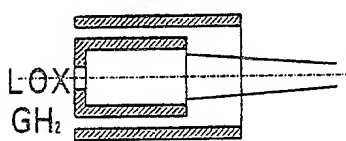
Establishment of design methodology for swirl-coaxial injectors with large injection elements.

Steady state characteristics were evaluated in relation to chamber pressure distributions, wall temperature distributions, and η_c 's with multi-element injectors with nominal thrusts of 14 kN and 10 kN and a chamber pressure of 3.5 MPa.

Stability characteristics were studied by introducing a bomb disturbance during steady state combustion. LOX/hydrogen and LOX/methane were used to see the effect of fuel density. Stability characteristics were evaluated based on amplitudes and frequencies of induced pressure disturbances.

Comparison of Steady State Combustion Characteristics

PARIS-France May 27-28, 1999



a: Shear-coaxial injectors

b: Swirl-coaxial injectors

Fig. 1 Comparison of non-swirl and swirl injectors



a: Non-recessed swirl-coaxial

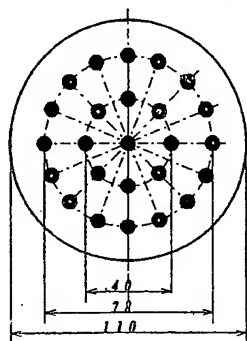


b: Recessed swirl-coaxial

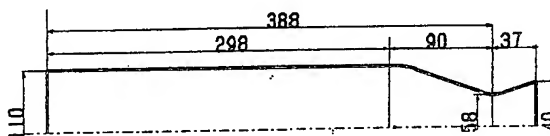
Fig. 2 Comparison of recessed and non-recessed swirl-coaxial injectors

Swirl-coaxial injectors with a recessed LOX post showed a self-pulsation of the spray. To avoid instability related to this self-pulsation, recessed injectors with swirl-coaxial was not used.

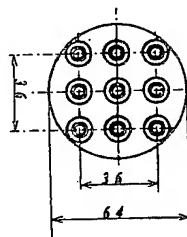
PARIS-France May 27-28, 1999



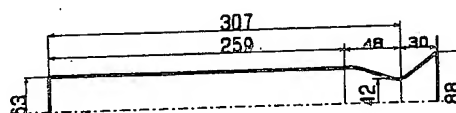
a: 14 kN injector



b: 14 kN chamber

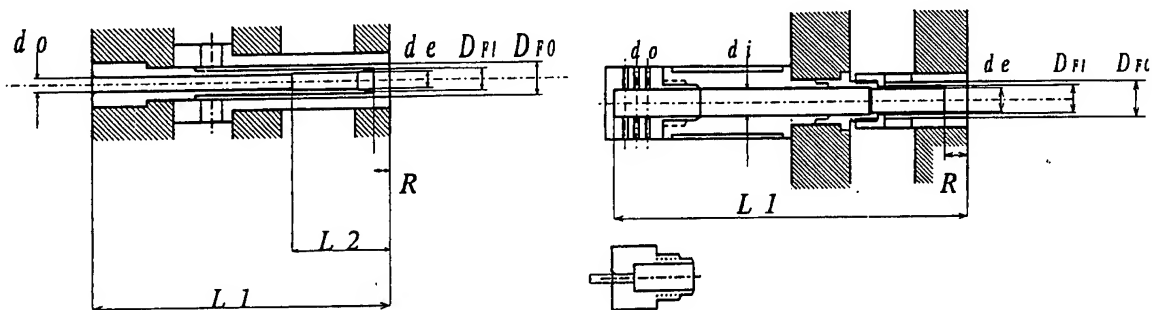


c: 10 kN injector



d: 10 kN chamber

Fig. 3 Configuration of injector and chamber

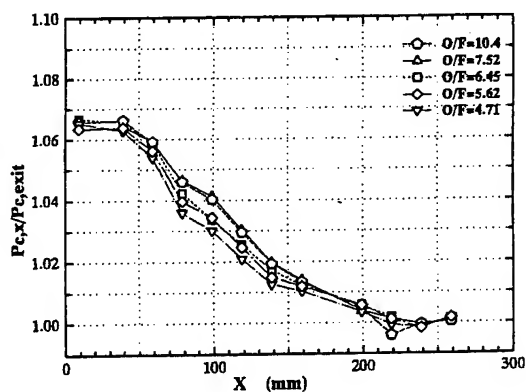


a: Details of 14 kN injector b: Details of 10 kN injector

Fig. 4 Injector configuration

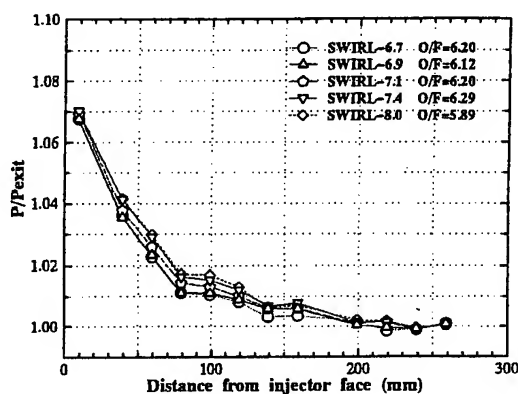
14 kN INJECTOR					10 kN INJECTOR						
Name	B	C	D	LD	Name	H1	C1	H2	C2	C3	C4
Type	coax	→	→	→	Type	coax	→	swirl	→	→	→
do	2.4	→	→	→	do	2.14	→	1.26x6	→	→	→
de	4.0	→	→	→	de	5.3	→	→	→	→	→
R	.0	→	→	→	R	5.3	→	0	→	→	→
DFI	4.4	→	→	→	DFI	6.3	→	→	→	→	→
DFO	5.5	6.4	7.0	7.0	DFO	10.0	9.0	10.0	7.4	8.0	9.0
L1	51	→	→	67.5	L2	77	→	73	→	→	→
L2	15	→	→	51							

PARIS-France May 27-28, 1999



a: Shear-coaxial injectors

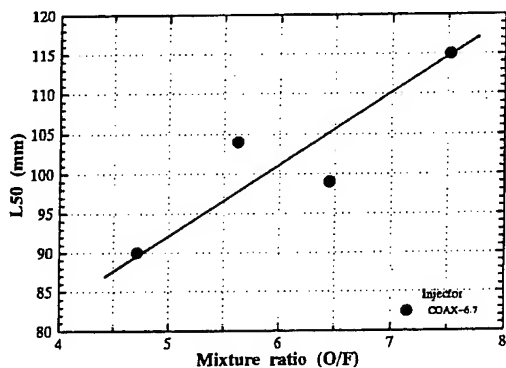
(10 kN injectors)



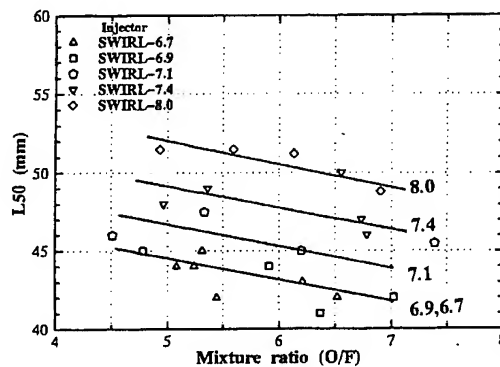
b: Swirl-coaxial injectors

Fig. 5 Comparison of axial pressure distribution

A pressure drop in a cylindrical section of the combustor is caused by the momentum pressure loss, thus pressure distribution indicates the progress of combustion.



a: Shear-coaxial injectors



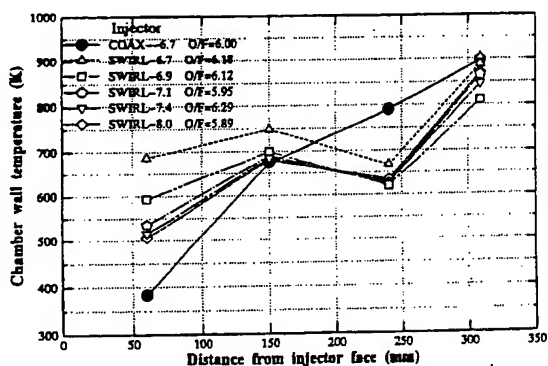
b: Swirl-coaxial injectors

(10 kN injectors)

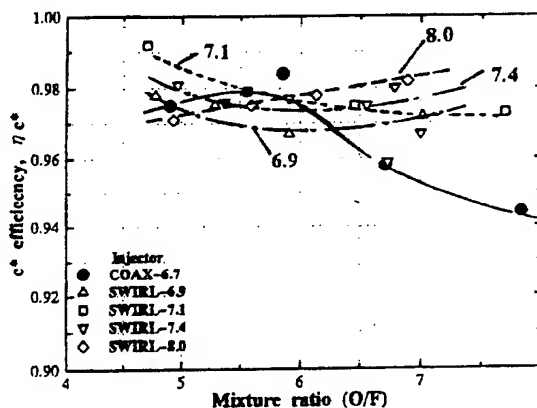
Fig. 6 Comparison of L50s as a function of mixture ratio

The length required for chamber pressure drop to the mean value of the chamber pressure, L50, is a measure for the required chamber length for complete combustion.

PARIS-France May 27-28, 1999



a: Axial wall temperature distribution



b: c* efficiency η c*

(10 kN chamber)

Fig. 7 Comparison of wall temperature distribution and ηc^*

Comparison of swirl-coaxial and shear-coaxial injectors	
Shear-coaxial injectors	Swirl-coaxial injectors
Coarse LOX spray	Fine LOX spray
Vaporization limited	Mixing limited
Large V_f/V_o improves η_c^*	Small V_f/V_o improves η_c^*
Combustion starts far injector face	Combustion starts near injector face
Low heat load near injector face	High heat load near injector face
Require longer chamber	Shorter chamber is possible

PARIS-France May 27-28, 1999

Comparison of Stability Characteristics

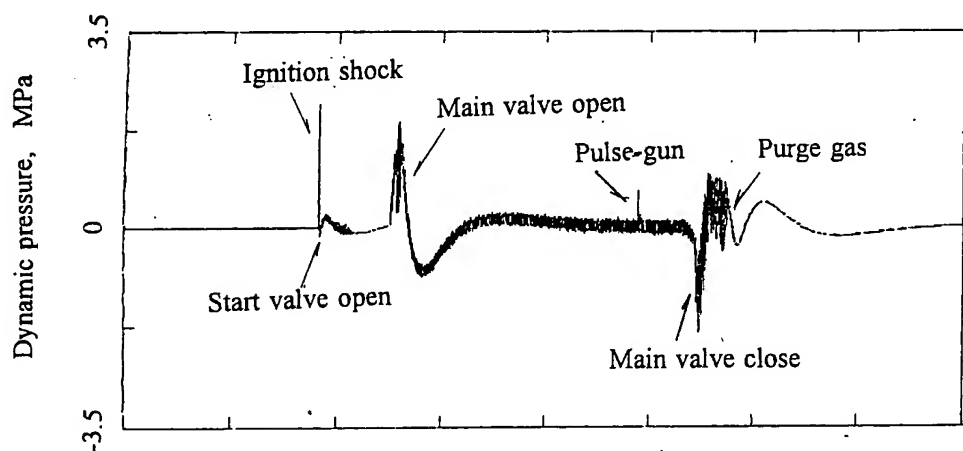
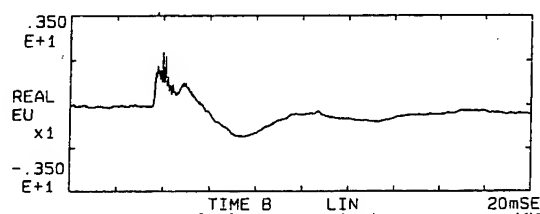


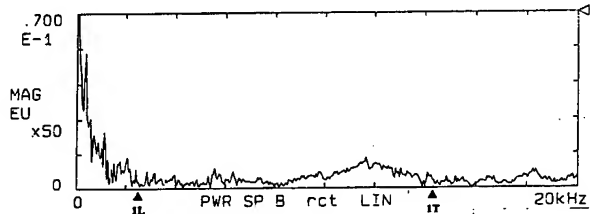
Fig. 8 Typical dynamic pressure trace

PARIS-France May 27-28, 1999

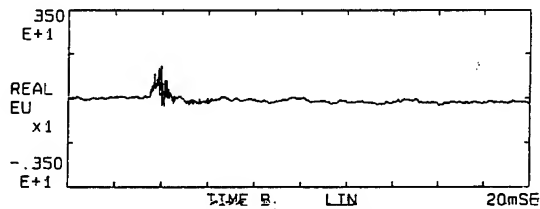


Dynamic pressure trace

a: Coaxial injector: H1, $P_c=3.44$ MPa, $O/F=6.16$, $V_f/V_o=29.1$, RDX= 2 grain

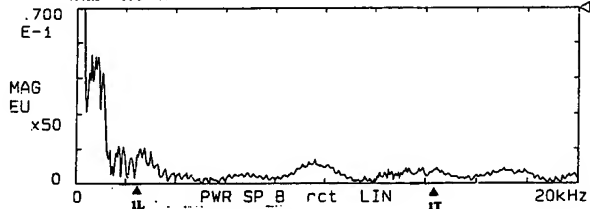


Pulse spectrum



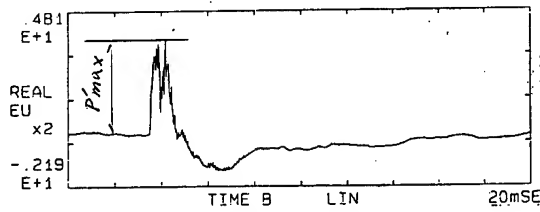
Dynamic pressure trace

b: Swirl injector: H2, $P_c=3.47$ MPa, $O/F=6.03$, $V_f/V_o=4.11$, RDX= 2 grain



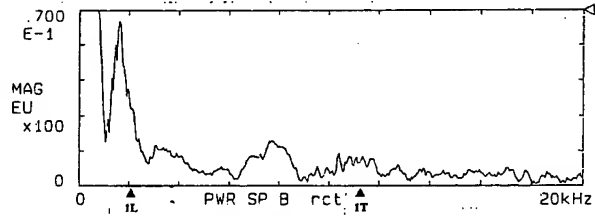
Pulse spectrum

**Fig. 9 Dynamic pressure trace and its pulse spectrum
(LOX/H₂, 10 kN injectors)**

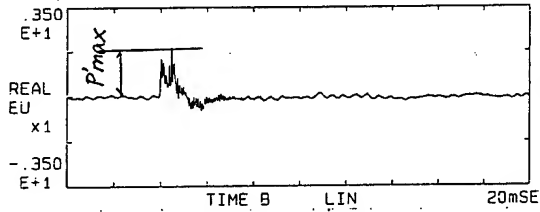


Dynamic pressure trace

a: Coaxial injector: C1, $P_c=3.59$ MPa, $O/F=3.69$, $V_f/V_o=12.7$, $RDX=2$ grain

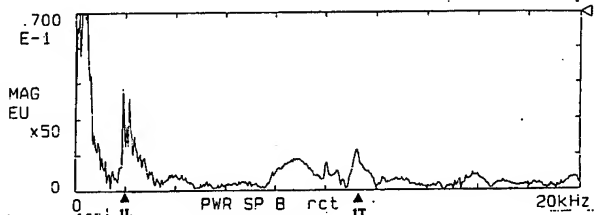


Pulse spectrum



Dynamic pressure trace

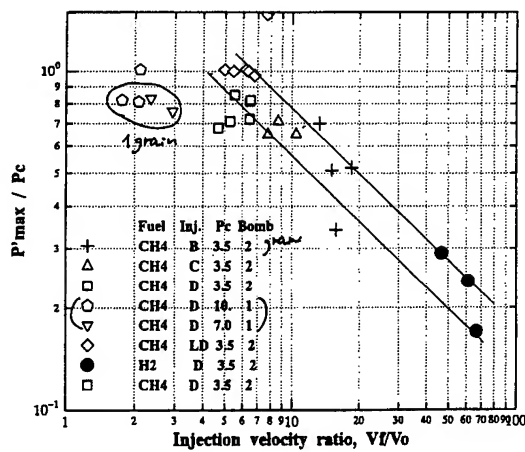
b: Swirl injector: C3, $P_c=3.66$ MPa, $O/F=3.57$, $V_f/V_o=1.25$, $RDX=2$ grain



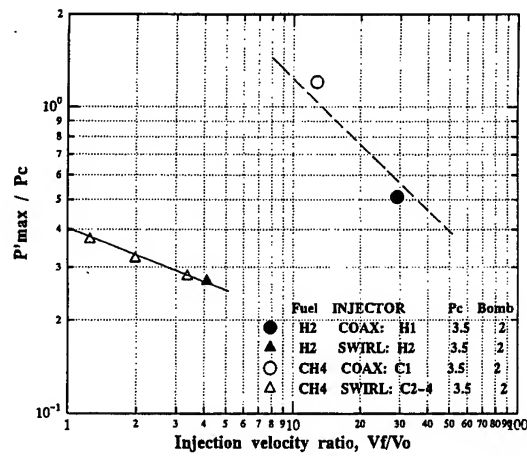
Pulse spectrum

Fig. 10 Dynamic pressure trace and its pulse spectrum (LOX/CH₄, 10 kN injectors)

PARIS-France May 27-28, 1999

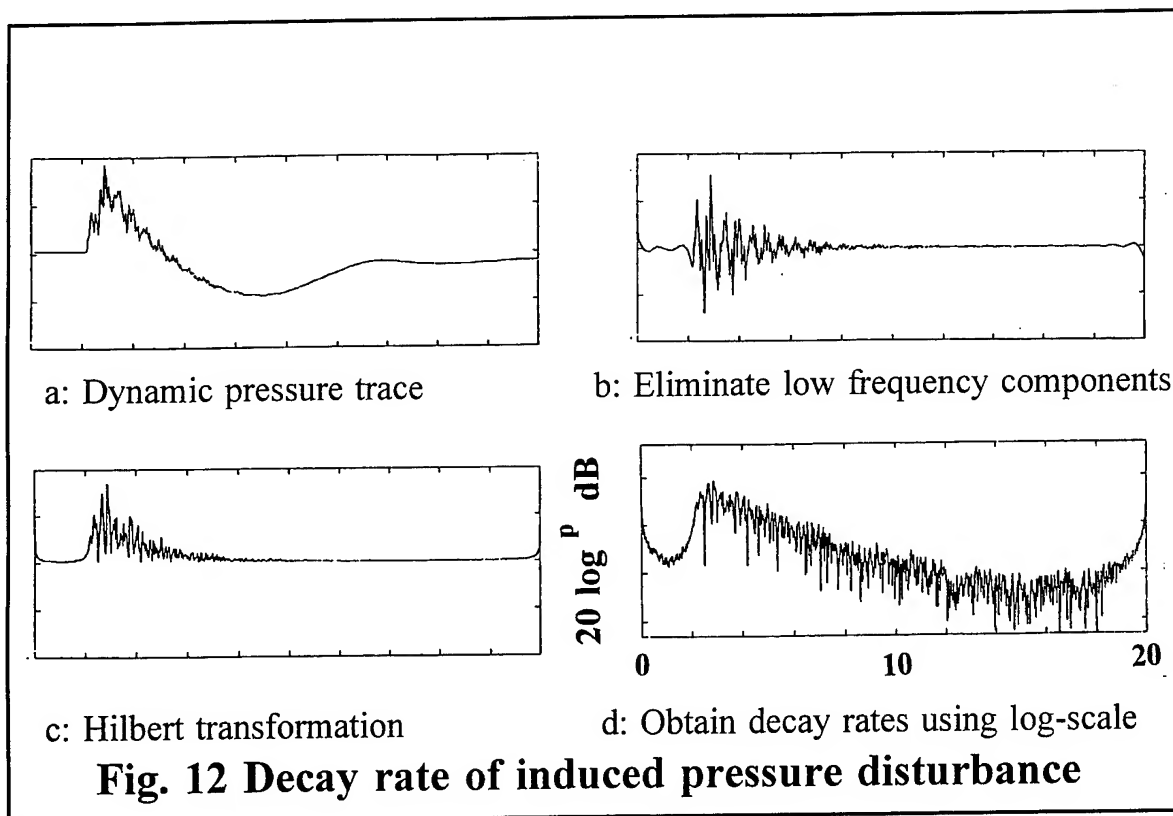


a: 14 kN chamber

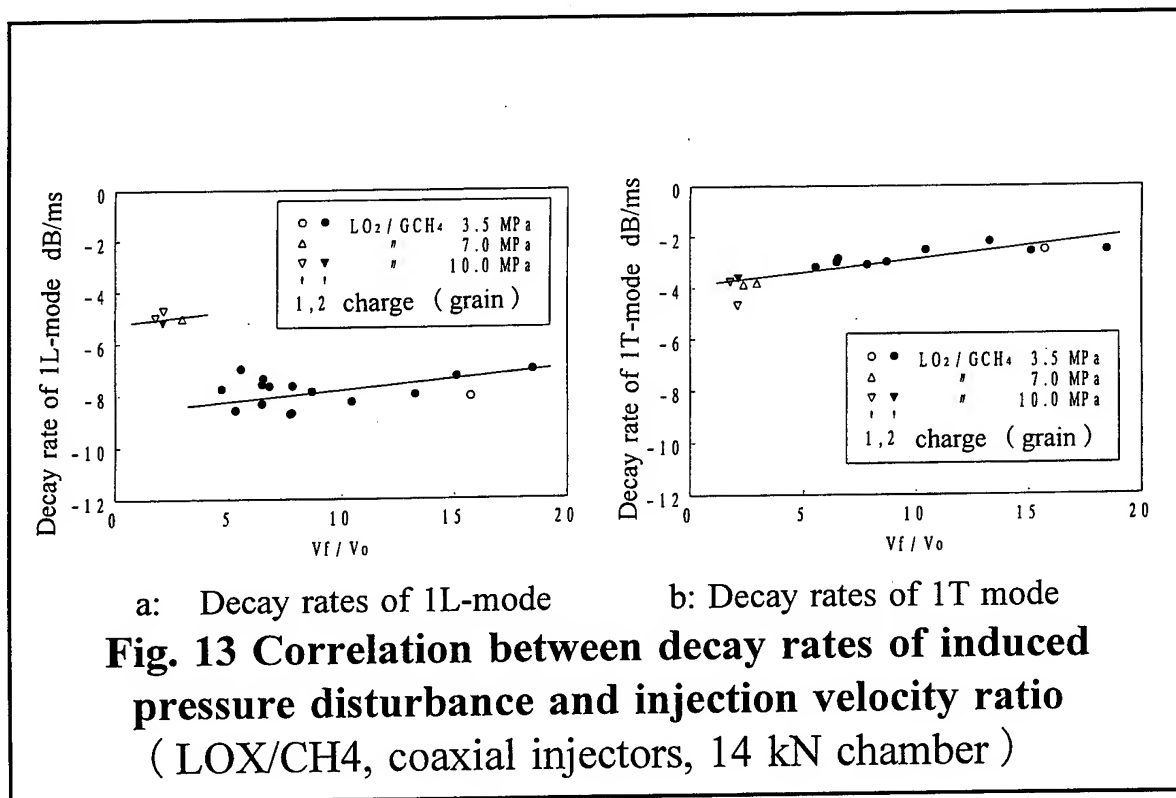


b: 10 kN chamber

Fig. 11 Induced maximum pressure, $P'max/P_c$, vs Injection velocity ratio, V_f/V_o



PARIS-France May 27-28, 1999



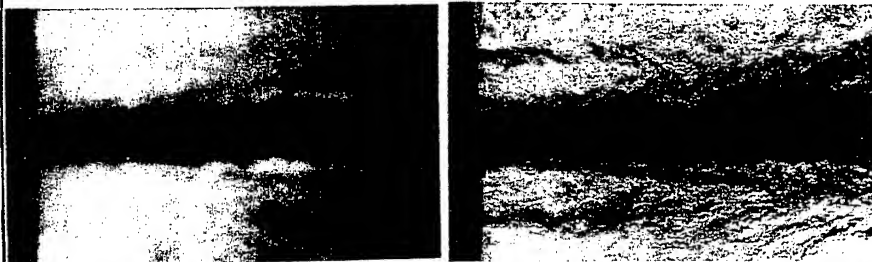
Summary of stability rating test results

- 1) Induced pressure disturbances, P'_{\max}/P_c , decreases with an increase of injection velocity ratio, V_f/V_o .
- 2) The P'_{\max}/P_c with swirl-coaxial injectors are smaller than those with coaxial injectors at the same V_f/V_o .
- 3) The correlation between P'_{\max}/P_c and V_f/V_o are able to be grouped in a single curve regardless of the difference of propellant combinations for coaxial and for swirl-coaxial injectors, respectively.
- 4) Observed correlations indicate existence of the interaction between the shock wave induced by a bomb and LOX droplets. That is, the larger the LOX droplets, the more the sensitivity to the shock disturbance.

PARIS-France May 27-28, 1999

Current program

A cooperative study between NAL and DLR is now on going. The purpose of the study is visualization of combustive flame during unstable combustion. The optically accessible rectangular chamber, its acoustic frequency is the same order to a typical large rocket engine, is designed. The chamber has 12-swirl and non-swirl coaxial injection elements. Bomb disturbance is plan to introduce.



W. Mayer and H. Tamura
"Flow Visualization of Super-critical Propellant Injection in a Firing LOX/GH₂ Rocket Engine," The Journal of Propulsion and Power, vol. 12 No. 5, 1996.

Our previous study on flow visualization in a LOX/H₂ rocket chamber (LOX/H₂, $P_c=4.5$ MPa, $V_o=30$ m/s, $V_f=300$ m/s, $d_o=1$ mm)

**INTERNATIONAL WORKSHOP ON
RESEARCH STATUS AND PERSPECTIVES
IN LIQUID ROCKET COMBUSTION CHAMBER FLOW DYNAMICS**

PARIS FRANCE (MAY 27-28 1999)

**EXPERIMENTAL INVESTIGATIONS OF CRYOGENIC
SPRAYS IN COMBUSTION**

by
Pierre GICQUEL, Lucien VINGERT
ONERA
29, Avenue de la Division Leclerc
92320 CHATILLON
France

ABSTRACT :

Three experimental investigations have been done on the cryogenic test bench MASCOTTE at ONERA Palaiseau center with the objective to study the LOX spray characteristics in combustion. Informations concerning the breakup process at 0.1 and 1 MPa were obtained by the mean of a visualization technique. Quantitative and qualitative description of the spray were then obtained by the use of a Phase Doppler system. A map of droplets size and velocity has been realized. The influence of the momentum ratio J on the first atomization process has been also shown.

Recently, with the objective to analyse the local Weber number by the mean of discrimination liquid and gas velocity, a last experiment has been performed with a 2D LDV system.

All those results participate for a better understanding of atomization in cryogenic sprays in combustion.

NOTATION

J	momentum ratio (gas/liquid)	V_m	axial mean velocity
D_0	initial droplet diameter	m_G	gas mass flowrate
t_e	evaporation time	m_L	liquid mass flowrate
t_s	residence time	MPa	pressure (in MPascal)
λ_{eff}	evaporation constant	V_L	liquid velocity
L	combustor length	V_G	gas velocity
V_g	droplet mean velocity	We	Weber number

INTRODUCTION

Cryogenic propellant combustion systems have been now applied successfully for many years in rocket engines (Ariane 1 to 5, SSME, ...). However, to improve the performance of this type of combustion systems and get a good modelling of the combustion, we need a better understanding of the elementary mechanisms, in particular atomization and vaporization processes.

A lot of works has been performed last 10 years to study the behaviour of many sprays. All those studies were more often conducted with simulant fluids (water for the main off them). It is of course because it's more difficult to performed those studies on real fluids with real hot fire conditions.

To contribute answering those questions a cryogenic test bench, called MASCOTTE, was built and a test program was conducted under a consortium of laboratories and manufacturers associating ONERA, CNRS, CNES and SEP. The main objective was to provide a good description of atomization and vaporization processes under hot fire conditions and, by this way, to have a better understanding of this kind of combustion.

This article describes experiments performed during combustion tests mainly focused on the LOX droplets size analysis.

First, with the goal to provide preliminary informations on the fluid dynamics of the LOX core breaking process, a visualization technique, using a stroboscopic laser sheet associated with a high speed camera (2000 frames/s), was used.

After those initial visualizations the main objective of this work consisted in measuring LOX droplets size and velocity on the axial and radial flow to get a good mapping of droplets size and velocity in the combustion

chamber. Two pressures have been performed, 0.1 and 1 MPa. A PDPA system with one component of velocity was used for those measurements.

The two experimental investigations (at 0.1 MPa and 1 MPa) give a good qualitative (by visualization) and quantitative (by Phase Doppler technique) description of the LOX spray in terms of atomization and vaporization process in hot fire conditions. At 0.1 MPa three different zones have been detected: near the post tip a first atomization zone, after a relative long ligaments zone and finally a well defined droplets spray.

A comparison between LOX droplets size and velocity at 0.1 and 1 MPa gives us information on the influence of the pressure on the atomization process.

The influence of the J number (momentum ratio) on the atomization has also been performed at 1 MPa.

A last characterization has been performed recently, for instance in cold flow conditions, with the objective to analyse the local Weber number by the mean of discrimination of liquid and gas velocity.

OPTICAL SETUP

Three optical configurations have been used during those experiments. On the picture of figure 1 the PDPA setup is shown on the test bench. Like is well known today the PDPA is a size and velocity particles optical measurement system. The PDPA complete theory has been described and explained in details in reference [1].

The schematic drawing of figure 2 shows the optical configuration used for the visualization tests. This visualization has been performed by the mean of a stroboscopic laser sheet associated with a high speed camera.

The laser sheet was formed by a stroboscopic copper laser beam (at $\lambda = 510.6$ nm) focused through a cylindrical and spherical lens. This sheet was about 70 mm wide and 1 mm thick near the chamber axis. The strobe frequency was 2 kHz and the pulse time duration about 40 ns. A high speed 16 mm movie camera (NAC E – 10) was used in association with black and white high speed sensibility movie film (500 ISO). This camera was used at 2000 frames/s and synchronised via an optical pick-up to the strobe frequency.

On the picture of figure 3 the optical 2D LDV system used recently for a 2D velocity analysis of both LOX and gas hydrogen is shown.

DROPLET SIZE AND VELOCITY RESULTS

The operating conditions are listed in the table 1. Those conditions were used for the two first campaigns in combustion (drop size and visualisation).

Case	Pressure MPa	V_L m/s	m_G g/s	V_G m/s	J	M	We 10^5	Re 10^5
A	0.1	2.21	15.00	893	13.4	3.30	0.598	0.67
A-10	1	2.23	23.70	308	14.5	2.10	0.20	0.67
C	0.1	2.21	10.00	628	6.3	5.00	0.304	0.67
C-10	1	2.23	15.80	207	6.5	3.20	0.09	0.67

Table 1 : Operating conditions

For all cases the LOX mass flowrate was maintained constant at 50 g/s.

Results at 0.1 MPa [2, 3, 4]

The LOX spray evolution in the combustion chamber has been described quantitatively and qualitatively. A map of the LOX droplet sizes and velocity has been done on all the length of the combustion chamber. One measurement point (on the axis) has been done also outside of the confining chamber and shows that droplets exist yet in this zone far from the front flame and cross it. Comparison between residence time (defined as: $t_r = L / V_g$), and evaporation time (defined as $t_e = (D_0)^2 / \lambda_{eff}$ by A. H. Lefebvre [5]) shows that at 0.1 MPa droplet size up to 200 μm was partially evaporated.

A comparison with computed empirical correlations [6, 7, 8] shows that the droplet size measurements are in the same order that results give by the empirical correlations. For more information see the reference [4].

An « artistic drawing » of the qualitative description of the spray is shown on figure 4.

Results at 1 MPa

Like above, for the 0.1 MPa campaign, a qualitative and quantitative description of the spray has been done. Those complementary results have allowed to do a comparison, at the same cross section of the chamber, between 0.1 MPa and 1 MPa. The results at 1 MPa show a lower number density but droplet size (D_{10} , D_{32}) are bigger than at 0.1 MPa (figure 5). The measurement validation rates are also better at 1 MPa. This shows that at high pressure all the small droplets are evaporated very quickly near the post tip of the injector and after only big structures and droplets are present in the spray.

A droplet size evolution versus J number has also demonstrated the importance of the momentum ratio for the first atomization process (figure 6).

VISUALIZATION RESULTS

Results at 0.1 MPa

During this first campaign only the zone near the injector has been analysed (from the injector post tip to 70 mm backward). A macro description of the breakup process has been done (figure 7) and has allowed to give an evolution, on 4 ms, of an attach ligament to simple droplets (spherical or not).

Results at 1 MPa

The aim of this test campaign at 1 MPa was to follow the LOX structure (if she exists) along the combustion chamber. Like a first result, a comparison with results at atmospheric pressure shows that the flame emission was clearly detectable at high pressure and not at 0.1 MPa. On figure 8 two pictures recorded during the test campaign are presented. First the phenomena were recorded without any filter to reject the luminous flame light (a). Here it is easily to see the LOX structure inside the flame. In a second configuration, a bandpass filter, centered at the wavelength of the laser beam, around 510 nm, was fitted in front of the camera lens. In this configuration only the scattered light of the liquid structure was visualized (b).

The analysis of the pictures at same axial positions confirms the PDPA results. The spray is denser at atmospheric pressure. Pictures far from the injector ($X/d > 30$) shows only big structures.

LDV TWO PHASES FLOW RESULTS

A last campaign, perform in 1999, has allowed to get a better description, in term of velocity, of a coaxial LOX structure with an anulus gas flowrate. The 2D LDV measurements has been done, for instant, in none reactif flow (LOX and gas N₂ and He). The main objective was to get the local Weber number by the mean of velocity discrimination between LOX droplets and gas. For gas velocity analysis a seeding system was added to to the gas distribution panel. The particles were chosen as zirconium oxide, with the objective to be used later in combustion tests.

A first theoretical analysis has been done by Onofri[9] to find the best optical configuration of the 2D LDV system. This analysis has given a numerical optimisation based on the diffusion of the two kind of particles (droplets and solid particles). For solid particles less than 1 μm , used for seeding the gas mass flowrate, and angular zone between 64° and 114° seem to be the best optical configuration.

For instance the first results show an important recirculation zone near the injector. An other important result shows that the seeding solid particles stay in the gas zone and never reach the two phases flow in the LOX spray. At the present time a software is on development with the objective to be able to analysed the raw signals and extract from the intensity levels of each particle the velocity of LOX droplets and seeding particles of the gas.

CONCLUSION

This paper has presented the main results got during a combustion test program performed on the ONERA cryogenic test bench MASCOTTE. Three experimental investigations were performed until today. Those investigations were mainly focused on the LOX droplet size and velocity analysis. The visualization technique give us first informations on the LOX structure and particularly the difference between tests at atmospheric pressure and 1 MPa. By the use of a PDPA measurement technique, a good mapping of droplet size and velocity around the LOX core has been obtained.

As main conclusions today we can say that we have got :

- a good qualitative (by visualization) and quantitative (by PDPA technique) description of the LOX sprays ;
- those results provide us informations on the atomization process under hot fire conditions, with a comparison between atmospheric pressure and 1 MPa ;
- the last step is yet under analysis, but would be able to help us to understand the local spray evolution by the knowledge of the local Weber number.

ACKNOWLEDGMENT

This work was supported by CNES and SEP under contract N° 875366 and 876691 ; the authors would like to express their thanks for this financial support.

REFERENCES:

- [1] **W. D. Bachalo, M. J. Houser**, *Phase Doppler spray analyser for simultaneous measurements of drop size and velocity*, Optical Engineering, volume 23, N° 5, 1984.
- [2] **P. Gicquel, L. Vingert D. Lourme, L. Menoret**, Coaxial Injectors Atomization, Progress in Astronautics and Aeronautics, vol. 169, Chap.6, pp. 145-189, 1995.
- [3] **P. Gicquel, L. Vingert et E. Brisson**, *Caractérisation expérimentale d'un brouillard LOX-GH2 en combustion issu d'un injecteur coaxial*. Actes du 5 ième « Colloque du GDR Combustion dans les moteurs fusées »
- [4] **P.Gicquel, E. Brisson, L. Vingert**, Experimental investigation of a LOX spray under hot fire conditions. ICLASS 97, Seoul (Korea), August 18-22, 1997.
- [5] **A. H. Lefebvre**, *Atomization and Sprays*, Hemisphere Press, NY, 1989
- [6] **S. Nukiyama and Y. Tanasawa**, *Experiments on the atomization of liquids in an air stream*, Trans. Soc. Mech. Eng. Jpn., vol. 5, N° 18, pp. 62-67, 1939.
- [7] **E.G. Lorenzetto and A.H. Lefebvre**, *Measurements of drops size on a plain jet airblast atomizer*, AIAA Journal, vol 2, N° 3, pp. 583-585, 1964.
- [8] **K. Y. Kim and W. R. Marchal** *Drop size distributions from pneumatic atomizers*, Journal of Am. Chem. Eng., vol 17, N° 3, pp. 575-584, 1971.
- [9] **F. Onofri**, *Optimisation numérique de la configuration expérimentale à adopter lors de la campagne de mesure des champs de vitesse particulaire/fluide du foyer LOX/GH2 « MASCOTTE »* Rapport d'étape CNRS du 3 sept. 1998

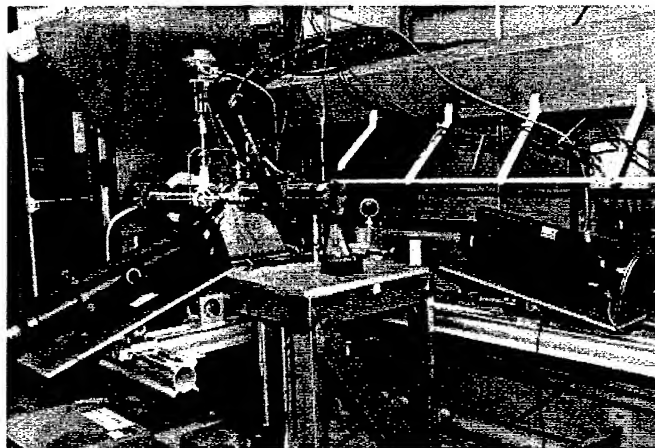


Fig 1. Optical PDPA arrangement on MASCOTTE test bench

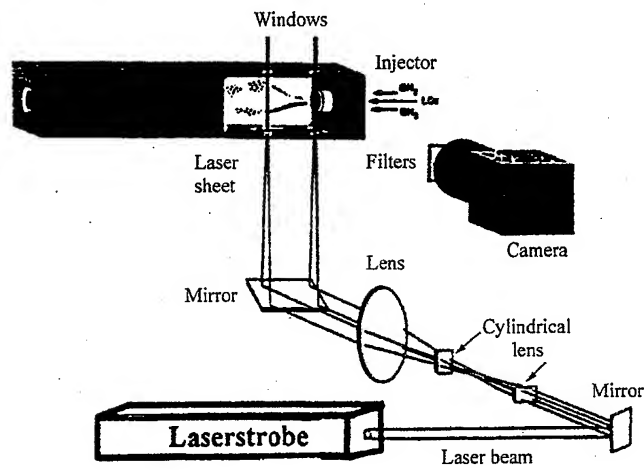


Fig 2. Optical visualization setup



Fig 3. 2D LDV system optical arrangement

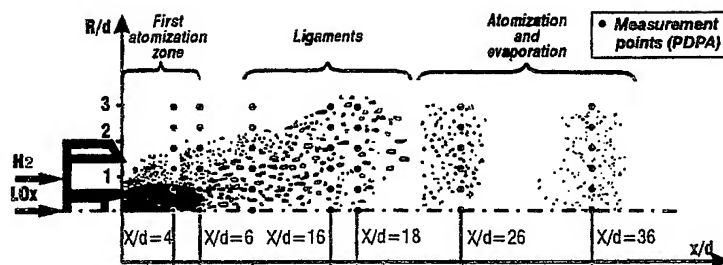


Fig 4. Qualitative description of the spray at 0.1MPa

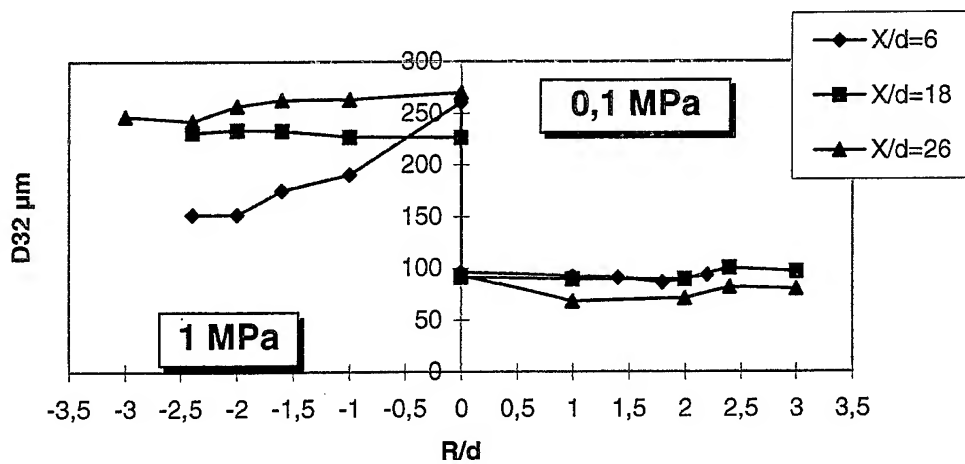


Fig 5. D_{32} comparison between 0.1 MPa et 1 Mpa

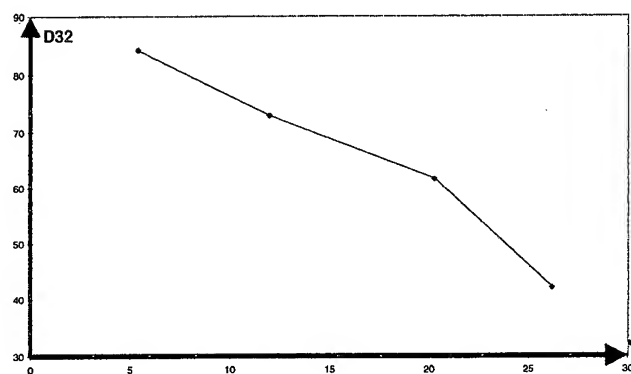


Fig 6. D_{32} evolution versus momentum ratio J



Fig 7. Evolution of the breakup process during 4 ms



(a) (b)
Fig 8. Visualization of flame and spray (a) and spray only with an additional green filter (b)

Quantitative Density Measurements in Supercritical LN2-Sprays Using Raman Scattering

M. Oschwald, A. Schik

Deutsches Zentrum für Luft- und Raumfahrt
Raumfahrtantriebe
Lampoldshausen

U.E. Mayer, W. Stricker

Deutsches Zentrum für Luft- und Raumfahrt
Institut für Verbrennungstechnik
Stuttgart

Motivation

conditions in a cryogenic high pressure rocket combustor:

Vulcaine-motor:

fuel: GH2
oxidizer: LOX

$T \approx 100\text{K}$ $P \approx 10\text{MPa}$

thermodynamic critical point of O_2 : $T_c = 165.6\text{K}$ $P_c = 5.04\text{MPa}$

in the trans- and supercritical region real-gas behavior influences

- atomization and mixing
- heat and species transport

basic experiment:

coaxial injection of LN2 and H2 (optional): $T_i = 100\text{K}-140\text{K}$ $P_i < 6\text{MPa}$
 thermodynamic critical point of N2: $T_c = 126.2\text{K}$ $P_c = 3.4\text{MPa}$

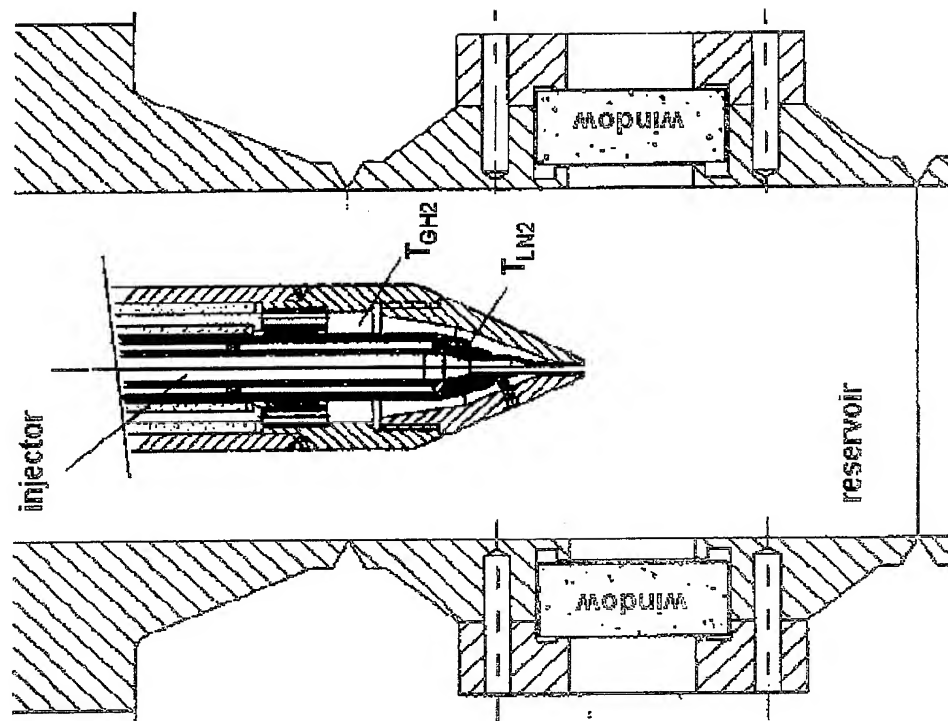
Laser diagnostics for **quantitative** investigation of the jet disintegration at conditions similar to rocket combustors:

thermodynamical state: $P_T/P_{C, \text{LN2}} \approx P_{CC}/P_{C, \text{LOX}}$

non-dimensional numbers: $Re, We, J (\text{LN2/GH2}) \approx Re, We, J (\text{LOX/GH2})$

idealized conditions: no combustion

Cryo-Injector Test Facility

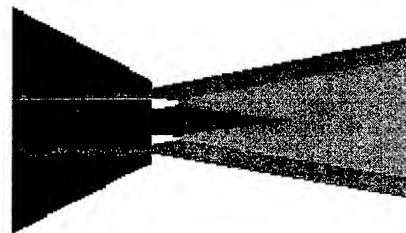


coaxial-injector

LN₂ Ø = 1.9mm

H₂ Ø_i = 2.4mm

Ø_o = 3.2mm



injection of H₂ is
optional



Optical Diagnostics at High Pressure

strong molecular interaction → line broadening
 strong gradients of the refractive index → laser beam steering
 high signal intensities → non-linear effects

Spontaneous Raman-Scattering

species-specific
 linear process, relative insensitive to molecular interaction
 signal intensity profits from high densities

pulsed lasers:

≈ 25MW/cm²

2D

good temporal resolution
 statistical characterization
 risk of gas break down
 non-linear effects

XeCl-excimer laser (351nm)

cw-lasers:

≈ 10kW/cm²

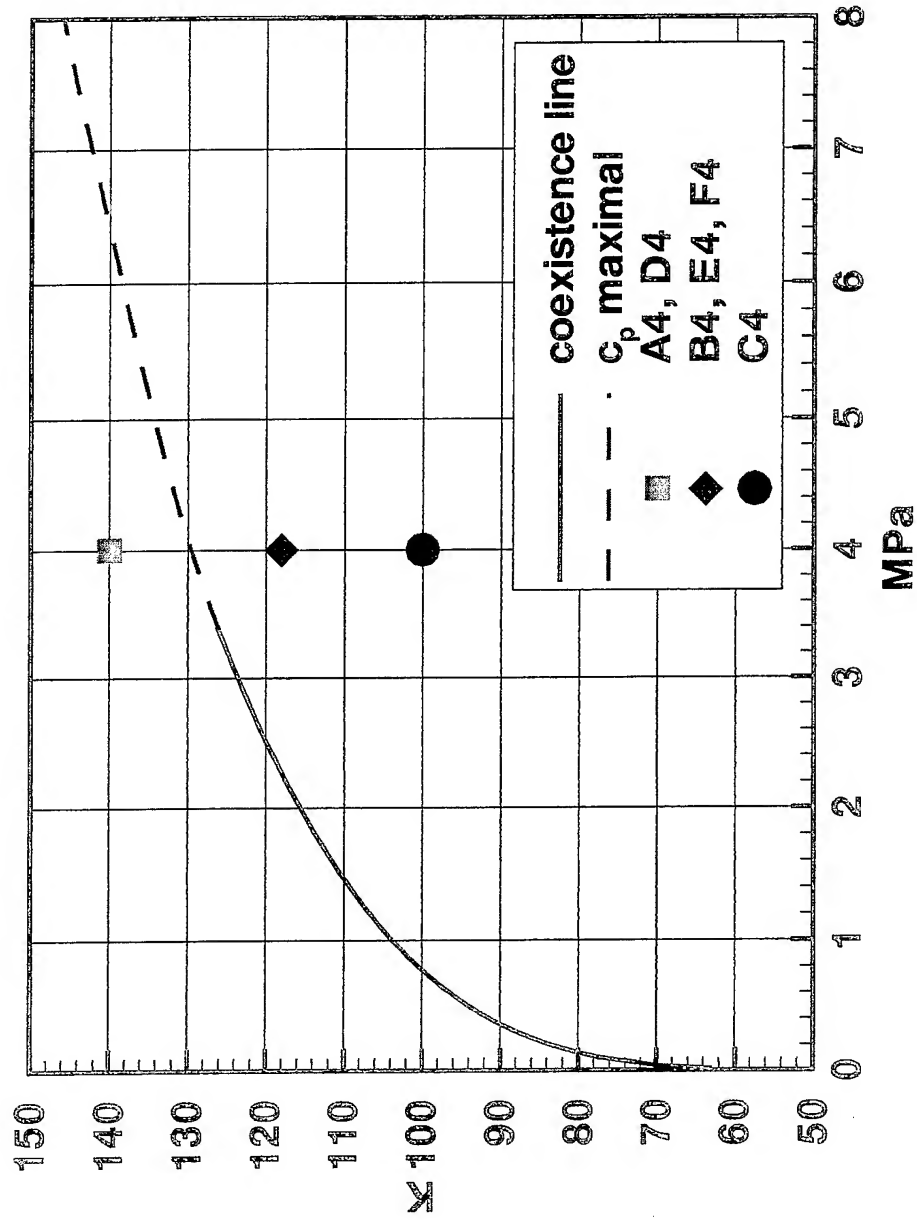
1D

temporal average
 mean values
 no gas break down, no non-linear effects
 simple experimental set-up

Ar-ion laser (488nm)

Nitrogen: Thermophysical Properties

4MPa

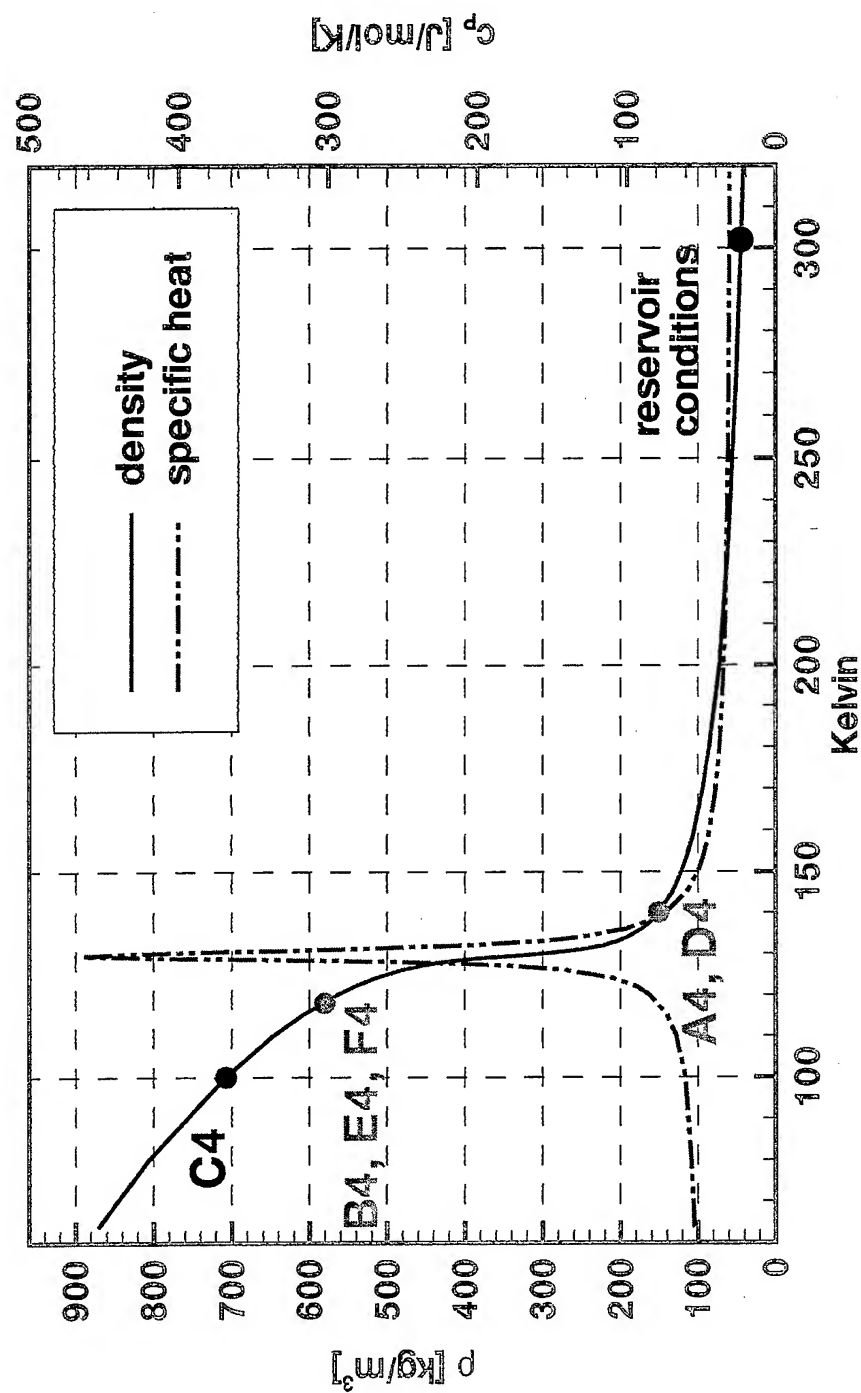


workshop May 27-28 1999.DOC



Nitrogen: Thermophysical Properties

4MPa



workshop May 27-28 1999.DOC



test cases

	V_{N_2} [m/s]	V_{H_2} [m/s]	T_{N_2} [K]	T_{H_2} [K]	ρ_{N_2} [kg/m ³]	ρ_{N_2}/ρ_{H_2}	$Re_{N_2}/1000$	$\rho v^2_{N_2}/\rho v^2_{H_2}$
A4	5		140		151		115	
B4	5		118		582		126	
C4	20		100		707		340	
D4	5	60	140	270	151	39	115	3.7
E4	5	120	118	270	582	151	126	3.8
F4	5	60	118	270	582	151	126	0.95

$$P_t = 4 \text{ MPa} \quad P_t/P_c = 1.17$$

1D-Raman Scattering

optical set-up

laser:

Ar⁺, 488nm,
1.5 Watt

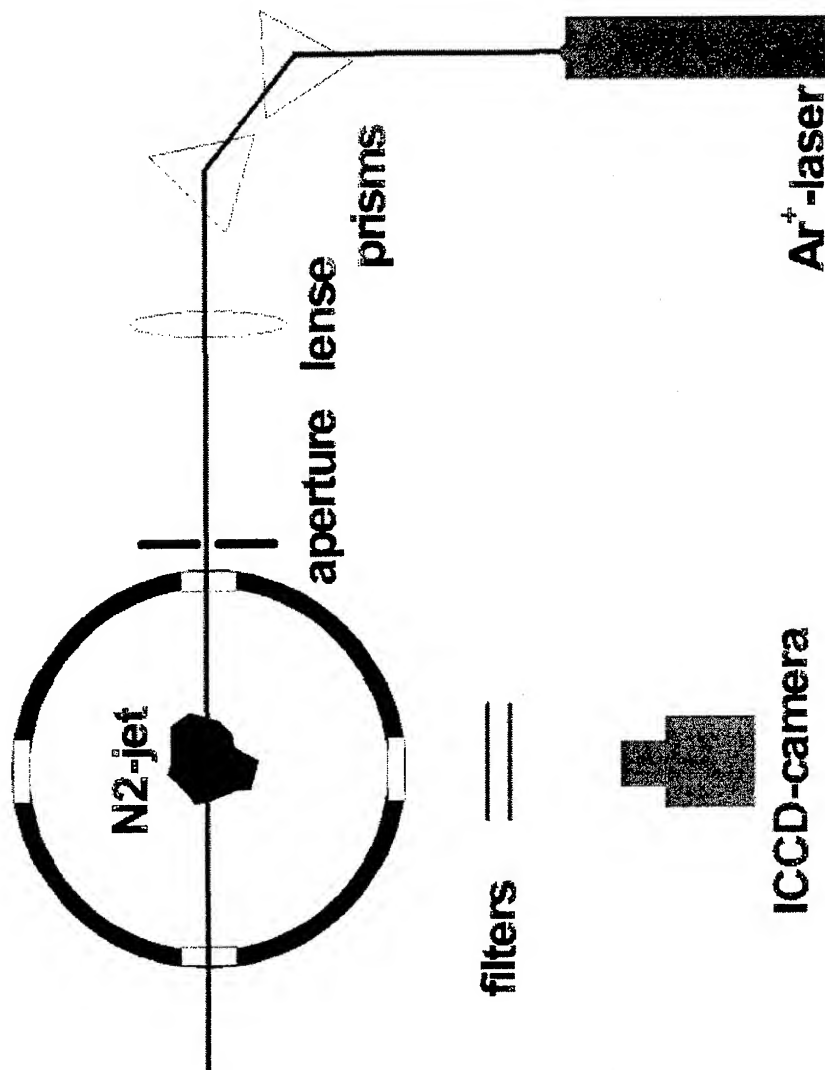
detector:

slow scan ICCD
integration "on chip"
1s

filter:

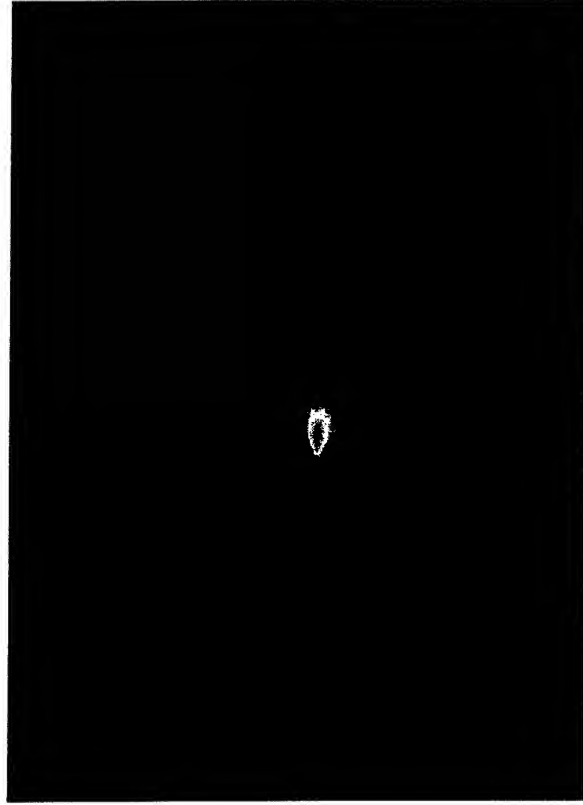
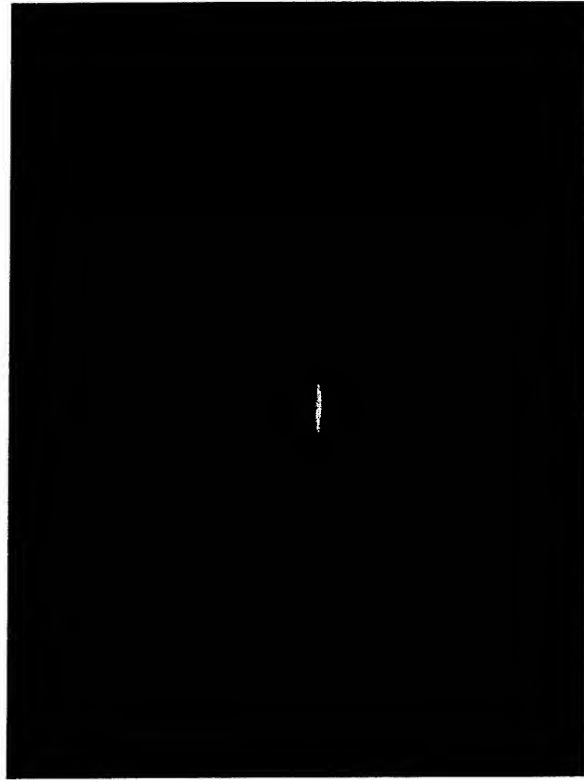
prisms and aperture;
OG550, Interference-filter
 $T(488\text{nm}) < 10^{-12}$
 $T(551\text{nm}) = 0.3$

S/N ~ 40 at 4MPa



Nitrogen Free-Jet row data

4MPa



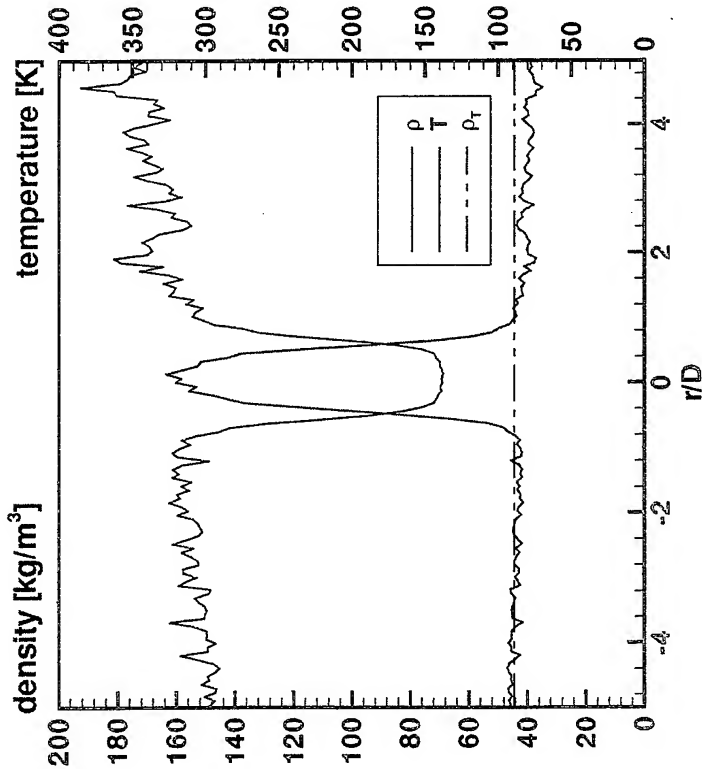
case A4
 $T_{N_2}=140K$
 $n_{1,2}=1.025$

case C4
 $T_{N_2}=100K$
 $n_{1,2}=1.157$

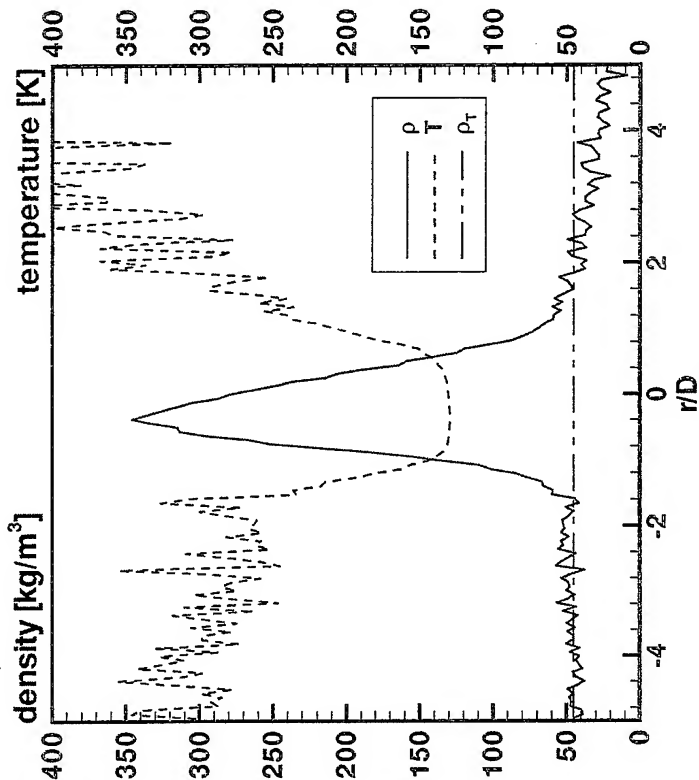
Nitrogen Free-Jet

case A4/B4

radial density and temperature profiles



case A4
 $x=2\text{mm}$

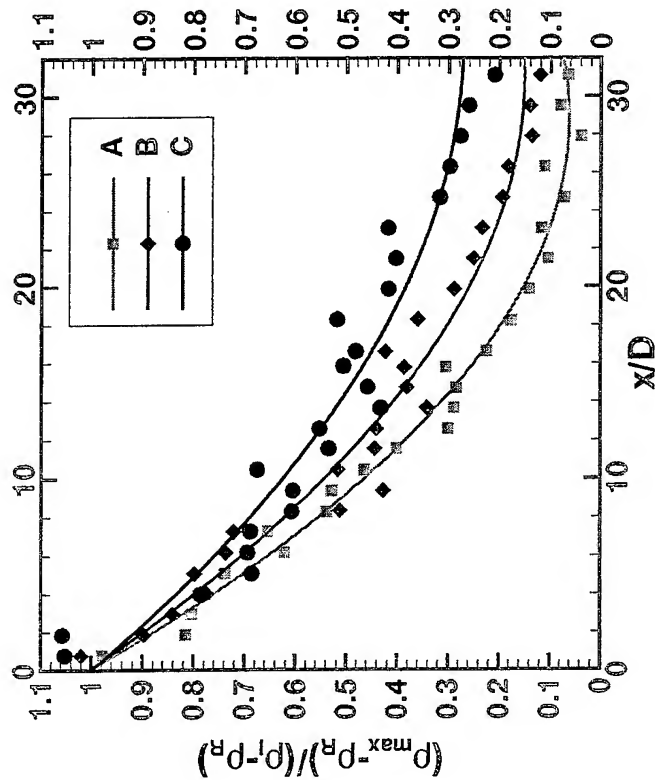


case B4
 $x=16\text{mm}$



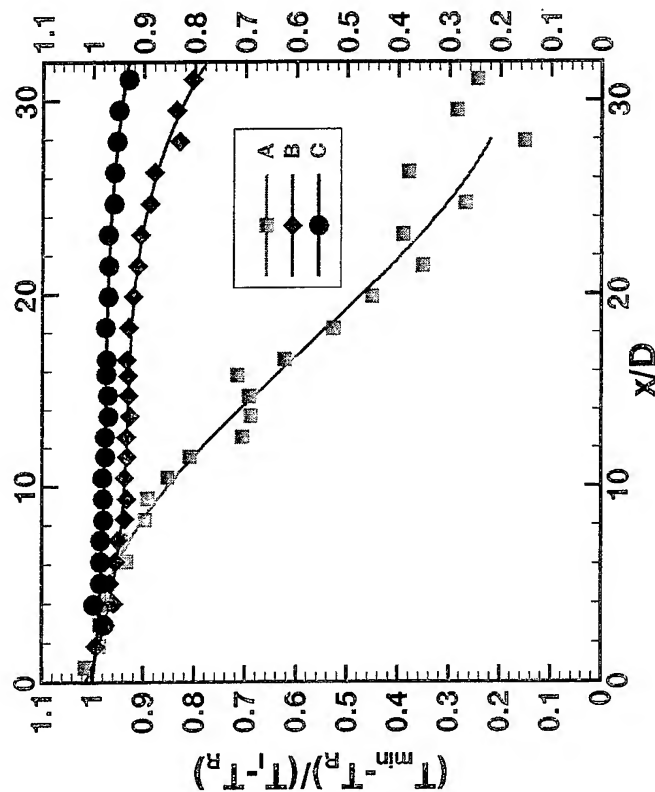
Nitrogen Free-Jet

4MPa



normalized density

normalized density/temperature



normalized temperature

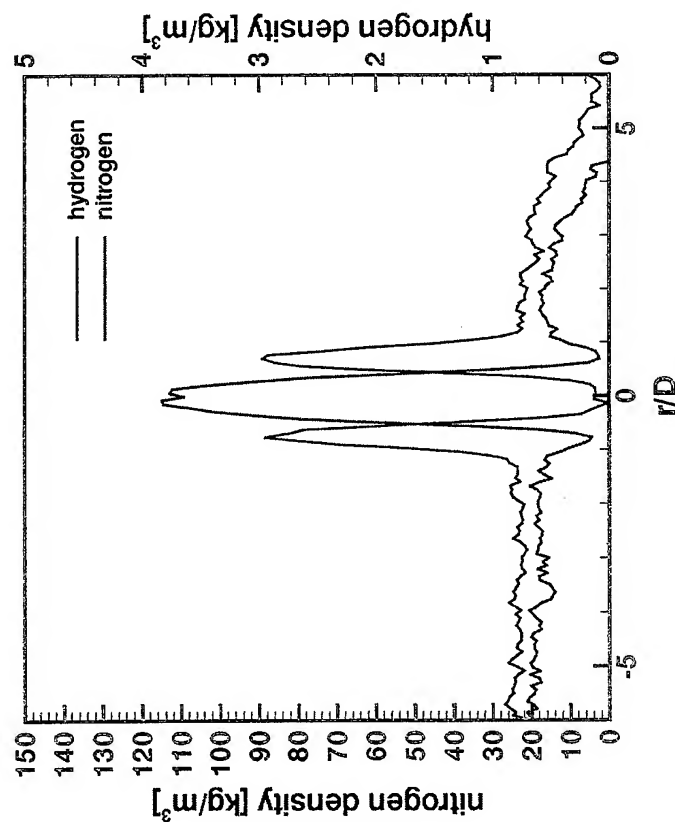
= 1: injector conditions
= 0: tank conditions



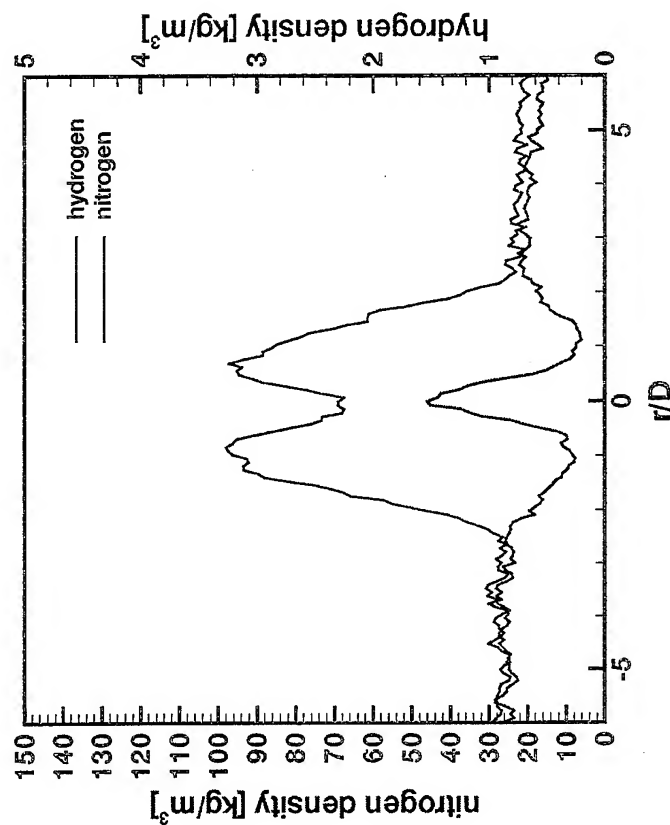
coaxial LN2/GH2-Injection

case D4

radial density profiles for nitrogen (140K) und hydrogen



$x=2\text{mm}$



$x=10\text{mm}$

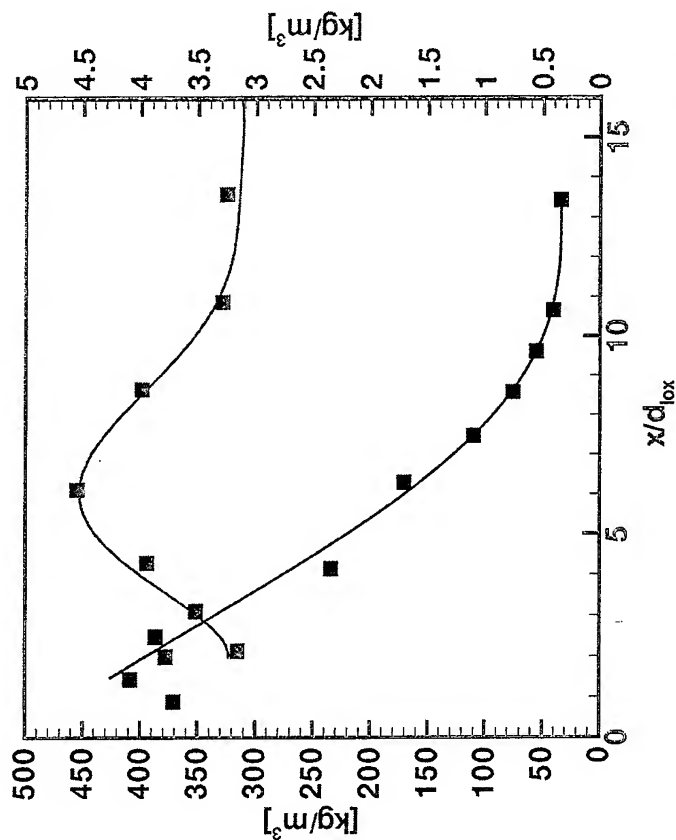
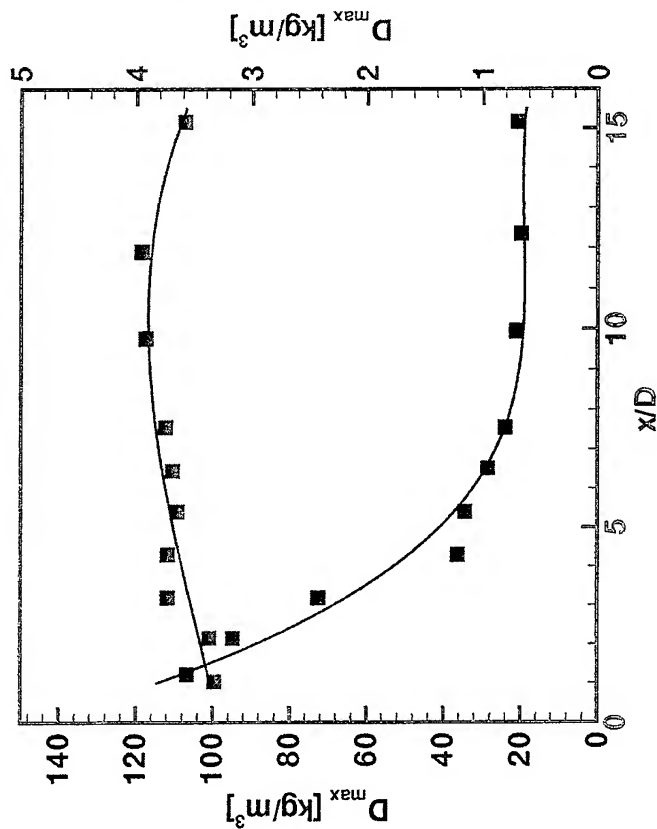


coaxial LN2/GH2-injection maximal density

4MPa

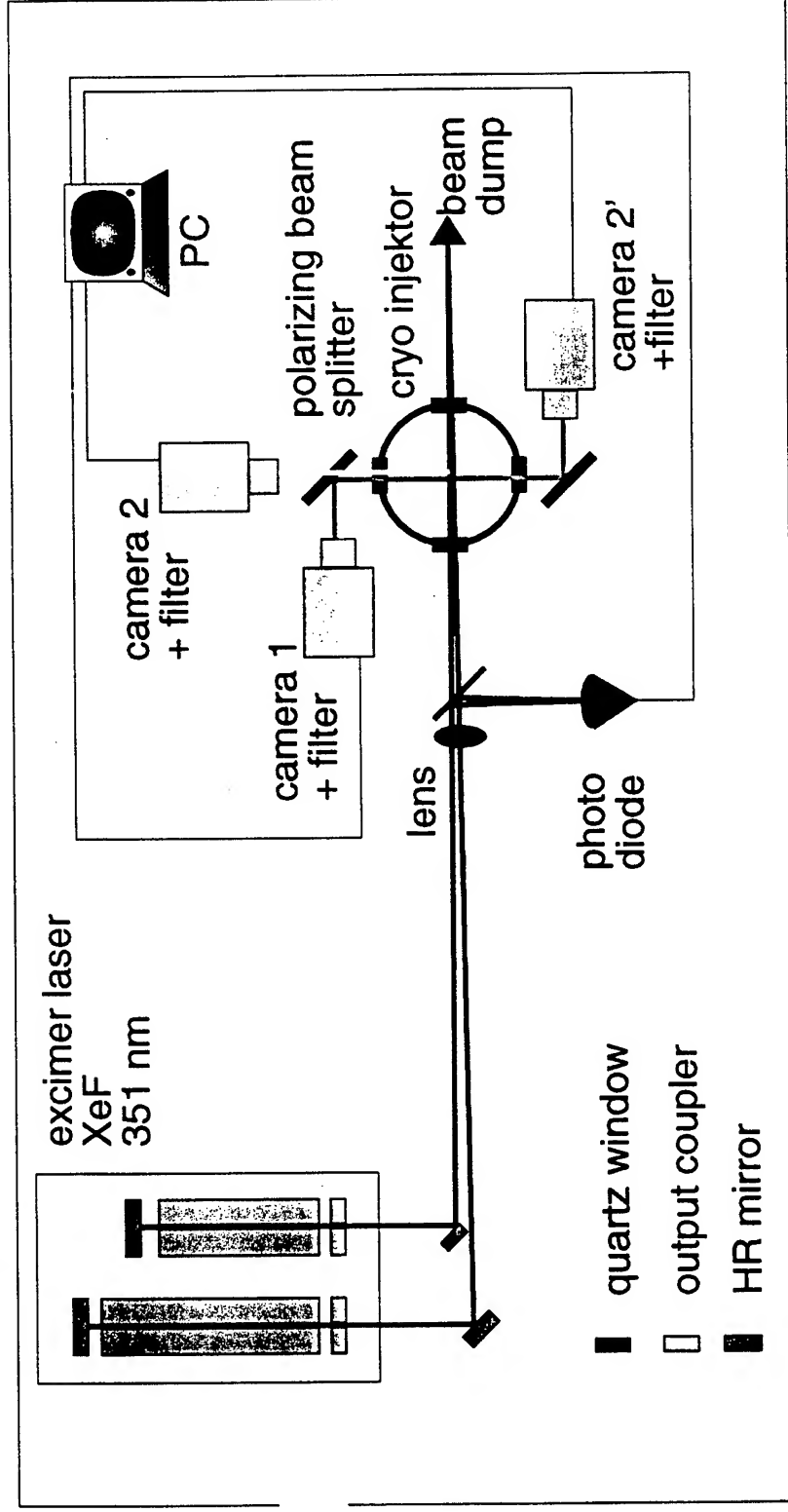
case D4: nitrogen (140K) / hydrogen

case E4: nitrogen (118K) / hydrogen



Experimental Arrangement

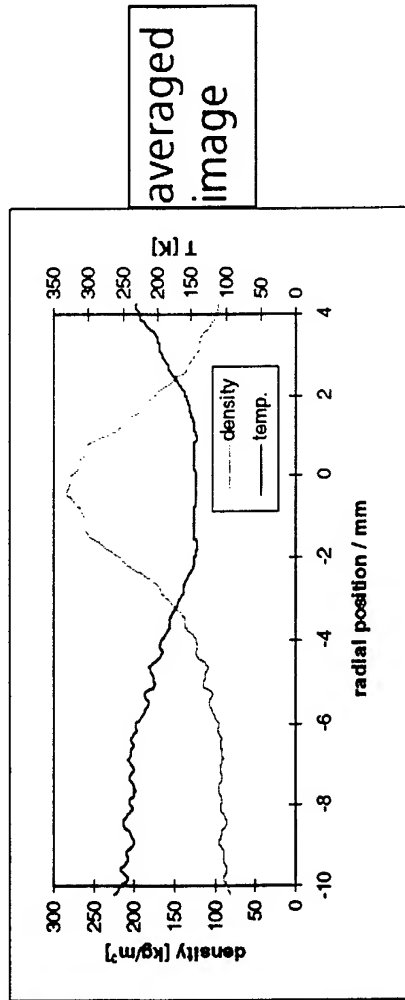
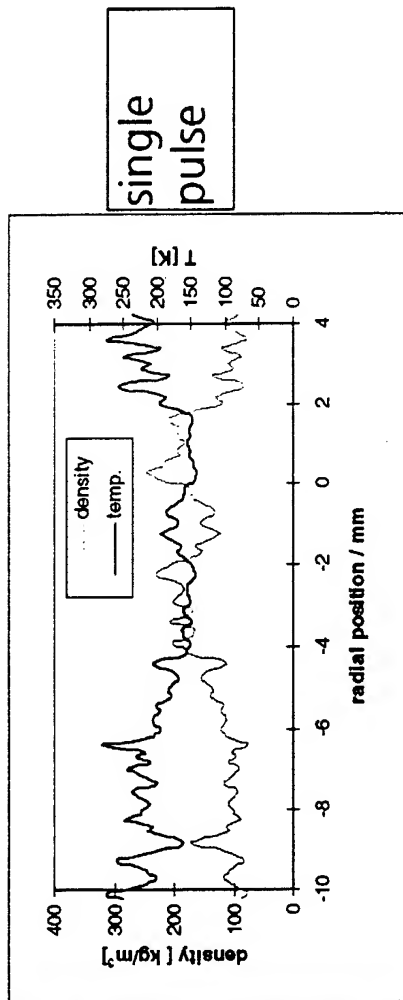
scattered light suppression by polarization or 2 species simultaneously



Institute for Physical Chemistry of Combustion, Stuttgart
Division Space Propulsion, Lampoldshausen

N₂ Densities and Temperatures

axial position 41.5 mm below injector; 60 bar, 20 m/s N₂ into N₂

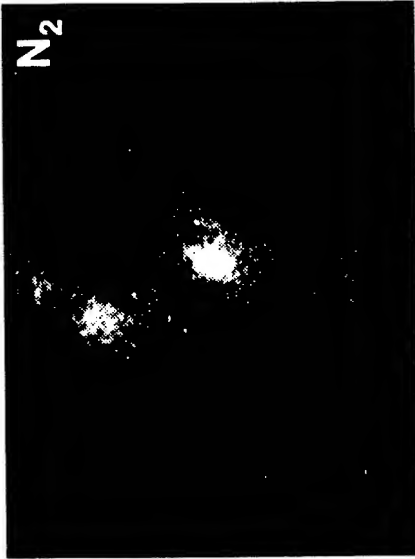
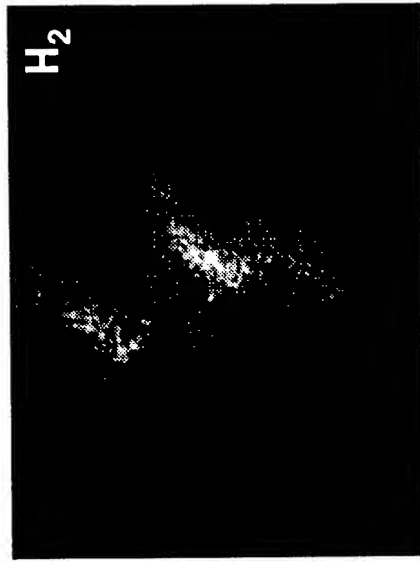


Institute for Physical Chemistry of Combustion, Stuttgart
Division Space Propulsion, Lampoldshausen



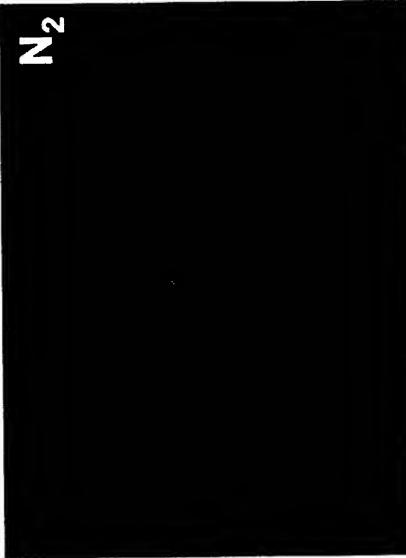
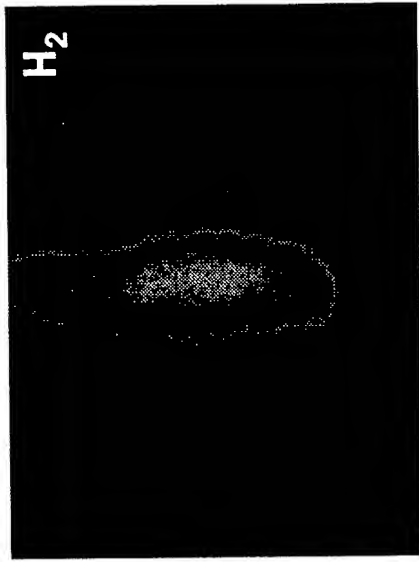
um970401.doc

Simultaneous Detection of H_2 and N_2 distance from injector 35-50 mm; no stray light suppression



15 m/s LN_2
150 m/s H_2
into
40 bar GN_2

single
pulse



averaged
images

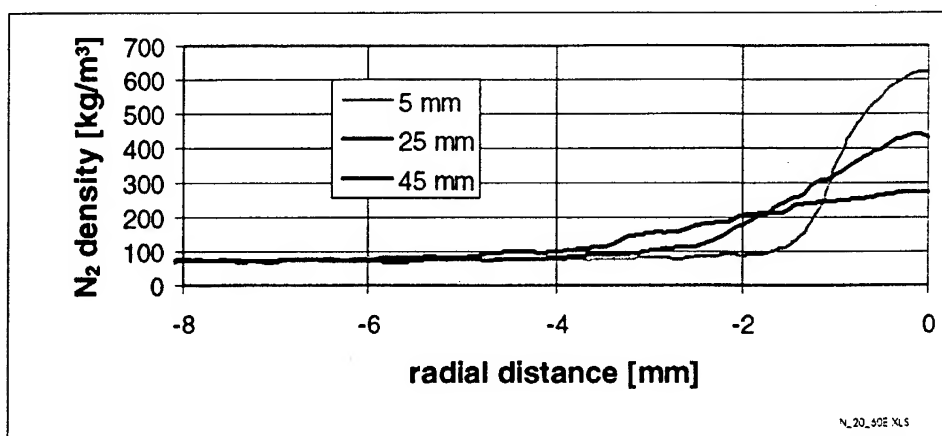


Institute for Physical Chemistry of Combustion, Stuttgart
Division Space Propulsion, Lampoldshausen

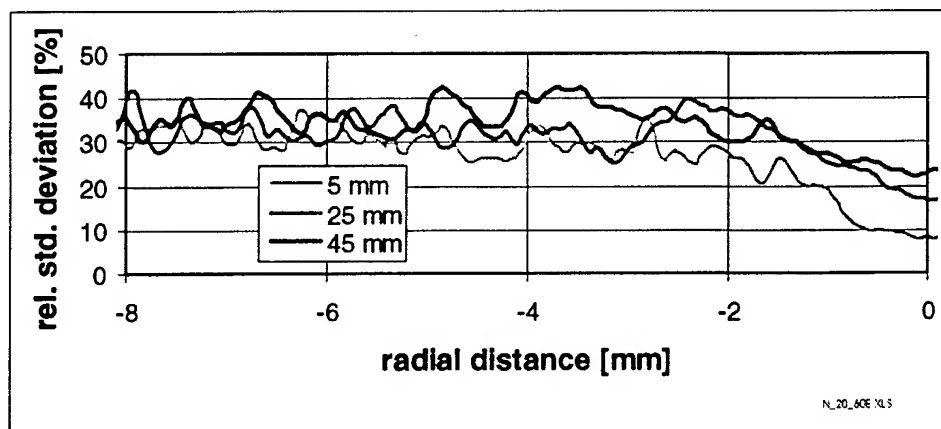
UM970428.CDF

20 m/s LN_2 into 6 MPa GN_2 : Average N_2 Densities and Std. Deviation

average density at three downstream positions



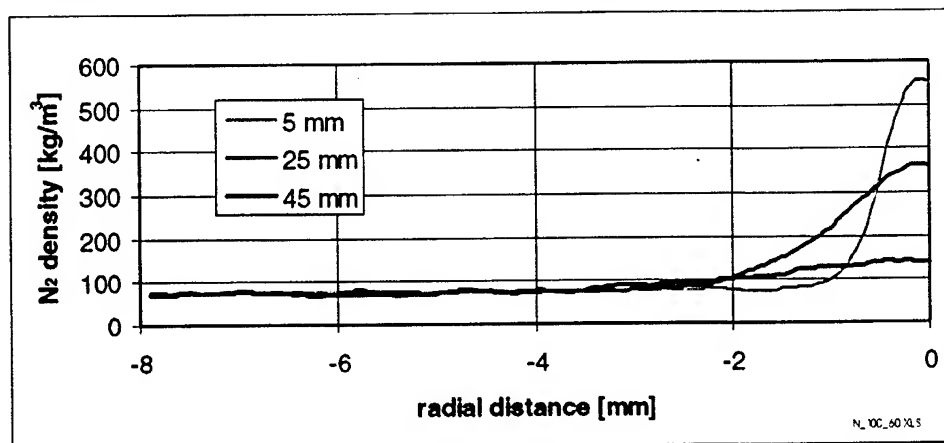
standard deviation



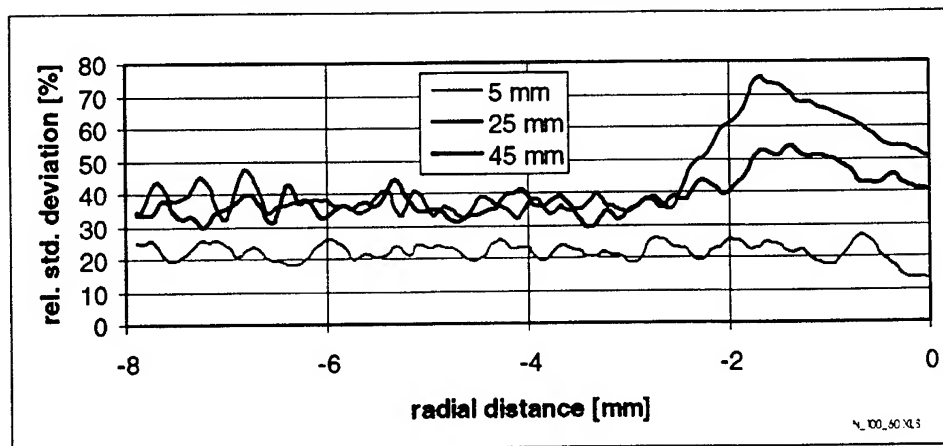
Institute for Physical Chemistry of Combustion, Stuttgart
Division Space Propulsion, Lampoldshausen

15 m/s LN_2 and 100 m/s H_2 into 6 MPa GN_2 : Average N_2 Densities and Std. Deviation

average density at three downstream positions



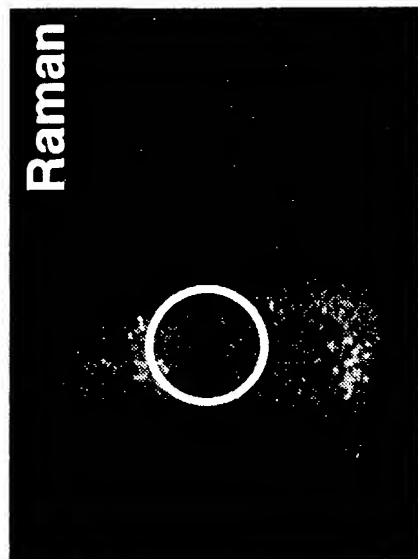
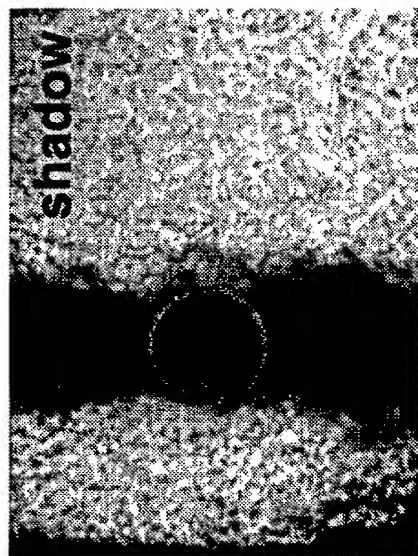
standard deviation



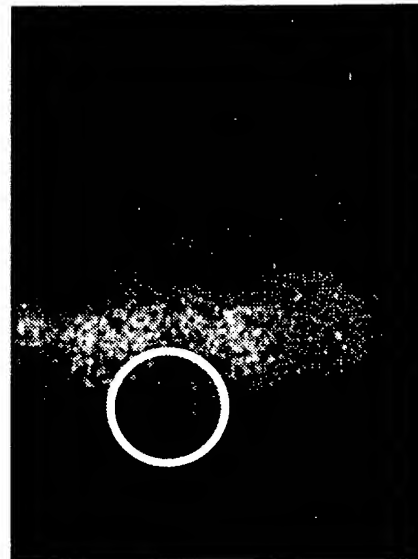
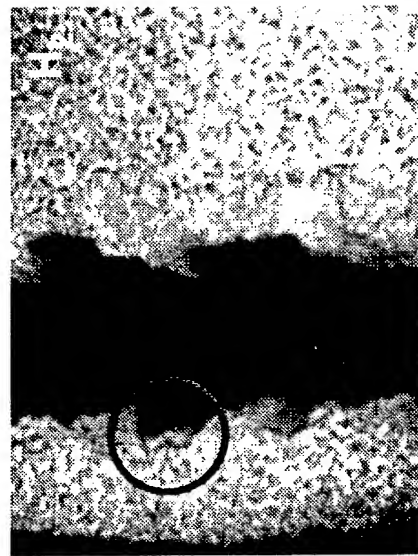
Institute for Physical Chemistry of Combustion, Stuttgart
Division Space Propulsion, Lampoldshausen



Comparison: Raman Imaging <-> Shadowgraphy distance from injector 35-50 mm; no stray light suppression



5 m/s LN₂
into
40 bar GN₂
single pulse



20m/s LN₂
into
40 bar GN₂
single pulse



Institute for Physical Chemistry of Combustion, Stuttgart
Division Space Propulsion, Lampoldshausen

UM970424.CDR

Summary

Spontaneous Raman Scattering

- cw-laser: no risk of interference due to gas break down and stimulated Raman scattering
- pulsed laser: with carefull adjustment of pulse energy and pulse length no interference due to gas break down and stimulated Raman scattering
- strong laser beam steering and elastic scattering in the near injector region due to gradients of the refractive index. Gradients increase with injection of H₂.
- at both excitation wavelengths (488nm, 351nm) broadband background signal observed; source not finally identified
- **quantitative density and temperature measurements possible with cw-laser and pulsed laser**

Summary

Nitrogen Free-Jet

- different development of and temperature and density distribution
- strong influence of the thermodynamical state on the development of the temperature profiles
- colder (more dense) N_2 -jet: slower disintegration

coaxial LN_2/GH_2 -injection

- constant density on the first few x/D in the core flow observed for $T_{N_2} < 130K$
- increased standard deviation in the boundary layer of the N_2 -jet as compared to the free jet case
- increasing H_2 -density downstreams the injector observed
- increasing $T(N_2) \Rightarrow$ more efficient atomization
- increasing H_2 -momentum flux \Rightarrow more efficient atomization

Studies on the Break-up Regimes of LOx Droplets

Bruno Vieille, Christian Chauveau and Iskender Gökalp
Laboratoire de Combustion et Systèmes Réactifs

CNRS - Orléans

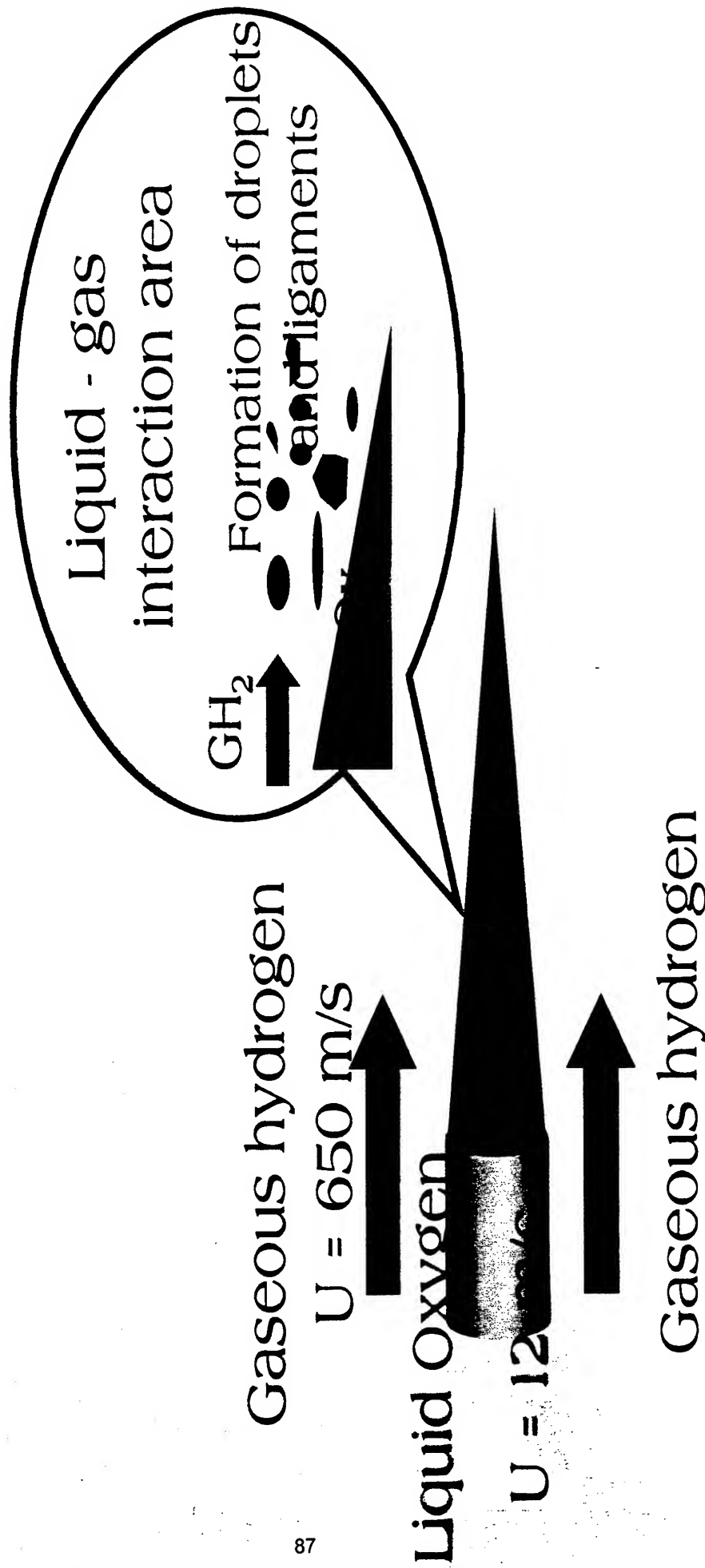
E-mail : vieille@cnrs-orleans.fr

Boris Gelfand, STC, RAS, Moscow

Contents

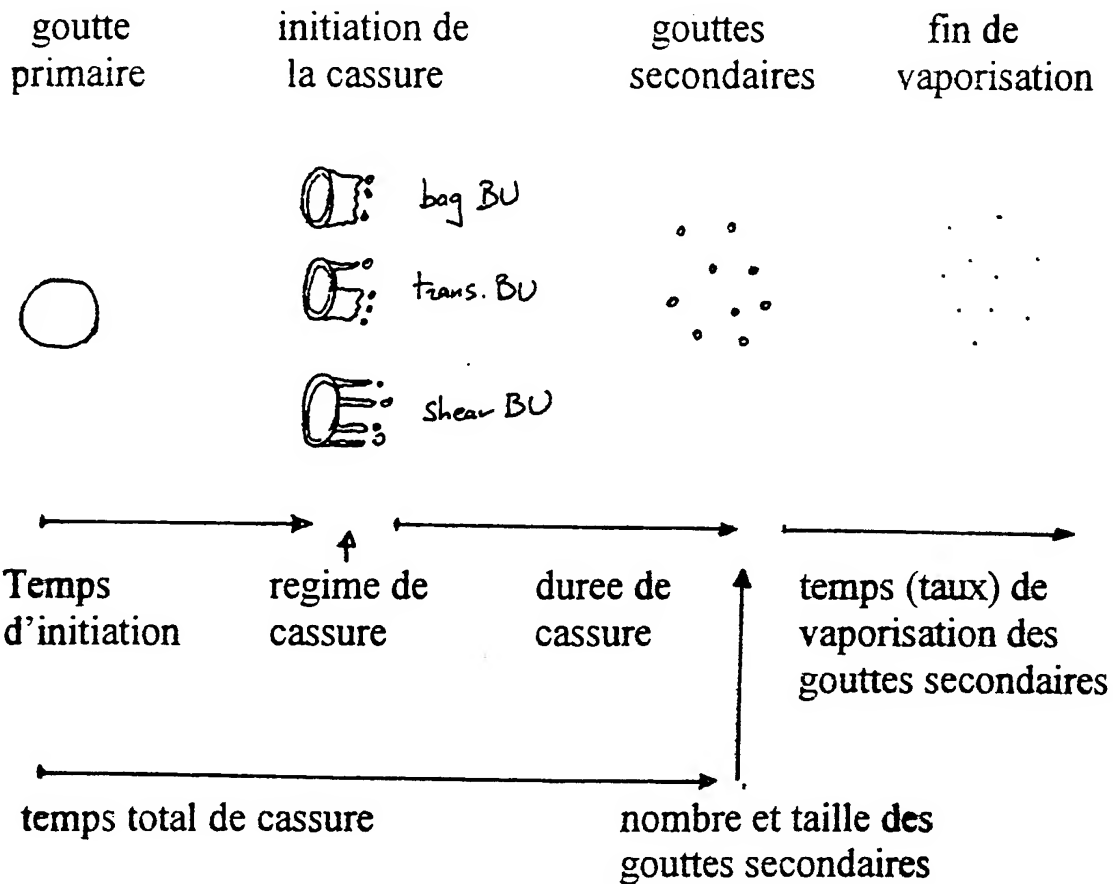
- Introduction
- Experimental set-up and diagnostics
- Results
 - Aerodynamic field
 - Break-up regimes
 - Characteristic times
- Conclusions

Vulcan coaxial injector



Activités du L.C.S.R.

Expérimentale : en configuration monogoutte :



Expérimentale : Spray inerte

Numérique : vaporisation / combustion goutte isolée

PARAMETRES INFLUANCANTS

Temps d'initiation et régime de cassure :

- Reynolds
- Weber
- Ohnesorge
- pression (via rapport de densité gaz/goutte)

Durée de la cassure (temps total – temps d'initiation) :

- Weber
- rapport de densités
→ indépendant de la pression

Nombre et taille des gouttes secondaires :

- Reynolds
- Weber
- pression
- D_0 (diamètre initial goutte primaire)

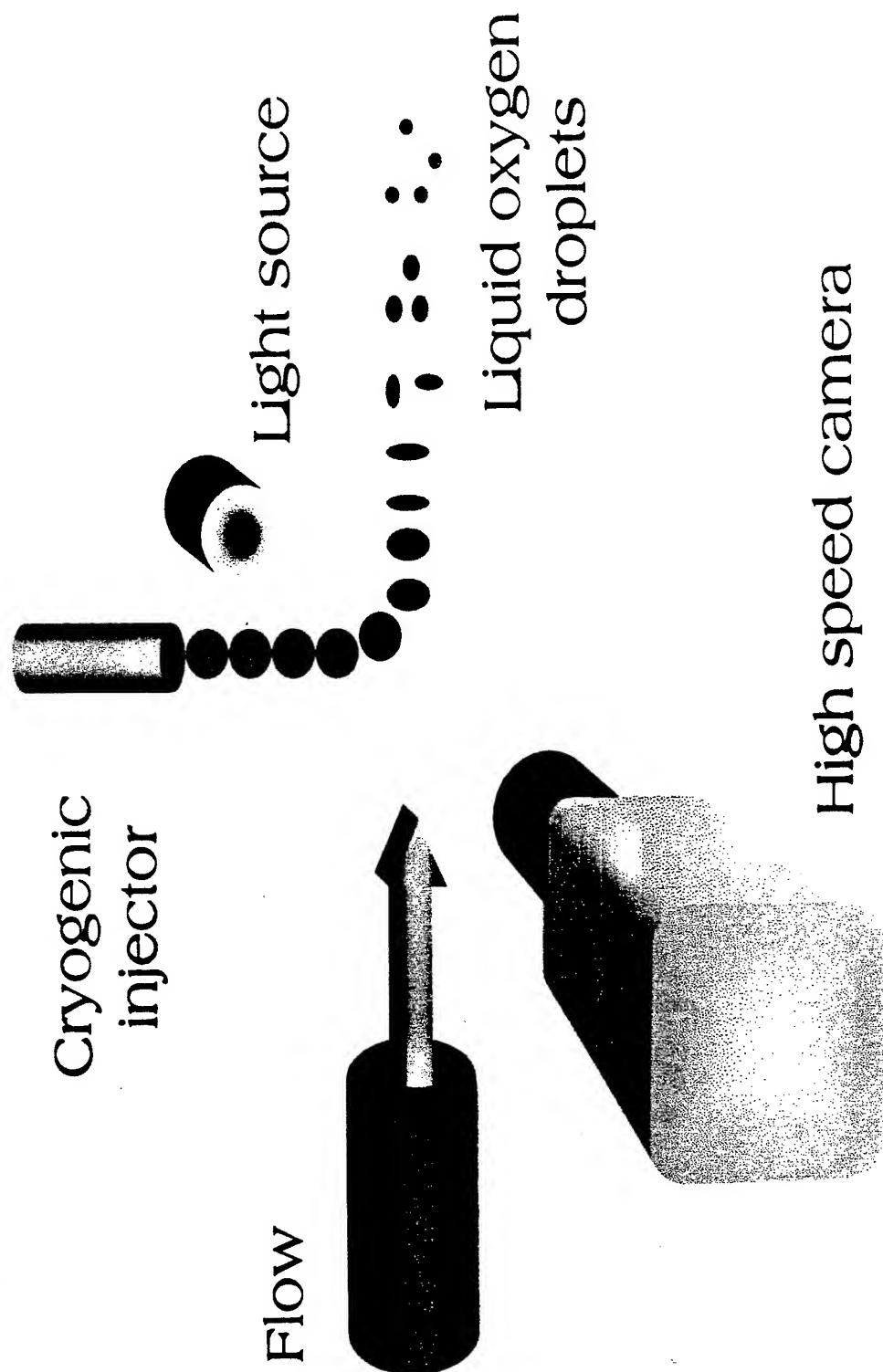
Temps de vaporisation :

- Reynolds turbulent $\frac{k^{1/2}d}{v_{\text{gaz}}}$
- Schmidt
- Schmidt turbulent $\frac{k^{1/2}L}{D_{12}}$
- Lewis
- Pression

Objectives

- To study the deformation and break-up regimes of liquid oxygen droplets subjected to aerodynamic shear forces under high pressure.
- To explore regimes in a very large range of the density ratio ($13 < \rho_l / \rho_g < 3500$) and of the droplet Weber and Reynolds numbers.
- To provide useful experimental data base to validate theoretical and numerical studies.

Droplet - jet interaction

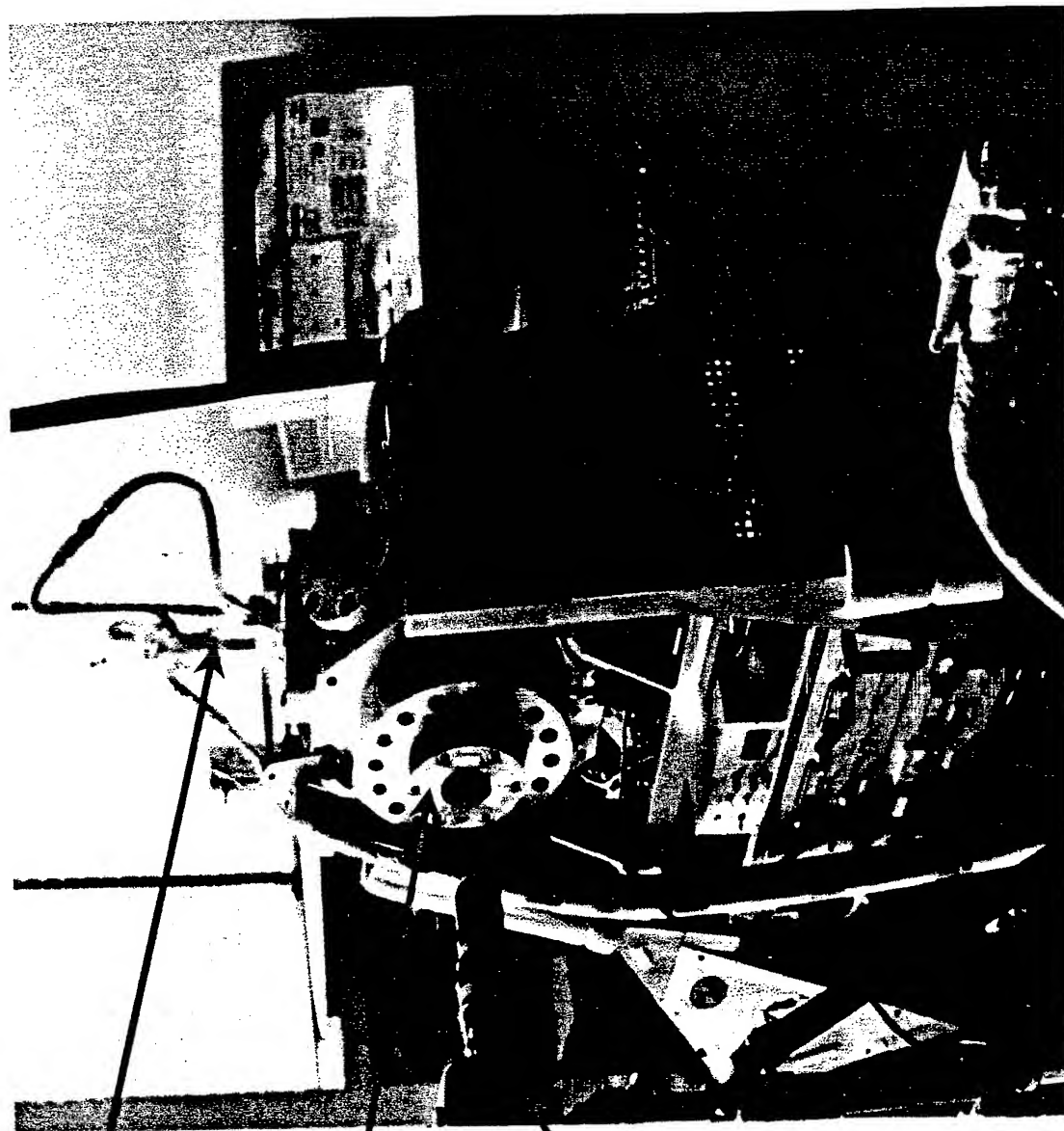


Experimental set-up

Cryogenic
injector

High pressure
chamber ($P_{\max} = 12 \text{ MPa}$)

Numerical high speed
camera (45 000 im/s)

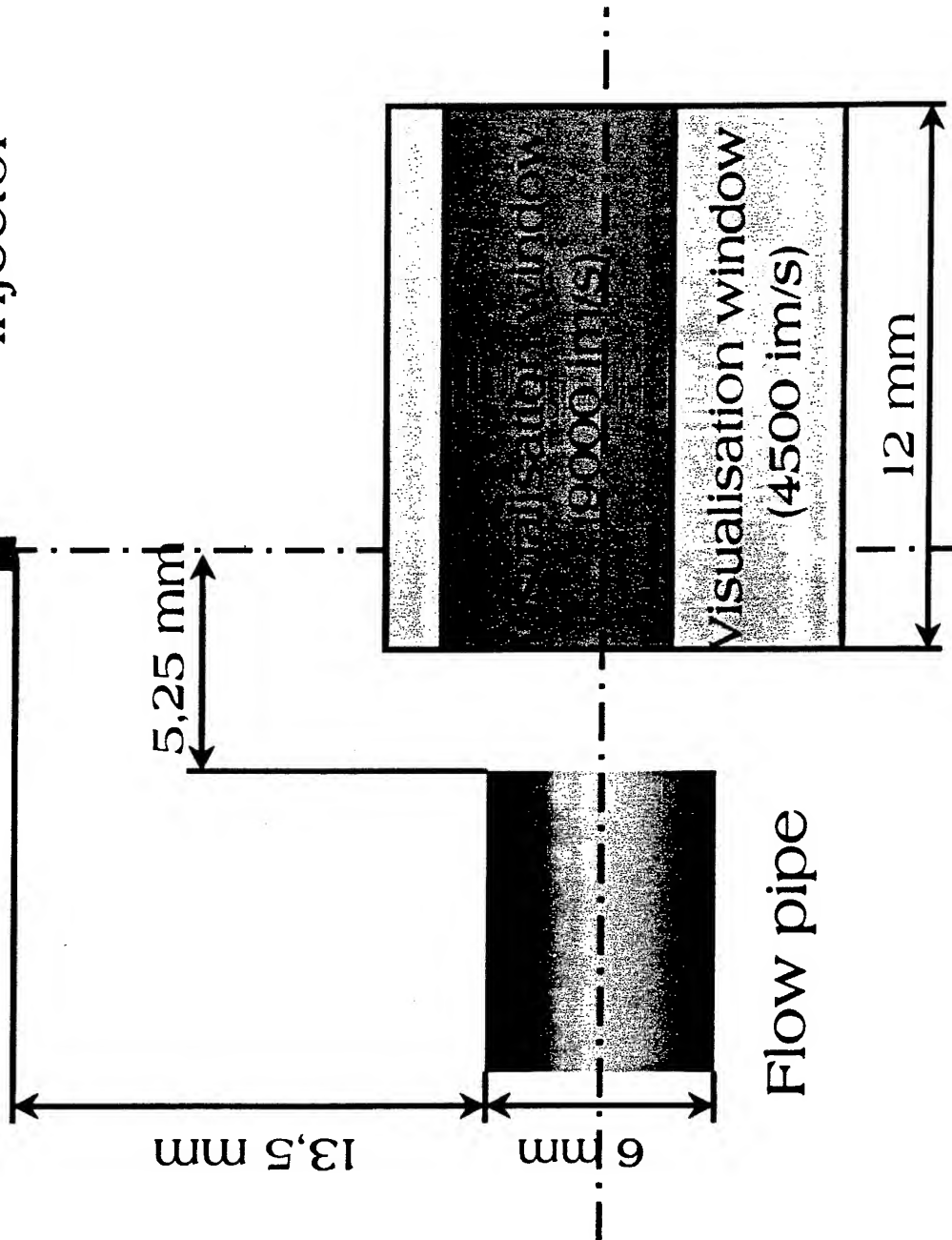


Diagnostics and image processing

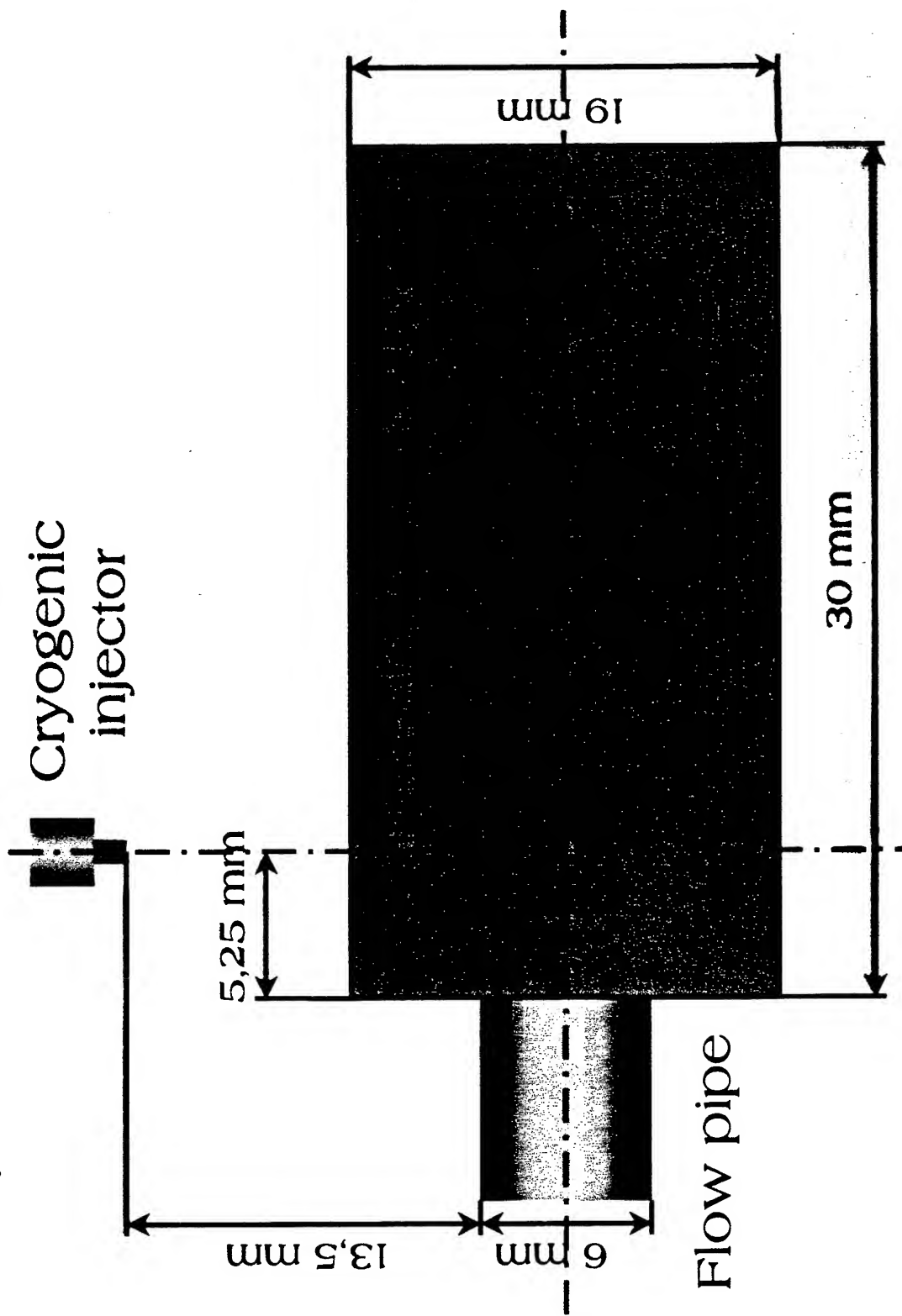
- Visualisation by numerical high speed camera up to 9000 images / second.
- Images processing based on Visilog software.
- Two components laser Doppler anemometry and particle image velocimetry for the characterisation of the aerodynamic field.

Exploration area by video camera

Cryogenic injector



Exploration area by PIV



Conditions explored for the aerodynamic field characterisation

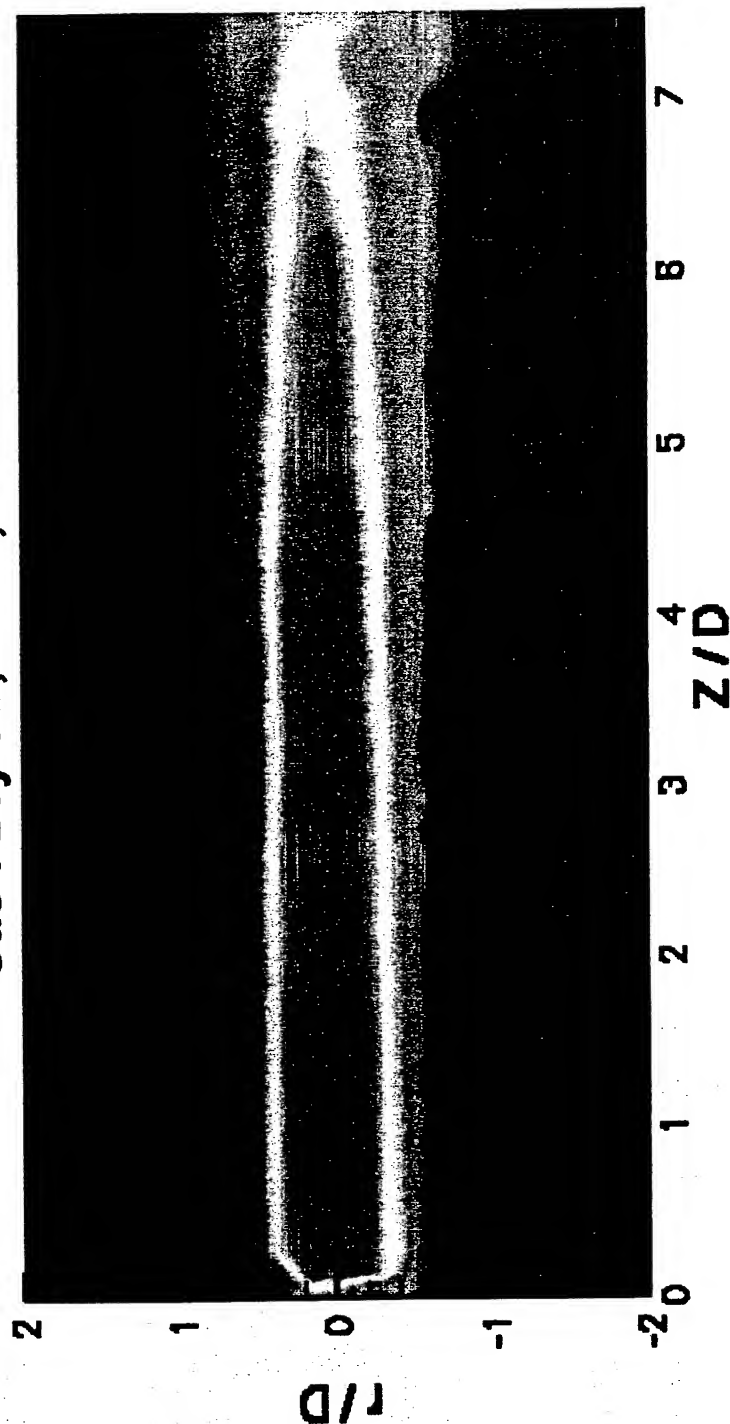
$$Re_{ec} = \frac{\rho_g U D}{\mu_g}, D : \text{flow pipe diameter}$$

Gas	Technique	Pressure (MPa)	Re_{ec}
Dry air	LDA	0,1 - 4	10000 - 30000
Helium	LDA	1	10000
Dry air	PIV	0,2 - 8	3000 - 9000

Aerodynamic field characterisation



Gas : Dry air, $P = 0,5 \text{ MPa}$



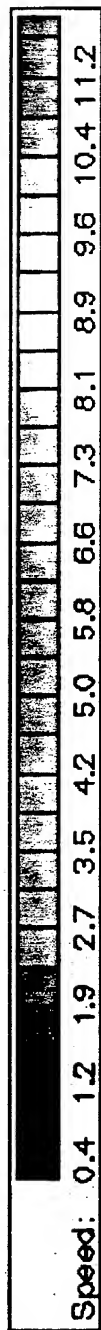
Conditions explored

$$DR = \frac{\rho_l}{\rho_g}, We = \frac{\rho_g U^2 D}{\sigma}, Re = \frac{\rho_g U D}{\mu_g}$$

D : initial droplet diameter

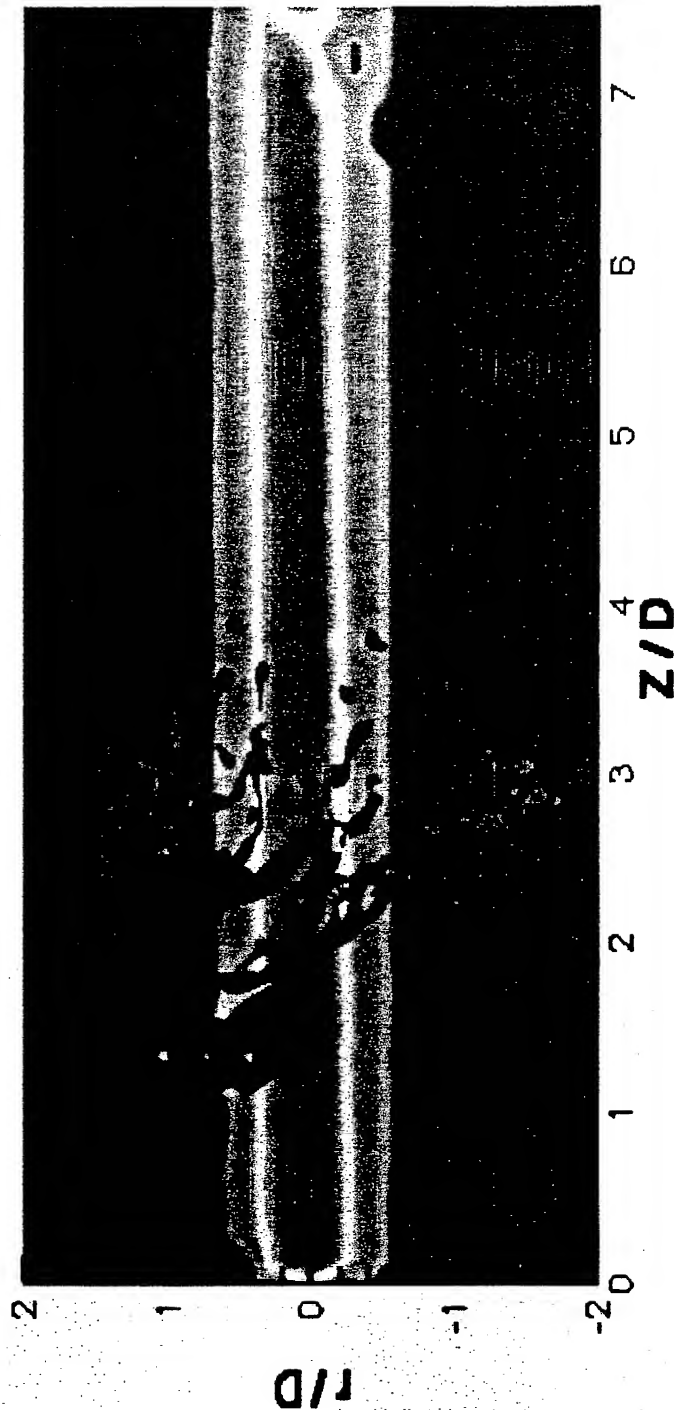
Liquid-gas couple	DR	We	Re
Ethanol / dry air	13 - 800	5 - 120	500 - 17000
Liquid oxygen / dry air	20 - 1030	2 - 850	600 - 7500
Liquid oxygen / helium	63 - 3500	1 - 180	320 - 3300

Superposition of the aerodynamic field and droplet break-up images

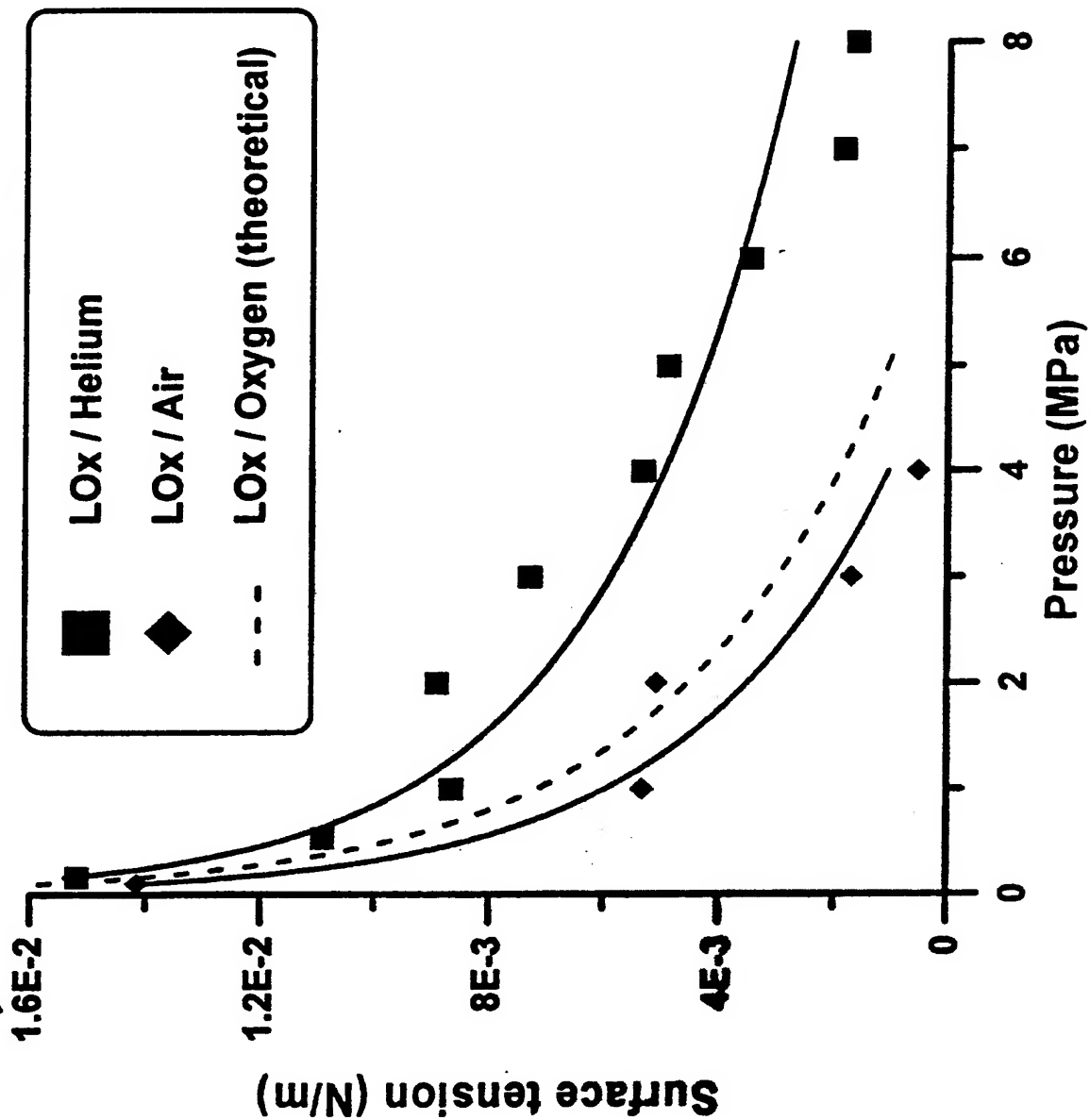


Liquid oxygen / Helium couple

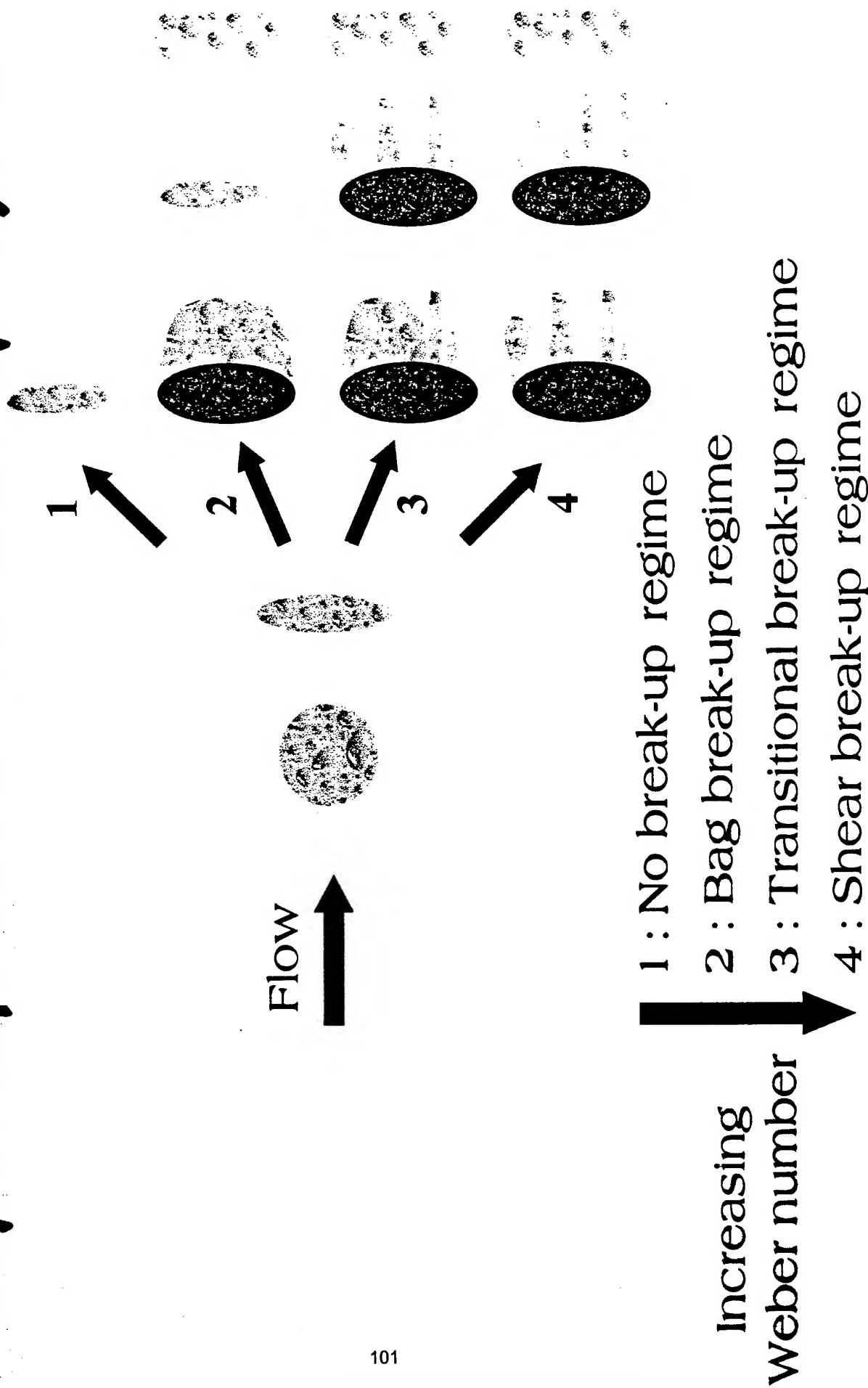
$P = 0,2 \text{ MPa}$, $We = 18$, $Re = 660$



Surface tension measurement



Droplet deformation and break-up regimes



Images for the LOx / Dry air couple

$P = 0,1 \text{ MPa}$, $DR = 1200$, $We = 48$, $Re = 1800$

Time between two images = $0,5 \text{ ms}$

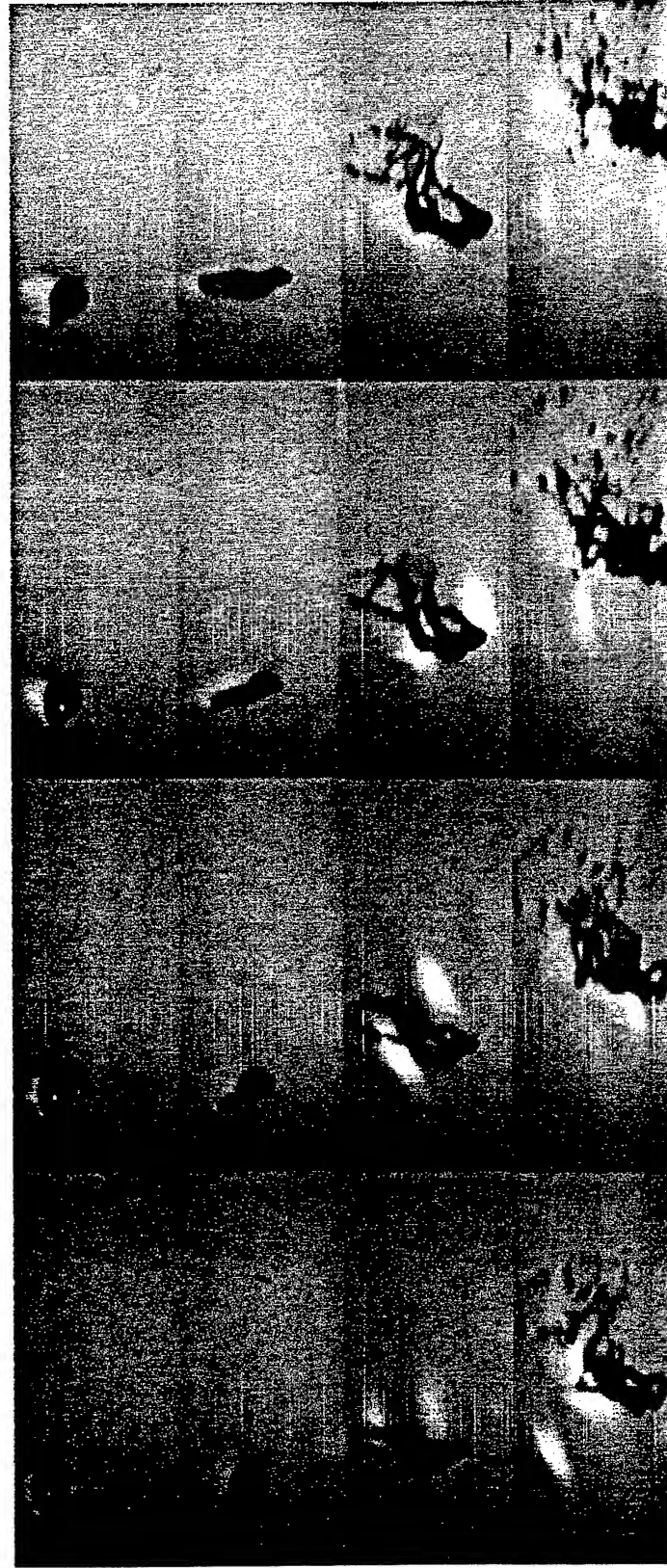
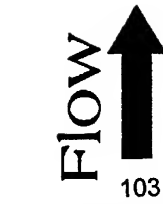
Flow
↑
102



Images for the L0x / Helium couple

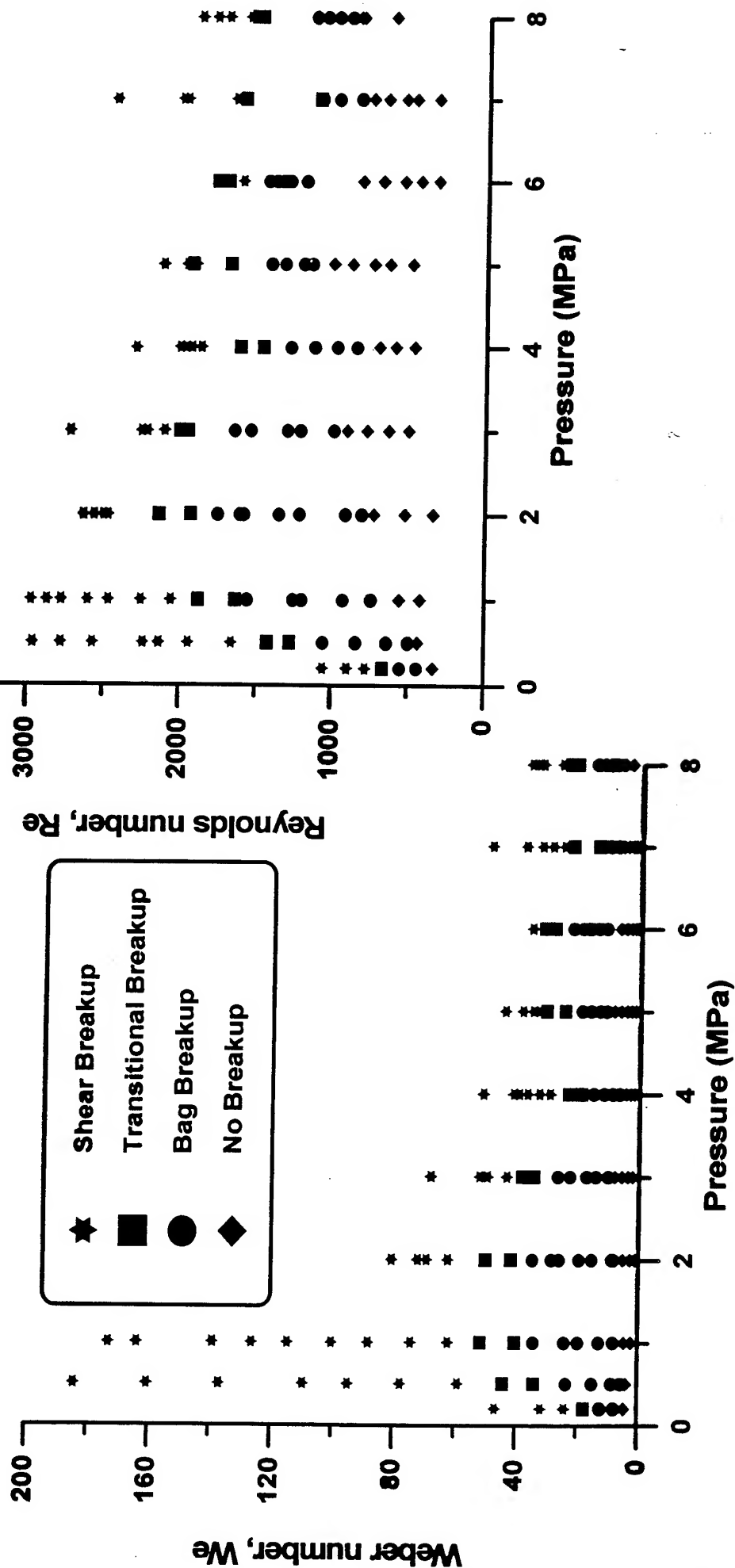
P = 2 MPa, DR = 350, We = 19, Re = 1350

Time between two images = 0,5 ms

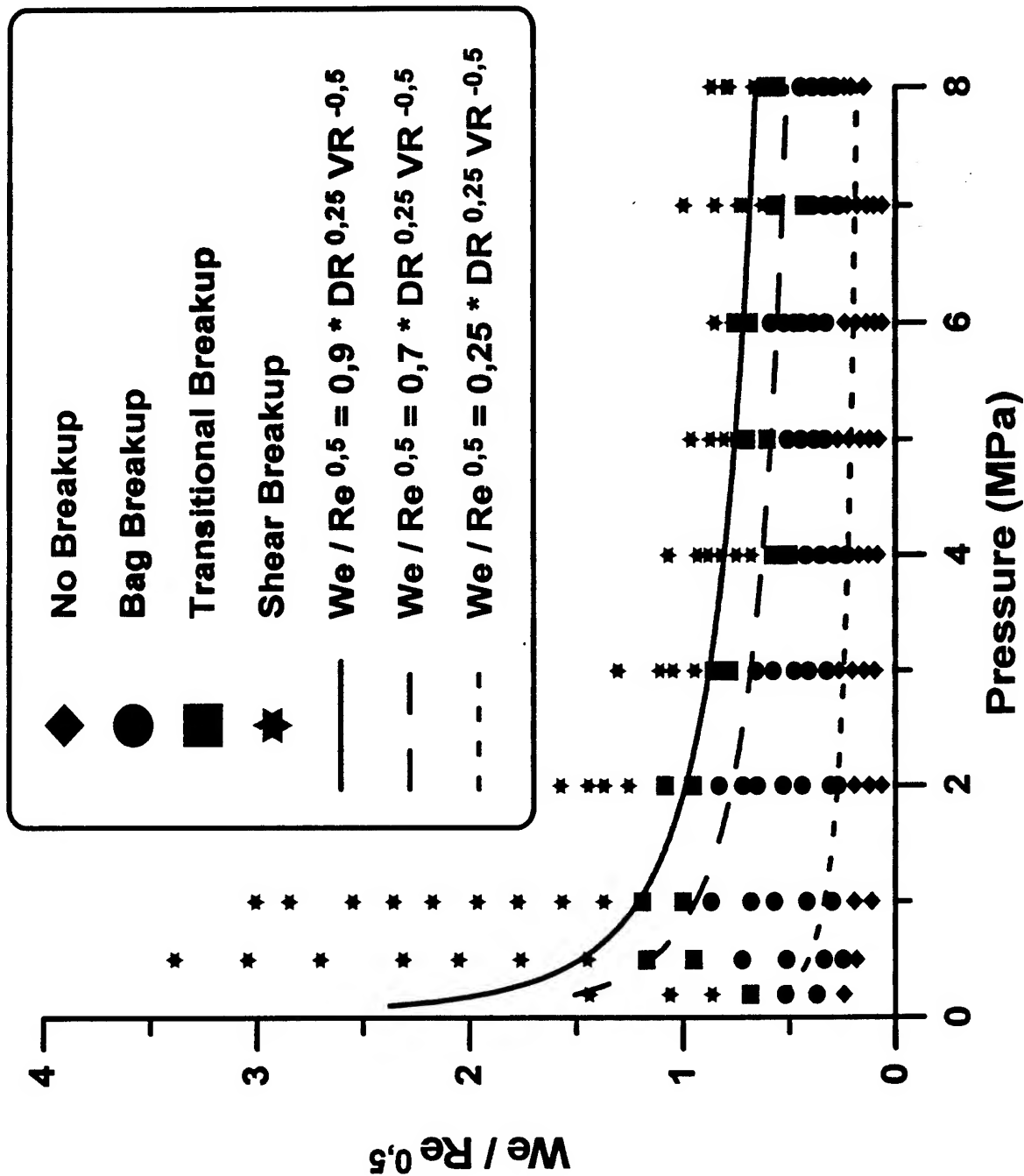


(p , We) and (p , Re) maps of the droplet deformation and break-up regimes

LOx / Helium couple

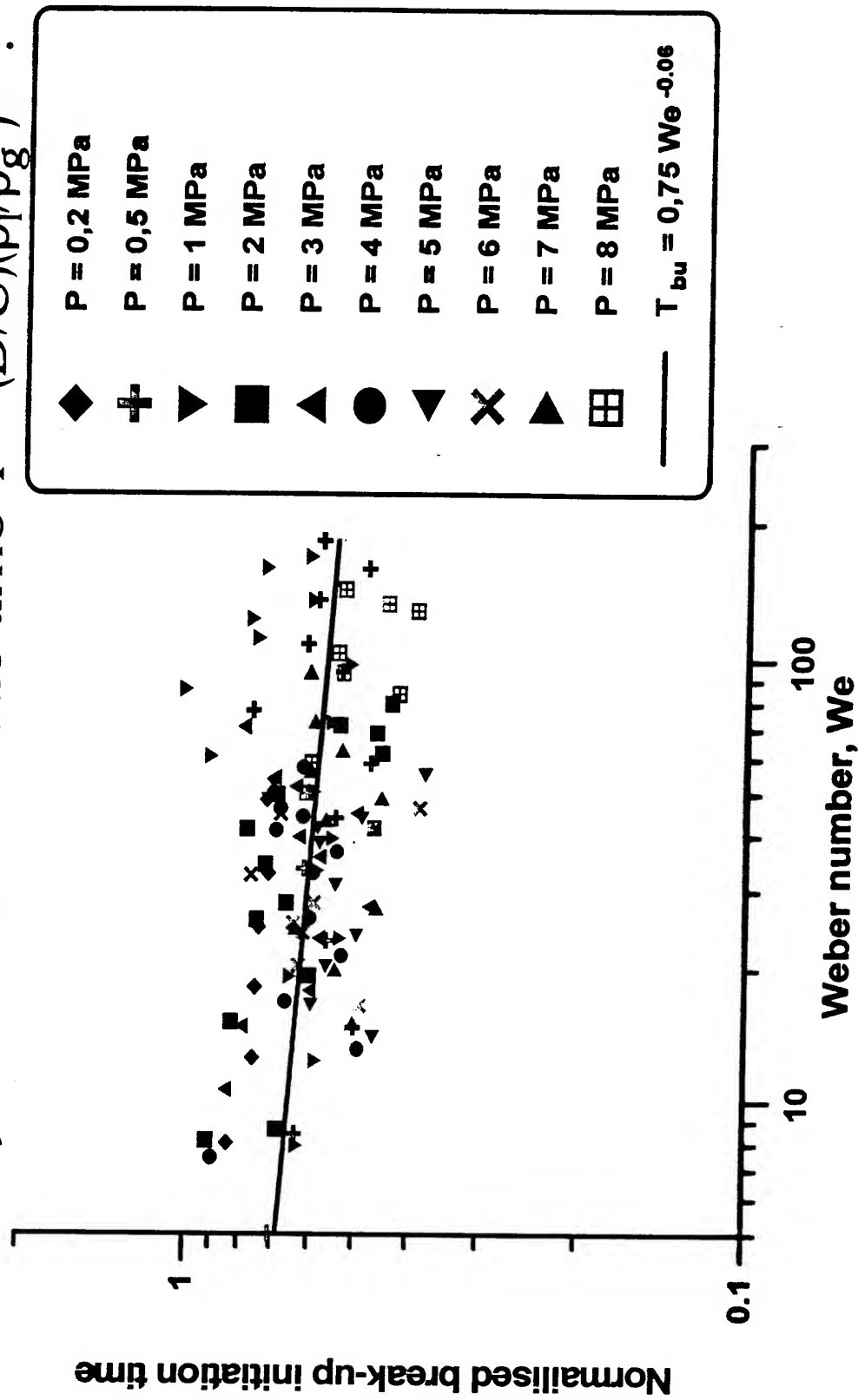


New correlation for the regime transitions

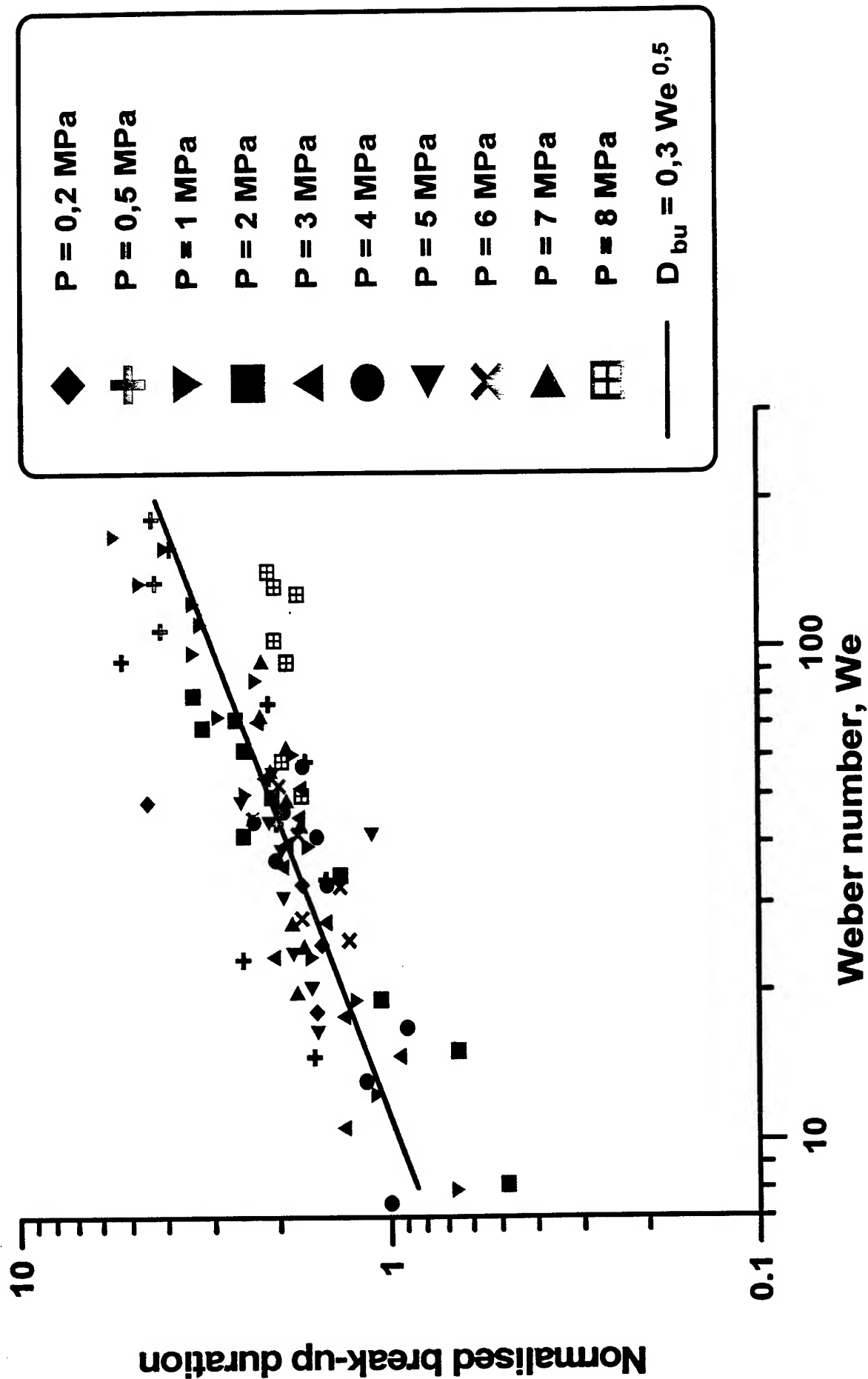


Normalised break-up initiation time

- Break-up initiation time measurements with images processing.
- Normalisation by the characteristic time $T = (D/U)(\rho_l/\rho_g)^{1/2}$.



Normalised break-up duration

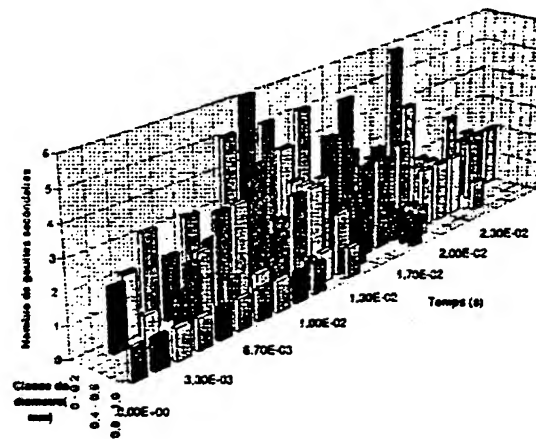


Nombre et taille des gouttes secondaires :

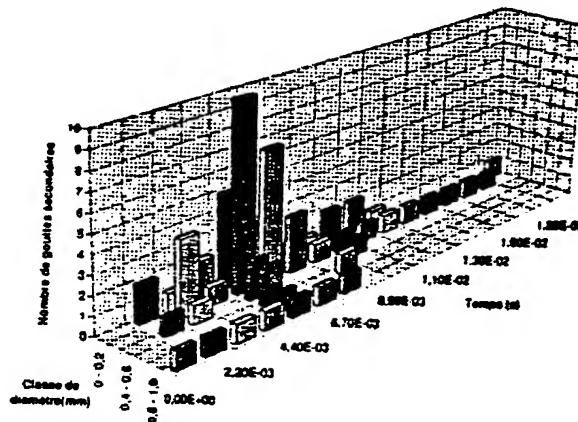
- difficile à déterminer expérimentalement
- résultats des différents auteurs peu concordants

Quelques résultats au L.C.S.R., mais plage de paramètres restreinte

→ pas de corrélation, mais tabulation et interpolation possible



oxygène liquide / hélium ($P = 0.5 \text{ MPa}$; $We = 137$; $Re = 2570$; $D_0 = 1.89 \text{ mm}$)



oxygène liquide / hélium ($P = 0.5 \text{ MPa}$; $We = 78$; $Re = 1940$; $D_0 = 1.90 \text{ mm}$)

Conclusions (1)

- An experimental system has been developed to investigate droplet-jet interaction regimes under various velocity and pressure conditions.
- About the atomisation regimes, the Weber number seems to be the relevant parameter for their apparitions.
- The transitions between different regimes are correctly predicted by correlation based on density and viscosity ratio.

Conclusions (2)

- For the normalised break-up initiation time, a law based on Weber number and density ratio is underlined.
- For the normalised break-up total time, its evolution follows a law $We^{0.25}$.
- The normalised break-up duration increases with $We^{0.5}$.

Financial support

Centre National de la Recherche Scientifique (CNRS)

Centre National d'Etudes Spatiales (CNES)

SEP (Snecma Division)

French Research Group 'Combustion in the Rocket
Engines'

Modeling of Supercritical Droplet and Spray Combustion

Vigor Yang
Propulsion Engineering Research Center
The Pennsylvania State University
University Park, Pennsylvania 16802, U.S.A.

phone: (814) 863-1502 fax: (814) 865-3389
email: vigor@psu.edu

Acknowledgment

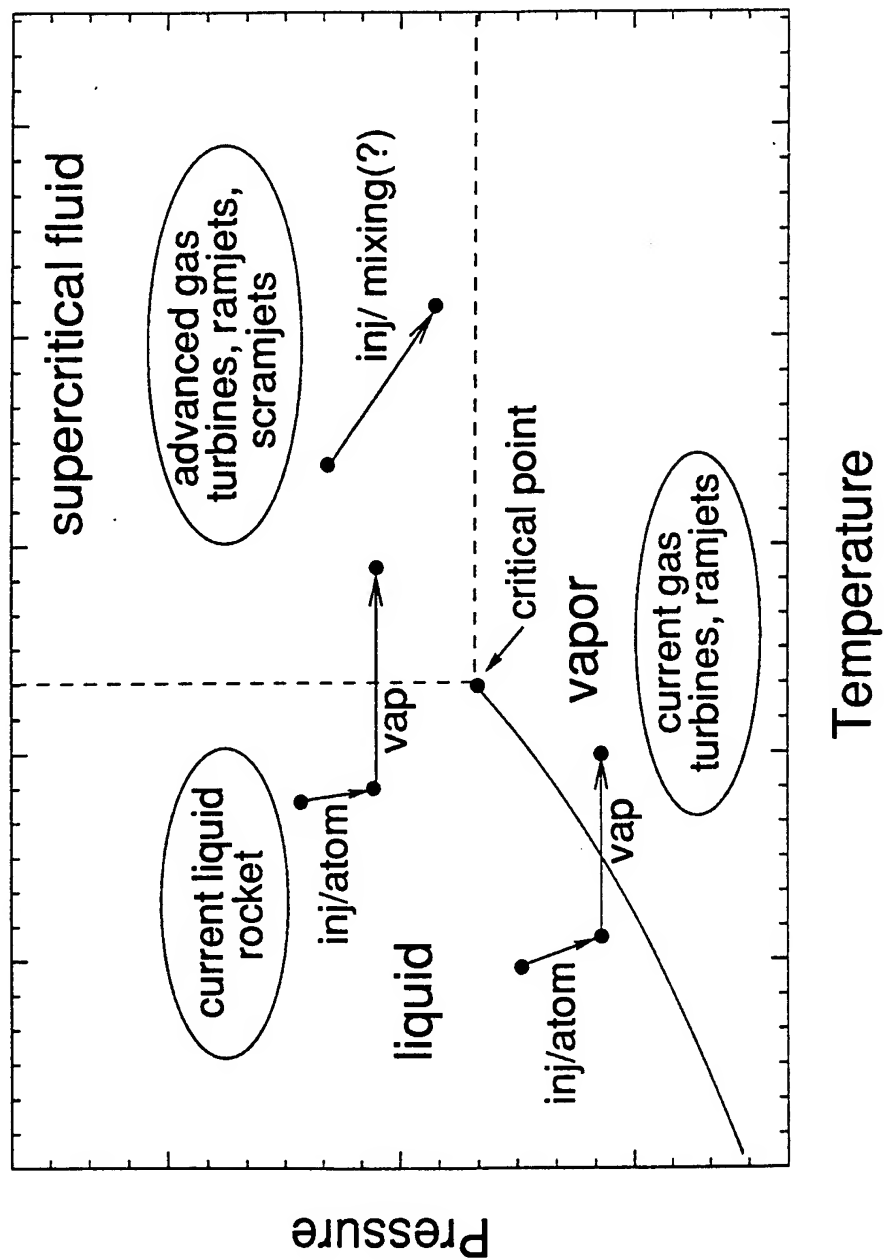
- Air Force Office of Scientific Research
- NASA Marshall Space Flight Center
- Penn State Propulsion Engineering Research Center

Collaboration

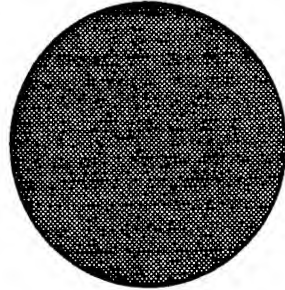
- Air Force Research Laboratory
- NASA Lewis (Glenn) Research Center
- l'Office National d'Etudes et de Recherches Aéronautiques

- thermodynamics
- transport phenomena
- droplet vaporization, combustion, and dynamics
- spray combustion
- mixing and flame holding/spreading

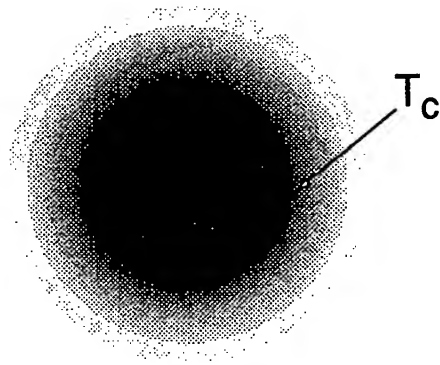
ADVANCED AIRBREATHING AND ROCKET ENGINES



Subcritical Droplet Vaporization



Supercritical Droplet Gasification



- Transient Diffusion
- Thermodynamic Non-ideality
- Property Variation
- Ambient Gas Solubility

SUPERCRITICAL DROPLET COMBUSTION AND DYNAMICS

- Property evaluation techniques and constitutive relations
- Droplet vaporization, combustion, and dynamics in convective environments
- Dynamic responses of droplet vaporization and combustion to ambient flow oscillations

Thermophysical Properties and Constitutive Relations

- Equations of state (p - v - T)
- Thermodynamic properties (e , h , s)
- Transport properties (μ , λ , D)

EQUATIONS OF STATE

- Soave-Redlich-Kwong (SRK)

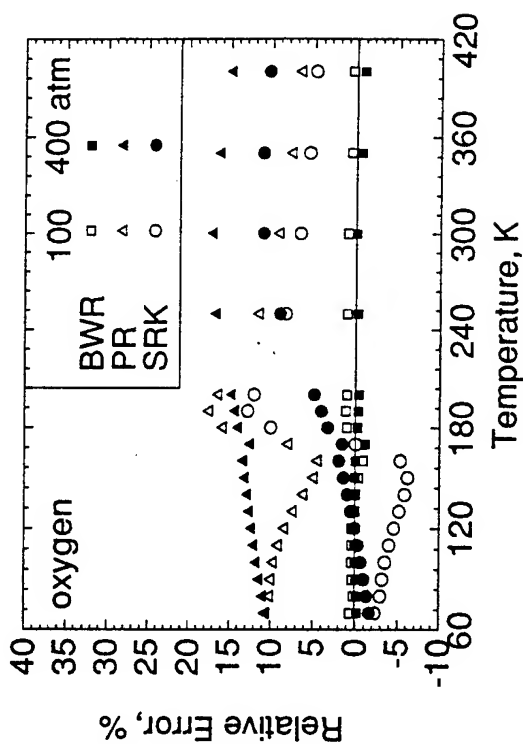
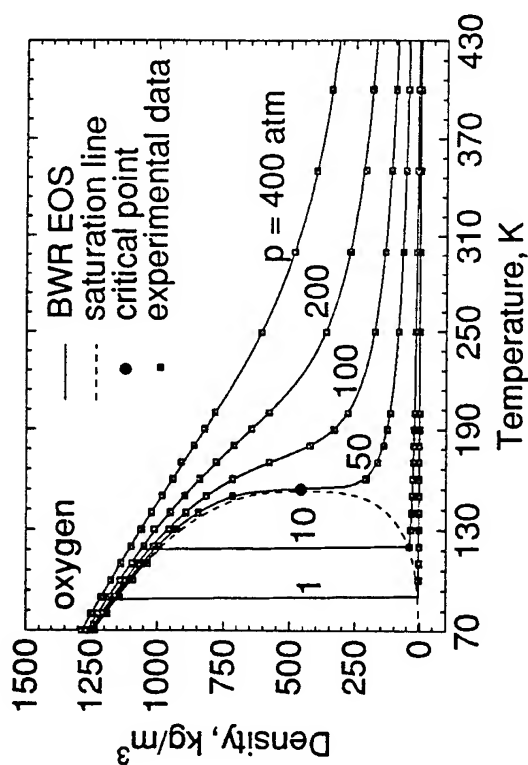
$$p = \frac{RT}{v-b} - \frac{a}{v(v+b)}$$

- Peng-Rubinson (PR)

$$p = \frac{RT}{v-b} - \frac{a}{v(v+b) + b(v-b)}$$

- Benedict-Webb-Rubin (BWR)

$$p = \sum_{n=1}^9 a_n \rho^n + \sum_{n=10}^{15} a_n \rho^{2n-17} e^{-\gamma \rho^2}$$



Evaluation of Thermodynamic Properties

- sensible enthalpy : $h(\rho, T) = h^0(T) + \Delta h_{exc}(\rho, T)$
- internal energy : $u(\rho, T) = u^0(T) + \Delta u_{exc}(\rho, T)$
- specific heat : $C_p(\rho, T) = C_p^0(T) + \Delta C_{p_{exc}}(\rho, T)$

where

$h^0(T), u^0(T), C_p^0(T) =$ values in dilute – gas limit

$\Delta h_{exc}, \Delta u_{exc}, \Delta C_{p_{exc}} =$ dense fluid corrections

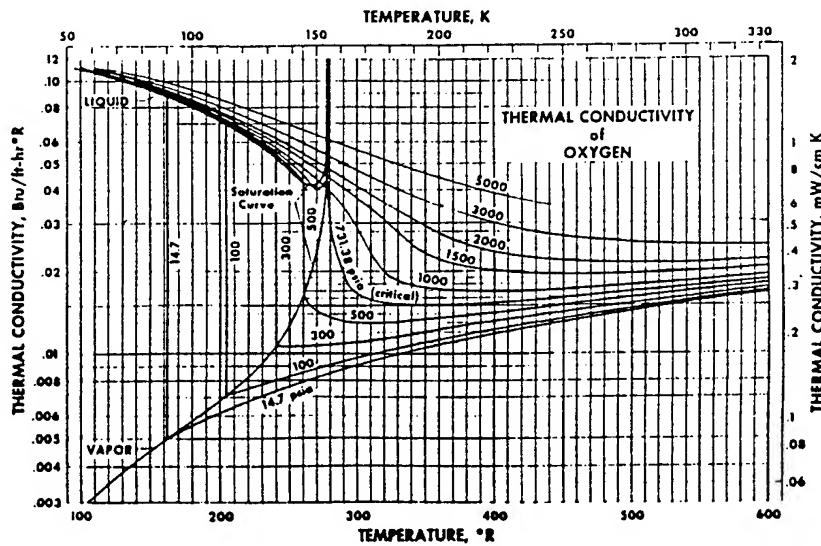
Pressure-explicit type of EOS:

$$\Delta h_{exc} = \int_0^p \left[\frac{p}{\rho^2} - \frac{T}{\rho^2} \left(\frac{\partial p}{\partial T} \right)_\rho \right] d\rho + RT(Z - 1)$$

$$\Delta u_{exc} = \int_0^p \left[\frac{p}{\rho^2} - \frac{T}{\rho^2} \left(\frac{\partial p}{\partial T} \right)_\rho \right] d\rho$$

$$\Delta C_{p_{exc}} = -T \int_0^p \frac{1}{\rho^2} \left(\frac{\partial^2 p}{\partial T^2} \right) d\rho + \frac{T(\partial p / \partial T)_\rho^2}{\rho^2 (\partial p / \partial \rho)_T} - R$$

Transport Properties of a Pure Substance

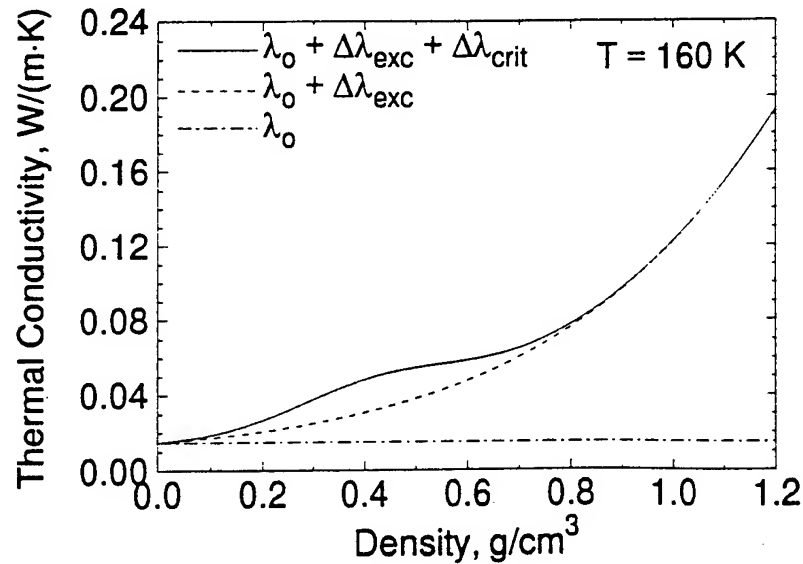


$$\lambda(\rho, T) = \lambda_0(T) + \Delta\lambda_{\text{exc}}(\rho, T) + \Delta\lambda_{\text{crit}}(\rho, T)$$

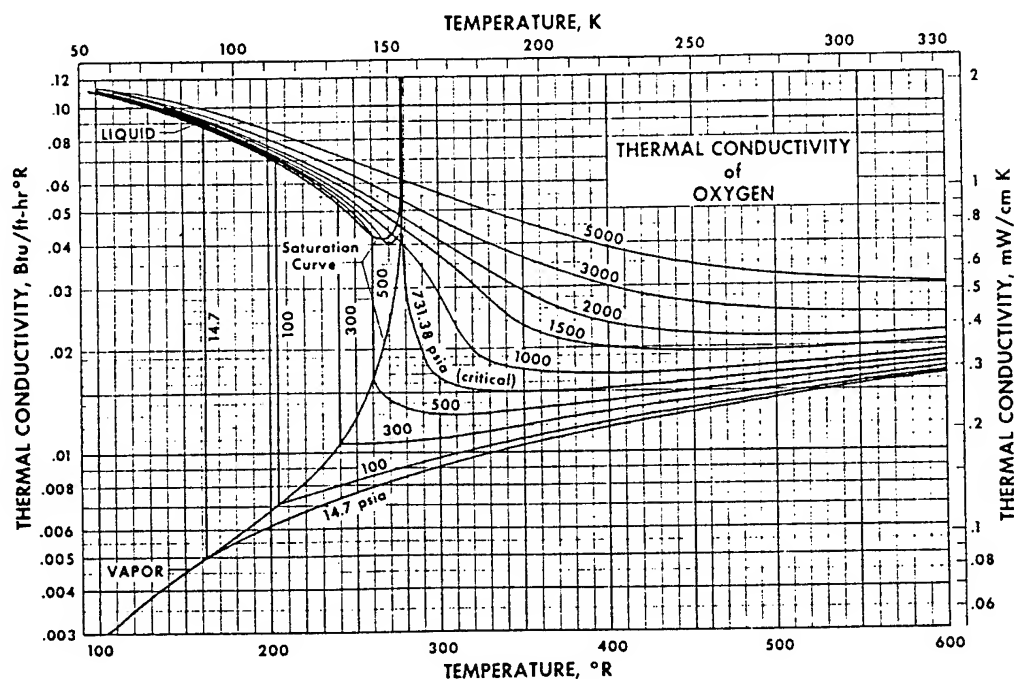
where λ_0 = dilute gas limit

$\Delta\lambda_{\text{exc}}$ = dense fluid correction

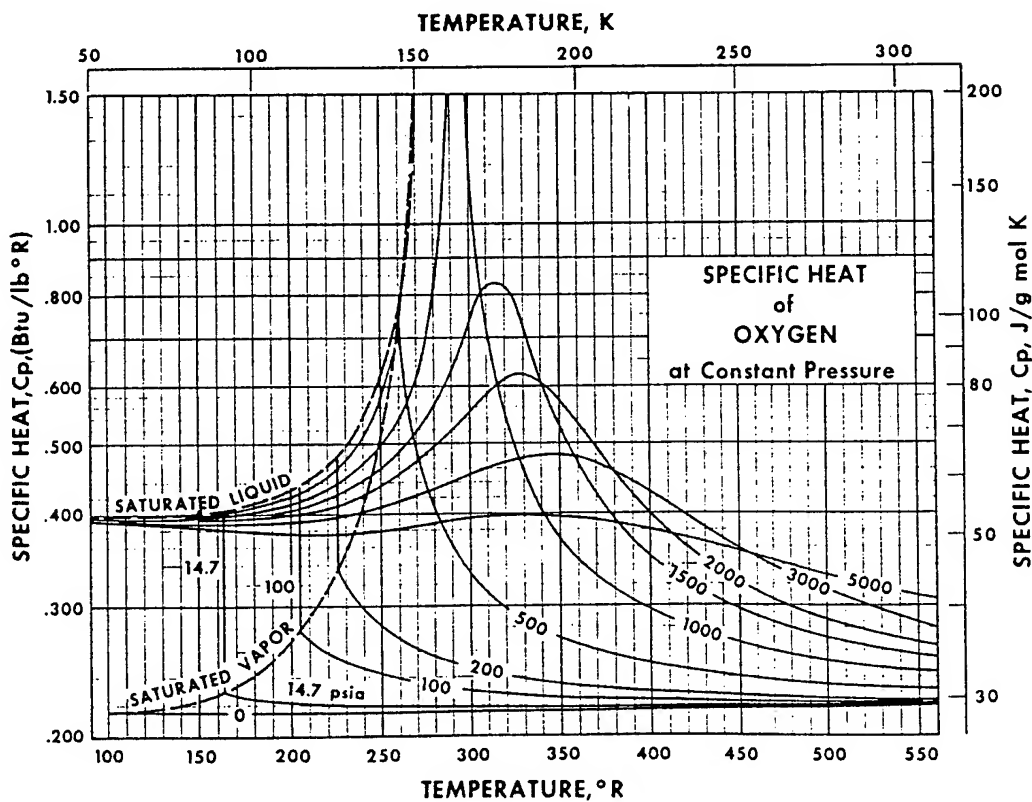
$\Delta\lambda_{\text{crit}}$ = critical enhancement



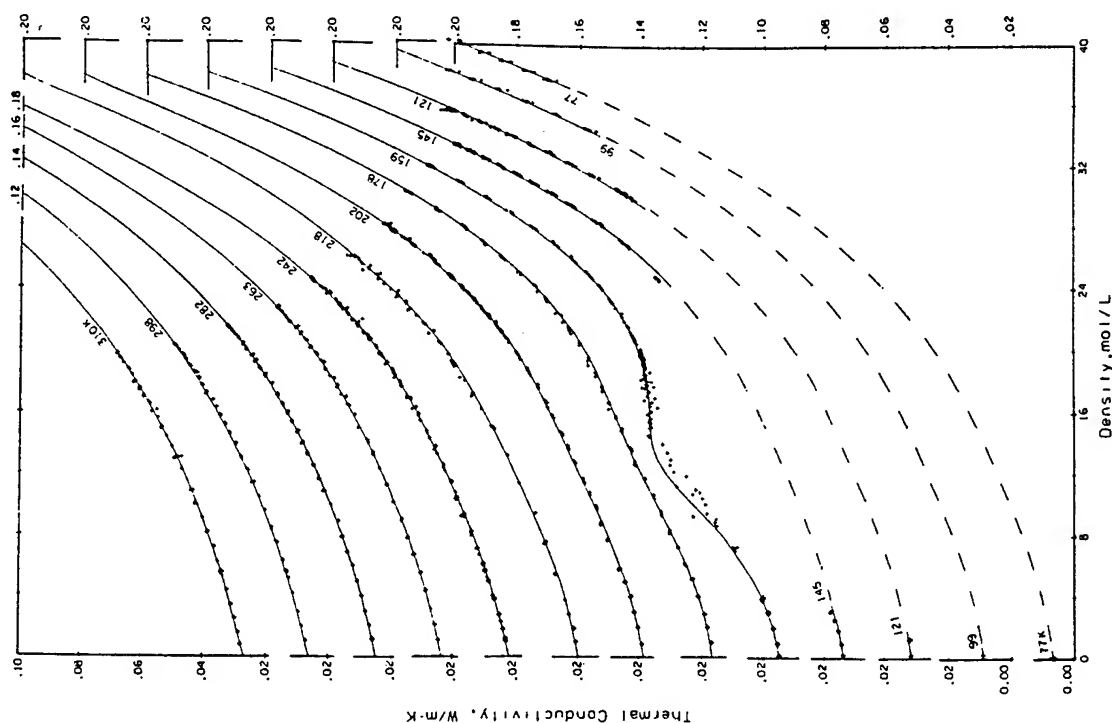
THERMAL CONDUCTIVITY OF OXYGEN



SPECIFIC HEAT OF OXYGEN



Correlation of Properties in terms of Density and Temperature

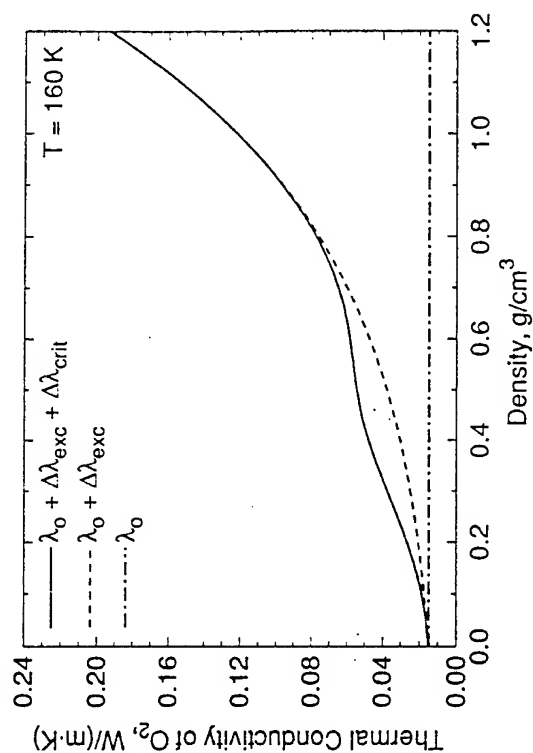


$$\lambda(\rho, T) = \lambda_0(T) + \Delta\lambda_{\text{exc}}(\rho, T) + \Delta\lambda_{\text{crit}}(\rho, T)$$

where λ_0 = dilute gas limit

$\Delta\lambda_{\text{exc}}$ = dense fluid correction

$\Delta\lambda_{\text{crit}}$ = critical enhancement

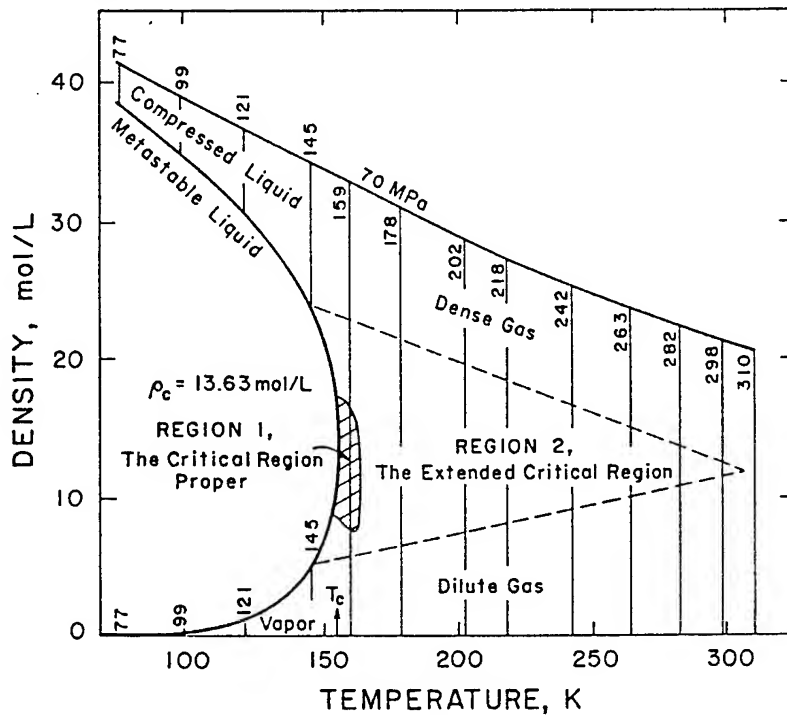


Critical Enhancement of Transport Properties

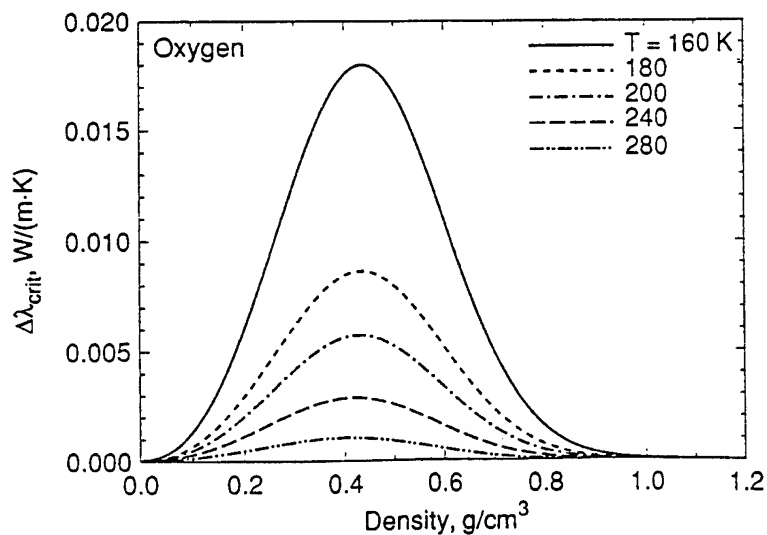
- Critical Region Proper : $|\Delta T^*| \leq 0.03$, $|\Delta \rho^*| \leq 0.25$

$$\Delta T^* = (T - T_c)/T_c \quad \text{and} \quad \Delta \rho^* = (\rho - \rho_c)/\rho_c$$

- Extended Critical Region



- Critical Enhancement of Thermal Conductivity

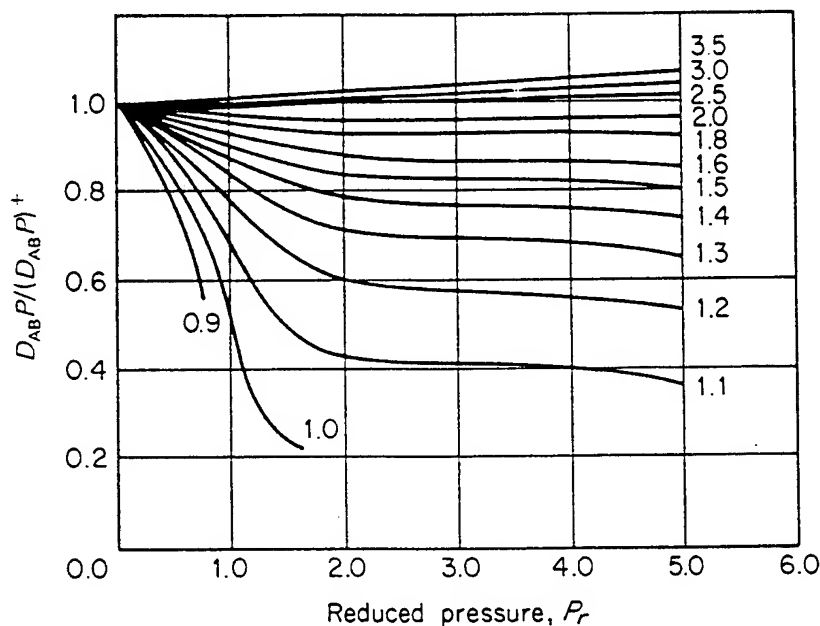


PROPERTY EVALUATION FOR MIXTURES

- Extended Corresponding-State Principle
 - Density based scheme
$$\eta_x(\rho, T) = \eta_0(\rho_0, T_0)F_\eta$$
 - BWR EOS for density at given pressure and temperature
 - Mapping function determined by
 - critical properties
 - Pitzer's acentric factor
 - Reference fluids based on methane or propane

Mass Diffusivity for Multicomponent Mixture

- Determine Binary Mass Diffusivity
 - Chapman-Enskog theory with Lennard-Jones intermolecular potential energy function
 - Corrected by the corresponding state approach of Takahashi



- Apply the mixing rule

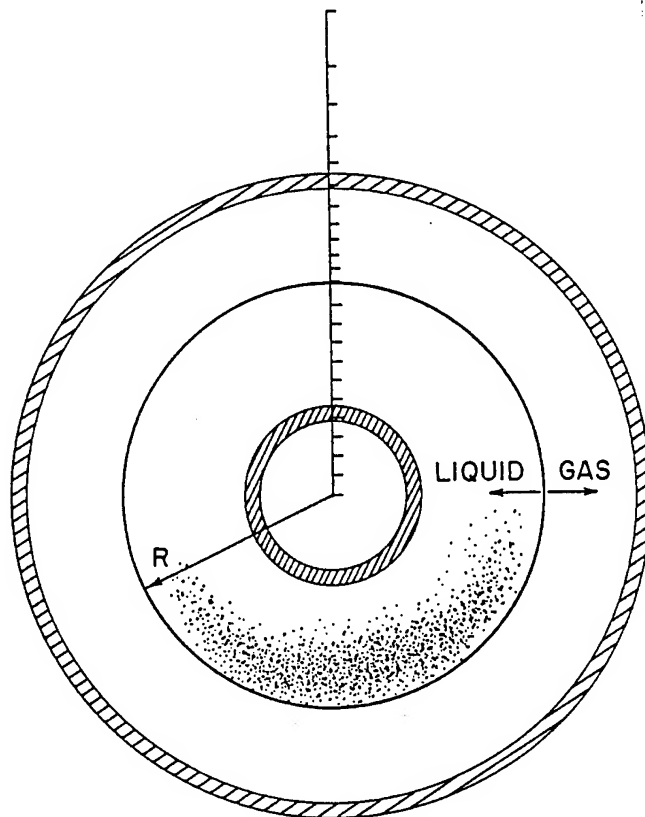
$$D_{im} = (1 - X_i) / \sum_{j \neq i}^N (X_j D_{ij}), \quad i=1, \dots, N$$

Droplet Vaporization and Combustion in Quiescent Environments

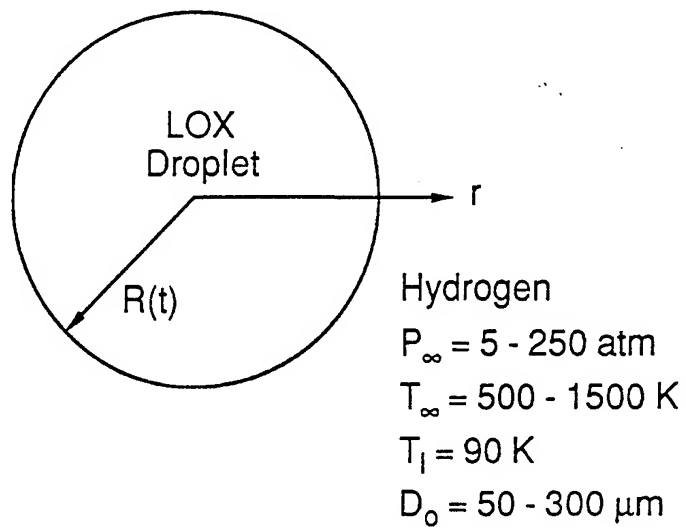
- **Liquid Oxygen (LOX) Droplet Vaporization in Gaseous Hydrogen**
5 < P_{∞} < 300 atm
500 < T_{∞} < 2500 K
50 < D_0 < 300 μm
- **Hydrocarbon Droplet Vaporization and Combustion in Air**
5 < P_{∞} < 200 atm
300 < T_{∞} < 2500 K
100 < D_0 < 1000 μm
- **Unsymmetrical Dimethylhydrazine (UDMH) Droplet Vaporization and Decomposition Combustion**
1 < P_{∞} < 180 atm

THEORETICAL FORMULATION

- Complete Time-Dependent Conservation Equations for Both Gas and Liquid Phases
 - mass
 - momentum
 - energy
 - species concentration
- Finite-Rate Chemical Kinetics for Gas-Phase Reaction
- Matching of Droplet Behavior with Ambient Gases
 - Continuities of mass and energy
 - Phase equilibrium



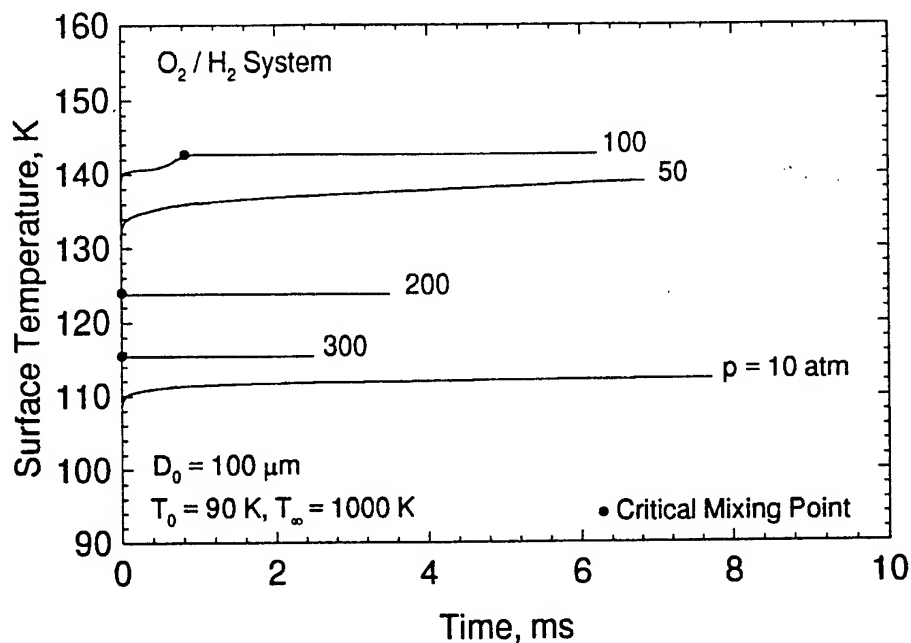
VAPORIZATION OF LOX DROPLET IN HYDROGEN FOR PRESSURES OF 5 - 250 atm



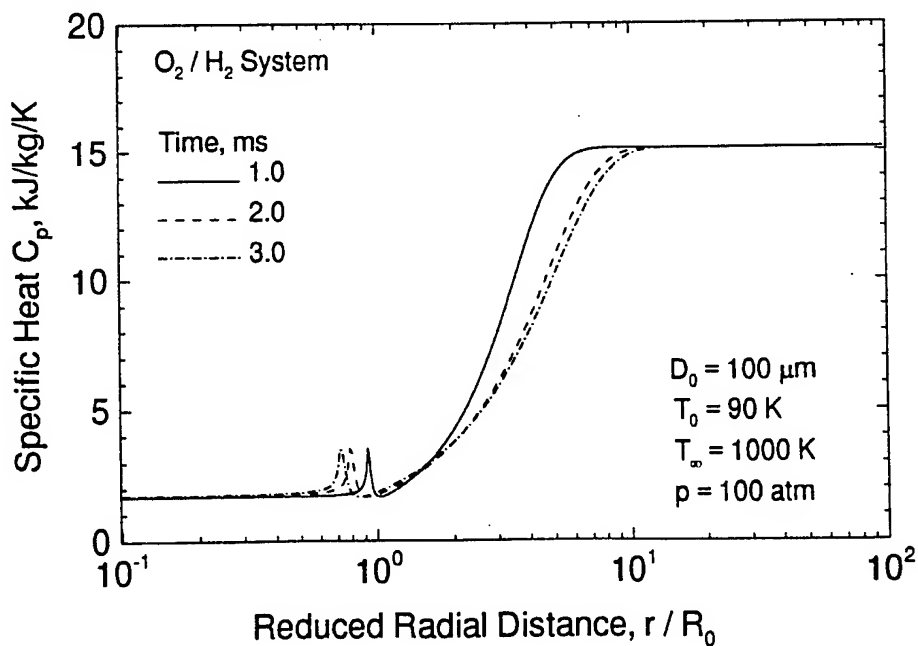
CRITICAL PROPERTIES OF OXYGEN AND HYDROGEN

	$T_c \text{ (K)}$	$P_c \text{ (atm)}$	$v_c \text{ (cm}^3\text{/g)}$	Z_c
OXYGEN	154.6	49.74	2.294	0.288
HYDROGEN	33.2	12.96	32.292	0.306

Time History of Droplet Surface Temperature

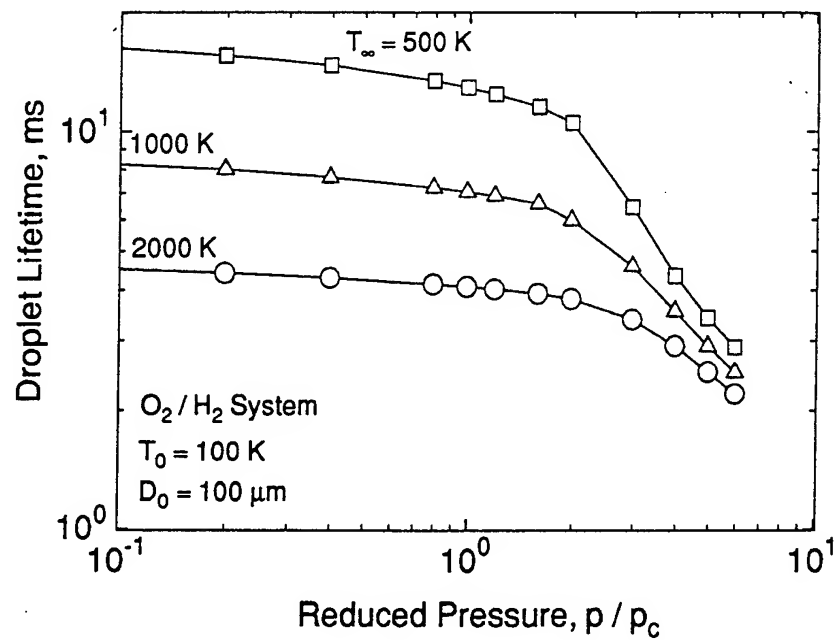


Distribution of Mixture Specific Heat



Effect of Pressure on Droplet Lifetime

$$500 < T_{\infty} < 2000 \text{ K}, 5 < p_{\infty} < 300 \text{ atm}$$



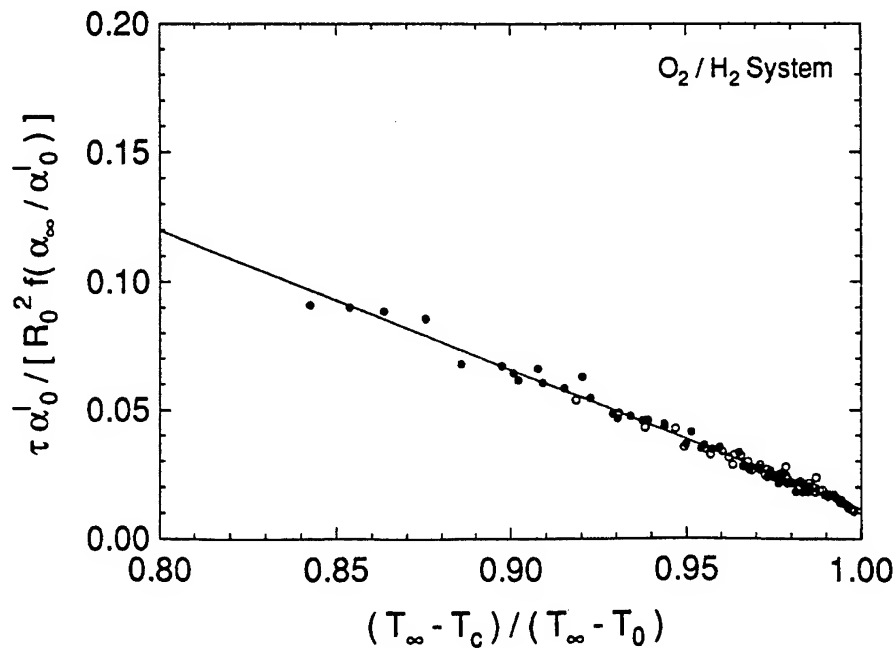
- Enthalpy of vaporization decreases with pressure
⇒ Enhancement of vaporization in subcritical regime
- Critical mixing temperature decreases with pressure
+ Gaseous thermal conductivity increases with pressure
⇒ Enhancement of vaporization in supercritical regime

Correlation of Droplet Lifetime

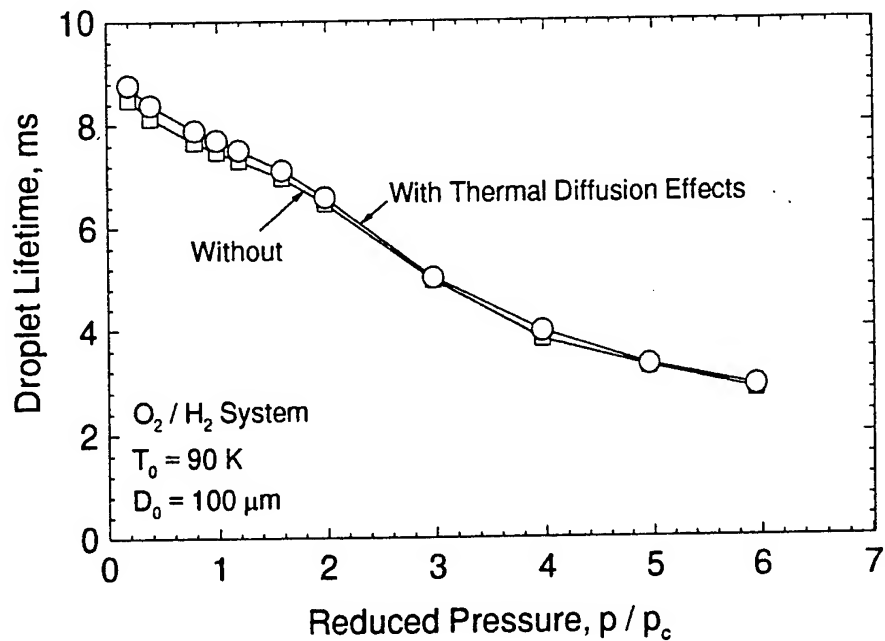
- Processes dominated by thermal diffusion in supercritical regime
- Simplified analysis based on thermal diffusion equation in terms of
 - thermal diffusivity α
 - initial droplet radius squared R_0^2
 - transfer number $(T_\infty - T_c) / (T_\infty - T_o)$
- Correlation of reduced droplet lifetime

$$\tau \frac{\alpha_o^l}{R_o^2} = \left[0.0115 + 0.542 \left(1 - \frac{T_\infty - T_c}{T_\infty - T_o} \right) \right] f \left(\frac{\alpha_\infty}{\alpha_o^l} \right)$$

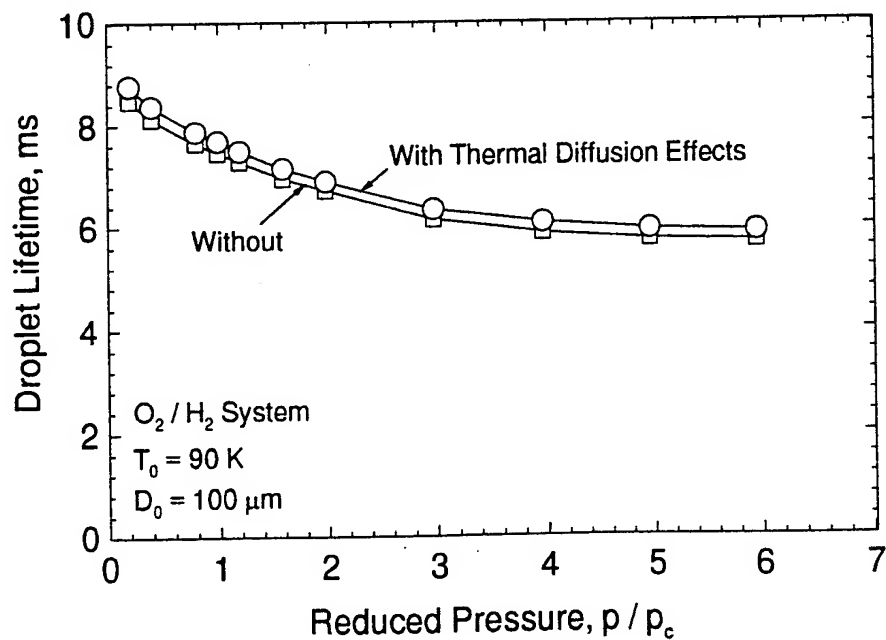
$$\text{where } f \left(\frac{\alpha_\infty}{\alpha_o^l} \right) = 1 + 3.9 \left[1 - \exp \left(-0.035 \left(\frac{\alpha_\infty}{\alpha_o^l} - 1 \right) \right) \right]$$



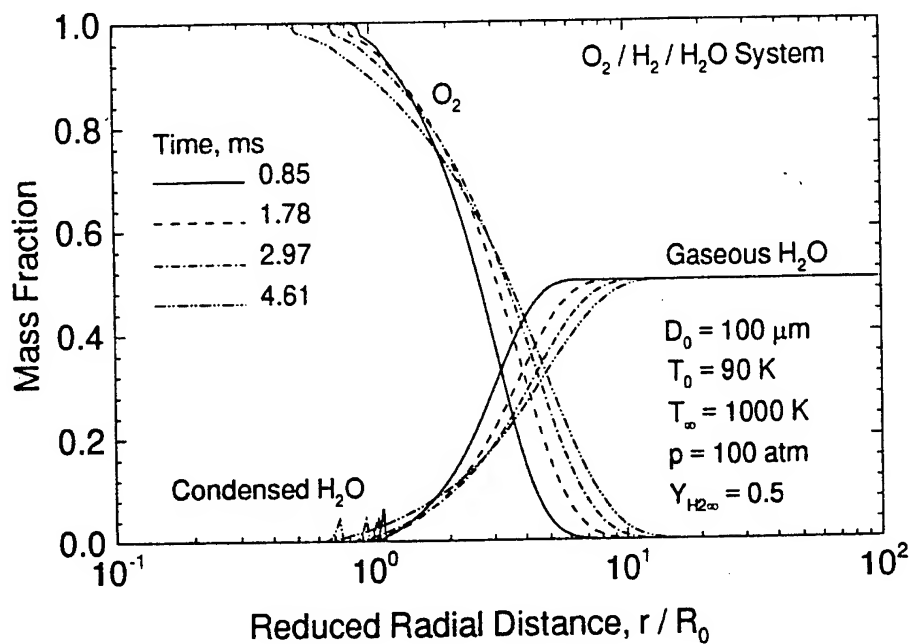
Effect of Thermal Diffusion on Droplet Lifetime (Critical Mixing Temperature)



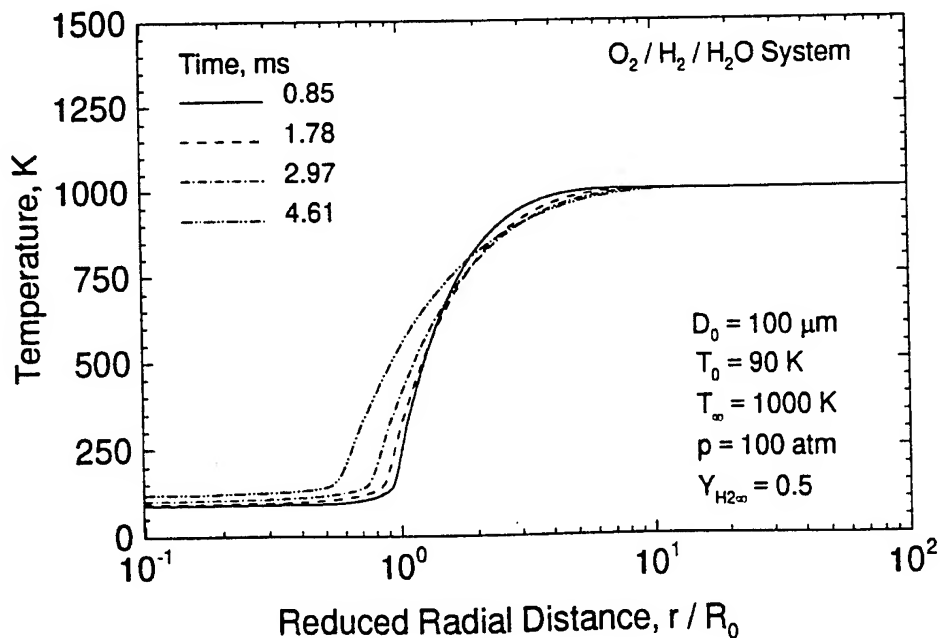
Effect of Thermal Diffusion on Droplet Lifetime (Critical Mixing Composition)



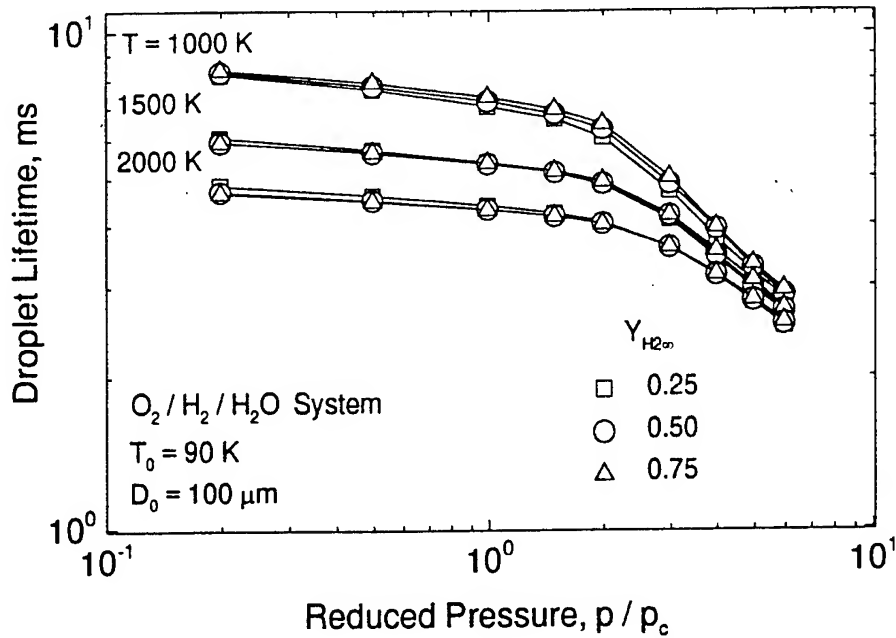
Species Composition in LOX/H₂/H₂O System



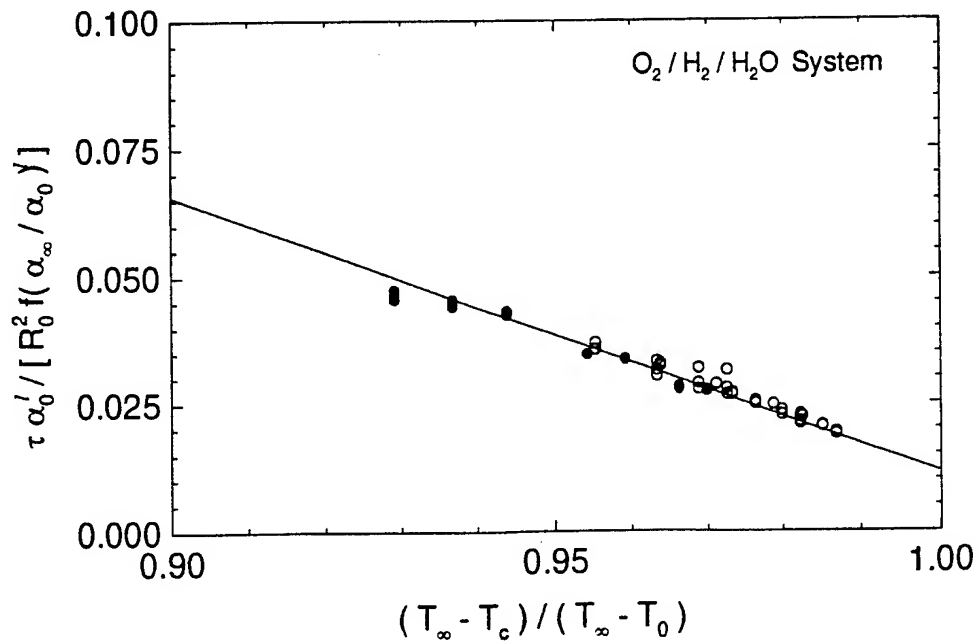
Temperature Distribution in LOX/H₂/H₂O System



Effect of Pressure on Droplet Lifetime (LOX/H₂/H₂O System)

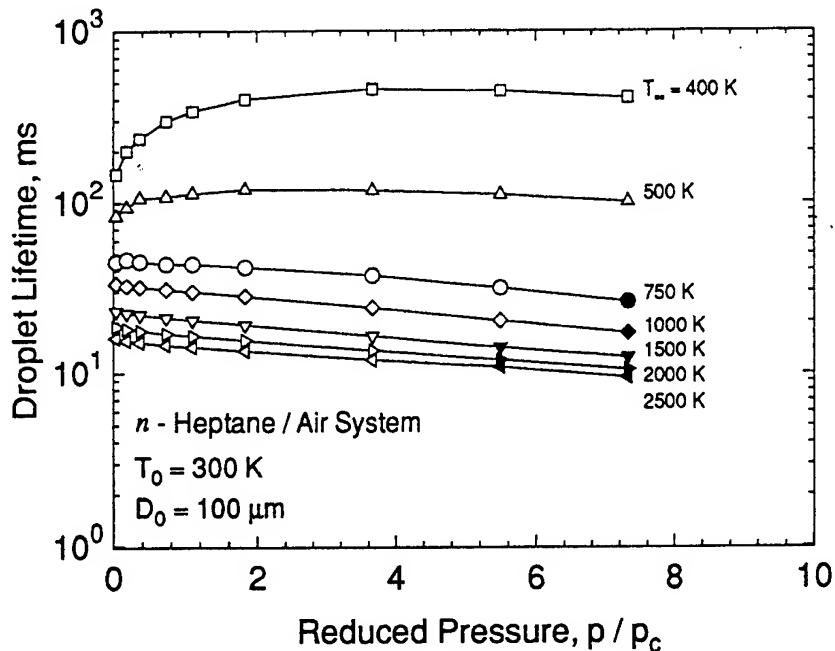


Correlation of Droplet Lifetime (LOX/H₂/H₂O System)



Effect of Pressure on Droplet Lifetime

$$400 < T_{\infty} < 2500 \text{ K}, 5 < p_{\infty} < 300 \text{ atm}$$



Subcritical Regime

- Low ambient temperature
 Molecular diffusion decreases with pressure
 \Rightarrow Nitrogen composition decreases at the interface
 \Rightarrow Surface temperature increases
 \Rightarrow Temperature gradient decreases at the surface
 \Rightarrow Droplet lifetime increases with pressure
- High ambient temperature
 Enthalpy of vaporization decreases with pressure
 \Rightarrow Enhancement of vaporization with pressure

Supercritical Regime

- Mixture critical temperature decreases with pressure
 + Gaseous thermal conductivity increases with pressure
 \Rightarrow Enhancement of vaporization in supercritical regime

Correlation of Droplet Lifetime

- High ambient temperature, $T_\infty > 1000\text{ K}$
- Various initial droplet temperatures, $T_o = 300, 325, 350\text{ K}$
- Reduced droplet lifetime correlated with pressure

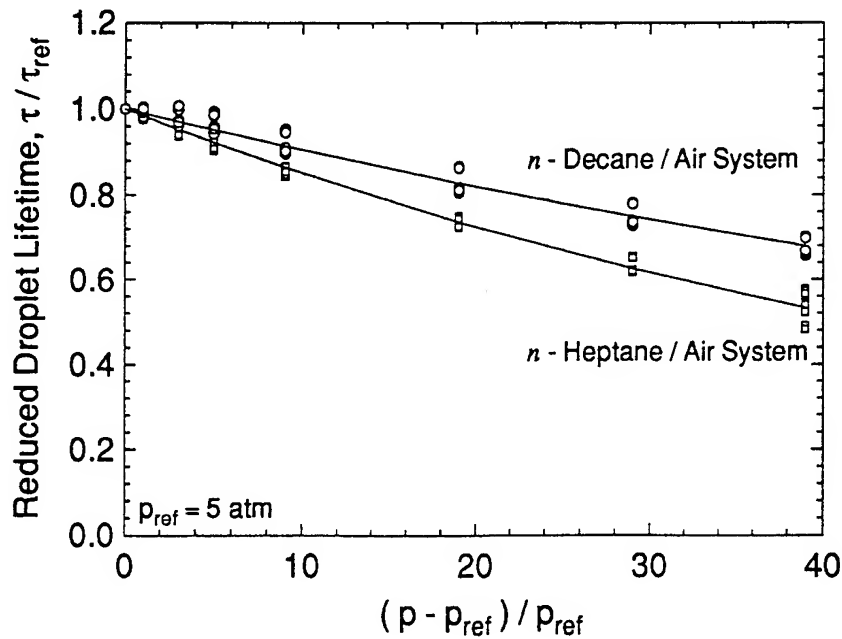
$$\tau_r = \frac{\tau}{\tau_{p_{ref}=5\text{ atm}}} = \exp\left[-a(p - p_{ref}) / p_{ref}\right]$$

where

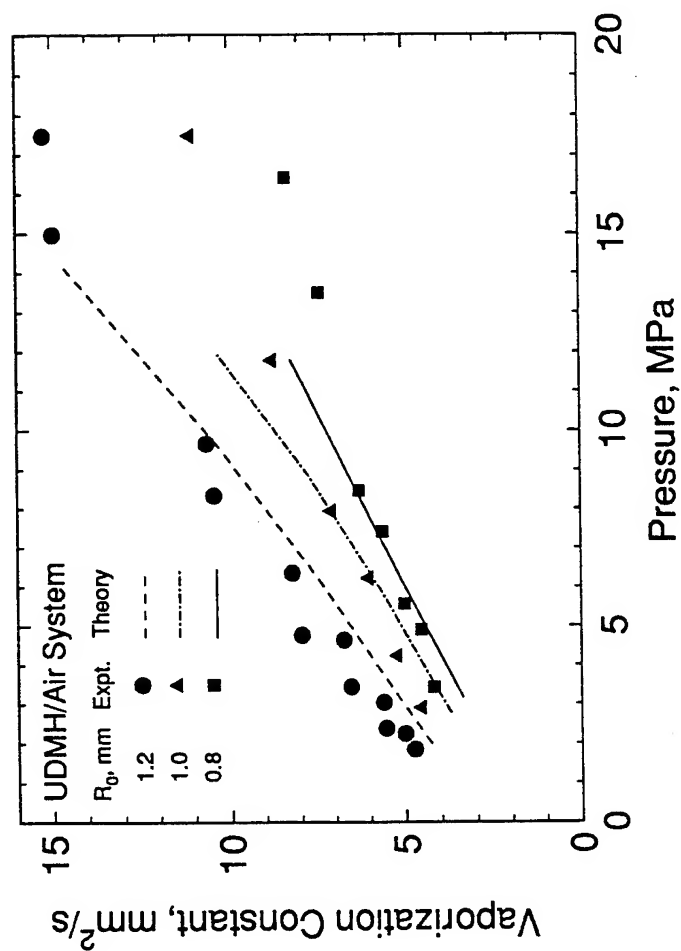
$a = 0.0161$ for n -heptane/air system

$a = 0.01$ for n -decane/air system

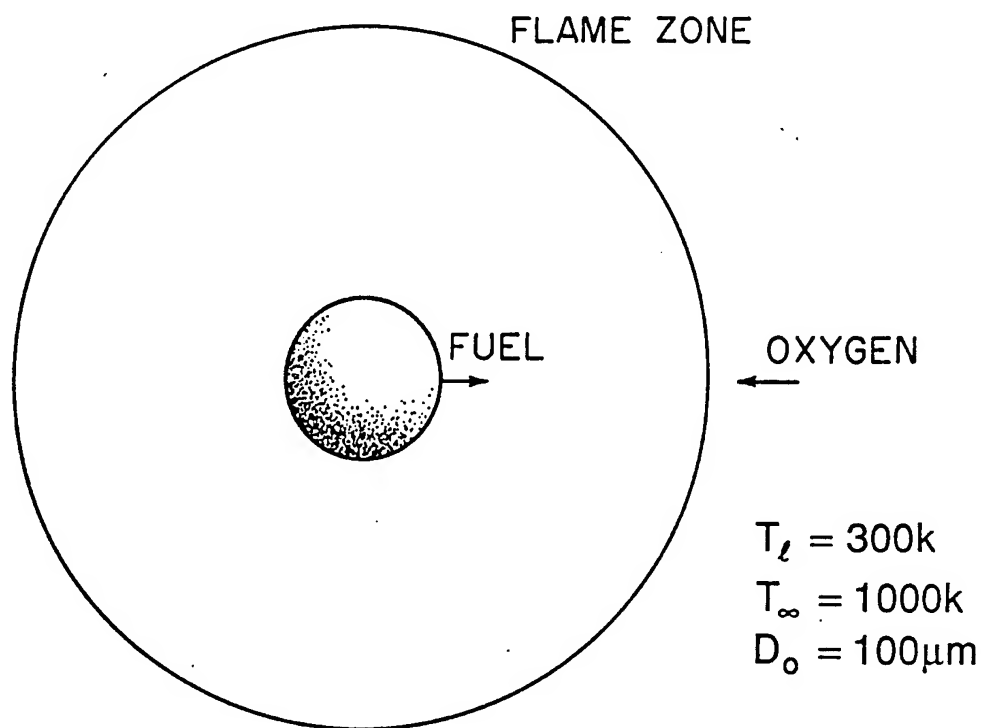
- Average deviation < 2 %



Effect of Pressure on Vaporization Rate of UDMH Droplet



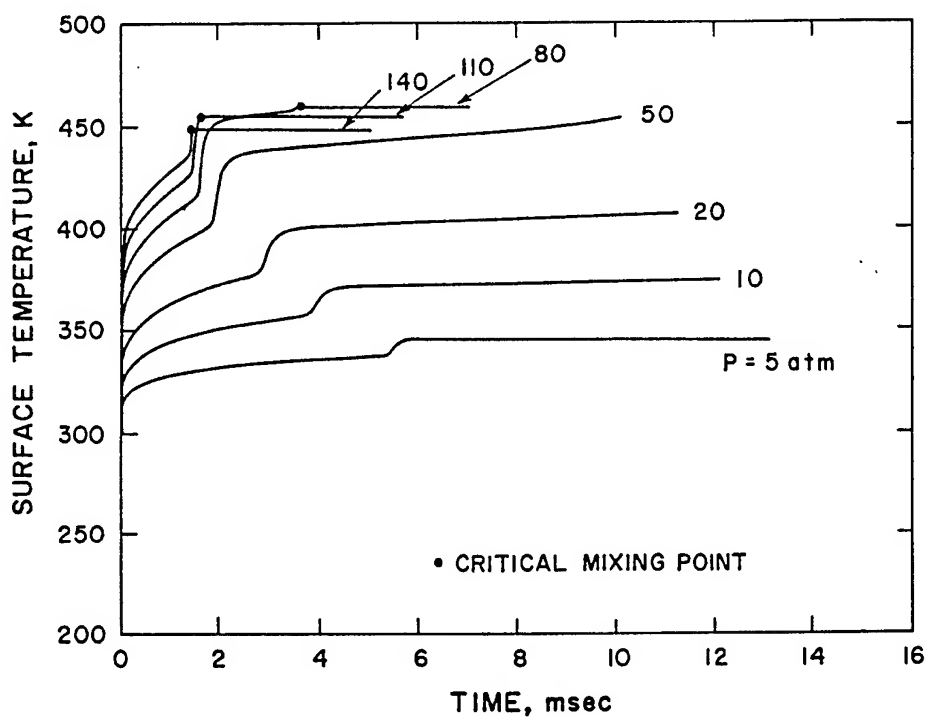
COMBUSTION OF n-PENTANE FUEL DROPLETS IN AIR FOR PRESSURES OF 5-140 atm



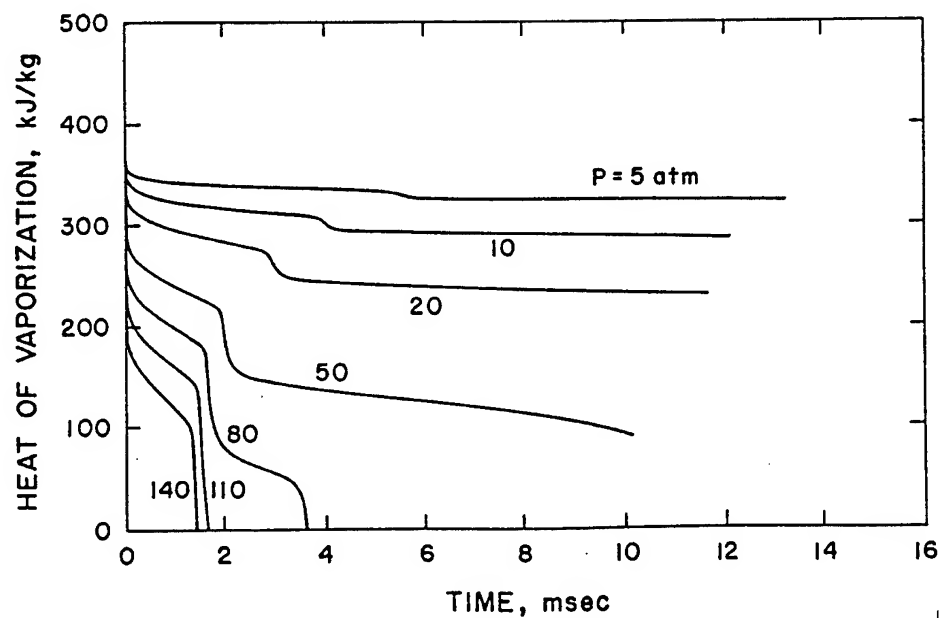
CRITICAL PROPERTIES OF CONSTITUENT SPECIES

	<u>n-C₅H₁₂</u>	<u>N₂</u>	<u>O₂</u>	<u>CO₂</u>	<u>H₂O</u>
Critical Temp.(k)	469.6	126.2	154.6	304.2	647.3
Critical Pressure (atm)	33.3	33.5	49.8	72.8	217.6

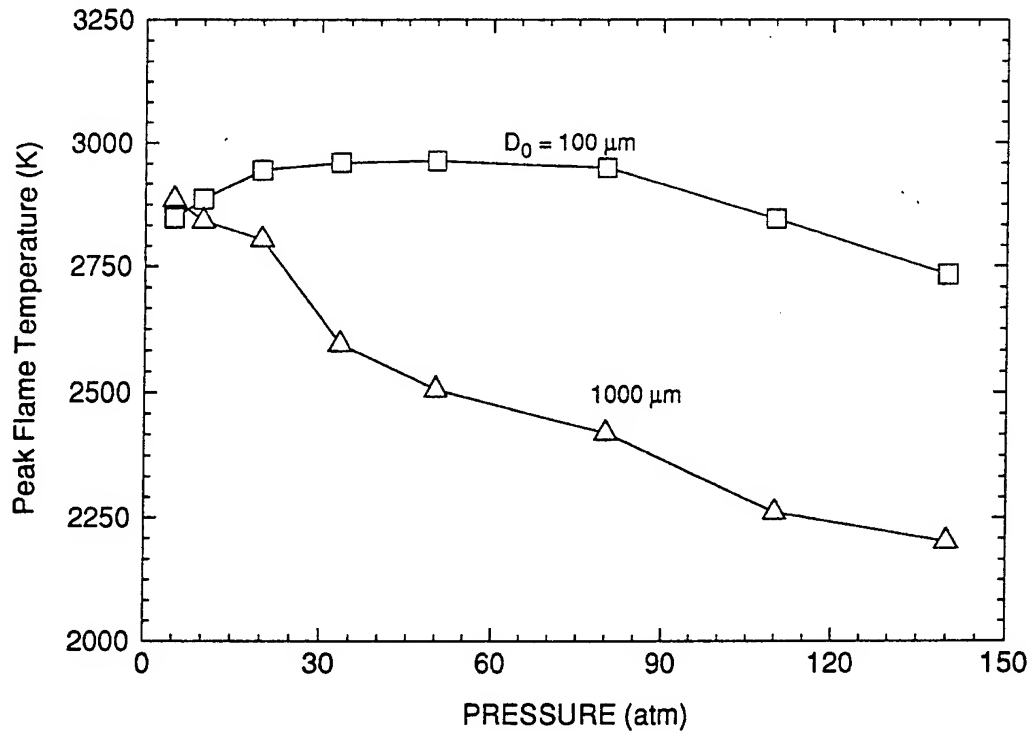
Time-Variations of Droplet Surface Temperature



Time-Variations of Latent Heat of Vaporization



Effect of Pressure on Peak Flame Temperature



- Thermal diffusivity decreases almost linearly with pressure,

$$\alpha \sim \frac{1}{P} \Rightarrow \text{less heat transfer from the flame zone.}$$

- Mass diffusivity decreases relatively fast with pressure,

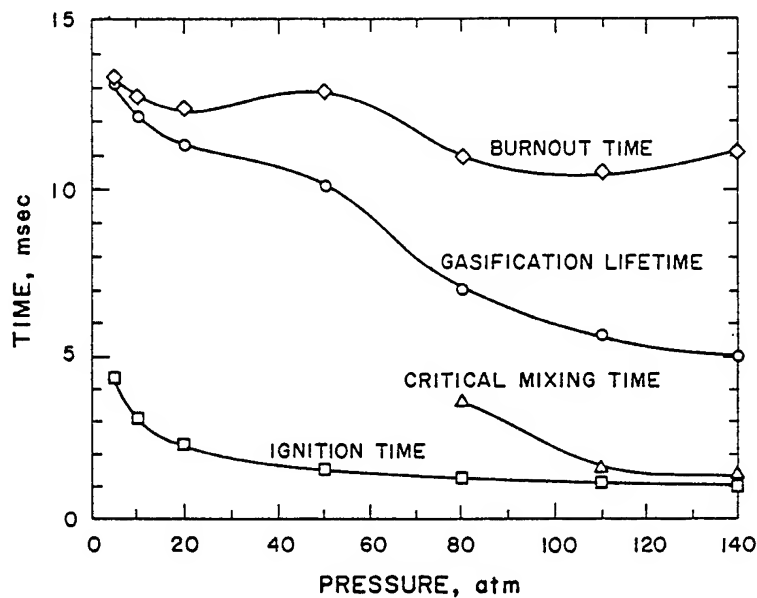
$$D < \frac{1}{P} \Rightarrow \text{much less fuel supply to the flame zone.}$$

- Lewis number increases with pressure,

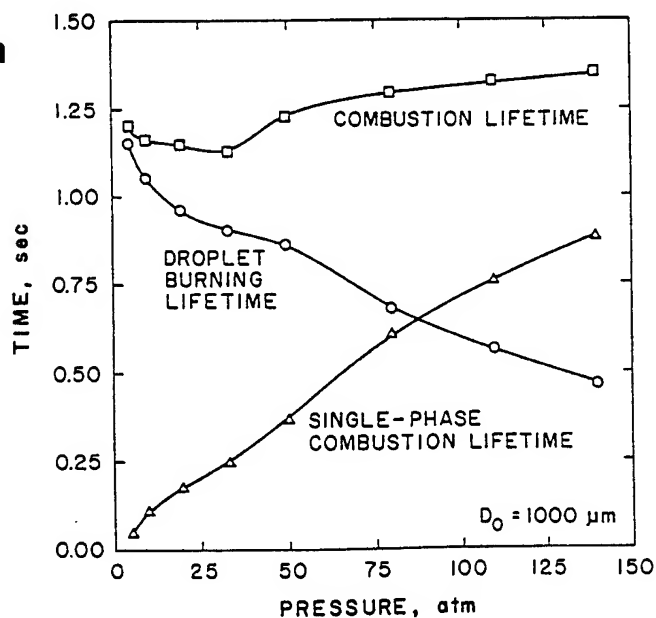
$$\text{Le} \equiv \frac{\alpha}{D} \uparrow \text{ as } P \uparrow$$

MILESTONE TIMES WITH DROPLET BURNING MECHANISMS

- $D_0 = 100 \mu\text{m}$



- $D_0 = 1000 \mu\text{m}$

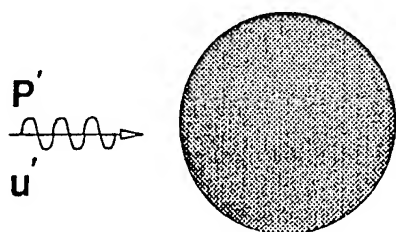


- At low pressures, gasification dominates.
- At high pressures, transient gas-phase diffusion dominates.

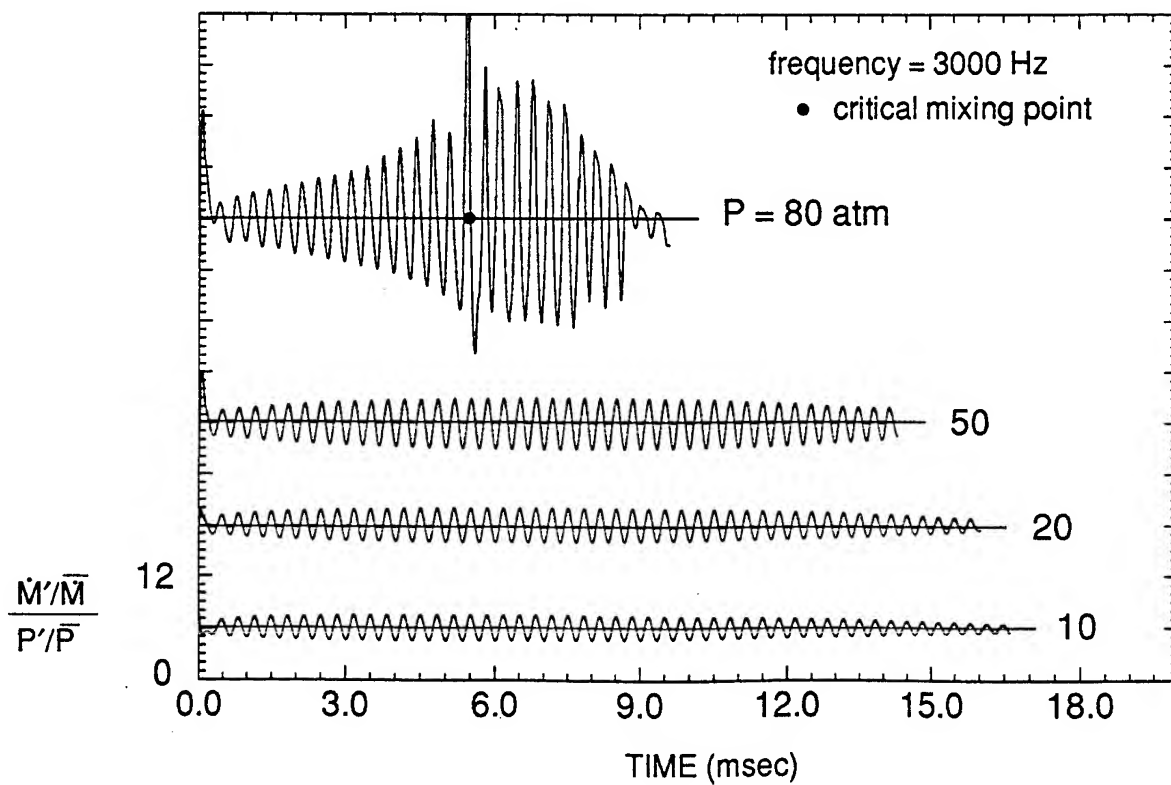
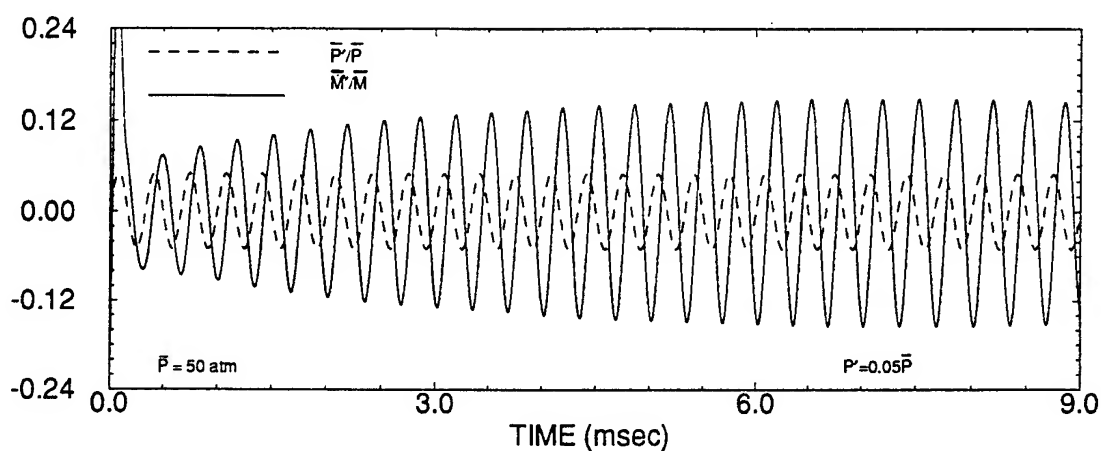
DYNAMIC RESPONSES OF DROPLET VAPORIZATION AND COMBUSTION TO AMBIENT FLOW OSCILLATIONS

- Pressure-Coupled Response
- Velocity-Coupled Response

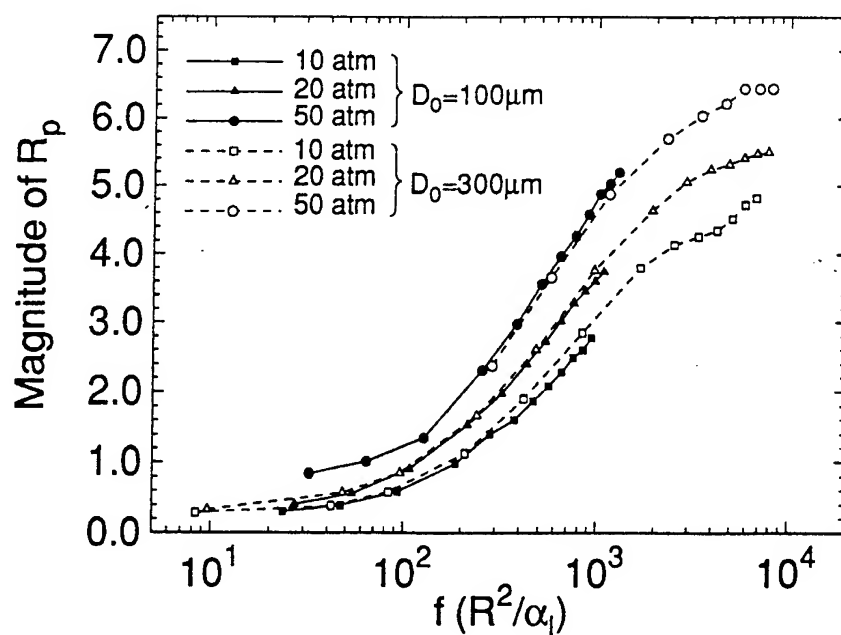
Droplet Vaporization Response



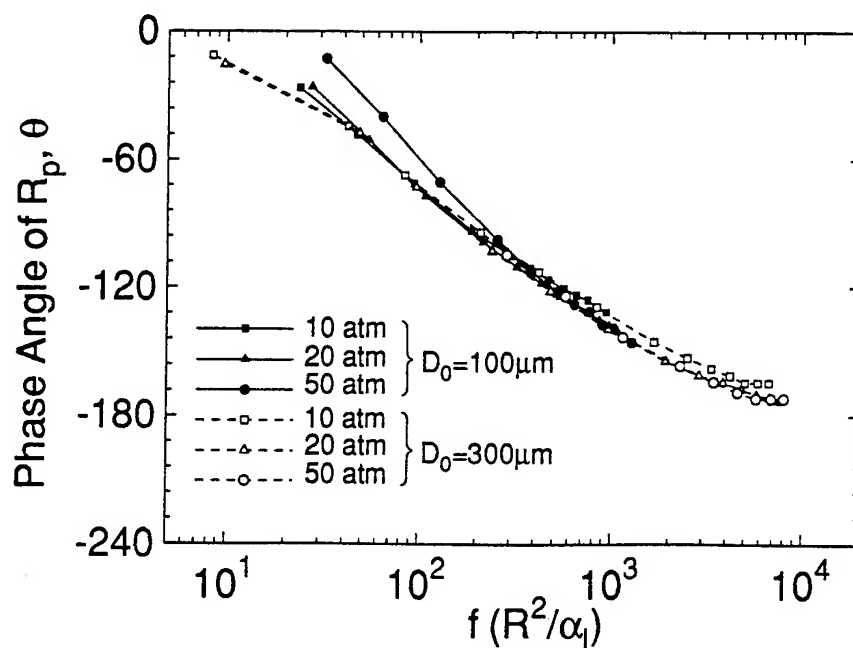
$$R_p = \frac{\left[\left(-\frac{dM}{dt} \right)_{\text{inst.}} - \left(-\frac{dM}{dt} \right)_{\text{s.s.}} \right]}{(p' / \bar{p})} \bigg/ \left(-\frac{dM}{dt} \right)_{\text{s.s.}}$$



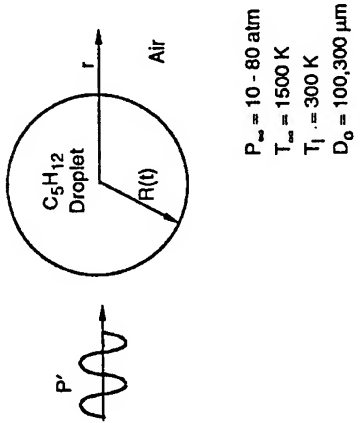
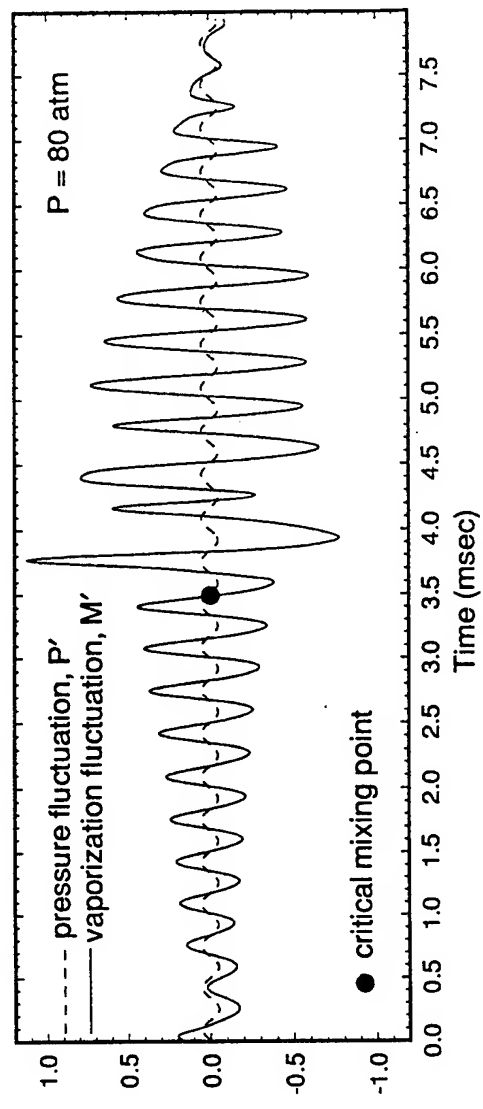
Magnitude of Droplet Vaporization Response



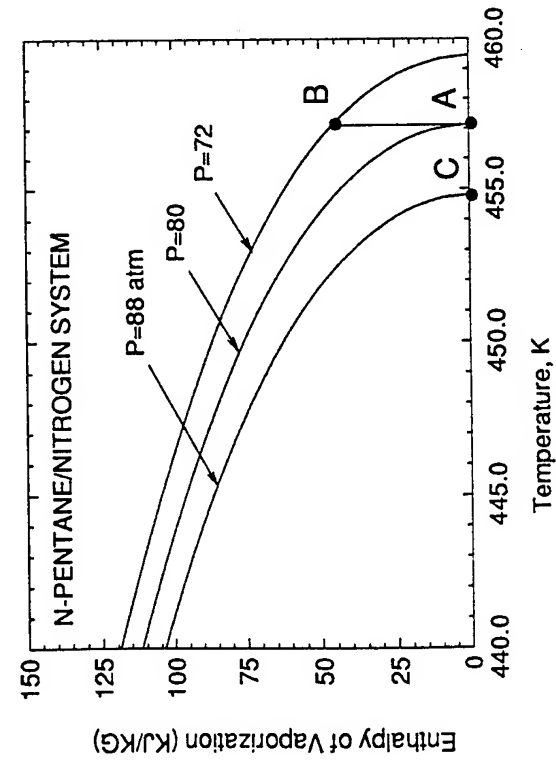
Phase Angle of Droplet Vaporization Response



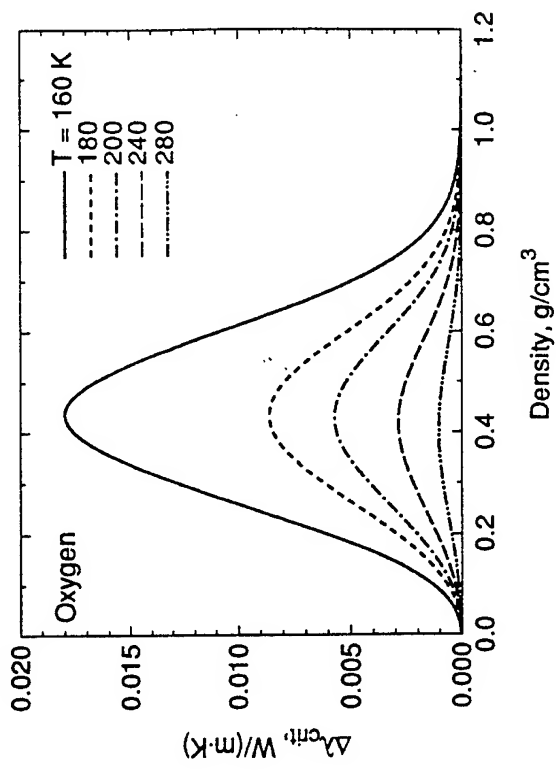
Abnormal Variations of Thermophysical Properties at Critical Point Cause Sharp Amplification of Droplet Vaporization Response



• enthalpy of vaporization



• critical enhancement of thermal conductivity, $\Delta\lambda_{crit}$



Supercritical Droplet Vaporization in Convective Environments

THEORETICAL FORMULATION

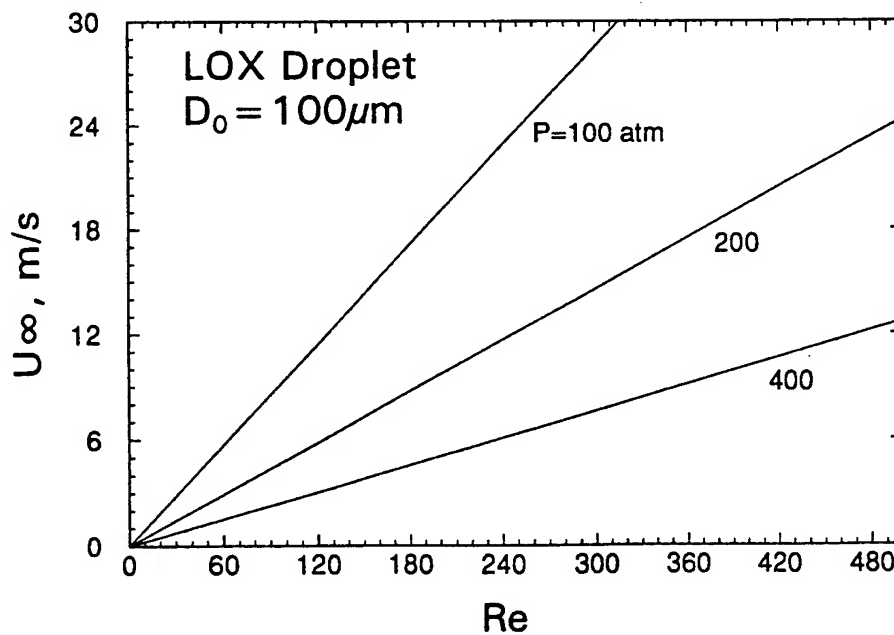
- complete time-dependent conservation equations for the entire field
 - mass
 - momentum
 - energy
 - species concentration
- thermodynamic nonideality
 - interfacial thermodynamics
 - dense-fluid phenomena
- transient diffusion
- property variation
- finite-rate chemical kinetics

SUPERCRITICAL DROPLET GASIFICATION IN CONVECTIVE ENVIRONMENTS

- Droplet Gasification
- Momentum Transfer
- Droplet Dynamics

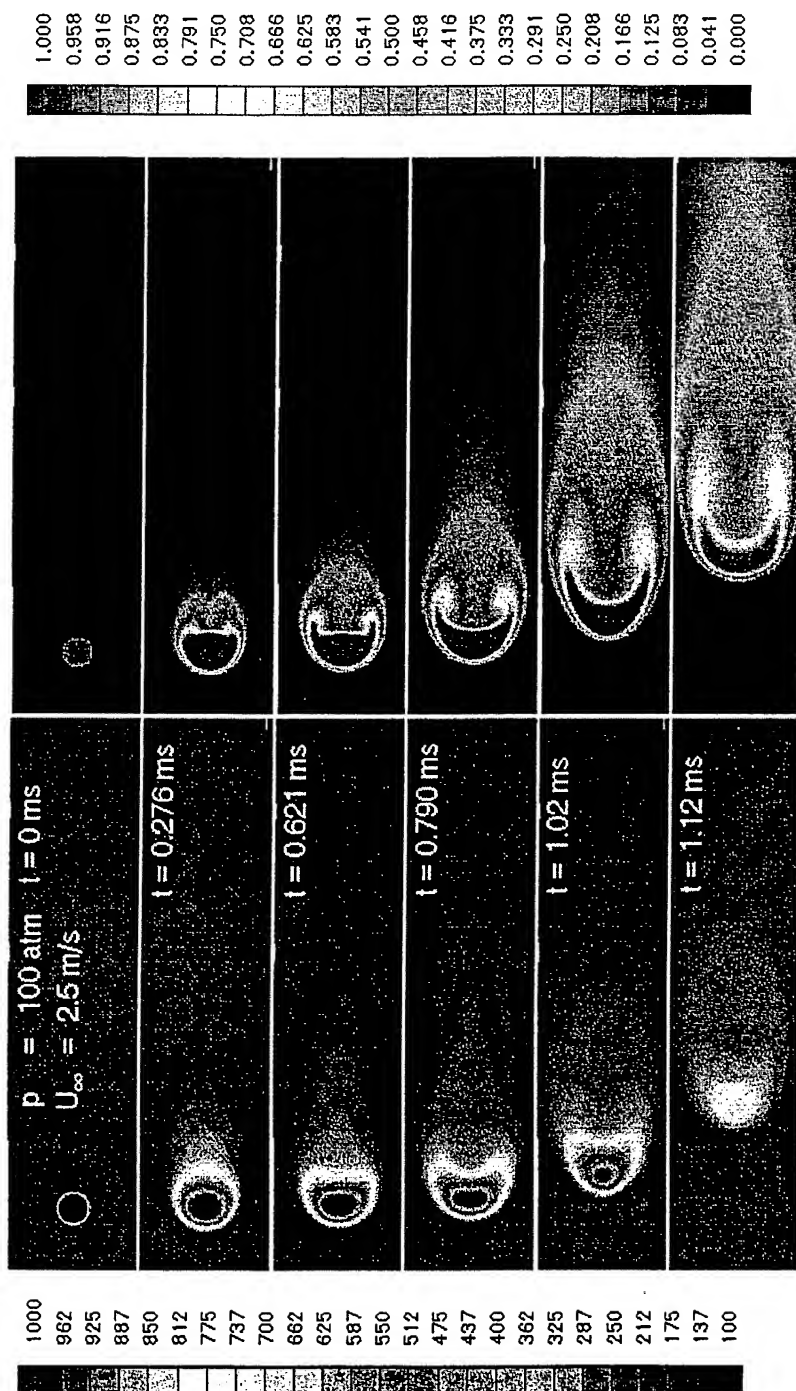
Key Parameters

- Reynolds number, $Re = \rho_{\infty} U_{\infty} D / \mu_{\infty}$
- Transfer number, $B = (Y_{FC} - Y_{F\infty}) / (1 - Y_{FC})$
- Lewis number, $Le = \alpha / D$
- Ambient density, ρ_{∞} , (or ambient pressure)



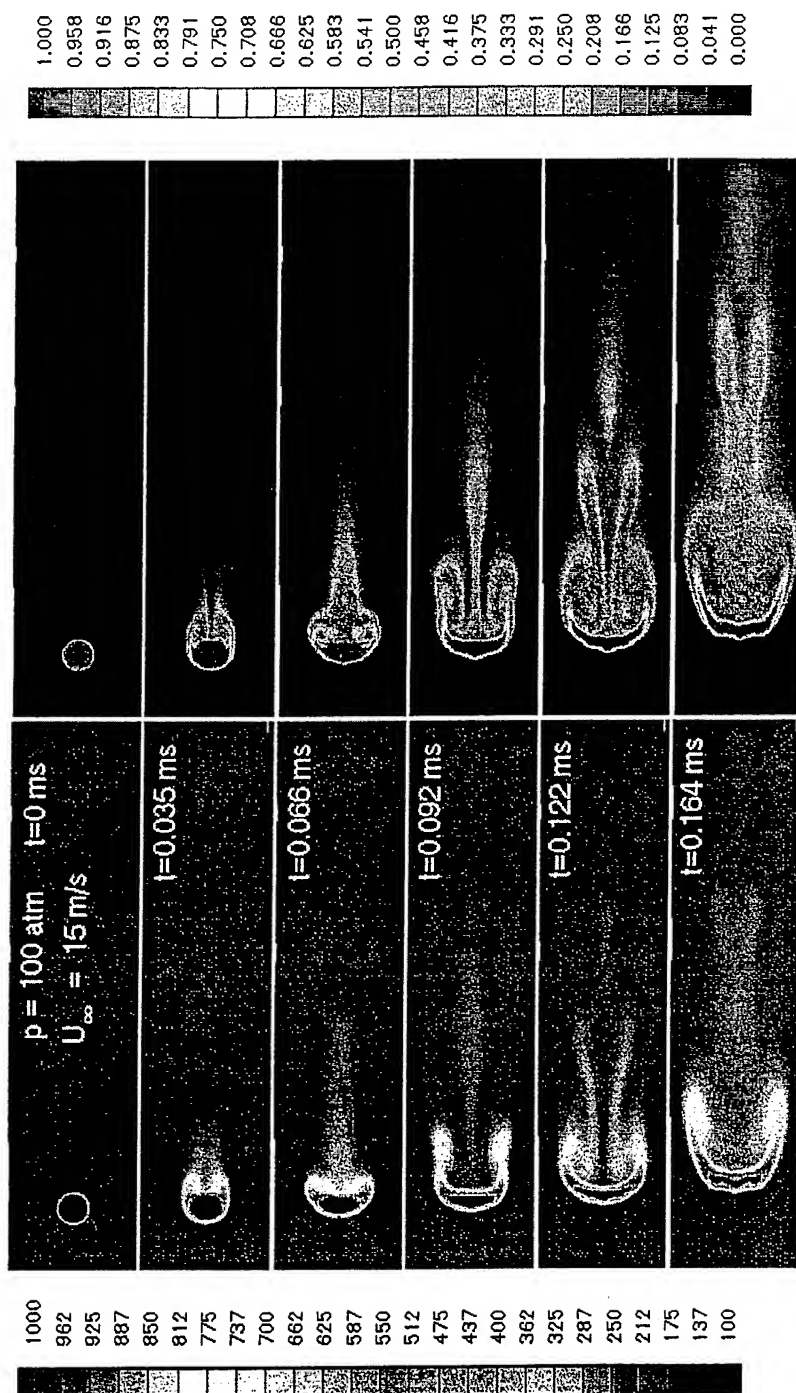
LOX DROPLET VAPORIZATION IN SUPERCRITICAL HYDROGEN

- Temperature
- O_2 Concentration



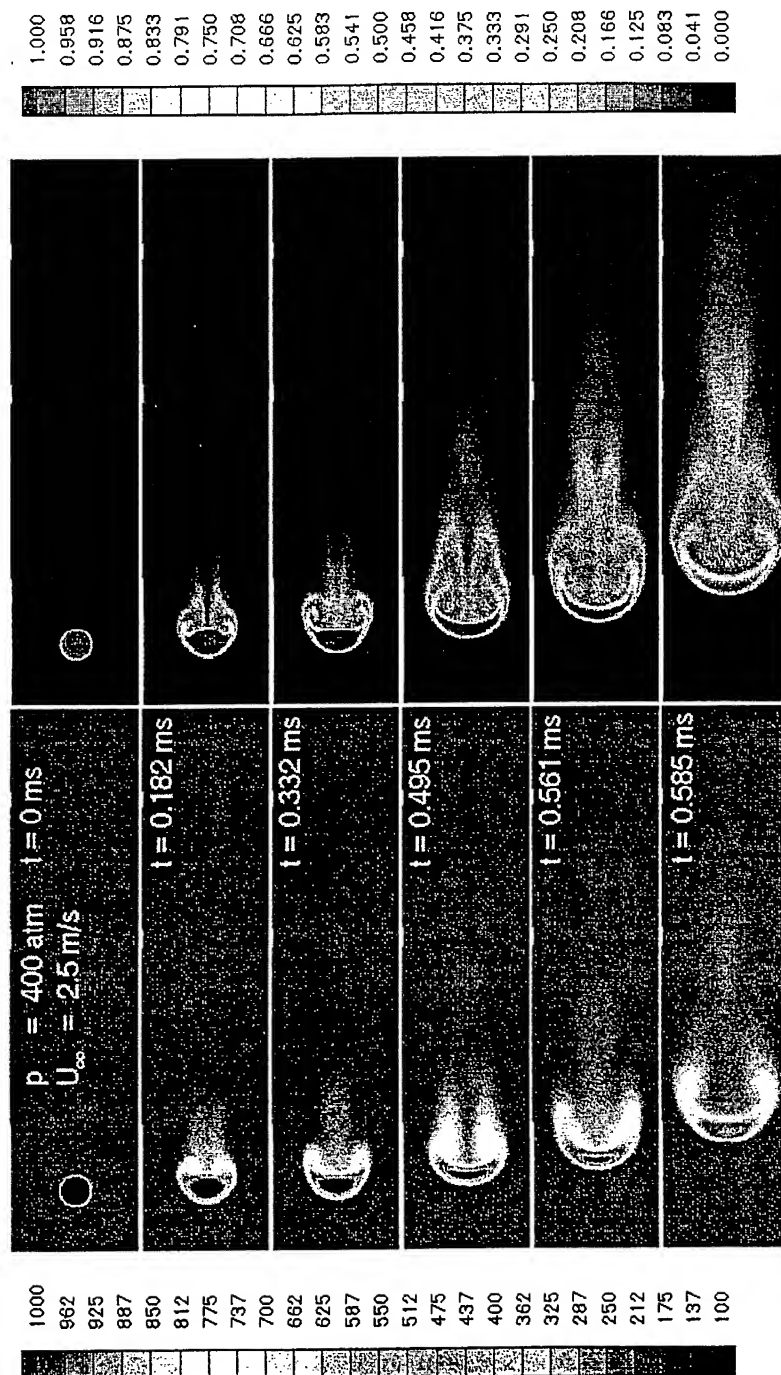
LOX DROPLET VAPORIZATION IN SUPERCRITICAL HYDROGEN

- Temperature
- O_2 Concentration



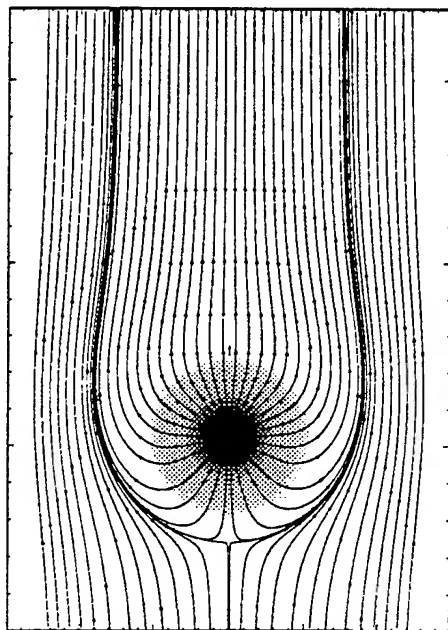
LOX DROPLET VAPORIZATION IN SUPERCRITICAL HYDROGEN

- Temperature
- O_2 Concentration

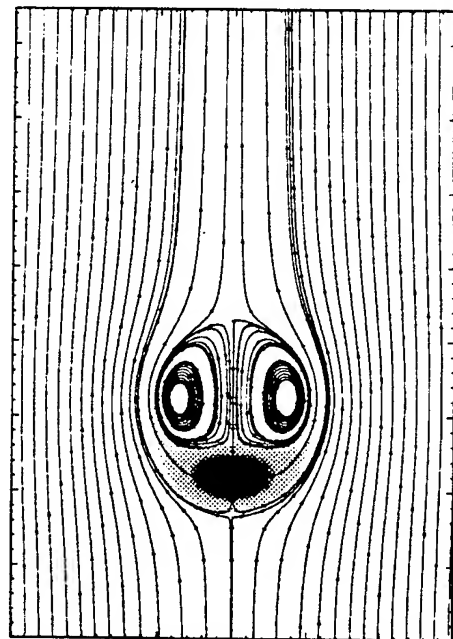


FOUR DIFFERENT MODES OF DROPLET EVOLUTION

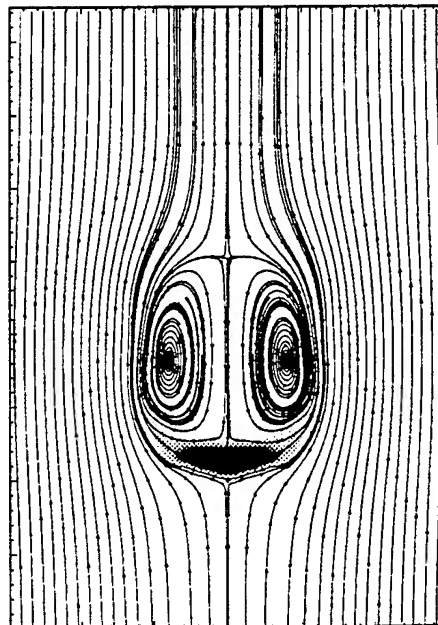
spherical(100 atm, 0.2 m/s; $t=610 \mu s$)



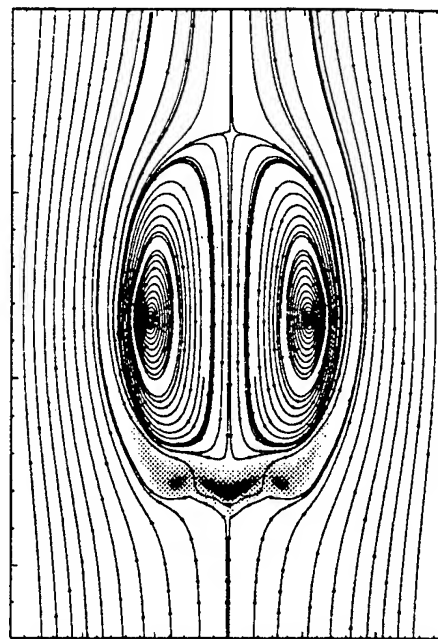
deformation(100 atm, 1.5 m/s; $t=610 \mu s$)



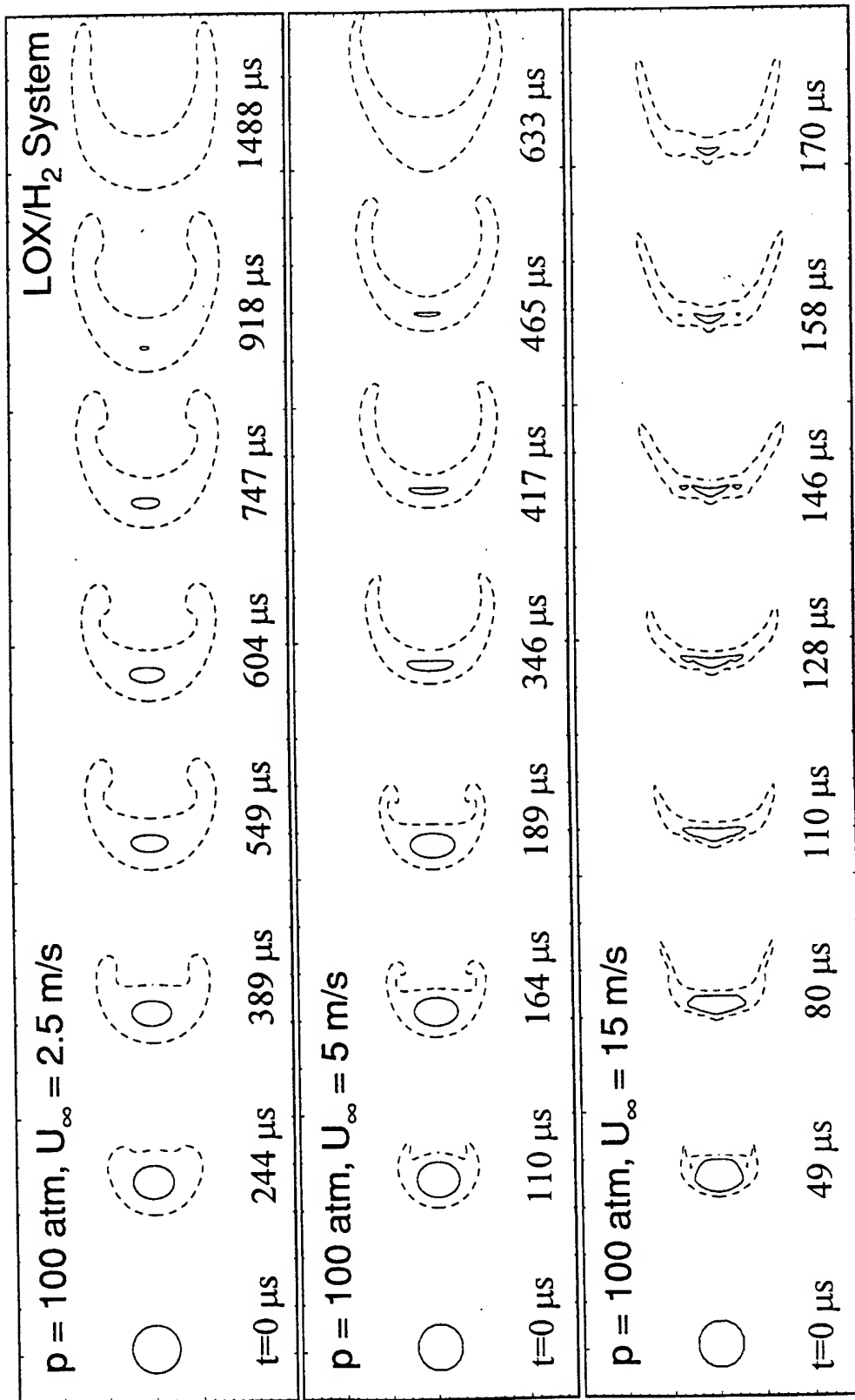
stripping(100 atm, 5 m/s; $t=170 \mu s$)



breakup(100 atm, 15 m/s; $t=170 \mu s$)

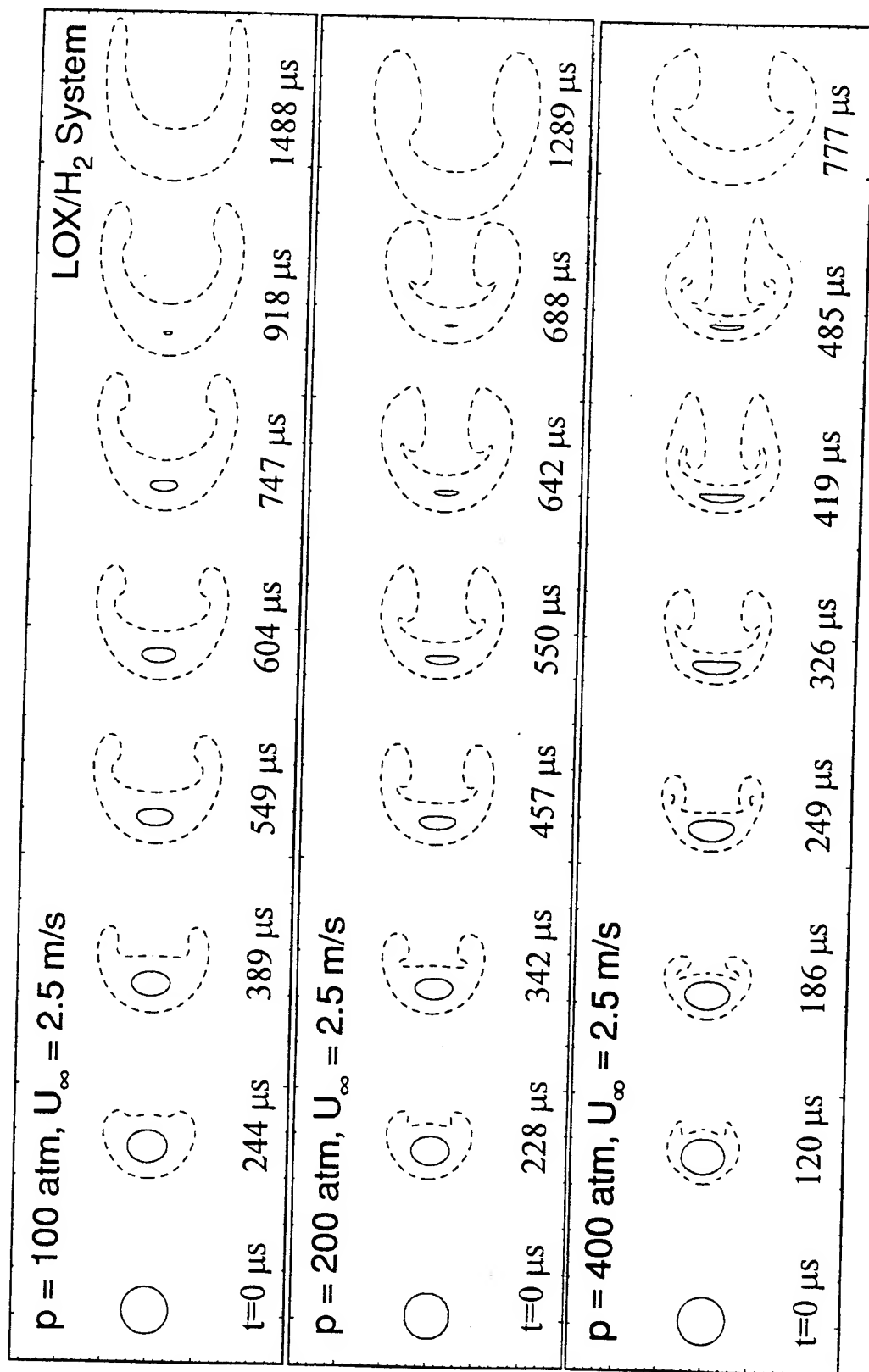


Evolution of Critical Surface



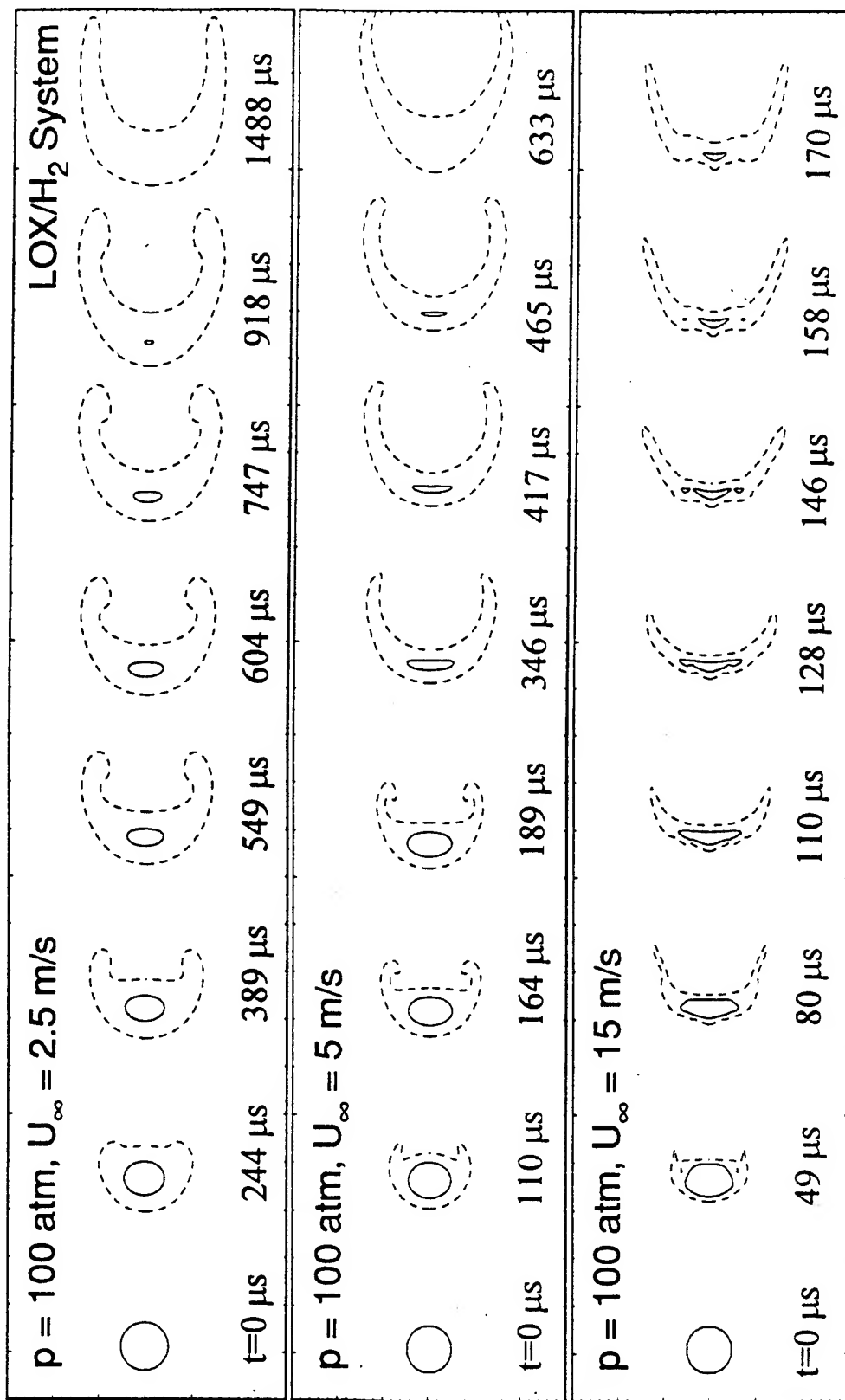
Critical Mixing Temperature
 Critical Mixing Composition

Evolution of Critical Surface



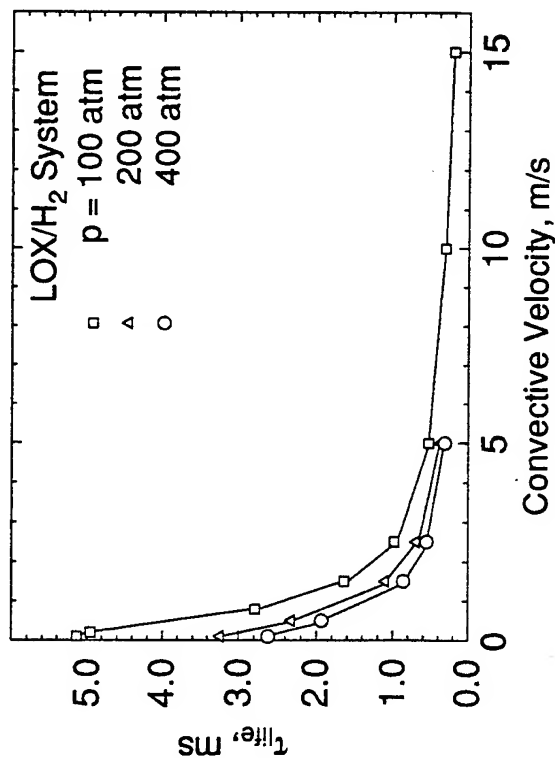
Critical Mixing Temperature
 Critical Mixing Composition

Supercritical LOX Droplet Vaporization in Convective Environments



Critical Mixing Temperature
 Critical Mixing Composition

Effects of Pressure and Velocity on Droplet Lifetime

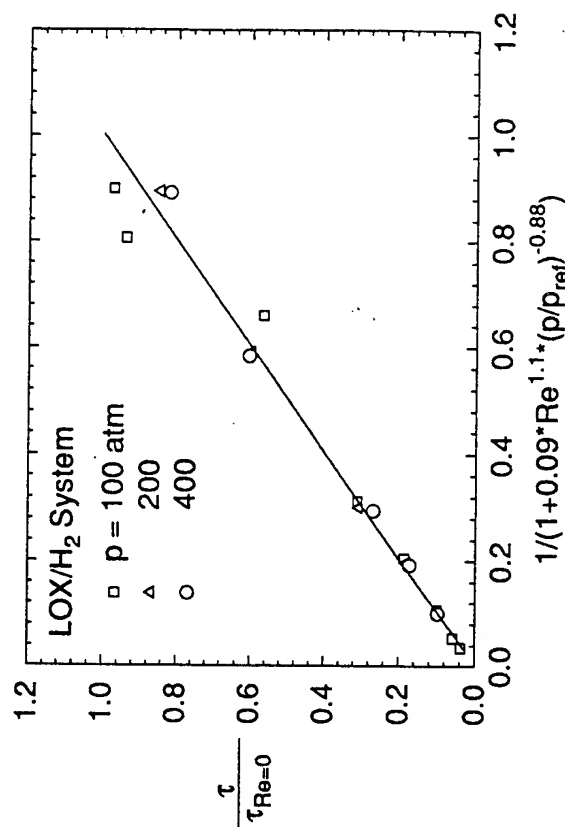


- Effect of Ambient Pressure on
 - thermophysical properties
 - critical mixing state
 - convective heat transfer
- Effect of Ambient Velocity on
 - convective heat transfer

- Atmospheric Conditions
 - Ranz and Marshall's correlation
- Supercritical Conditions
 - LOX/hydrogen system

$$\frac{\tau_f}{\tau_{f, Re=0}} \propto \frac{h_{Re=0}}{h} = \frac{1}{1 + 0.3 Re^{1/2} Pr^{1/3}}$$

$$\frac{\tau_f}{\tau_{f, Re=0}} = \frac{1}{1 + 0.165634 Re^{1.1} (p_r, o_2)^{-0.88}}$$



Droplet Drag Coefficient

- Hard Sphere (Putnum, 1963)

$$C_D^0 = \frac{24}{Re} \left[1 + \frac{1}{6} Re^{2/3} \right]$$

- Subcritical Droplet Vaporization
- Chiang et al. (1992)

$$C_D = \frac{C_D^0}{[1+B]^{0.2}} \quad \text{with} \quad B = \frac{C_p(T_\infty - T_s)}{\Delta h_v}$$

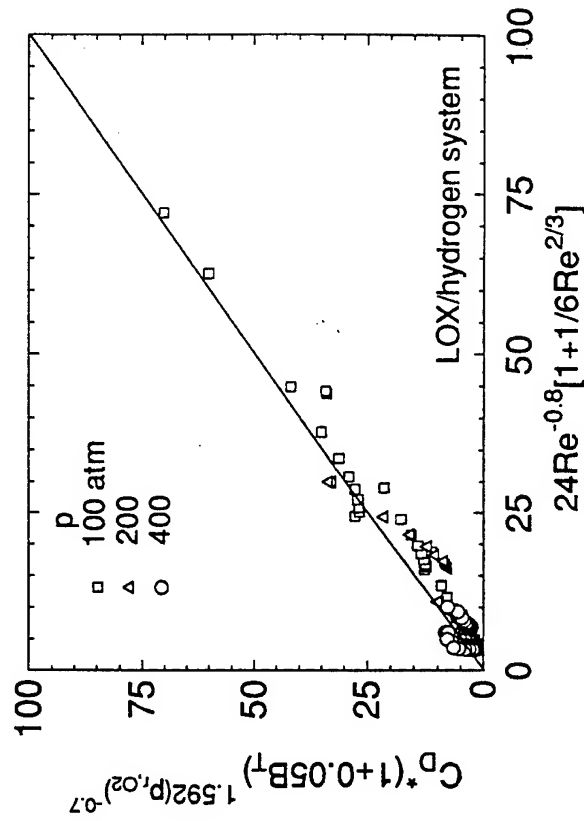
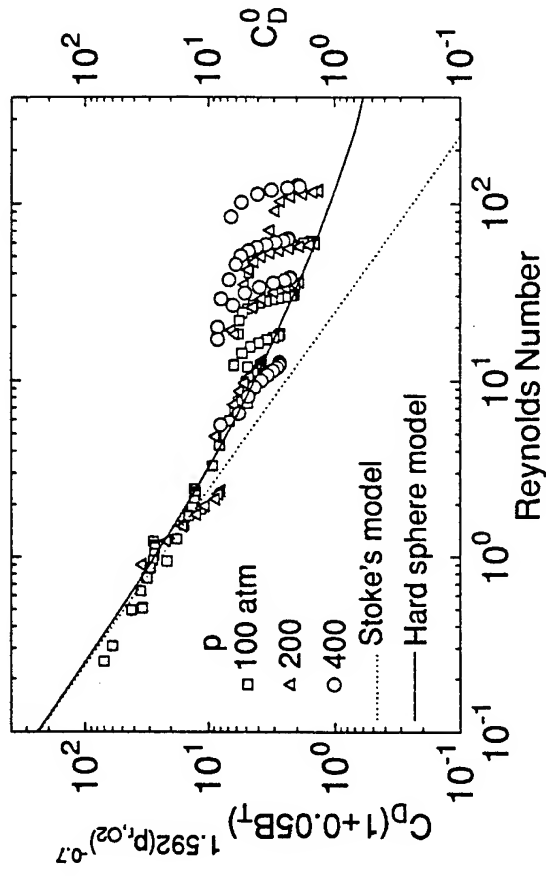
- Supercritical Droplet Vaporization
- equivalent sphere model

$$C_D = \frac{C_D^0}{(1+aB_T)^b} \quad \text{with} \quad B_T = \left(\frac{T_\infty - T_s}{T_s - T_l} \right)$$

$$a = 0.05; \quad b = 1.592(p_{r,O_2})^{-0.7}$$

- correction for droplet deformation

$$C_D = \frac{C_D^0 Re^{0.2}}{(1 + aB_T)^b}$$



Supercritical Droplet Combustion in Convective Environments

H₂-O₂ REACTION MECHANISMS

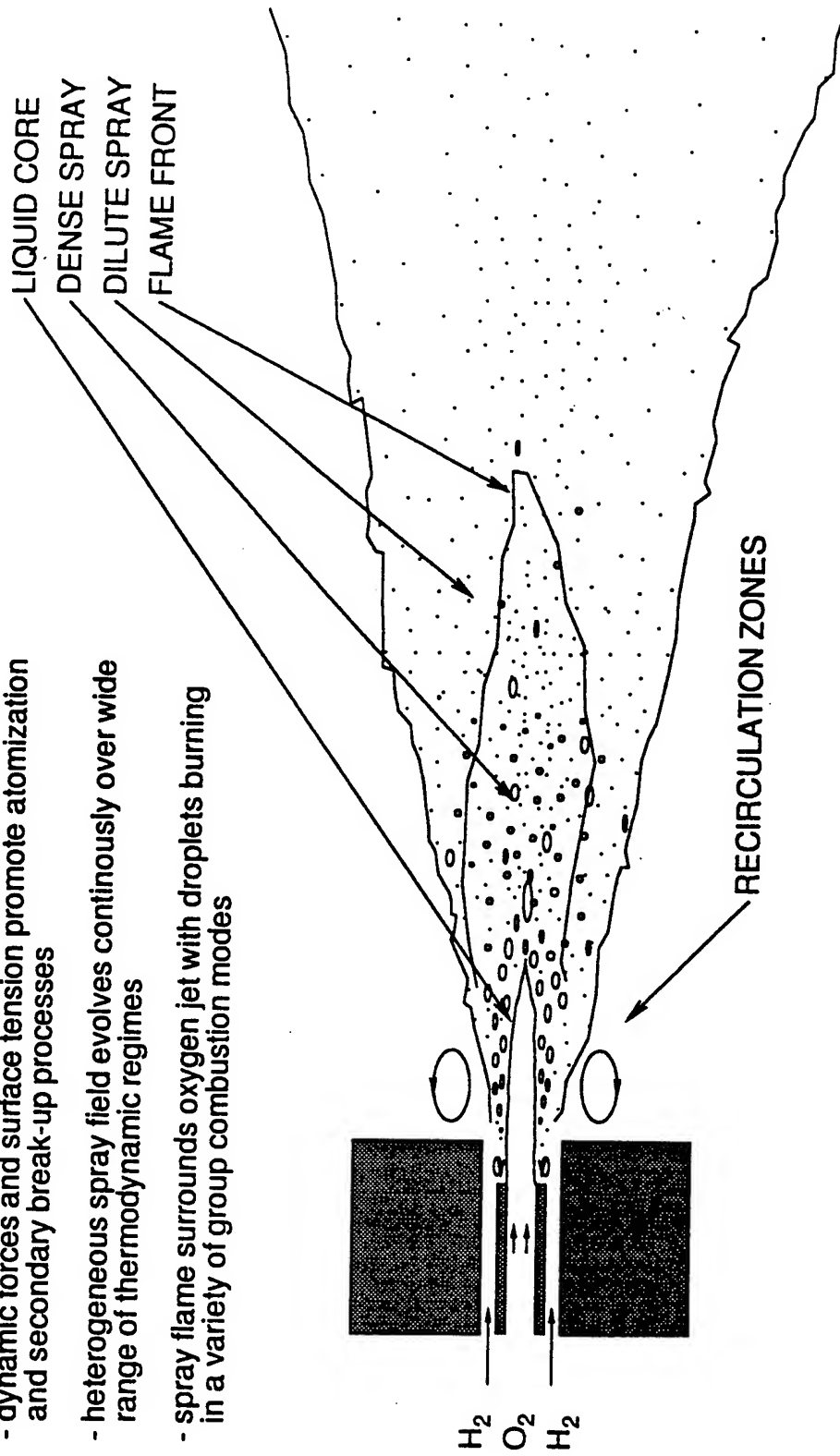
Eight Species Involved : H₂, O₂, H₂O, OH, O, H, HO₂, and H₂O₂

- **Initiation Reaction**
$$\text{H}_2 + \text{M} \rightarrow \text{H} + \text{H} + \text{M}$$
$$\text{H}_2 + \text{O}_2 \rightarrow \text{HO}_2 + \text{H}$$
- **Chain Reaction Involving O, H, and OH**
$$\text{H} + \text{O}_2 \rightarrow \text{O} + \text{OH}$$
$$\text{O} + \text{H}_2 \rightarrow \text{H} + \text{OH}$$
$$\text{H}_2 + \text{OH} \rightarrow \text{H}_2\text{O} + \text{H}$$
$$\text{O} + \text{H}_2\text{O} \rightarrow \text{OH} + \text{OH}$$
- **Chain Termination Involving O, H, and OH**
$$\text{H} + \text{H} + \text{M} \rightarrow \text{H}_2 + \text{M}$$
$$\text{O} + \text{O} + \text{M} \rightarrow \text{O}_2 + \text{M}$$
$$\text{H} + \text{O} + \text{M} \rightarrow \text{OH} + \text{M}$$
$$\text{H} + \text{OH} + \text{M} \rightarrow \text{H}_2\text{O} + \text{M}$$
- **Reaction Involving HO₂**
$$\text{H} + \text{O}_2 + \text{M} \rightarrow \text{HO}_2 + \text{M}$$
$$\text{HO}_2 + \text{H} \rightarrow \text{OH} + \text{OH}$$
$$\text{HO}_2 + \text{H} \rightarrow \text{H}_2\text{O} + \text{O}$$
$$\text{HO}_2 + \text{O} \rightarrow \text{O}_2 + \text{OH}$$
$$\text{HO}_2 + \text{HO}_2 \rightarrow \text{H}_2\text{O}_2 + \text{O}_2$$
$$\text{HO}_2 + \text{H}_2 \rightarrow \text{H}_2\text{O}_2 + \text{H}$$
- **Reaction Involving H₂O₂**
$$\text{H}_2\text{O}_2 + \text{OH} \rightarrow \text{H}_2\text{O} + \text{HO}_2$$
$$\text{H}_2\text{O}_2 + \text{H} \rightarrow \text{H}_2\text{O} + \text{OH}$$
$$\text{H}_2\text{O}_2 + \text{H} \rightarrow \text{HO}_2 + \text{H}_2$$
$$\text{H}_2\text{O}_2 + \text{M} \rightarrow \text{OH} + \text{OH} + \text{M}$$

LIMITING EXTREMES: 1) INERTIAL PROCESSES DOMINATE

- "Low" Heating Rates

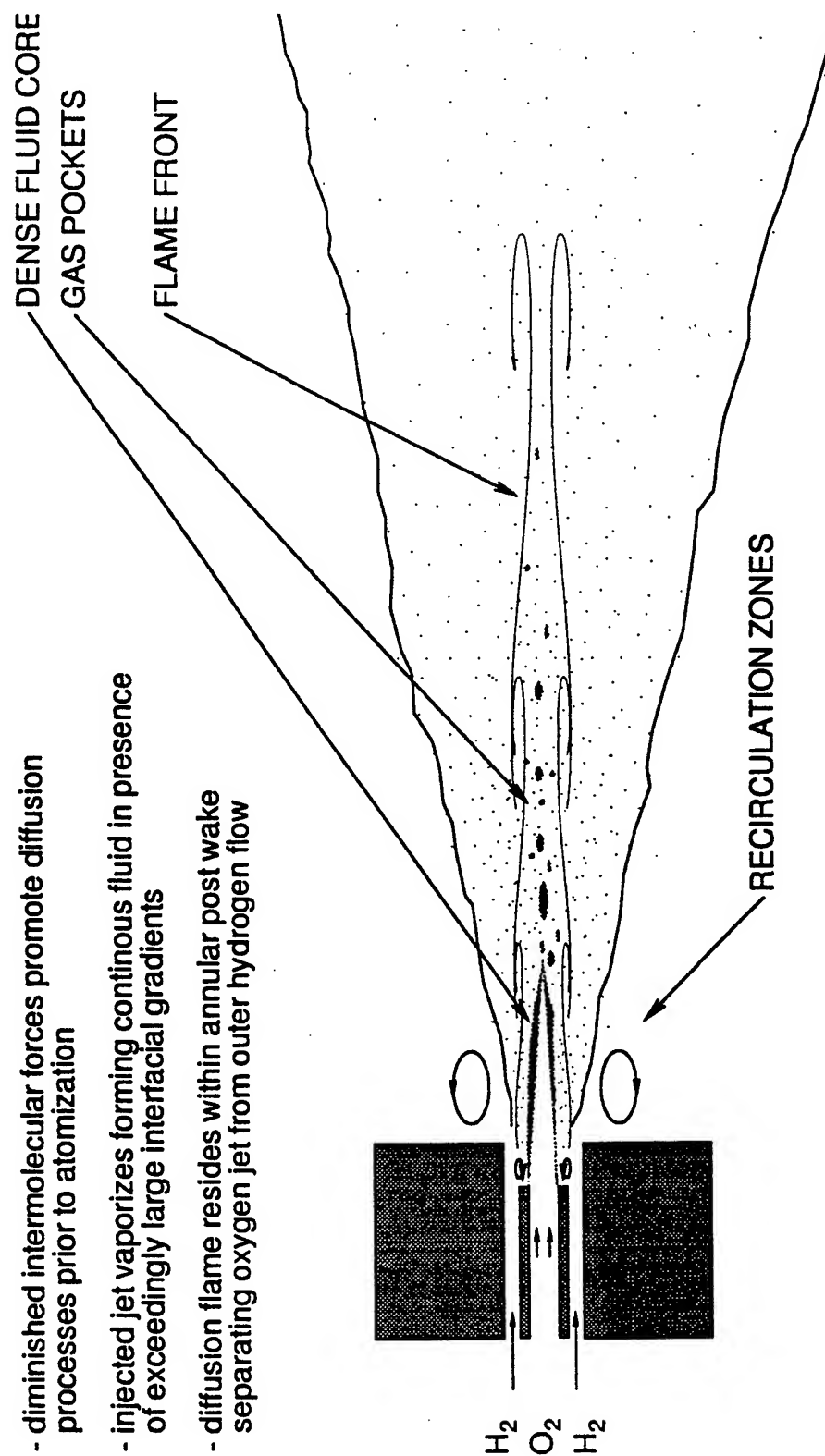
- dynamic forces and surface tension promote atomization and secondary break-up processes
- heterogeneous spray field evolves continuously over wide range of thermodynamic regimes
- spray flame surrounds oxygen jet with droplets burning in a variety of group combustion modes



LIMITING EXTREMES: 2) DIFFUSION PROCESSES DOMINATE

- "High" Heating Rates

- diminished intermolecular forces promote diffusion processes prior to atomization
- injected jet vaporizes forming continuous fluid in presence of exceedingly large interfacial gradients
- diffusion flame resides within annular post wake separating oxygen jet from outer hydrogen flow



FILTERED CONSERVATION EQUATIONS

Mass:

$$\frac{\partial}{\partial t}(\theta \bar{p}) + \nabla \cdot (\theta \bar{p} \tilde{\mathbf{u}}) = \dot{\rho}_s$$

Momentum:

$$\frac{\partial}{\partial t}(\theta \bar{p} \tilde{\mathbf{u}}) + \nabla \cdot [\theta (\bar{p} \tilde{\mathbf{u}} \tilde{\mathbf{u}} + \bar{p} \mathbf{I})] = \nabla \cdot (\theta \bar{\tau}) - \nabla \cdot (\theta \mathbf{T}) + \dot{\mathbf{F}}_s$$

Energy:

$$\begin{aligned} \frac{\partial}{\partial t}(\theta \bar{p} \tilde{e}_t) + \nabla \cdot [\theta (\bar{p} \tilde{e}_t + \bar{p}) \tilde{\mathbf{u}}] &= \nabla \cdot (\theta \bar{\mathbf{q}}_e) + \nabla \cdot (\theta \bar{\tau} \cdot \tilde{\mathbf{u}}) \\ &- \nabla \cdot (\theta \mathbf{Q}) - \nabla \cdot (\theta \mathbf{T} \cdot \tilde{\mathbf{u}}) \\ &- \nabla \cdot \left[\theta \frac{1}{2} tr(\mathbf{T} \tilde{\mathbf{u}} \tilde{\mathbf{u}}) \right] + \nabla \cdot [\theta (\bar{\tau} \cdot \tilde{\mathbf{u}})] + \dot{Q}_s \end{aligned}$$

Species:

$$\frac{\partial}{\partial t}(\theta \bar{p} \tilde{Y}_i) + \nabla \cdot (\theta \bar{p} \tilde{Y}_i \tilde{\mathbf{u}}) = \nabla \cdot (\theta \bar{\mathbf{q}}_i) - \nabla \cdot (\theta S_i) + \theta \bar{\omega}_i + \dot{\omega}_{s,i} \quad i = 1, \dots, N$$

CLOSURE REQUIREMENTS

Thermodynamic and Transport Properties:

$$Z, C_p, \mu, \lambda, D_{im}$$

Subgrid-Scale Turbulence Interactions:

$$T, Q, S_i$$

Subgrid-Scale Particulate Interactions:

$$\theta, \dot{\rho}_s, \dot{F}_s, \dot{Q}_s, \dot{\omega}_{s,i}$$

Chemical Kinetics:

$$\bar{\omega}_i$$

EXTENDED CORRESPONDING STATES PRINCIPLE

- Expresses generalization that equilibrium properties which depend on intermolecular forces are related to critical properties in universal manner
- Basic assumptions:

- 1) Configurational properties of mixture can be equated to those of a hypothetical pure fluid

$$\eta_m(\rho, T, X_1, \dots, X_N) = \eta_z(\rho, T)$$

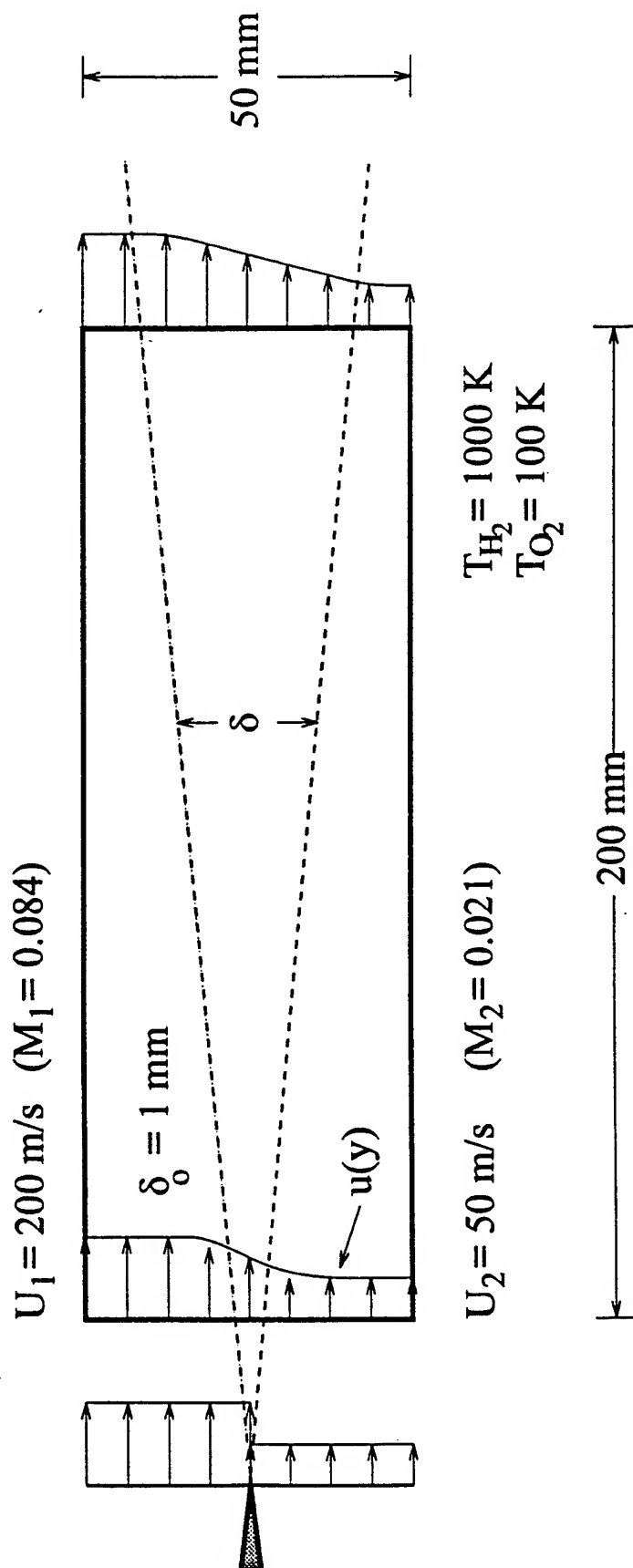
- 2) Properties of the hypothetical fluid obey classical two parameter corresponding states formalism

$$\eta_z(\rho, T) = \eta_o F_\eta(W_o, W_x, \hbar_x, f_x)$$

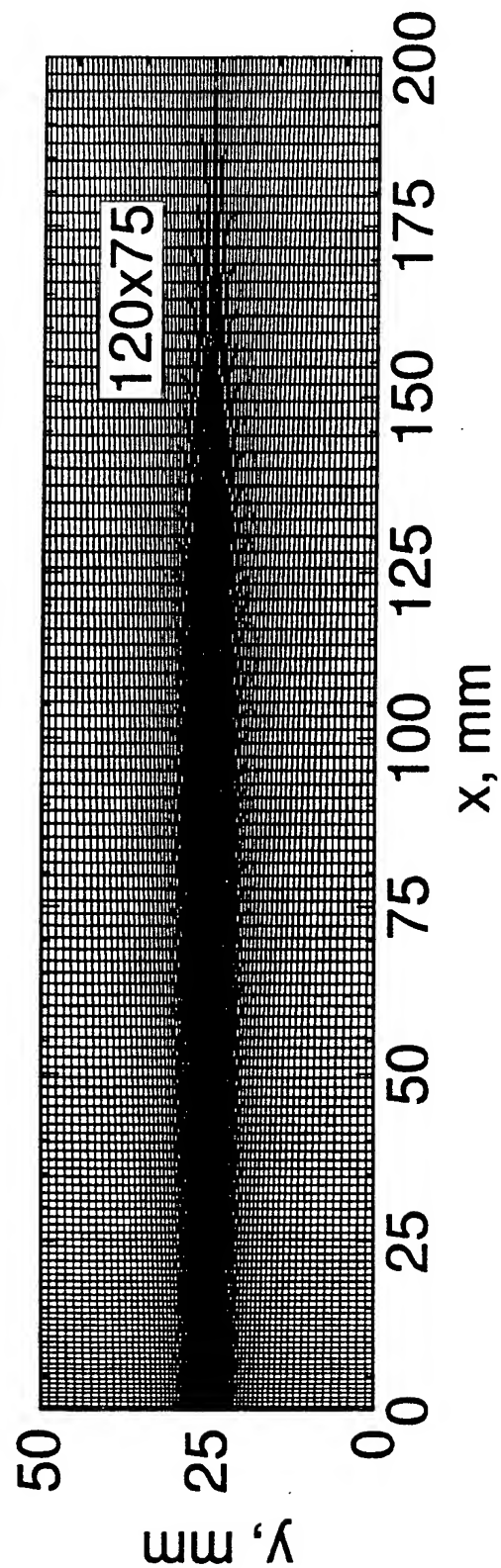
- 3) Reference fluid density and temperature obey extended equilibrium corresponding states principle

$$\rho_o = \rho \hbar_x \quad T_o = T / f_x$$

HIGH-PRESSURE SPRAY FIELD DYNAMICS

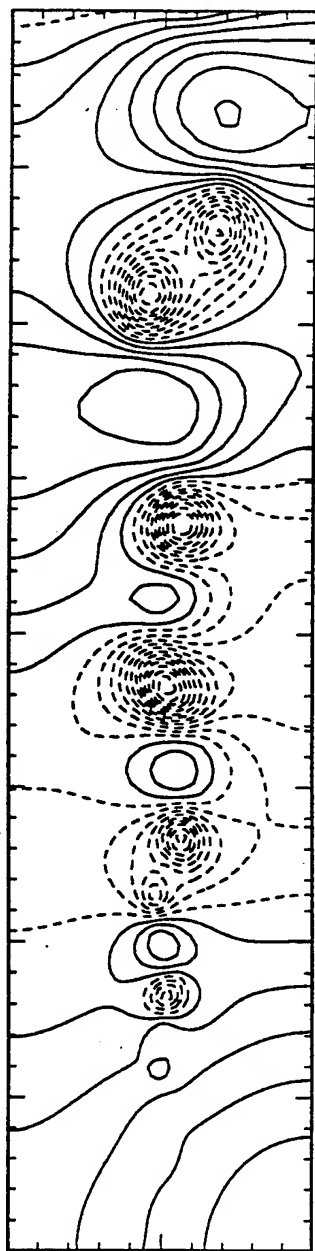


GRID DISTRIBUTION

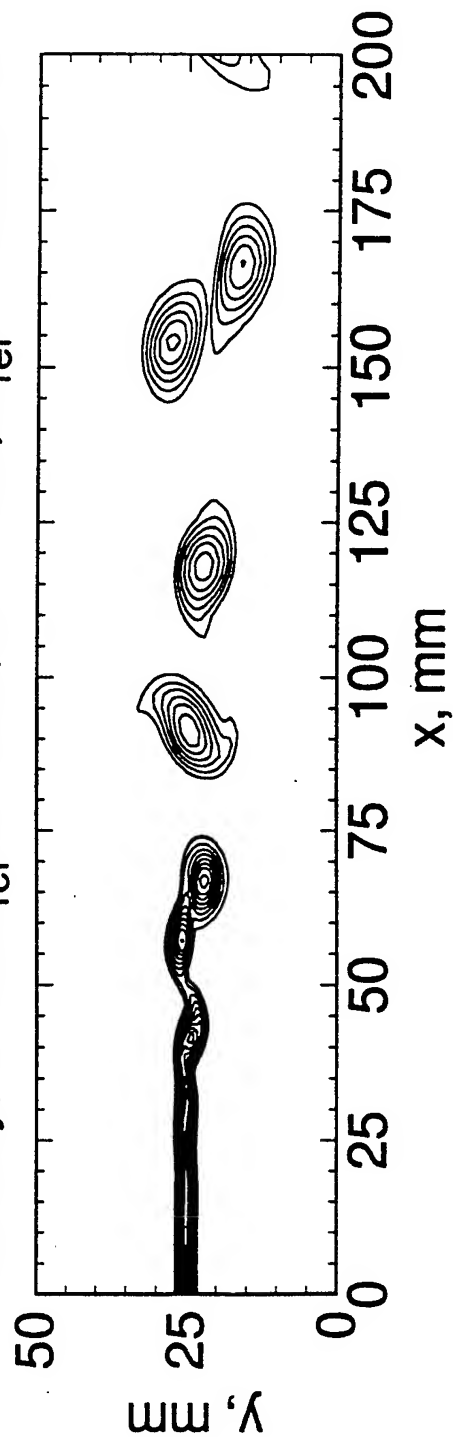


BASELINE FLOW CHARACTERISTICS

Pressure, $-0.2336 \leq (p - p_{\text{ref}})/p_{\text{ref}} \leq 0.1415\%$, $\Delta = 0.02\%$

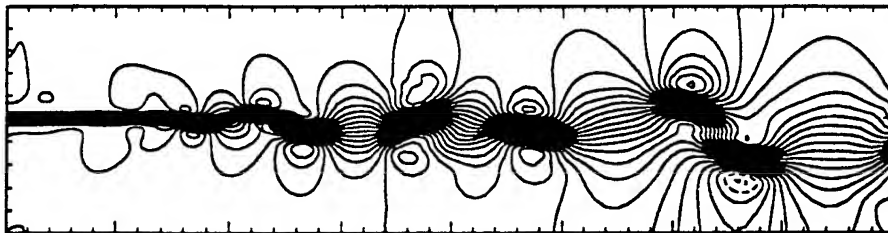


Vorticity, $0 \leq \omega/\omega_{\text{ref}} \leq 100\%$, $\Delta = 10\%$, $\omega_{\text{ref}} = -74 \times 10^3 \text{ s}^{-1}$

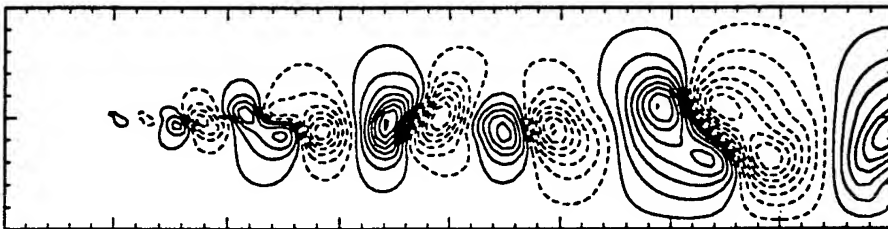


BASELINE FLOW CHARACTERISTICS

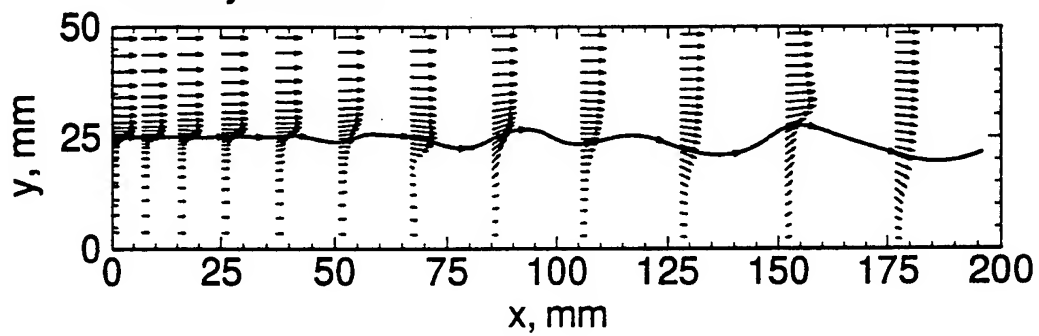
u-Velocity, $-20 \leq u \leq 250$ m/s, $\Delta = 10$ m/s



v-Velocity, $-75 \leq v \leq 75$ m/s, $\Delta = 10$ m/s



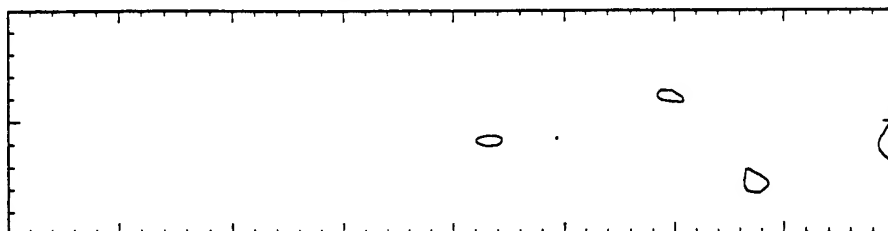
Velocity Vectors



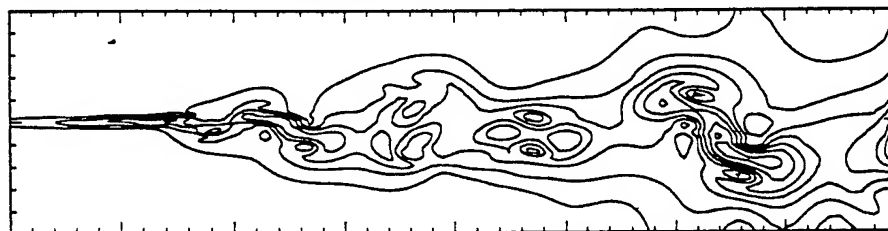
BASELINE FLOW CHARACTERISTICS

Viscosity Ratio

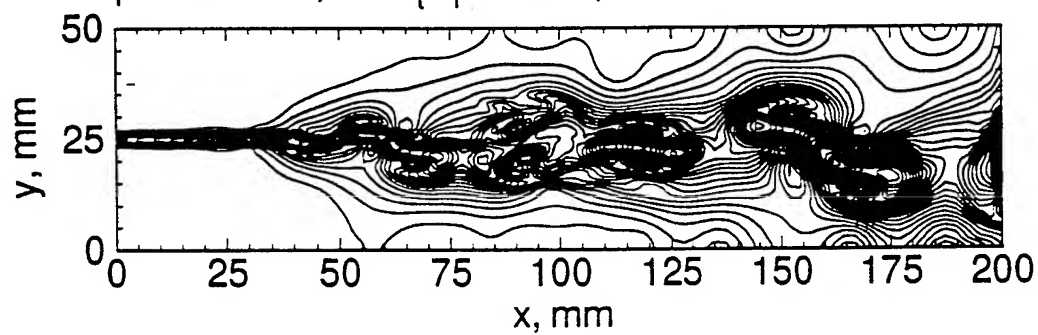
$p = 1 \text{ atm}$, $0 \leq v_t/v_l \leq 0.2704$



$p = 100 \text{ atm}$, $0 \leq v_t/v_l \leq 37.80$, $\Delta = 5$

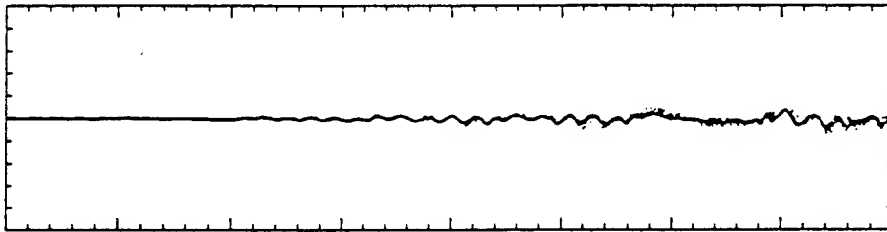


$p = 400 \text{ atm}$, $0 \leq v_t/v_l \leq 156.3$, $\Delta = 5$

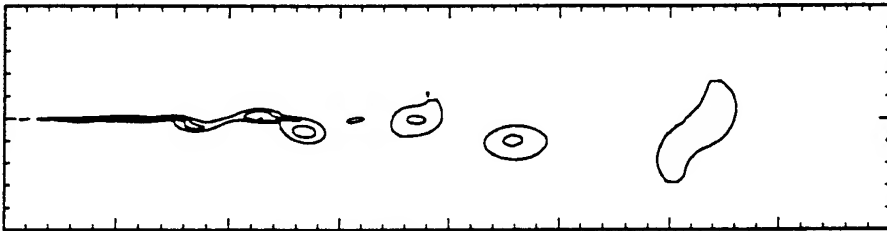


1 atm, O/F = 4

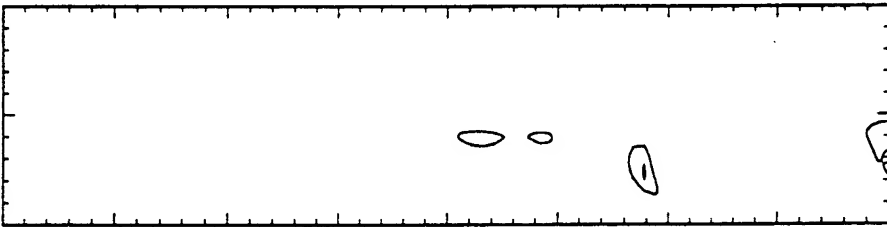
Spray Distribution, 2576 Parcels, 6.3×10^4 Particles



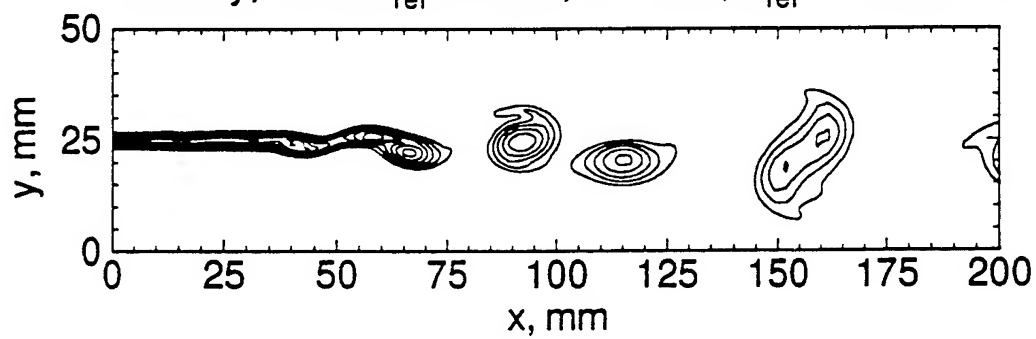
Mass Fraction, $0.8132 \leq Y_{H_2} \leq 1$, $\Delta = 0.05$



Viscosity Ratio, $0 \leq \nu_t/\nu_l \leq 0.2947$

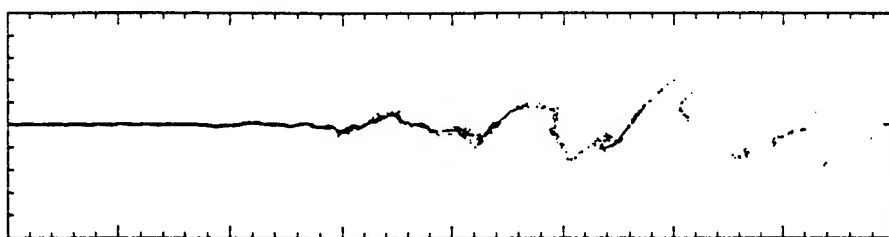


Vorticity, $0 \leq \omega/\omega_{ref} \leq 100\%$, $\Delta = 10\%$, $\omega_{ref} = -74 \times 10^3 \text{ s}^{-1}$

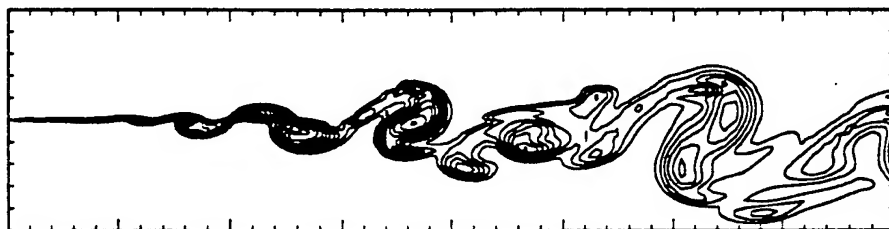


100 atm, O/F = 4

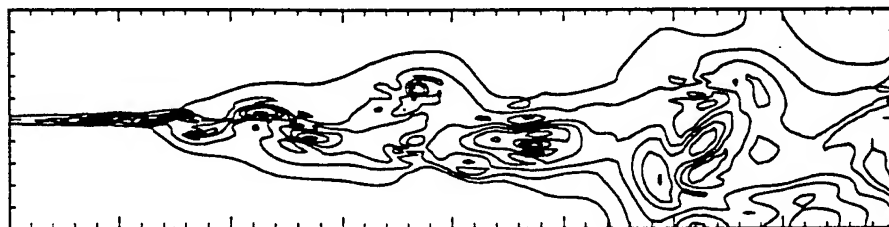
Spray Distribution, 2680 Parcels, 2.8×10^6 Particles



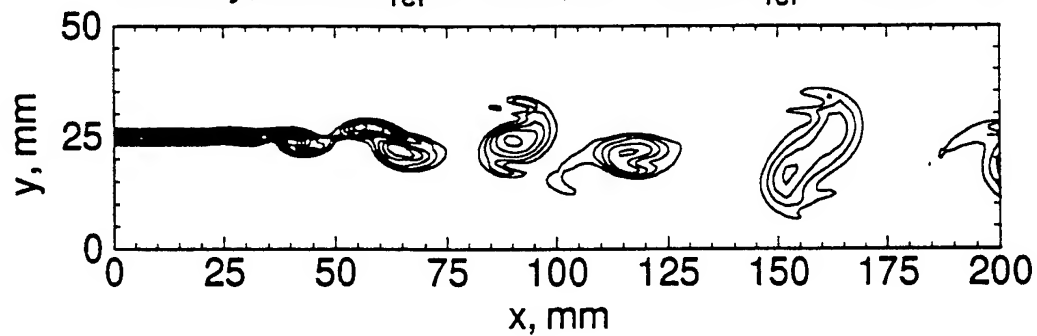
Mass Fraction, $0.4032 \leq Y_{H_2} \leq 1$, $\Delta = 0.05$



Viscosity Ratio, $0 \leq \nu_t/\nu_l \leq 35.52$, $\Delta = 5$

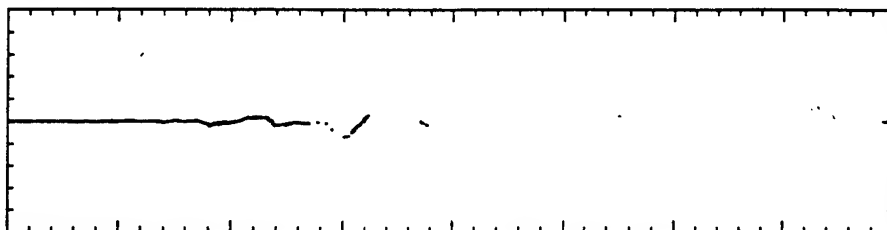


Vorticity, $0 \leq \omega/\omega_{ref} \leq 100\%$, $\Delta = 10\%$, $\omega_{ref} = -74 \times 10^3 \text{ s}^{-1}$

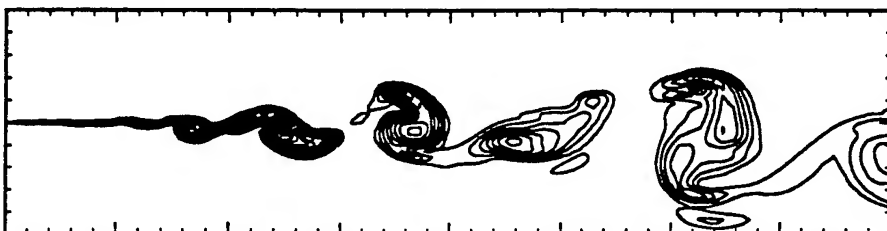


400 atm, O/F = 4

Spray Distribution, 1363 Parcels, 5.1×10^6 Particles



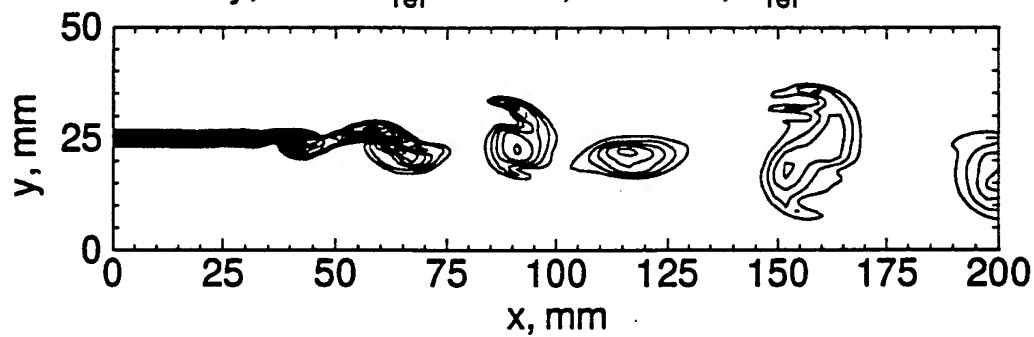
Mass Fraction, $0.2102 \leq Y_{H_2} \leq 1$, $\Delta = 0.05$



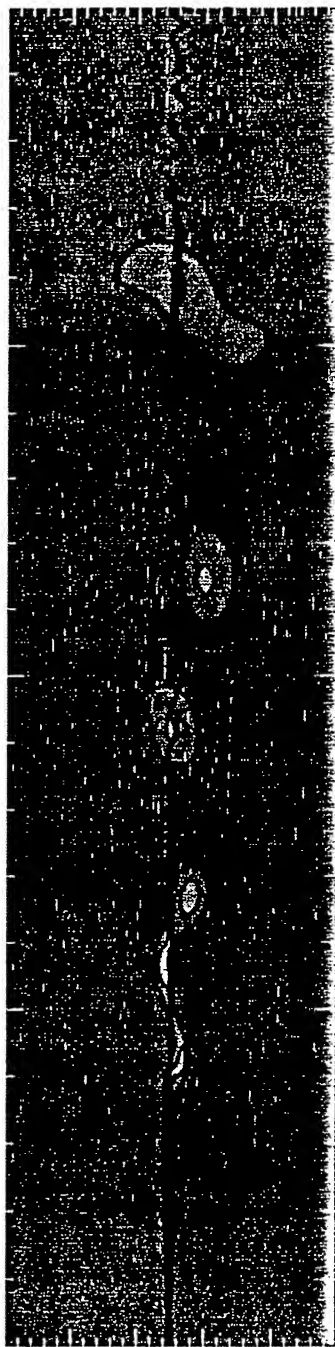
Viscosity Ratio, $0 \leq \nu_t/\nu_l \leq 195.0$, $\Delta = 5$



Vorticity, $0 \leq \omega/\omega_{ref} \leq 100\%$, $\Delta = 10\%$, $\omega_{ref} = -74 \times 10^3 \text{ s}^{-1}$



1 atm



100 atm



SHEAR COAXIAL UNI-ELEMENT INJECTOR

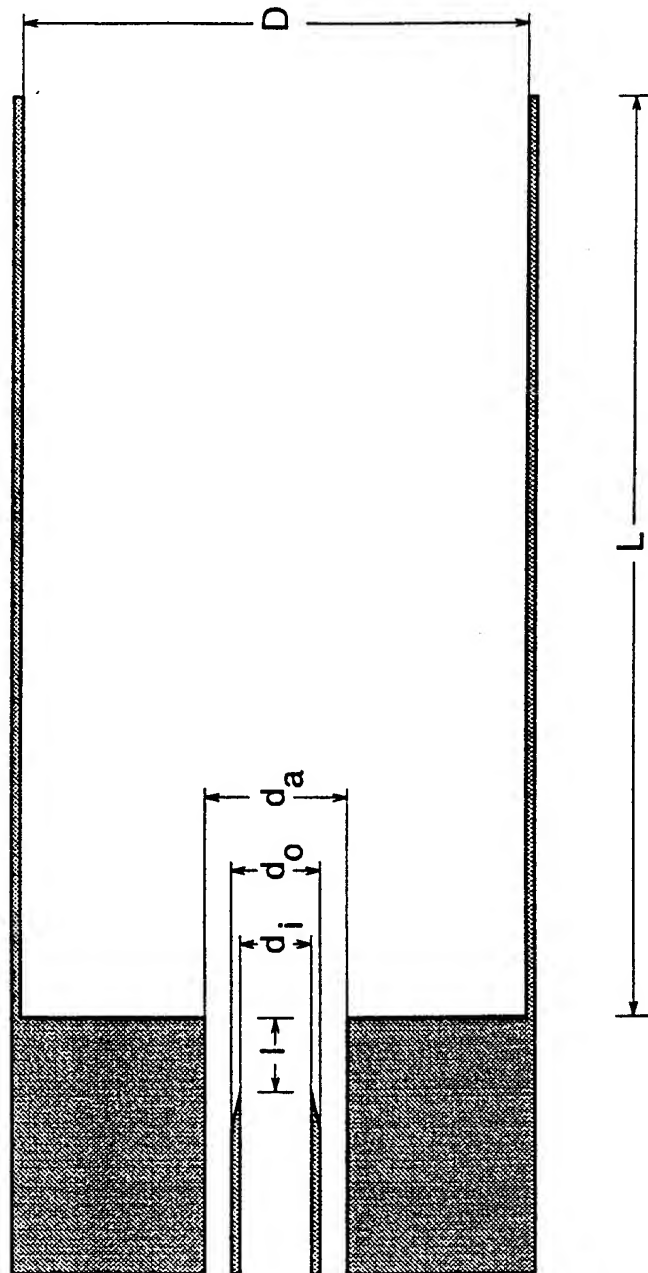


Table 5: Inlet conditions employed for the analysis of high-pressure hydrogen-oxygen mixing and combustion processes. Subscript 1 denotes the hydrogen stream, subscript 2 denotes the oxygen stream.

	1	2	3	4	5	6
p [atm]	100	100	100	100	100	100
T_1 [K]	150	150	150	300	300	300
T_2 [K]	100	100	100	300	300	300
T_2/T_1	0.6667	0.6667	0.6667	1	1	1
ρ_1 [kg/m ³]	15.37	15.37	15.37	7.752	7.752	7.752
ρ_2 [kg/m ³]	1118	1118	1118	134.7	134.7	134.7
ρ_2/ρ_1	72.75	72.75	72.75	17.37	17.37	17.37
U_1 [m/s]	500	250	125	250	125	62.5
U_2 [m/s]	30	30	30	30	30	30
U_2/U_1	0.06	0.12	0.24	0.12	0.24	0.48
$\rho_2 U_2 / \rho_1 U_1$	4.365	8.730	17.46	2.084	4.169	8.338
$\rho_2 U_2^2 / \rho_1 U_1^2$	0.2619	1.048	4.190	0.2501	1.001	4.002
M_1	0.4828	0.2414	0.1207	0.1786	0.08931	0.04465
M_2	0.04572	0.04572	0.04572	0.09203	0.09203	0.09203
Re_{δ_1}	1424000	715700	359400	243200	121900	60990
Re_{δ_2}	245000	245000	245000	201700	201700	201700
Pr_1	0.7842	0.7842	0.7842	0.6913	0.6913	0.6913
Pr_2	1.917	1.917	1.917	0.7832	0.7832	0.7832
Sc_1	1.560	1.560	1.560	1.365	1.365	1.365
Sc_2	89.09	89.09	89.09	0.2207	0.2207	0.2207
Le_1	1.964	1.964	1.964	1.975	1.975	1.975
Le_2	46.48	46.48	46.48	0.2817	0.2817	0.2817

$Re_\delta \equiv U_e \delta / \nu$ where U_e represents the edge velocity and δ the channel half width.

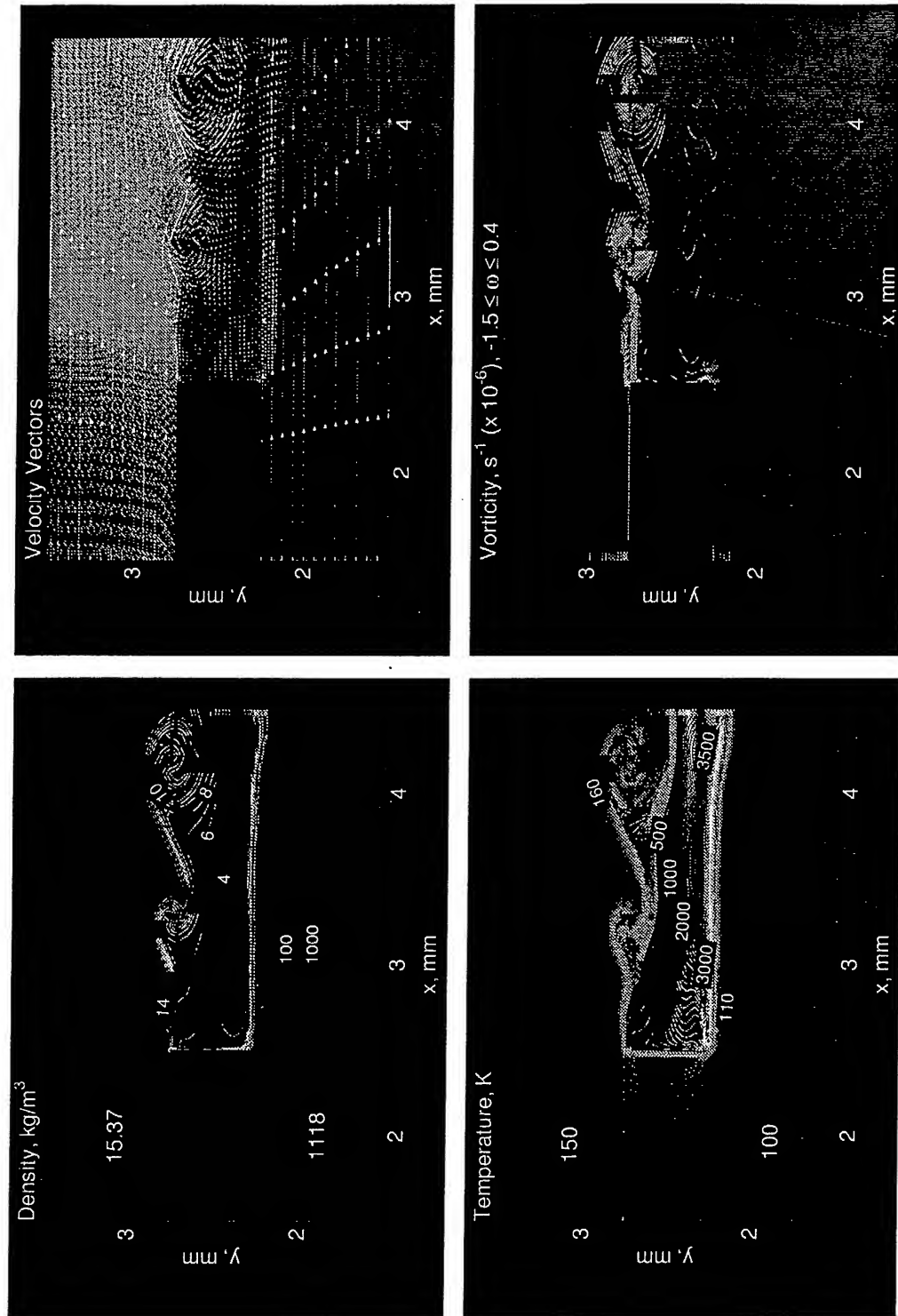


Figure 19: Contours of density, temperature, velocity, and vorticity in the near-field region of the splitter plate for inlet condition-3 in Table 5.

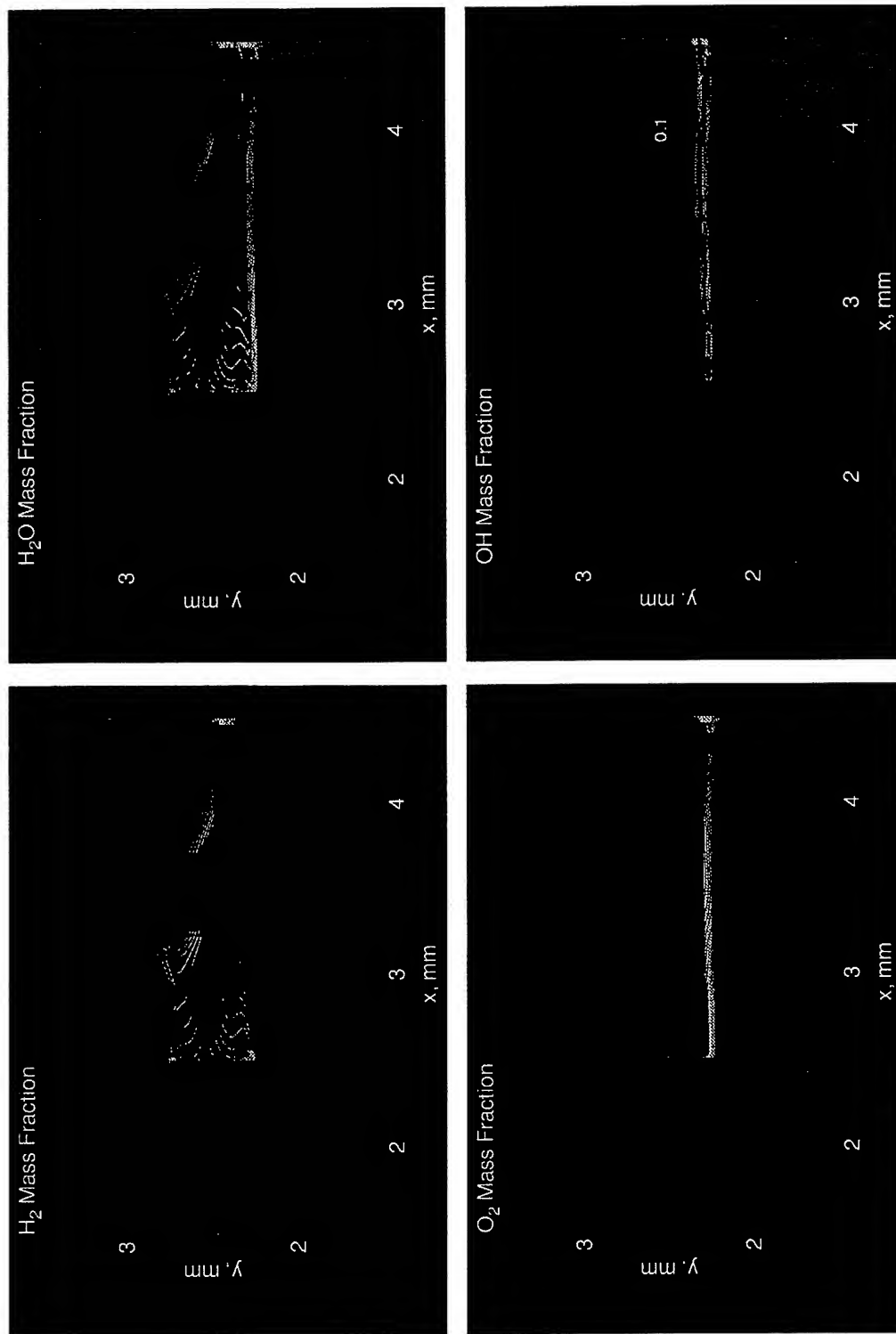


Figure 20: Contours of H_2 , O_2 , H_2O , and OH mass fraction in the near-field region of the splitter plate for inlet condition 3 in Table-5.

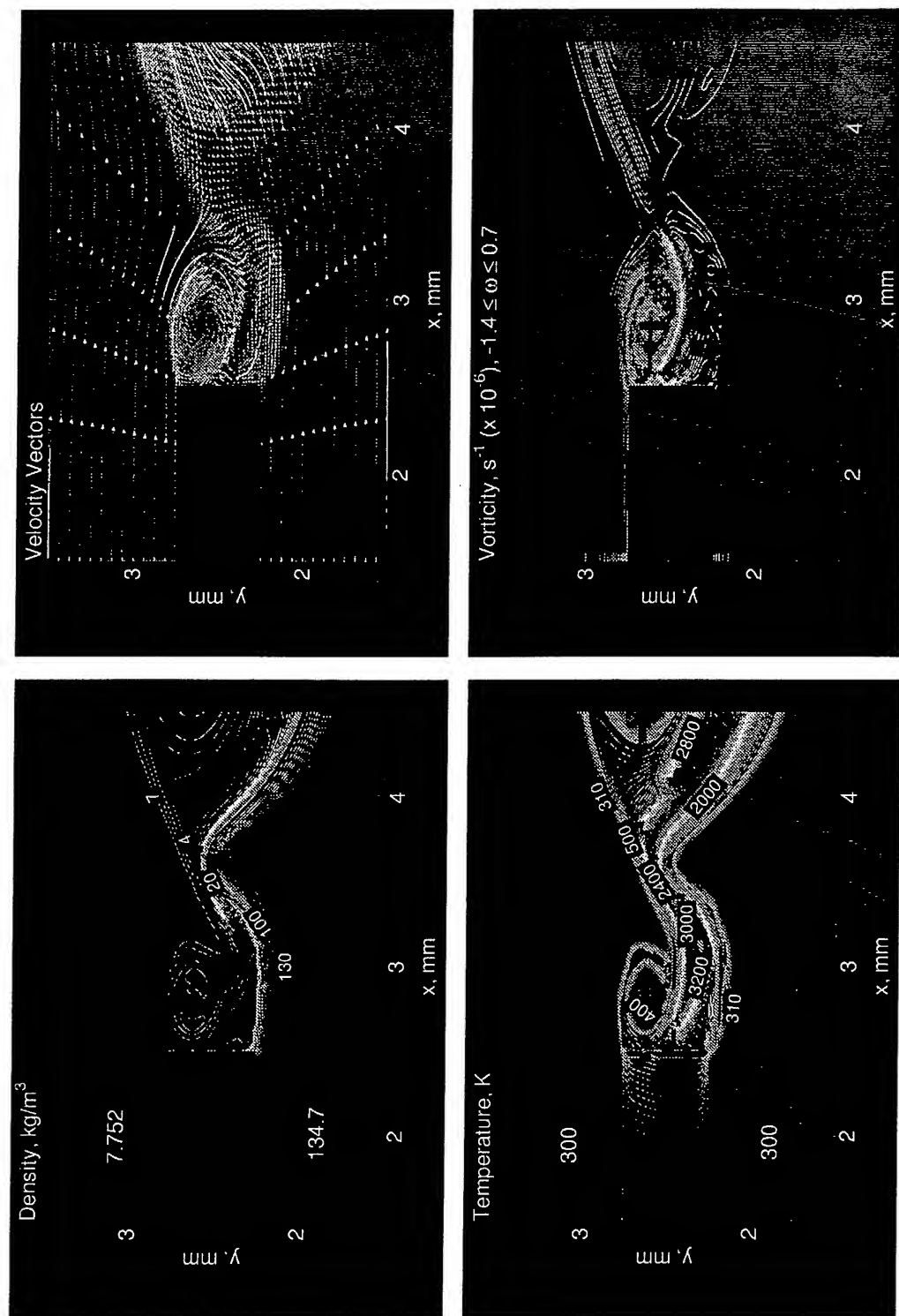


Figure 21: Contours of density, temperature, velocity, and vorticity in the near-field region of the splitter plate for inlet condition 5 in Table 5.

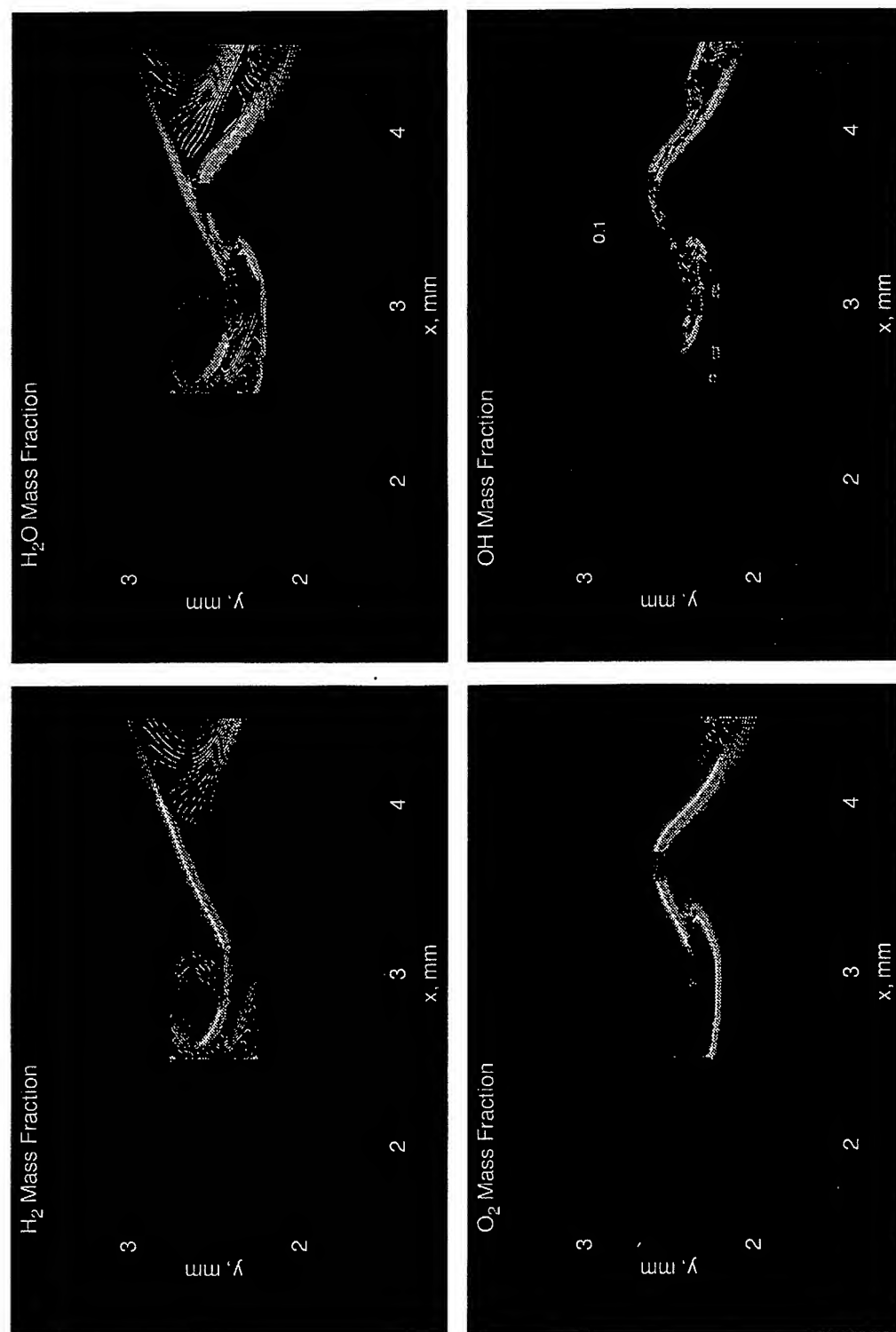
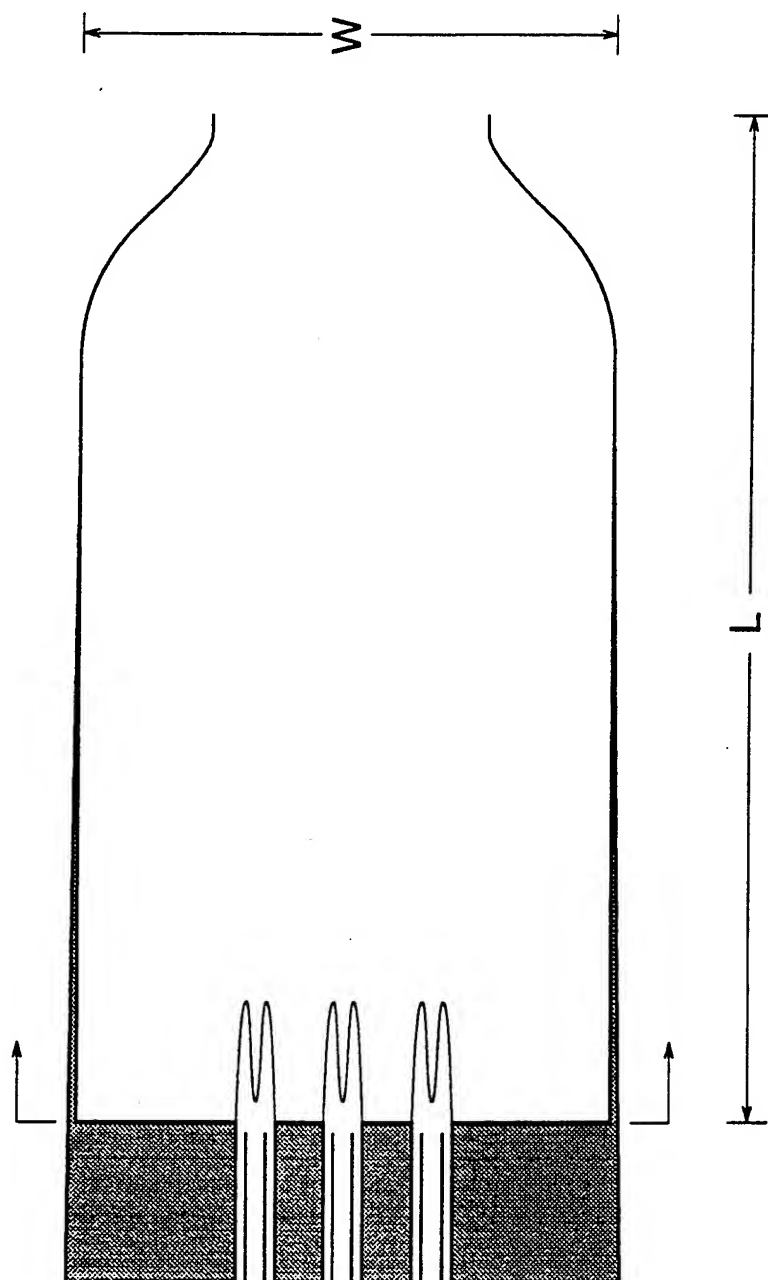


Figure 22: Contours of H_2 , O_2 , H_2O , and OH mass fraction in the near-field region of the splitter plate for inlet condition 5 in Table-5.

PLANAR COAXIAL TRI-ELEMENT ARRAY



Cryogenic Combustion Modelling

—
B. Barbeau, F. Lacas, G. Rymmer and S. Candel

—
*Labo EM2C du CNRS et de l'ECP, Grande Voie des Vignes,
F-92295 Châtenay Malabry, France*

INTRODUCTION :

- Simulation conditions
- Numerical solver
- Combustion model
- Spray model
- Computational domain
- Results



General

- Finite volume (ALE), basic equations in integral form
- Structured mesh with hexaedric cells

Spray

- Statistical Eulerian Lagrangian method
- Vaporizing droplets, Turbulent movement
- No collision, No breakup

Combustion model

- Coherent Flame Model

- 1 droplet is representative of n droplets of identical size, velocity and temperature.
- Droplets turbulent movement : t_k characteristic turbulent correlation time, Δt timestep
 - If $\frac{\Delta t}{t_k} < 1$ then $\mathbf{v_d} = \mathbf{v_d}'$
 - If $\frac{\Delta t}{t_k} > 1$ then $\mathbf{v_d} = \mathbf{v_d}'$ and $\mathbf{x_d} = \mathbf{x_d} + \mathbf{x_d}'$



- Vaporization law : Wet Bulb Temperature model

$$\dot{r} = \frac{-\rho D(\bar{T})}{2\rho_{Lox}r} B Sh_d$$

- with $B = \frac{Y_{O_2}^* - \bar{Y}_{O_2}}{1 - Y_{O_2}^*}$
- and $Sh_d = (2 + 0.6 Re_d^{0.5} Sc_d^{1/3}) \frac{\log(1+B)}{B}$
- $Y_{O_2}^*$ is the gaseous oxygen mass fraction at droplet surface.



Mean reaction rate $\overline{\dot{\omega}_c}$ is given by $\overline{\dot{\omega}_c} = -\bar{\rho} S_d \bar{\Sigma}$, where $\bar{\Sigma}$ is described by the following transport equation

$$\frac{\partial \bar{\Sigma}}{\partial t} + \nabla \cdot \tilde{\mathbf{u}} \bar{\Sigma} = \nabla \cdot \frac{\nu \Sigma}{\sigma \Sigma} \nabla \bar{\Sigma} + E_s \bar{\Sigma} - \beta \left(\frac{S_d}{Y_{H_2}} + s \frac{S_d}{Y_{O_2}} \right) \bar{\Sigma}^2$$

E_s is the turbulent strain rate

$$E_s = \alpha_{\tilde{k}} \tilde{\epsilon} \text{ and } \Phi = s Y_{H_2^0} / Y_{O_2^0}$$

and S_d oxygen consumption velocity is given by

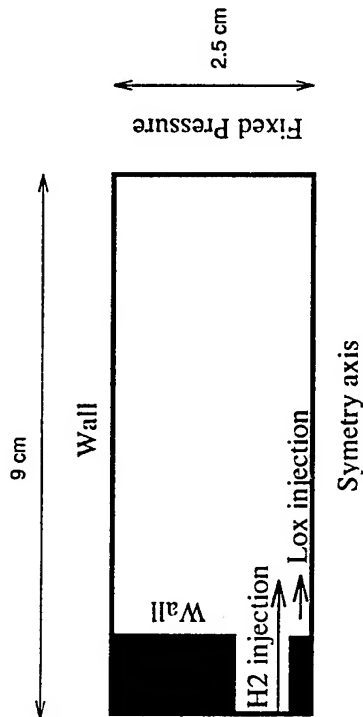
$$S_d = Y_{o\infty} \left(\frac{D E_s}{2\pi} \right)^{1/2} \frac{\Phi + 1}{\Phi} \exp \left(\operatorname{erf}^{-1} \left(\left(\frac{\Phi - 1}{\Phi + 1} \right)^2 \right) \right)$$



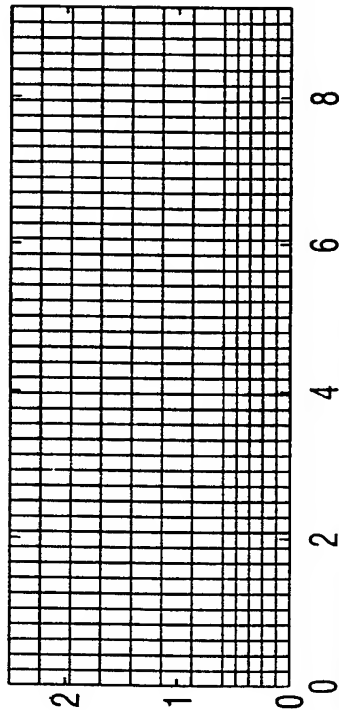
Laboratoire E.M2.C.



Without recess
size : 2.5 × 9 cm



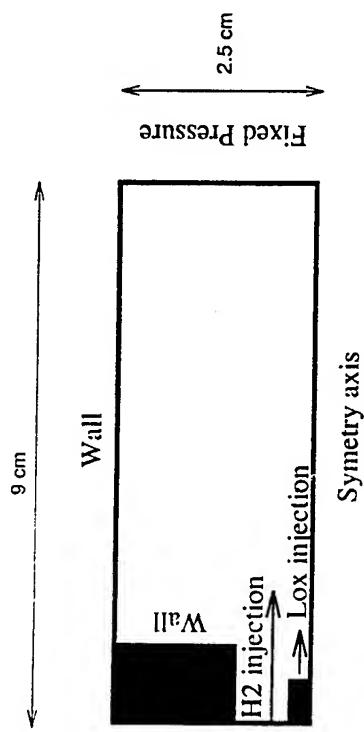
mesh : 13 × 45



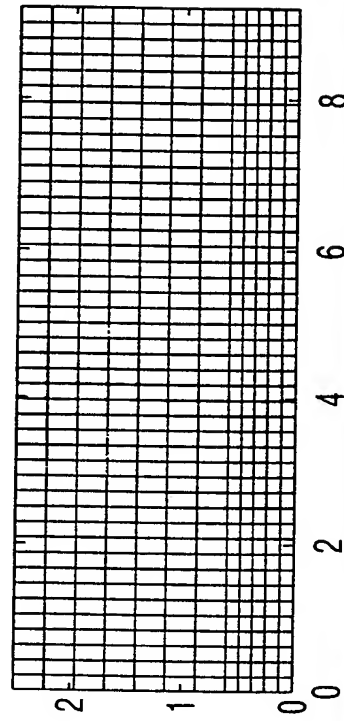
COMPUTATIONAL DOMAIN : Configuration and mesh

With recess

size : 2.5×9 cm; recess = D_{Lox}



mesh : 13×45



Laboratoire E.M2.C.



SIMULATION CONDITIONS : general inflow conditions

And for all simulation points :

Species	Variable	Value
H_2	Temperature (K)	300
	Density (kg/m^3)	0.8
O_2	Temperature (K)	80
	Density (kg/m^3)	1170
	Pressure (bars)	10

SIMULATION CONDITIONS : 4 different inflow conditions

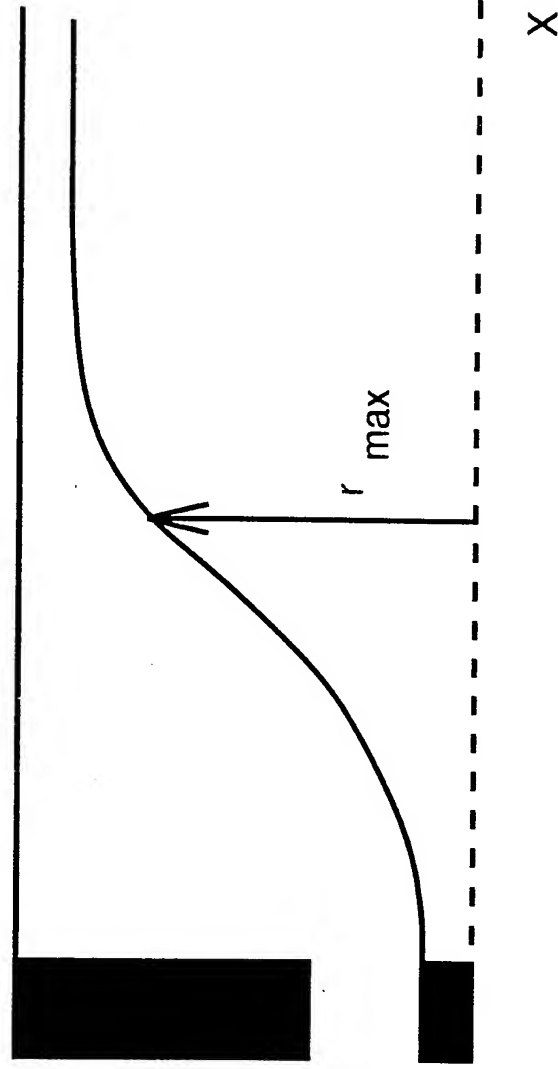
General propellant inflow conditions (with and without recess)

Species	Variable	Point A	Point C
H_2	Velocity (m/s)	308	207
LOx	Velocity (m/s)	2.23	2.23
	$We.10^{-3}$	28.2	12.6
	$Re_{Lox} .10^{-3}$	67	67
	J	14.5	6.5



Without recess

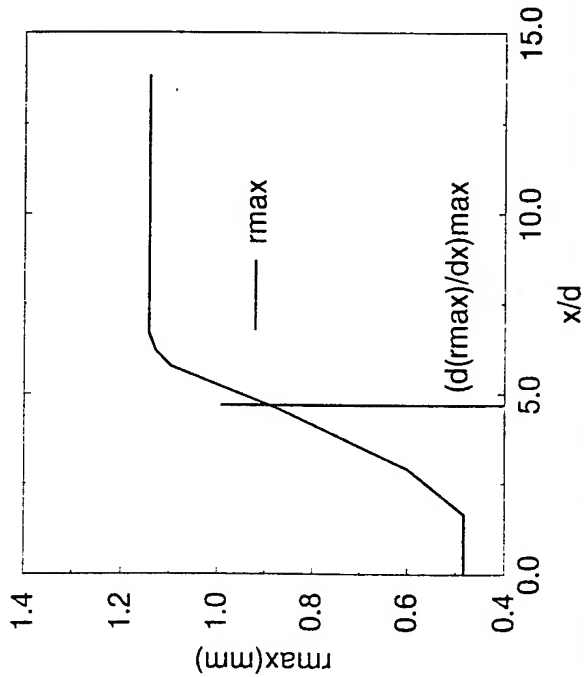
- Locate flame's maximum expansion rate (x_d)
- Compare x_d with experimental trends of the flame



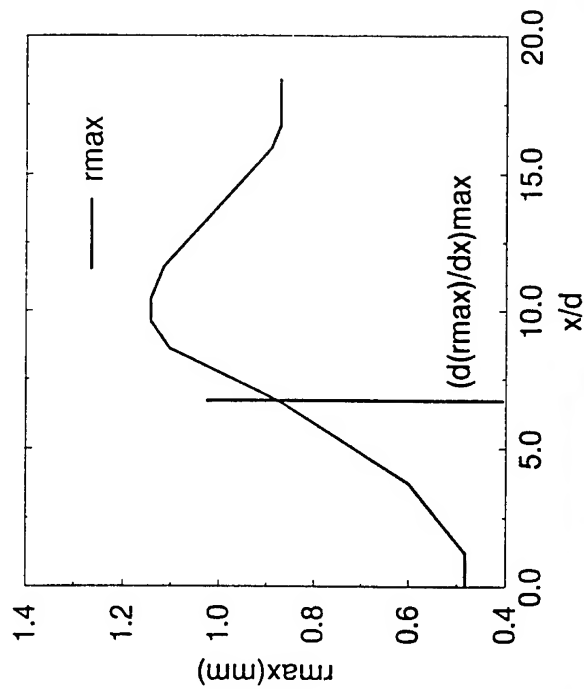
Without recess

	x_d (comp)	x_d (exp)
Point A	4.6	1.0
Point C	6.6	3.0

Point A



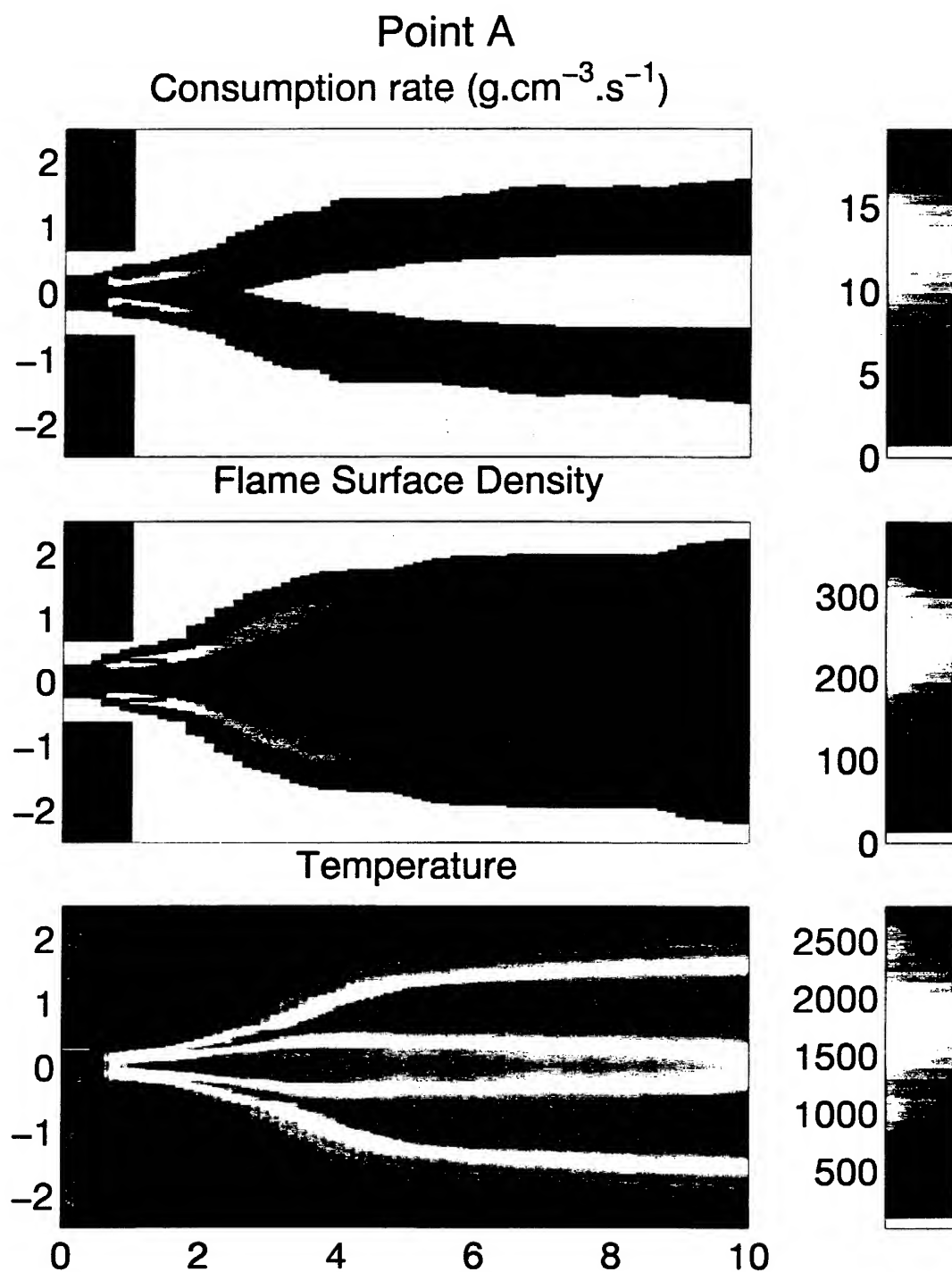
Point C



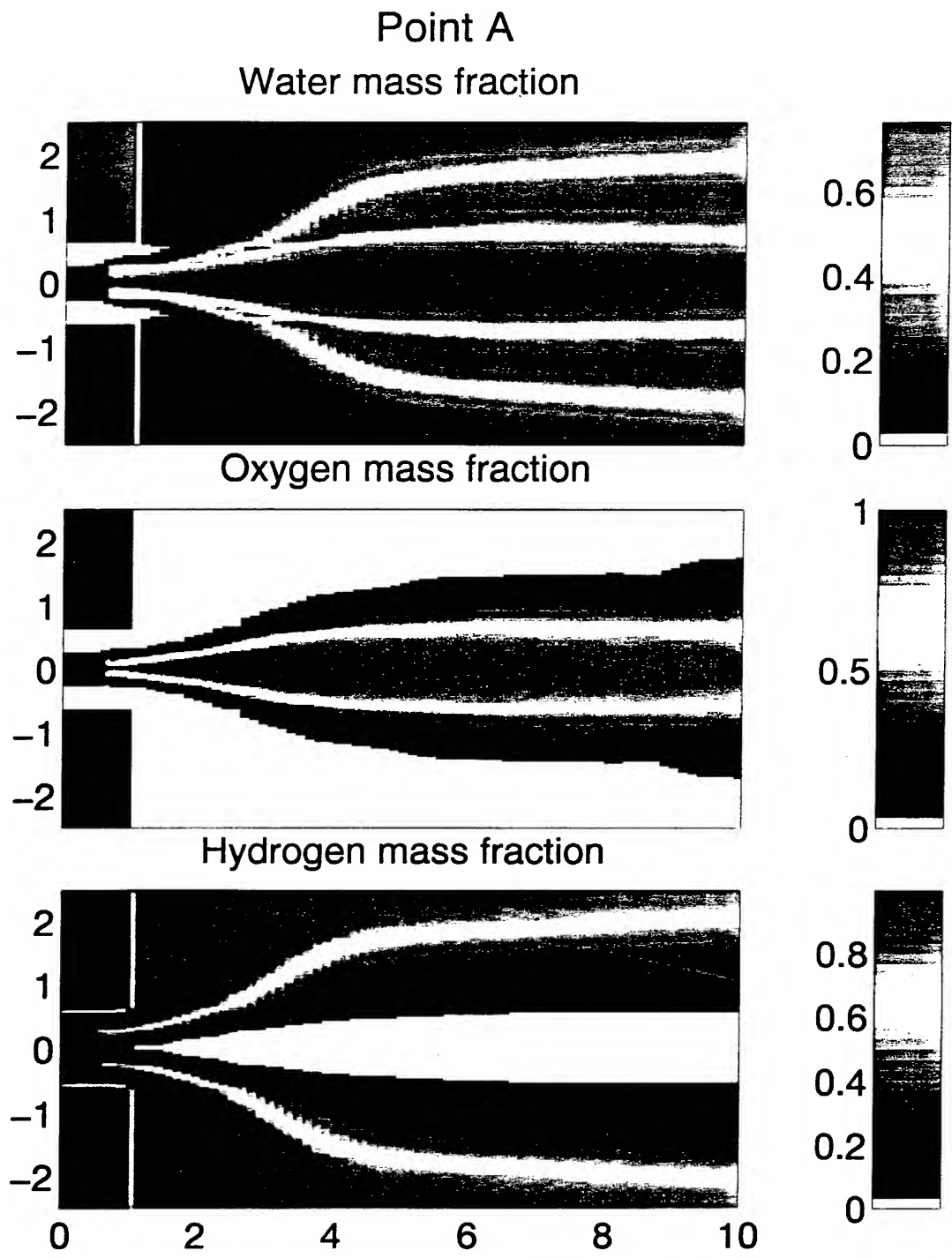
Laboratoire E.M2.C.



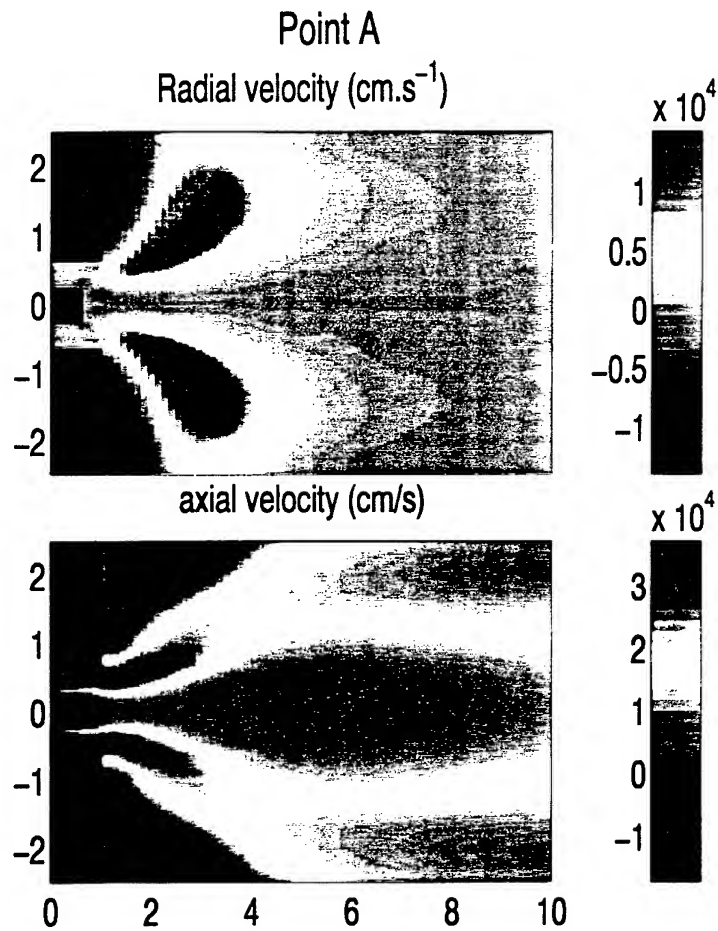
RESULTS : Point A, with recess



RESULTS : Point A, with recess



RESULTS : Point A, with recess



Point A with recess



Point A without recess



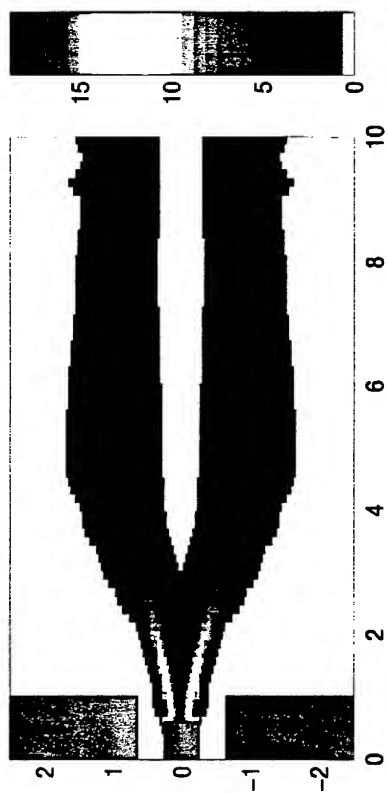
Point C with recess



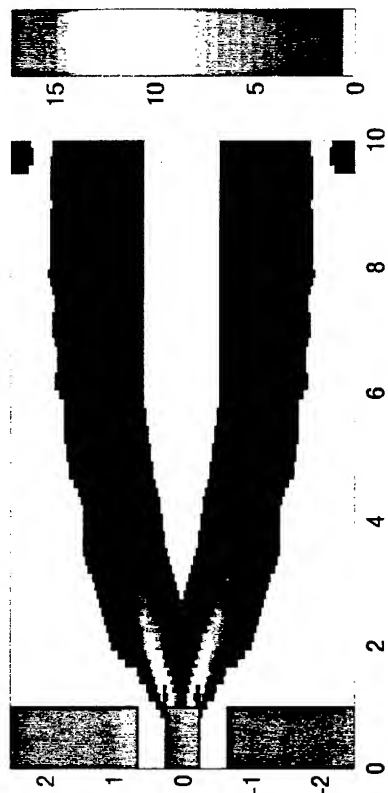
Point C without recess



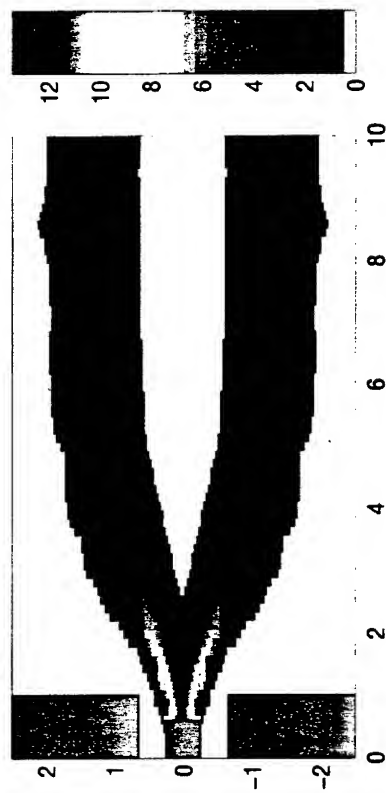
Point A avec retrait



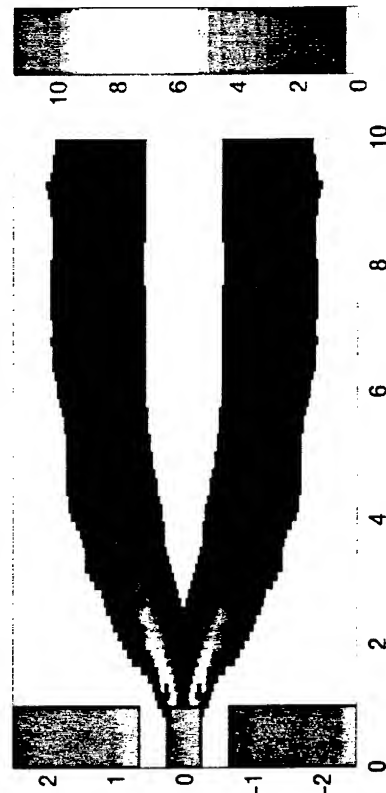
Point A sans retrait



Point C avec retrait

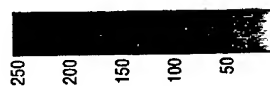
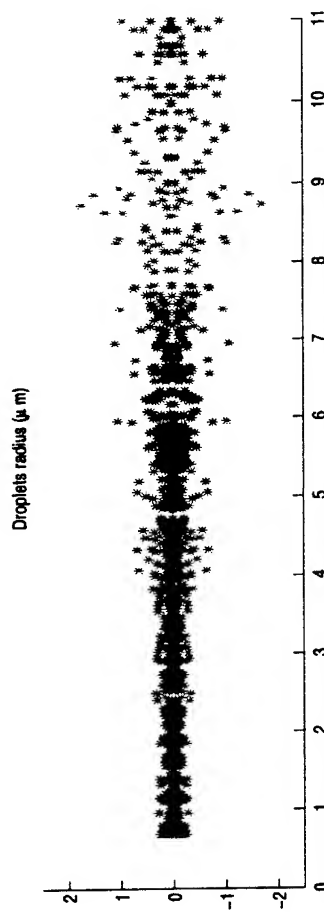
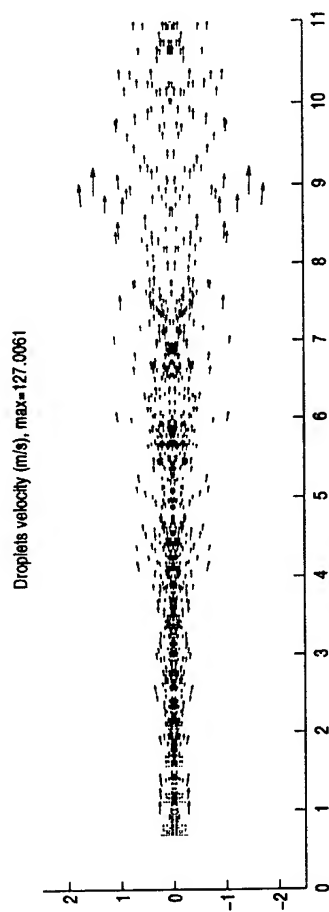


Point C sans retrait

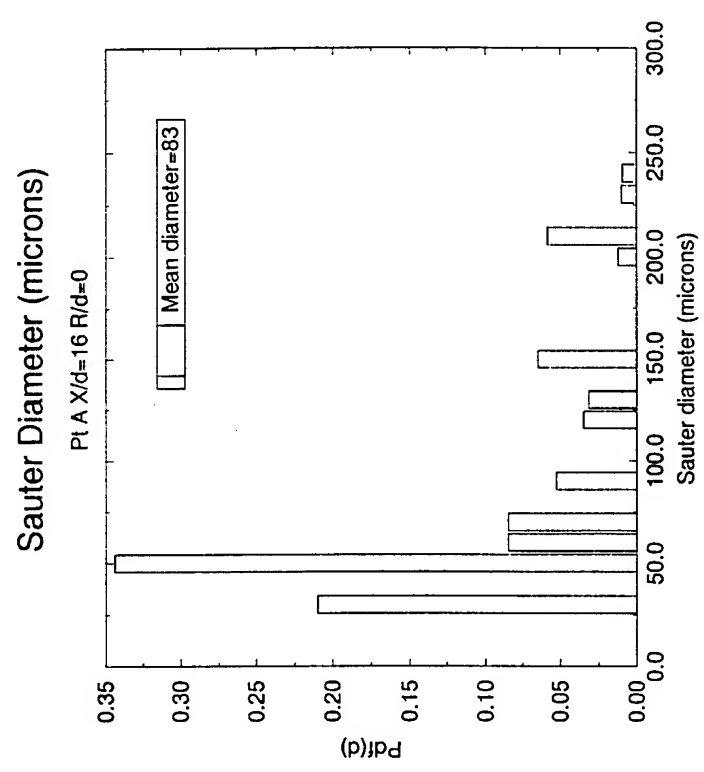
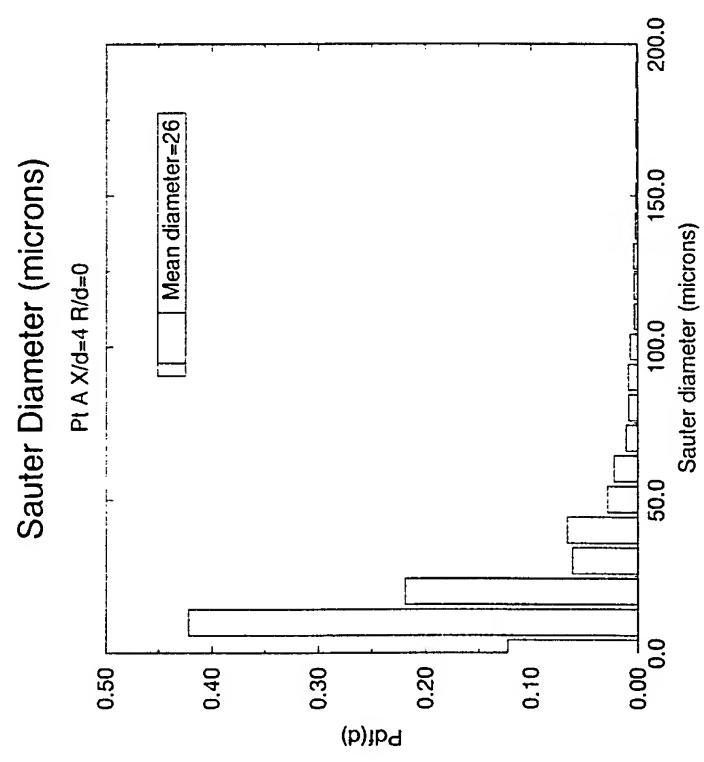


RESULTS : Point A, without recess

- Droplets velocities
- Droplets positions



Point A without recess



$x/d = 4$

Measured SMD : 59.9 μm

$x/d = 16$

Measured SMD : 102.8 μm

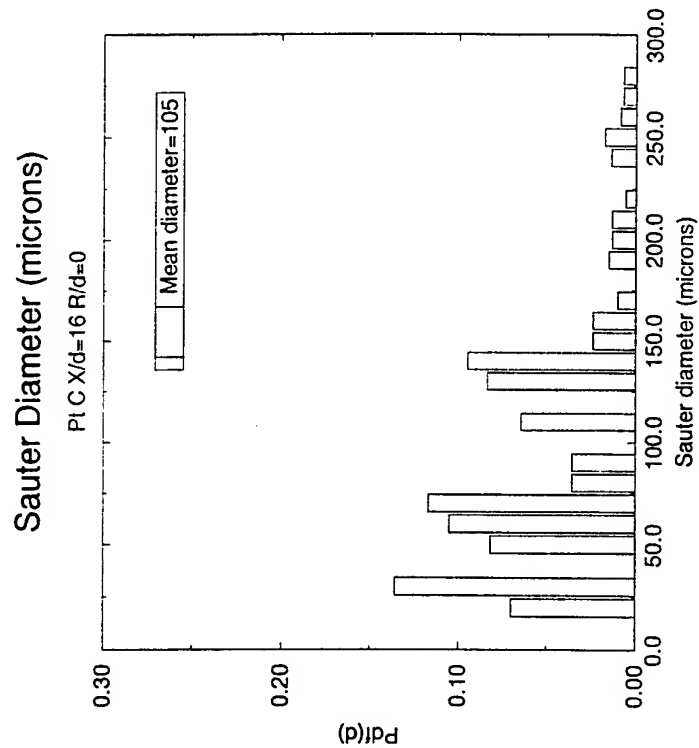
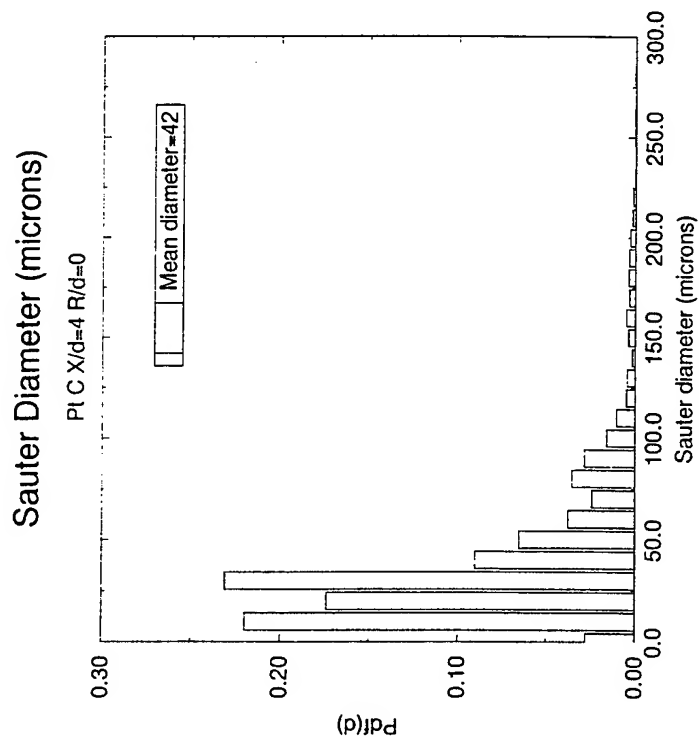


Laboratoire E.M2.C.



COMPARISON WITH EXPERIMENT : PDA/simulation

Point C without recess



$x/d = 4$

Measured SMD : 73.4 μm

$x/d = 16$

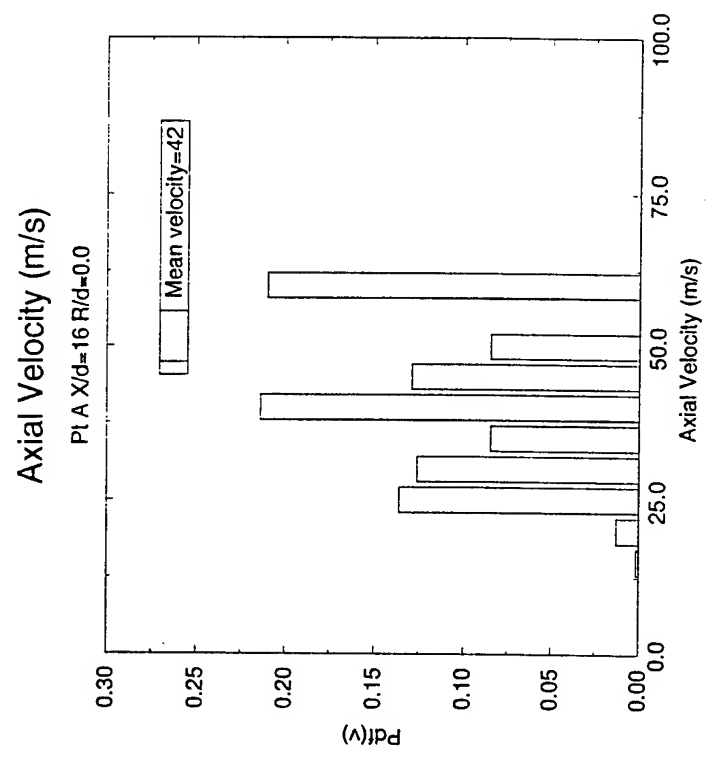
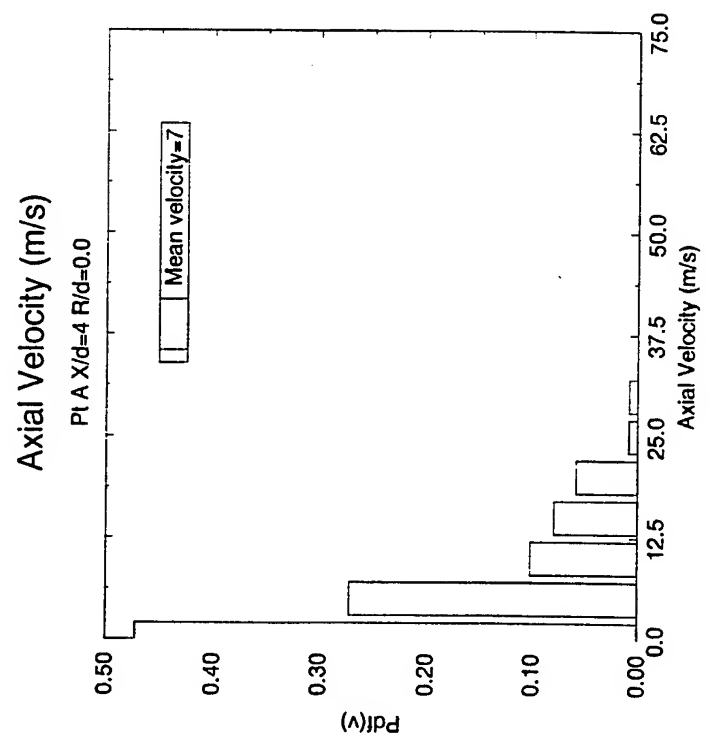
Measured SMD : 103.5 μm



Laboratoire F. M. C.



Point A without recess



$x/d = 4$
Mean Velocity 26.2 ms^{-1}

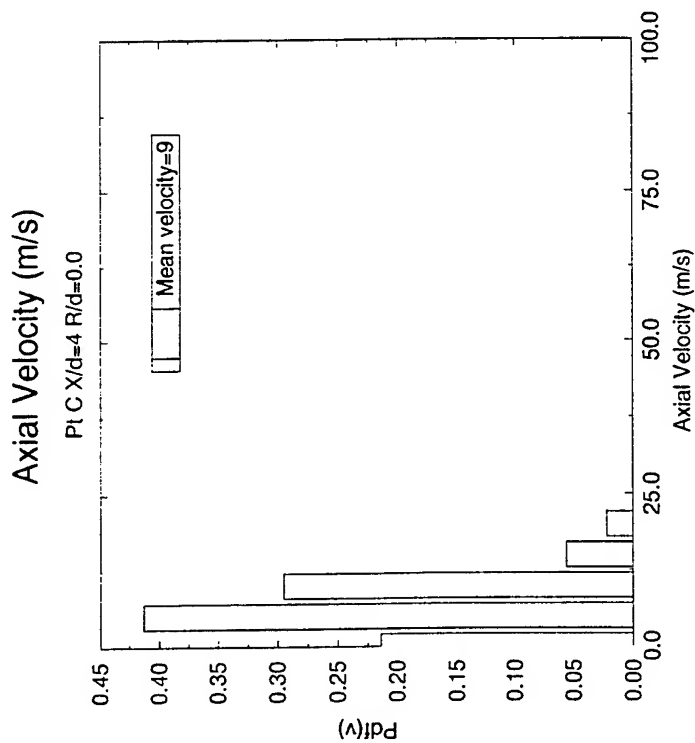
$x/d = 16$
Mean Velocity 8.6 ms^{-1}



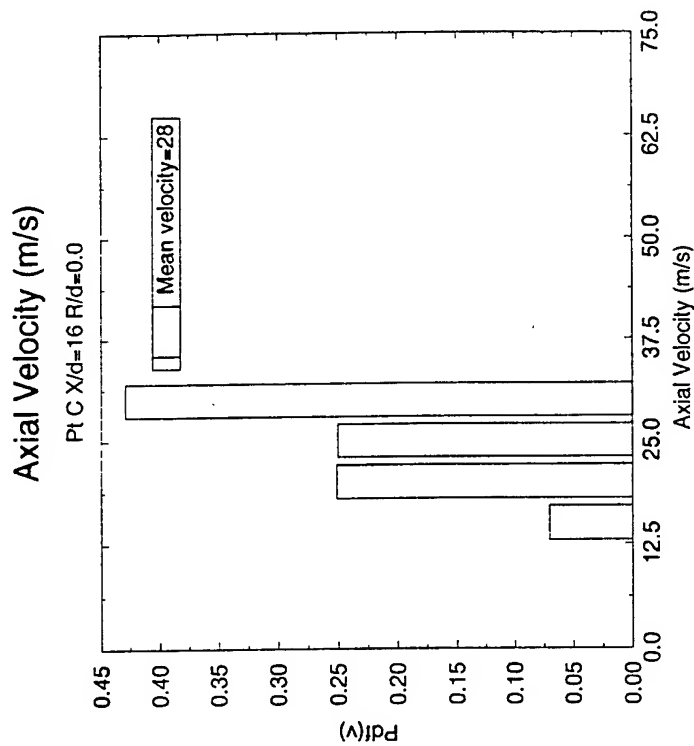
Laboratoire E.M2.C.



Point C without recess



$x/d = 4$
Mean Velocity 16.8 m s^{-1}



$x/d = 16$
Mean Velocity 8.3 m s^{-1}



Laboratoire E.M2.C.



Good agreements :

- Flame shape
- Flame shape's dependence with momentum ratio
- Droplets sizes

Problems :

- Flame stabilization
- Atomization

Comparison Simulation/Experiment needs postprocessing of computation results

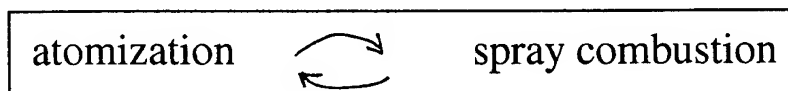
**Thin Film Dynamics
and the
Physics of Atomization**

Dirk Meinköhn
Deutsches Zentrum für Luft- und Raumfahrt DLR
D-74239 Hardthausen
e-mail: dirk.meinkoehn@dlr.de

Liquid Rocket Combustion Chamber Flow Dynamics
International Workshop CNES (Paris), May 27-28 (1999)

General Remarks

- liquid propellants: **combustion**
 - gasification
 - mixing processes
 - combustion: efficiency
 - motor operations: stability
- **spray states**: intermediate, important
- feedback loop:



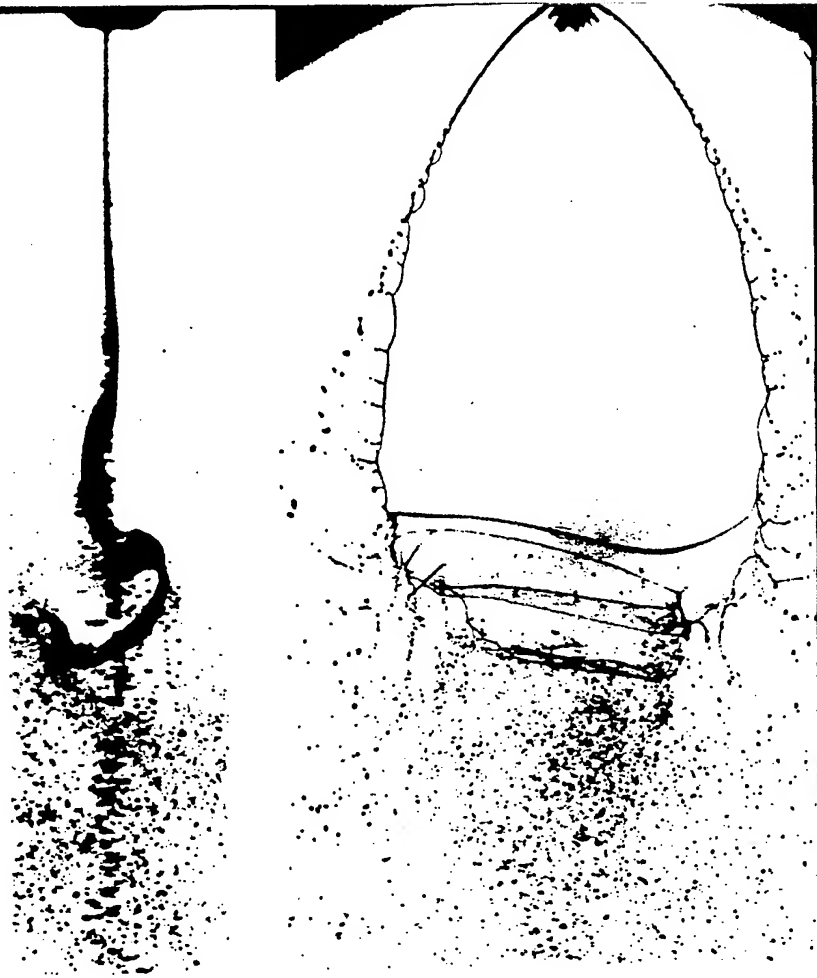
- atomization problematics: no comprehensive model available
- atomization → hydrodynamic process
 - liquid membranes/ligaments: flow processes
 - liquid edges: formation/dynamics
 - droplet detachment: neck formation/pinching/rupture
- **asymptotic descriptions**

Atomization Processes

- forcing process:
 - nozzle flow → jet
 - air assist/electrostatic/ultrasonic/ ...
 - generation of liquid membranes/filaments
- decomposition of membranes/filaments
 - droplets/spray formation
- investigation: **applications oriented**/empirical approach
 - forcing process: technicalities/devices
 - spray properties: empirical
 - feed-back from downstream combustion: neglected
- investigation: **physics orientated**/predictive approach
 - liquid flow processes in membranes/filaments: 2-d/1-d
 - interaction with 3-d environment:
 - * **formation/dynamics of liquid edges**
 - * **criticality** (→ static equilibrium of liquid edges)
 - * **propagation of perturbations** in liquid membranes
 - * **rupture/necking/pinching**
 - * **feedback processes**
- **deductive approach → predictive approach**

(van Dyke)

147. Kelvin-Helmholtz waves on a thin liquid sheet. Water is ejected downward in the form of a thinning sheet from a fan-spray nozzle that is vibrated sinusoidally normal to the plane of the sheet at a frequency giving wave instability. A side view shows the initial exponential growth predicted by two-dimensional theory and the development of a complex wave form as the amplitude increases. The stream of drops along the axis at the bottom is seen in the plan view to result from collapse of the rims of the sheet. *Crapper, Dombrowski, Jepson & Pyott 1973*



droplet detachment: role of liquid edges



Daimler-Benz Aerospace

Raumfahrt-Infrastruktur



Third French-German Colloquium on

Research on Liquid Rocket Propulsion

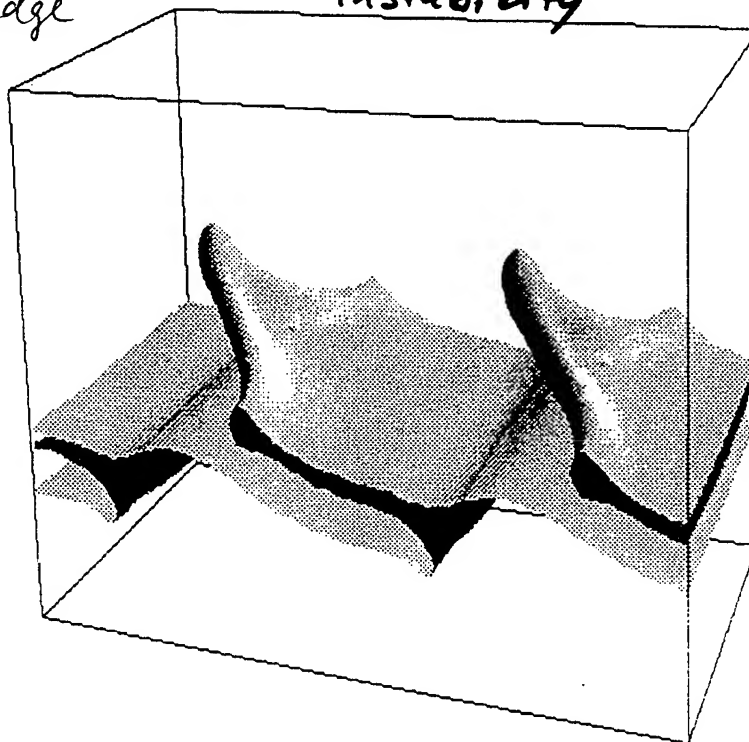
example: formation of
a liquid edge



• Kelvin-Helmholtz
instability

Topics :

- Heat Transfer
- Diagnostics
- Modelling
- Atomisation



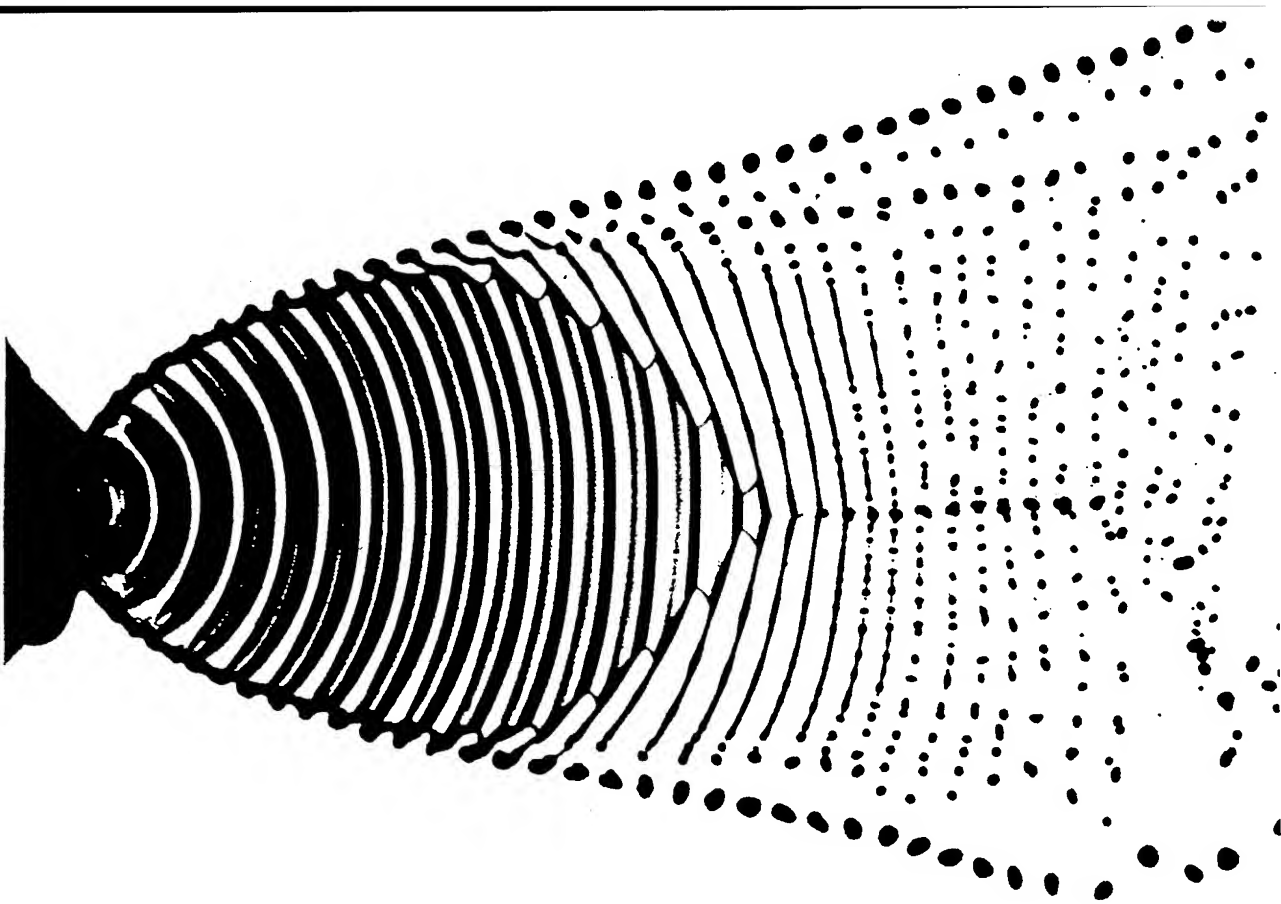
5-6 June 1997

Marseilles (France)

3-D Simulation of liquid-gas shear layer. S Zaleski & J.Li

*Rapp. final de Synthèse
1995, ZIRA CNRS 22*

prepared by the
CNES SEP DASA DLR joint programme group
organised by the CNRS (IRPHE) in partnership with
the Université de la Méditerranée and the city of Marseilles



149. Breakup of a liquid sheet. Studies of drop formation in sprays show that the production of filaments generally constitutes an intermediate stage. Controlled filament formation should therefore provide a means of regulating the size of drops. One approach is to subject the nozzle to

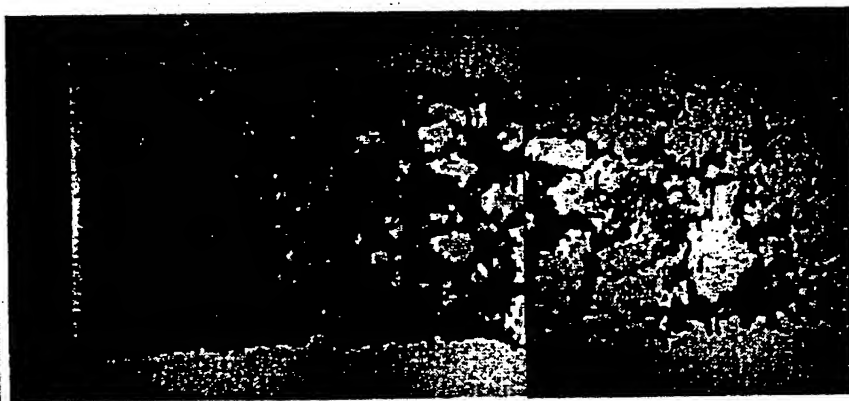
forced vibrations. This photograph shows a flat laminar sheet of water issuing from a fan-spray nozzle that is oscillated axially at resonant frequency. Photograph by N. Dombrowski

liquid edges and droplet detachment

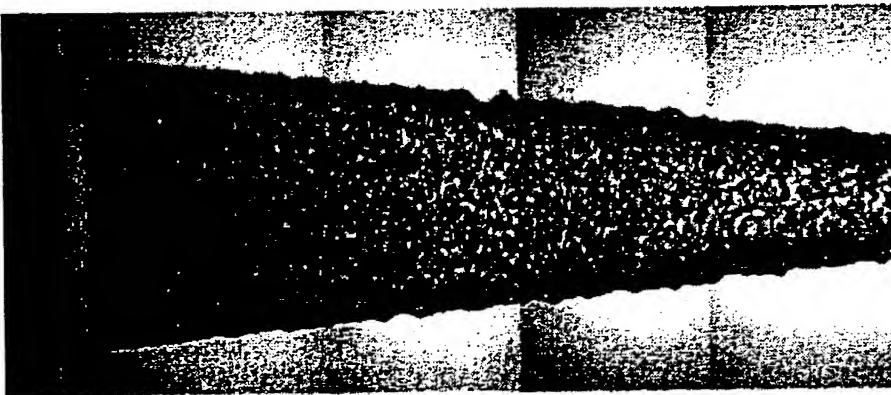


$U_L = 4.3 \text{ m/s}$

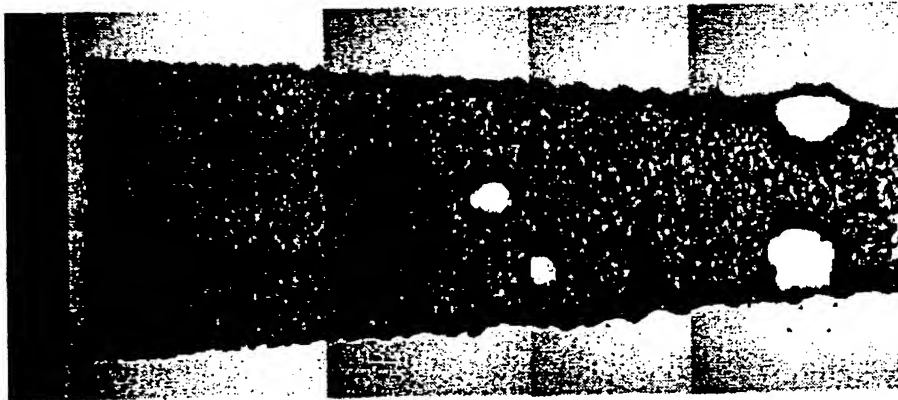
$Re = 2400$



$U_1 = U_2 = 20 \text{ m/s}$

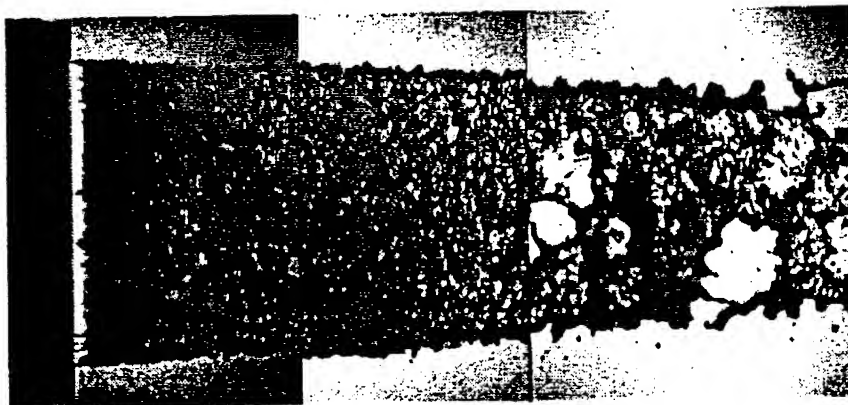


$U_1 = U_2 = 0$



$U_L = 6.4 \text{ m/s}$

$Re = 4200$



$U_1 = U_2 = 20 \text{ m/s}$

Physical Characterization

- flow processes → **hydrodynamics**

1. liquid membranes/filaments: deformation → propagation of pressure perturbations
2. propagation of existing free edges
3. rupture processes for membranes/filaments
4. formation of free edges

- **long wave theory:**

reference wave length λ large → **reduction in dimensionality**

** 2-d membranes / 1-d filaments **

- characteristic dimensions: *cm* , *sec* , *g*
- characteristic variables

(relative) flow velocity	u	[<i>cm/sec</i>]
characteristic length	h	[<i>cm</i>]
density	ρ	[<i>g/cm</i> ³]
kinematic viscosity	ν	[<i>cm</i> ² / <i>sec</i>]
surface tension	σ	[<i>g/sec</i> ²]

- characteristic groups

Reynolds $Re = uh/\nu$

Capillary $Ca = u\rho\nu/\sigma$

Weber $We = \sigma/h\rho u^2 = \frac{1}{ReCa}$

Ohnesorge $Oh = \nu\sqrt{\rho/\sigma h} = \frac{\sqrt{We}}{Re} = \sqrt{\frac{Ca}{Re}}$

Bond $Bo = \rho gh^2/\sigma$

Hydrodynamic Models

- Navier-Stokes equations → **continuum-theoretic**

$$\nabla \cdot \vec{v} = 0 \quad , \quad \rho = \text{const}$$

$$\partial_t \vec{v} + (\vec{v} \cdot \nabla) \vec{v} = \frac{1}{\rho} \nabla p + \nu (\nabla \cdot \nabla) \vec{v}$$

- **thin** liquid membranes/ligaments

$$p = \sigma \kappa$$

- 2 limit cases (no gravity):

case 1: Weber-number hydrodynamics

- no viscosity/no dissipation
- propagation/dynamics:
 - * pressure perturbations
 - * free edges

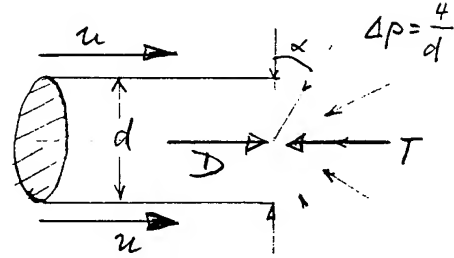
case 2: Ohnesorge-number hydrodynamics

- viscosity important/strong dissipation
- rupture processes:
 - * continuum-theoretic asymptotics
 - * needle's-eye-role of microphysics

Weber Number Hydrodynamics

- **static criticality:** drag force D = surface tension force T

$$D = \frac{1}{2} c_D \frac{\pi d_{crit}^2}{4} \rho_{air} u^2 = T = \pi \sigma d_{crit}$$



- typical estimate: **diameter of maximal drop** d_{max}

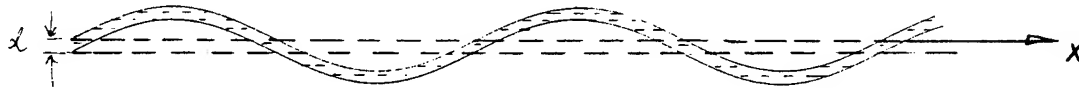
$$d_{max} \simeq d_{crit} = \frac{8\sigma}{\rho_{air} u^2} \frac{1}{c_D} = \left(\frac{8}{c_D} d_0\right) We$$

reference diameter d_0

- **dynamics:** propagation of perturbations

$z \perp$

antisymmetric wave



- velocity $\vec{v} = \{u, v\} = -\nabla \Phi \rightarrow$ velocity potential Φ

- wave equation (Taylor):

$$\rho \partial_{tt}^2 \Phi = \sigma \partial_z \left(\partial_{xx}^2 \Phi \right) \Big|_{z=\pm d/2}$$

- antisymmetric waves:

$$u = a w_{as} \kappa \sinh(\kappa z) \cos(\kappa[x - w_{as}t])$$

$$v = a w_{as} \kappa \cosh(\kappa z) \cos(\kappa[x - w_{as}t])$$

- wave speed $w_{as} \rightarrow$ **dispersion relation**

$$w_{as}^2 = \frac{2\sigma}{\rho d} \{(\kappa d/2) \coth(\kappa d/2)\}$$

- case $\kappa d \ll 1$:

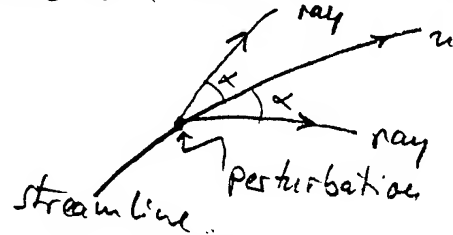
$$w_{as}^2 = \frac{2\sigma}{\rho d}$$

\rightarrow long wave approx.: nondispersive

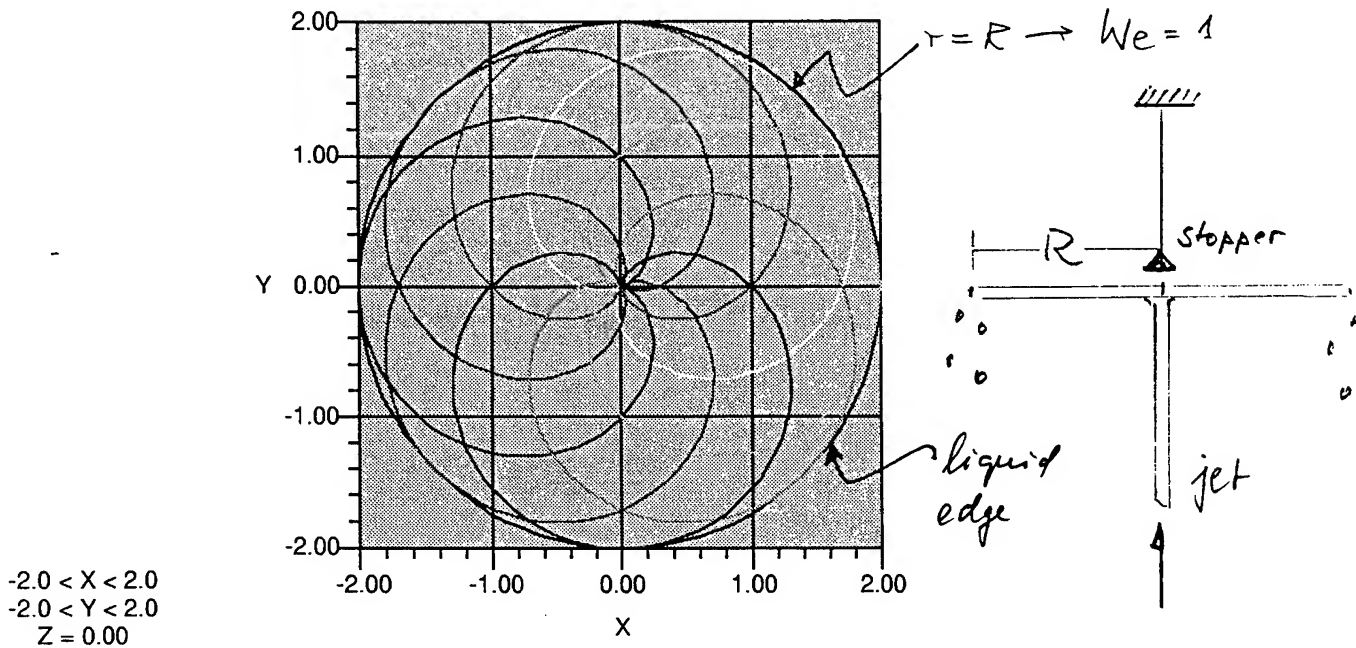
Geometric Acoustics: Rays

- antisymmetric waves: nondispersive \rightarrow hyperbolic
- stationary perturbations: influence spreading along rays (compare: Mach lines)

$$\sin^2(\alpha) = w_{as}^2/u^2 = \frac{2\sigma}{\rho du^2} = We$$



- example (Taylor): impinging jet \rightarrow radially expanding free sheet



- solution method: ray tracing \rightarrow eikonal method

$$\sin^2(\alpha) = \frac{2\sigma}{\rho du^2} = \frac{4\pi\sigma}{\rho Qu} r = r/R$$

$$\rightarrow We = r/R$$

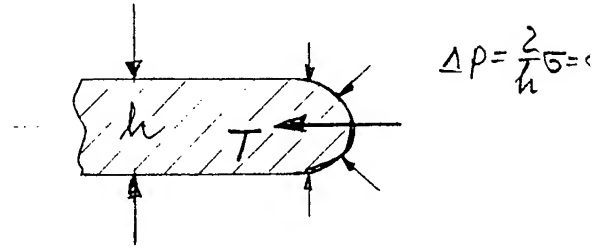
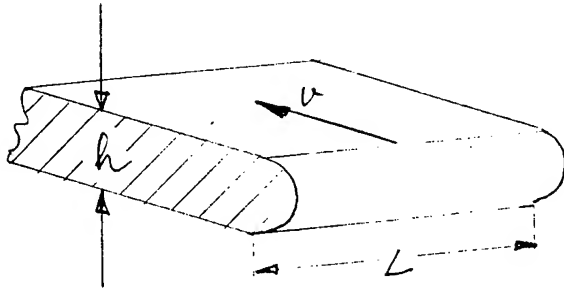
parameter $R = \frac{\rho Qu}{4\pi\sigma}$

kinematic mass flux $Q = 2\pi r du = const$

flow velocity $u = const$

Liquid Sheets: Edge Dynamics

- edge retraction



cylindrical edge

- cylindrical edge:

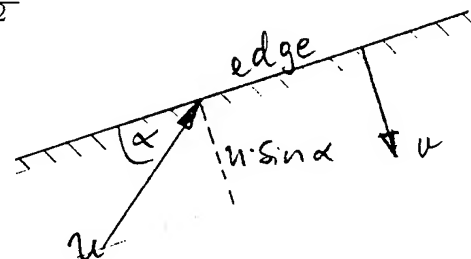
- retraction velocity = v
- tension force (per unit length of edge):

$$T = \int_0^\pi (h/2) d\alpha \cdot 2\sigma/h \sin(\alpha) = 2\sigma$$

- mass (per unit length of edge): $dM = \rho h dx \rightarrow M = \rho h x$

- edge dynamics: $T = 2\sigma = \frac{d}{dt} \left(M \frac{dx}{dt} \right) = (\rho h/2) \frac{d^2 x^2}{dt^2}$

- solution: $x/\tau \equiv v = \sqrt{\frac{2\sigma}{\rho h}} = w_{as}$



- stationary edge \rightarrow **geometric acoustics**

liquid edge = acoustic ray

\rightarrow

$$\sin^2(\alpha) = v^2/u^2 = w_{as}^2/u^2 = We$$

- **conclusion:**

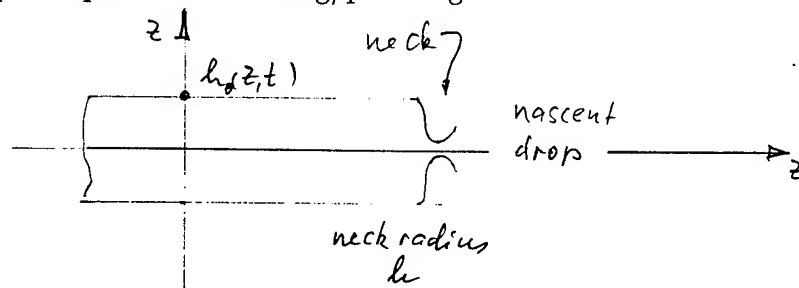
1. importance of Weber number for edge dynamics
2. analogy Weber number with Mach number (gas dynamics)
3. ray tracing, method of characteristics

Droplet Detachment: Necking/Pinching Phenomenon

- acoustic theory: inertia, surface tension, no viscosity

characteristic time: $t_{ref} = h^3 \rho / \sigma \ll 1$

- droplet separation: necking/pinching



- large curvature $\kappa \sim 1/h$, large surface tension forces
- well-posedness: dissipation/viscosity necessary
- Ohnesorge hydrodynamics

- modelling: full Navier-Stokes + continuity \rightarrow

inertia + surface tension + viscosity

viscous time scale: $t_{vis} = h^2 / \nu$

- (Keller/Miksis 1983, Eggers/Dupont 1994) pinching \rightarrow **asymptotic phenomenon**

- long wave approximation
- large neck curvature \rightarrow boundary values negligible \rightarrow **self-similar solution**
- new scales for length and time: surface tension as well as viscosity

$$\ell_{neck} = \nu^2 \rho / \sigma = h Oh^2$$

$$t_{neck} = \nu^3 \rho^2 / \sigma^2 = \frac{h^2}{\nu} Oh^4 = t_{vis} Oh^4$$

$$Oh^2 = \frac{\nu^2 \rho}{h \sigma}$$

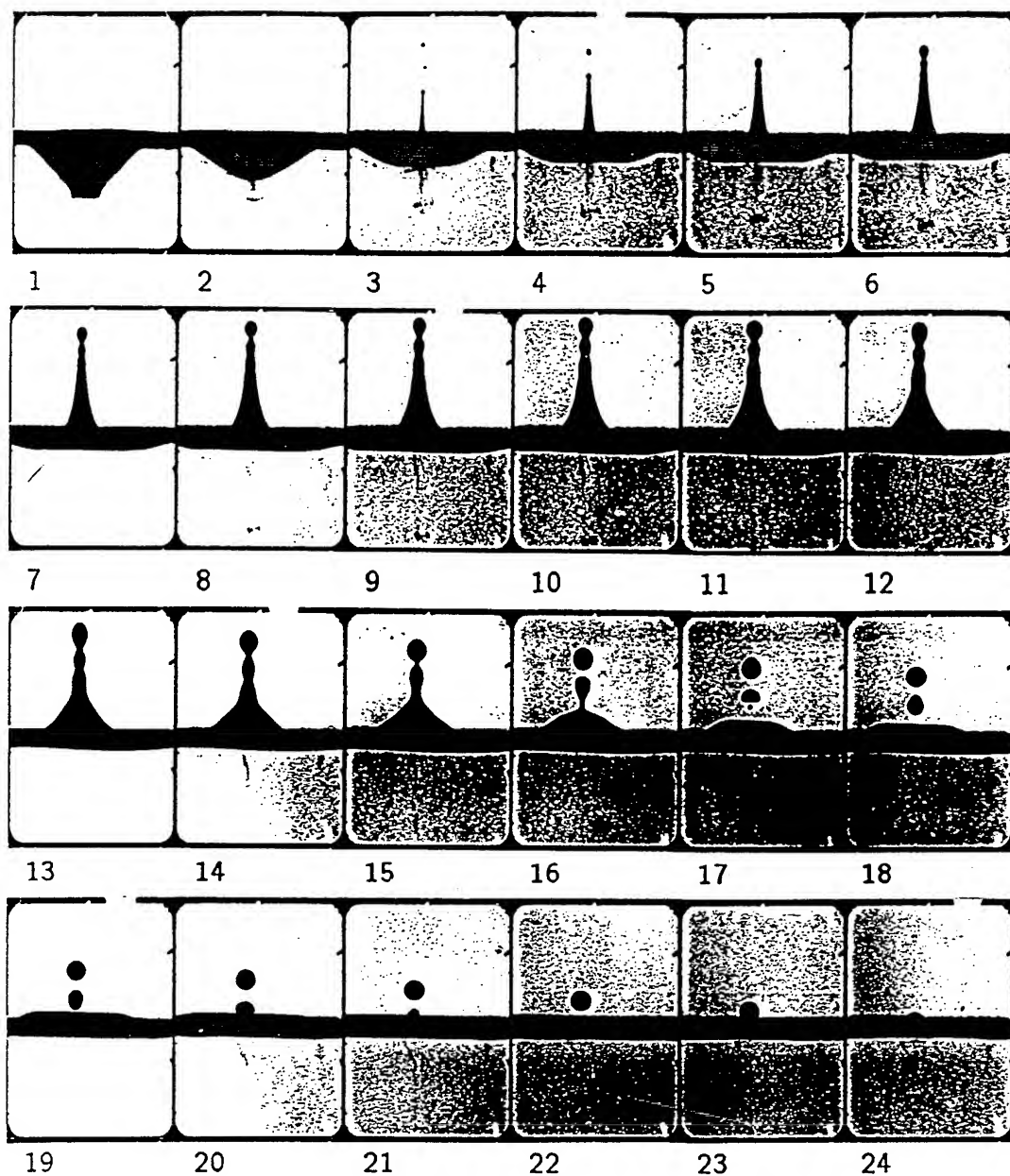


Fig. 7 from :
M. Rein , JFM 306 (1996) 145

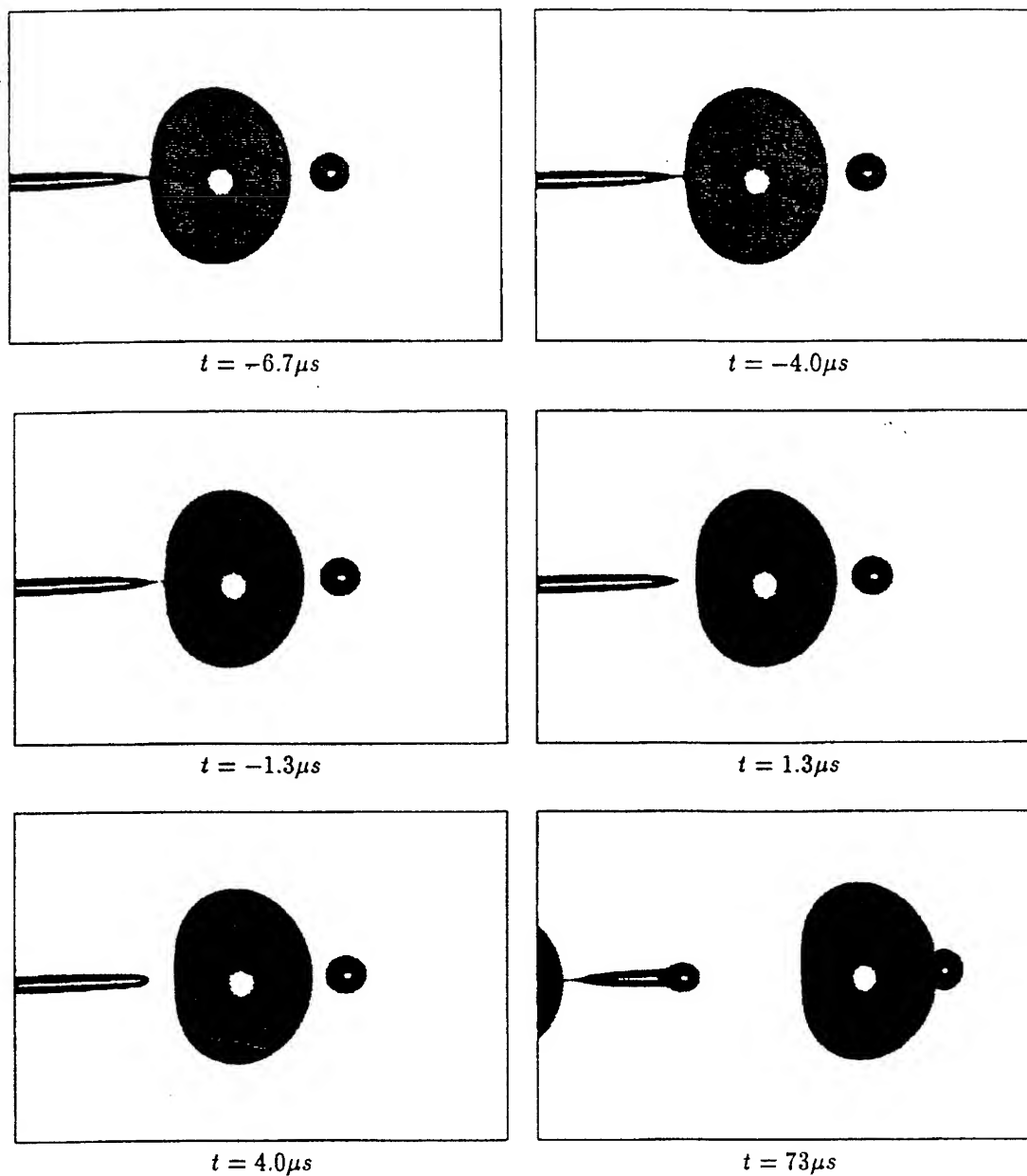


Fig. 3. Separation of the droplet from the liquid jet of radius $r_j = 98.5 \mu m$. Time is given relative to the moment of the jet breakup. Liquid medium of relatively low viscosity (MIXD). The width of one frame corresponds to 1 mm

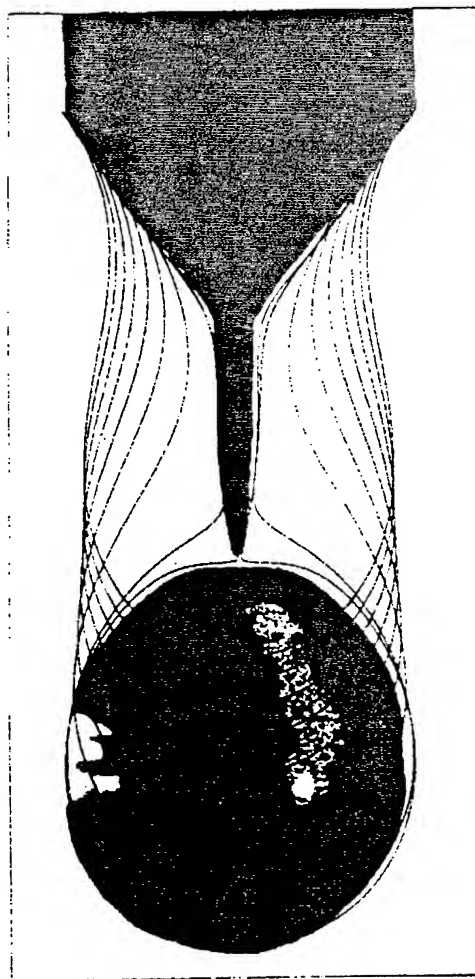


FIGURE 2. Simulation of a drop of water suspended from a circular orifice of radius $r_0 = 0.26$ cm. This gives parameter values $l_c/r_0 = 0.992$ and $l_v/r_0 = 4.89 \times 10^{-6}$, compare table 1. The time distance between profiles is $0.4(r_0^3 \rho / \gamma)^{1/2}$, starting from a point where the drop is already falling. We also superimpose a profile at the snap-off and the corresponding experimental picture from Peregrine *et al.* (1990). There is no adjustable parameter in the comparison. To enhance contrast, we erased the background in the original photograph.

Conclusions

- physics of atomization:
 - deformation processes/instability of liquid membranes/ligaments:
Weber number hydrodynamics, acoustics → **hyperbolic PDE**
 - pinching/rupture of liquid membranes/ligaments:
Ohnesorge number hydrodynamics → **parabolic PDE**
 - post-rupture processes: edge dynamics/secondary rupturing/satellite droplets
- modelling efforts:
 - no comprehensive, all-encompassing model available as yet
 - available: partial models covering asymptotic aspects
 - interaction/coupling with external acoustics: partially possible
- goal: physical characterization of atomization
 - process duration
 - droplet size distribution
 - fully coupled with external acoustics → **elliptic PDE**
- compare: state-of-the-art in phase transition modelling
 - no closed comprehensive model
 - two asymptotic partial models:
 - * nucleation
 - * late-stage ripening/Ostwald ripening

International Workshop on Research Status and Perspectives in Liquid Rocket Combustion Chamber Flow Dynamics

May 27, 1999

CNES/Paris

Computation of Spray Combustion using PDF-equation approach

P. Durand¹, M. Gorokhovski¹, R. Borghi²

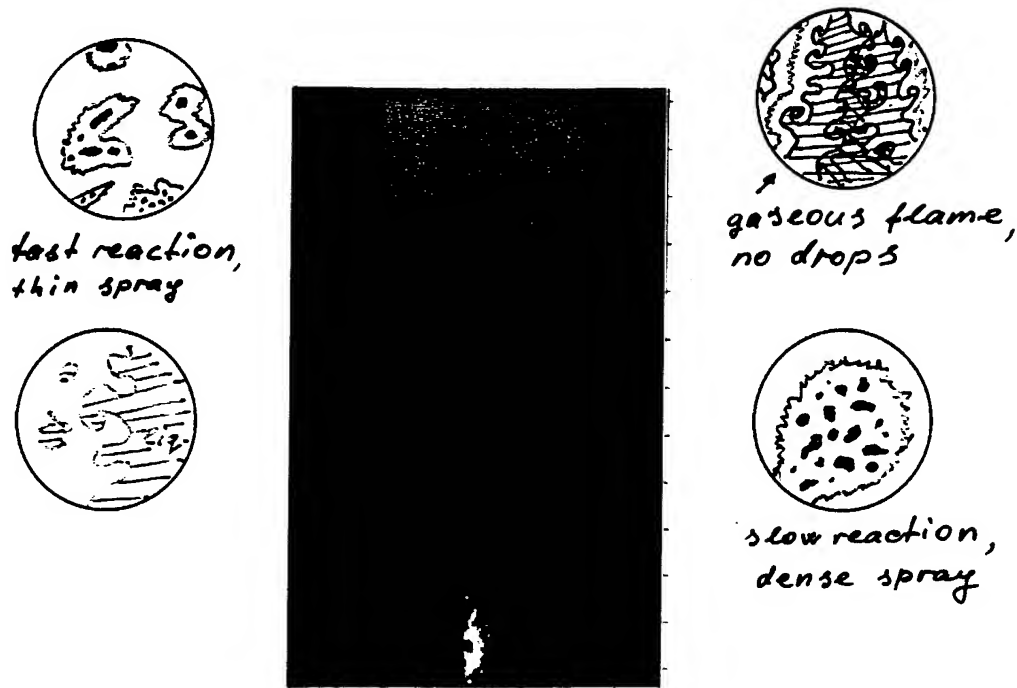
1 : UMR 6614-CNRS

CORIA / Université et INSA de Rouen
FR-76821 Mont-Saint-Aignan Cedex

2 : UMR 6594-CNRS

IRPHE / Université Aix Marseille
FR-13451 Marseille Cedex

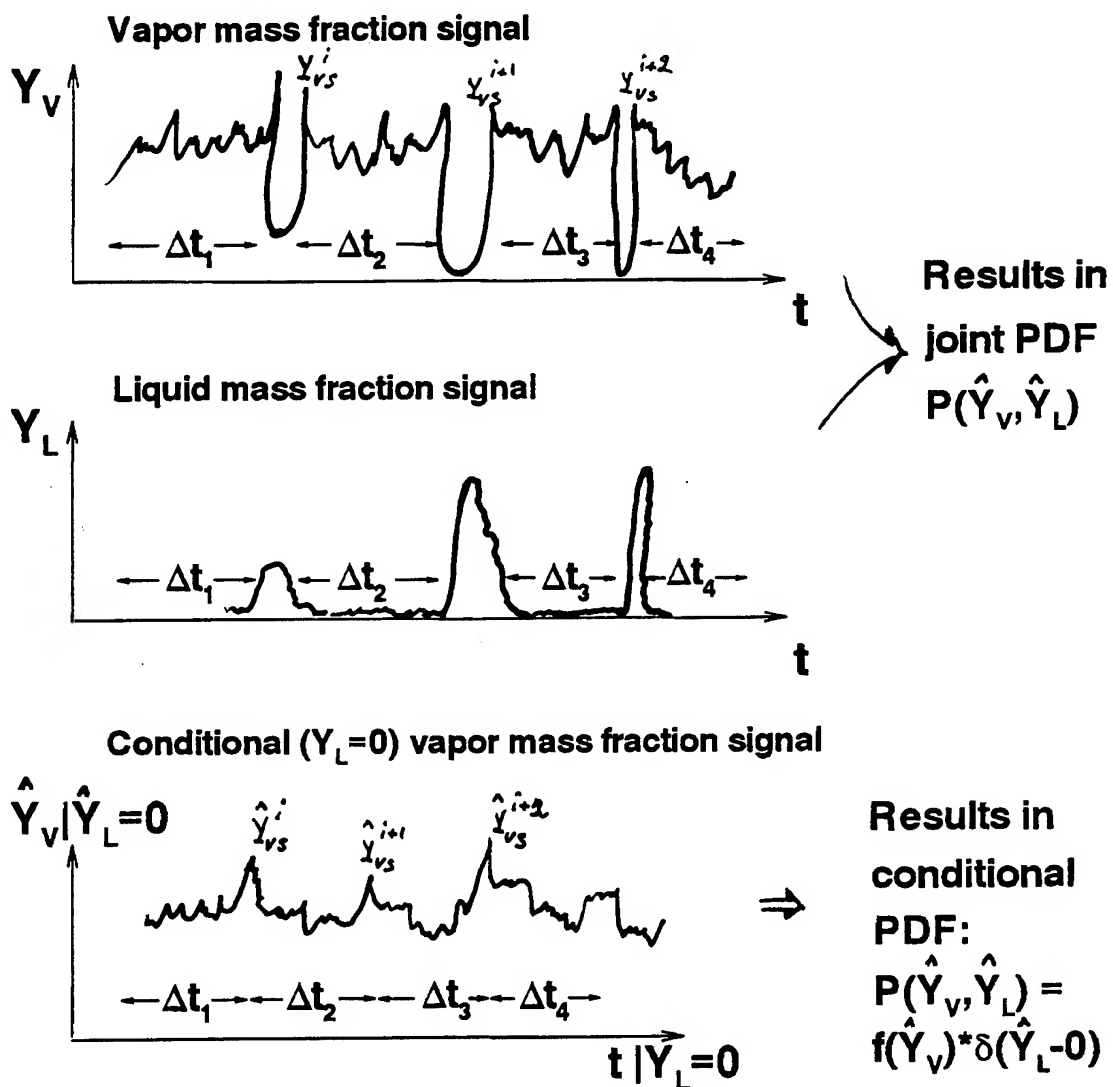
•Resulting "spray flame" is controlled by the turbulent scalar mixing and the turbulent dispersion of droplets.



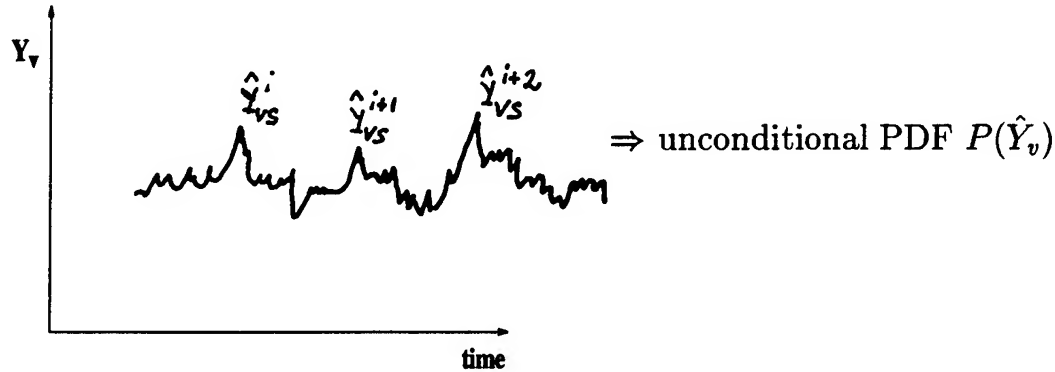
Laser Mie scattering of the reacting spray. The green and blue colors correspond to the droplet scattering and the flame emission respectively. (Stepowski et al., 1992)

- The random positions and properties of evaporating droplets intervene in the turbulent micro-mixing in the gas mixture.
- It modifies the probability distribution of temperature and concentrations and eventually the mean local rate of chemical reactions.
- Models of turbulent gaseous flames that accounts for turbulence-chemistry interaction are often based on the PDF-equation method. The objective here is to extend the PDF-equation approach to the spray combustion.

PDF-Equation Approach in Multicontinua Formulation:
Example for vapor and liquid mass fractions



From the stochastic differential equation to the PDF-equation



- Fluctuations (Y_i, T) in the gas are caused by the random velocity field and by the random rate of vaporization/condensation. The set of all events constitutes a sample space.
- Instantaneous continuity for the vapor mass fraction :

$$\rho \frac{\partial Y_v}{\partial t} + \rho \vec{V} \cdot \nabla Y_v = \nabla (D \rho \nabla Y_v) + \rho \dot{\omega}_{lg} (1 - Y_v) + \rho \dot{\omega}_{chem}$$

- Instantaneous continuity for the gas mixture density :

$$\frac{\partial \rho}{\partial t} + \nabla \cdot (\rho \vec{V}) = \rho \dot{\omega}_{lg}$$

- Vaporization rate : $\dot{\omega}_{lg} = \rho_v V_{vap,s} \cdot \Sigma$;

→ $\Sigma = |\nabla Y_v| \delta(Y_v - Y_{vs})$ - instantaneous interface per unit volume
 $V_{vap,s}$ - vapor velocity relatively to the displacement of interface
 $\dot{\omega}_{lg} = 0$ if $V_{vap,s} = 0$ (or $Y_v \neq Y_{vs}$)

→ $\dot{\omega}_{chem}$ - chemical reaction rate

- Unconditional PDF balance equation :

$$\frac{\partial}{\partial t} \left(\langle \rho | Y_v = \hat{Y}_v \rangle P(\hat{Y}_v) \right) + \nabla \left[\langle \rho \vec{V} | Y_v = \hat{Y}_v \rangle P(\hat{Y}_v) \right] = \langle \rho \dot{\omega}_{lg} | Y_v = \hat{Y}_v \rangle P(\hat{Y}_v)$$

*evolution
in the phase
space*

$$\left\{ \begin{array}{l} -\frac{\partial}{\partial \hat{Y}_v} \left[\langle \nabla (\rho D \nabla Y_v) | Y_v = \hat{Y}_v \rangle P(\hat{Y}_v) \right] \\ -\frac{\partial}{\partial \hat{Y}_v} \left[P(\hat{Y}_v) \langle \rho \dot{\omega}_{lg} | Y_v = \hat{Y}_v \rangle (1 - \hat{Y}_v) \right] \\ -\frac{\partial}{\partial \hat{Y}_v} \left[P(\hat{Y}_v) \langle \rho \omega_{chem} | Y_v = \hat{Y}_v \rangle \right] \end{array} \right.$$

- Integration over all spectrum of \hat{Y}_v leads to the averaged continuity equation :

$$\frac{\partial \bar{\rho}}{\partial t} + \nabla \cdot (\overline{\rho \vec{V}}) = \overline{\rho \omega_{lg}}$$

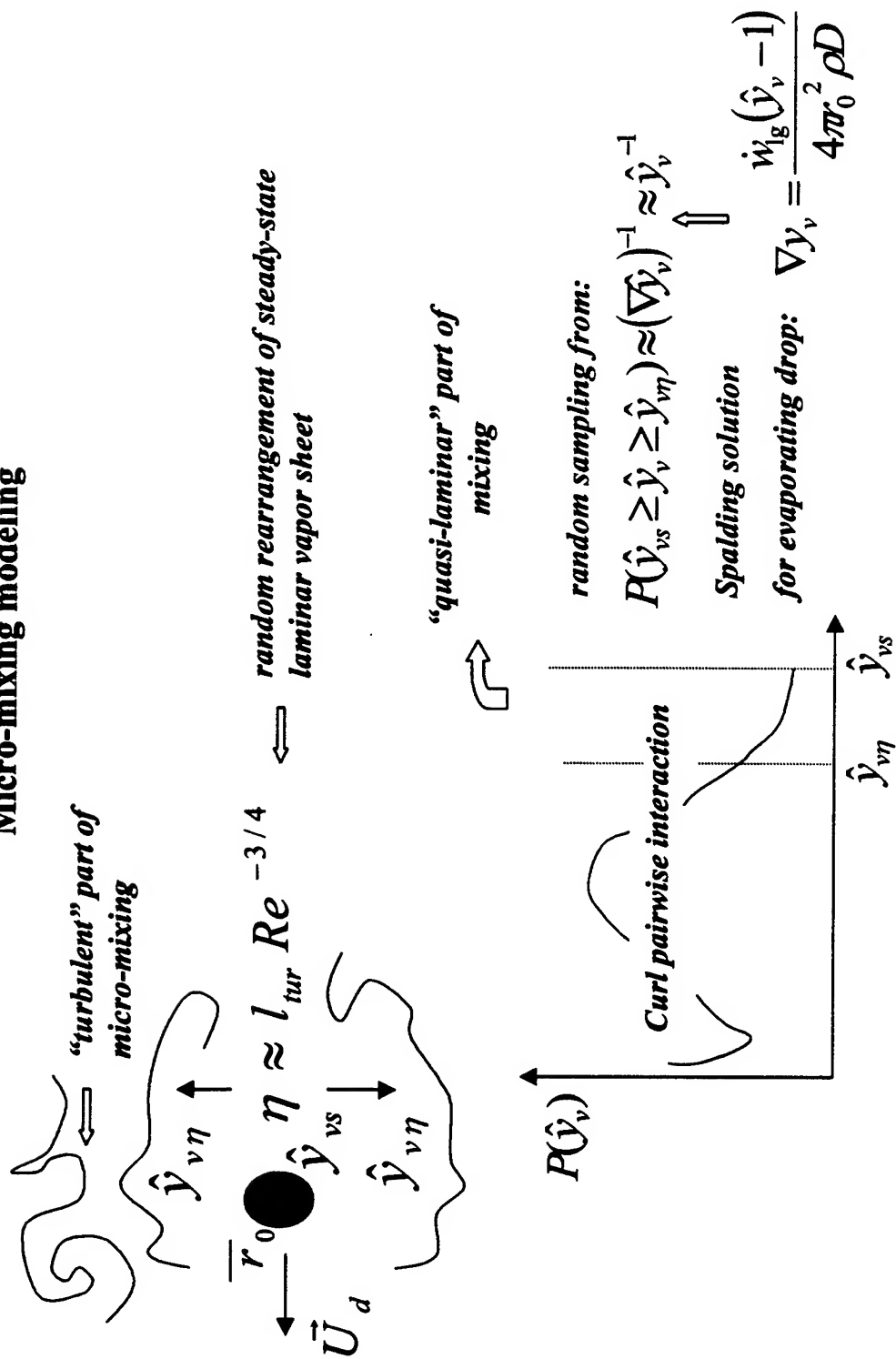
- Vaporization/condensation rate is explicitly available from Lagrangian tracking of the droplets
- Non-linear chemical reaction term is presented in exact form

Unconditional joint PDF-equation for gas mixture
(gaseous species and gas enthalpy) :

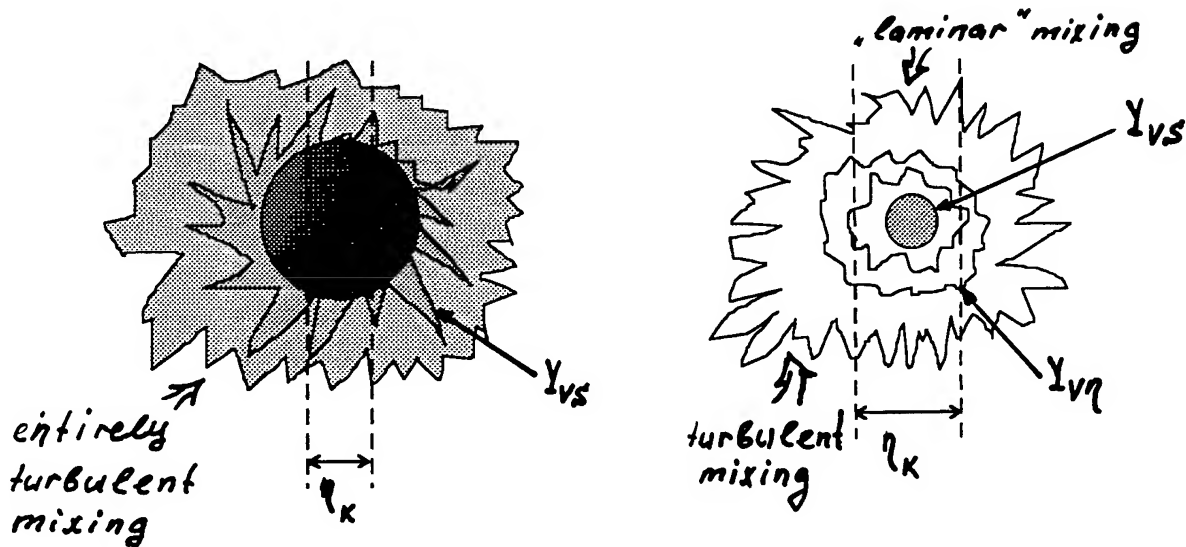
$$\begin{aligned}
& \frac{\partial}{\partial t} \langle \rho \rangle P(\hat{Y}_1, \dots, \hat{Y}_M, \hat{h}) + \nabla \left[\langle \rho \vec{V} \rangle P(\hat{Y}_1, \dots, \hat{Y}_M, \hat{h}) \right] = \langle \rho \dot{\omega}_{lg} \rangle P(\hat{Y}_1, \dots, \hat{Y}_M, \hat{h}) \\
& - \sum_{i=1}^M \frac{\partial}{\partial \hat{Y}_i} \left[\left(\langle \nabla (\rho D \nabla Y_i) \rangle - \langle \rho \dot{\omega}_{lg} \rangle Y_i + \langle \rho \dot{\omega}_{lg} \rangle \delta_{iv} \right) P(\hat{Y}_1, \dots, \hat{Y}_M, \hat{h}) \right] \\
& - \frac{\partial}{\partial \hat{h}} \left[\left(\langle \nabla (\rho D \nabla h) \rangle + \langle \rho \dot{q}_{lg} \rangle \right) P(\hat{Y}_1, \dots, \hat{Y}_M, \hat{h}) \right] \\
& - \sum_{i=1}^M \frac{\partial}{\partial \hat{Y}_i} \langle \rho \omega_{chem} \rangle P(\hat{Y}_1, \dots, \hat{Y}_M, \hat{h})
\end{aligned}$$

- Enthalpy source (or sink) due to the droplets \dot{q}_{lg} is explicitly available from Lagrangian tracking of the droplets ; $\dot{q}_{lg} = 0$ if the heat exchange at the interface = latent heat
- Alongside with the CFD, the modeling of PDF-equation supplies each cell with the probability distributions in order to calculate the mean combustion rate

Micro-mixing modeling



Laminar and turbulent parts in the mixing



At what conditions entirely turbulent mixing occurs?

For stagnant droplet:

$$t_{evap} \propto \frac{d_0^2}{8D} \cdot \frac{\rho_{liq}}{\rho_{gas}}; \quad t_{tur} \propto \frac{k}{\epsilon};$$

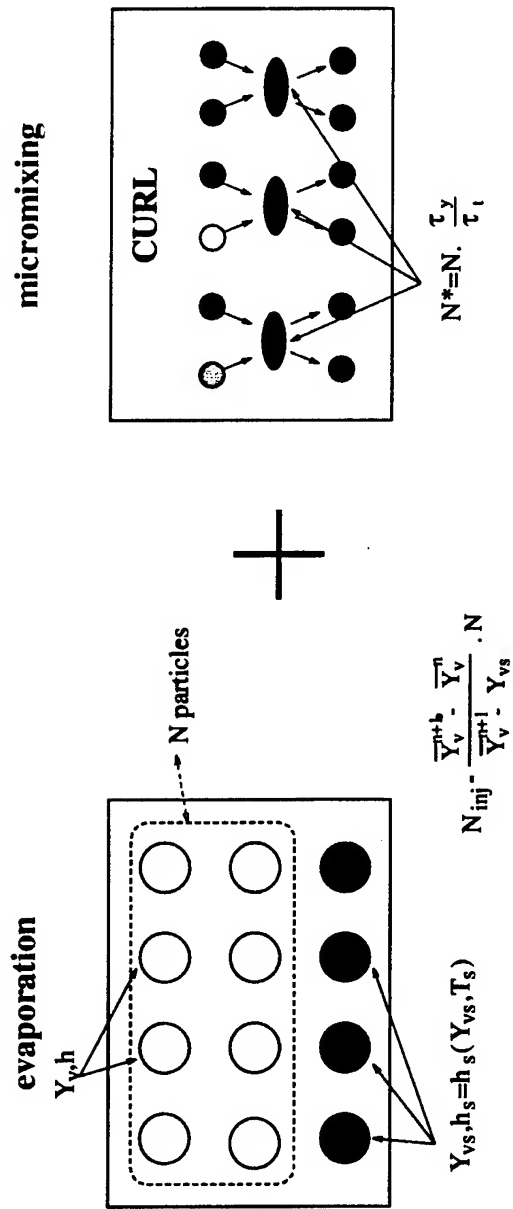
$$\frac{t_{evap}}{t_{tur}} \propto \frac{d_0^2}{8\eta^2} \cdot \frac{\rho_{liq}}{\rho_{gas}} \cdot \frac{V_\eta}{k} \propto \dots \left| \frac{V_\eta}{\Delta U} \propto Re^{-1/4} \right| \dots \propto \frac{1}{8Re^{1/2}} \cdot \left(\frac{d_0}{\eta} \right)^2 \cdot \frac{\rho_{liq}}{\rho_{gas}}$$

$$\left(\frac{\eta}{d_0} \right)^2 \propto \frac{1}{8Re^{1/2}} \cdot \frac{\rho_{liq}}{\rho_{gas}} \cdot \frac{t_{tur}}{t_{evap}}; \quad \underline{d_0 > \eta} \Rightarrow \text{mixing is turbulent.}$$

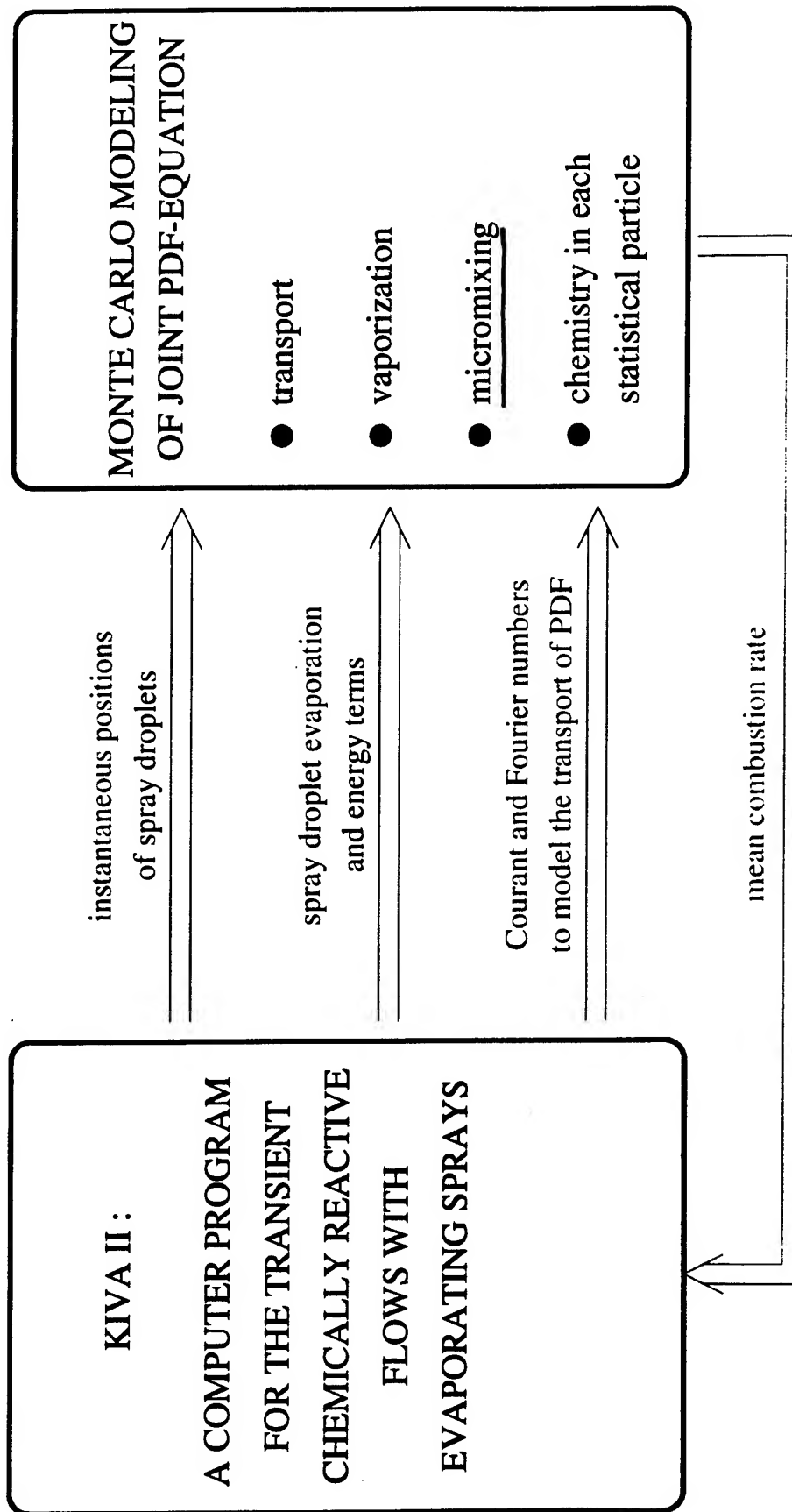
For mobile droplet:

$$\underline{|u_d - u_{gas}| > V_\eta} \Rightarrow \text{mixing is turbulent.}$$

SCHEMATIC

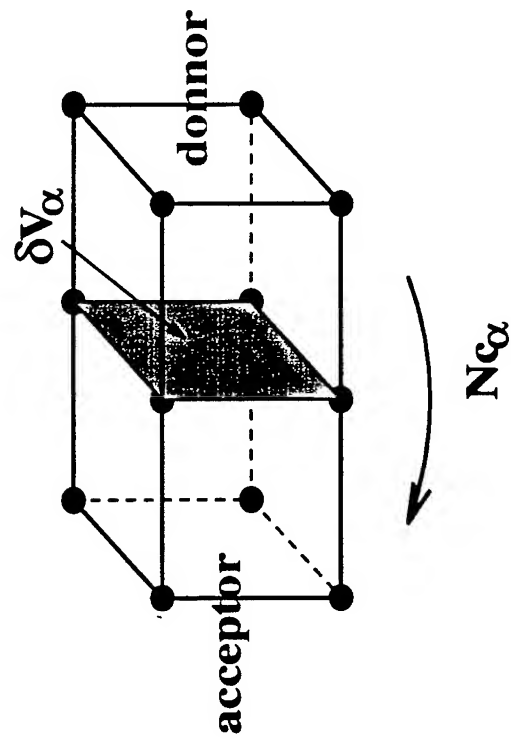


$$\frac{\int_{Y_{vs}}^{Y_v} P(\hat{Y}_v) d\hat{Y}_v}{\int_{Y_{vs}}^{Y_{v\eta}} P(\hat{Y}_v) d\hat{Y}_v} = rnd \in [0, 1] \Rightarrow \hat{Y}_v = \hat{Y}_{v\eta} \left(\frac{\hat{Y}_{vs}}{\hat{Y}_{v\eta}} \right)^{rnd}$$



Simulation of convective transport

Donnor/acceptor scheme :

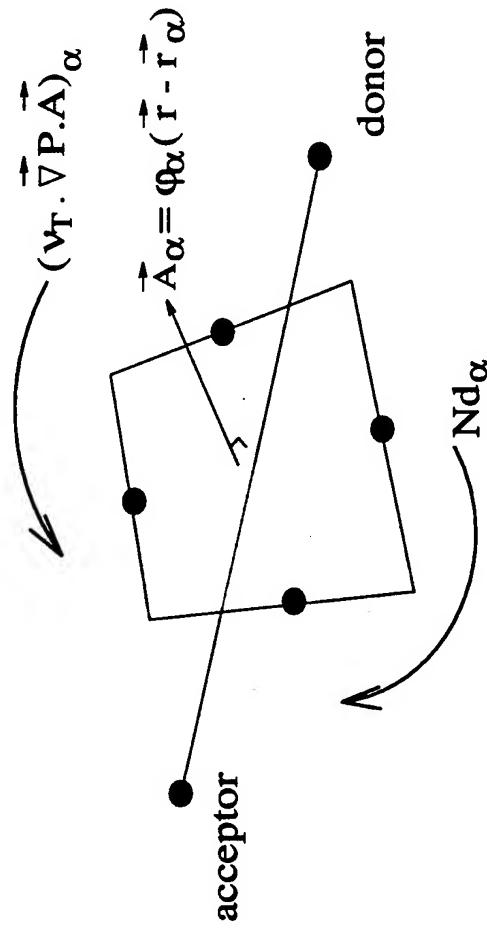


$$P_a = P_a + \frac{\delta V_\alpha}{V} P_d$$

→ Exchange of Nc_α statistical particles

→ $Nc_\alpha = \text{int} [N.C_\alpha]$ where C_α is an effective Courant number

Simulation of diffusive transport



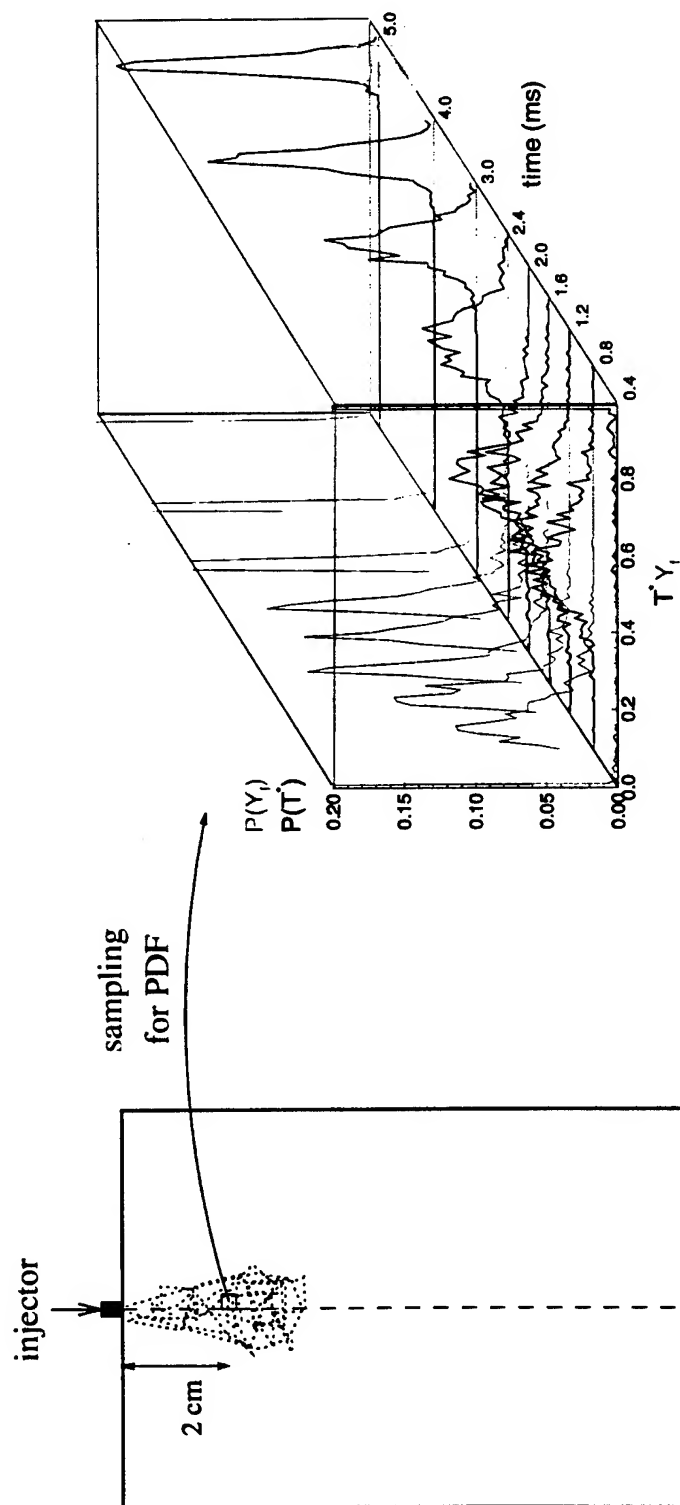
$$P_a = P_a(1 - F_\alpha) + F_\alpha P_d$$

→ Exchange of Nd_α statistical particles

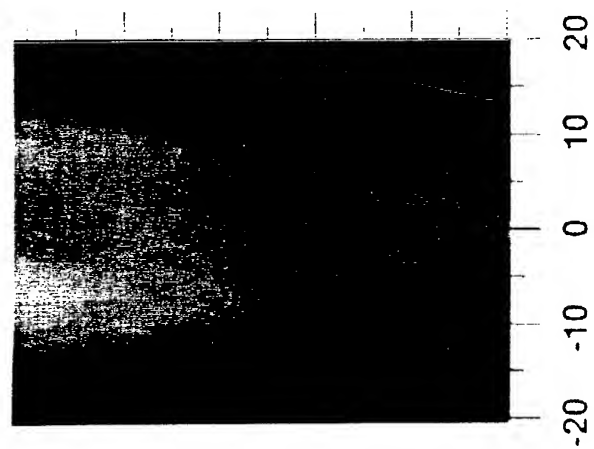
→ $Nd_\alpha = \text{int}[N \cdot F_\alpha]$ where F_α is an effective Fourier number

Spray in the constant volume bomb. (inert case)

PDF distribution computed

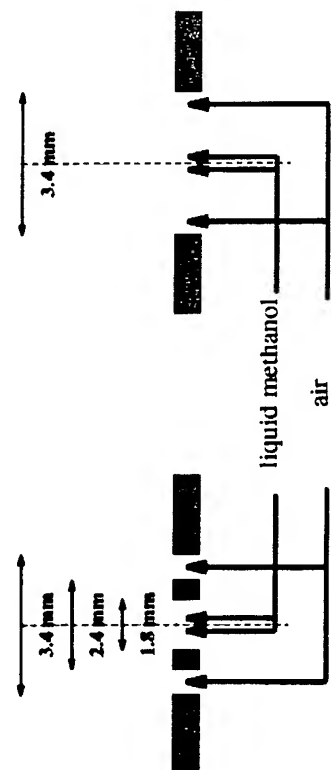


Experimental and numerical inlet setup



Experiment

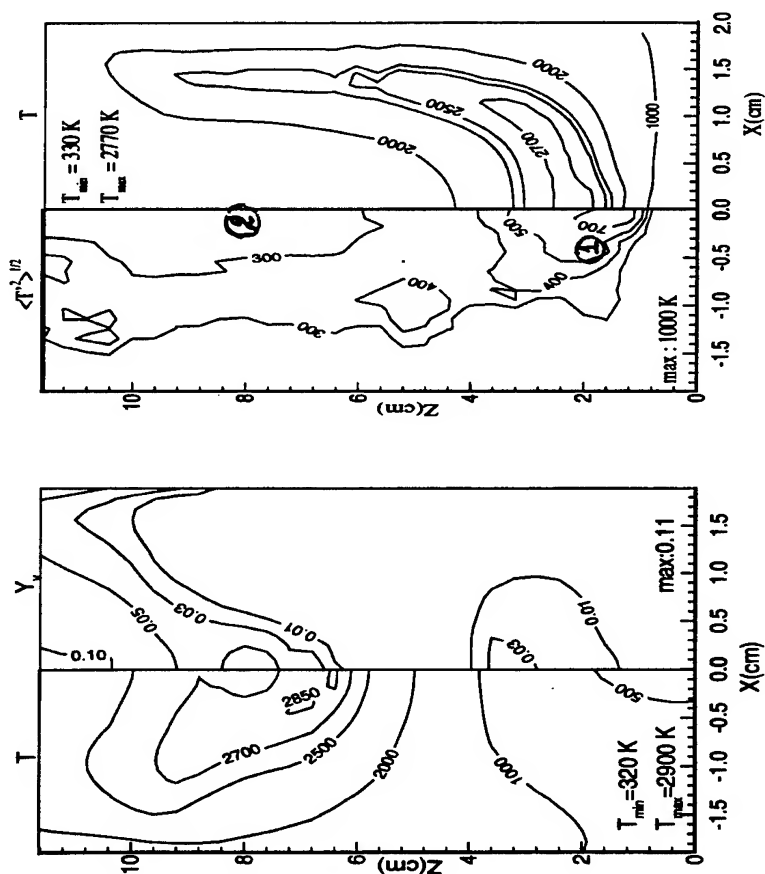
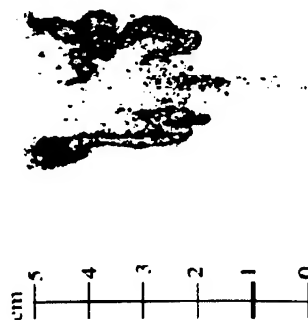
Modeling



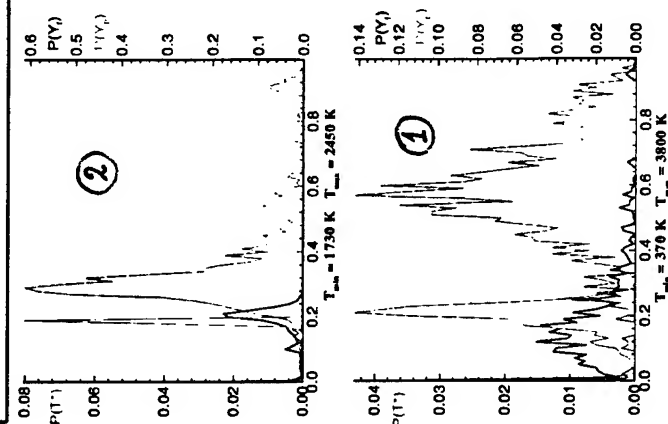
Computations of temperature and vapor distributions
using Eddy-Break-Up combustion model (middle) and PDF approach (right)

Experimental pattern of
OH emission

$V = 110 \text{ m/s}$ $Q_{\text{CH}_3\text{OH}} = 1 \text{ g/s}$



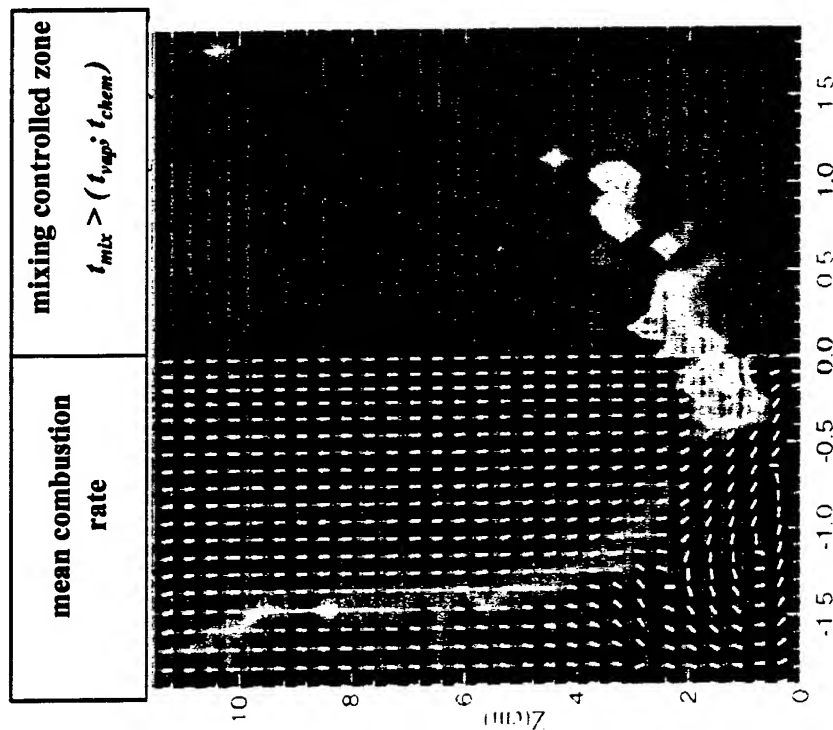
Probability distributions
of vapor mass fraction
and temperature in two
different locations



PDF

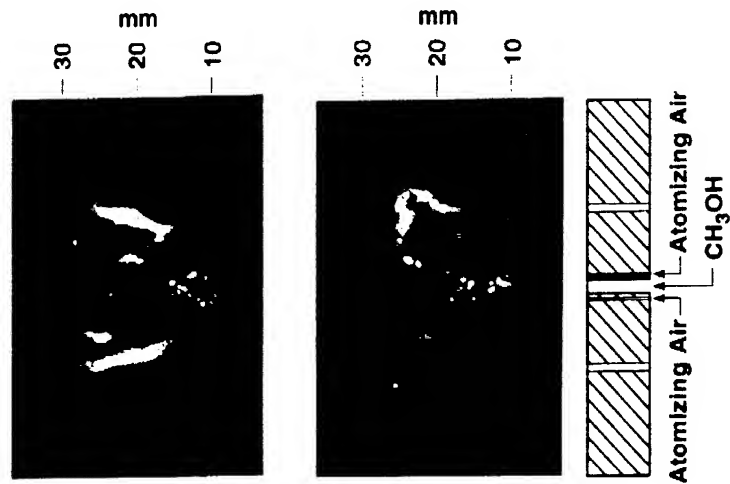
EBU

Computed results

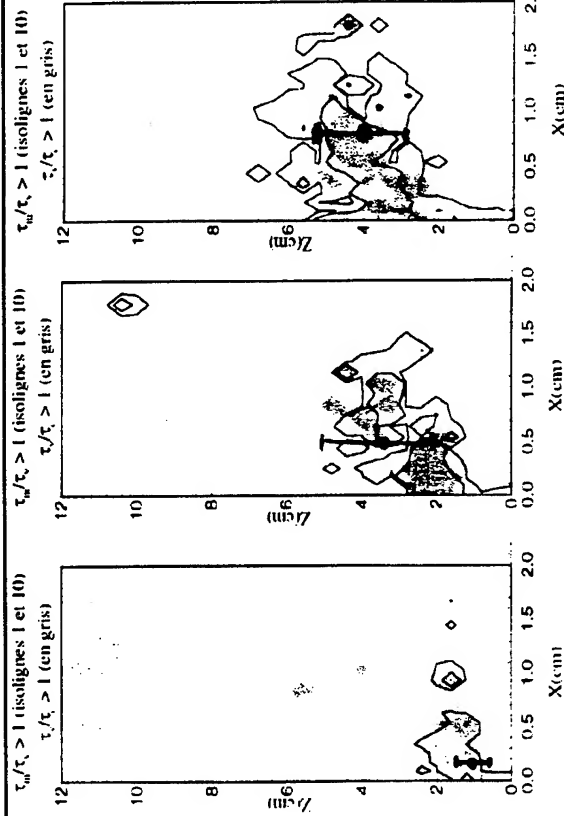


Stepowski et al., 1994:

OH planar laser-induced fluorescence images of the reacting spray. Images represent two snapshots taken for $V_{conow} = 110\text{m/s}$

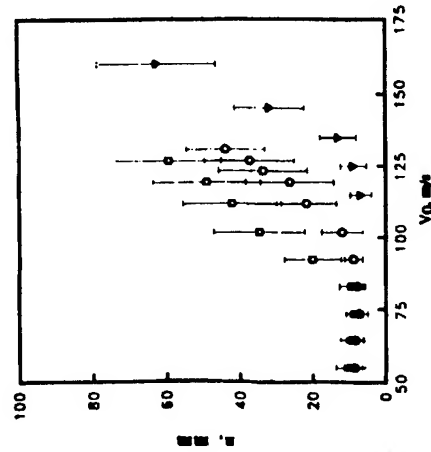


Computed probable zone of stabilized
combustion for three coflow velocities



$U_{cof} = 70 \text{ m/s}$ $U_{cof} = 110 \text{ m/s}$ $U_{cof} = 150 \text{ m/s}$

Stepowski et al., 1994:
Experimental lift-off
location versus air coflow
velocities



ROCKET INJECTOR CHALLENGES: Performance, Stability and Reliability at Low Cost

R. J. Santoro

Propulsion Engineering Research Center
and
Department of Mechanical and Nuclear Engineering
The Pennsylvania State University

INTERNATIONAL WORKSHOP ON
RESEARCH STATUS AND PERSPECTIVES
IN LIQUID ROCKET COMBUSTION CHAMBER FLOW DYNAMICS

May 27-28, 1999
PARIS - France

PENNSTATE



ACKNOWLEDGMENTS

Penn State

Dr. Sibtosch Pal
Dr. Roger Woodward
Mr. Matt Lehman
Ms. Amy Reeb
Mr. Larry Schaaf

Moscow Aviation Institute

Prof. Vladimir Bazarov (Visiting at Penn State)

Funding

NASA MSFC, AFOSR

PENNSTATE



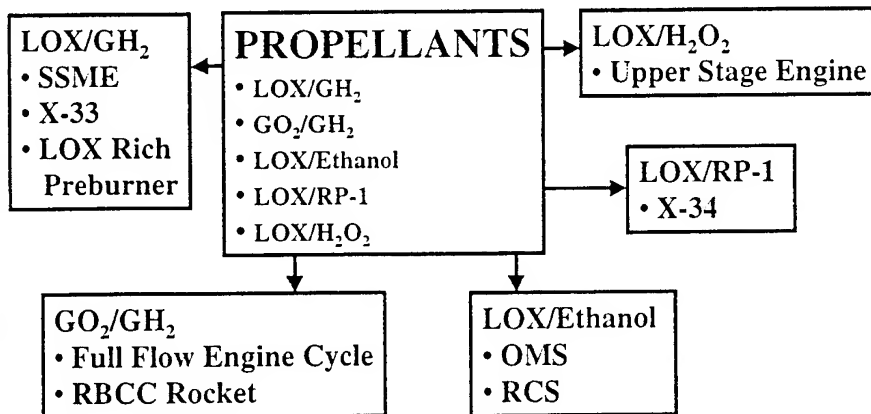
OVERVIEW

- Rocket Injector Design Criteria
 - ⇒ Propellant Combination
 - ⇒ Performance, Stability and Reliability Aspects
 - ⇒ Low Cost
- Focused Application-oriented Injector Research at Penn State
 - ⇒ LOX-rich Preburner - LOX/GH₂ Propellants
 - ⇒ Orbital Maneuvering System (OMS) Upgrade - LOX/Ethanol Propellants
 - ⇒ Gas/Gas Injector Technology - GO₂/GH₂ Propellants
- Injector Flowfield Research at Penn State
 - ⇒ Dynamics of Impinging Jet Injectors
 - ⇒ Chamber Mach Number Effects on Injector Flowfield - GO₂/GH₂ and LOX/GH₂ Propellants
- Summary/Future Plans



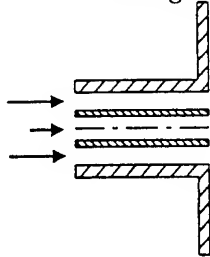
ROCKET INJECTOR DESIGN

Application Defines Propellants/Injector Design

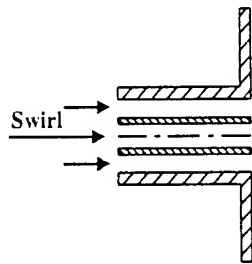


ROCKET INJECTOR DESIGN

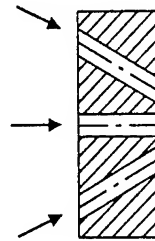
Injectors Depend on Shear and/or Flow Impingement for Mixing and/or Atomization



Shear Coaxial Injector



Swirl Coaxial Injector



Impinging Injector

Generic Injector Types



PERFORMANCE

- Combustion Efficiency Is Typically High, Particularly, for H_2/O_2 Systems (99%).
 - Performance Gains Through Compact Combustors
 - Increased Lifetime
- Combustion Performance - Instability Trade-off Critical for Liquid-liquid Systems Such As LOX/RP-1.
- Route to Improved Performance Is Advance Design Methodologies That Are CFD Model Based.
 - Gas/Gas Injector Studies Have Been Pursued As a First Step



INJECTOR RESEARCH AT PENN STATE

• Focused Application-oriented Injector Research at Penn State

- ⇒ Gas/Gas Injector Technology - GO_2/GH_2 Propellants
 - Shear Coaxial Injector
 - Swirl Coaxial Injector
 - Impinging Injector
- ⇒ LOX-rich Preburner - LOX/ GH_2 Propellants
 - Swirl Coaxial Injector
- ⇒ Orbital Maneuvering System (OMS) Upgrade - LOX/Ethanol Propellants
 - Pintle Injector
 - Bi-centrifugal Coaxial Swirl Injector

PENNSTATE



GAS/GAS INJECTOR TECHNOLOGY

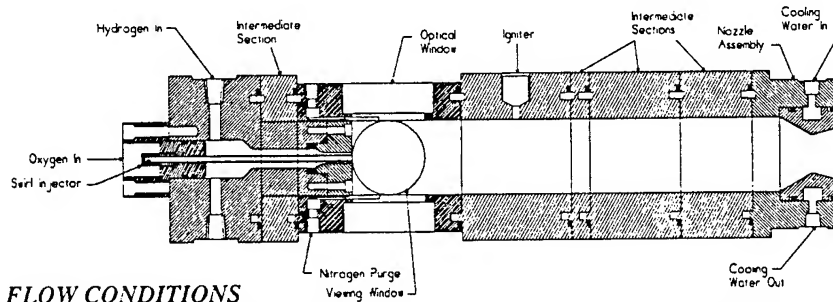
Motivation

- Data Base on Gas/Gas Combustion for Rocket Application Is Limited To Studies of Global Characteristics
 - Aerojet Report (1973)
- Gas/Gas Injector Design Requires a Data Base On Local Phenomena
 - Mixing and Combustion Characteristics
 - Injector Face and Wall Heat Transfer Issues
- Laser-based Diagnostic Techniques and CFD Models Have Matured, and Can Be Used As Design Tools for Next-generation Technology (RLV) Development

PENNSTATE



GAS/GAS INJECTOR TECHNOLOGY



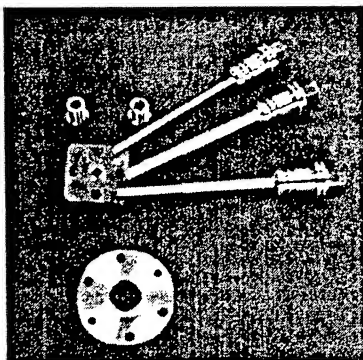
FLOW CONDITIONS

GH ₂ Mass Flow Rate	1.9×10^{-2} kg/s (4.2×10^{-2} lbm/s)
GO ₂ Mass Flow Rate	0.11 kg/s (0.25 lbm/s)
GO ₂ /GH ₂ Mass Flow Ratio	6.0
Inlet Gas Temperature	300 K
Chamber Pressure	6.9 MPa (1000 psia)

PENNSTATE



GAS/GAS INJECTOR TECHNOLOGY



Injectors Tested

- Swirl Coaxial Injectors
⇒ 60°, 75° and 90° GO₂ Swirl
- Shear Coaxial Injectors
⇒ H₂/O₂ Velocity Ratios of 4, 6, 7 and 8
- O-F-O and F-O-F Triplet Injectors
⇒ *Excessive Heat Transfer Noted at Lower Pressure Experiments (Not Tested at 1000 psia)*

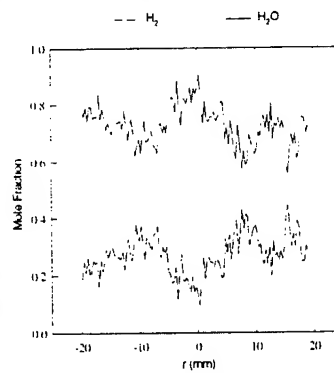
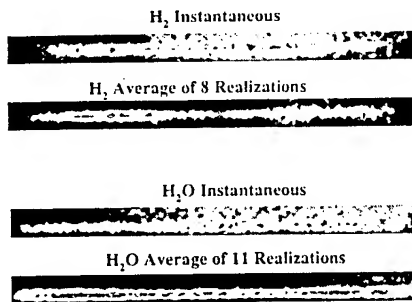
Injector Posts for 60°, 75° and 90° GO₂ Swirl

PENNSTATE



GAS/GAS INJECTOR TECHNOLOGY

O/F=6 Raman Species Measurements for 60° Swirl Injector



$P_c=993$ psia; $x=3.5$ in.

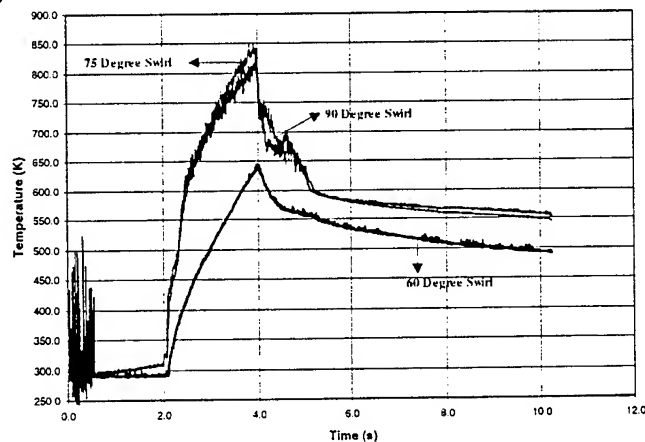
$X=89$ mm

Near-Complete Mixing and Combustion Within 90 mm



GAS/GAS INJECTOR TECHNOLOGY

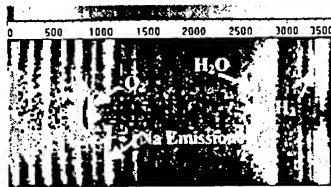
O/F=6 Injector Face Temperature for Swirl Injectors



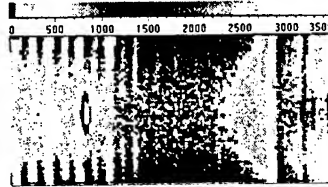
GAS/GAS INJECTOR TECHNOLOGY

O/F=6

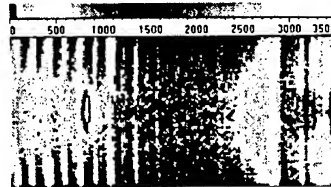
X=127 mm



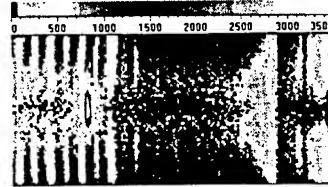
H₂/O₂ Velocity Ratio=8.0



H₂/O₂ Velocity Ratio=6.8



H₂/O₂ Velocity Ratio=5.9



H₂/O₂ Velocity Ratio=3.9

PENNSTATE



GAS/GAS INJECTOR TECHNOLOGY

Summary

Swirl Coaxial Injector

- Mixing and Combustion Is Extremely Fast
- Heat Release Achieved Within a Short Distance
- Face Temperature Increases With Swirl Angle
- Use of Swirl Coaxial Injector Will Require Effective Face Cooling Strategies

Shear Coaxial Injector

- Mixing and Combustion Is Slower Than Swirl Coaxial Injector
- Mixing and Combustion Increases With GH₂ to GO₂ Velocity Ratio

PENNSTATE



LOX-RICH PREBURNER

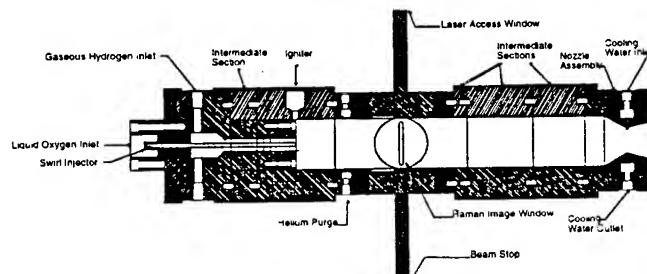
Motivation

- Improve Understanding of LOX/GH₂ Combustion at LOX-rich Conditions
- Conduct Detailed Study of Swirl Coaxial Injector Performance
- Data Base to Validate/improve Computational Combustion Tools

PENNSTATE



LOX-RICH PREBURNER

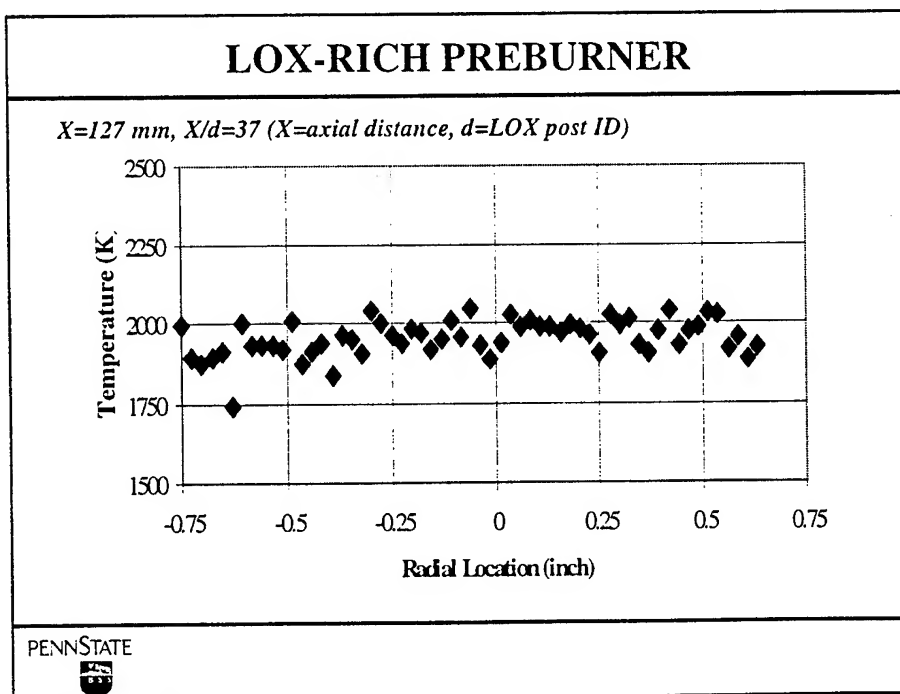
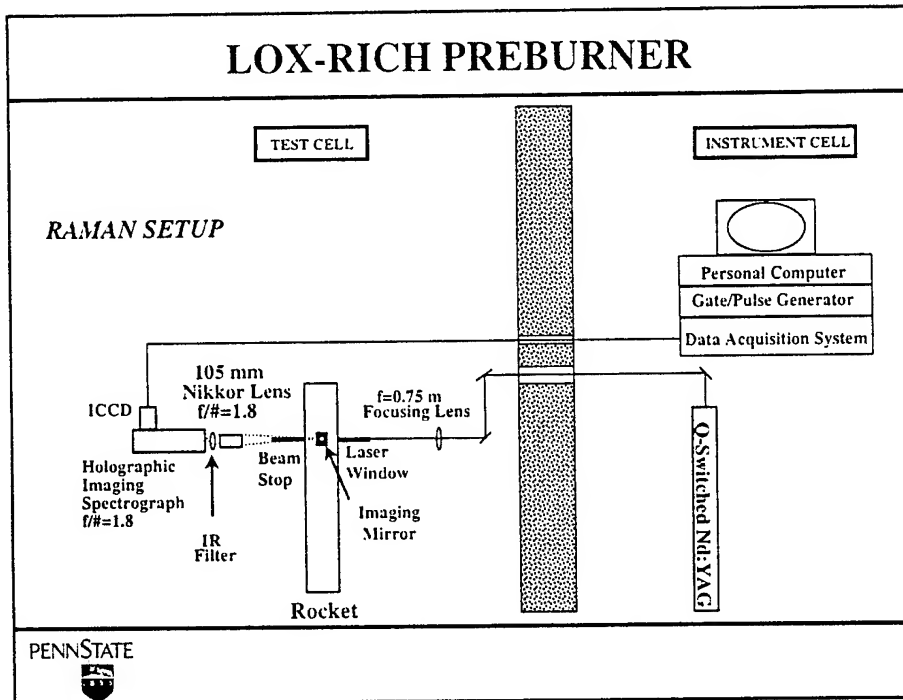


TEST CONDITIONS

CASE	LO ₂ Flowrate (lb _m /s)	GH ₂ Flowrate (lb _m /s)	(O/F) _{mix}	T _{adiabatic} K	P _{chamber} psia	c* Efficiency	LO ₂ Velocity ft/s	GH ₂ Velocity ft/s
A	0.2	0.004	50	1806	300	0.6	110	110
B	0.2	0.005	40	2114	333	0.8	110	140
C	0.2	0.008	25	2724	337	0.9	110	224

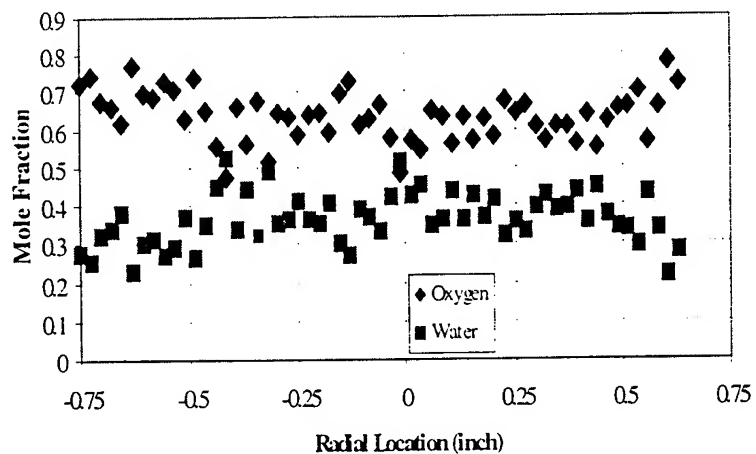
PENNSTATE





LOX-RICH PREBURNER

$X=127\text{ mm}$, $X/d=37$ (X =axial distance, d =LOX post ID)



PENNSTATE


LOX-RICH PREBURNER

Summary

- Single Shot Linewise Multi-species Raman Images Of LOX/GH₂ Rocket Combustion Obtained For Oxidizer-rich Conditions
- Resultant Temperature And Major Species Profiles Yield Expected Values
- Swirl Coaxial Injector Mixedness Is Further Evaluated

PENNSTATE

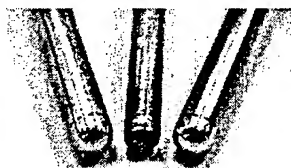

OMS UPGRADE

Motivation

- NASA Is Investigating the Feasibility of a Non-toxic OMS/RCS Upgrade for the Space Shuttle to Eliminate the Safety and Cost Issues Associated With Hypergolic Propellants
- Broad Objectives
To Provide NASA and Contractors With an Objective Base From Which Future Injector Design Decisions Can Be Made for OMS and Future HEDS Applications
- Specific Objectives
To Measure and Analyze Detailed Combustion Characteristics of LOX/Ethanol Propellant Combinations at Representative Thrust Chamber Conditions for Various Candidate Injectors

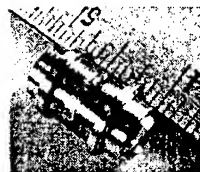
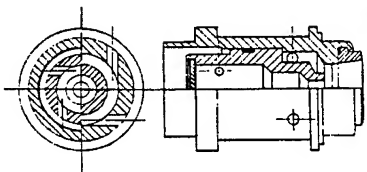
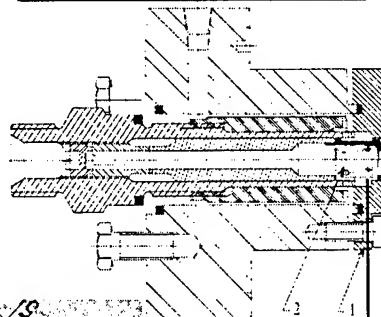


OMS UPGRADE



PINTLE INJECTOR TIP

BI-CENTRIFUGAL SWIRLER



OMS UPGRADE

OMS Engine Design

Thrust: 27 kN (6000 lbf)

Isp: 326 sec

Mixture Ratio: 1.7

Propellant Flowrate: 8.3 kg/s (18.4 lbm/s)

-Oxygen: 5.26 kg/s (11.6 lbm/s)

-Ethanol: 3.08 kg/s (6.8 lbm/s)

Sub-Scale Engine Design

1/60 of Full Scale-mass flowrate

Mixture Ratio: 1.7

Propellant Flowrate: 0.14 kg/s (0.307 lbm/s)

-Oxygen: 0.088 kg/s (0.193 lbm/s)

-Ethanol: 0.052 kg/s (0.114 lbm/s)

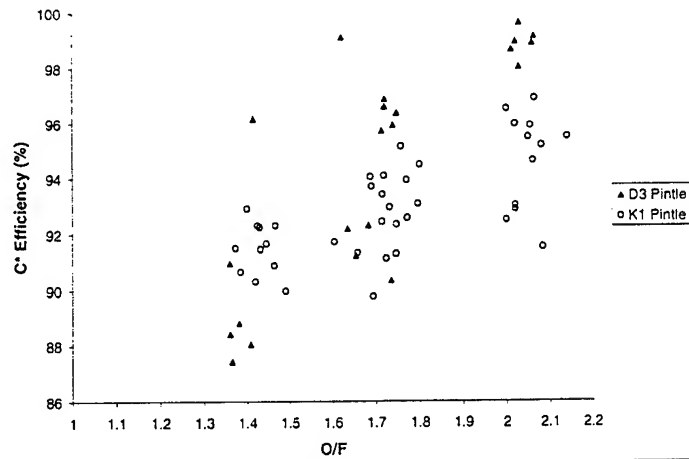
Case #	1	2	3	4	5	6
P_c (MPa)	1.10	1.10	1.10	2.07	2.07	2.07
O/F	2.0	1.7	1.4	2.0	1.7	1.4
LOX flowrate (kg/s)	0.095	0.088	0.082	0.177	0.163	0.155
ethanol flowrate (kg/s)	0.048	0.052	0.059	0.088	0.096	0.111
GN2 flowrate (kg/s)	0.014	0.014	0.014	0.014	0.014	0.014
Nozzle Diameter (mm)	16.51	16.51	16.51	16.51	16.51	16.51

PENNSTATE



OMS UPGRADE

• Over 100 LOX/Ethanol Tests Were Conducted on Pintle Injectors

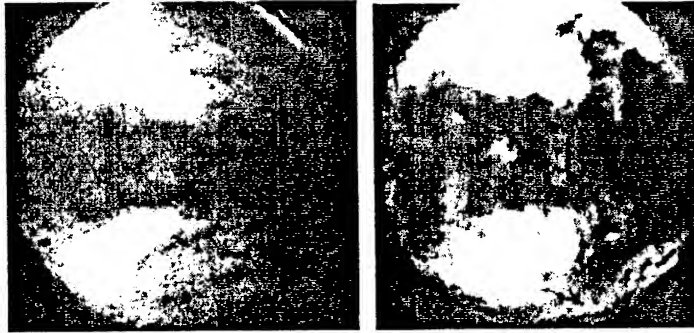


PENNSTATE



OMS UPGRADE

BI-CENTRIFUGAL NEAR INJECTOR FLOWFIELD



2M injector, Case 2

Flow

2M injector, Case 6

Outer LOX flow is separated from inner ethanol cone by layer of vaporized oxygen



OMS UPGRADE

MODIFIED BI-CENTRIFUGAL INJECTOR WITH LARGE RECESS

•2M w/large recess face plate exhibits good mixing and combustion over wide range of operating conditions and is insensitive to LOX quality



Case 3

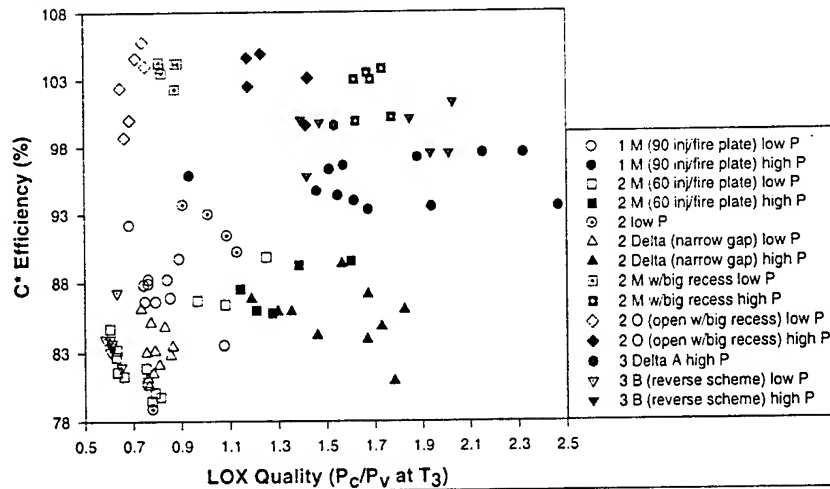
Flow

Case 4



OMS UPGRADE

PERFORMANCE OF BI-CENTRIFUGAL INJECTOR



PENNSTATE



OMS UPGRADE

Summary

PINTLE INJECTOR

- Pintle Injector Designed for OMS Conditions Operated in a Stable Manner
- For Pintle Injector, c^* Efficiency Increase With O/F

BI-CENTRIFUGAL SWIRLER

- Marginal LOX Quality Influenced Combustion Efficiency for All Injector Configurations
- Shadowgraph Imaging Was Instrumental in Assessing Flow Phenomena Which Caused Lower Than Expected Performance
- Use of Recess Is Reasonable Solution to Spray Cone Separation Problem:
 - Recess Insensitive to LOX Quality (of Significance to OMS Upgrade), Stable Under All Conditions Tested, LOX Cooling of Injector Face Effective Here

PENNSTATE



INJECTOR RESEARCH AT PENN STATE

Injector Flowfield Research at Penn State

- ⇒ Dynamics of Impinging Jet Injectors
 - Like-on-like Impinging Injectors
- ⇒ Chamber Mach Number Effects on Injector Flowfield - GO_2/GH_2 and LOX/GH_2 Propellants
 - Shear Coaxial Injectors



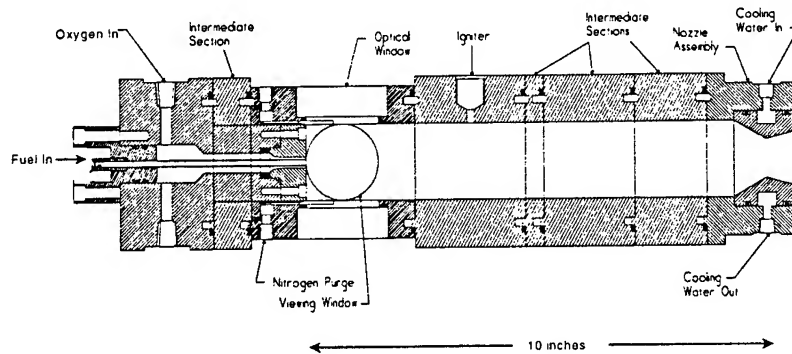
DYNAMICS OF IMPINGING JET INJECTORS

Motivation

- Determine Conditions Under Which Impinging Jet Injector Periodic Atomization Can Cause Combustion Instabilities
 - ⇒ Longitudinal Mode Excitation for GO_2 /ethanol Propellants in Model Rocket Chamber
 - ⇒ Electromechanical Drivers Controlling Individual Ethanol Jets (*of Impinging Jet Injector*)



DYNAMICS OF IMPINGING JET INJECTORS

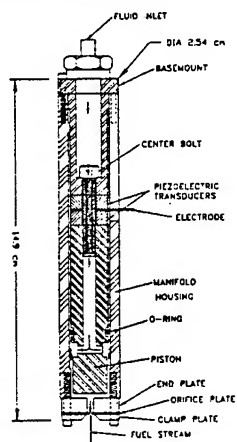


- Ethanol Impinging Jet Injector
(Individual Electromechanical Drivers)
- Annular Flow of GO_2

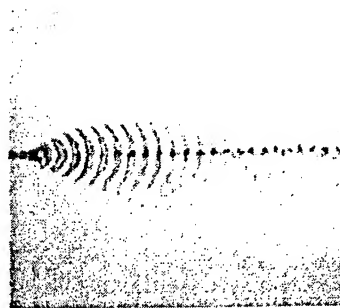


DYNAMICS OF IMPINGING JET INJECTORS

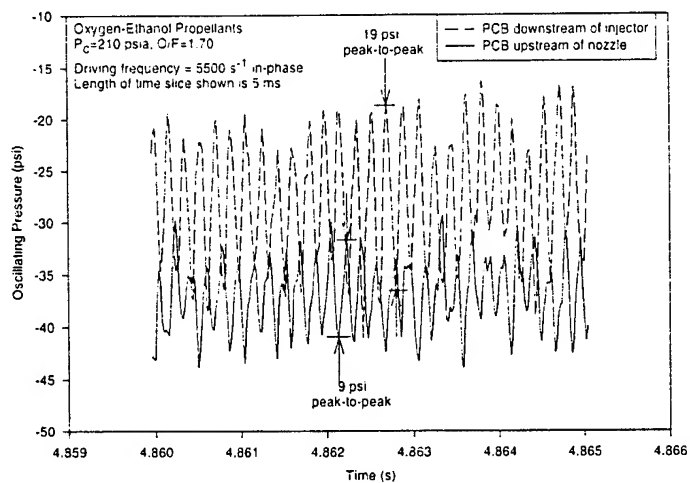
ELECTROMECHANICALLY DRIVEN INJECTOR ASSEMBLY



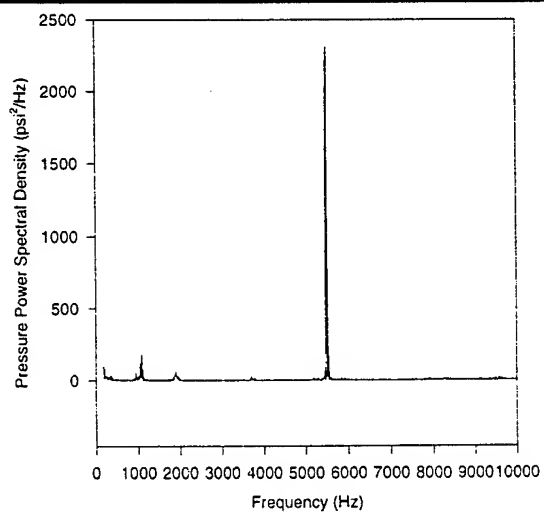
IMPINGING INJECTOR JETS
PERTURBED OUT-OF-PHASE
AT 2500 Hz



DYNAMICS OF IMPINGING JET INJECTORS



DYNAMICS OF IMPINGING JET INJECTORS



DYNAMICS OF IMPINGING JET INJECTORS

Summary

- Successful Demonstration of Combustion Instability by Periodic Atomization for Impinging Jet Injector
- Technique Has Potential As Active Control of Combustion Instability

PENNSTATE

CHAMBER MACH # EFFECT STUDIES

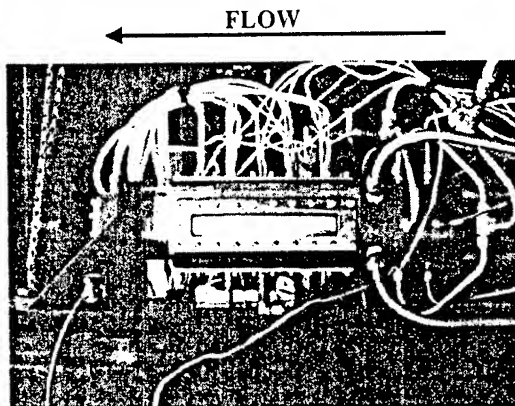
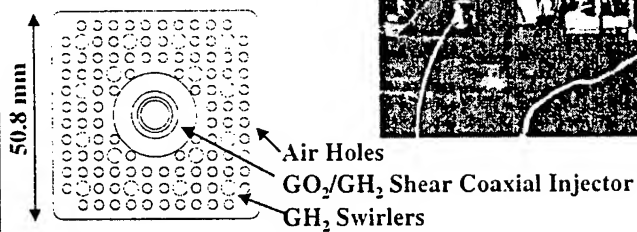
Motivation

- Document Effect of Chamber Mach # on Mixing and Combustion Characteristics of Shear Coaxial Injector for Both GO_2/GH_2 and LOX/GH_2 (*Currently in Progress*) Propellants
- Obtain Data Base for CFD Code Validation

PENNSTATE

CHAMBER MACH # EFFECT STUDIES

- GO_2/GH_2 Study Injector
- $\text{O/F} \approx 4$ GO_2/GH_2 Combustion
- Background Air/ GH_2 Flow
- 1200 K Background Flow
- Chamber Pressure ≈ 1.3 MPa
(190 psia)
- Chamber Mach # Varied
 \Rightarrow for M# of $\approx 0, 0.1, 0.2, 0.3$



PENNSTATE

CHAMBER MACH # EFFECT STUDIES

Flow Conditions

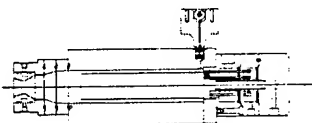
Case	Chamber Mach Number	O ₂ mass flow rate (lbm/s)	Main H ₂ mass flow rate (lbm/s)	Air mass flow rate (lbm/s)	Background H ₂ mass flow rate (lbm/s)
1	0.1	0.093	0.024	0.730	0.007
2	0.2	0.093	0.024	1.887	0.016
3	0.3	0.093	0.024	3.197	0.030

Case	O/F Main	O/F Background	O/F total
1	3.818	111.4	26.7
2	3.818	115.4	48.8
3	3.818	107.2	60.8

PENNSTATE

CHAMBER MACH # EFFECT STUDIES

Focused Laser Beam Passes
Vertically Through Rocket
Chamber



50mm Lens

ICCD Camera

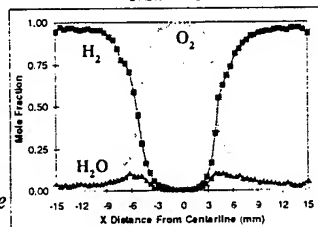
Imaging Spectrograph

PENNSTATE

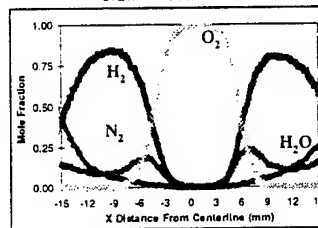
CHAMBER MACH # EFFECT STUDIES

$P_c = 1.3 \text{ MPa}$
 $X = 51 \text{ mm}$
 $X/d = 6.5$
 $X = \text{Axial Distance}$
 $d = \text{GO}_2 \text{ Post ID}$

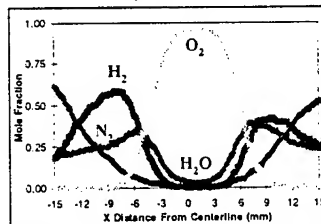
$M \# \approx 0$



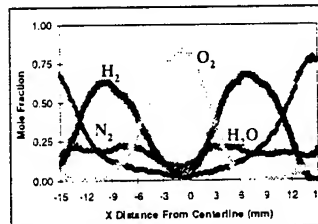
$M \# \approx 0.1$



$M \# \approx 0.2$



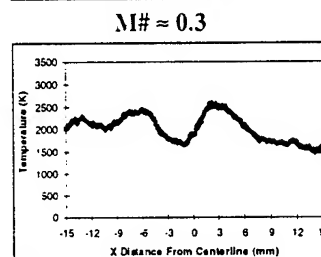
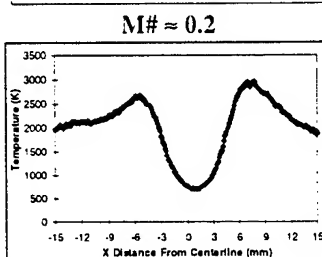
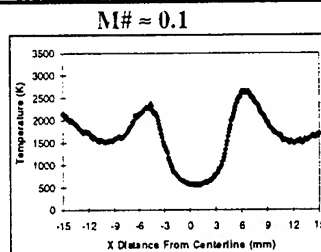
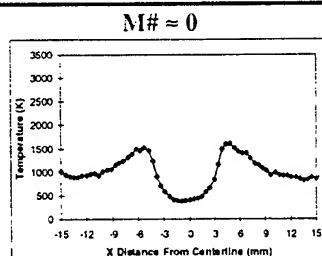
$M \# \approx 0.3$



PENNSTATE

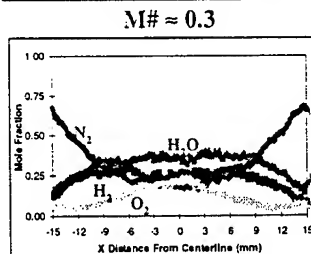
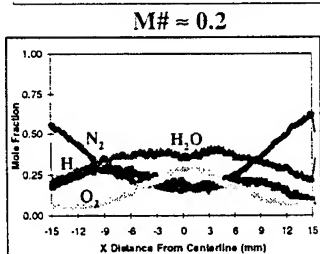
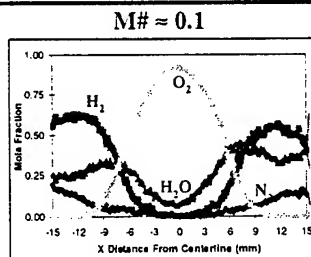
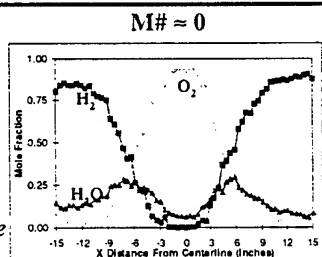
CHAMBER MACH # EFFECT STUDIES

$P_c = 1.3 \text{ MPa}$
 $X = 51 \text{ mm}$
 $X/d = 6.5$
 $X = \text{Axial Distance}$
 $d = \text{GO}_2 \text{ Post ID}$



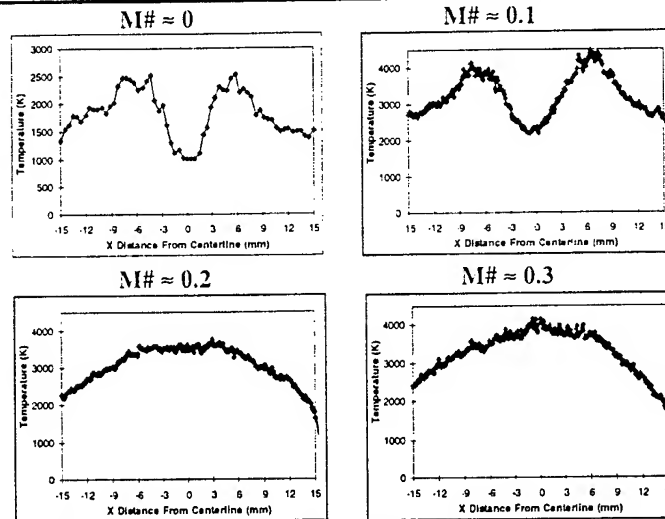
CHAMBER MACH # EFFECT STUDIES

$P_c = 1.3 \text{ MPa}$
 $X = 127 \text{ mm}$
 $X/d = 16.2$
 $X = \text{Axial Distance}$
 $d = \text{GO}_2 \text{ Post ID}$



CHAMBER MACH # EFFECT STUDIES

$P_c = 1.3 \text{ MPa}$
 $X = 127 \text{ mm}$
 $X/d = 16.2$
 $X = \text{Axial Distance}$
 $d = GO_2 \text{ Post ID}$

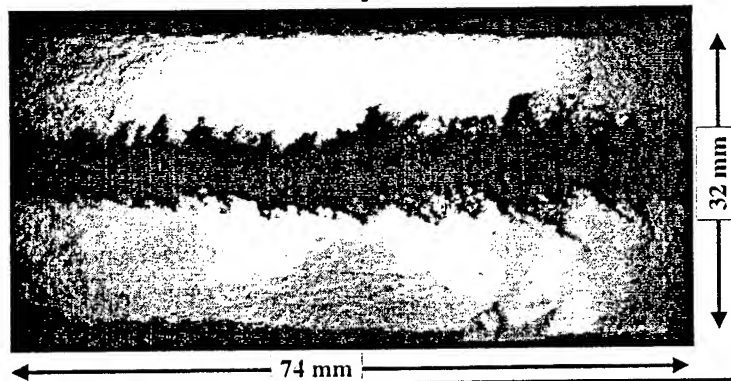


PENNSTATE

CHAMBER MACH # EFFECT STUDIES

SHADOWGRAPH IMAGE OF LOX IN COMBUSTION ZONE

- LOX/GH₂ O/F=4 For Shear Coaxial Injector
- Chamber Pressure = 1.38 MPa (200 psia)
- Chamber Mach# = 0.2 (Air/GH₂ Combustion; 1280 K)



PENNSTATE

CHAMBER MACH # EFFECT STUDIES

Summary

- Initial Experiments for a GO_2/GH_2 Shear Coaxial Injector Involving Raman Spectroscopy Indicate That Chamber Mach # Increases Mixing
- Experiments Are Currently Underway for a LOX/GH_2 Shear Coaxial Injector

PENNSTATE



Summary/Future Work

- Broad Rocket Propulsion Interests Are Driving Diverse Studies of Injector Types and Propellant Combinations.
- Current Interest in Low Cost Access to Space Is Currently Focusing Research On Propellants That Provide Operations Advantages and Robust Injector/Chamber Concepts That Increase Lifetime.
- Advanced Concepts Such As Rocket Based Combined Cycle and Pulse Detonation Engines Are Also Competing Increasing Interest.
- Future Research Efforts At Penn State's Cryogenic Combustion Laboratory Reflect These Developments.

PENNSTATE



Recent Studies on Preburner Injector Characteristics for the Hydrogen-Oxygen Engine

J.Wang, S.Q.Cheng, L.Z.Song, P.X.Hu

11th Research Institute of China Aerospace Corporation

Abstract In order to develop the technology for high performance hydrogen-oxygen staged combustion rocket engine, four kinds of preburner injector have been studied theoretically and experimentally. By using the Phase Doppler Particle Analyzer(PDPA), the spray characteristics of these injectors are investigated, through varying liquid-to-air pressure drop ratio, liquid mass flow, and back pressure in the high pressure rig. Fire tests have also been completed for demonstration. The spray performance, gas temperature distribution, combustion stability and ignition performance for different injector configurations are revealed.

1. Introduction

The preburner is a key component for the staged combustion cycle engine, owing to its higher pressure and flowrate than that of the gas generator cycle engine. Its combustion performance and stability, gas temperature distribution at exit are closely related to its injector configurations. In order to develop high performance preburner injector, recently we studied four kinds of injector configurations theoretically and experimentally.

Four kinds of injector configurations are depicted in fig.1-3. The coaxial injector with swirler of liquid oxygen in centre can get high performance and commonly used in china Hydrogen Oxygen Rocket Engine, The coaxial injector with straight stream of liquid oxygen in centre use the successful experiences of the SSME/LE-7 preburner injectors and it has a well-earned reputation for its reliable operation and processing; The bi-coaxial injector is a new kind of injector configuration we designed specially. Its hydrogen sleeve consist of two segments, hydrogen and oxygen burn at near stoichiometric mixture ratio in the first segment. In the second segment, is injected the remainder of hydrogen which mix and cool the stream exited from first segment. Turbulent diffusion combustion is transformed into premixture combustion for this injector, so that its combustion rate increases. Its spray and mixture performance are as same as that of the shear coaxial injector.

Preburner injector unit is made of injector face plate, central ignition port and four injector, as shown in Fig.4. The ignition port diameter is 16mm. Four injectors with same configuration are equally located at a circle of diameter 32mm. Four injector configurations, namely A,B,C,D are used respectively in their injector elements for testing.

we employed the Phase Doppler Analyzer(PDPA) to study spray droplet size and flowrate distribution for different injector configuration, using air and water as imitation agents, varying liquid-to-air injector pressure drop ratio, liquid mass flowrate and back pressure in the high pressure rig. Theoretical approach is to calculate the atomization combustion model which consider gaseous phase, droplet phase, turbulence and combustion effects. Changing the measured spray data into inlet conditions of the imitation calculation, we can get the spray combustion efficiency and gas temperature distribution and other parameters for the four kinds of injector configuration. The injector elements are also undertaken fire testings, it's chamber pressure ranges 6.85-7.73 MPa, it's mixture ratio ranges 0.639-0.845. Combustion efficiency, gas temperature distribution and vibration are measured .

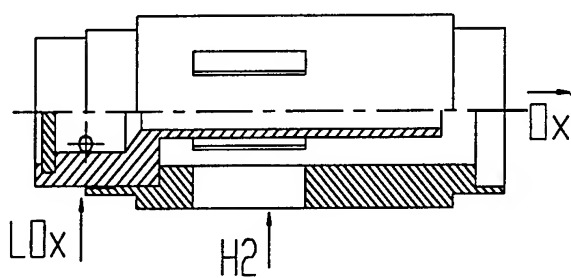


Fig.1 Swirl coaxial injector(A)

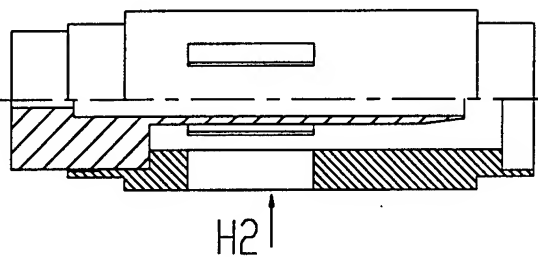
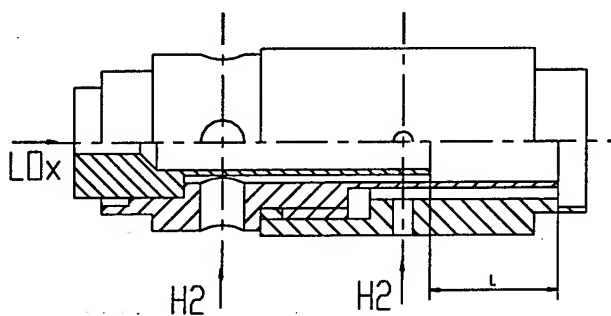
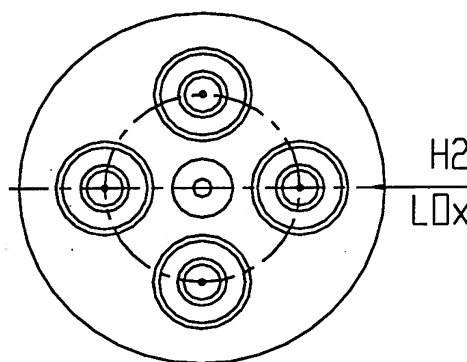


Fig.2 Shear coaxial injector(B)



$$L = \begin{cases} 17mm \\ 27mm \end{cases}$$

Fig.3 bi-coaxial injector



Injector arrangement

Fig.4 injector unit

2. Test Facilities

Injector spray testing goes on in the high pressure rig, as shown in Fig. 5. Normal pressure in the rig is 3.5 MPa, it's internal diameter 320mm, highness 1200mm. There are four windows on it's flank, inserted with plate glass of thickness 25mm and diameter 100mm, used for PDPA light emission, receive and monitor. Safety valve and pressure gauge are mounted on the upper cover, the regulator on bottom is used to keep chamber pressure.

Fire test system for preburner injector, in Fig.6, consist of hydrogen flow lines, liquid oxygen flow lines, nitrogen pressurization system, nitrogen cutoff system and measurement system. The venturi orifice and sonic nozzle are respectively set on liquid oxygen flow line and gaseous hydrogen flow line. The measured data include propellant flowrate, inlet injector pressure, gas average pressure and fluctuation pressure, vibrations corresponding to axial, radial, tangential direction at injector element head. Three temperature gauges are mounted on exhaust duct to measure gas temperature distribution.

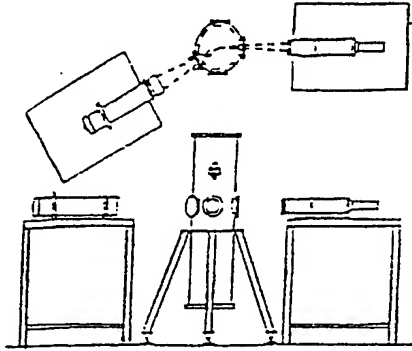


Fig.5 spray measurement system

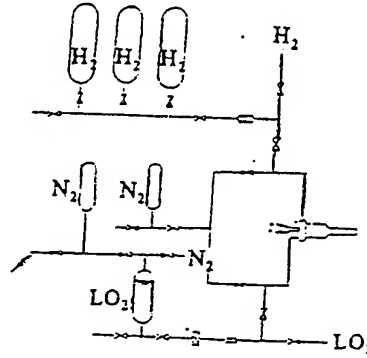


Fig.6 fire testing system

3. Theoretical Model

the spray combustion model in [4] is adopted for theoretical calculation. The model consider gas phases combustion, as well as droplet behavior in gas phases and their interaction. These processes are coupled each other, so that the calculation of the spray combustion model should be done by solving equation system of gas phase equation, droplet equation, combustion and turbulence equation.

3.1 Gas Phase Governing Equations

We can get the gas phase governing equations concerning the continuity, momentum, energy and composition in the following average form:

$$\left\{ \begin{array}{l} \frac{\partial \bar{\rho}}{\partial t} + \frac{\partial}{\partial x_j} (\bar{\rho} u_j) = S_{pm} \\ \frac{\partial}{\partial t} (\bar{\rho} u_j) + \frac{\partial}{\partial x_j} (\bar{\rho} u_j u_j) + \frac{\partial}{\partial x_j} (\bar{\rho} u_j' u_j') = - \frac{\partial \bar{p}}{\partial x_j} + \frac{\partial \bar{\tau}_{ij}}{\partial x_j} + \bar{p} F_j + S_{pui} \\ \frac{\partial}{\partial t} (\bar{\rho} \bar{H}) + \frac{\partial}{\partial x_j} (\bar{\rho} u_j \bar{H} + \bar{\rho} u_j' \bar{H}') = \frac{\partial \bar{p}}{\partial t} + \frac{\partial}{\partial x_j} \left(\frac{\mu}{Pr} \frac{\partial \bar{H}}{\partial x_j} \right) + \\ \frac{\partial}{\partial x_j} (\bar{\tau}_{ij} u_i - \mu u_i \frac{\partial \bar{u}_i}{\partial x_j}) + \frac{\partial \bar{q}_{ij}}{\partial x_j} + S_{pH} \end{array} \right.$$

$$\left\{ \frac{\partial}{\partial t}(\bar{\rho}\bar{Y}_s) + \frac{\partial}{\partial x_j}(\bar{\rho}\bar{Y}_s\bar{u}_j) + \bar{\rho}\bar{Y}'_s\bar{u}'_j \right\} = \frac{\partial}{\partial x_j}(\bar{\rho}D_s \frac{\partial \bar{Y}_s}{\partial x_j}) - \bar{W}_s + S_{Ys} \quad (1)$$

Turbulence model employs $\kappa - \epsilon$ equations, namely

$$\left\{ \begin{aligned} \frac{\partial}{\partial t}(\bar{\rho}k) + \frac{\partial}{\partial x_j}(\bar{\rho}u_j k) &= \frac{\partial}{\partial x_j}[\Gamma_k \frac{\partial k}{\partial x_j}] + G_k - \bar{\rho}\epsilon \\ \frac{\partial}{\partial t}(\bar{\rho}\epsilon) + \frac{\partial}{\partial x_j}(\bar{\rho}u_j \epsilon) &= \frac{\partial}{\partial x_j}[\Gamma_\epsilon \frac{\partial \epsilon}{\partial x_j}] + C_1 \frac{\epsilon}{k} G_k - C_2 \frac{\bar{\rho}}{k} \epsilon^2 \end{aligned} \right. \quad (2)$$

Assuming that stress is proportional to average strain, the expression of Reynold's strain is as following:

$$-\bar{\rho} \overline{u'_i u'_j} = \mu_i \left[\frac{\partial \bar{u}_j}{\partial x_i} + \frac{\partial \bar{u}_i}{\partial x_j} \right] - \frac{2}{3} \rho k \delta_{ij} \quad (3)$$

3.2 Droplet Governing Equations

Considering turbulence diffusion effects, droplet movement equation is written as:

$$\left\{ \begin{aligned} \dot{m}_d \frac{dU_d}{dt} &= C_D \frac{A_d}{2} \frac{\mu Re}{D} \{ U - (U_d + U_{diff}) \} \\ \dot{m}_d \frac{dV_d}{dt} &= C_D \frac{A_d}{2} \frac{\mu Re}{D} \{ V - (V_d + V_{diff}) \} + \dot{m}_d \frac{W_d^2}{r} \\ \dot{m}_d \frac{dW_d}{dt} &= C_D \frac{A_d}{2} \frac{\mu Re}{D} \{ W - W_d \} + \dot{m}_d \frac{V_d W_d}{r} \end{aligned} \right. \quad (4)$$

When droplet collide with wall, the droplet rebounds with same axial velocity and opposite radial velocity. It's trajectory equation is :

$$\frac{dx_d}{dt} = U_d, \quad \frac{dr_d}{dt} = V_d, \quad r \frac{d\theta}{dt} = W_d \quad (5)$$

3.3 Droplet Vaporization Model

Droplet vaporization rate can be calculated by following formula:

$$\dot{m}_{v.s} = \frac{2\pi r_l \rho_g D_g N_{um}}{AB} \ln\left(\frac{1 - Y_{v.\infty}}{Y_{v.s}}\right) \quad (6)$$

here $A = 1 + \frac{4\pi r_l^2 \rho_{us}}{\dot{m}_{v.s}} \frac{\partial r_l}{\partial t}$, $B = 1 + \frac{\rho_{e.s}}{\rho_{v.s}} (1 - \frac{1}{A})$

The droplet radius variation can be written as the following:

$$\frac{dr_l}{dt} = -\frac{\dot{m}_{v,s}}{\pi D^2 \rho_l} - \frac{D}{6 \rho_l} \frac{d\rho_l}{dt} \quad (7)$$

Droplet energy equation is:

$$\frac{dT_l}{dt} = \frac{3\lambda_g N_{uT} Z_1}{2C_{pl} r_l^2 \rho_l} \left\{ \frac{T_g - T_l}{e^{Z_1} - 1} - \frac{\Delta H_v}{Z_2} \right\} \quad (8)$$

here $Z_1 = \frac{\dot{m}_{vs} Z_2}{\pi D \lambda_g N_{uT}}$, $Z_2 = AC_{pv} + (A - 1) C_{pe} \frac{\rho_{ls}}{\rho_{e,s}}$

3.4 Combustion Model

We use Spalding's EBU model to imitate droplet combustion, assuming that turbulent combustion zone consist of large quantity of flammable gas messes and burned gas messes. Chemical reaction take place at interfaces between messes. Chemical reaction rate depends on flammable gas messes break rate which is directly proportional to turbulence fluctuation energy decay rate.

$$\begin{cases} R_{f,g} = -\min(|R_f|, |R_g|) \\ R_f = -AM_f \left(\frac{\rho_{yf}}{M_f} \right)^a \left(\frac{pY_{ox}}{M_{ox}} \right)^b \exp(-E/RT) \\ R_g = -C_k \rho_g^{0.5} \frac{\epsilon}{k} \end{cases} \quad (9)$$

here $C_k=1.07$; A stands for reaction constant;

4. Results and Discussion

4.1 Spray Measurement

The spray is measured downstream at a section of 110 mm distance from nozzle exit. At different radius ,we measure droplet density Nd, average volume diameter D30,average area diameter D20 ,then calculate average droplet diameter D32 by following formula:

$$D_{32} = \frac{\int_0^R N_d(r) D_{30}(r) dr}{\int_0^R N_d(r) D_{20}(r) dr} \quad (10)$$

Varying gas/liquid injector pressure drop ratio, back pressure in high pressure rig and liquid flowrate, we can obtain the relation between D32 and $\Delta PG / \Delta PG, PB, m L$, as seen in Fig.7-9. The Fig. 10 show liquid flowrate distribution v.s radius. It can be seen that it's average spray droplet diameter is smallest for centrifugal coaxial injector;

For shear coaxial injector and bi-coaxial injector, their spray droplet diameters are closely; For bi-coaxial injector, when it's oxygen post recess increases, it's average spray droplet diameter will decrease. For all four injector configurations, their average spray droplet diameters will decrease when injector pressure drop ratio increase, and their average spray droplet diameters will increase when back pressure and liquid flowrate increase. Fig.10 show that for shear coaxial injector and bi-coaxial injector, their flowrate distribution concentrate on spray centre; for swirl coaxial injector, it's flowrate distribution is well distributed, that benefits mixture ratio distribution.

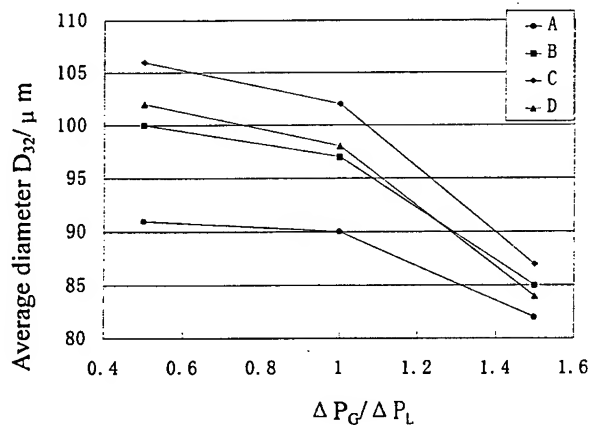


Fig.7 gas/liquid injector pressure drop ratio effects on D32

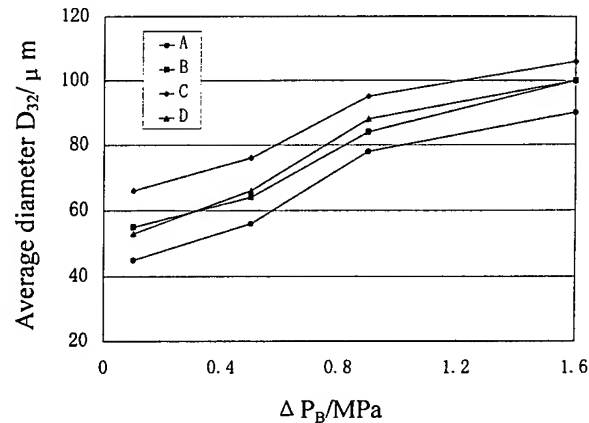


Fig.8 back pressure effects on D32

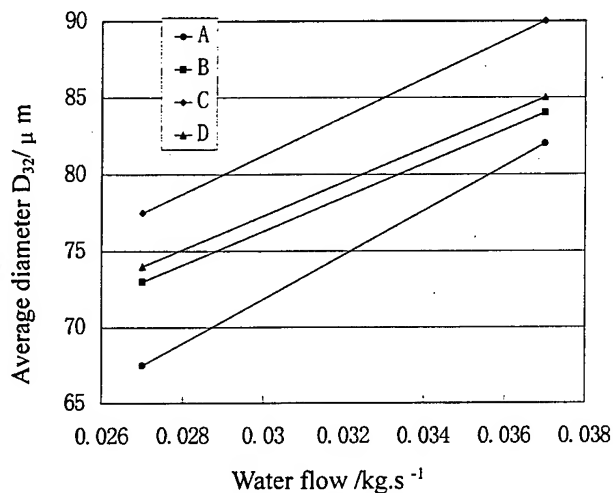


Fig.9 flowrate effects on D32

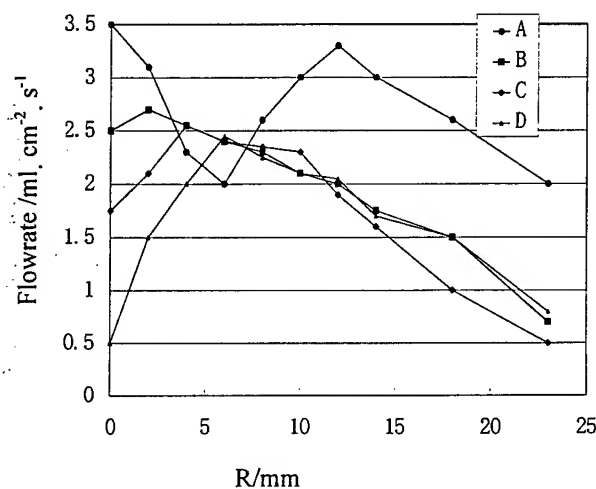


Fig.10 flowrate distribution

4.2 Theoretical Calculation

Cartesian coordinates grid system are used for theoretical calculation. We will change the non-regular physical plane into regular rectangular plane for calculating. The grids distribution is made exponentially. In order to ensure calculation

convergence and accuracy, we make denser grids at near injector face and convergent section, where there are great variation in chemical reaction and flow conditions.

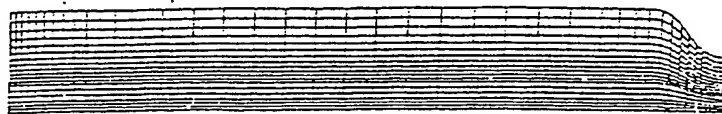


Fig.11 Calculation domain and grid plane

We make the equations(1) and (2) discretization. The liquid phase governing equations (4) and (5) are coupled with gas phase governing equations through diffusion velocities. We can directly integrate the liquid phase governing equations, while assuming that gas phase field is known. The time interval required for droplet movement from position k to $k+1$ is decided by following expression:

$$\Delta t_k = \min \left\{ \frac{\Delta \xi}{U_{d,k}} \cdot \frac{\Delta \eta}{V_{d,k}} \right\} \quad (11)$$

here $U_{d,k}$, $V_{d,k}$ denote droplet axial and radial velocities at position k . The SIMPLE was used to solve the equation system. The pressure field is indirectly given by continuity equation, so that we can put the pressure field into momentum equation to get velocity field. As soon as the velocity field meets continuity requirements, the calculation will go to the end, otherwise the calculation repeats after revising pressure field again. In calculation, we assume that all flux at symmetric axis are equated to zero, the wall is adiabatic, fixed and can't be penetrated, and there is sonic velocity at preburner exit. The flow conditions are greatly coupled with throat choke conditions. The inlet parameters are:

liquid flowrate 0.0885 kg/s; liquid oxygen temperature 90K; gaseous hydrogen temperature 300K.

Mixture ratio variation can be realized by changing gaseous hydrogen flowrate. For centrifugal injector, liquid oxygen tangential velocity should be given. For bi-coaxial injector, gaseous hydrogen velocity at different entrance is given to corresponding entrance grids.

Initial spray droplet size is obtained by spray testing data. Dividing the measured droplet size into 10 groups, inputting diameter and mass percentage of each group, the calculation begin and the results will display on plane.

For four kinds of preburner injector, the pictures are almost same. Now we take straight coaxial injector as example to explain the results. Velocity vector field is depicted in Fig.12. It show that there is a recirculation zone near injector face. Fig.13 show temperature field, it imply that there is great temperature variation in the range of 30-70mm downstream injector face, where exists strong combustion reaction. Liquid oxygen droplets injecting from injector move forward along it's trajectory,

owing to their vaporization, around them exist strong combustion zones. The oxygen vapor immediately reacts with gaseous hydrogen before it's sufficient diffusion, so that exists higher local mixture ratio. The highest temperature can reach about 3000K. The chemical reaction basically stops in excess of 70mm downstream injector face. Gas temperature gradually become closely and the final temperature is about 1000K. At different axial distance, the temperature variation relations with radius are depicted in Fig.14. The temperature near injector face ($X < 26.5\text{mm}$) is under 800K, that imply combustion don't take place. The combustion begins until the distance is in excess of 26.5mm and stops about at $X = 78.9$. The low temperature zones near injector face are produced by recirculation. After combustion begin, exists initial temperature peak in radial direction about at $Y = 5\text{mm}$, then the peak move gradually toward the centre. In excess of $X = 79.9\text{mm}$, gas temperatures are almost equal. Radial distribution of axial velocities is shown in Fig.15. It imply that recirculation zones exist at 0-43mm axial distance and the flow finally become stable accompanying with the end of combustion. Fig.16 show that radial velocities in combustion zone are relatively higher, owing to turbulence mixture and then they decrease gradually. The radial velocities are almost equal to zero before the convergent section ($X = 173.9$). That means diffusion and mixture are very weak, the flow is in equilibrium.

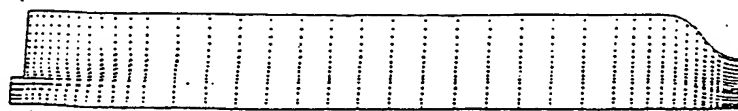


Fig.12 velocity vector field

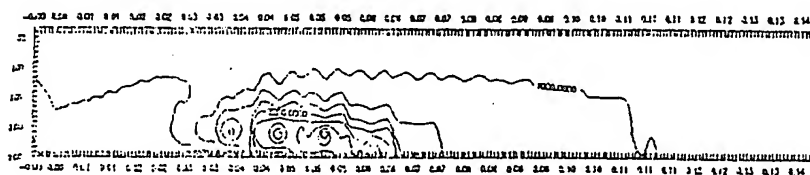


Fig.13 isothermal field

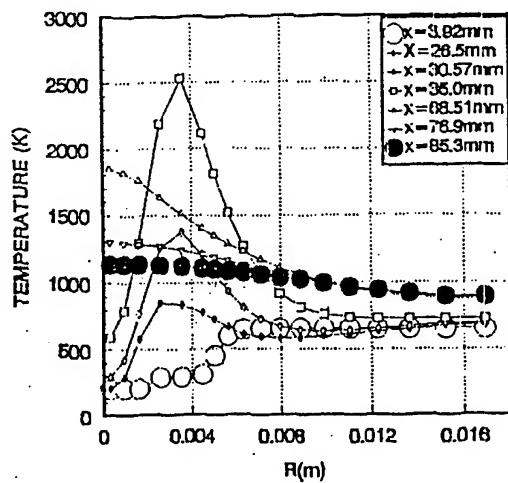


Fig.14 gas temperature radial distribution at different sections

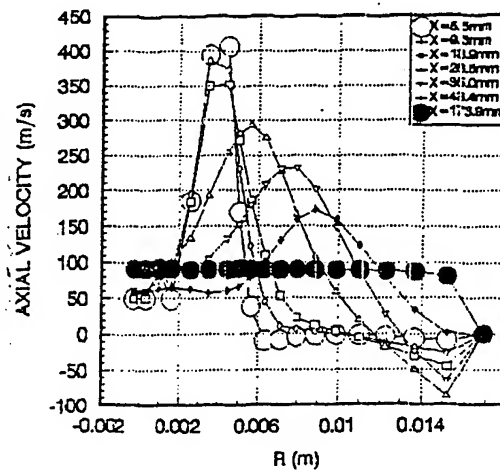


Fig.15 radial distribution of axial velocity at different sections

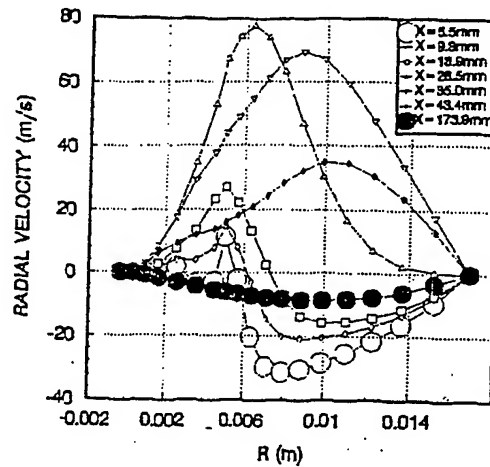


Fig.16 radial distribution of radial velocity at different sections

4.3 Fire Testing Results

Six fire testings for preburner have been finished. The testing measured data are summarized in table 1.

Table 1 testing data

mode	YR01	YR02	YR03	YR04	YR06 _I	YR06 _{II}
preburner pressure Pf, MPa	7.400	7.585	7.489	7.080	7,732	6.848
OX flow Gy, kg/s	0.370	0.376	0.375	0.369	0.367	0.322

H2 flow Gr, kg/s	0.438	0.448	0.461	0.461	0.497	0.470
mixture ratio, r	0.845	0.838	0.813	0.799	0.738	0.673
characteristic velocity C, m/s	2435	2475	2408	2269	2308	2272
gas temperature Tf1, K	1151	1121	/	/	1003	900
gas temperature Tf2, K	1163	1123	1091	1058	953	866
gas temperature Tf3, K	1134	1103	1056	1054	989	896
theoretical temperature Tf _{Th} , K	1118	1108	1082	1072	1044	954
biggest temperature difference ΔT_p , K	28.98	20.09	35.6	4.2	50.23	34.73

A. Combustion Efficiency. It can be calculated by the following:

$$\eta_c = C_{ex}^* / C_{th}^* \quad C_{ex}^* = P_r A_t / G_\Sigma \quad (12)$$

here C_{ex}^* is experimental characteristic velocity;
 C_{th}^* is theoretical characteristic velocity, corrected by supply
gas hydrogen temperature
 A_t is throat area of exhaust duct

The other measured data are all close to 100%, this is owing to having bigger hardware volume. Theoretical calculation show that the propellant combustion goes on to the end in 100mm downstream injector face. combustion efficiencies greater than 100% result in the measurement error. Comparing four preburner configurations, we found that option D has higher combustion efficiency and lower for B.

B. Gas Temperature Distribution

Gas temperatures are measured at different locations in a same exhaust duct section. The increase rate of measured temperature with mixture ratio is more rapid than that of theoretical calculation. Comparison of the temperature difference show that the gas temperature is well distributed for D, $\Delta T_f = 20.09$, and it's temperature distribution is poor for B, $\Delta T_f = 50.23$.

C. Vibration

Vibration gauges were mounted at the head cover of injector elements in axial, radial and tangential directions. The measured vibration data are given in table 2, the

peak frequency and its amplitude are given in table 3. Comparing their vibration data of different injector configurations, there is lower vibration for D, its complex vibration is 325.4 m/s^2 , and its component vibration is 36.8 m/s^2 (3025 Hz). The option B has higher vibration, its complex vibration is 686 m/s^2 , component vibration is 196.4 (5575 Hz). The measured gas pressure fluctuation shows that there is no combustion instability, the peak to peak pressure fluctuation is less than 4% of rated chamber pressure.

Table 2 mechanical vibration

parameter name	YR01	YR02	YR03	YR04	YR06
option	C	D	A	B	B
axial acceleration $a_1, \text{m/s}^2$	306.3	261.7	514.5	196	356.7
radial acceleration $a_2, \text{m/s}^2$	414.5	279.6	676.2	686	541
tangential acceleration $a_3, \text{m/s}^2$	232	325	/	174	278

Table 3 mechanical vibration

parameter name		YR01	YR02	YR03	YR04	YR06
axial frequency	Hz	6375	3025	3425	7825	5650
axial amplitude	m/s^2	12.6	36.8	38.9	32	63.8
radial frequency	Hz	6975	8975	3450	5675	5575
radial amplitude	m/s^2	47.2	33.4	59	47.7	196.4
tangential frequency	Hz	4275	7950	3450	3200	5575
tangential amplitude	m/s^2	15.1	22.4	59	18	36.4

D. Ignition Performance

We employ pyrotechnic ignitor AN8100-00B which has 150mm flame length and about four second burning duration. Pressure peaks occur at about 0.6 s. After liquid oxygen and gaseous hydrogen inject into preburner, the chamber pressure rapidly increases up to peak value. there is a time interval between hydrogen entering time and ignition time, which were given in table 4. The ignition performance is closely related to the time interval, and the shorter interval means well ignition performance. The data show that option A has shorter time interval and it is longest for option B. this may be related to mixture ratio distribution (Fig.10). For swirl coaxial injector, oxygen injection flow has strong transversal penetrability into hydrogen, so that it can improve mixture ratio distribution and ignition performance.

Table 4 Ignition delay

parameters name	YR01	YR02	YR03	YR04	YR06
option	C	D	A	B	B
hydrogen enter time, s	0.4	0.4	0.7	0.4	0.4
ignition time, s	1.6	1.6	1.6	1.8	1.8
time interval, s	1.2	1.2	0.9	1.4	1.4

5. Concluding Remarks

A. Gas/liquid coaxial injector spray droplet diameters decrease with the increase of gas/liquid injector pressure drop and increase with the increase of liquid flowrate and back pressure.

B. Average spray droplet diameter for swirl coaxial injector is smaller than that of shear coaxial injector. It has good transversal penetrability and ignition performance.

C. The bi-coaxial injector (option D) has the advantage of high combustion efficiency and stability, uniform temperature distribution but it needs to further improve its ignition performance.

D. For gas/liquid coaxial injectors, there are recirculation zones in the range of 0-43mm downstream injector face, and the combustion occurs in range of 30-70mm from injector face.

Reference

1. Sankar S .V, Zhu J.Y, Bachalo W.D. Experimental studies on the behavior of coaxial rocket injector spray. Areome Tric, Sunnyvale, CA, U.S.A. 1994
2. Lefebvre A.H. Atomization and spray Hemisphere Pub. XO, 1989
3. Yost M.C. Preburner of staged combustion rocket engine, NASA CR-135356
- 4 Z.G.Wang Combustion Processes imitation calculation for liquid rocket engine, National Defence Science and Technology University, China, 1995.

Numerical simulation of reactive flow within the MASCOTTE combustor

Mani POUROUCHOTTAMANE ←

Victor BURNLEY

Francis DUPOIRIEUX

Guillaume DEUCHST

Isabelle DUBOIS

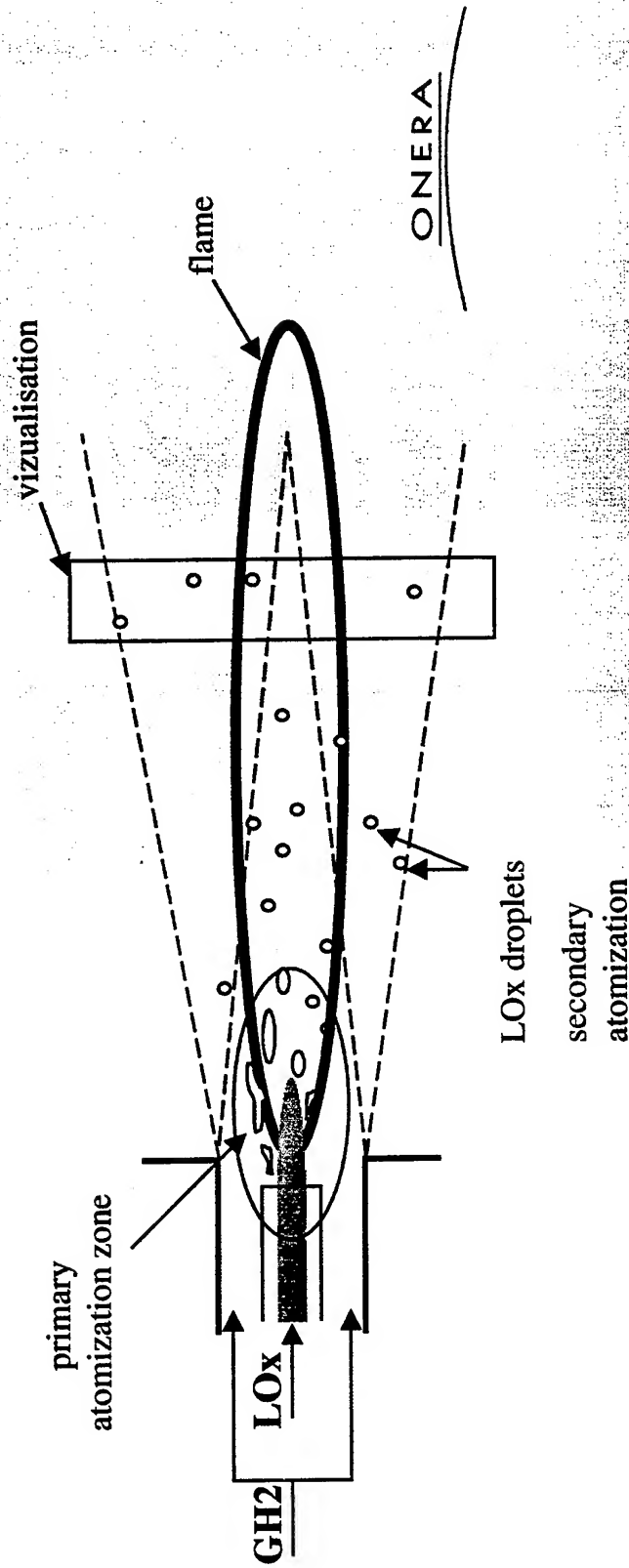
Pascale GILBANK

Department of Fundamental and Applied Energetics (DEFA) - ONERA

The MASCOTTE combustor

Mascotte operating domain (V03 version)

Gaseous hydrogen mass flow rate : 5 to 75 g/s
Gaseous hydrogen temperature : 298 K or cooled down to 100 K
Liquid oxygen mass flow rate : 40 to 400 g/s
Liquid oxygen temperature : 85 K
Pressure in the combustion chamber : 1 to 100 bars



The CFD code MSD2.2

- calculation code of DEFA - ONERA
- version : 2.2 (released in March 1999)
- current applications : propulsion (liquid, solid, airbreathing)
turbomachinery
aerothermics

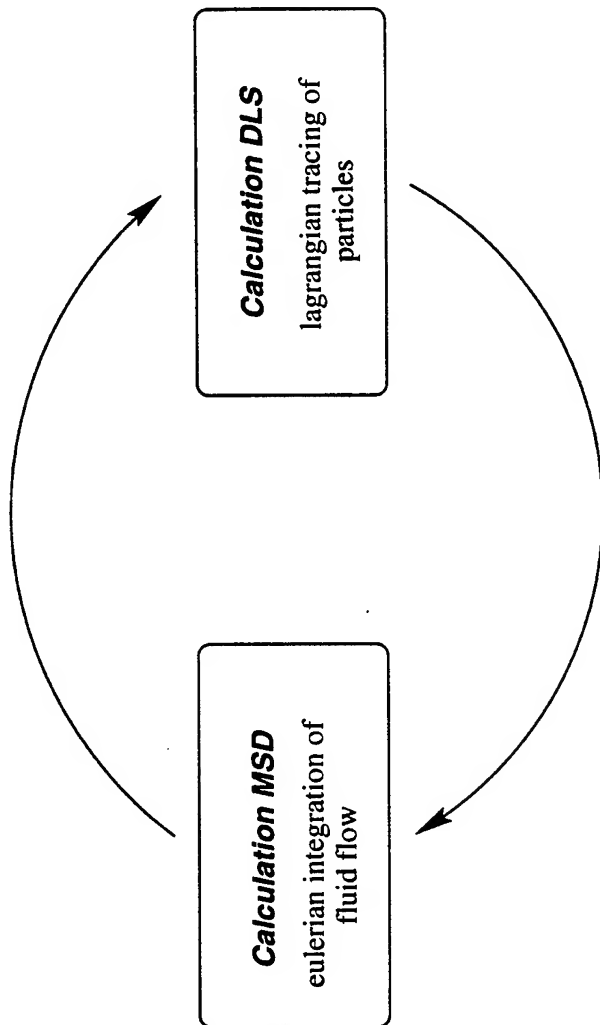
Specifications of MSD 2.2

- finite difference finite volume
- structured mesh : fixed or deforming
- multidomain
- multispecies
- schemes : explicit and implicit
- multigrid : V , W and F cycles
- turbulence : k - ϵ , k - l, RNG
- combustion : various models
- dispersed two-phase flow : Eulerian (DE), Lagrangian (DLS)

Calculation of MASCOTTE

stochastic Eulerian-Lagrangian approach

mean flow field



source terms (interfacial transfer)

ONERA

Equations for the Lagrangian tracing of particles

$$\frac{d\vec{X}_p}{dt} = \vec{V}_p$$

$$m \frac{d\vec{V}_p}{dt} = \vec{F}$$

$$\frac{dm}{dt} = \omega_{\text{vap}}$$

$$m \frac{dh}{dt} = \phi$$

with :

$$\vec{F} = \frac{\pi}{8} D_p^2 C_D \left| \vec{U}_G - \vec{V}_p \right| (\vec{U}_G - \vec{V}_p)$$

$$\omega_{\text{vap}} = 2\pi \rho D_p D \ln(1 + B_M)$$

$$\phi = \pi D N_u \lambda (T - T_s) - \omega_{\text{vap}} L_{\text{vap}}$$

Equations solved by MSD

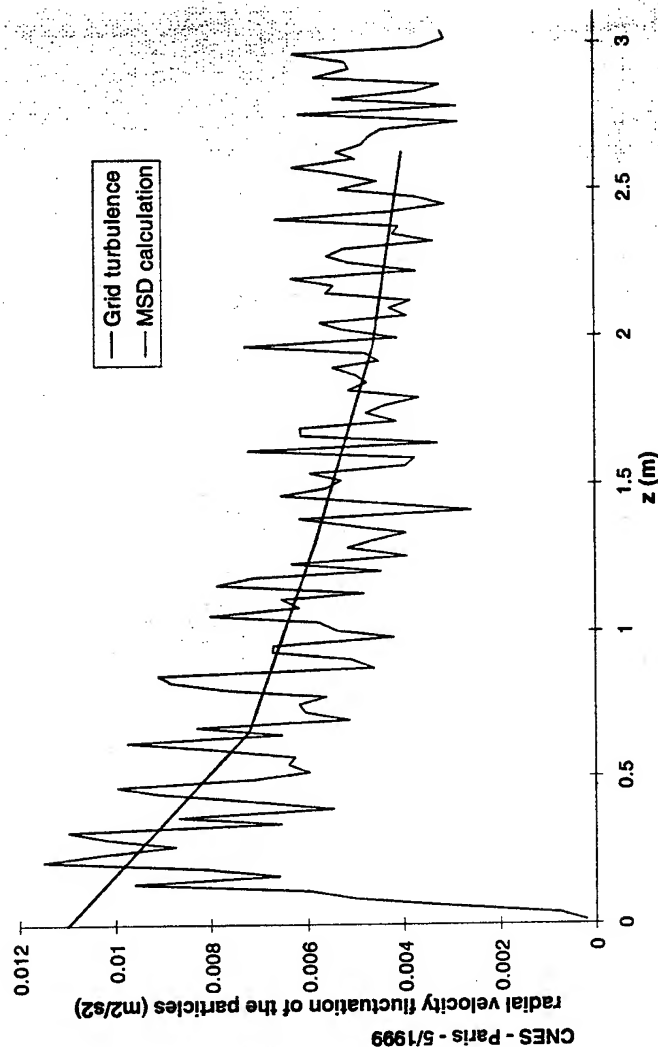
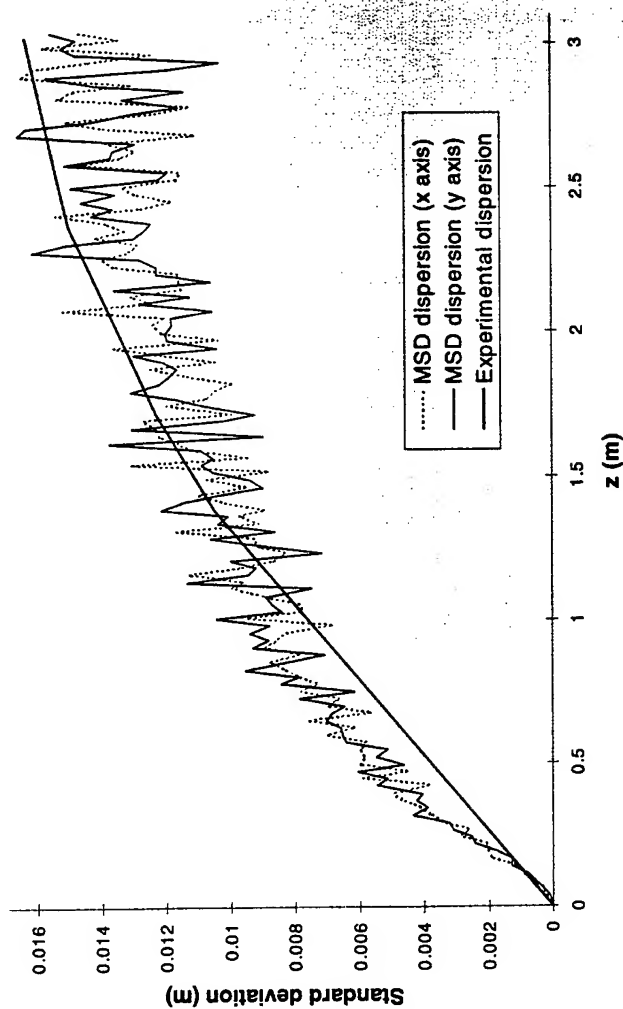
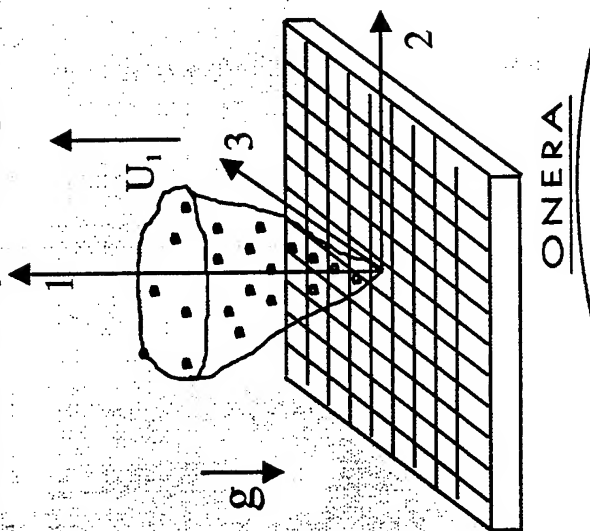
$$\frac{\partial}{\partial t} \begin{pmatrix} \rho \\ \rho \vec{U} \\ \rho H \\ \rho Y_\alpha \\ \rho k \\ \rho \varepsilon \end{pmatrix} + \vec{\nabla} \cdot \begin{pmatrix} \rho \vec{U} \\ \rho \vec{U} \vec{U} + P \mathbf{I} \\ \rho H \vec{U} \\ \rho Y_\alpha \vec{U} \\ \rho k \vec{U} \\ \rho \varepsilon \vec{U} \end{pmatrix} + \overrightarrow{FLUX}_{viscous} = \begin{pmatrix} S_\rho + \Gamma \\ S_{\rho \vec{U}} + \vec{\Gamma} \\ S_{\rho H} + \Pi \\ S_{\rho Y_\alpha} + (\Gamma) \\ S_{\rho k} + .. \\ S_{\rho \varepsilon} + .. \end{pmatrix}$$

In bold : interfacial exchange terms between phases (→ given by DLS)

Dispersion validation

The Snyder & Lumley experiment

- Air mean velocity : 6.55 m/s
- Mesh length : 2.54 cm
- Particle diameter : 87 μm
- Particle density : 1000 kg/m³

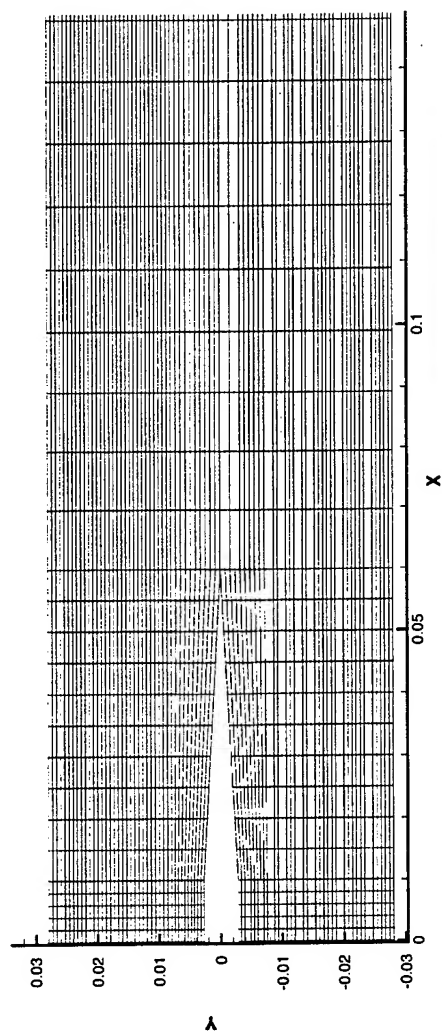
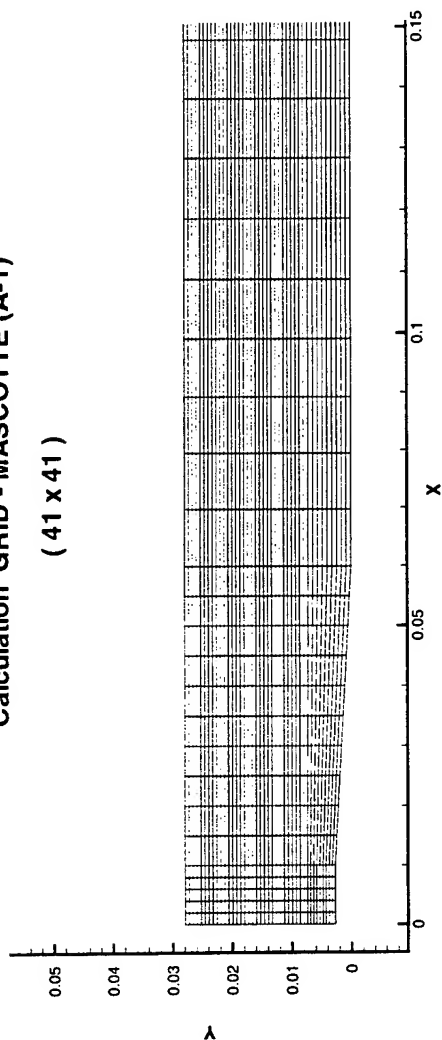


ONERA

MASCOTTE simulation at 1 bar

Calculation GRID - MASCOTTE (A-1)

(41 x 41)



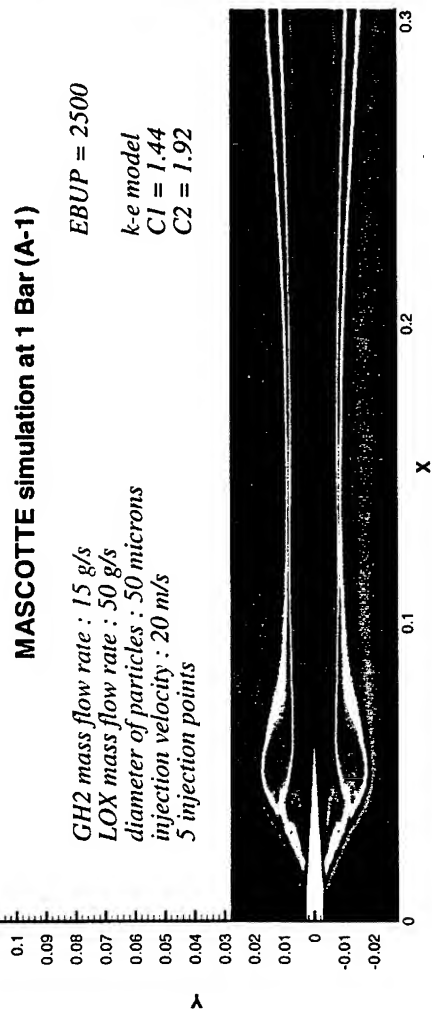
ONERA

MASCOTTE simulation at 1 Bar (A-1)

GH2 mass flow rate : 15 g/s
 LOX mass flow rate : 50 g/s
 diameter of particles : 50 microns
 injection velocity : 20 m/s
 5 injection points

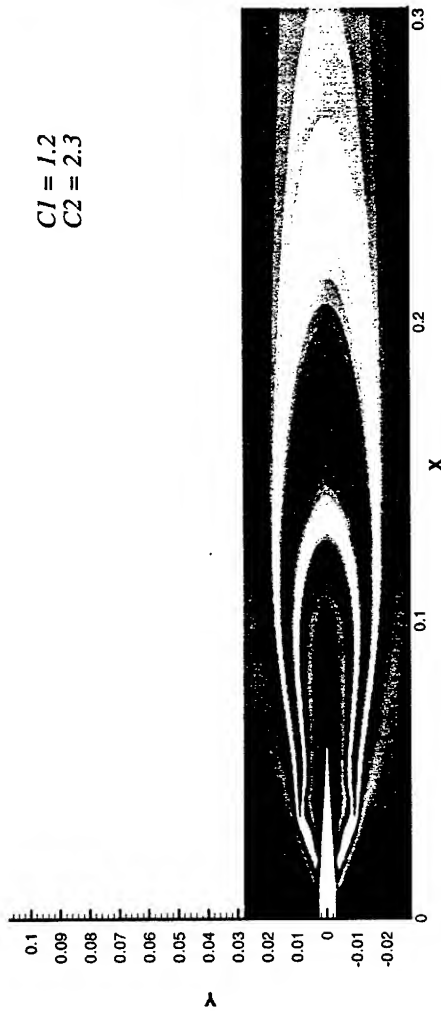
EBUP = 2500

k-e model
 C1 = 1.44
 C2 = 1.92



Temperature
4142.29
4011.48
3880.67
3749.85
3619.04
3488.22
3357.41
3226.59
3095.76
2964.95
2834.13
2703.31
2572.50
2441.68
2310.86
2180.04
2049.22
1918.40
1787.58
1656.76
1525.94
1395.12
1264.30
1133.48
1002.66
871.84
741.02
610.20
479.38
348.56

C1 = 1.2
 C2 = 2.3



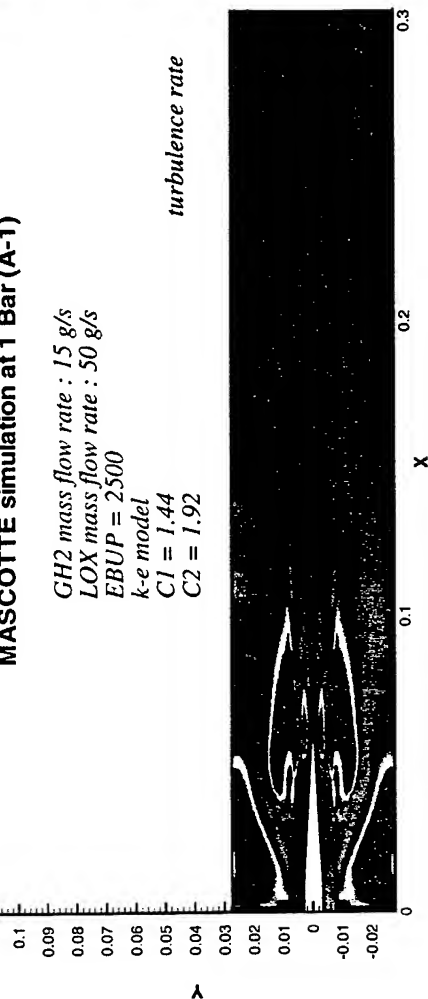
Temperature
4279.43
4144.96
4010.49
3876.02
3741.55
3607.08
3472.6
3338.13
3203.66
3069.19
2934.72
2800.25
2665.78
2531.31
2396.84
2262.37
2127.9
1993.43
1858.96
1724.49
1590.02
1455.55
1321.08
1186.61
1052.14
917.67
783.20
648.73
514.26
379.79

ONERA

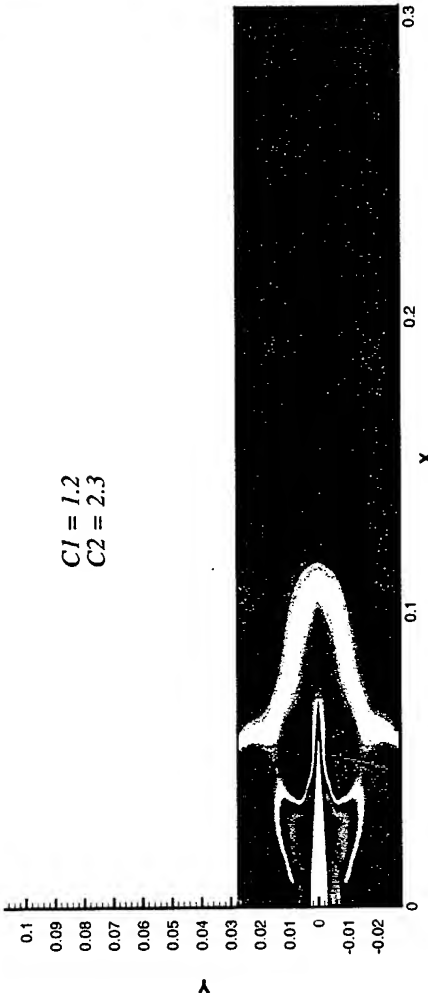
MASCOTTE simulation at 1 Bar (A-1)

GH2 mass flow rate : 15 g/s
 LOX mass flow rate : 50 g/s
 EBUP = 2500
 k-e model
 C1 = 1.44
 C2 = 1.92

turbulence rate



C1 = 1.2
 C2 = 2.3

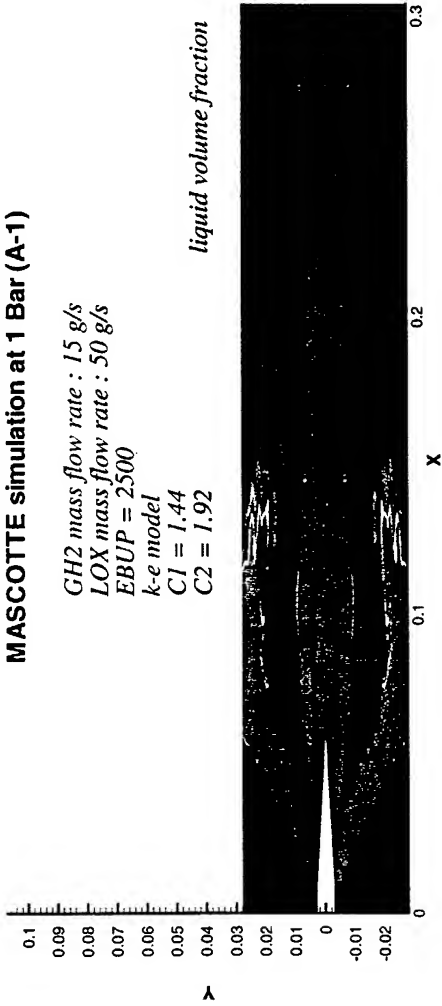


ONERA

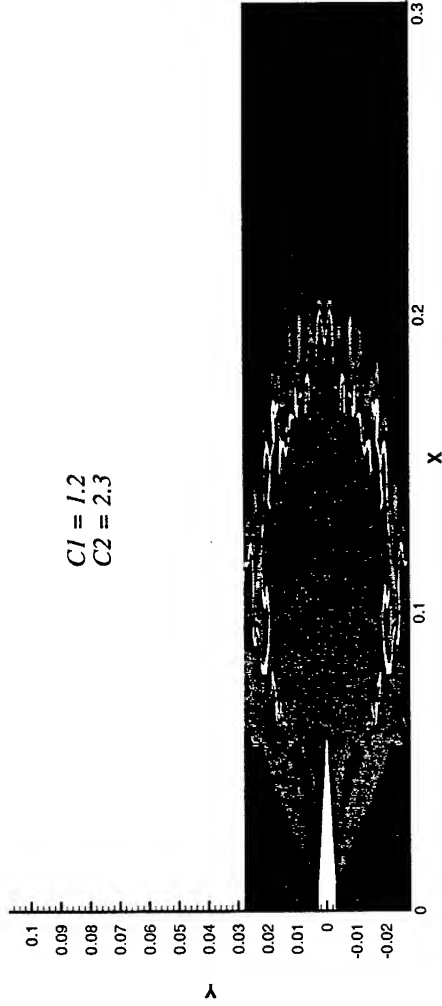
MASCOTTE simulation at 1 Bar (A-1)

GH2 mass flow rate : 15 g/s
LOX mass flow rate : 50 g/s
EBUP = 2500
k-e model
C1 = 1.44
C2 = 1.92

liquid volume fraction



C1 = 1.2
C2 = 2.3

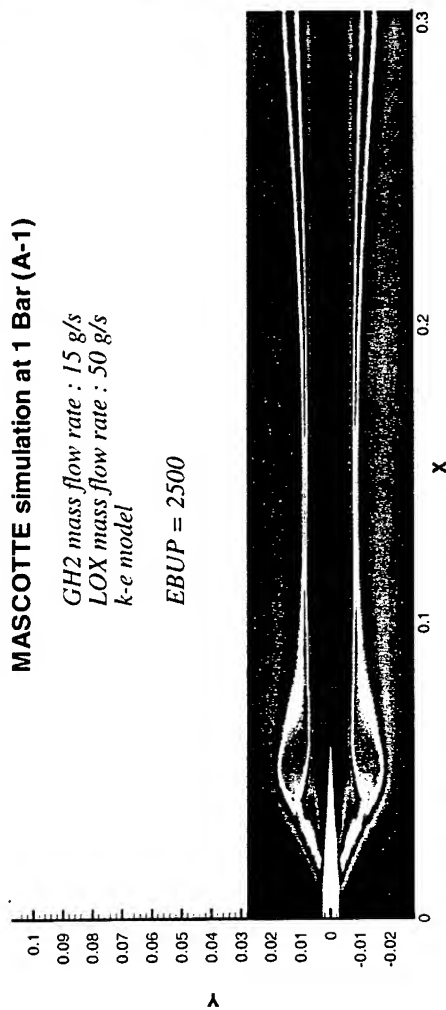


ONERA

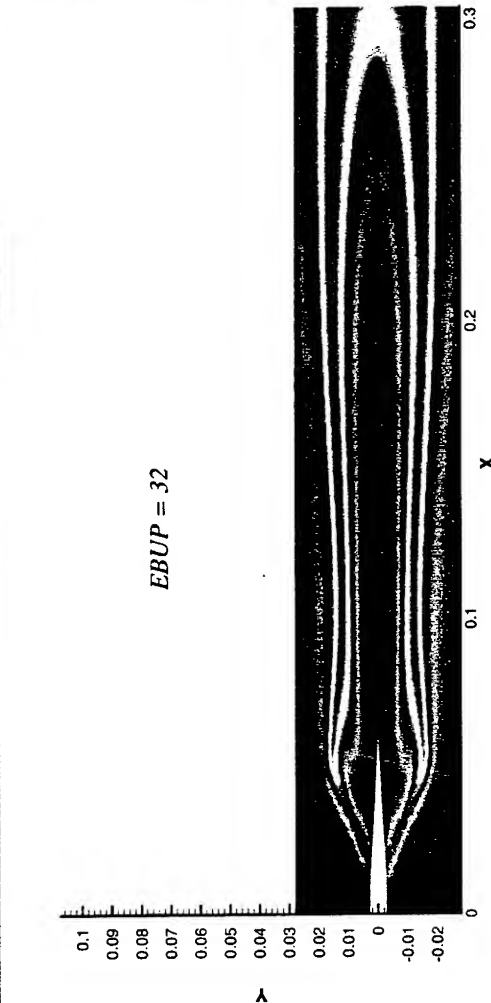
MASCOTTE simulation at 1 Bar (A-1)

GH2 mass flow rate : 15 g/s
LOX mass flow rate : 50 g/s
k-e model

EBUP = 2500



EBUP = 32

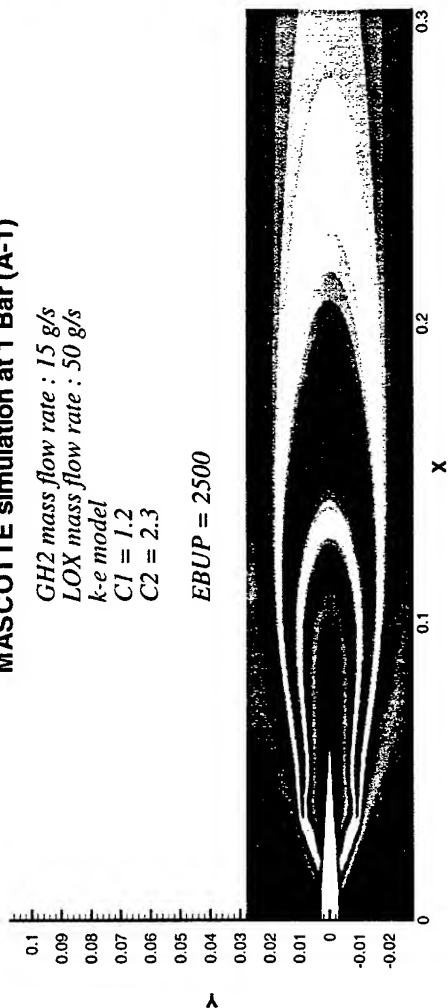


ONERA

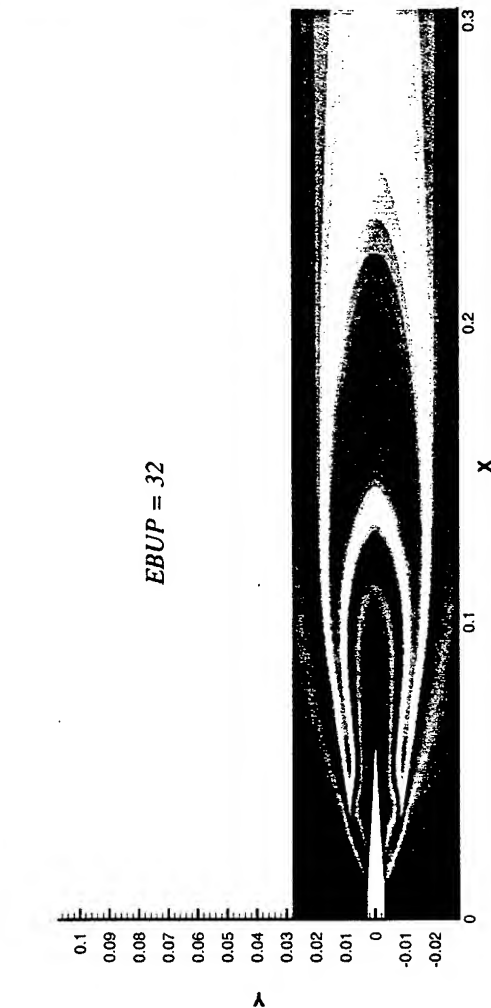
MASCOTTE simulation at 1 Bar (A-1)

GH2 mass flow rate : 15 g/s
 LOX mass flow rate : 50 g/s
 k-e model
 C1 = 1.2
 C2 = 2.3

EBUP = 2500



EBUP = 32



ONERA

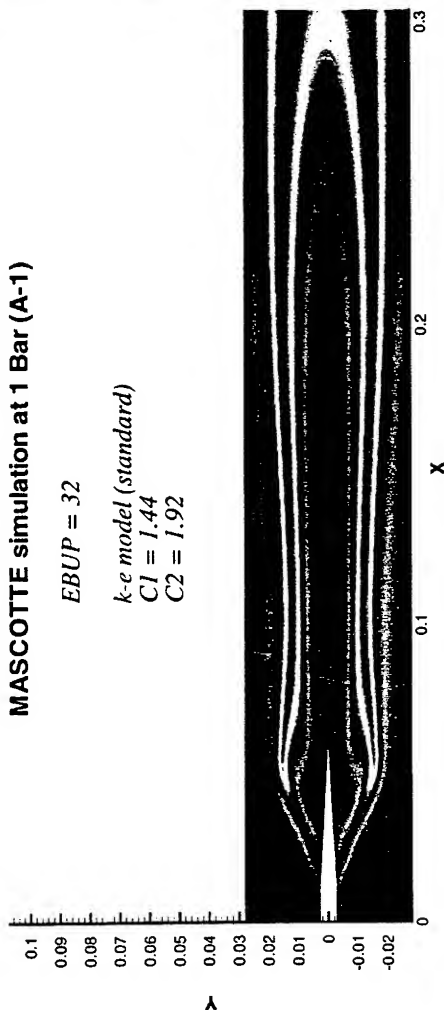
MASCOTTE simulation at 1 Bar (A-1)

EBUP = 32

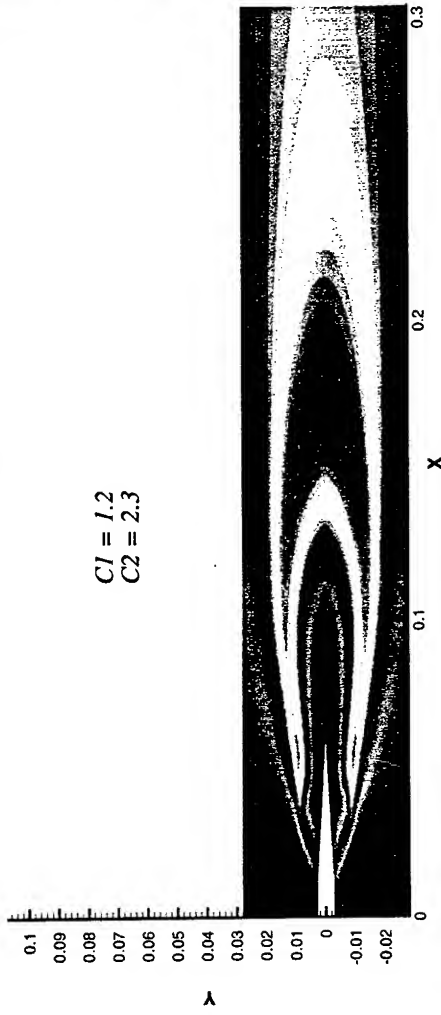
k-e model (standard)

C1 = 1.44

C2 = 1.92



C1 = 1.2
C2 = 2.3



ONERA

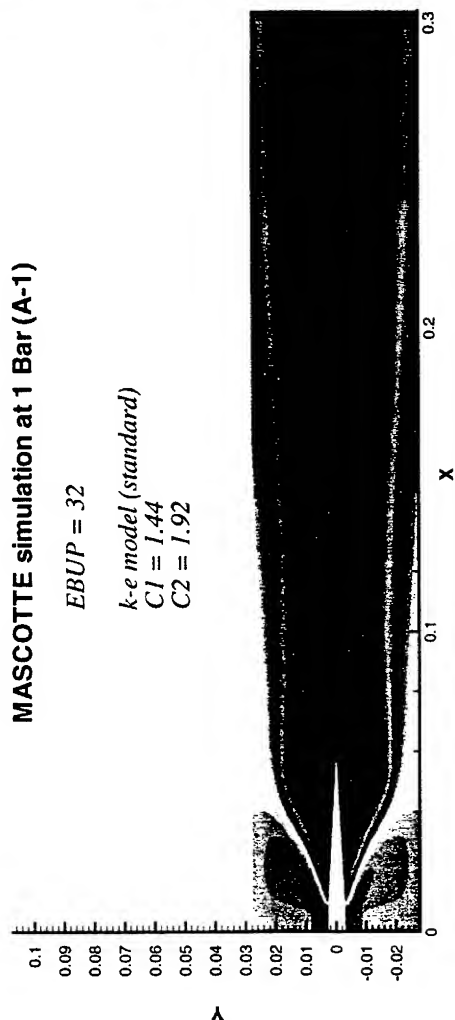
MASCOTTE simulation at 1 Bar (A-1)

EBUP = 32

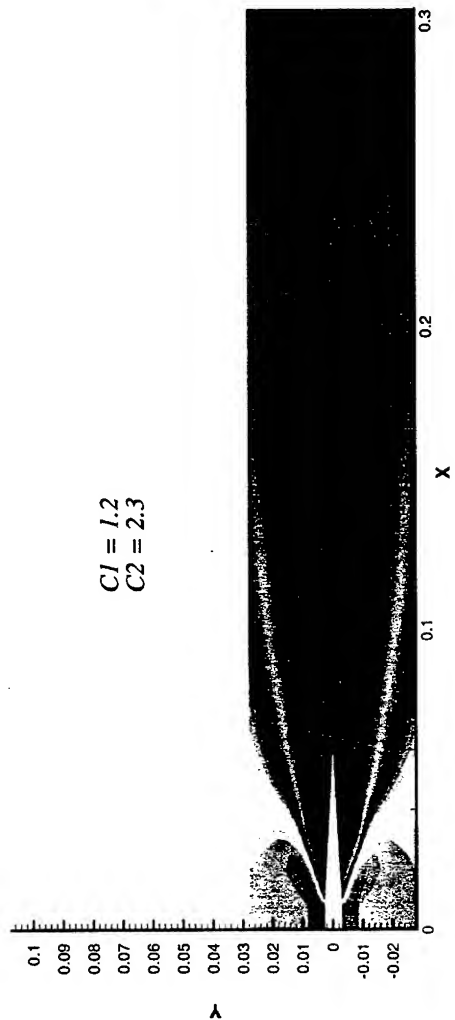
k-e model (standard)

$C1 = 1.44$

$C2 = 1.92$



$C1 = 1.2$
 $C2 = 2.3$



ONERA

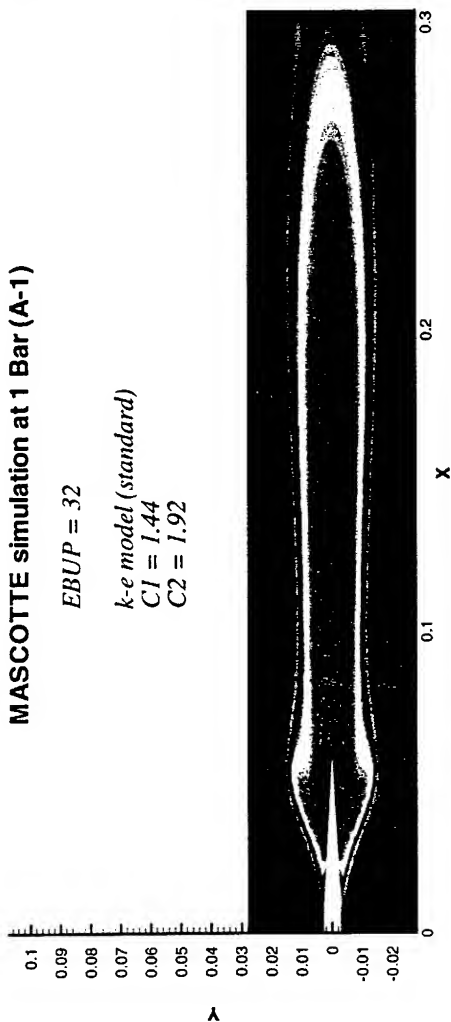
MASCOTTE simulation at 1 Bar (A-1)

EBUP = 32

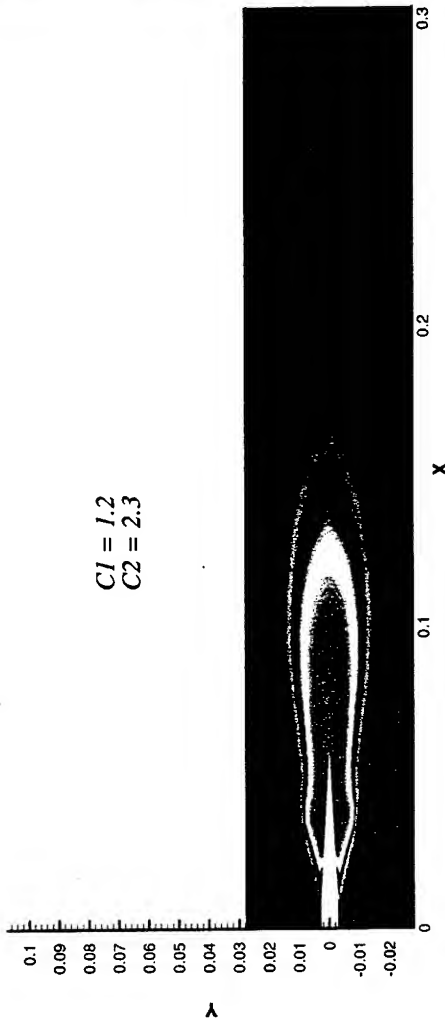
k-e model (standard)

CI = 1.44

C2 = 1.92



CI = 1.2
C2 = 2.3



ONERA

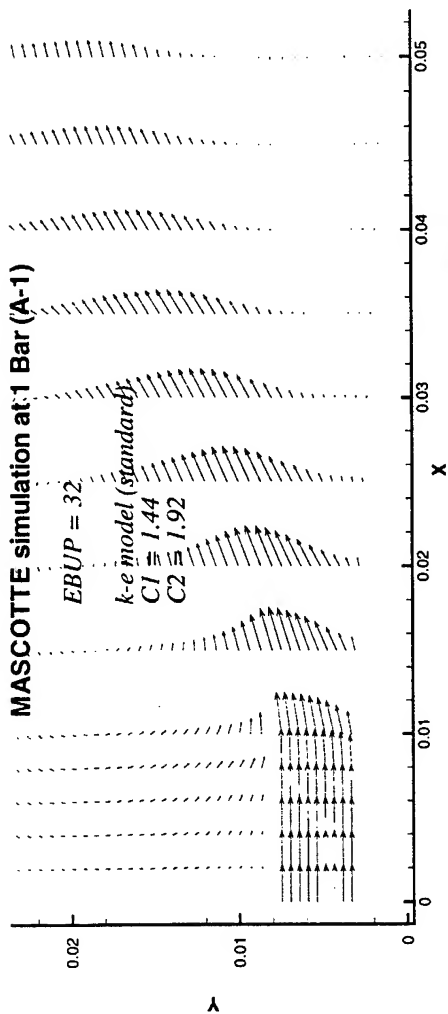
MASCOTTE simulation at 1 Bar (A-1)

EBUP = 32

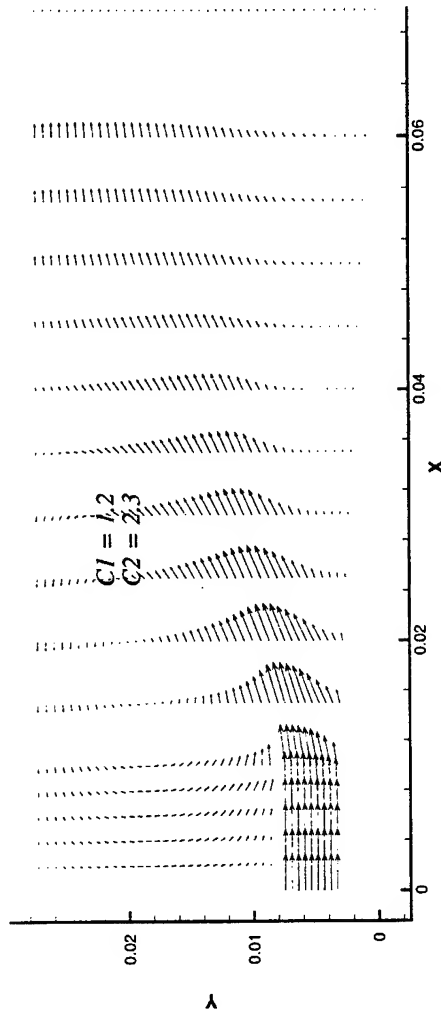
k-e model (standard)

C1 = 1.44

C2 = 1.92



C1 = 1.2
C2 = 2.3



ONERA

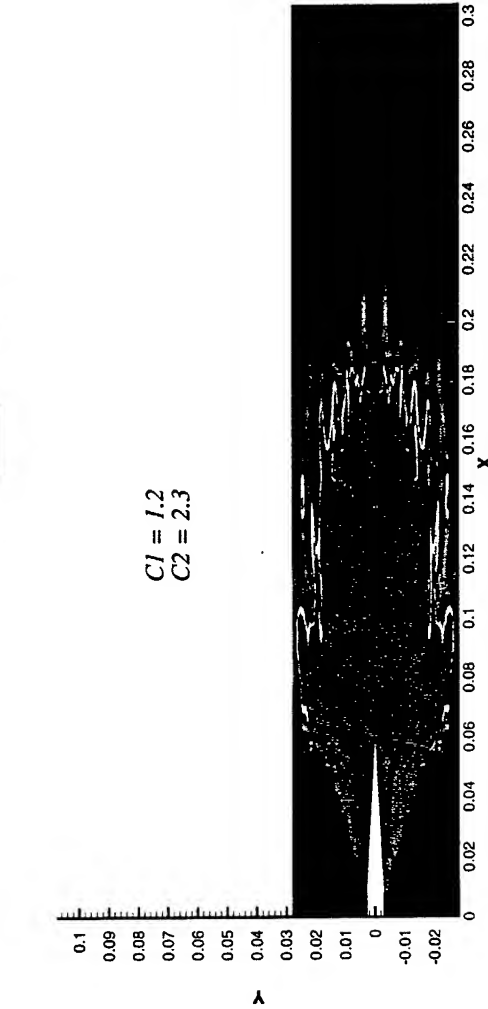
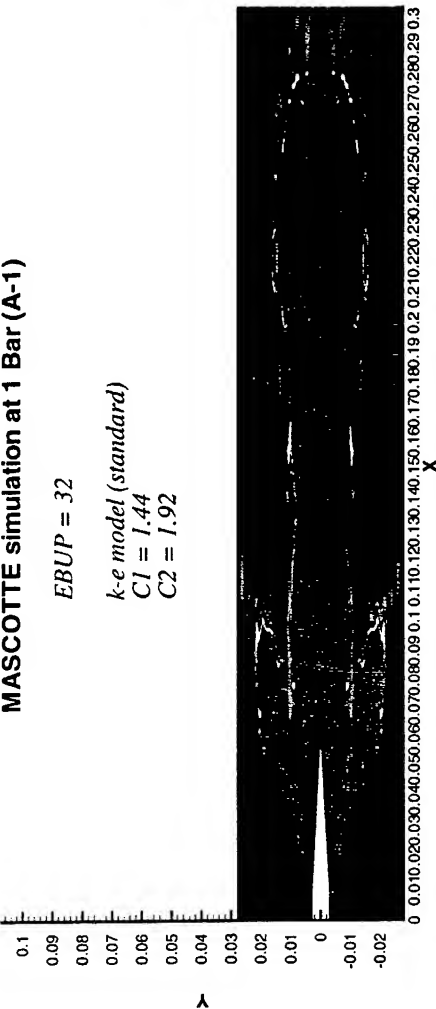
MASCOTTE simulation at 1 Bar (A-1)

EBUP = 32

k-e model (standard)

C1 = 1.44

C2 = 1.92



C1 = 1.2
C2 = 2.3

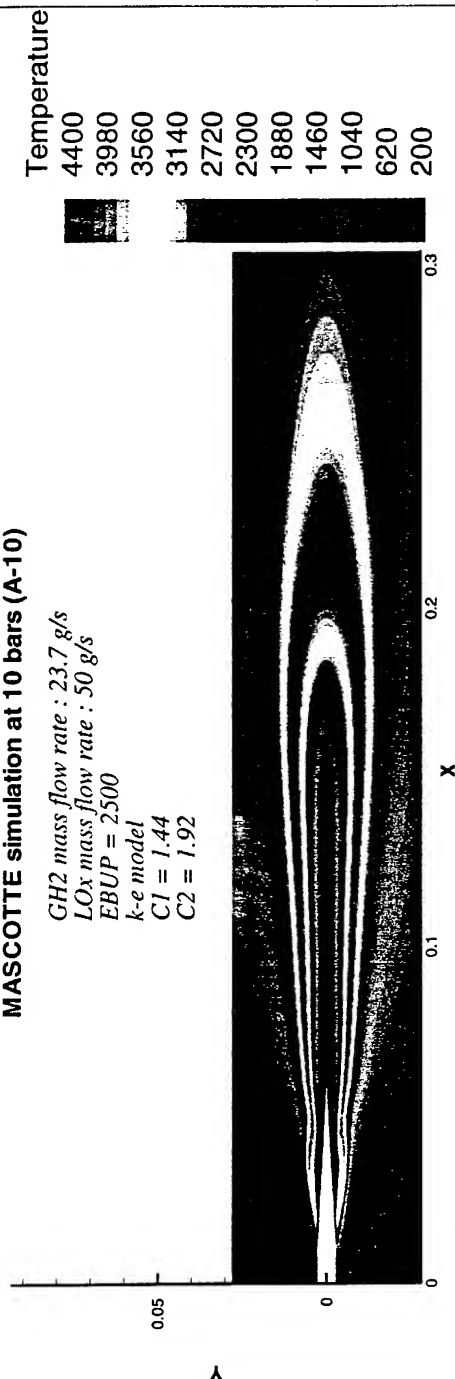
ONERA

ONERA

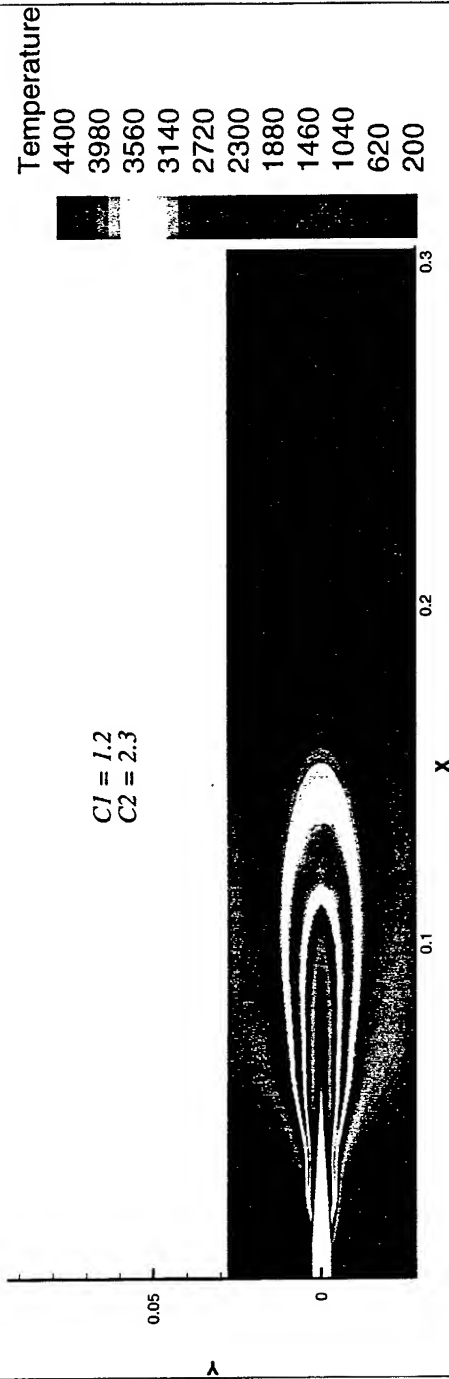
MASCOTTE simulation at 10 bars

MASCOTTE simulation at 10 bars (A-10)

GH2 mass flow rate : 23.7 g/s
 LOx mass flow rate : 50 g/s
 EBU_P = 2500
 k-e model
 C₁ = 1.44
 C₂ = 1.92



C₁ = 1.2
 C₂ = 2.3

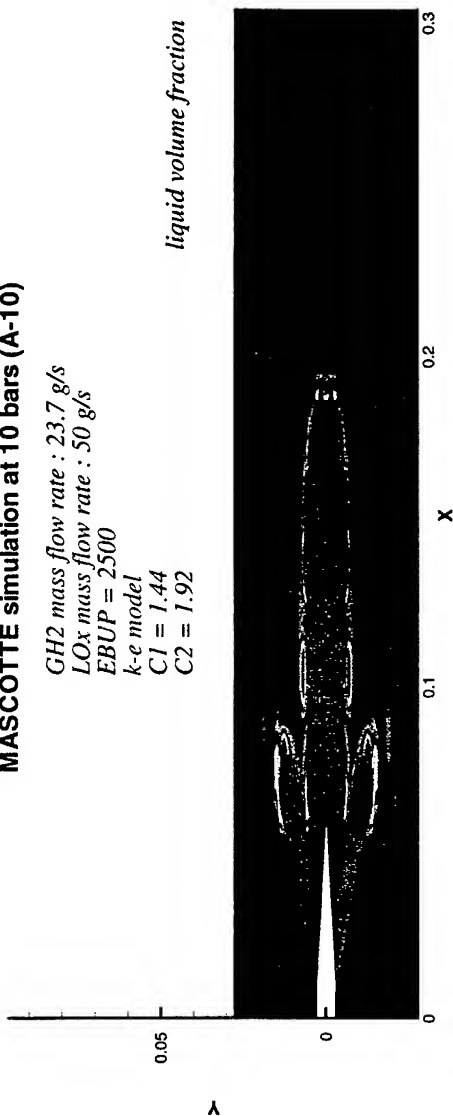


ONERA

MASCOTTE simulation at 10 bars (A-10)

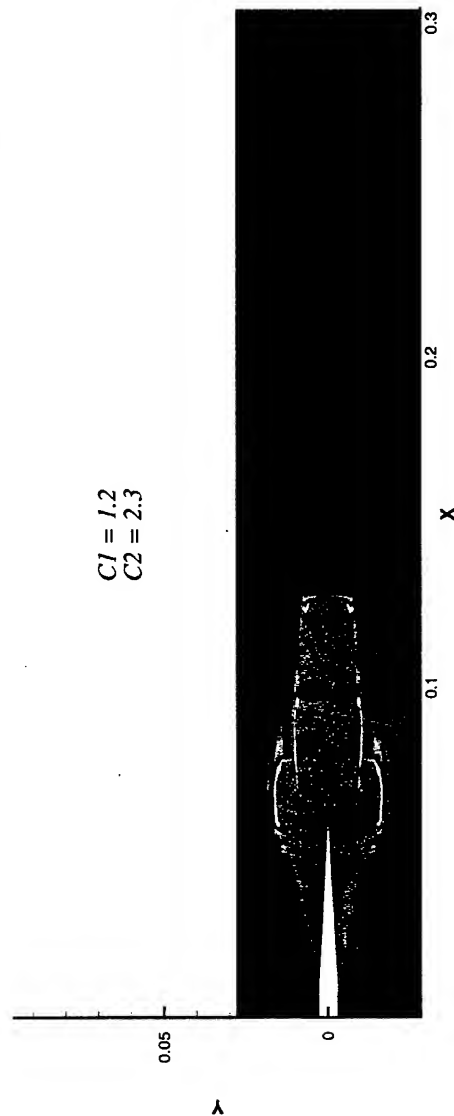
GH2 mass flow rate : 23.7 g/s
 LOx mass flow rate : 50 g/s
 EBUP = 2500
 k-e model
 C1 = 1.44
 C2 = 1.92

liquid volume fraction



Taux ^{kg} /reference ^{kg}
1E-06
9.58333E-07
9.16667E-07
8.75E-07
8.33333E-07
7.91667E-07
7.5E-07
7.08333E-07
6.66667E-07
6.25E-07
5.83333E-07
5.41667E-07
5E-07
4.58333E-07
4.16667E-07
3.75E-07
3.33333E-07
2.91667E-07
2.5E-07
2.08333E-07
1.66667E-07
1.25E-07
8.33333E-08
4.16667E-08
0

C1 = 1.2
 C2 = 2.3



Taux ^{kg} /reference ^{kg}
1E-06
9.58333E-07
9.16667E-07
8.75E-07
8.33333E-07
7.91667E-07
7.5E-07
7.08333E-07
6.66667E-07
6.25E-07
5.83333E-07
5.41667E-07
5E-07
4.58333E-07
4.16667E-07
3.75E-07
3.33333E-07
2.91667E-07
2.5E-07
2.08333E-07
1.66667E-07
1.25E-07
8.33333E-08
4.16667E-08
0

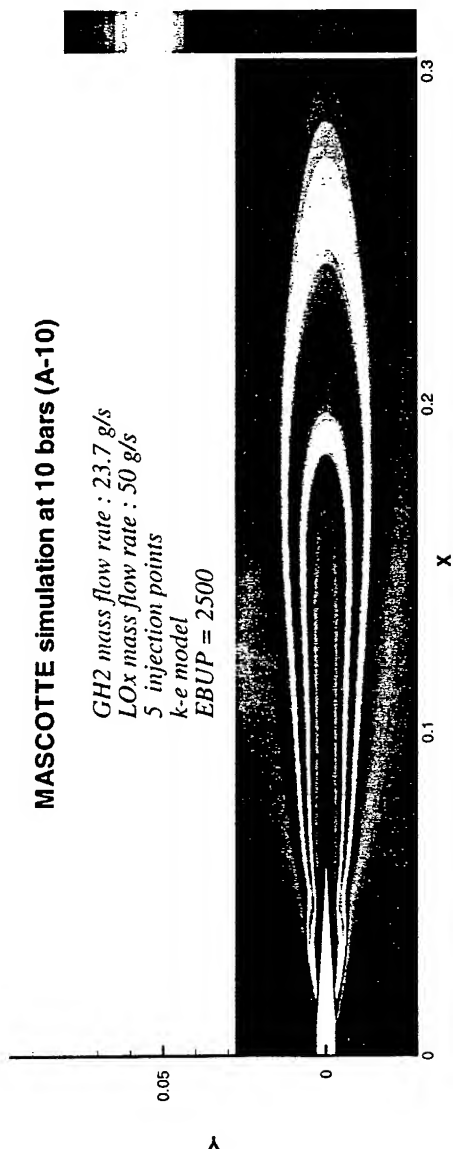
ONERA

ONERA

Temperature
4400
3980
3560
3140
2720
2300
1880
1460
1040
620
200

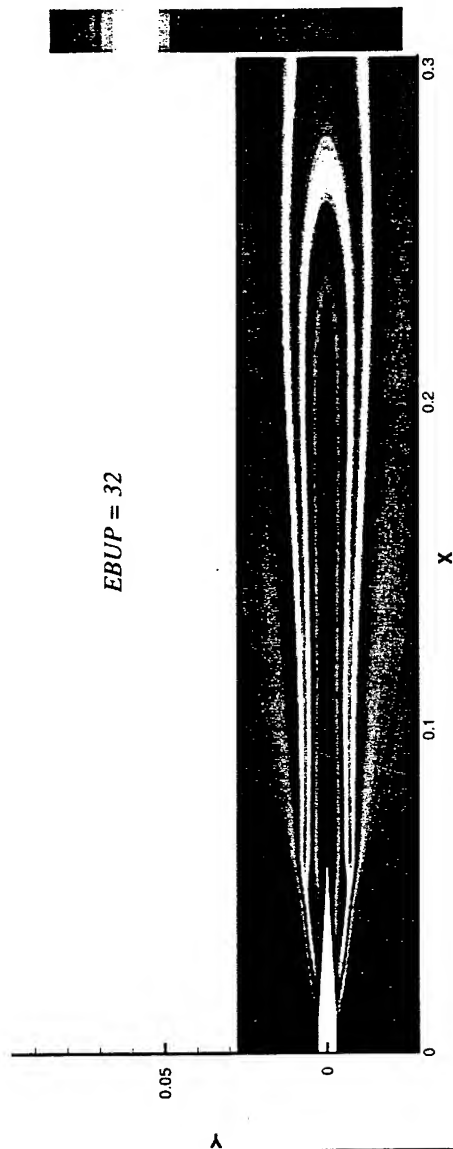
MASCOTTE simulation at 10 bars (A-10)

GH2 mass flow rate : 23.7 g/s
LOx mass flow rate : 50 g/s
5 injection points
k-e model
EBUP = 2500



Temperature
4400
3980
3560
3140
2720
2300
1880
1460
1040
620
200

EBUP = 32



Preliminary Results

- validation of the functioning of DLS (Lagrangian solver)
- results qualitatively in good agreement with experiments
- high sensitivity to turbulence

Work in progress

- Introduction of source terms for the equations of k and ε
- Introduction of the volume fraction of liquid in the equations
in prediction of :
 - calculation of dense regions of the two-phase flow (near the core)
 - Eulerian modeling of the flow

Conservation equations for the continuous phase

$$\frac{\partial}{\partial t}(\alpha\rho) + \frac{\partial}{\partial x_j}(\alpha\rho U_j) = \Gamma$$

$$\frac{\partial}{\partial t}(\alpha\rho U_i) + \frac{\partial}{\partial x_j}(\alpha\rho U_i U_j) = -\alpha \frac{\partial P}{\partial x_i} + \frac{\partial}{\partial x_j}(\alpha T_{ij} - \langle \rho \chi u_i'' u_j'' \rangle) + F_i + I_i$$

$$\frac{\partial}{\partial t}(\alpha\rho E) + \frac{\partial}{\partial x_j}(\alpha\rho H U_j) = -P \frac{\partial \alpha}{\partial t} - \frac{\partial}{\partial x_j}(\alpha Q_j + \langle \rho \chi h'' u_j'' \rangle) + S + \Pi$$

In bold : interfacial exchange terms between phases (\rightarrow modeled)

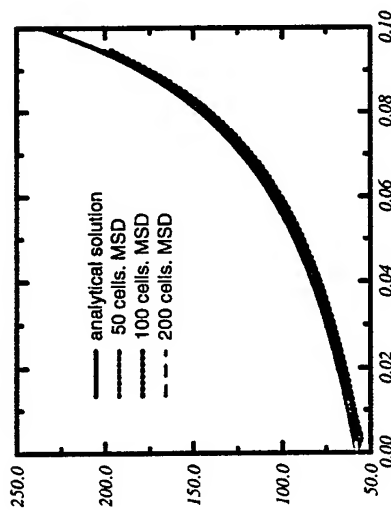
Work done : introduction of α in MSD

ONERA

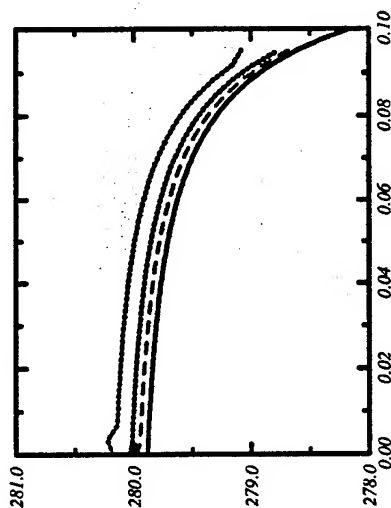
Introduction of α in MSD : 1D validation

H_2
 $\rho U = 5.$
 $T = 280$
 $p = 97800$

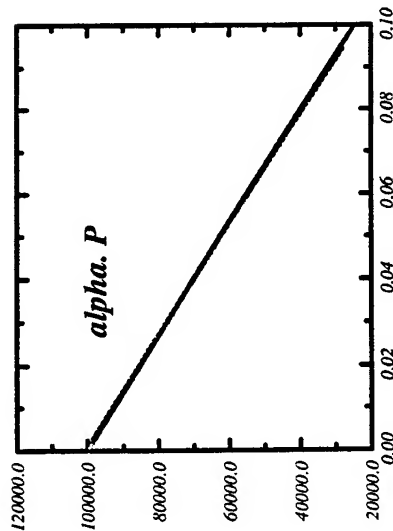
axial velocity



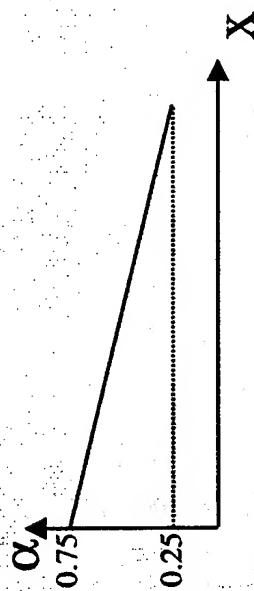
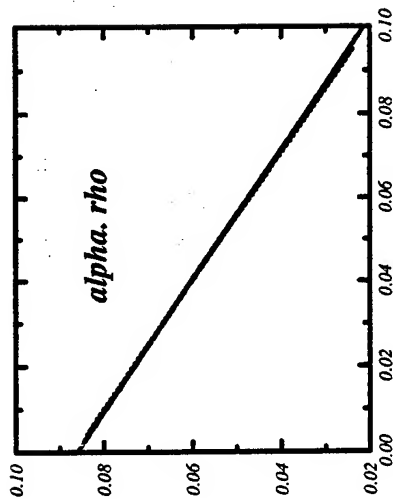
temperature



α . P



α . rho



α : volume fraction of gas

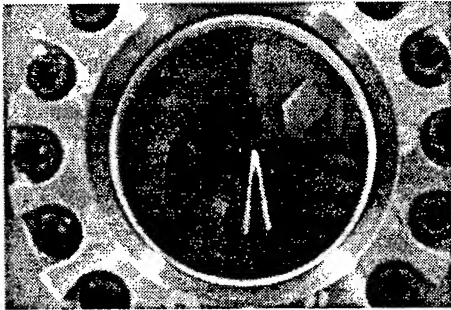
ONERA

Work to be done

- improvement of thermodynamics → better prediction of temperature
- improvement of turbulence by evaluating source terms for k and ε → right length of flame
- other developments :
 - introduction of volume fraction of phases
 - secondary break-up and coalescence
 - evaporation at high pressure (above critical pressure of LOx)
- Eulerian modeling : two-fluid model ?



Basic Research in Liquid Rocket Combustion at the Air Force Research Laboratory



Doug Talley
Propulsion Sciences
and Advanced
Concepts Division

27-28 May 1999



Required Injector Characteristics

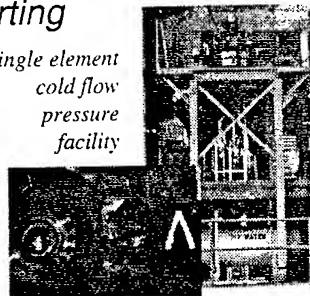
- Complete combustion in the shortest possible length
 - Main injectors: performance vs weight tradeoffs
 - Preburners/GG's: downstream component interactions, eg, turbine blades, etc
- Acoustically stable
 - Chamber modes
 - Feed system coupling
- Chamber/wall compatibility
 - Heat transfer/cooling
 - Oxygen blanching
- Minimize pressure drop
- Throttling
- Ignitable; minimum ignition transients
- Cost, weight
- The "ilities:"
 - Reliability
 - Maintainability
 - Manufacturability
 - Durability
 - Operability



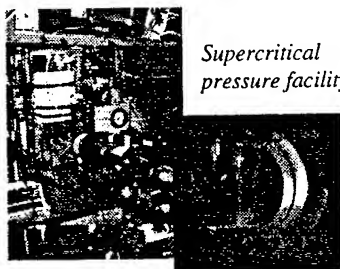
Facilities currently supporting basic research

- All facilities designed to provide optical access at pressures to 2000 psi (136 atm).

Single element cold flow pressure facility



Supercritical pressure facility



Subscale hot fire facility



Single element cold flow pressure facility

Gas simulants	N ₂ (g), He(g)
Liquid simulant	H ₂ O(l), others
Window Purge gas	N ₂ (g), He(g)
N ₂ mass flow rate	.20 lbm/s (.09 Kg/s)
He mass flow rate	.20 lbm/s (.09 Kg/s)
H ₂ O mass flow rate	4.0 lbm/s (1.8 Kg/s)
Max. test art. press.	2000 psi (136 atm)
Max. Fuel sim. press.	3000 psi. (204 atm)
Max. Ox sim. press.	3000 psi. (204 atm)

Windowed test chamber with 5.5" (14 cm) of axial injector travel and a linear translating injector stage with 5" (13 cm) total radial travel inside chamber.

Ability to simulate manifold cross velocities to 30 ft/s (9.1 m/s).

27 tube traversable mechanical patternator

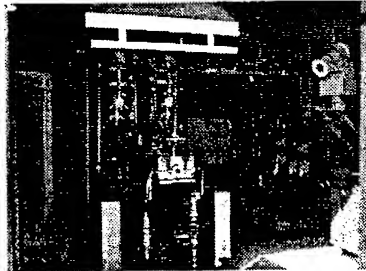
Phase Doppler, Malvern, other diagnostics





Subscale hot fire facility

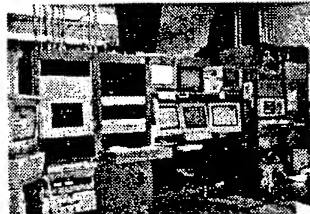
Fuel	H ₂ (g), CH ₄ (g)
Oxidizer	O ₂ (g)
Purge gas	N ₂ (g), He(g)
H ₂ mass flow rate	.15 lbm/s (.07 Kg/s)
CH ₄ mass flow rate	.25 lbm/s (.11 Kg/s)
O ₂ mass flow rate	1.0 lbm/s (.45 Kg/s)
N ₂ mass flow rate	.5 lbm/s (.23 Kg/s)
Water flow rate	16 lbm/s (7 Kg/s)
Max. system press.	2640 psi. (179 atm)



128 ch, 200 kbs scanning A/D
16 ch, 2 MHz per ch A/D, independently controlled
Central laser/optics room

Installing in 1999

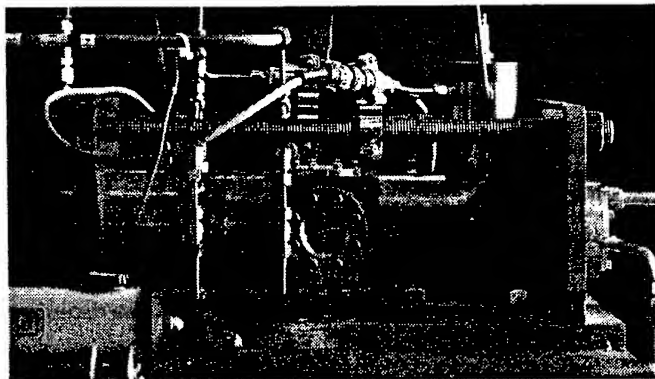
2000 psi liquid hydrocarbon capability



2000
LOX capability



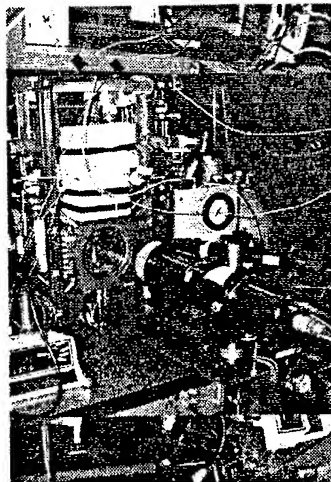
Gas/gas hardware





Supercritical pressure facility

Chamber	Stainless
Optical access	2 facing sapphire 13 cm dia windows 2 facing slot-shaped quartz (12 x 1.3 cm)
Max chamb. press.	2000 psi (136 atm)
Chamb. temp.	473 K
Injected fluid	O ₂ , N ₂ , HC, and mixtures
Ambient fluid	N ₂ , He, and mixtures
Injected mass flow rate	400 mg/s
Cryogenic cooler	85 K
Mass flow meters	up to 10,000 SLPM

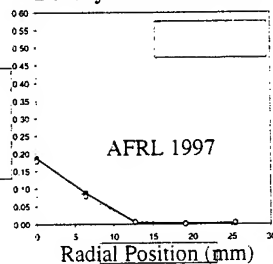
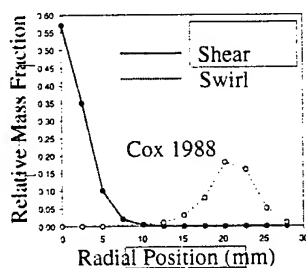


Air Force Research Laboratory Pressure Capability Matches More Scaling Parameters

Atmospheric Pressure
Geometry Scaling=1.0
Velocity Ratio O/F=.084
Ma=0.25

Pc=416 psig
Geometry Scaling=1.0
Velocity Ratio O/F=.084
Ma=0.25
Momentum Ratio O/F=.079
Density Ratio O/F=29.2

AFRL/NASA study



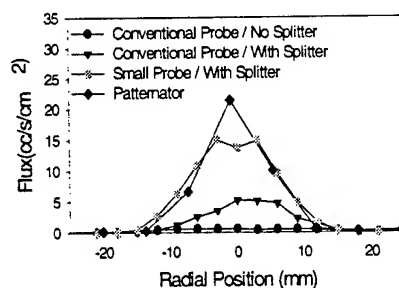
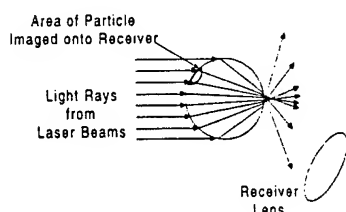
- H₂/O₂ fuel preburner coax injector tests demonstrate reduced effectiveness of swirl on macro-scale mixing at pressure.



Dense Spray Diagnostics

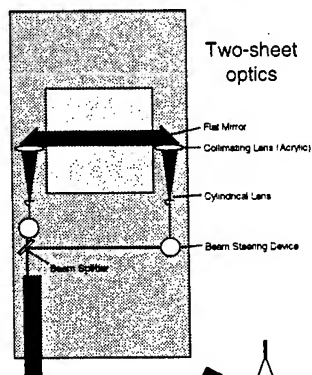
Strakey, et. al., ILASS Americas '98

- Goal - Extend existing diagnostic techniques into the dense spray regime where $N > 10^5 \text{ cc}^{-1}$.
- The combination of a small probe volume and a flow splitter resulted in a dramatic improvement in PDPA volume flux measurements in a dense spray.



Two Sheet Correction for Laser Sheet Extinction

Talley, et. al., AIAA 96-0469



20 deg viewing angle corrected for perspective

Camera response*

$$G = KI\rho$$

Along a ray,

$$\frac{dG_I}{G_I} = \frac{dI_I}{I_I} + \frac{d\rho}{\rho}$$

$$\frac{dG_T}{G_T} = \frac{dI_T}{I_T} + \frac{d\rho}{\rho}$$

Beer's law scattering is the same in both directions at any dx . Thus

Adding,

$$\frac{dG_I}{G_I} + \frac{dG_T}{G_T} = 2 \frac{d\rho}{\rho}$$

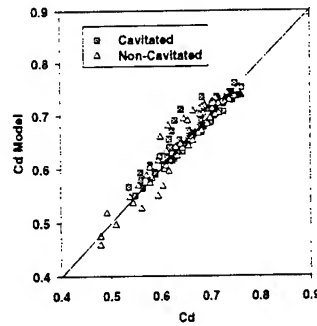
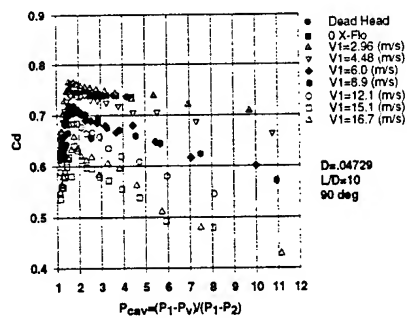
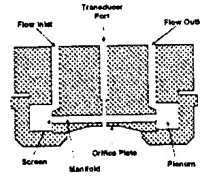
Independent of laser sheet intensity.

* G is gray level, I is laser sheet intensity, ρ is spray mass density, and K is a constant



Effect of Crossflow on Orifice Discharge Coefficients

Strakey, et. al., *Atomization and Sprays*, vol. 9, no. 1, 1998



$D = 1.19 \text{ mm}$, $L/D = 10$, $P_1 = 0.69 \text{ MPa}$



Evolution of Mixing Layers in Transition from a Subcritical to a Supercritical State

Acknowledgements:

Bruce Chehroudi

Roger Woodward

Ed Coy

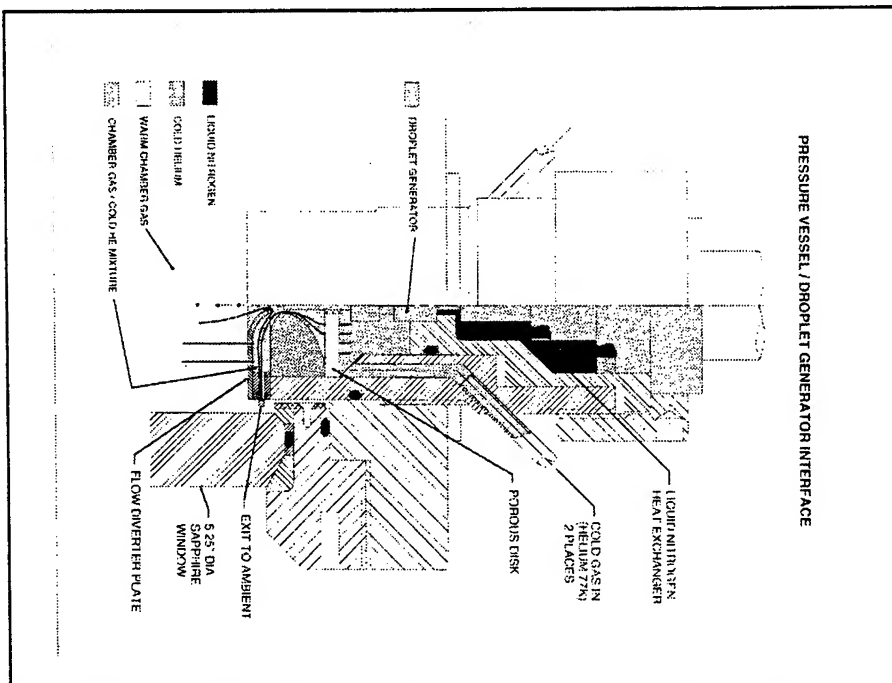


Overall Objectives

Determine the impact of thermodynamic state relative to the critical point on the transport and mixing of droplets, jets, and sprays

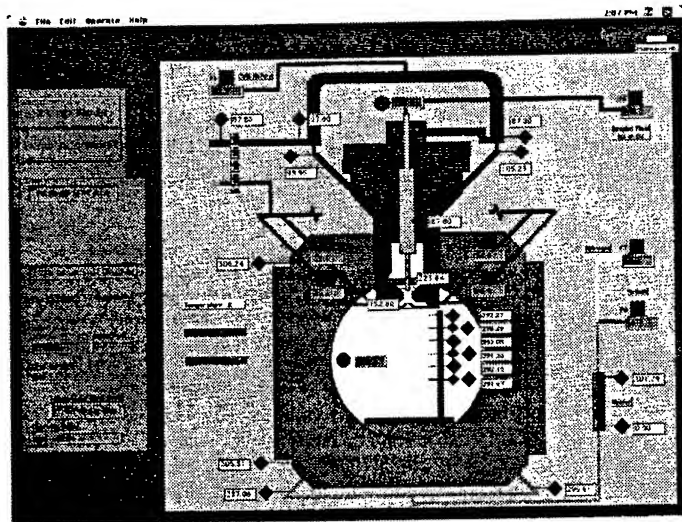
Issues

- Vanishing surface tension and heat of vaporization
- Equivalent gas/liquid densities
- Enhanced gas/liquid solubility
- Mixing induced critical point variations

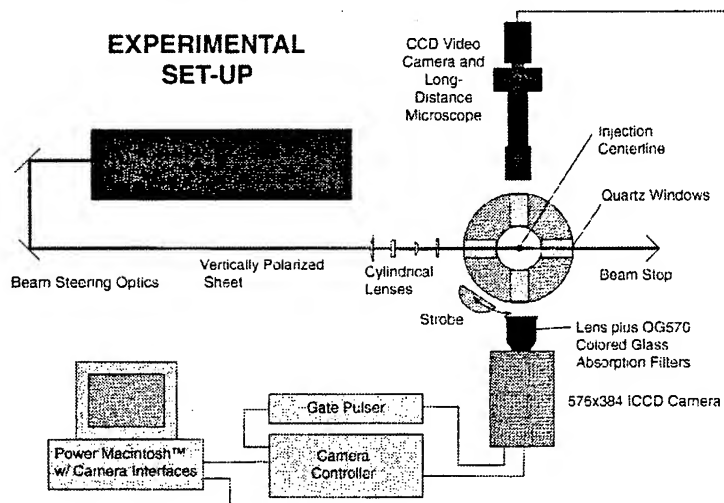




Pressure Vessel Schematic



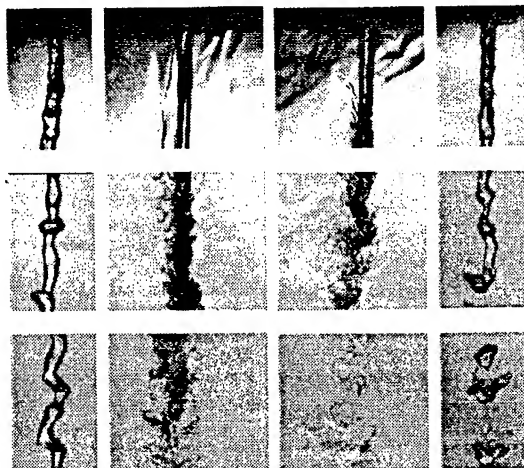
Raman Measurements





Low Reynolds Number N₂ Jets

Woodward and Talley, AIAA 96-0468



into:

N₂
Pr=0.83

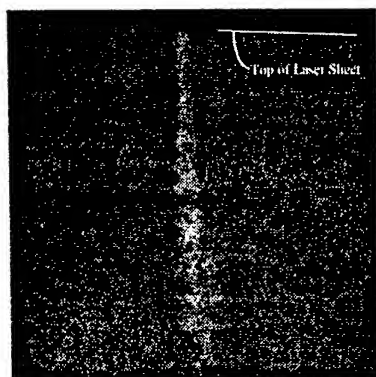
N₂
Pr=1.03

N₂
Pr=2.03

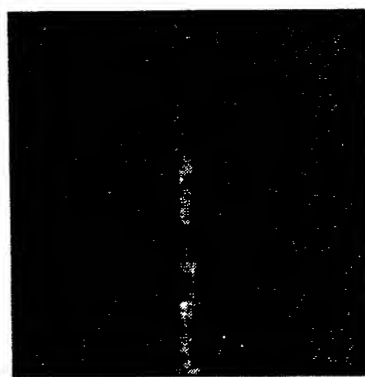
N₂/He, MR=3.9
Pr=2.03



Raman images of LN₂ jet at 69 atm into (a) gaseous nitrogen and (b) helium



(a)

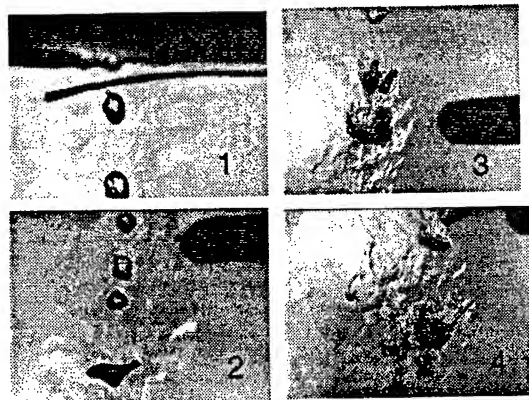


(b)



Transcritical Injection of LOX Droplets

Mayer et. al., *J. Propulsion and Power*, vol. 14, no. 5, 1998

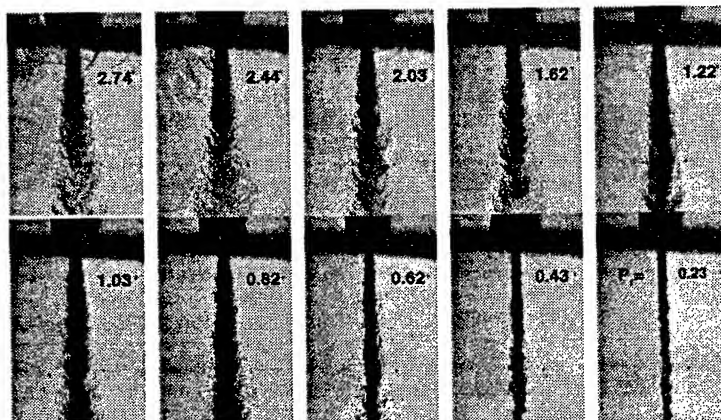


Ambient: N₂ @ 970 psig, 290K. O₂ Injector Temperature: 177K.
Drops formed in chilled helium, nitrogen flowing across stream.
Sequence corresponds to increasing distance downstream.



N₂ into N₂

Back-illuminated images. Chamber is at a fixed supercritical temperature of 300 K but varying sub- to supercritical pressures ($P_{\text{critical}} = 3.39$ MPa). $Re = 25,000$ to $75,000$. Injection velocity: 10-15 m/s. Froude number = 40,000 to 110,000. Injectant temperature = 99 to 120 K.





PRESSURE DEPENDENT MIXING LAYER STRUCTURE

Nitrogen/nitrogen system ($P_{cr} = 3.39 \text{ MPa}$, $T_{cr} = 126 \text{ K}$)

$T_{inj} = 128 \text{ K}$, $T_{amb} = 300 \text{ K}$, mass flow = 350 mg/s



Low Pres.
Subcritical
Droplets



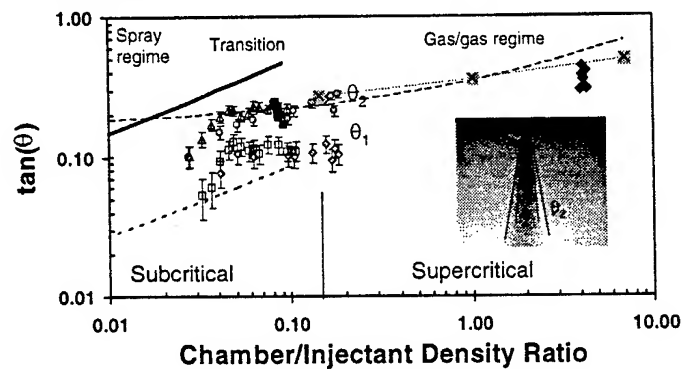
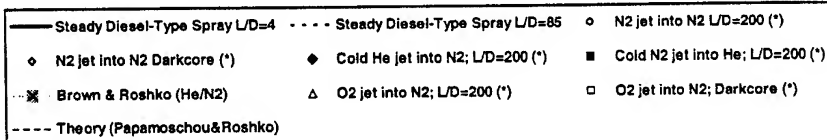
Mod. Pres.
Supercritical
Ligaments



High Pres.
Supercritical
Gas layers

Air Force Research Laboratory Sub- and Super-critical Mixing Layer Physics

Chehrودي et. al., AIAA 99-0206, AIAA 99-2489





Characteristic Times

- Characteristic bulge formation time (τ_b) at the jet interface (Tseng et al.): $(\rho_l L^3 / \sigma)^{1/2}$; ρ_l , L , σ are liquid density, characteristic dimension of turbulent eddy, and surface tension, respectively.
- Characteristic time for gasification (τ_g) (D-square law): D^2/K ; D and K are drop diameter and vaporization constant.
- A Hypothesis: If these two characteristic times (calculated for appropriate length scales) are comparable then an interface bulge may not be separated as an unattached entity (onset of the gas-jet behavior at supercritical condition)



Similar equation format for different cases

- Theoretical isothermal liquid spray growth rate (θ_s) based on Orr-Sommerfeld equation and stability analysis to find the wavelength of the most unstable interface wave:
 $\theta_s \cong 0.27 [0 + (\rho_g/\rho_l)^{0.5}]$
- Papamoschou/Rashko theory for incompressible variable-density gaseous mixing layer/jet:
 $\theta_{P/R} \cong 0.17 [1 + (\rho_g/\rho_l)^{0.5}]$
- Dimotakis theory for incompressible variable-density gaseous mixing layer/jet:
 $\theta_D \cong 0.212 [0.59 + (\rho_g/\rho_l)^{0.5}]$
- ALL HAVE THE SQUARE ROOT OF DENSITY RATIO AND THE SAME EQUATION FORMAT



Correlation

Based of the information of the previous slide the following correlation is proposed for both sub- and supercritical measured growth rates:

$$\theta_{ch} \equiv 0.27 [(\tau_b/(\tau_b + \tau_g)) + (\rho_j/\rho_i)^{0.5}] \quad \text{N2 into N2}$$

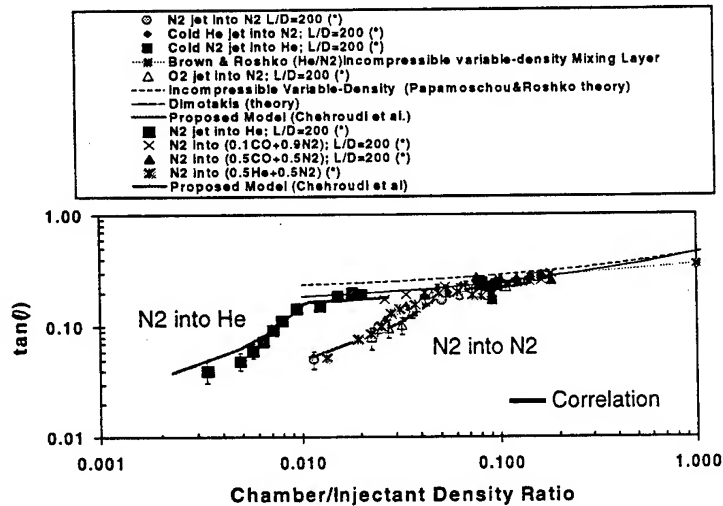
$$\theta_{ch} \equiv 0.27 [(\tau_b/(\tau_b + \tau_g)) + \{(\rho_j/\rho_i) - 0.8(\rho_g/\rho_i)\}^{0.5}] \quad \text{N2 into He}$$

Note:

- For isothermal liquid case: $\tau_g \gg \tau_b$ and $\tau_g \rightarrow \infty$. It then collapses to the isothermal spray case.
- For subcritical the $(\tau_b/(\tau_b + \tau_g))$ is calculated until it reaches 0.5. After that it is maintained constant at 0.5 for supercritical jet. The transition point is found to be approximately when $(\tau_b/(\tau_b + \tau_g)) \equiv 0.5$.
- Only a horizontal axis variable transformation is needed to fit with the N₂-into-He experimental growth rate data.



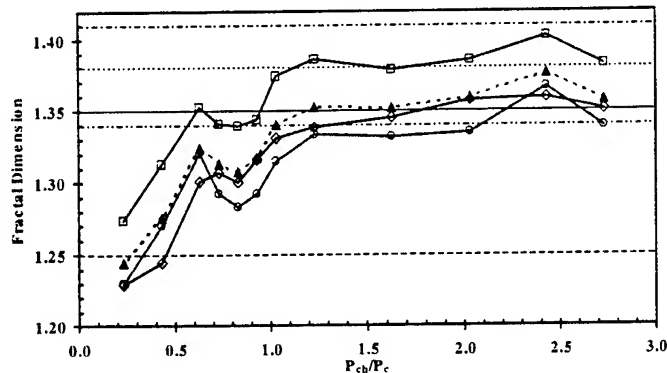
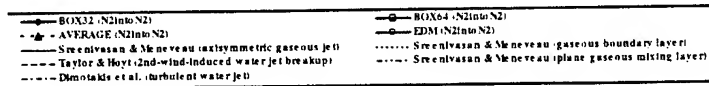
Empirical Correlation Results





Fractal Dimension vs Reduced Pressure

Chehroudi et. al., AIAA 99-2489



Summary and Conclusions

- Structural differences in cryogenic jets have been observed below and above the thermodynamic critical point.
- Liquid-Jet like appearance occurs up to near the critical point, similar to second wind-induced liquid jet breakup regime.
- Gas-jet like appearance occurs above the critical point. No drops are observed.
 - Supercritical spreading rate measurements agree quantitatively with incompressible variable density mixing layer experiments and theory.
 - Supercritical fractal dimensions agree quantitatively with gas jet measurements.
- New and existing mixing layer growth rate experiments and theory have for the first time been consolidated into a single plot as a function of density ratio, where the density ratio spans three orders of magnitude.
- A physical mechanism and correlation have been proposed to describe the transition from spray to gas jet behavior.



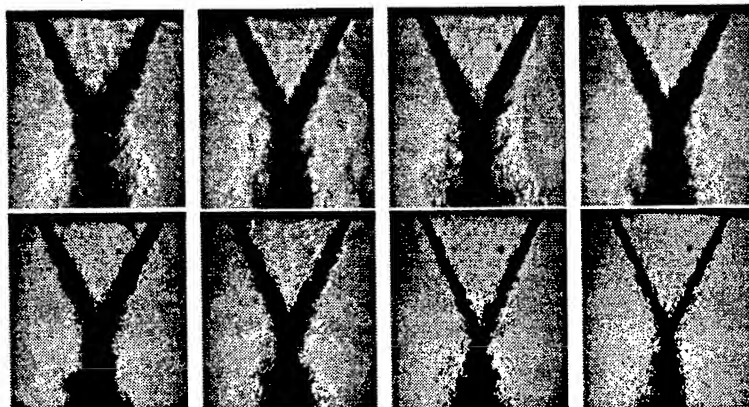
Instantaneous Images of Sub- and Supercritical Impinging Jets

N_2 into N_2

($P_{critical} = 3.39$ MPa; $T_c = 126.2$ K)

($P_{ch} = 5.5, 4.2, 3.5, 2.8, 2.5, 2.1, 1.5, 0.8$ MPa; from upper left to lower right)

($Re = 25,000$ to $70,000$; injection velocity: $10-15$ m/s)



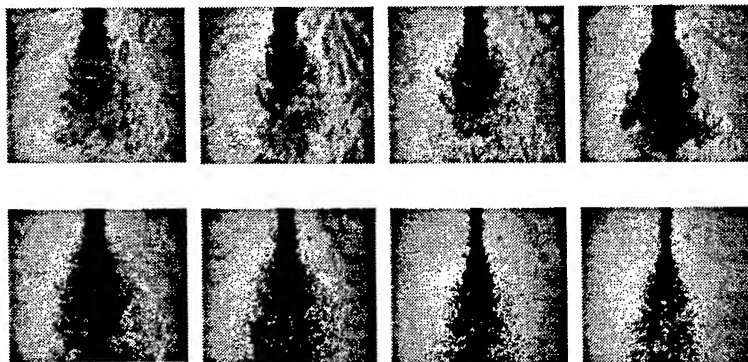
Instantaneous Images of Sub- and Supercritical Impinging Jets

N_2 into N_2

($P_{critical} = 3.39$ MPa; $T_c = 126.2$ K)

($P_{ch} = 5.5, 4.2, 3.5, 2.8, 2.5, 2.1, 1.5, 0.8$ MPa; from upper left to lower right)

($Re = 25,000$ to $70,000$; injection velocity: $10-15$ m/s)





Opportunities for Future Research

1990's at AFRL

- High pressures, "steady."
- Gas/gas injection

Future: 1990's topics remain relevant. Add:

- Injector/chamber interactions
- Transients
 - Organized
 - Un-organized
- Revolutionary cycles
 - Pulsed detonation propulsion
 - Combined cycle

THE STRUCTURE OF CRYOGENIC JET FLAMES INFERRED FROM EXPERIMENTS

A. Tripathi,^{*} M. Juniper,[†] P. Scoufflaire,[‡]
D. Durox,[§] C. Rolon,[¶] S. Candel,[¶]

EM2C Laboratory, CNRS, Ecole Centrale Paris
F-92295 Châtenay-Malabry, France

L. Vingert,[°] and M. Habiballah,[◊]
ONERA, 91120 Palaiseau, France

Abstract

This article reports new experimental results on cryogenic jet flames formed by a coaxial injector. This element fed with liquid oxygen and gaseous hydrogen is placed in a square combustion chamber equipped with quartz windows. The flame is studied with a set of optical methods : light emission from OH radicals and from H₂O molecules, laser induced fluorescence of OH, elastic scattering from the liquid oxygen jet, shadowgraphy. These techniques are used to examine flame spreading near the injection plane. The instantaneous flame location was previously described with simultaneous light elastic scattering images and laser induced fluorescence of OH. More recently, the mean flame structure was extracted from average emission images treated with Abel's transform. This numerical transformation provides the local volumetric light emission of the species being imaged. Previous studies concerned radiation from OH radicals. New measurements have been carried out by imaging a band of wavelengths which characterizes H₂O radiation. The transformed images of OH yield a structure which is indicative of the location of reaction while the transformed images of H₂O radiation portray the distribution of products or temperature in the flame. This combined imaging provides further information on the flame structure. Additional clues on

Prepared for presentation at the International Workshop on Liquid Rocket Propulsion, CNES, Paris, May 27-28, 1999.

^{*} PhD student, EM2C Laboratory, [†] PhD student, EM2C Laboratory,

[‡] Engineer, EM2C Laboratory, [§] Research Engineer, EM2C Laboratory,

[¶] Professor, Ecole Centrale Paris, [¶] Professor, Ecole Centrale Paris,

[°] Research Scientist, ONERA, [◊] Research Scientist, ONERA,

the flow near the injector are provided by shadowgraph images. Systematic experiments have been carried out by varying the operating parameters and the chamber pressure. Effects of LOX tube recess have also been examined at various pressures and for a set of operating conditions. The data provide a unified picture of the flame in the vicinity of the injection plane. Results may be used to describe effects of pressure and analyze the modification in the flame pattern induced by recess. The experimental investigation serves as a basis for modeling efforts described in a companion paper and in a previous article cited in reference.

This work was carried-out with support from CNES, SEP, ONERA and CNRS.

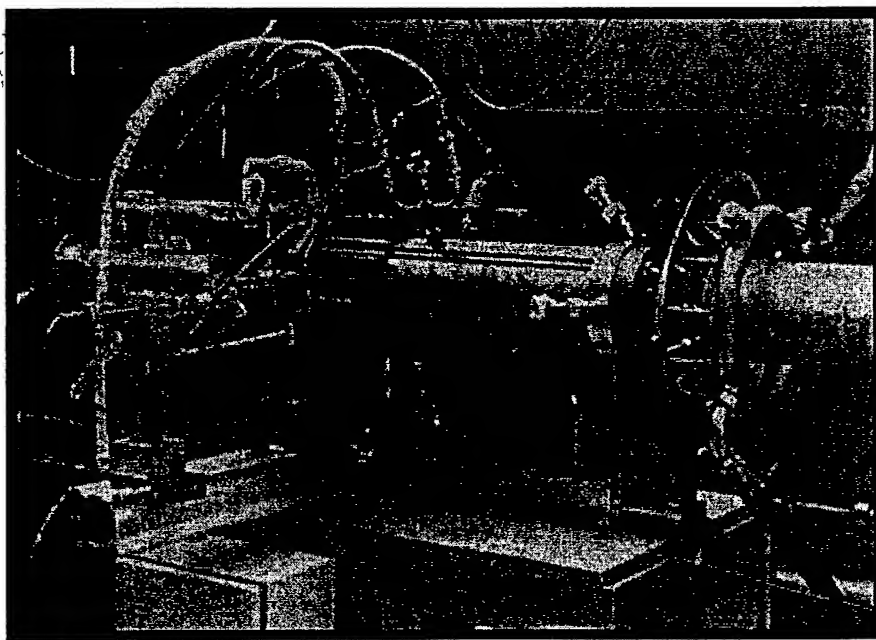
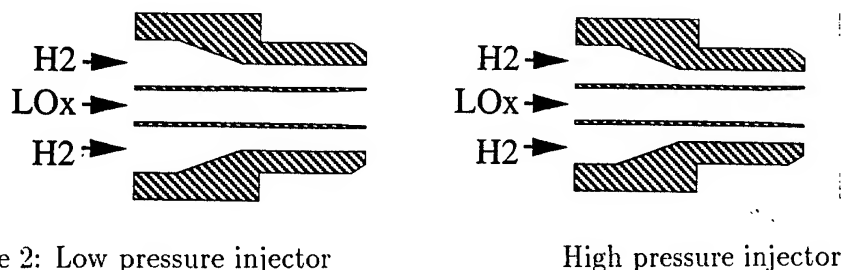


Figure 1: Cryogenic combustion facility

1 Experimental Facility

The experimental facility, called Mascotte, shown in Figure 1, is situated at ONERA, Palaiseau. It consists of a coaxial injector in which an annulus of hydrogen at high velocity is injected around a jet of liquid oxygen at low velocity. The dimensions of the injector are in the same range as those used in the Vulcain rocket motor of Ariane 5. A pressure of 60 bar can be maintained



within the chamber, which is square. The first few centimetres of the flame can be examined through quartz windows on each side of the chamber.

Cold flow studies have shown the importance of the momentum ratio, defined as $J = \rho_g u_g^2 / \rho_l u_l^2$, in determining jet break-up mechanism. This parameter is kept constant on changing pressure, which requires a reduction of the hydrogen flow cross-section at high pressure. The injector geometries are shown in Figure 2.

Our laboratory has carried out five series of experiments on Mascotte, the details of which are summarised in Table (1). Versions VO1 and VO2 of the combustion facility permitted pressures up to 10 bar. At these pressures, the flame position was determined using planar laser-induced fluorescence. The liquid surface position was found simultaneously by observing the elastic scattering of the laser sheet. It is known that LIF and elastic scattering are less effective at high pressure, as well as being technically complicated. It is more suitable to use visualisation techniques based on emission and shadowgraphy. These techniques are simpler, but quite effective.

2 Experiments at 1, 5 and 10 bar

A diagram of the apparatus used for planar laser-induced fluorescence is shown in Figure 3. The laser sheet excites OH radicals in the $Q_1(6)$ band, which decay emitting a photon at a different wavelength. The emission intensity is found to be almost independent of temperature in a range between 1500 and 3000K. The signal then mainly depends on the concentration of hydroxyl (OH) radicals. These radicals are an intermediate in the global reaction of H_2 with O_2 and regions of high level of OH mark the flame front. Filters exclude all but the fluorescence wavelength and thus the flame position is recorded by an intensified CCD camera. Simultaneously, a second CCD camera records the scattering of the laser sheet by the liquid surface.

Version of rig	Dates	Pressure	Visualisation technique
VO1 VO2	3 series of tests	1,5,10 bar	Laser-induced fluorescence Elastic scattering OH emission
VO3	June 1998 March 1999	10,60 bar	OH emission H2O emission Spectroscopy Shadowgraphy

Table 1: Experiments on MASCOTTE by Laboratoire EM2C

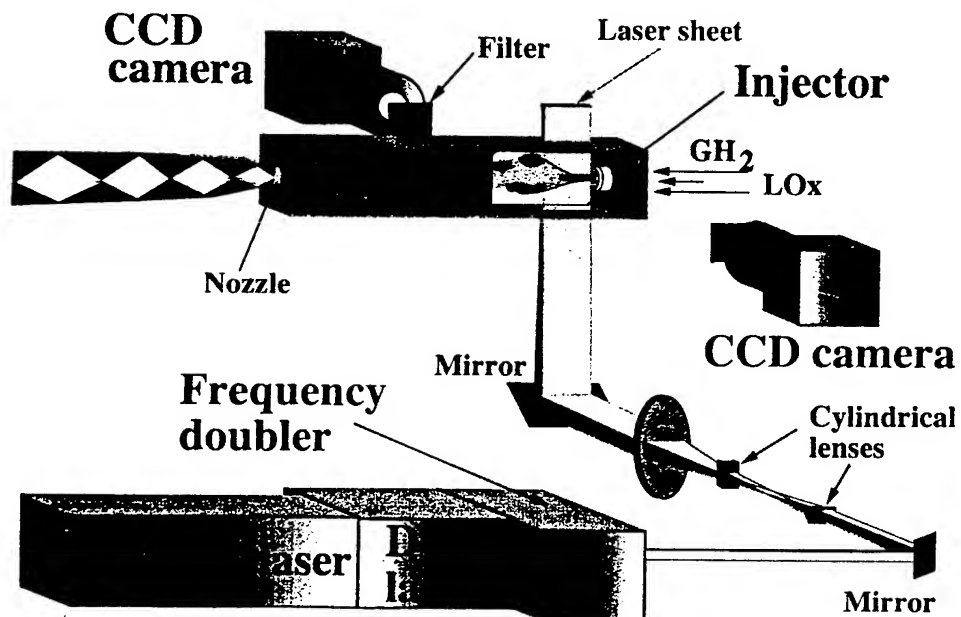


Figure 3: Set-up for simultaneous Planar Laser-induced Fluorescence and Elastic Scattering imaging

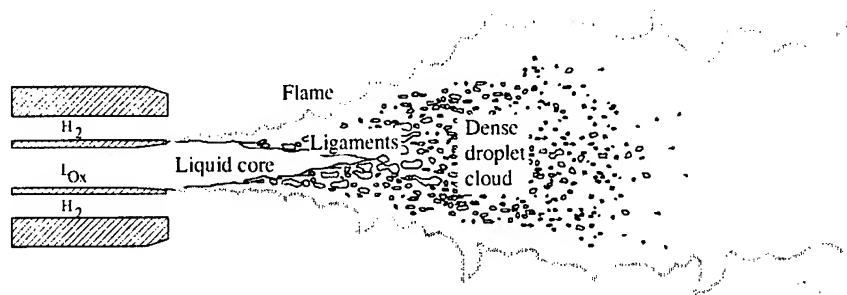


Figure 4: Schematic diagram of the flame between 1 and 10 bar, below the critical pressure of oxygen

This gives the position of the jet and droplets.

The flame front ¹ in red, is not seen in the top half of the images because very little of the laser sheet passes undisturbed through the jet. The bottom half shows that the flame front is highly wrinkled. Scattering from the liquid surface is shown in blue. Further from the injector, the intensity is lower, which is due to the fact that the droplets are smaller. Also the thicker droplet cloud masks the sheet of droplets which are illuminated by the laser. The scattered signal is outside the dynamic range of the CCD camera.

Some important points can be made about the flame shape. The flame starts at the oxygen injector lip and then burns extremely close to the liquid jet. The liquid jet breaks up into a dense cloud of droplets. The inter droplet distance divided by the droplet diameter is estimated to be around $b/d = 6$. Because the cloud is so dense, external group combustion takes place and the flame surrounds but does not penetrate the cloud. A schematic diagram of the flame shape between 1 and 10 bar is shown in Figure 4.

3 Application of The Abel Inversion

Given the reduced signal level of PLIF at high pressures, other techniques were considered. One of these is the Abel inversion of natural emission images. The spectrum of the flame shows that it is possible to isolate the natural emission of OH^* and H_2O^* radicals, as shown in Figure 5.

The Abel inversion is frequently used to obtain the radial intensity distribution of an axisymmetric object from a projection on a plane placed on

¹Colour images can be found in Candel et al: "Experimental investigation of shear coaxial cryogenic jet flames," *Journal of Propulsion and Power*, Vol. 14, 1998, pp. 826-834

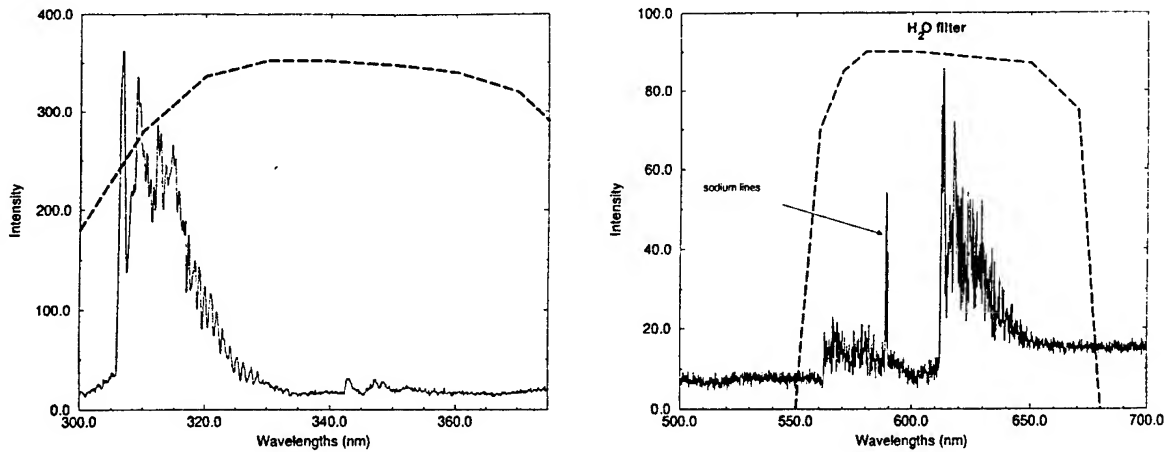


Figure 5: Spectrum of the flame at 10 bar a) $300 < \lambda < 400\text{nm}$; UV region
b) $500 < \lambda < 700\text{nm}$; green-red region

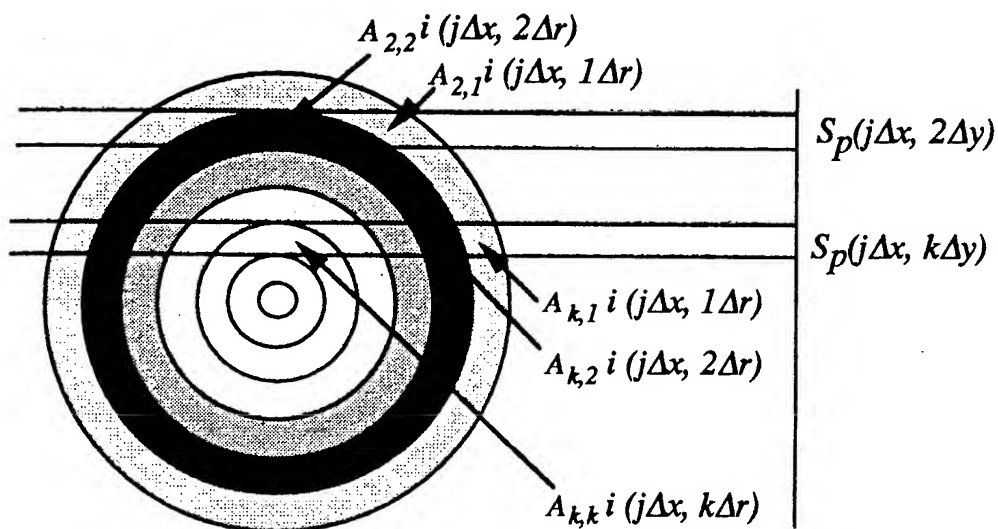


Figure 6: Principle of the Abel inversion, the radial structure is deduced from the projected distribution

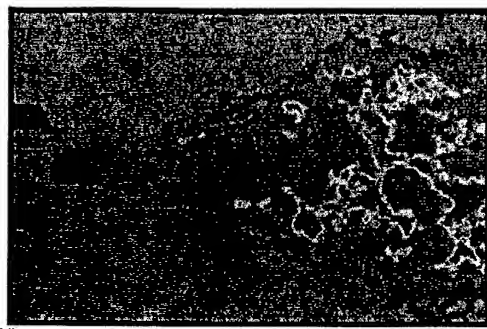


Figure 7: Instantaneous image of the OH^* emission of a turbulent flame, 10 bar, $J = 14.5$



Figure 8: Averaged images of a turbulent flame. This gives the OH^* Intensity \times Residence fraction summed along the line of sight. 10 bar, $J = 14.5$

the side. The principle is shown in Figure 6. The axisymmetric distribution is assumed to be made up of a series of co-centric rings. To calculate the contribution of an inside ring, the contribution of the rings outside it is subtracted from the cumulative image along the line of sight. Working from the outside to the inside, this enables the contribution from each ring to be determined. Around the axis, the process is particularly sensitive to noise.

Care is required when applying the Abel transform to a non-axisymmetric turbulent flame, as indicated in Figure 7. Averaging over several images gives an axisymmetric field: intensity \times residence fraction, which is summed over the line of sight, as in Figure 8. The residence fraction corresponds to the fraction of the time that the flame spends at a particular point, on average. The Abel inversion can be applied to this field, giving a slice through the injector plane of the intensity of OH^* radical natural emission \times residence fraction, Figure 9. This can be compared with the average of the PLIF



Figure 9: The Abel inversion of the averaged images. This gives a slice of the OH^* Intensity \times the Residence fraction. 10 bar, $J = 14.5$

images, which gives a slice of the intensity of OH radical stimulated emission \times residence fraction, as in Figure 10. This indicates a slightly wider high intensity region than that found in the Abel-inverted images. However, this is to be expected because the PLIF images show all OH radicals, whereas the Abel-inverted images show only the excited OH^* radicals. The OH^* radical has a short lifetime compared with characteristic flow times and will not be seen away from the flame front. However, it is likely that a small quantity of OH radicals will exist in the high temperature regions around the flame. The corresponding intensity of these radicals on the PLIF images will be small but the residence fraction will be high. This accounts for the thick flame zone on the averaged PLIF images.

To compare the averaged images more exactly it is necessary to make the reasonable assumption that the regions where OH concentration is high correspond to the regions of OH^* . Thus when the low intensity regions of the PLIF images are removed and the images averaged, the result should be similar to the intensity of $\text{OH}^* \times$ Residence fraction. The comparison turns out to be excellent. Figure 11 shows the positions of maximum intensity for the Abel inverted images and for the average of the PLIF images.

Whenever the Abel inversion is used, it should be remembered that the slices are of emission intensity \times residence fraction, rather than just intensity. The highest values are usually seen near the injector, where the residence fraction is high. The Abel-inverted images give a good idea of the change in the average flame shape when injection conditions are altered. It should also be noted that the Abel inversion assumes that no light is absorbed or deflected by the flame.

The Abel-inverted images of OH^* and H_2O^* radical emission are shown in Figures 12 and 13. To a first approximation, the intensity of OH^* emission

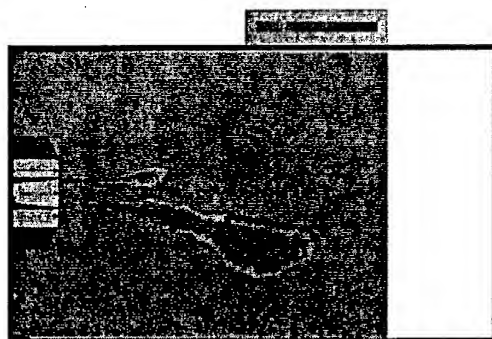


Figure 10: Averaged PLIF images. This gives a slice of the OH Intensity \times the Residence fraction

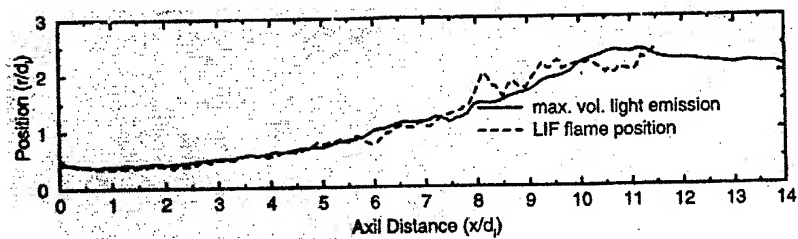


Figure 11: Position of maximum intensity of the Abel-inverted emission images compared with that of the average PLIF images

is a function of the reaction rate and the intensity of the thermally excited reaction product H_2O^* is a function of temperature. From these images, taken with an oxygen tube recess of $1 \times d_{\text{LO}_2}$, it can be seen that the maximum H_2O^* emission is somewhat further downstream than the maximum OH^* emission, as would be expected.

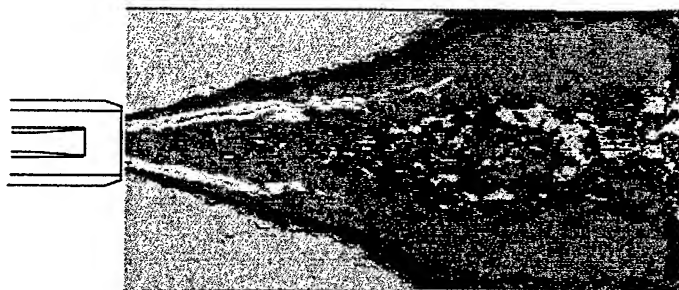


Figure 12: OH^* Intensity \times Residence fraction at 10 bar in a slice through the axial plane

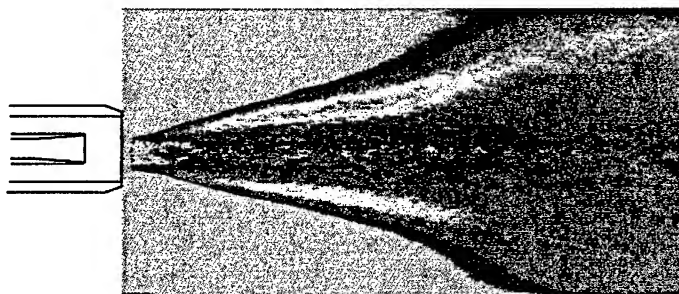


Figure 13: H_2O^* Intensity \times Residence fraction at 10 bar in a slice through the axial plane

4 Supercritical effects

The critical point of oxygen is 50.8 bar, 155K. The Pressure-Temperature phase equilibrium diagram is shown in Figure 14. Conditions achieved in Mascotte version VO1, VO3 and in the Vulcain motor are also shown in this figure. The important point is that the oxygen will have no definite phase

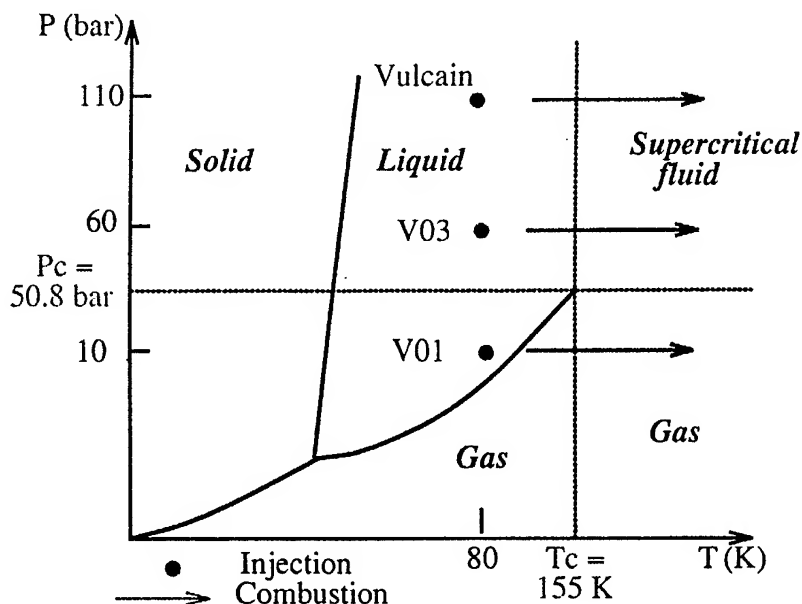


Figure 14: Pressure-Temperature diagram for oxygen, with the operating points of Mascotte versions VO1, VO3 and the Vulcain rocket motor

boundary in VO3 and in Vulcain, unlike the low pressure VO1. This is likely to lead to differences in jet and droplet break-up, since surface tension is a factor at low pressure. Above the critical pressure, two gases of very different density mix.

Studies by Delplanque and Sirignano indicate that the oxygen jet will have a dense, liquid-like core, where the temperature is low. Towards the edge of the jet, where the temperature is higher, the oxygen will be supercritical. There will be very high temperature and density gradients in this region, but no discontinuous surface. Around the critical point, small temperature variations lead to large density variations. The fluid becomes almost opaque to incident light.

5 Experiments at 60 bar

The apparatus for flame and jet visualisation at high pressure is shown in Figure 15. The techniques used are listed below:

- Spectroscopy: The spectrum of the flame at 60 bar was obtained over the course of the campaign. It showed that OH* radical emission is well isolated by the filters.
- Images of OH* radical emission

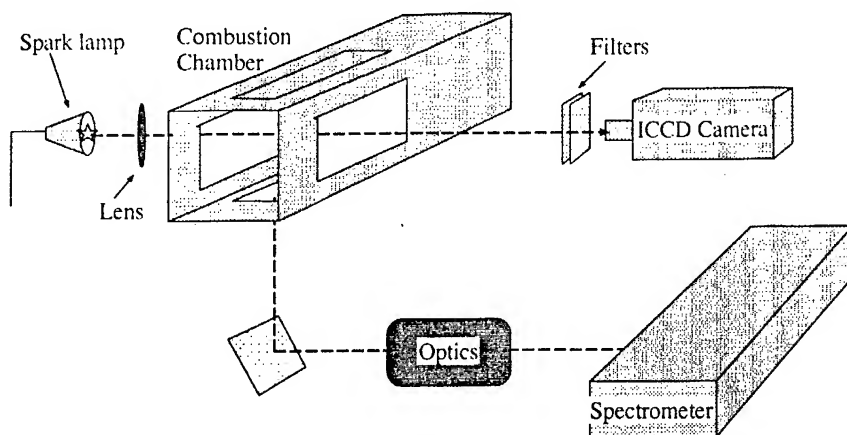


Figure 15: Experimental set-up used in the high pressure tests

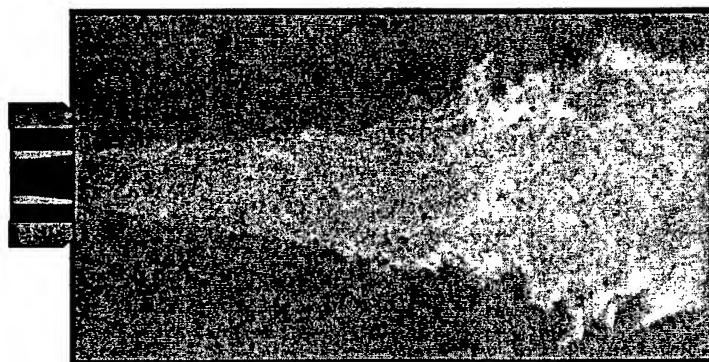


Figure 16: OH* radical emission at low pressure ($P \approx 30\text{bar}$)

- Shadowgraphy: In order to eliminate as much of the flame's natural emission as possible, the ICCD camera had a very short exposure time (300ns) and was synchronised with the spark lamp. In addition, after passing through the chamber, the light was focussed through an iris. This cut out a large proportion of the flame's natural emission. Finally, the light was filtered to remove as much natural emission as possible, while passing the wavelength in which the spark was most intense, between 420 and 500 nm.

Some close-up images of the near-injector region were also taken.

The far-field results are shown in Figures 16 to 19. During each run the pressure took 30 seconds to build up to 60 bar and then was stable for 7 seconds. Thus images at low pressure were obtained, but it should be stressed that the conditions were not steady and do not correspond to those of version



Figure 17: OH* radical emission at 60 bar

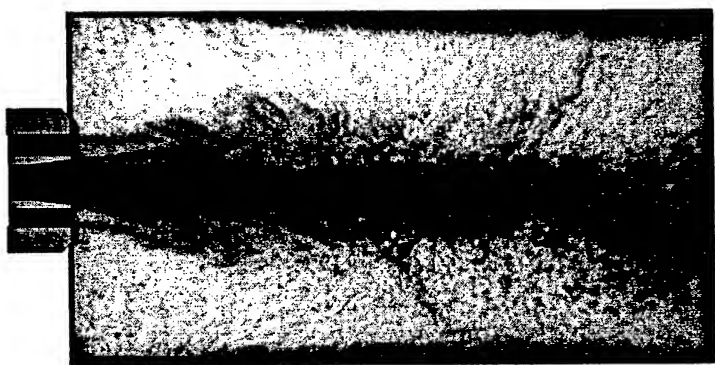


Figure 18: Shadowgraphy at low pressure ($P \approx 30\text{bar}$)



Figure 19: Shadowgraphy at 60 bar

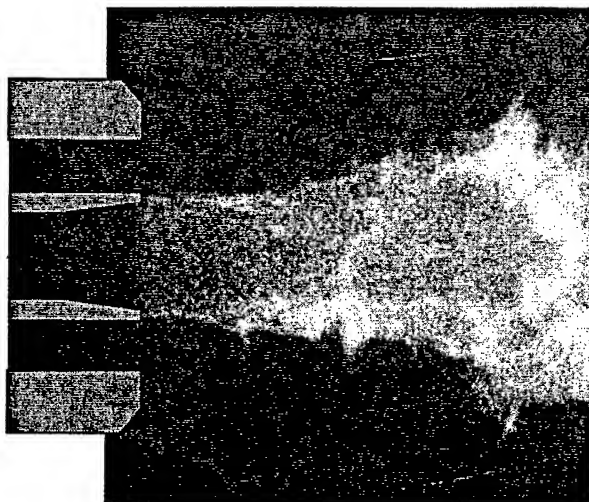


Figure 20: Emission above 400nm at low pressure, near injector

VO1 and VO2 of Mascotte. It is clear from the shadowgraphy images that the shape of the oxygen jet is different at high pressure. Droplets are no longer visible and it is more clumpy and stringy. Emission is more intense at high pressure and, compared with the stable images at 1,5 and 10 bar from version VO1 and VO2, the flame expands less rapidly.

The near-field emission images are shown in Figures 20 and 21. The flame is stabilised just behind the oxygen injector lip. This effect has also been noted by Mayer and Tamura on the cryogenic combustion facility in Japan, on which the diameter of the oxygen jet is smaller and the oxygen lip proportionally much larger, figure (22). The near-field shadowgraphy images require some explanation. Typical samples are shown in Figures 23 and 24. Where the light from the spark lamp has been deflected only slightly, a shadowgraphy effect can be seen, characterised by a light and a dark band. Where the light has been deflected more, it is not captured by the lens and a schlieren effect can be seen. This is simply a dark region. A shadowgraphy effect can be seen at the outside edge of the hydrogen jet and in some parts of the gaseous phase in the low pressure image. The 60 bar image is almost entirely determined by schlieren effects. Light is deflected by refractive index gradients perpendicular to the ray direction. Refractive index gradients will be large at the edge of the oxygen jet and at the edges of the flame. If the flame is very close to the oxygen jet, the two will be indistinguishable.

The images show the expansion of the hydrogen annulus, the wake of the oxygen tube lip, the position of the oxygen jet (or the inner edge of the flame) and the outer edge of the flame. An image taken by Mayer and Tamura is

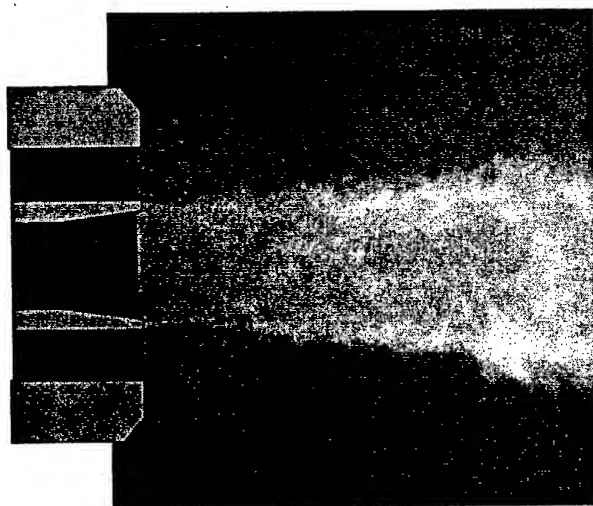


Figure 21: Emission above 400nm at 60 bar, near injector

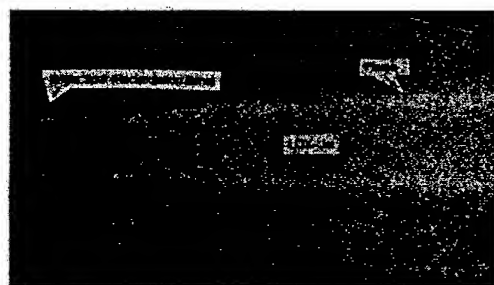


Figure 22: OH* radical emission at 45 bar from Mayer and Tamura, *Journal of Propulsion and Power* Vol 12, 1996

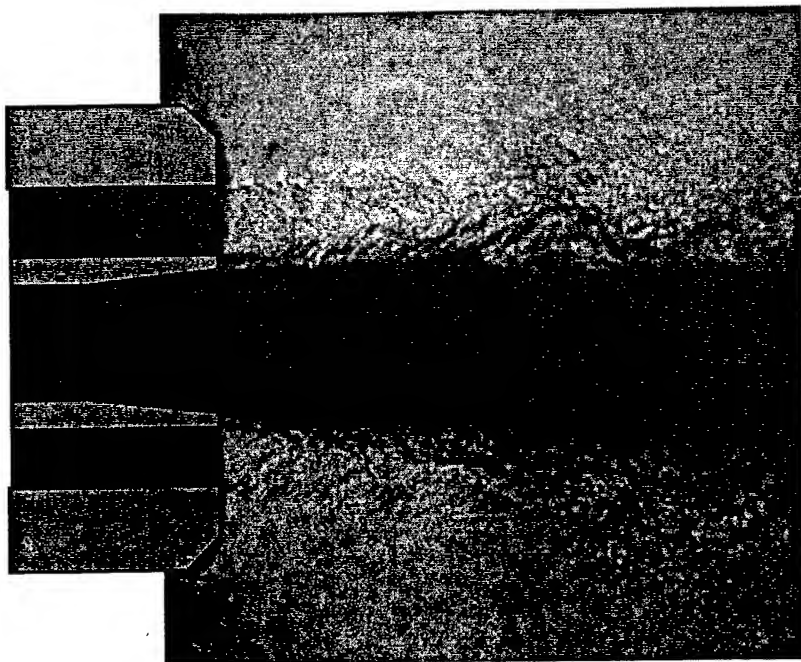


Figure 23: Shadowgraphy at low pressure ($P \approx 30$ bar), near injector

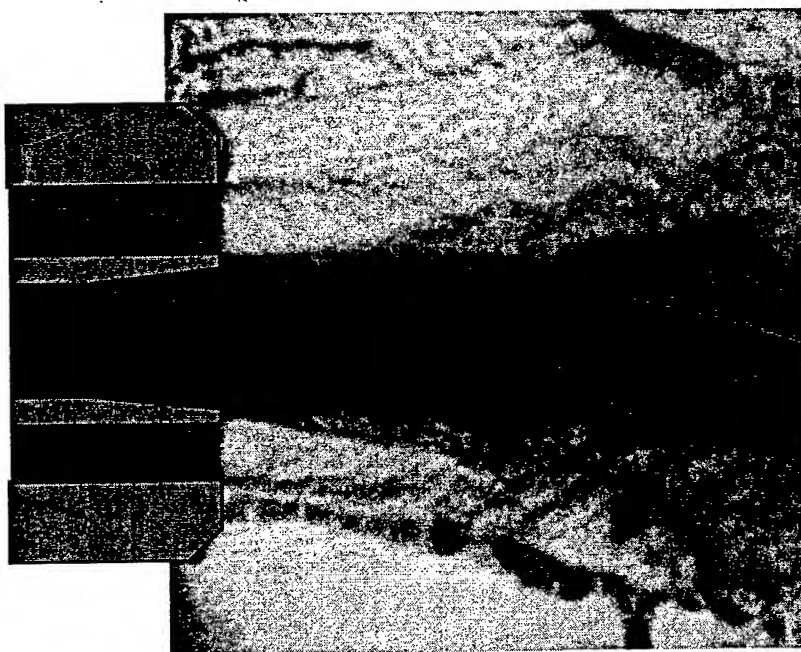


Figure 24: Shadowgraphy at 60 bar, near injector

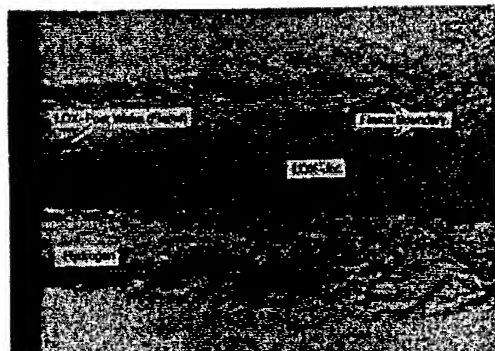


Figure 25: Shadowgraphy at 45 bar, from Mayer and Tamura, *Journal of Propulsion and Power* Vol 12, 1996

shown in Figure 25 for comparison.

An Abel inversion of the near-injector emission images at 60 bar is shown in Figure 26. This will not be valid in the central region where the jet partially shields the far side of the flame. The images show the proximity of the flame to the oxygen jet. The bright spot behind the oxygen injector lip is smaller and less intense than that observed by Mayer and Tamura on the 1mm diameter injector.

Important points can be made about the flame shape at 60 bar. The flame and the oxygen jet are extremely turbulent. The jet breaks up into packets, rather than droplets. The flame is stabilized on the oxygen injector lip in a recirculation zone and then grows in intensity. This is schematized in Figure 28.

6 Conclusion

Structure of subcritical and supercritical cryogenic flames are examined using imaging techniques. The flame is stabilized in the near vicinity of the oxygen tube and initially spreads around the oxygen core as a corrugated surface. The momentum ratio has a decisive effect in the subcritical cases. It has a less visible effect in the supercritical case but this aspect needs further study. Subcritical and supercritical flames differ notably in their structure and corresponding rate of expansion.

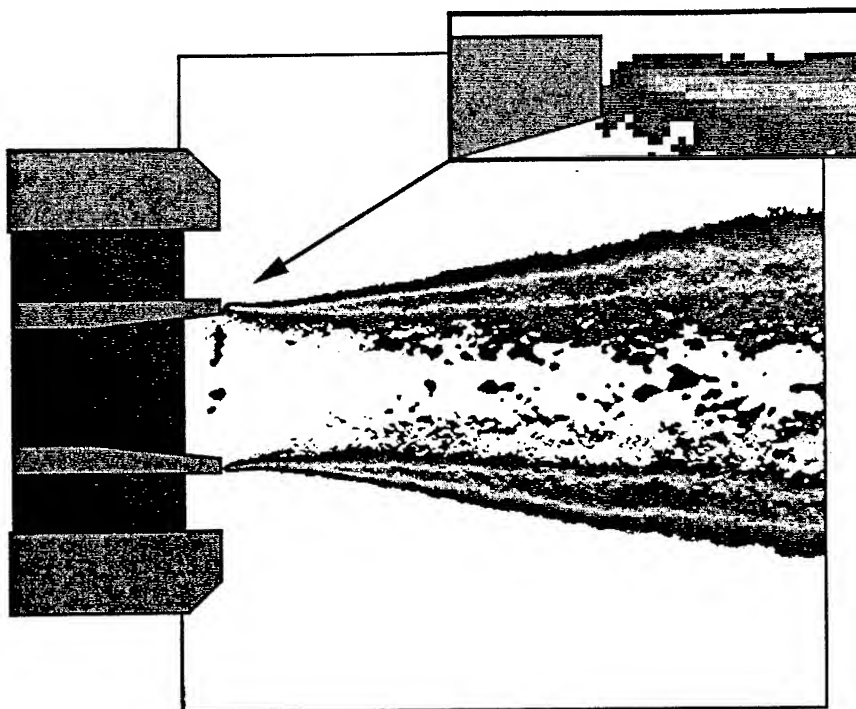


Figure 26: Abel inversion of the near-injector emission images

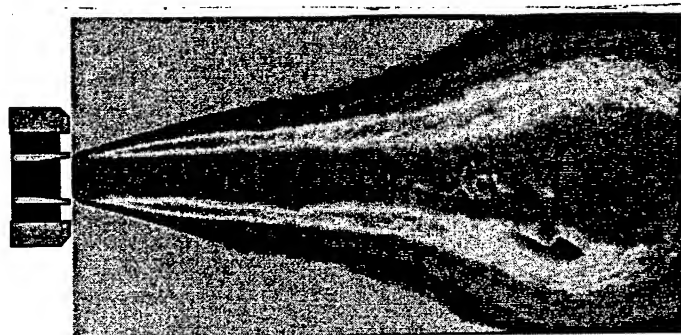


Figure 27: Abel transform of the averaged images at 60 bar

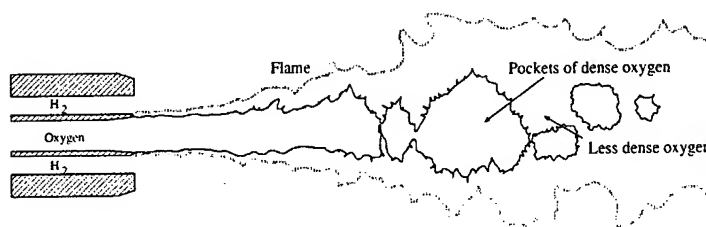


Figure 28: Schematic representation of the flame shape at 60 bar

References

¹Herding, G., Snyder, R., Scoufflaire, P., Rolon, C. and Candel, S., "Emission and laser induced fluorescence imaging of cryogenic propellant combustion," *Proceedings of the Conference on Propulsive Flows in Space Transportation Systems* (Bordeaux, France), CNES, 1995. pp. 1-14

²Snyder, R., Herding, G., Rolon, C. and Candel, S., "Analysis of flame patterns in cryogenic propellant combustion," *Combustion Science and Technology*, Vol. 124 , 1997, pp. 333-373.

³Herding, G., Snyder, R., Scoufflaire, P., Rolon, C. and Candel, S., "Flame stabilization in cryogenic propellant combustion," *26th Symposium (International) on Combustion*, The Combustion Institute, Pittsburgh, 1996, pp. 2041-2047.

⁴Herding, G., Snyder, R., Rolon, C. and Candel, S., "Investigation of cryogenic propellant flames using computerized tomography of OH emission images," *Journal of Propulsion and Power*, Vol. 13, pp. 146-151 , 1998.

⁵Brummund, U., Cessou, A., Oschwald, M., Vogel, A., Grisch, F., Bouchardy, P., Pealat, M., Vingert, L., Habiballah, M., Snyder, R., Herding, G., Scoufflaire, P., Rolon, C. and Candel, S., "Laser diagnostics for cryogenic propellant Combustion Studies," *Proceedings of the 2nd International Symposium on Liquid Rocket Propulsion* (Chatillon, France), 1995. pp. 19.1-19.22.

⁶Candel, S., Herding, G., Snyder, R., Scoufflaire, P., Rolon, C., Vingert, L., Habiballah, M., Grisch, F., Pealat, M., Bouchardy, P., Stepowsky, D., Cessou, A. and Colin, P., Experimental investigation of shear coaxial cryogenic jet flames," *Journal of Propulsion and Power*, Vol. 14 , 1998, pp. 826-834.

⁷Kendrick, D., Herding, G., Scoufflaire, P., Rolon, C. and Candel, S., Effects of recess on cryogenic flame stabilization," *In press, Combustion and Flame* 1999.

⁸Tripathi, A., Juniper, M., Scoufflaire, P., Rolon, C., Durox, D. and Candel, S., LOX tube recess in cryogenic flames investigated using OH and H₂O emission," AIAA paper 99-2490, 1999.

⁹Barbeau, B., Lacas, F., Rymer, G. and Candel, S., Cryogenic flame modeling in a coaxial flame configuration," AIAA paper 99-0207, 1999.

Coherent anti-Stokes Raman Scattering (CARS) Measurements in a Shear-Coaxial Cryogenic Jet Flame

P. BOUCHARDY, F. GRISCH

ONERA - LAERTE
Département Mesures Physiques
Diagnostics optiques et plasmas
Fort de Palaiseau - 91120 PALAISEAU

W. CLAUSS

German Aerospace Research Establishment (DLR)
Germany

CNES01a



ONERA



Objective

- Improve design and optimization of high performance LOX-GH2 Rocket Engines
- Development of optical Diagnostics for combustion studies at high pressure (10 MPa)
 - CARS technique
Instantaneous measurements of temperature - concentration
 - Heat Release
Turbulence mixing of hot reaction products and Hydrogen

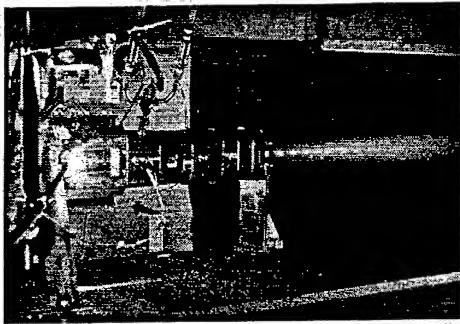
CNES02a



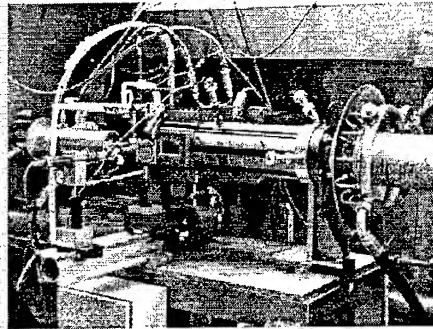
ONERA



MASCOTTE Combustion chamber



10 bar Facility



High Pressure Facility

CNES13a



ONERA

Multiplex CARS technique on MASCOTTE

- Detection of H_2 (fuel species)
- Single-shot measurements at 5 Hz frequency
 - ◇ 150 measurements during a run ($\Delta t=30s$) at 1 bar
 - 100 measurements (20 s) at higher pressure
- Temporal resolution: 10 ns
- Planar BOXCARS arrangement for H_2 with 200 mm focal lens
 - ◇ probe volume: 1.2 mm-long \times 100 μm diameter

CNES09a

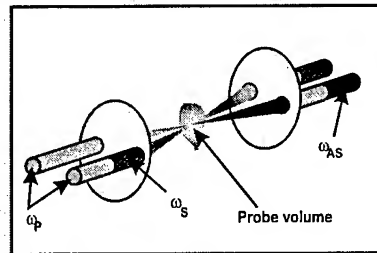


ONERA

The CARS technique (coherent anti-Stokes Raman spectroscopy)

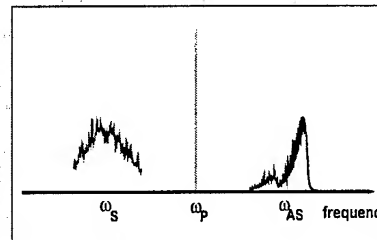
- Three laser beams are applied simultaneously to the gas mixture

- two pump beams
- one probe beam



- A new laser beam is created

- Its amplitude is strong when the difference $(\omega_p - \omega_s)$ matches a Raman frequency ω_v



- Multiplex CARS spectroscopy

- Use of a monochromatic laser for ω_p and a broadband dye laser for ω_s
- Instantaneous Measurements
- Spatially Resolved Measurements

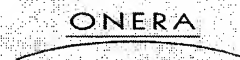
CNES03a



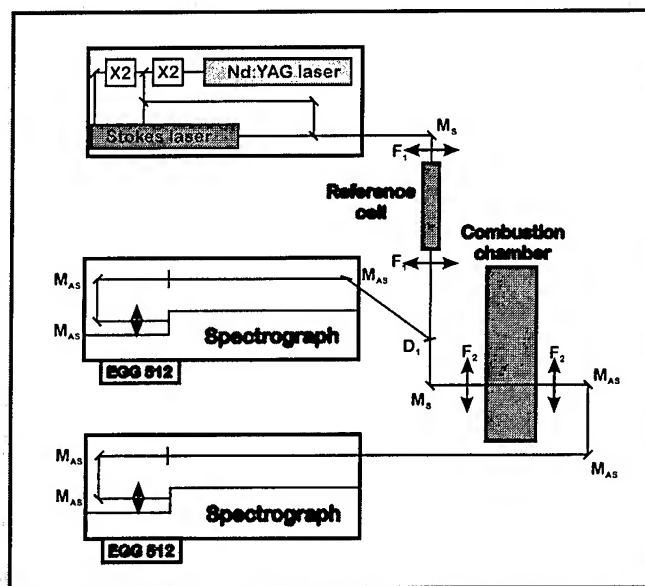
Multiplex CARS technique on MASCOTTE

- Detection of H_2 (fuel species)
- Single-shot measurements at 5 Hz frequency
 - ⇒ 150 measurements during a run ($\Delta t = 30s$) at 1 bar
 - 100 measurements (20 s) at higher pressure
- Temporal resolution: 10 ns
- Planar BOXCARS arrangement for H_2 with 200 mm focal lens
 - ⇒ probe volume: 1.2 mm-long \times 100 μm diameter

CNES05a



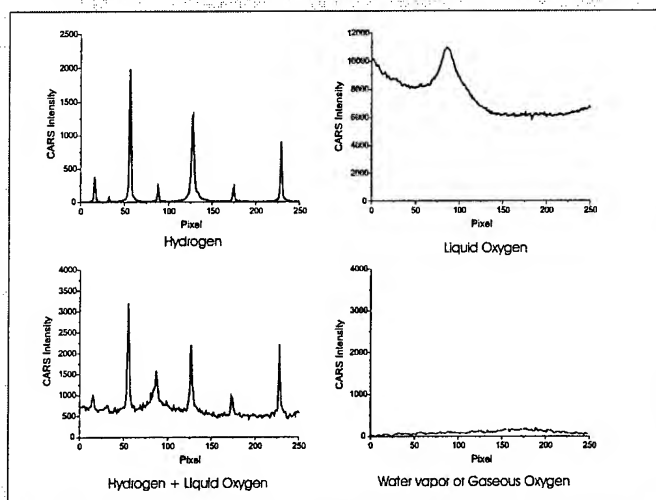
Experimental CARS setup



CNES04a
DLR

ONERA

Two-Phase Flow Effect on the single-shot H_2 CARS spectra

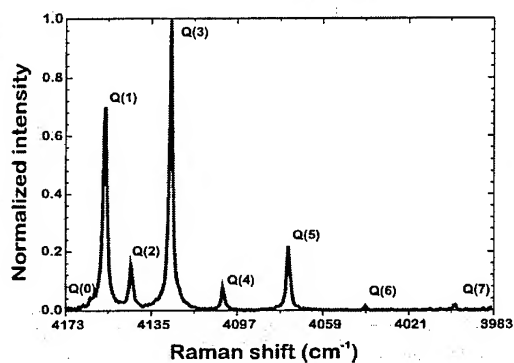


$X = 80 \text{ mm}$, $Y = 5 \text{ mm}$, $P = 1 \text{ bar}$

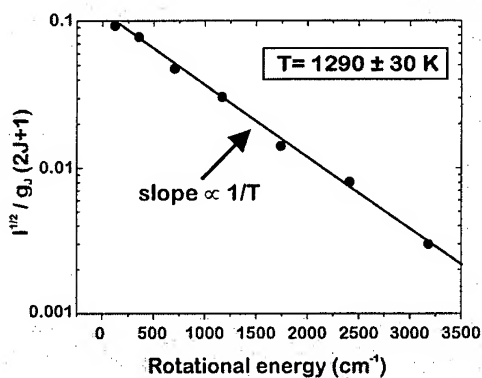
CNES 15a
DLR

ONERA

Temperature measurement on H_2 at atmospheric pressure



Single-shot spectrum of H_2



Boltzmann diagram

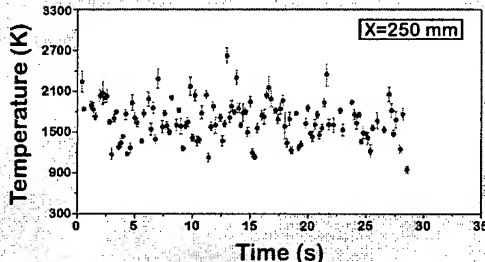
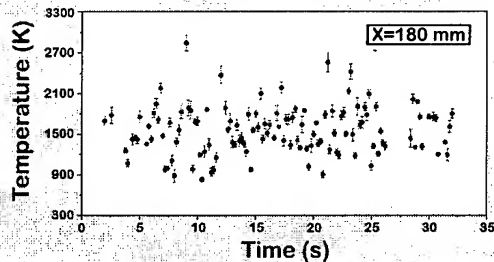
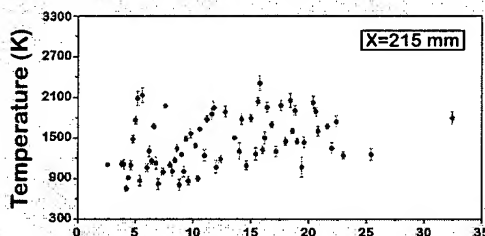
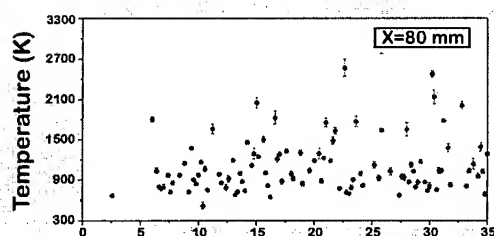
$\gamma_{\text{doppler}} \gg \gamma_{\text{collisional}}$ for all rotational lines

CNES05a



ONERA

Single-shot temperature *versus* time at 1 bar



Position: Y=20 mm

X: axial position from the injector, Y: radial position from the flow axis

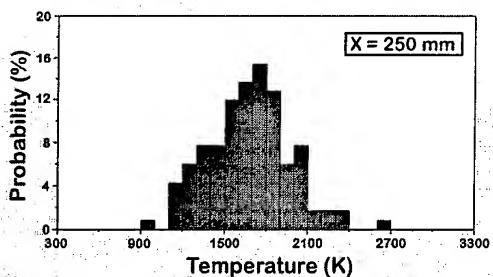
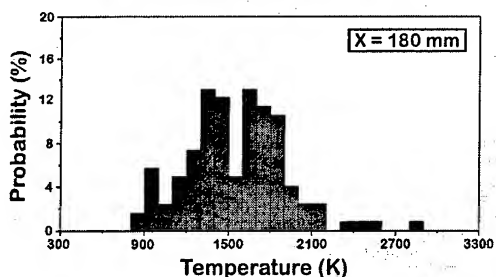
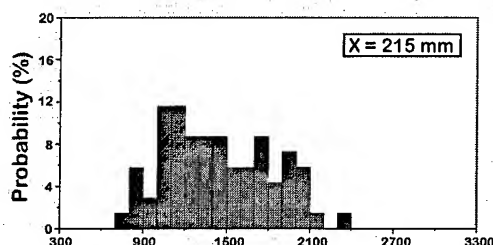
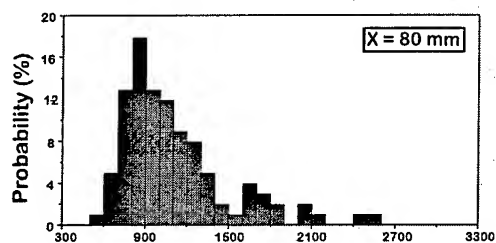
CNES12a



ONERA

P.D.F. of single-shot temperature at 1 bar

Position: Y=20 mm



CNES11a

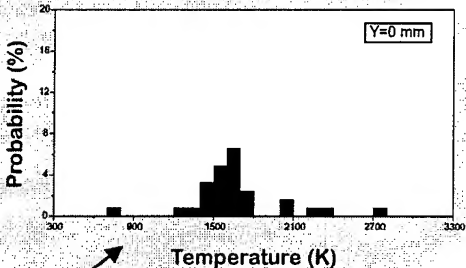
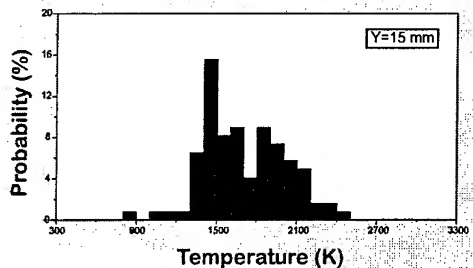
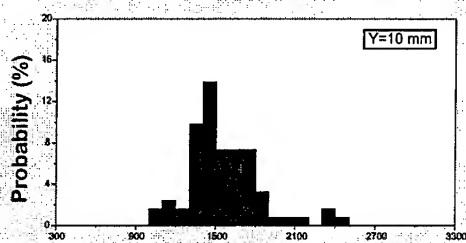
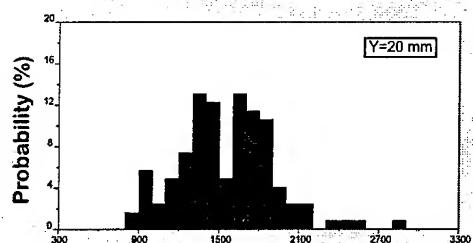


→ mean temperature and standard deviation

ONERA

P.D.F. of single-shot temperature at 1 bar

X=180 mm from the injector



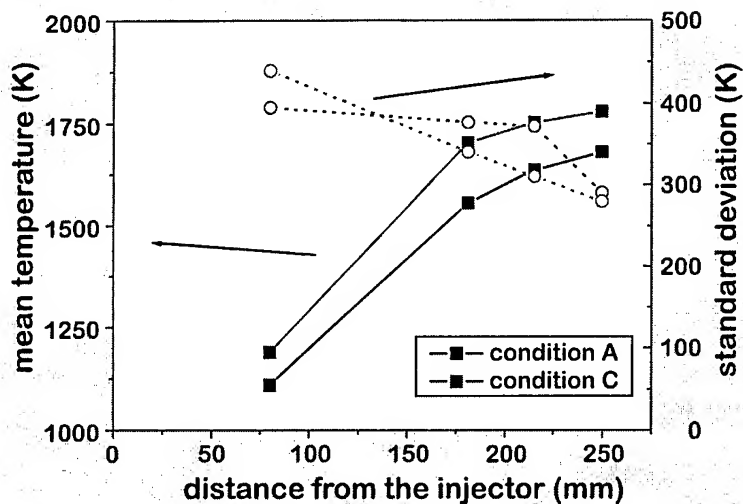
CNES23a



mean temperature and standard deviation ?

ONERA

Temperature Profile at Y=20 mm P=1 bar



Condition A: 50 g/s LOX, 15 g/s H₂

Condition C: 50 g/s LOX, 10 g/s H₂

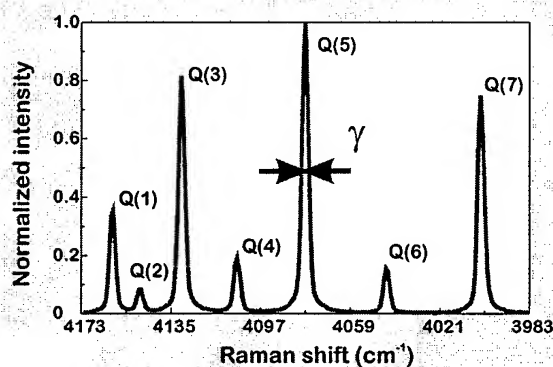
CNES16a



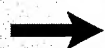
ONERA

High pressure condition

- CARS line depends on the linewidth γ (Doppler + collisional)
- Collisional broadening + Dicke effect become significant.
- Dependence on the rotational state J
- Influence of the collisional partners for H₂ (H₂, O₂, H₂O)



Single-shot spectrum at 10 bar



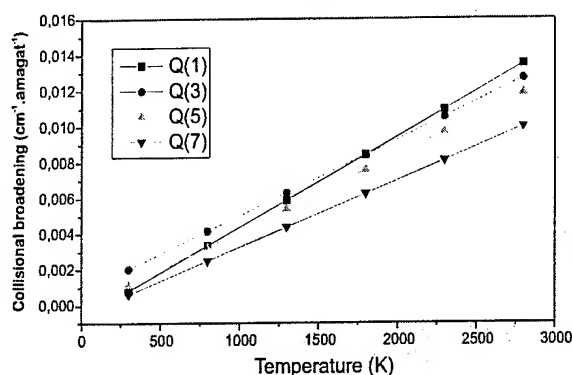
Impossibility to use the Boltzmann Diagram Technique

CNES07a



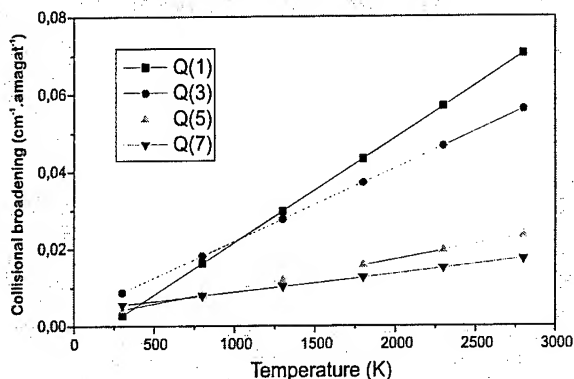
ONERA

Collisional Linewidths for H₂-H₂ and H₂-H₂O



H₂-H₂

Courtesy of X. Michaut and H. Berger
(University of Dijon)



H₂-H₂O

$$\rightarrow \gamma = C_{H_2} \gamma_{H_2-H_2} + C_{H_2O} \gamma_{H_2-H_2O}$$

CNES08a



ONERA

Temperature measurement at high pressure

- Temperatures are deduced by fitting experimental spectra with the theoretical ones calculated for different temperatures and for different molar fractions of H₂ and H₂O
- Effects of O₂ are merged with those of H₂
(same collisional behavior of H₂-H₂ and H₂-O₂)
- The fitting technique used is a simple least squares where the error function is given by

$$F = \sum \omega_j (I_j^{\text{exp}} - I_j^{\text{theory}}(T, x_{H_2}, x_{H_2O}))^2$$

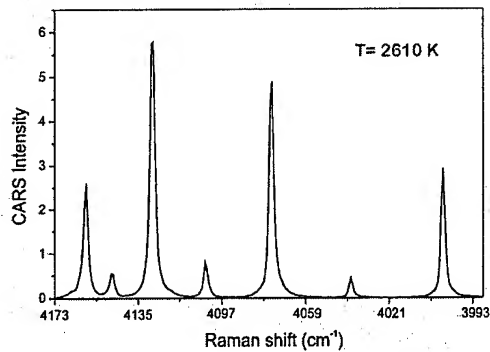
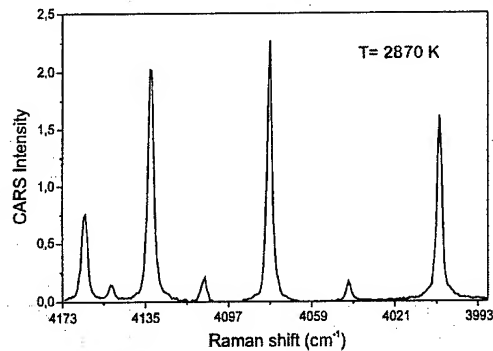
$$x_{H_2} = 1 - x_{H_2O} \text{ by assumption}$$

CNES09a



ONERA

High Pressure H₂ CARS spectra

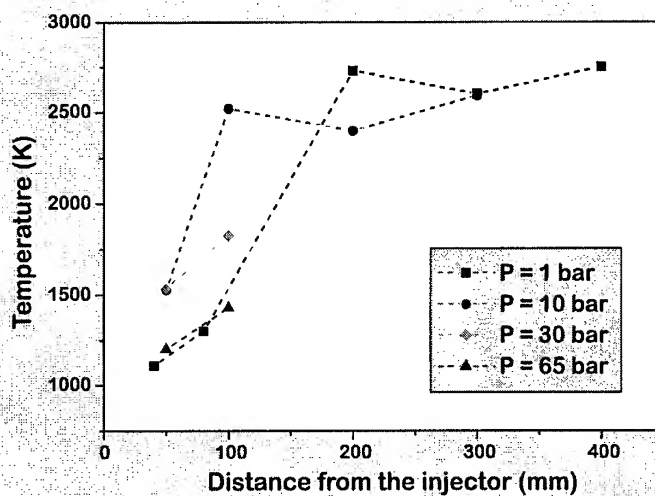


CNES/04



ONERA

Temperature evolution *versus* pressure



Condition C

Radial position: 15 mm from the flow axis

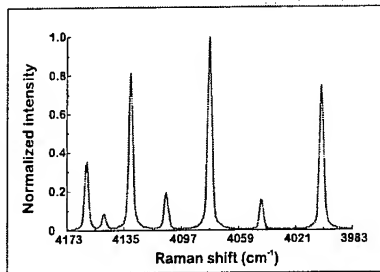
CNES/23



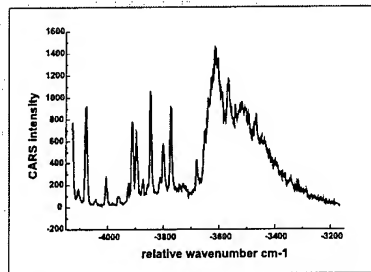
ONERA

Principle of measurement

- Simultaneous detection of two species: H_2 and H_2O



H_2 CARS spectrum



H_2O CARS spectrum

- Data processing
 - H_2O concentration estimated from the intensity of the H_2O CARS spectra
 - Species composition for the collisional linewidth can be estimated
 - Temperature deduced from the H_2 and H_2O spectral profiles

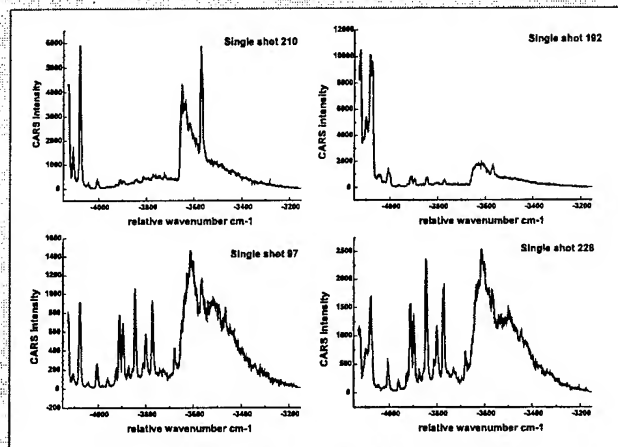
CNES19a



ONERA

Results

- Simultaneous detection of H_2 and H_2O using CARS have been performed for pressures up to 65 bar.
- H_2O CARS spectra



- Data processing still in progress (recent experiment)

CNES20a



ONERA

Conclusion

- Detection of H_2 (and H_2O) using CARS have been successfully performed for pressures up to 65 bar in a cryogenic combustor.
- Temperature and concentration can be deduced from the experimental CARS signals
- Data base for the validation of combustion solvers
- Measurements will be performed on the P8 combustor (DLR) at 60 bar next year

CNES21a



DLR

ONERA

Statistical Investigation of the Turbulent Flame Geometrical Structures in a Liquid Oxygen / Gaseous Hydrogen Shear-Coaxial Jet

Armelle CESSOU, Pascal COLIN, Denis STEPOWSKI

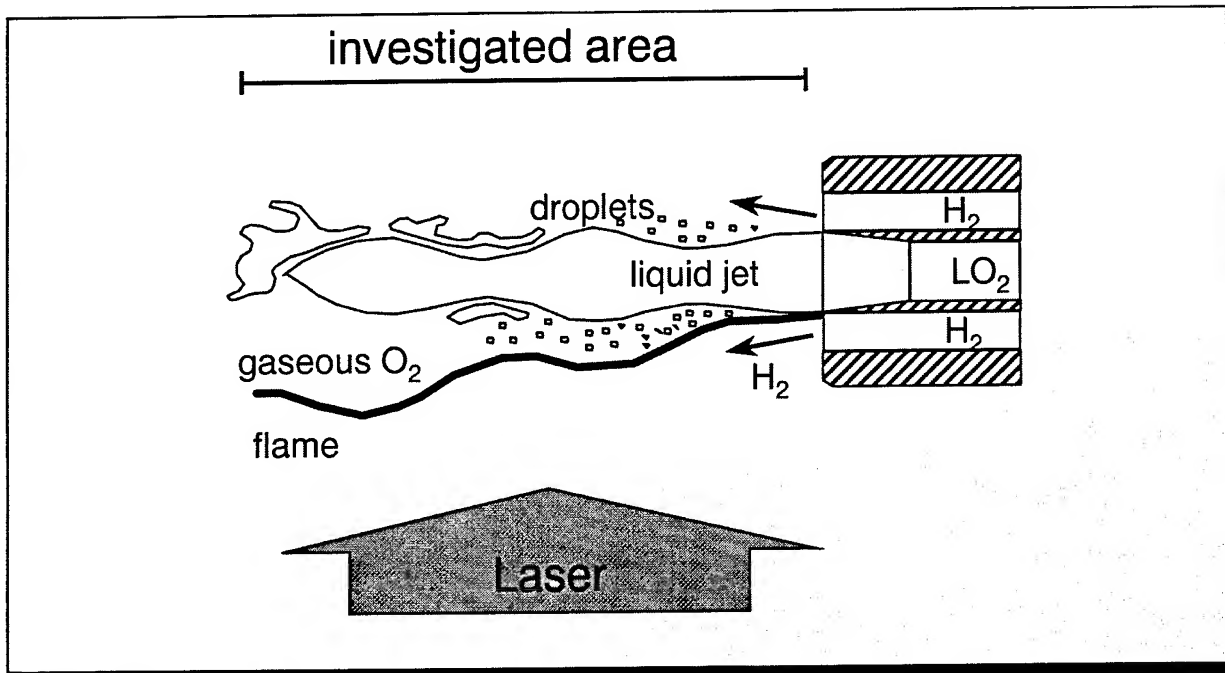
***CORIA UMR 6614
CNRS - Université & INSA de Rouen
Place Emile Blondel
76821 Mont Saint Aignan, France***



Context

- **rocket engine application**
- **cryogenic propellant combustion facility :**
 - MASCOTTE test bench of ONERA**
- **developed for better understanding of physical phenomena encountered in rocket engines :**
 - *atomization*
 - *vaporization*
 - *turbulent mixing*
 - *two-phase combustion*
- **Investigation by planar laser induced fluorescence**

Investigated Area



Flame Description

- Flame always anchored at the lip of the injector
- Non-premixed character
- conserved scalar : mixture fraction

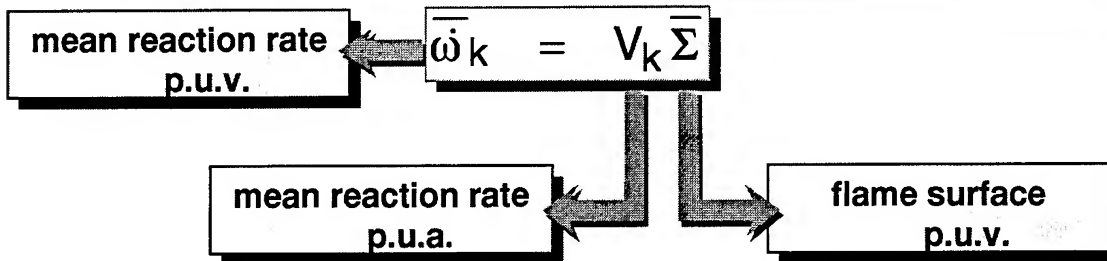
$$Z = \frac{\nu Y_F - Y_O + Y_O^\infty}{\nu Y_F^\infty + Y_O^\infty}$$

- Description : constant-property surface
- Hyp. : infinitely fast chemistry \Rightarrow flame at stoichiometric mixture

constant-property surface $Z = Z_s \Rightarrow$ Flame

Flame Description

- chemistry decoupled from turbulence



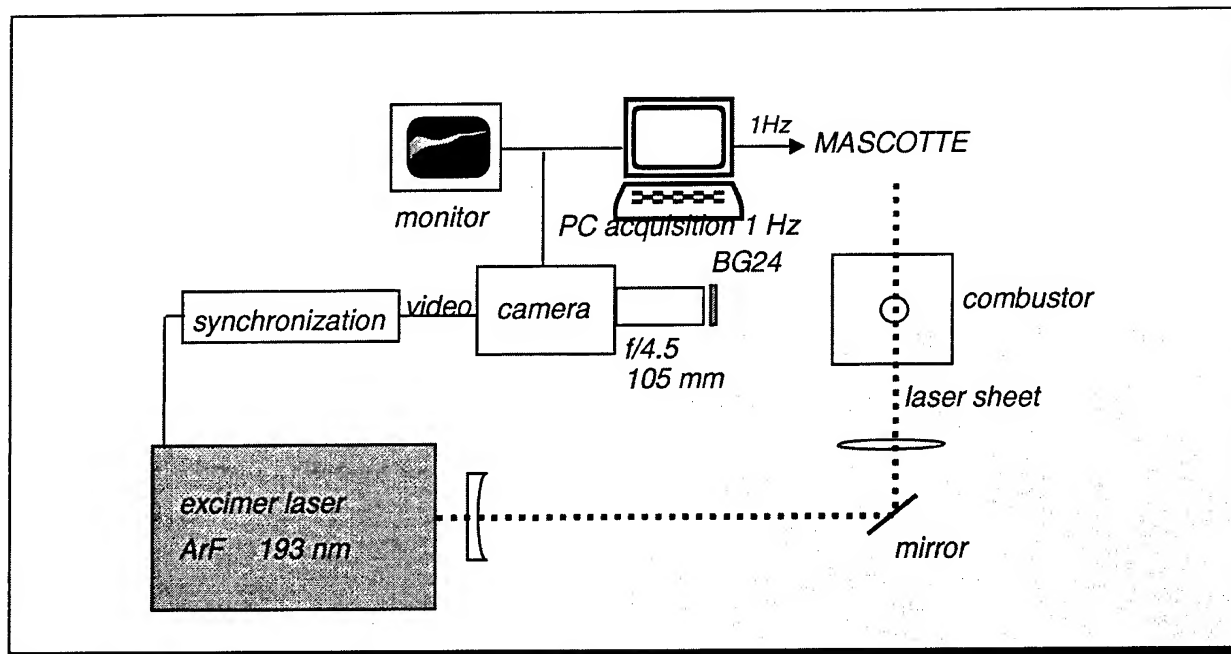
- local geometry of constant-property surface
 - presence probability
 - normal to the surface
 - curvature
 - flame surface production



Operating Conditions

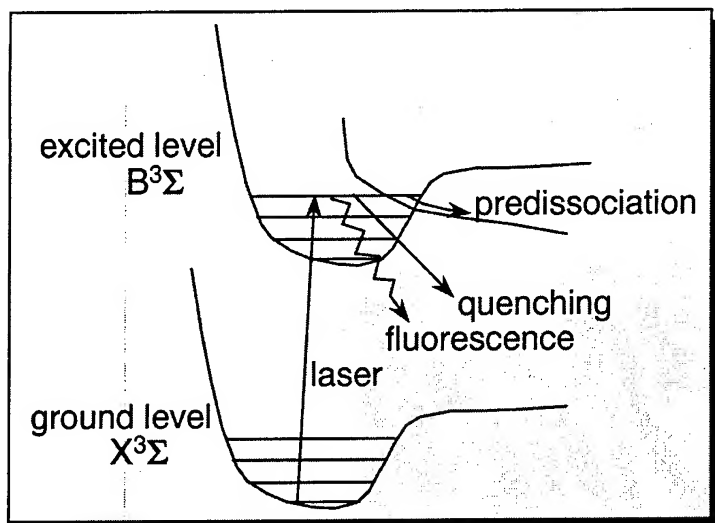
Point	m_l g/s	m_g g/s	P bar	T_{GH2} K	V_{lox} m/s	V_{GH2} m/s	Re_l $\times 10^3$	J	We $\times 10^3$	image number
C1	50	9.5	1	289	2.18	620	67	6	12.5	151
C1p	50	9.5	8	289	2.18	163	67	3.2	6.5	182
F1	50	9.5	1	94	2.18	419	67	8.1	16.9	274

Experimental Set-up



coRia
UMR 6614
CNRS - UNIVERSITE et INSA de ROUEN

Fluorescence Scheme

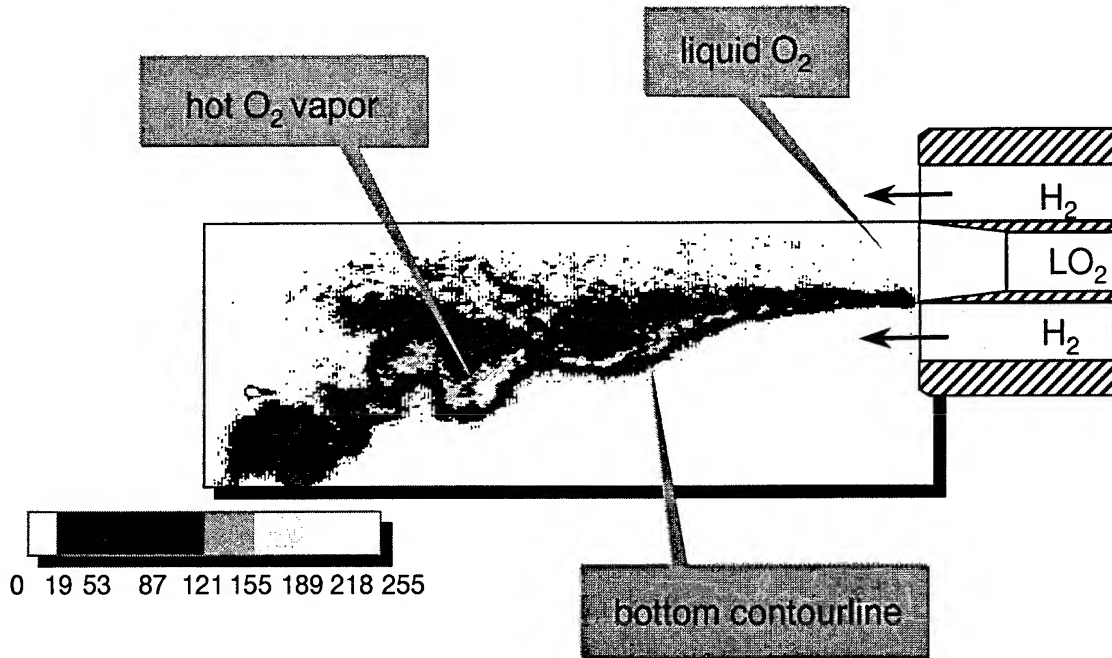


- **broadband ArF laser, 193 nm**
- **predissociative fluorescence of O_2**
- **hot vibrational bands**
 - $(v'=0, v''=4)$
 - $(v'=1, v''=7)$
 - $(v'=2, v''=10)$
 - $(v'=3, v''=15)$

- **Effective absorption cross section**
 - **Fluorescence efficiency**
- } **strongly increase with temperature**

coRia
UMR 6614
CNRS - UNIVERSITE et INSA de ROUEN

Instantaneous Image



Flame Identification

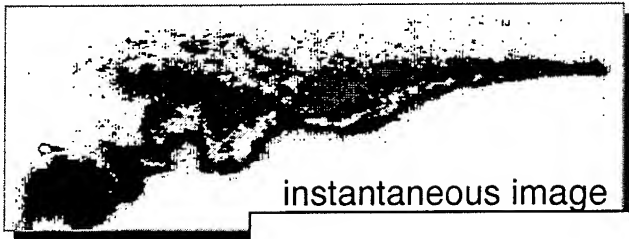
- reverse configuration
laser irradiance not altered
before reaching the flame

- at adiabatic flame temperature
detection limit : $Z = 0.109$
while $Z_s = 0.11$

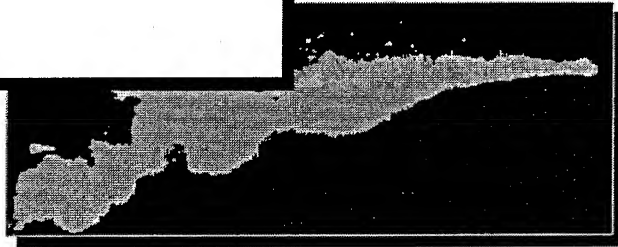
- Hyp. : infinitely fast chemistry for H₂/O₂

bottom outline of fluorescence
called flame

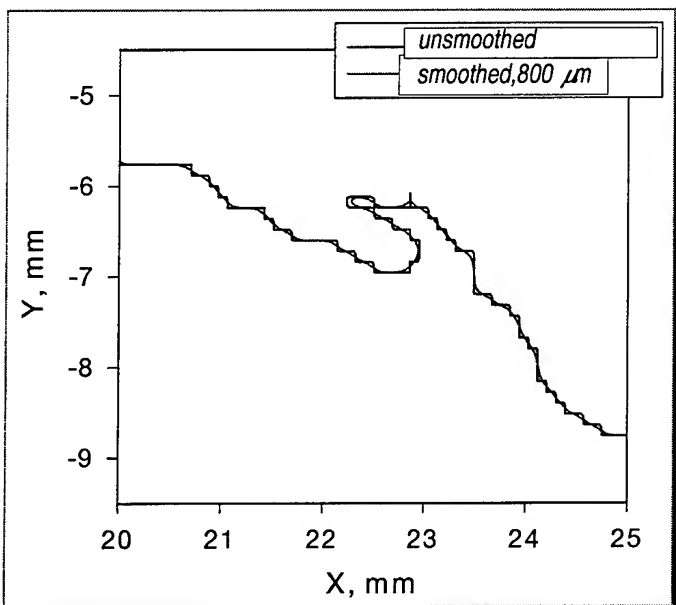
Contourline Determination



- Binarization $S_i > \text{threshold} \Rightarrow S = 100$
 $S_i < \text{threshold} \Rightarrow S = 0$
- median filter (3 x 3)
- contourline detection



High frequency filtering

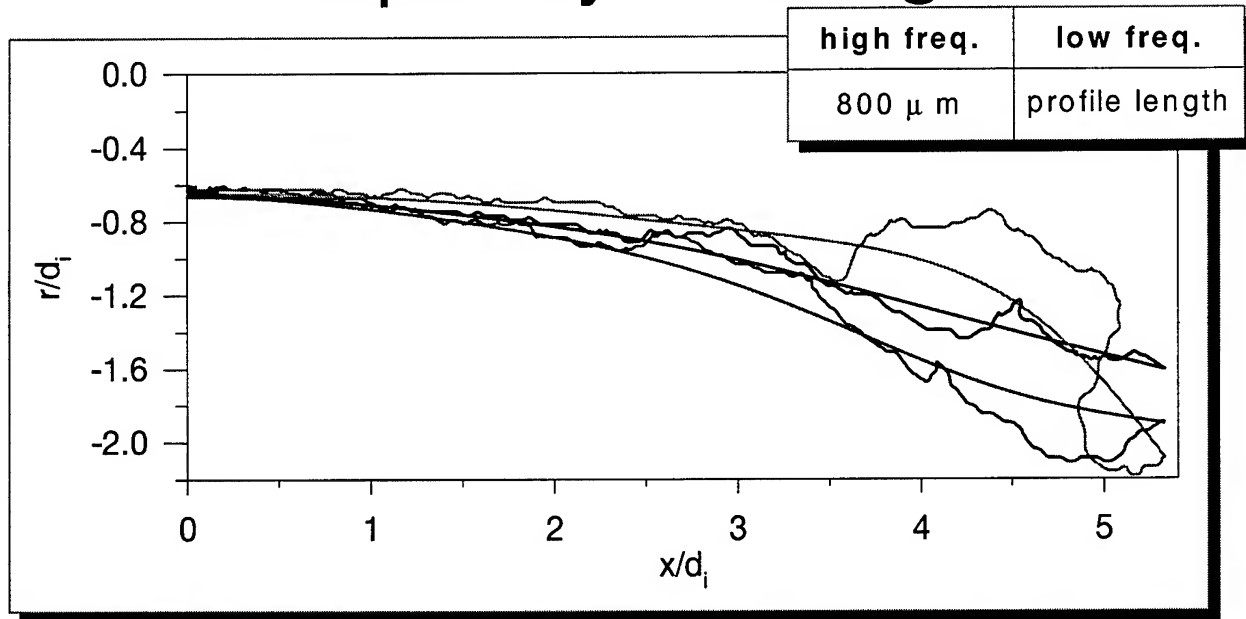


- sampled at evenly spaced intervals

$$ds = \sqrt{dx^2 + dy^2}$$

- smoothed through a gaussian filtering (800 μm)

High and Low Frequency Filterings

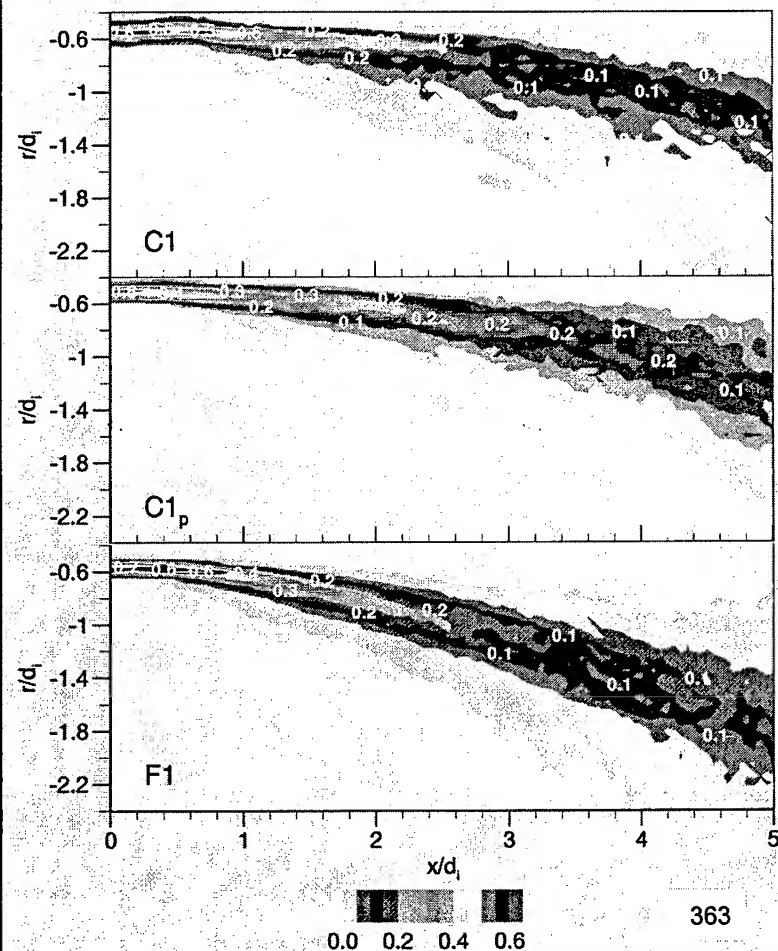


Presence Probability

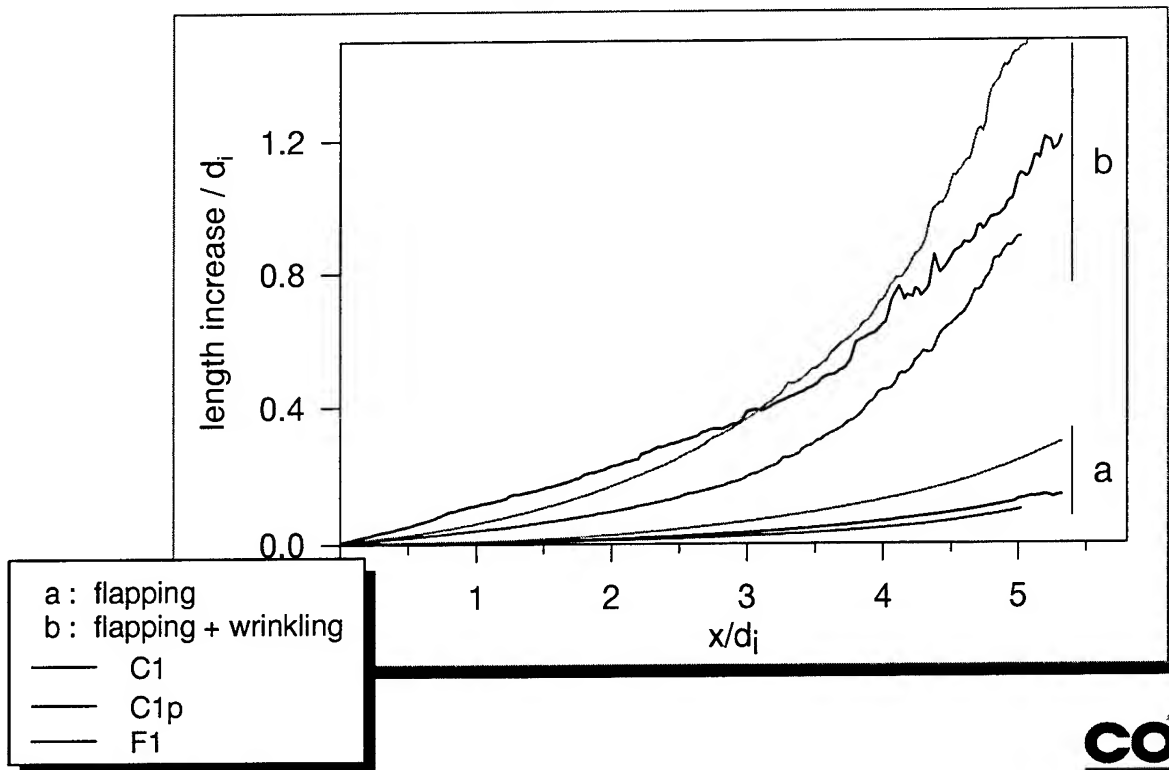
- mesh 0.25 x 0.25 mm²
- $x < d_i$ sharp distribution
- $x < 2d_i$

flame bows

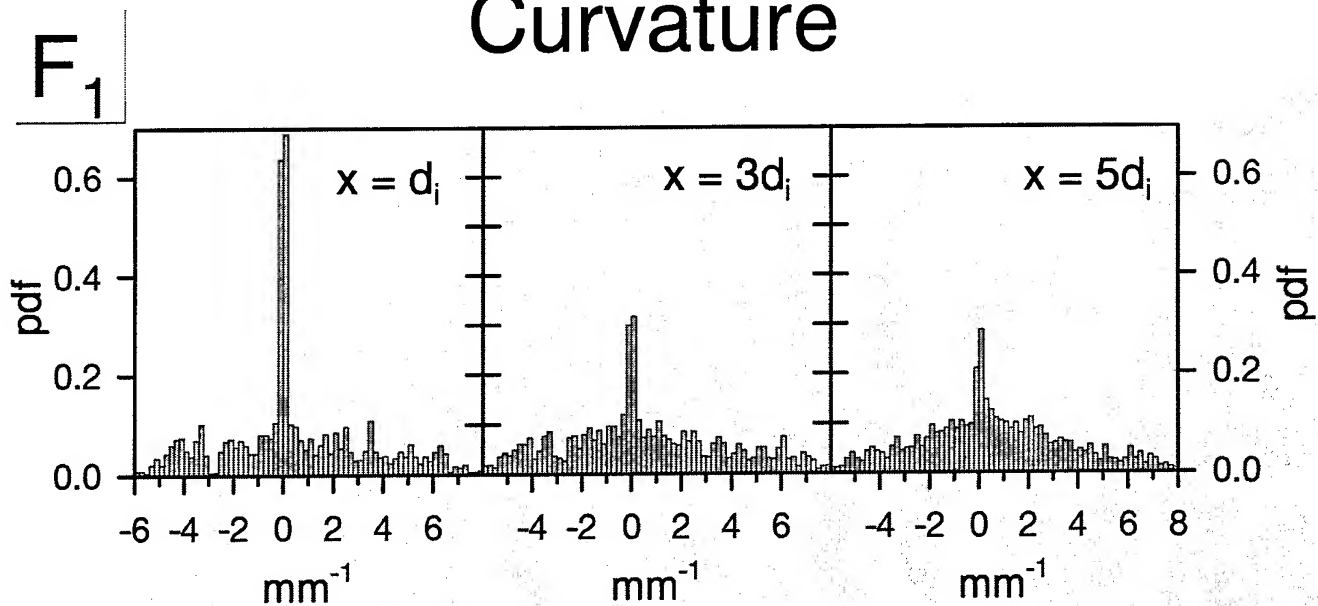
large distribution



Length Increase

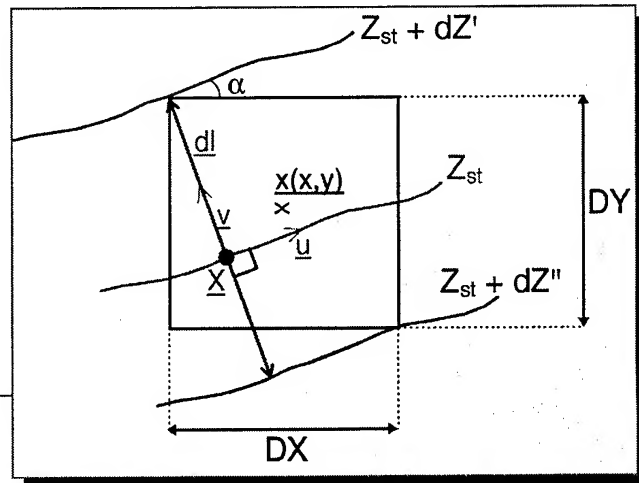


Curvature



$$h_i = \frac{\dot{x}(s_i)\ddot{y}(s_i) - \dot{y}(s_i)\ddot{x}(s_i)}{(\dot{x}^2(s_i) + \dot{y}^2(s_i))^{3/2}}$$

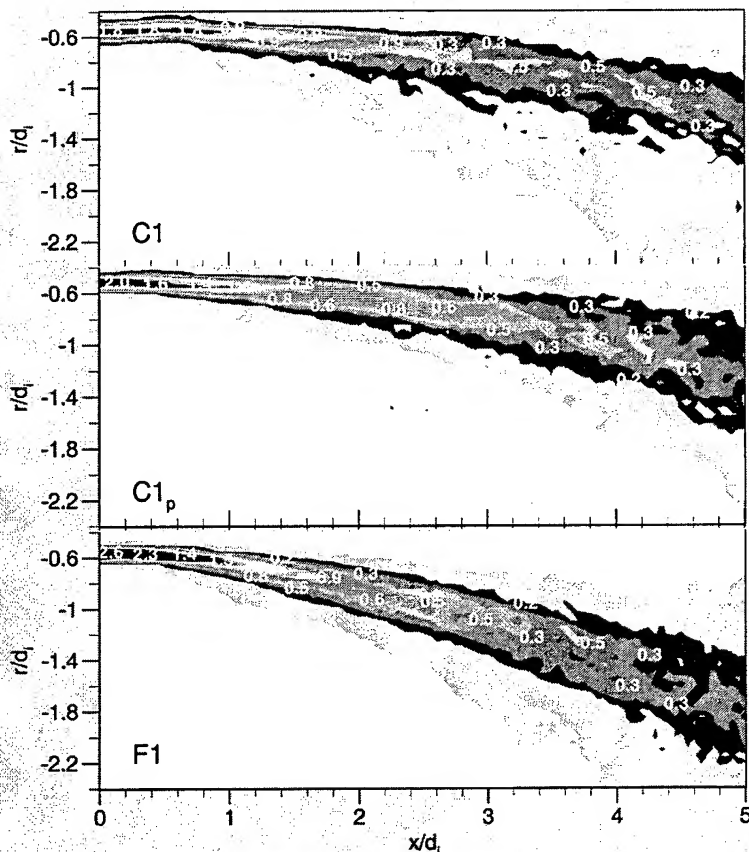
Flame Surface Density



$$\bar{\Sigma}(\underline{X}, Z_{st}) = f_Z(Z_{st}; \underline{X}) \cdot \langle |\nabla Z| | Z_{st}; \underline{X} \rangle$$

$$dl(u, v, DX, DY, Z) = DX \cdot \sin(\bar{u}, \bar{x}) + DY \cdot \cos(\bar{u}, \bar{x})$$

$$\bar{\Sigma}(\underline{X}, Z_{st}) = P(Z_{st} < Z < Z_{st} + \langle dZ | Z_{st}; \underline{X} \rangle) \cdot \left\langle \frac{1}{dl} \middle| Z_{st}; \underline{X} \right\rangle$$



Σ

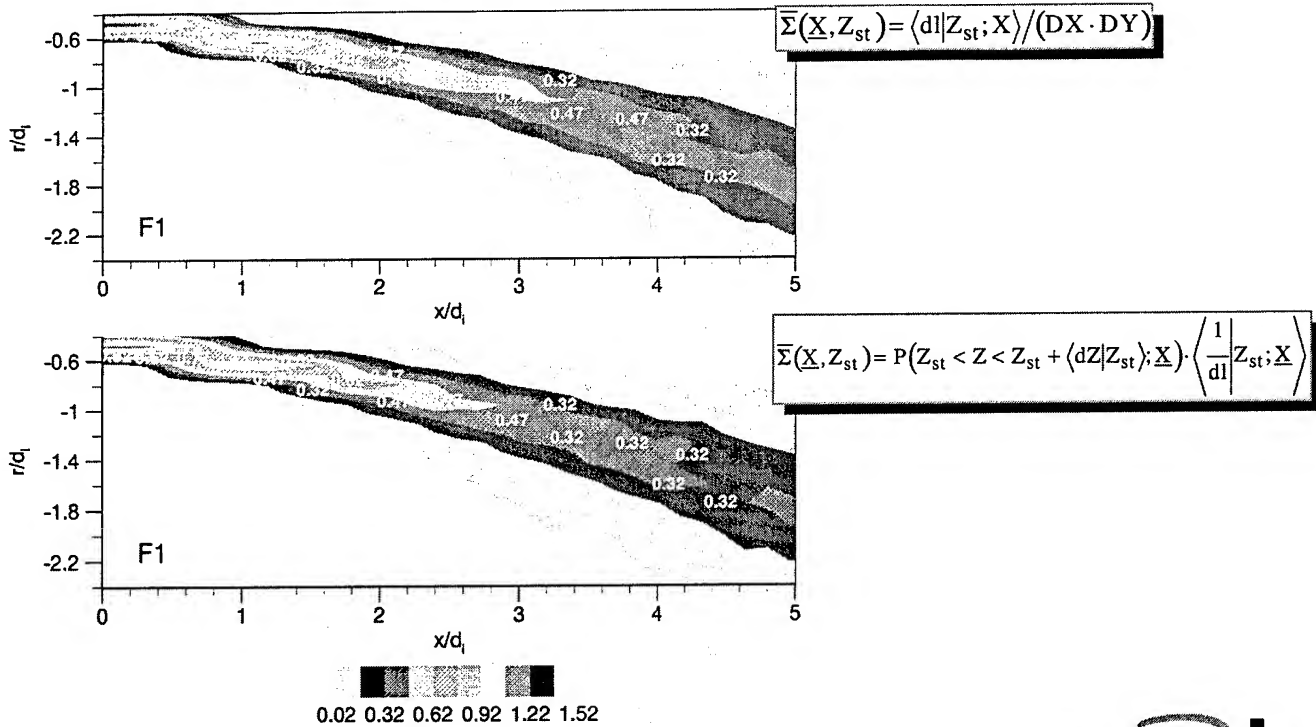
- $\Sigma = P \times \langle 1/dl | Z_s \rangle$
 - mesh $0.25 \times 0.25 \text{ mm}^2$
 - $x < 2d_i$
- Σ underestimated

from

$$\left\langle \frac{1}{dl} \middle| Z_{st}; \underline{X} \right\rangle = \left\langle \frac{1}{DX \times dy/ds + DY \times dx/ds} \right\rangle$$



Comparison



Conclusion

- – reverse configuration
(oxygen within the flame envelope)
 - – O₂ fluorescence
- } stoichiometric iso-surface
- statistical description of flame surface properties



- validation tools for numerical modeling

Acknowledgment

- **GDR «Combustion dans les moteurs fusées»
(CNES, SEP, CNRS, ONERA)**
- **M. Habiballah, L. Vingert, A. Mouthon, R. Barraud
of ONERA (MASCOTTE test bench)**



SOME POSSIBLE CONSEQUENCES OF BIFURCATIONS IN COMBUSTORS

F.E.C. Culick

California Institute of Technology

~ ~ ~

International Workshop on Research Status and
Perspectives in Liquid Rocket Chamber
Dynamics

~ ~ ~

Work Supported by:

California Institute of Technology

Airforce Office of Scientific Research (Dr. M. Birkan)

ENEL (Dr. G. Benelli)

ONR (Dr. J. Goldwasser)

DoE, AGTSR Program (Dr. D. Fant)

Held at CNES, 1 Place Maurice Quentin,
Paris, France

27-28 May 1999



OUTLINE

- I Introduction
- II Bifurcation of Dynamical States in a Dump Combustor
- III Bifurcation of Steady Combustion with Recirculation Zones
- IV Incorporating Bifurcation of Combustion in Analysis of Combustor Dynamics
- V Some Consequences of Subcritical Bifurcations with Noise
- VI Concluding Remarks



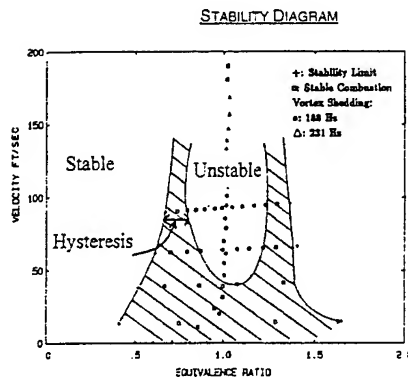
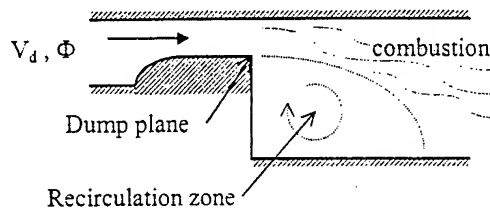
I INTRODUCTION



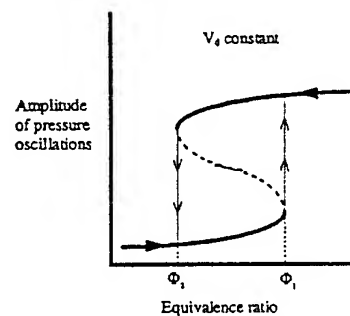
HISTORICAL BACKGROUND

Bifurcation of Dynamical States of Combustion

- In the mid-1980's, hysteresis was discovered at the boundary between stable and unstable operation of the Caltech dump combustor (Smith, 1985; Sterling, 1987)



HYSTERESIS OF AMPLITUDE



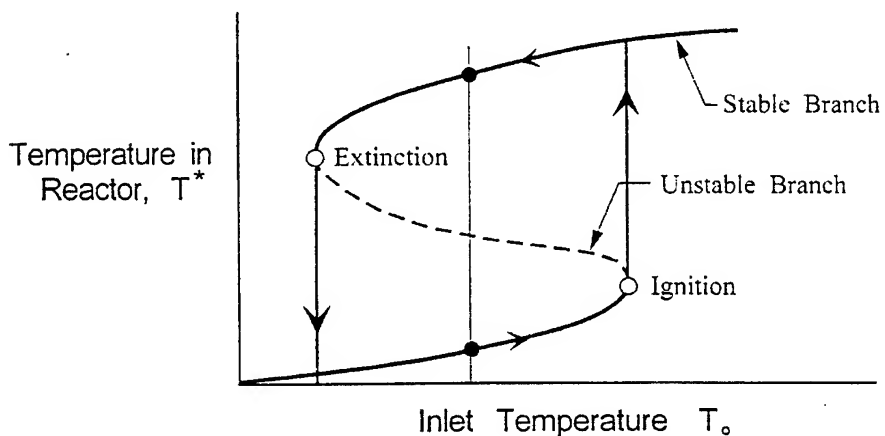
- These results suggest bifurcation of dynamical states of combustion (limit cycles?)
- The behavior has since been found by others [Cohen (UTRC); Richards (METC)]



HISTORICAL BACKGROUND (cont'd)

Bifurcation of Steady States of Combustion

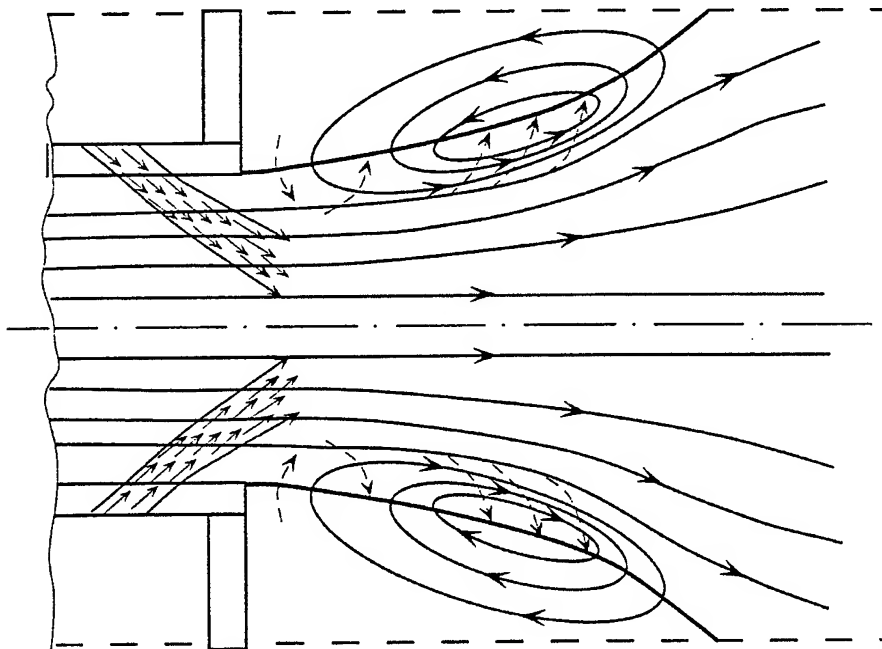
- In the 1970's, Natanzon et al proposed and investigated the stability of bifurcated steady states of combustion as a possible mechanism for random occurrences of combustion instabilities.
- The reasoning rests on bifurcation of steady combustion in a recirculation zone (Natanzon et al, 1992)



HISTORICAL BACKGROUND (cont'd)

Bifurcation of Steady States of Combustion (cont'd)

- One state (cold recirculation zone) is more unstable and prone to produce combustion instabilities.
- Which state is reached depends on history (e.g. during ignition or shut-down); the final state depends on random 'accidents' of that history.
- Hence random occurrences of combustion instabilities may be observed.
- Analysis of the recirculation zone is an extension of that for a perfectly stirred (homogeneous) reactor

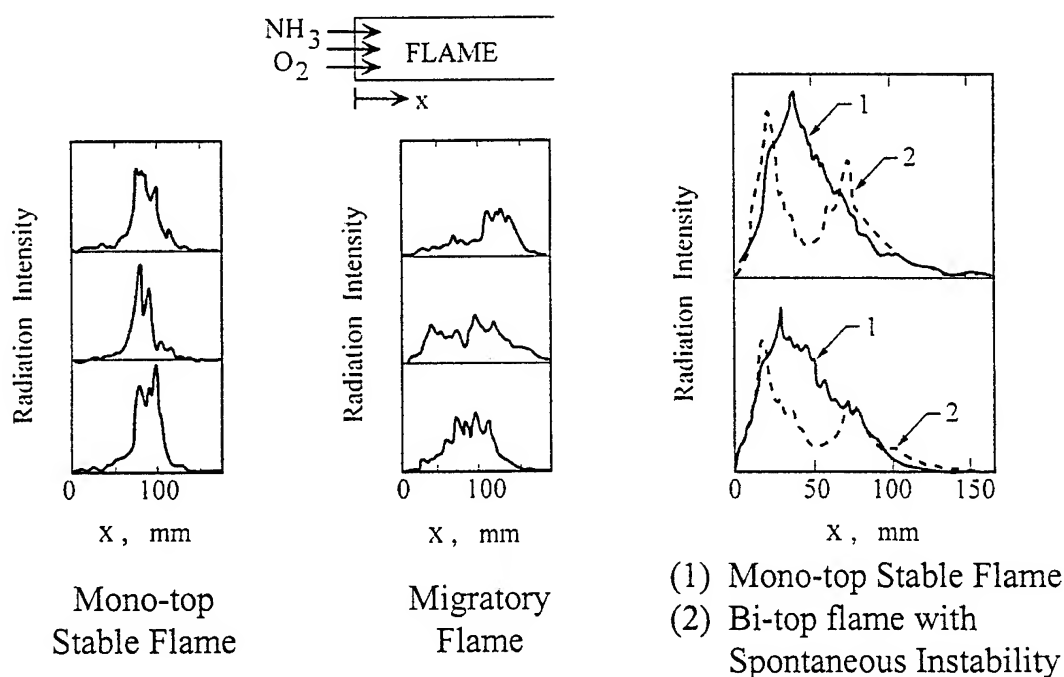


HISTORICAL BACKGROUND (cont'd)

- Doulatov et al (1998) (independently) proposed existence of 'multiple modes' of combustion, based on statistical analysis of pressure records

“...statistical error equaled almost 100% while the instrumentation error was no more than 15%...”

- Observations of flame structure in a small NH_3/O_2 engine (Beliy et al, 1983; Abulkanov et al, 1974) showed correlation between presence of instabilities and spatial characteristics of the flame structure.



Dependence of radiation intensity (ICuH) on the chamber length; a) typical mono-top stable flame; b) an example of migratory flame; c) mono-top stable flame and bi-top flame created by the spontaneous instability in the combustion chamber from a single experiment.



HISTORICAL BACKGROUND (cont'd)

- Note the connection in the Russian reports between statistical analysis of pressure records (both multiple and single firings) and the conclusion that bifurcation of the combustion process exists [Ref. 1st International Symposium on Liquid Propellant Rocket Engines, Pennsylvania State University (1993)]
- In numerical simulations it may be difficult to identify bifurcations except with special intentions (?)
- Presence of hysteresis constitutes a basis for control by injecting pulses to cause transitions between two stable states.



SOME REMARKS ON AFFECTING COMBUSTION INSTABILITIES

- The problem of linear stability of motions in a combustion chamber can be reduced to a general form of Rayleigh's Criterion.
- Rayleigh's original criterion was based on excitation of acoustic waves in a tube (e.g. a Rijke tube) by energy addition in the form of heat transfer or energy released in combustion processes.
- The criterion states (roughly) that energy addition tends to destabilize (i.e. encourage) a pressure disturbance if the rate of energy addition is increasing locally where the pressure disturbance is also increasing.

\dot{Q} : rate of energy addition/volume

$\frac{\partial \dot{Q}^{(r)}}{\partial t}$: component of rate of change of \dot{Q} in phase
with the pressure disturbance δp

Change of energy if the disturbance $\sim \frac{\partial \dot{Q}^{(r)'}}{\partial t} \delta p$

- Formally:

$$\nabla^2 p' - \frac{1}{\bar{a}^2} \frac{\partial^2 p'}{\partial t^2} = h ; \quad h = \frac{1}{\bar{a}^2} \frac{R}{C_v} \frac{\partial \dot{Q}'}{\partial t} + h_2$$

$$\hat{n} \cdot \nabla p' = -f$$



SOME REMARKS ON AFFECTING COMBUSTION INSTABILITIES (cont'd)

Modal expansion and spatial averaging:

$$p'(\vec{r};t) = \bar{p} \sum \eta_i(t) \psi_i(t) : \frac{d^2 \eta_n}{dt^2} + \omega_n^2 \eta_n = F_n$$

$$F_n = -\frac{\bar{a}^2}{\bar{p}E_n^2} \left\{ \int h \psi_n dV + \oint f \psi_n dS \right\} \quad E_n^2 = \int \psi_n^2 dV$$

Change of energy of an oscillator in one cycle

$$\Delta \xi_n = \int_t^{t+\tau_n} \Re \{ F_n \dot{\eta}_n \} dt = \frac{\bar{R}/\bar{C}_v}{\bar{p}E_n^2} \int \psi_n dV \int_t^{t+\tau_n} \dot{\eta}_n \frac{\partial \dot{Q}'}{\partial t} dt' + \dots$$

“Rayleigh’s Criterion”

$$\Delta \xi_n = \frac{\bar{R}/\bar{C}_v}{\bar{p}E_n^2} \int \psi_n dV \int_t^{t+\tau_n} \dot{\eta}_n \frac{\partial \dot{Q}'}{\partial t} dt' > 0 \Rightarrow \text{instability}$$



SOME REMARKS ON AFFECTING COMBUSTION INSTABILITIES (cont'd)

- The destabilizing tendency of energy addition depends on the local phase relation and spatial disturbance.
- Stabilizing or controlling combustion instabilities “according to Rayleigh’s criterion” means altering the spatial distribution and phasing of the energy released by combustion.
 - e.g. modulate the primary or a secondary supply of fuel.
- Neither successes nor failures in treating combustion instabilities in liquid rockets are well-understood; notably the amplitudes of oscillations before and after application of a method to improve stability have not been predicted.
 - Why? Because the mechanisms are not well-understood: relying only on Rayleigh’s criterion for interpreting problems of combustion instabilities produces no information about the mechanisms unless a theory for $\partial\dot{Q}/\partial t$ is given.
 - The situation is somewhat better for solid rockets because the overwhelming dominant mechanism is associated with the dynamics of combustion processes at a burning solid surface. A secondary cause of instabilities is vortex shedding, strongly dependent on details of the internal geometry.
- Consideration of bifurcations means paying attention to a special class of mechanisms.



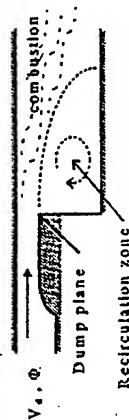
II BIFURCATION OF DYNAMICAL STATES IN A DUMP COMBUSTOR

References:

- D. Smith (1985)** "An Experimental Study of Acoustically Excited, Vortex Driven, Combustion Instability Within a Rearward Facing Step Combustor," Ph.D. Dissertation, Jet propulsion Center, California Institute of Technology.
- J. Sterling (1987)** "Longitudinal Mode Instabilities in Air Breathing Engines," Ph.D. Dissertation, Jet Propulsion Center California Institute of Technology.
- P. Knoop, F.E.C. Culick, and E.E. Zukoski (1996)** "Extension of the Stability of Motions in a Combustion Chamber by Nonlinear Active Control Based on Hysteresis," *Combustion Science and Technology* V. 123, 1-6, p. 363.
- G. Isella, C. Seywert, F.E.C. Culick, and E.E. Zukoski (1997)** "A Further Note on Active Control of Combustion Instabilities Based on Hysteresis," *Combustion Science and Technology* V. 126, pp. 381-388.

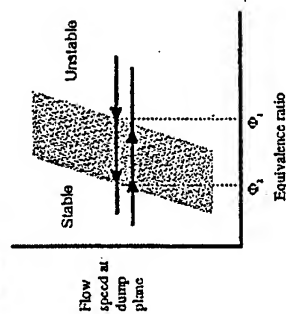


STABILITY AND HYSTERESIS IN A DUMP COMBUSTOR

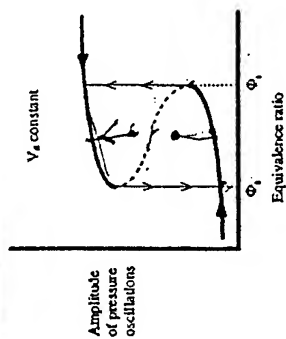


Tests with a dump combustor have revealed hysteretic behaviour in the stability boundary (V_d, ϕ) [Smith 1985, Sterling 1987]:

STABILITY BOUNDARY



HYSTERESIS OF AMPLITUDE



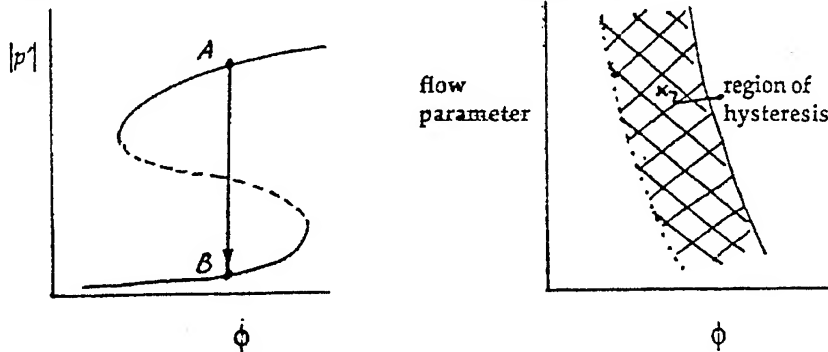
Observations:

- 1) As ϕ is increased, keeping V_d constant, the system becomes unstable for $\phi \geq \phi_1$.
- 2) If ϕ is then decreased, oscillations persist until $\phi \approx \phi_2 < \phi_1$.



POTENTIAL SIGNIFICANCE OF HYSTERESIS

- In combustors for which hysteresis exists, the range of stable operation (with active control) can be extended.



If a disturbance causes the system to be unstable in state A, active control of pulsing can produce transition to the stable state B.

- Understanding hysteresis means understanding true nonlinear behavior and may lead to a method of nonlinear control in the regions of vigorous instabilities, possibly more efficient than methods of linear control.
- However, when it exists, hysteresis occurs in some lean range of mixture ratio, i.e. in the region including the lean blowout limit.

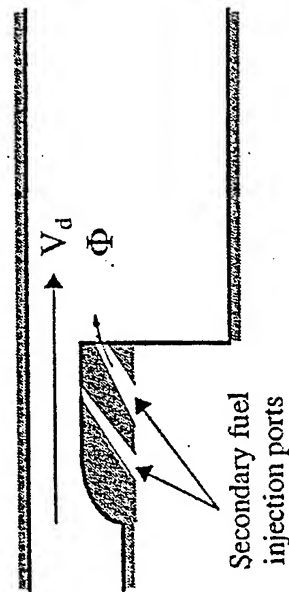
Hence a practical strategy for design of operational combustors may be

- design the combustor for stable operation for moderate and high mixture ratios, by using 'passive' control (geometry, flow field ...)
- use active control based on the presence of hysteresis in the range of low mixture ratios

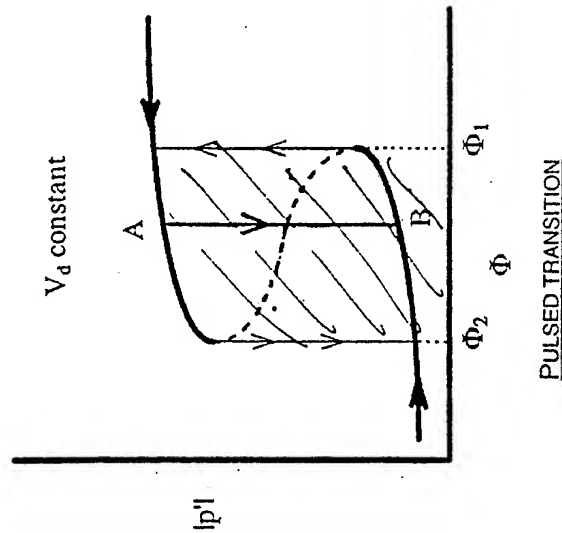


IMPLICATIONS OF HYSTERESIS

- ◊ The existence of hysteresis means that the system possesses two types of dynamic behaviour - two dynamical states - corresponding to the upper and lower branches.
- ◊ Recent experiments confirm that discrete pulses of secondary fuel injected in the region of the dump plane can cause the transition from the upper branch, point A, to the lower branch, B. The third intermediate branch is unstable.



PULSED INJECTION OF SECONDARY FUEL



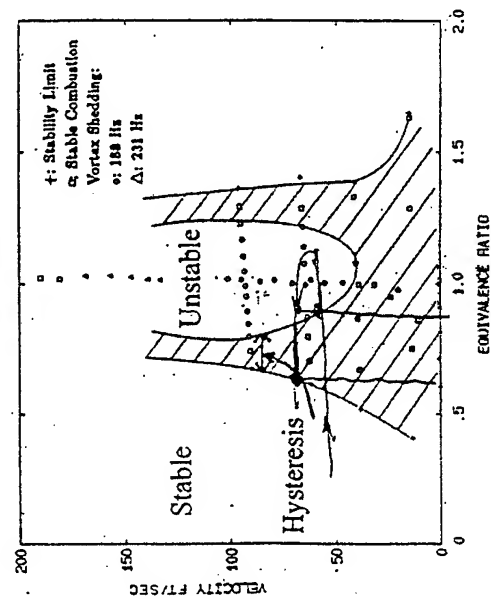
QUESTIONS ON THE ROLE OF HYSTERESIS IN ACTIVE CONTROL OF COMBUSTORS

- **How general is hysteresis in combustors?**
- **Under what conditions does hysteresis exist?**
- **What distinguishes the conditions under which:**
 - (i) **a pulse causes no transition?; and**
 - (ii) **a pulse generates transition to the lower branch?**



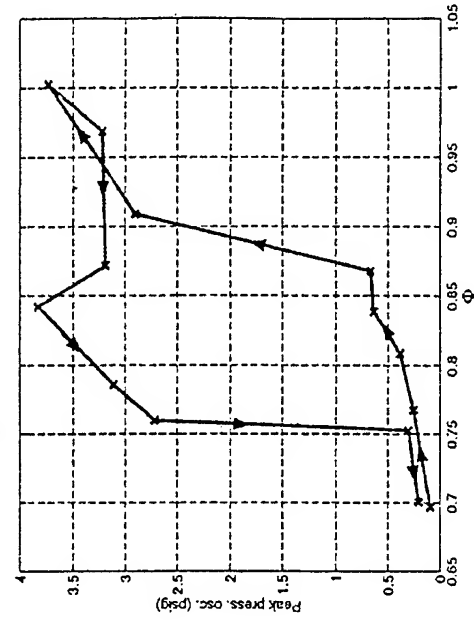
MEASURED STABILITY BOUNDARY AND HYSTERESIS LOOP

STABILITY DIAGRAM



Sterling (1987)

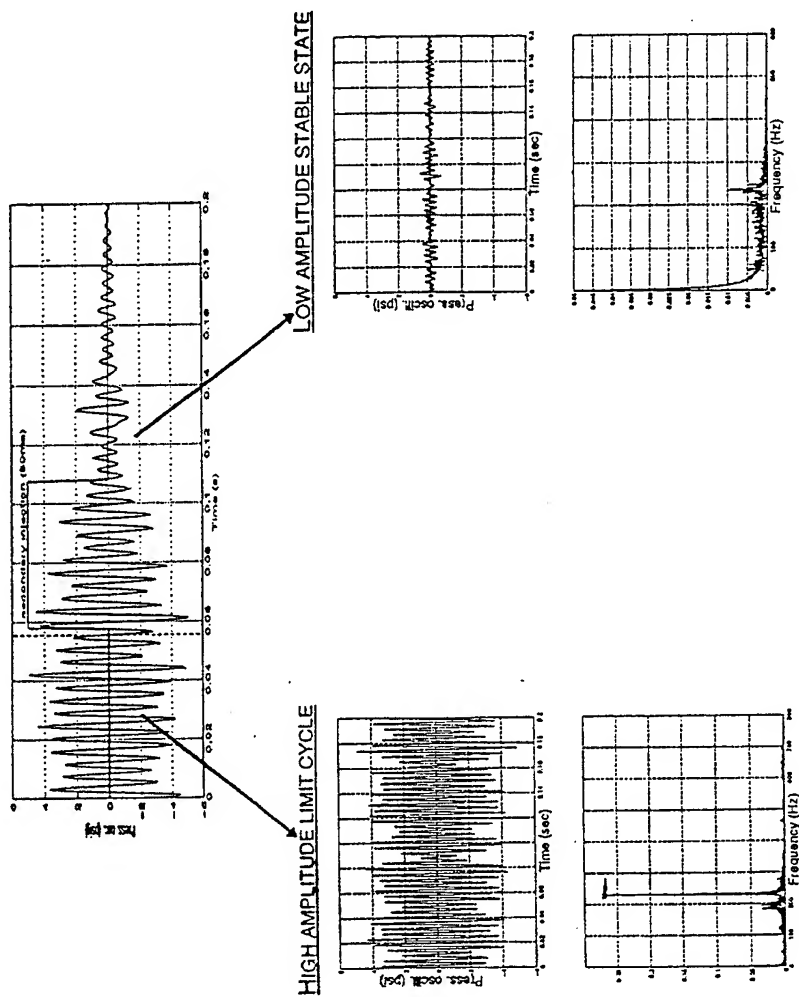
HYSTERESIS LOOP



Isella et al. (1996)



EXAMPLE OF A PULSED TRANSITION



III BIFURCATION OF STEADY STATE COMBUSTION WITH RECIRCULATION ZONES

References:

Dubinkin, B.N., Natanzon, M.S., and Cham'yan, A.E. (1978) "Two Regimes of Combustion in a Combustion chamber with a Recirculation Zone," *Physics of Combustion and Explosion*, Vol. 14, No. 6, (pp. 693-700).

Natanzon, M.S. and Men'shikova, O.M. (1992) "Bifurcation of Steady Combustion Regimes and Their Influence on the Onset of High-Frequency Oscillations in Combustion Chambers," *Physics of Combustion and Explosion*, Vol. 28, No. 4, (pp. 10-18).

Natanzon, M.S. (1999) Unsteady Combustion in Liquid Rocket Engines translated from the Russian edition (1984) with revised Chapter 8 on bifurcations. Translation editor, F.E.C. Culick.



3.1 BIFURCATION OF COMBUSTION IN A PERFECTLY-STIRRED REACTOR

References:

Bifurcations in Combustion:

Semenov, N. N. (1928) Russian Physico-Chemical Association Journal, V. 60, No. 3 (pp. 241-250).

Zel'dovich, Y. B. Barenblatt, G. I. And Librovich, V. B. (1985) Mathematical Theory of Combustion and Explosion.

Bifurcations in Perfectly-Stirred Reactors:

Vulis, L. A. (1960) Thermal Regimes of Combustion, McGraw-Hill Book Company, New York.

Longwell, J. P. and Weiss, M. A. (1955) "High Temperature Reaction Rates in Hydrocarbon Combustion," *Industrial and Engineering Chemistry*, Vol. 47, pp. 1634ff-1643.

Spalding, D. B. (1957) "Theoretical Relationships Between Combustion Intensity and Pressure Drop for One-Stream Combustion Chambers," A.R.C. 19,180 C.F. 393, Aeronautical Research Council, Great Britain.



3.1 BIFURCATION OF COMBUSTION IN A PERFECTLY-STIRRED REACTOR (cont'd)

References:

Bifurcations in Perfectly-Stirred Reactors (cont'd):

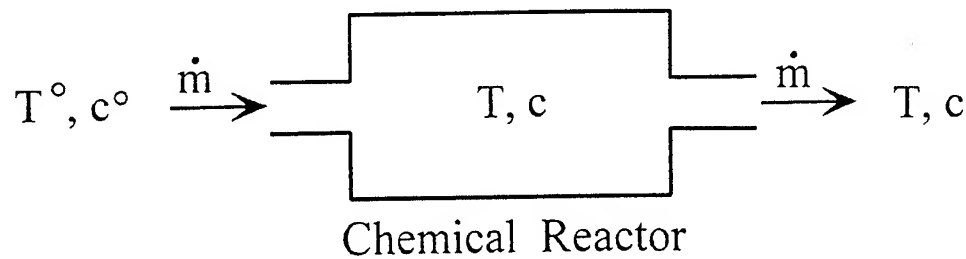
Hottel, H. C., Williams, G. C. and Bonnell, A. H.
(1958) "Application of Well-Stirred Reactor Theory to the Prediction of Combustor Performance."

- Spalding and Hottel et al treat a model of a combustor comprising a perfectly stirred reactor (mixing of reactants and recirculated products; no combustion) followed by a plug flow reactor (recirculation zone with combustion).



3.1 BIFURCATION OF COMBUSTION IN A PERFECTLY-STIRRED REACTOR (cont'd)

Reference: Vulis, L. A. Thermal Regimes of Combustion



- Assumption: Instantaneous complete mixing of inlet flow, producing uniform conditions in the volume.

$$\tau_r: \text{residence time, } \tau_r = \frac{\text{mass of reactants in volume}}{\text{mass flow rate}} = \frac{\rho V}{\dot{m}} (s)$$

$$w: \text{reaction rate, } w = \frac{c_0 - c}{\tau_r} (s^{-1})$$

Q : heat of combustion per unit mass (Energy/mass)

- Assumption: Ignore heat losses through the boundary condition for steady reaction (combustion).

c : mass concentration of reactant mixture

V : volume of reactor

ρ : density of products



3.1 BIFURCATION OF COMBUSTION IN A PERFECTLY-STIRRED REACTOR (cont'd)

Rate of Energy Release by Combustion = Net Rate of Energy Loss with Flow

$$Q_I = Q_{II} \quad (\text{per unit mass of reactants in the volume})$$

$$Q_I = wQ = \frac{c_0 - c}{\tau_s} Q = [k_0 c e^{-E/RT}] Q \quad \text{for a first order reaction}$$

$$Q_{II} = \frac{\dot{m} c_p (T - T_0)}{\rho V} = \frac{1}{\tau_s} c_p (T - T_0)$$

Rewrite the condition in terms of four dimensionless parameters

$$\theta = \frac{RT}{E} \quad (\text{temperature})$$

$$\theta_0 = \frac{RT_0}{E} \quad (\text{inlet temperature})$$

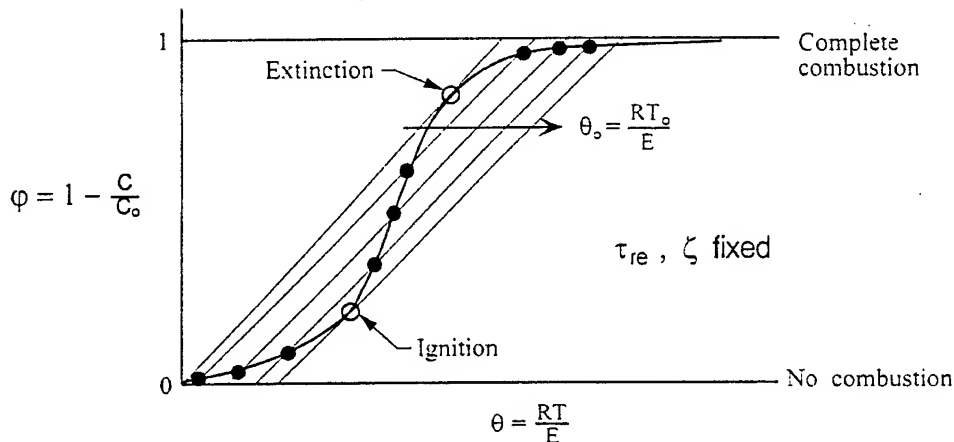
$$\xi = \frac{R c_0 Q}{c_p E} \quad (\text{heat of combustion})$$

$$\tau_{rc} = \tau_r k_0 = \frac{\tau_r}{\tau_c} \quad \left(\frac{\text{residence time}}{\text{reaction time}} \right)$$

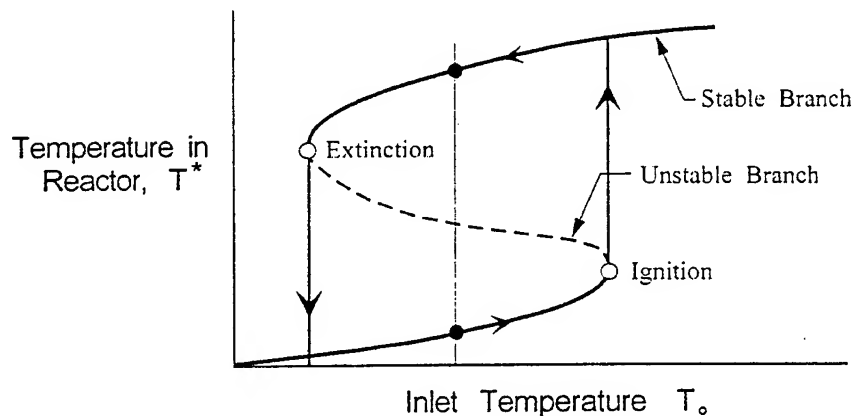


3.1 BIFURCATION OF COMBUSTION IN A PERFECTLY-STIRRED REACTOR (cont'd)

Define: $\phi = 1 - \frac{c}{c_0}$ concentration of reacted mixture leaving the reactor.



Replot to show hysteresis loop:



Subcritical bifurcation with turning points occurs because:

- 1) Energy loss is a linear function of temperature
- 2) Energy gain is a nonlinear function of temperature having a 'special' form

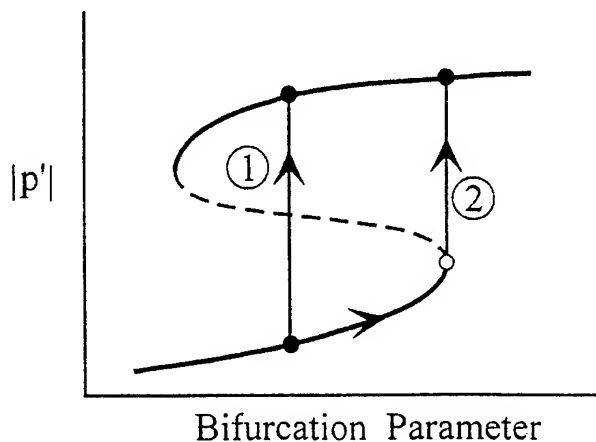


3.2 BIFURCATION OF STEADY COMBUSTION WITH RECIRCULATION ZONES; Connections With Loss of Stability

Reference: Natanzon et al.

Motivation

- In general there are two classes of mechanisms for loss of stability:
 - linear instability: 'soft excitation', supercritical bifurcation
 - nonlinear instability: 'hard excitation', subcritical bifurcation
- Instabilities arising from subcritical bifurcations may be generated in two ways:
 - 1) sufficiently large disturbances applied to the system operating in the lower branch;
 - 2) during transient changes the system may be taken to the lower turning point, then making the transition to the upper branch:



3.2 BIFURCATION OF STEADY COMBUSTION WITH RECIRCULATION ZONES; Connections With Loss of Stability (cont'd)

- If instabilities are found far from the linear stability boundary, a possible cause is subcritical bifurcation of combustion.
 - In the absence of large disturbances, path ② may be the cause, identified by connection with the history of the operating state.

Idea:

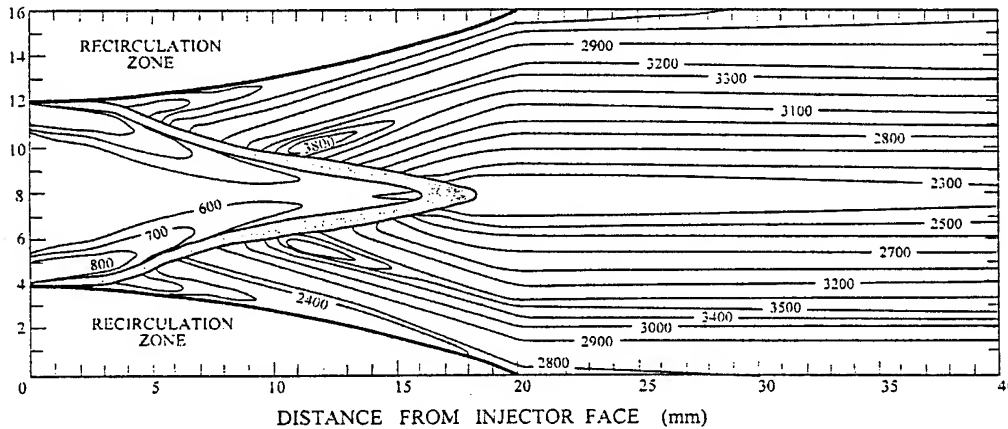
- Bifurcation of steady combustion is associated with behavior of recirculation zones treated as one-dimensional perfectly stirred (homogeneous) reactors.
- The length of the recirculation zone becomes the bifurcation parameter.
- An essential assumption is that local ignition of the injected reactants (gas/gas or liquid/gas) may occur in two ways.
 - 1) presence of hot combustion products from the recirculation zone;
 - 2) 'self-ignition' of the injected reactants due to high initial temperature at the injector outlet, or low activation energy.



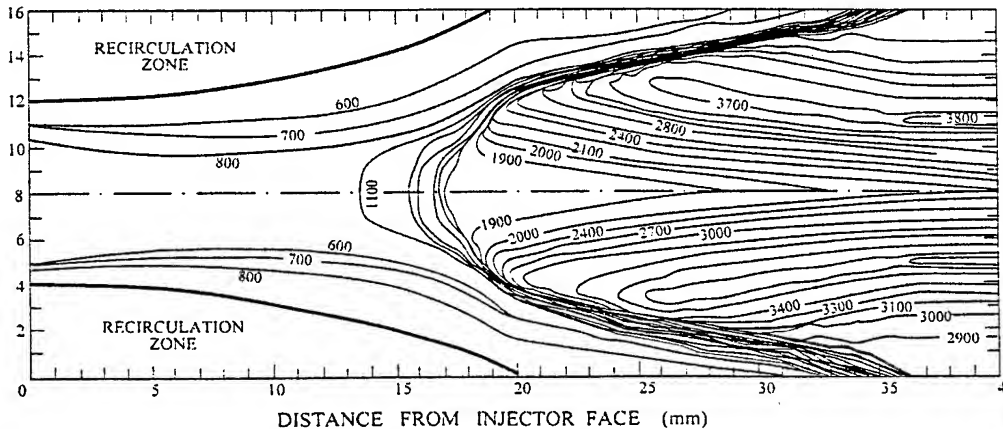
Connections With Loss of Stability (cont'd)

- injector.

Ignition by Recirculation Zone



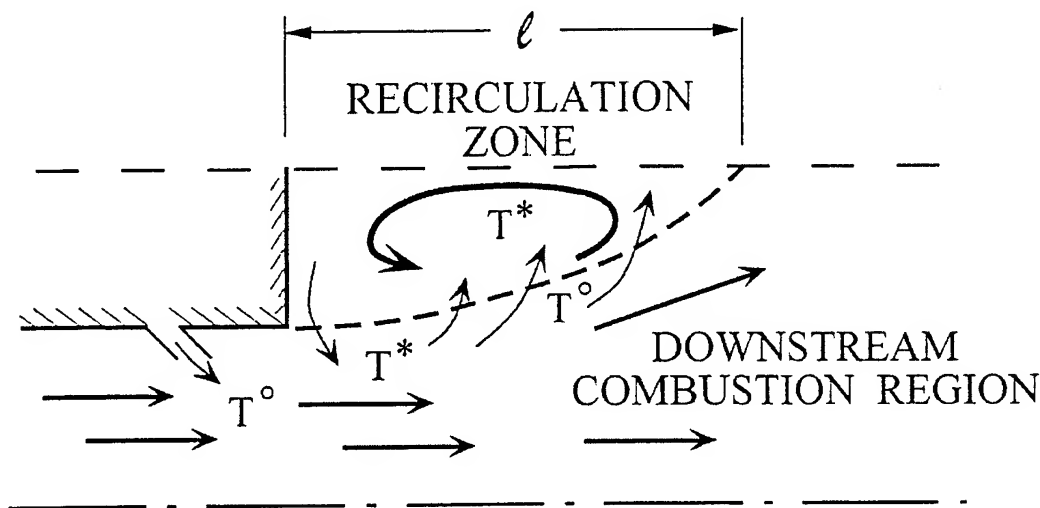
Self-Ignition in the Bulk Flow



3.3 NATANZON'S ANALYSIS OF COMBUSTION WITH RECIRCULATION ZONES

- The analysis is based on a simplified physical model: the results should be regarded as suggestive of the behavior described above

Physical Model:



- The field is approximated as a one-dimensional steady flow:
- Recirculation zone is followed by the combustion region downstream.



3.3 NATANZON'S ANALYSIS OF COMBUSTION WITH RECIRCULATION ZONES (cont'd)

- A condition for steady combustion in the recirculation zone is set in analogy with the condition $Q_I = Q_{II}$ constructed for a perfectly stirred reactor, but flow enters due to entrainment and leaves at the upstream face, having the temperature T^* of the zone.
- For analysis of the recirculation zone, the external flow from the injection port is implicit, being the source of the entrained flow.
- As for the perfectly stirred reactor, there exist conditions under which steady states exist: one is stable, and two are unstable.
 - i) Low temperature stable state with 'no' combustion in the recirculation zone. The main flow must 'self-ignite' at the end or downstream of the recirculation zone.
 - ii) High temperature stable state representing combustion in the recirculation zone. The flow leaving the zone at the injector face ignites the main flow.



3.3 NATANZON'S ANALYSIS OF COMBUSTION WITH RECIRCULATION ZONES (cont'd)

Condition for steady combustion:

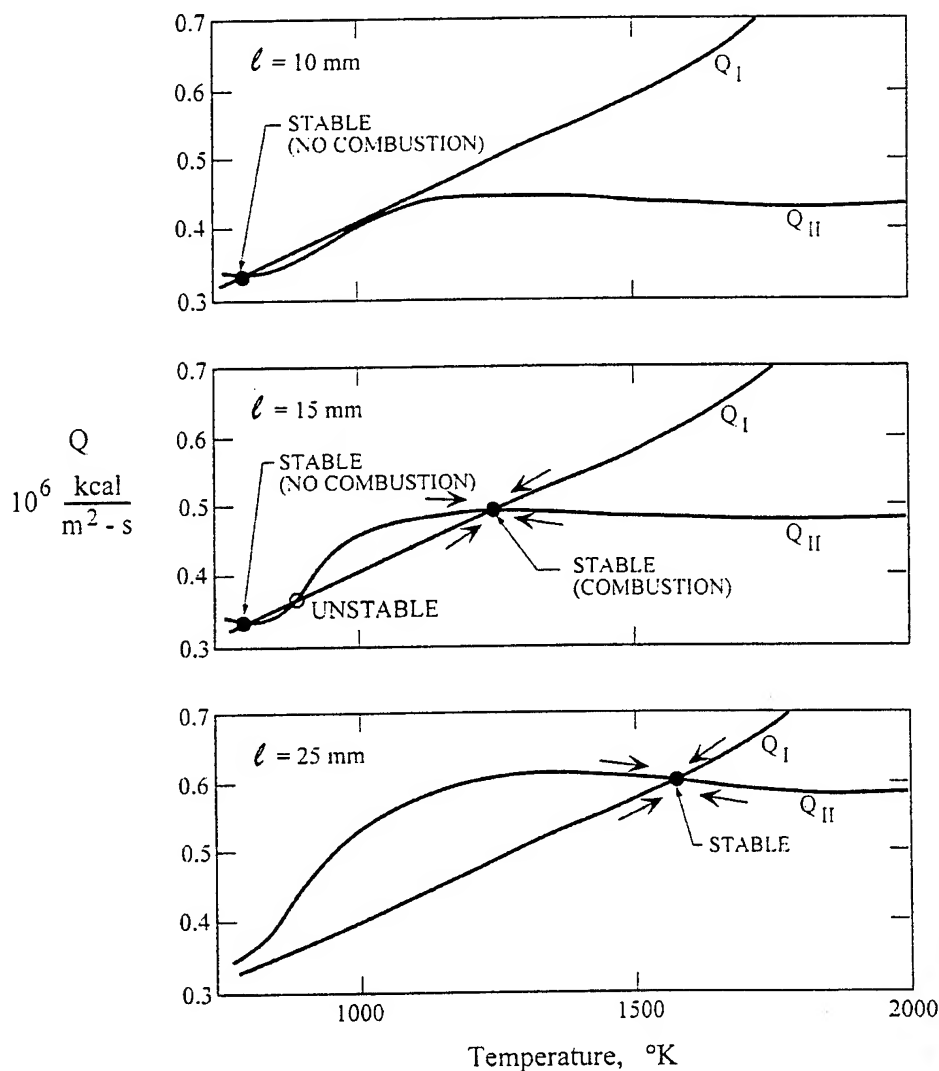
$$Q_I(T^*) = Q_{II}(T^*)$$

$$(\rho u C_p \tilde{T})^* - (\rho u C_p T)^0 = w H_o \ell - B \Delta \rho u$$

Net Energy Flow
out of
Recirculation
Zone

Energy
Released
by
Combustion

Energy
Absorbed
by
Liquid Fuel



3.3 NATANZON'S ANALYSIS OF COMBUSTION WITH RECIRCULATION ZONES (cont'd)

Equations Solved for Recirculation Zone

Gas Flow:

$$\frac{d}{dx}(\rho u) = G_{\rho u}$$

$$\Rightarrow \Delta(\rho u) = G_{\rho u} \ell$$

$G_{\rho u}$: vaporization rate

v_f, v_o, v_p : mass concentrations

$$v_f + v_o + v_p = 1$$

Combustion Products:

$$\frac{d}{dx}(\rho u v_p) = w$$

$$\Rightarrow v_p \Delta(\rho u) = w \ell$$

$$\Delta(\rho u) = (\rho u)^* - (\rho u)^o$$

Fuel Vapor:

$$\frac{d}{dx}(\rho u v_f) = G_{\rho u} - \frac{1}{1+k_0} w$$

$$\Rightarrow v_f \Delta(\rho u) = \Delta(\rho u) - \frac{1}{1+k_0} w \ell$$

$G_{\rho u}$: vaporization rate
of fuel drops



3.3 NATANZON'S ANALYSIS OF COMBUSTION WITH RECIRCULATION ZONES (cont'd)

Energy:

$$\frac{d}{dx}(\rho u h) = w H_0 - G_{\rho u} [C_f (T_s - T_s^0) + \xi (T_s)] + G_{\rho u} C_p T_s$$

T_s : surface temperature of fuel drops

C_f : heat capacity of fuel

ξ : heat of vaporization

$$\Rightarrow (\rho u C_p \tilde{T})^* - (\rho u C_p \tilde{T})^0 = w H_0 \ell - B \Delta(\rho u)$$

$$B := C_f (T_s - T_s^0) + \xi (T_s) - C_p T_s$$

$$\tilde{T} := T + h_d / C_p$$

Motions of Fuel Drops:

$$\frac{dv}{dx} = G_v \quad ; \quad \frac{dm}{dx} = G_m$$

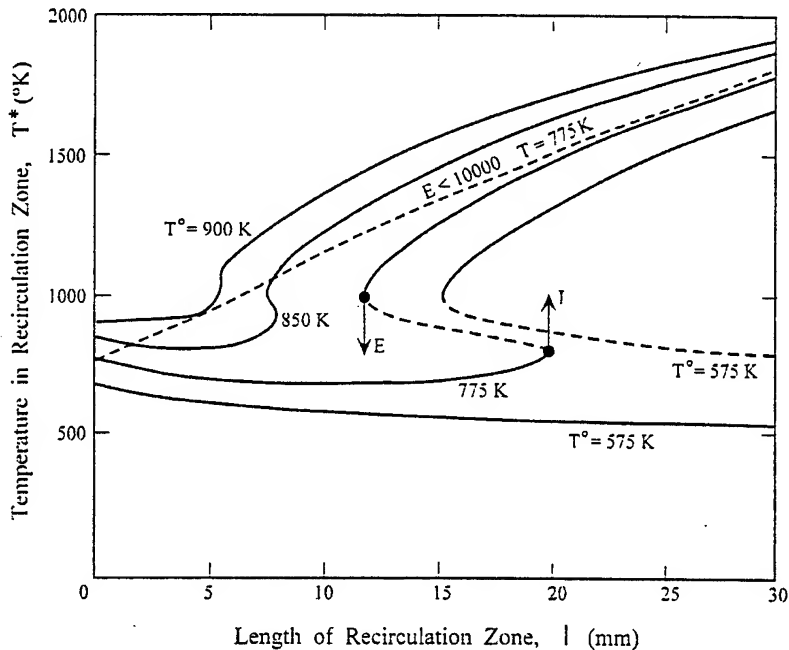
v: velocity

m: mass



3.3 NATANZON'S ANALYSIS OF COMBUSTION WITH RECIRCULATION ZONES (cont'd)

- The true meaning of the model and the calculations is NOT clear in the two references but it appears that the model is virtually identical to that for a PSR.
- Solution is obtained by iteration giving the results sketched above.
- The results of the calculations for the recirculation zone can be displayed in the bifurcation diagram, a replot of the results given above:



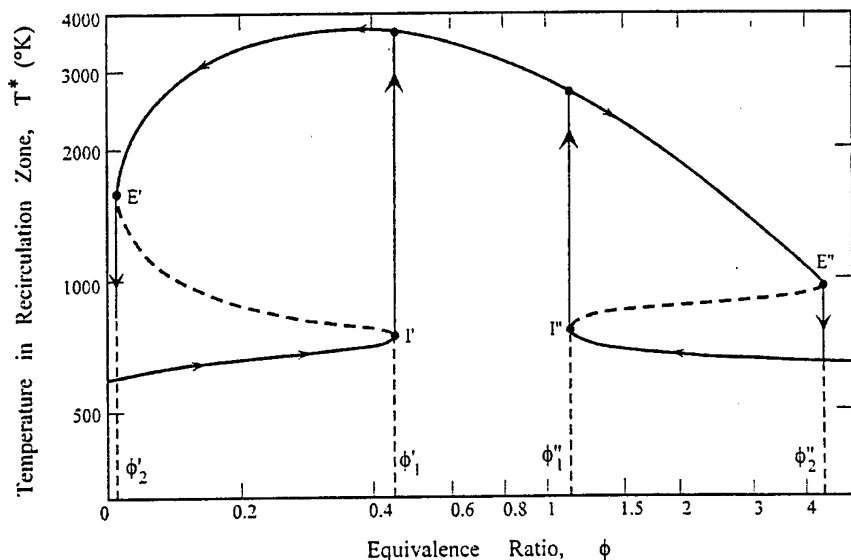
- This figure shows that for initial temperatures T^0 higher than about 830°K only the high temperature state of combustion exists in the recirculation zone.



3.3 NATANZON'S ANALYSIS OF COMBUSTION WITH RECIRCULATION ZONES (cont'd)

- For a range of $T^0 < 830^\circ\text{K}$, say $T^0 = 775^\circ\text{K}$, two stable states are possible for, in this case, $1.2\text{cm} < \ell < 2.0\text{cm}$.
 - For $T^0 = 775^\circ\text{K}$, as ℓ increases, the temperature remains low in the recirculation zone until $\ell \approx 2\text{cm}$ when ignition occurs.
 - Then ℓ is reduced, combustion is sustained until $\ell \approx 1.2\text{cm}$ when extinction occurs.
- Multiple states can also be obtained if for a fixed length of recirculation zone the equivalence ratio α (i.e. the F/O mixture ratio) is changed, consequently changed the heat of combustion.

The next figure shows the bifurcation diagram in the coordinates: temperature T^* in the recirculation zone versus ϕ , the equivalence ratio.



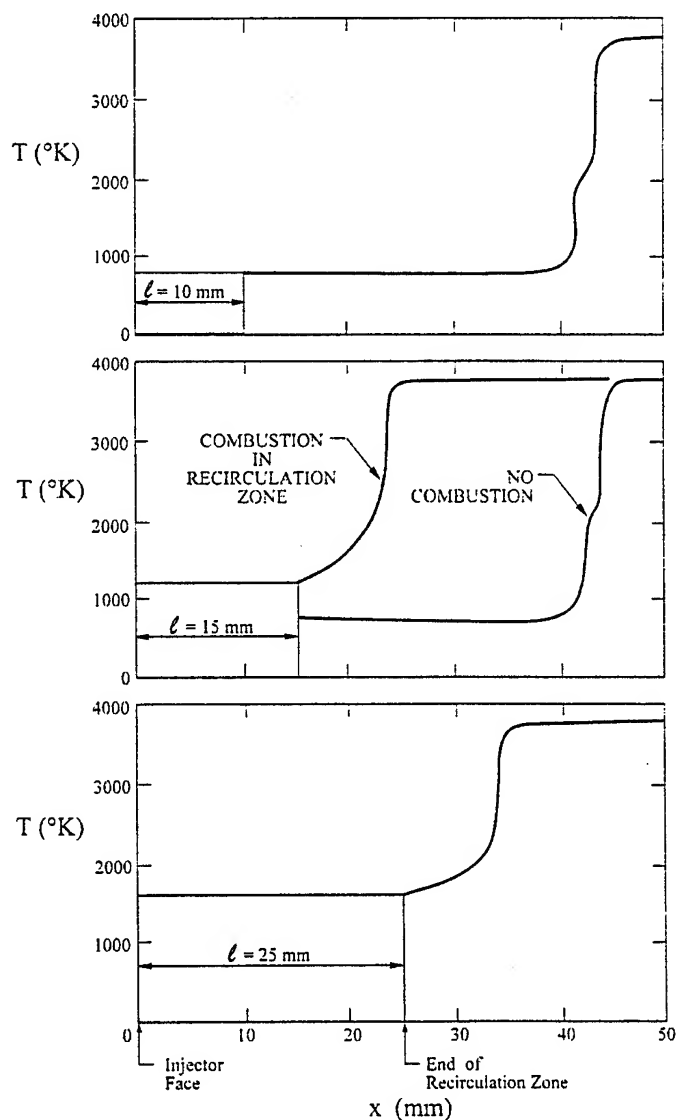
- Note that in this setting two hysteresis loops exist.



3.3 NATANZON'S ANALYSIS OF COMBUSTION WITH RECIRCULATION ZONES (cont'd)

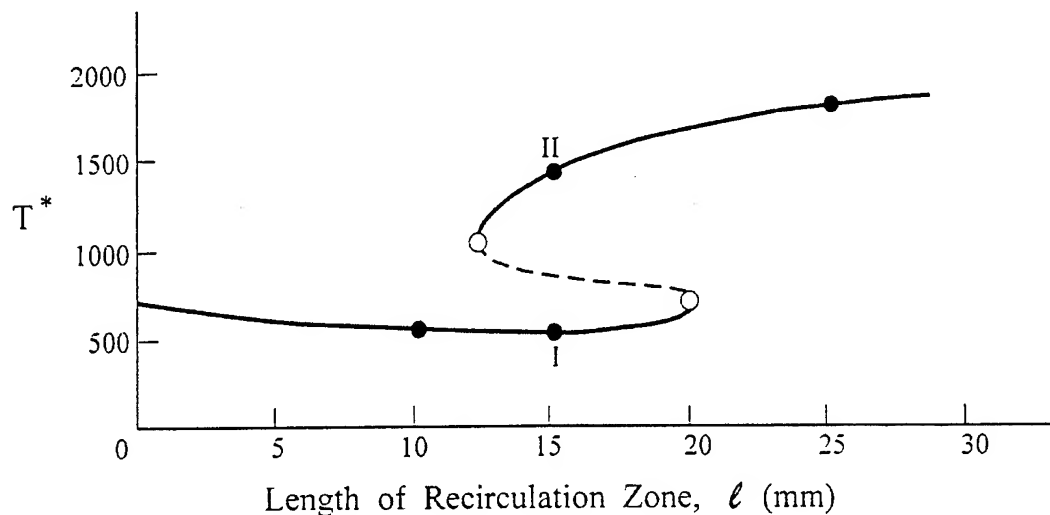
Combustion and The Temperature Field Outside the Recirculation Zone

- Natanzon and Men'shikova (1992) have reported the following results for the temperature field outside the recirculation zone, obtained by solving one-dimensional equations with $T^0 = 775^\circ\text{K}$ and $\phi = ?$



3.3 NATANZON'S ANALYSIS OF COMBUSTION WITH RECIRCULATION ZONES (cont'd)

- The sequence of these cases falls as shown in the bifurcation diagram:



- Some of the detailed behavior of these curves depends on the model of droplet combustion, fragmentation,...
- Note that the overall steady combustion process in the chamber is hardly affected by the particular condition in the recirculation zone:
 - ~ if the chamber is sufficiently long, the combustion efficiency and exit temperature are essentially identical in all cases
- In respect to the excitation of combustion instabilities, when there are multiple steady states, the question is:

Which of the steady states is less stable?

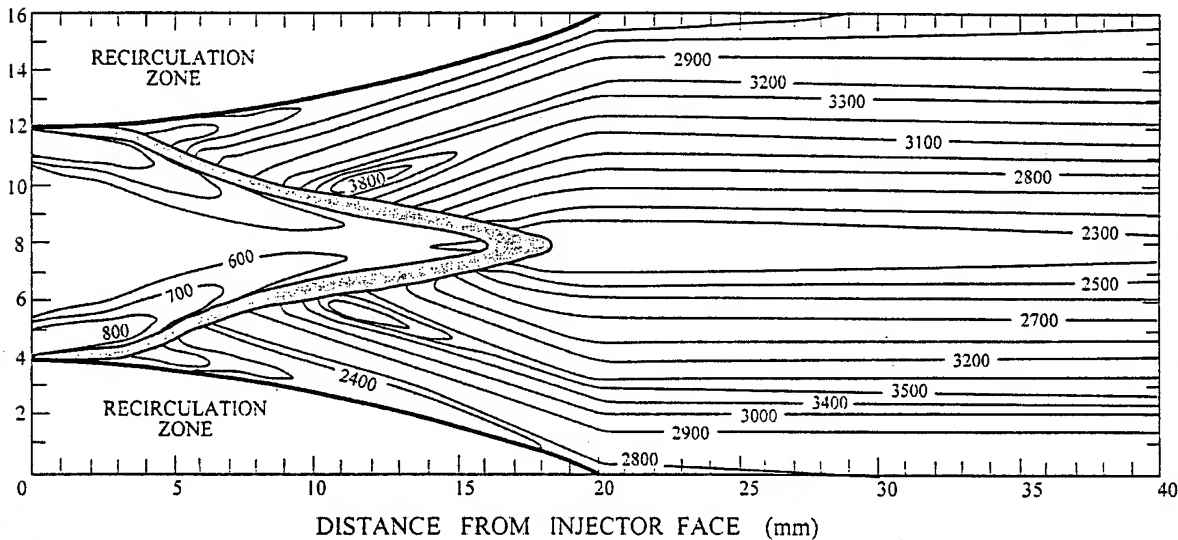


3.3 NATANZON'S ANALYSIS OF COMBUSTION WITH RECIRCULATION ZONES (cont'd)

- Because the current existence of a particular steady state depends on the history of the operating point of the chamber, the possibility for ‘randomly’ occurring instabilities is exposed.

A Two-Dimensional Model for Combustion with Bifurcations

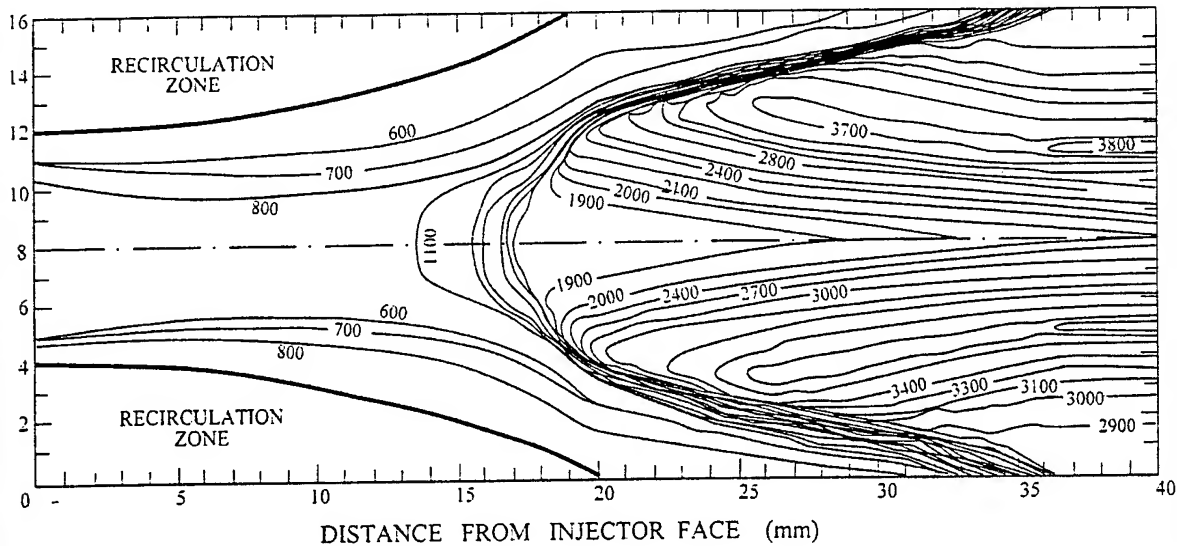
- A model is constructed for gas/gas reactants.
- The recirculation zone is treated as a perfectly stirred reactor but flows in and out are included.
 - A condition for stationary combustion enforced.
- Details of the flow outside the recirculation zones are incomplete.
- Results show the existence of two states of steady combustion:



Ignition by Recirculation Zone



3.3 NATANZON'S ANALYSIS OF COMBUSTION WITH RECIRCULATION ZONES (cont'd)



Self-Ignition in the Bulk Flow

Stability of the Two States of Steady Combustion

- Natanzon establishes the stability of the two steady states by applying his method based on the amplitude-phase-frequency characteristic (APFC) interpreted as a "hodograph."
- A recirculation zone is a passive capacitance, providing distributed sources along its boundary.



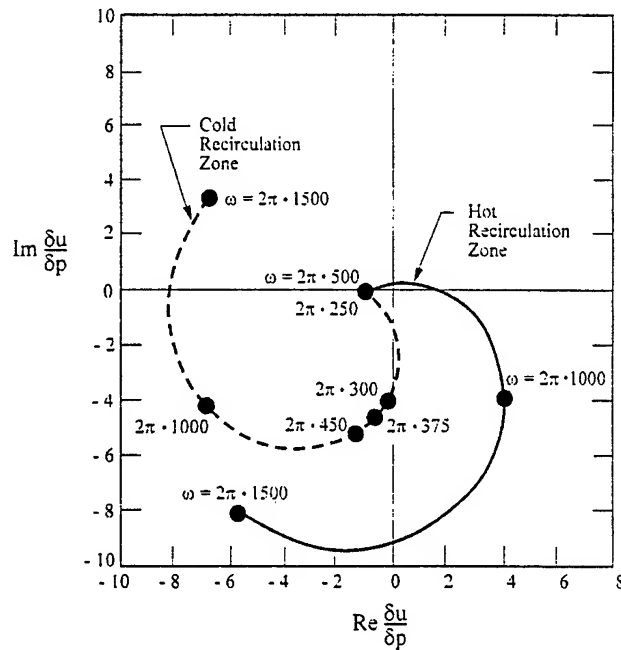
3.3 NATANZON'S ANALYSIS OF COMBUSTION WITH RECIRCULATION ZONES (cont'd)

- The method comes down to examining the behavior of the transfer function $R(i\omega)$ for the combustion zone:

$$R(i\omega) = \frac{\delta u}{\delta p}$$

δu : velocity fluctuation at the

δp : pressure fluctuation



- $\mathcal{R}e\left(\frac{\delta u}{\delta p}\right) > 0 \Rightarrow$ tendency to instability. (Natanzon)
- Consistent with Rayleigh: move Q where p is high

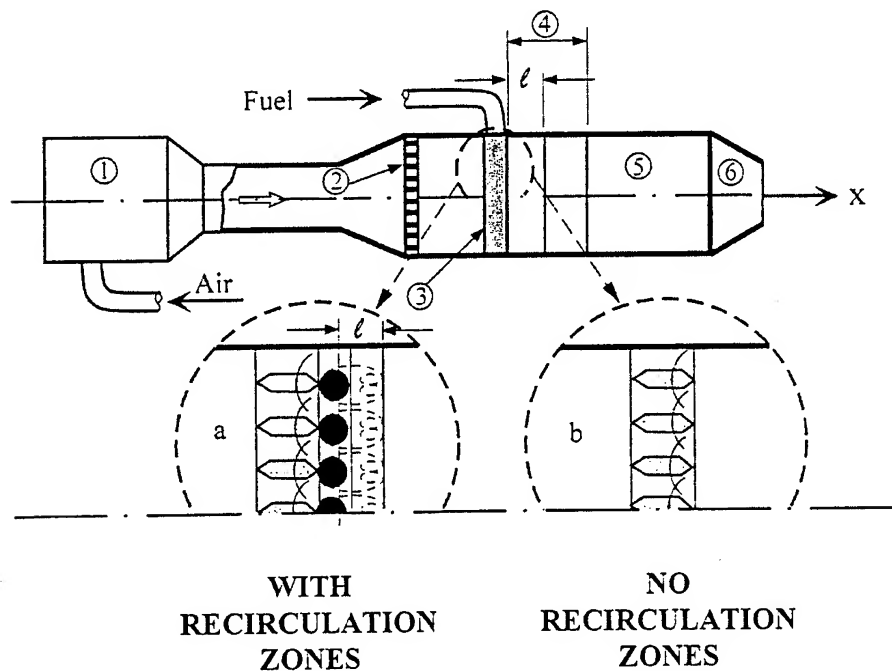
HENCE the state with a hot (combusting)
recirculation zone is more unstable.



3.3 NATANZON'S ANALYSIS OF COMBUSTION WITH RECIRCULATION ZONES (cont'd)

Experimental Results Confirming the Possible Influences of Recirculation Zones

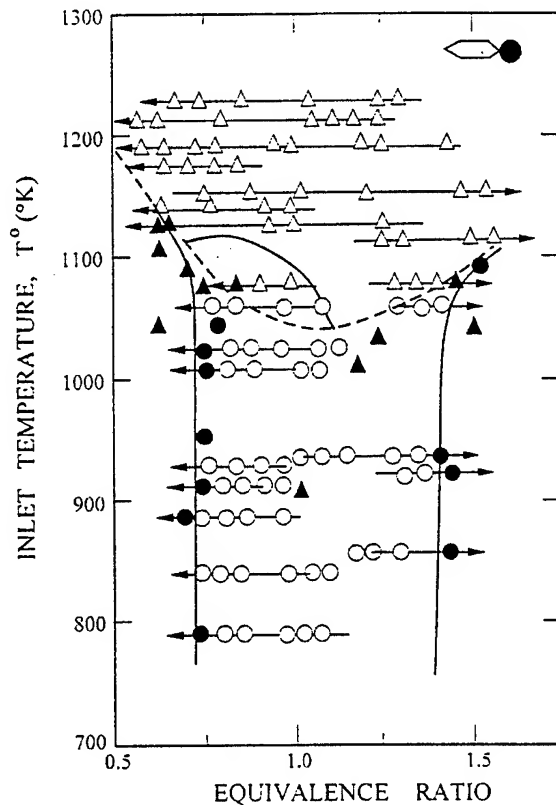
- The figure shows laboratory apparatus specially constructed to demonstrate qualitative changes of stability when recirculation zones are present.
 - Tests were run with and without recirculation zones; recirculation zones were created by mounting a cascade of rods immediately downstream of the pylons through which fuel was injected in an air stream.



- In all tests, the chief experimental variables were the temperature T^0 of the inlet air and the equivalent ratio.
- The reactants were liquid fuel and heated air.



3.3 NATANZON'S ANALYSIS OF COMBUSTION WITH RECIRCULATION ZONES (cont'd)

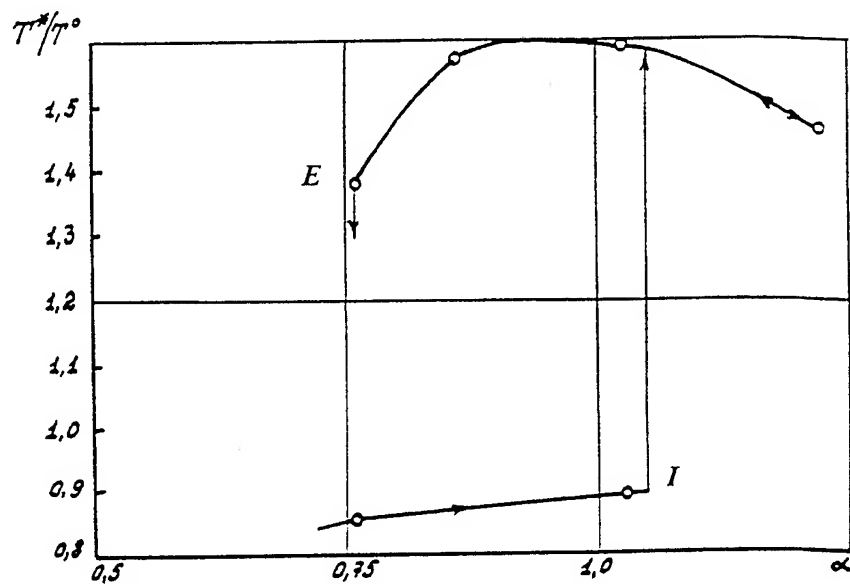


- Tests with no recirculation zones showing the conditions for combustion and no ignition or extinction.
 - boundary of extinction
 - Δ steady combustion
 - \blacktriangle no combustion
- The extinction boundary is essentially coincident with the boundary of self-ignition (apparently no ignition was used) and T^0 is minimum when $\phi = 1$.
- Tests with turbulence-inducing cascade (and recirculation zones)
 - boundaries of extinction
 - \circ steady combustion
 - \bullet no combustion
 - \blacksquare region in which hysteresis is observed



3.3 NATANZON'S ANALYSIS OF COMBUSTION WITH RECIRCULATION ZONES (cont'd)

- Experimental results for hysteresis are shown in the figure below.



IV INCORPORATING BIFURCATION OF COMBUSTION IN ANALYSIS OF COMBUSTOR DYNAMICS

References:

Culick, F. E. C., Paparizos, L., Sterling, J., and Burnley, V. (1992) "Combustion Noise and combustion Instabilities in Propulsion Systems," AGARD CP 512.

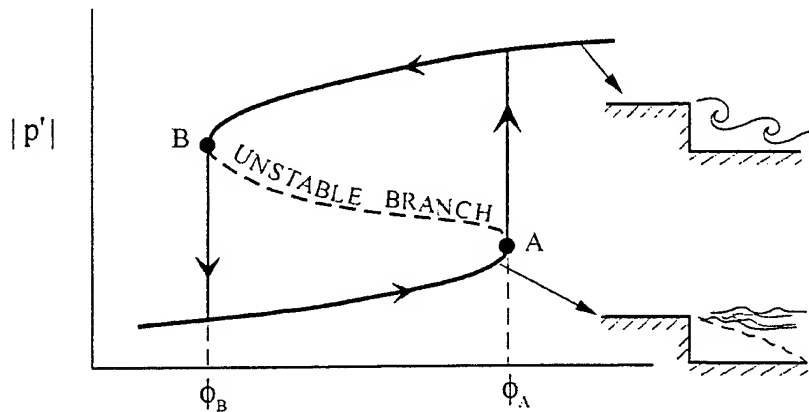
Burnley, V. (1990) "Nonlinear Combustion Instabilities and Stochastic Sources," Ph.D. Dissertation, California Institute of Technology.



INCORPORATING A GLOBAL BIFURCATION OF COMBUSTION IN ANALYSIS OF COMBUSTOR DYNAMICS

- Two apparently different types of subcritical bifurcations have been described, both involving recirculation zones in essential ways.

1) Bifurcation of dynamical states, showing the existence of two steady oscillatory states in a dump combustor:



- A: loss of linear stability and development of steady limit cycles for all $\phi \geq \phi_n$
 B: absolute linear stability for $\phi \geq \phi_B$

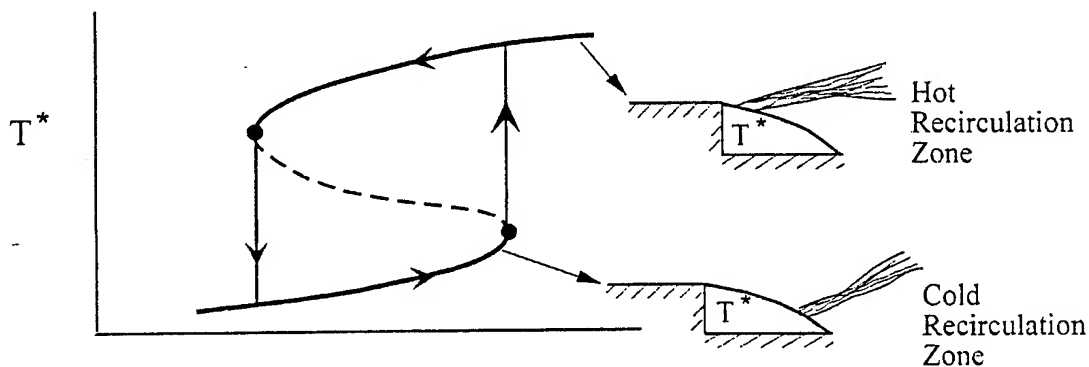
Lower branch: weak oscillations: stable linear modes driven by noise sources independent of the acoustic field.

Upper branch: strong oscillations in stable limit cycles characterized by the balance of energy (power) gains and losses; the behavior is intrinsically nonlinear (gains of losses or both).



INCORPORATING A GLOBAL BIFURCATION OF COMBUSTION IN ANALYSIS OF COMBUSTOR DYNAMICS (cont'd)

- 2) Bifurcation of steady states, one of which is linearly stable and one linearly unstable, developing stable limit cycles.



- The two types of bifurcation involve physical behavior differing in detail but which can be formally accommodated in the same theoretical framework.
- Note that the scales of the recirculation zones differ in the two cases because the scales of the combustor differ.
- In liquid rockets, many 'small' recirculation zones exist at the injector face. The problem of cooperative behavior to produce a bifurcation of dynamical behavior in the combustor remains unsolved: interactions among the zones is sufficient and probably necessary.



INCORPORATING A GLOBAL BIFURCATION OF COMBUSTION IN ANALYSIS OF COMBUSTOR DYNAMICS (cont'd)

- Analysis based on modal expansion and spatial averaging suggests the strategy to follow.

Modal Expansion

$$p'(\vec{r};t) = \bar{p} \sum \eta_i(t) \psi_i(\vec{r})$$

Spatial Averaging

$$\frac{d^2 \eta_n}{dt^2} + \omega_n^2 \eta_n = F_n$$

$$F_n = -\frac{\bar{a}^2}{\bar{p} E_n^2} \left\{ \int h \psi_n dV + \oint f \psi_n dV \right\}$$

where h, f represent volumetric and surface sources of pressure disturbances:

$$\nabla^2 p' - \frac{1}{\bar{a}^2} \frac{\partial^2 p'}{\partial t^2} = h ; \quad \hat{n} \cdot \nabla p' = -f$$

- The functions h and f contain purely gasdynamical parts and sources of mass, momentum, and energy due, primarily, to combustion processes and interaction between gaseous and condensed phases.
- Some of the sources may be due to actuation associated with some means of active control.



INCORPORATING A GLOBAL BIFURCATION OF COMBUSTION IN ANALYSIS OF COMBUSTOR DYNAMICS (cont'd)

- Gasdynamics alone cannot produce subcritical bifurcations. Hence the behavior sought must be associated with other sources, in particular the dynamics of the energy release accompanying combustion processes.
- As a result of the spatial averaging, the dynamical consequences of volumetric and surface sources (h , f) are equivalent.

$$\nabla^2 p' - \frac{1}{\bar{a}^2} \frac{\partial^2 p'}{\partial t^2} = h \qquad \hat{n} \cdot \nabla p' = -f$$

Modal Expansion and Spatial Averaging:

$$\frac{d^2 \eta_n}{dt^2} + \omega_n^2 \eta_n = 0 ; \quad F_n = -\frac{\bar{a}^2}{\bar{p} E_n^2} \left\{ \int h \psi_n dV + \oint f \psi_n dS \right\}$$

With volumetric energy release Q_R and mass injection at the lateral boundary:

$$(F_n)_{\text{COMB}} = \frac{\bar{a}^2}{\bar{p} E_n^2} \left\{ \frac{\gamma-1}{\bar{a}^2} \int \frac{\partial \dot{Q}'_R}{\partial t} \psi_n dV + \oint \frac{\partial m'_b}{\partial t} \psi_n dS + \oint \frac{\partial p'}{\partial t} [\bar{u}_b + (u'_b)_{\text{linear}}] \psi_n dS \right\}$$

Accounting for volumetric energy addition only:

$$(F_n)_{\text{COMB}} = \frac{\gamma-1}{\bar{p} E_n^2} \int \frac{\partial \dot{Q}'_R}{\partial t} \psi_n dV$$



INCORPORATING A GLOBAL BIFURCATION OF COMBUSTION IN ANALYSIS OF COMBUSTOR DYNAMICS (cont'd)

QUESTION: What nonlinear behavior of \dot{Q}'_R is necessary to produce a subcritical bifurcation in the chamber dynamics?

Two proposals:

A. Sterling (1993) "Nonlinear Analysis and Modeling of Combustion Instabilities in a Laboratory Combustor," Combustion Science and Technology, Vol. 89 (pp. 167-179)

- Modeling time-dependent heat release associated with combustion in periodically shed vortices to explain nonlinear behavior in the Caltech dump combustor.
- Rayleigh's Criterion is used to obtain an estimate for a Poincaré map:

$$\Delta \xi_n = \frac{\gamma-1}{\bar{p}E_n^2} \omega_n^2 \int \psi_n dV \int_t^{t+\tau} \eta_n \dot{Q}' dt'$$

The map displays the cycle-to-cycle increments of the energy in a modal oscillator.



INCORPORATING A GLOBAL BIFURCATION OF COMBUSTION IN ANALYSIS OF COMBUSTOR DYNAMICS (cont'd)

- Two models of \dot{Q}_r' proposed:

1) Periodic Delayed Combustion Response

Physical Basis: (observations)

- (i) For small amplitudes, a small shed vortex is surrounded by hot combustion products from the previous cycle: shorter time delay and less energy released.
- (ii) For large amplitudes, a large shed vortex interacts with the wall, creating a region of cold reactants: a longer time delay is associated with larger energy release.

Model: Energy released in the vortex shedding is proportional to the acoustic velocity, with a time delay (relative to the pressure oscillation) linear in the acoustic oscillator energy



INCORPORATING A GLOBAL BIFURCATION OF COMBUSTION IN ANALYSIS OF COMBUSTOR DYNAMICS (cont'd)

Realization:

$$\dot{Q}' = Q(\bar{r})\dot{\eta}(t-\tau)$$

$$\eta = \sqrt{\xi} \sin \omega t \quad (\text{Single Mode})$$

$$\tau = c_1 \xi$$

Substitute in Rayleigh's Criterion

$$\xi_{j+1} = \xi_j [1 + c_2 \sin \xi_j]$$

A one-dimensional map with bifurcation parameter c_2 .

2) "Twice-Kicked" Oscillator

Physical Basis: (observations)

- (i) A vortex is shed when the velocity at the dump plane is rising during each cycle.
- (ii) For 'small' vortices, combustion occurs later in the cycle, nearly to completion, producing a broad 'pulse' of pressure.
- (iii) For 'large' vortices, combustion is not complete in the first pulse and occasionally smaller secondary pulses of pressure occur.



INCORPORATING A GLOBAL BIFURCATION OF COMBUSTION IN ANALYSIS OF COMBUSTOR DYNAMICS (cont'd)

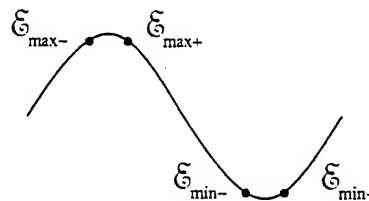
Model: The energy released is modeled as two pulses (δ -functions) in time. A large amplitude pulse always occurs when the pressure is near maximum, and rising, causing growth. For 'large' amplitudes a pulse also occurs when the pressure is minimum, tending to alternate the oscillations.

Realization:

Use Rayleigh's Criterion to construct the relations for energies at maxima and minima of pressure:

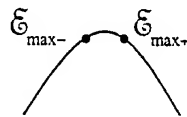
Free Oscillation:

$$\xi_{\max+} = \xi_{\min-}$$



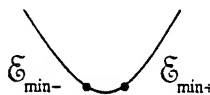
Pulse near p_{\max} :

$$\xi_{\max+} = \xi_{\max-} + c_1 \xi_{\max-}$$



Pulse near p_{\min} :

$$\xi_{\min+} = \xi_{\min-} - c_2 \xi_{\min-}$$



Combine and renormalize:

$$\xi_{j+1} = c_3 (\xi_j - c_4 \xi_j^2)$$

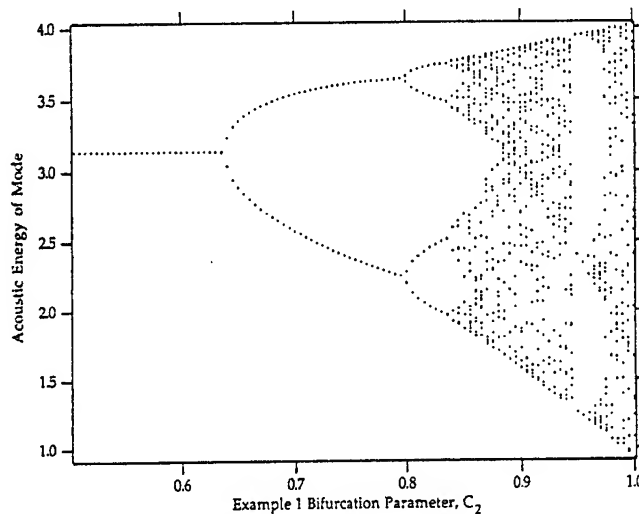
Bifurcation parameter
 c_3 for c_4 fixed



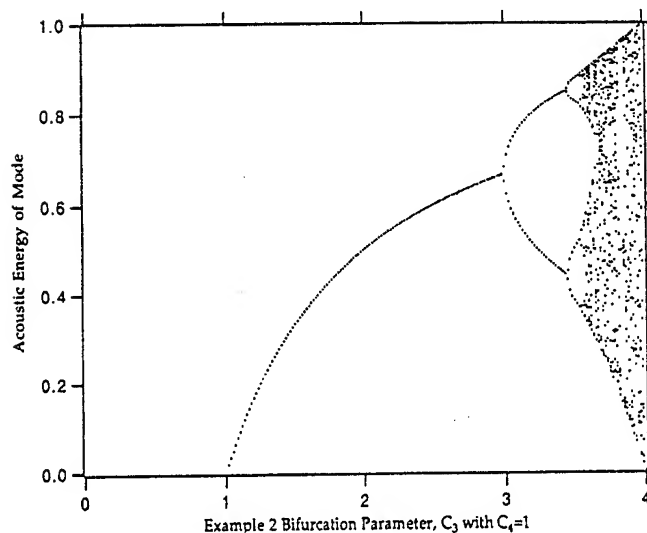
INCORPORATING A GLOBAL BIFURCATION OF COMBUSTION IN ANALYSIS OF COMBUSTOR DYNAMICS (cont'd)

The bifurcation diagrams for the two cases are shown in the following two figures. In each case, period-doubling bifurcations occur, leading to chaotic behavior not observed in the experimental results.

DELAYED COMBUSTION RESPONSE



"TWICE-KICKED" OSCILLATOR



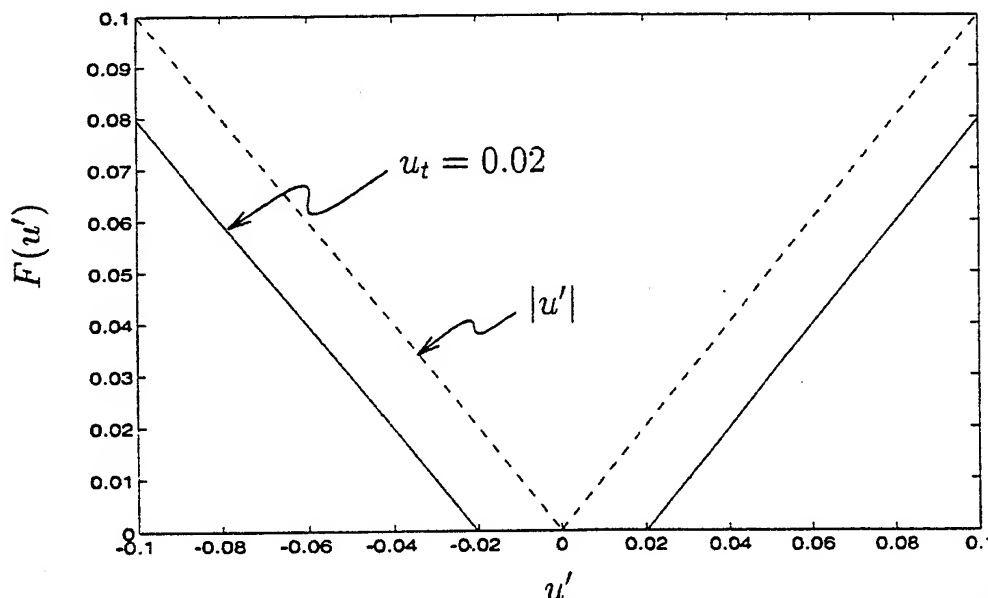
INCORPORATING A GLOBAL BIFURCATION OF COMBUSTION IN ANALYSIS OF COMBUSTOR DYNAMICS (cont'd)

- The question remains: can these ideas be adapted in such a fashion as to provide an explanation for the subcritical bifurcation and hysteresis shown by the experimental results?

V. Burnley (1996) "Nonlinear Combustion Instabilities and Stochastic Sources," Ph.D. Thesis, California Institute of Technology.

- Modeling the time-dependent heat release for distributed combustion following the models of Levine and Baum(1983) and Greene (1990).

$$\dot{m}' = \bar{m} R_{vc} F(|\bar{u}' - \bar{u}_t|) \quad \text{or} \quad \dot{Q}' = \bar{Q} q_{vc} F(|\bar{u}' - \bar{u}_t|)$$



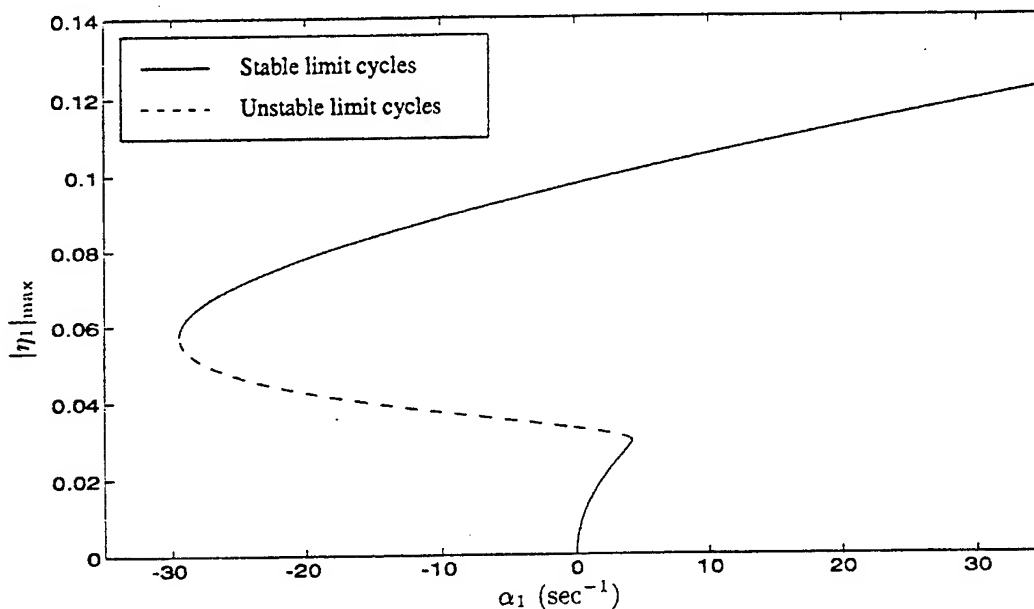
- The threshold velocity u_t is necessary to give a subcritical bifurcation.



INCORPORATING A GLOBAL BIFURCATION OF COMBUSTION IN ANALYSIS OF COMBUSTOR DYNAMICS (cont'd)

- With the above representation of \dot{m}' or \dot{Q}' , application of a continuation method gives the following bifurcation diagram:

BIFURCATION DIAGRAM FOR THE DETERMINISTIC SYSTEM;
THRESHOLD VELOCITY MODEL OF NONLINEAR COMBUSTION



- For reasons not known, the usual supercritical bifurcation occurs at $\alpha_1 = 0$, followed by two turning points, giving the possibility for hysteresis and nonlinear (pulsed) instabilities.

Note: existence of a threshold velocity $\neq 0$ is essential for this result: the reasons are not known.



V SOME CONSEQUENCES OF SUBCRITICAL BIFURCATIONS WITH NOISE



5.1 REPRESENTING NOISE IN ANALYSIS OF THE GLOBAL DYNAMICS

- There are three sorts of problems:
 - Formal construction of noise (stochastic) sources in the framework of spatial averaging equations for the fluctuating motions (oscillator equations).
 - Modeling the noise sources
 - Solving the stochastic differential equations

A Construction of Noise Sources in the Oscillator Equations

- The first step is application of the principle of splitting small disturbances.

Chu, B.T. and Kovazonay, L.S.G. (1958) "Nonlinear Interactions in a Viscous Heat-Conducting Compressible Gas," Journal of Fluid Mechanics, V. 3, No. 5 (pp. 494-514).



5.1 REPRESENTING NOISE IN ANALYSIS OF THE GLOBAL DYNAMICS (cont'd)

SPLITTING THE UNSTEADY FLOW FIELD

- Chu and Kovazsnay (1958)
 - In the limit of small amplitudes, disturbances in a compressible fluid may be synthesized of three types of waves: acoustic waves, vorticity waves, and entropy waves.
 - acoustic waves carry pressure and velocity
 - vorticity waves carry vorticity and velocity
 - entropy waves carry entropy and velocity

$$p' = p'_a$$

$$\bar{\Omega}' = \bar{\Omega}'_{\Omega}$$

$$s' = s'_s$$

$$\bar{u}' = \bar{u}'_a + \bar{u}'_{\Omega} + \bar{u}'_s$$

- To second order, acoustic waves remain free of entropy and vorticity.
- Apply the principle of additive splitting to problems of second-order acoustics and nonuniform mean flow.



5.1 REPRESENTING NOISE IN ANALYSIS OF THE GLOBAL DYNAMICS (cont'd)

- Apply the principle of additive splitting to problems of second-order acoustics and nonuniform mean flow. Write the flow variables as sums of the three contributions:

$$p' = p'_a + p'_\Omega + p'_s$$

$$\bar{\Omega}' = \bar{\Omega}'_a + \bar{\Omega}'_\Omega + \bar{\Omega}'_s$$

$$s' = s'_a + s'_\Omega + s'_s$$

To first order;

$$\text{Acoustic Waves: } p' = p'_a \quad p'_\Omega = p'_s = 0$$

$$\text{Vorticity Waves: } \Omega' = \Omega'_\Omega \quad \Omega'_a = \Omega'_s = 0$$

$$\text{Entropy Waves: } s' = s'_s \quad s'_a = s'_\Omega = 0$$

The velocity field contains all three:

$$\bar{u}' = \bar{u}'_a + \bar{u}'_\Omega + \bar{u}'_s$$

Note: The vorticity field may contain, to first order, random contributions (noise) and terms arising, for example, from generation of vorticity at a lateral surface with mass injection.



5.1 REPRESENTING NOISE IN ANALYSIS OF THE GLOBAL DYNAMICS (cont'd)

A. Procedure:

(i) Write $p = \bar{p} + p'$, $\vec{u} = \bar{\vec{u}} + \vec{u}'$ etc. in the general conservation equations expanded to 3rd order in ()'

(ii) Form the nonlinear wave equation for the pressure

(iii) Assume $p' = \bar{p} \sum \eta_i \psi_i$ and spatial average to give the oscillator equations $\ddot{\eta}_n + \omega_n^2 \eta_n = F_n$:

$$-\frac{\bar{p} E_n^2}{\bar{a}^2} F_n = \bar{\rho} I_1 + \frac{1}{\bar{a}^2} I_2 + \bar{\rho} I_3 + \frac{1}{\bar{a}^2} I_4 + \bar{\rho} I_5$$

$$+ \oint \bar{\rho} \frac{\partial \vec{u}'}{\partial t} \cdot \hat{n} \psi_n dS - \int \vec{\mathcal{T}} \cdot \nabla \psi_n dV + \frac{1}{\bar{a}^2} \int \frac{\partial p'}{\partial t} \psi_n dV$$

$$I_1 = \int [\bar{\vec{u}} \cdot \nabla \vec{u} + \vec{u}' \cdot \nabla \bar{\vec{u}}] \cdot \nabla \psi_n dV$$

⋮

etc

(iv) Apply the splitting principle and rewrite I_1, \dots

$$I_1 = I_1^a + I_1^\Omega + I_1^s$$

$$I_1^a = \int [\nabla (\bar{\vec{u}} \cdot \vec{u}'_a) - \vec{u}'_a \times \nabla \times \bar{\vec{u}}] \cdot \nabla \psi_n dV$$

⋮



5.1 REPRESENTING NOISE IN ANALYSIS OF THE GLOBAL DYNAMICS (cont'd)

- (v) The fluctuations appearing in I_1, \dots must be modeled:

Assume to first order,

$$u'_a = \sum \frac{\dot{\eta}_j \cdot(t)}{\gamma k_j^2} \nabla \psi_j$$

and set $p'_\Omega = p'_s = 0$

To second order the oscillator equations have the form

$$\ddot{\eta}_n + \omega_n^2 \eta_n = 2\alpha_n \dot{\eta}_n + 2\omega_n \theta_n \eta_n - \sum_{i=1}^{\infty} \sum_{j=1}^{\infty} [A_{nij} \dot{\eta}_i \dot{\eta}_j + B_{nij} \eta_i \eta_j] + \sum [\xi_{ni}^v \dot{\eta}_i + \xi_{ni} \eta_i] + \Xi_n + (F_n)_{\text{other}}^{\text{NL}}$$

$\xi_{ni}^v, \xi_{ni}, \Xi_n$ are stochastic sources defined as integrals but they must be modeled.

B. Modeling the Noise Sources

- No modeling based on experimental, theoretical, or phenomenological results has been accomplished.
- Approximate the sources ξ_{ni}^v, ξ_{ni} and Ξ_n as white noise processes.



5.1 REPRESENTING NOISE IN ANALYSIS OF THE GLOBAL DYNAMICS (cont'd)

C. Solving the Stochastic Differential Equations

- The random character of the stochastic sources will appear as randomness imposed in the amplitudes $\eta_n(t)$ of the modes.
- Thus the Fourier synthesis of the pressure field serves in the first instance as an approximate representation of the deterministic (acoustics) part of the unsteady motions and good results can be obtained by retaining only a small number of terms in the modal expansion.
- Results have been obtained only for the simplest case of two modes, with noise sources only in the fundamental mode. Nonlinear gasdynamic coupling transfers stochastic behavior to the second mode.



5.1 REPRESENTING NOISE IN ANALYSIS OF THE GLOBAL DYNAMICS (cont'd)

C. Solving the Stochastic Differential Equations (cont'd)

- There are two types of stochastic influences included here:
 - (i) ξ_{ni}, ξ_{ni}^v represent stochastic influences on the 'spring' of natural frequency and in the damping of growth rate of the n^{th} mode;
 - (ii) Ξ_n represents a stochastic driving source causing excitation of the n^{th} mode even in the absence of driving by combustion processes [cf. Russian interpretation of test results and analysis by R. Hessler for solid rockets in the 1970's – 1980's.
- The equations to be solved are (Burnley, 1996)

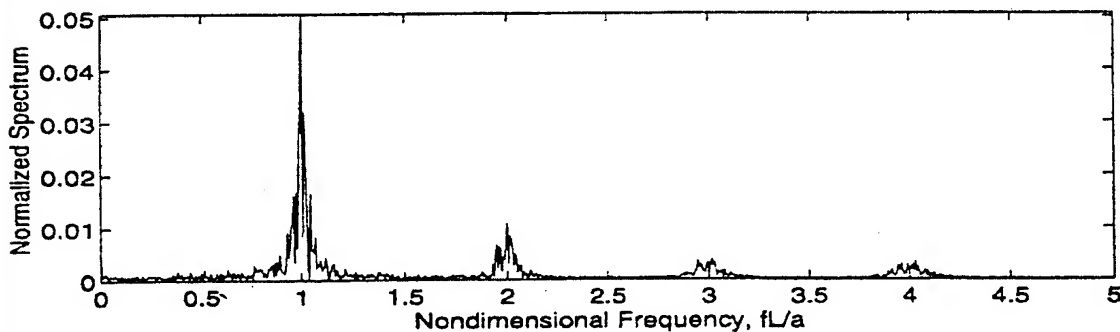
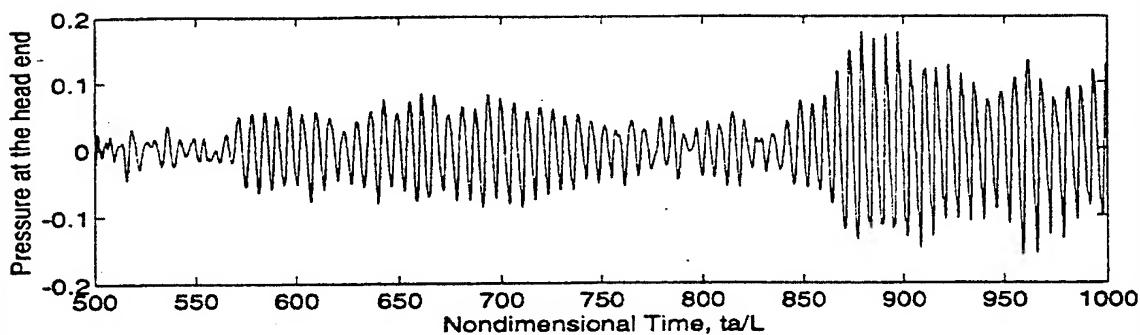
$$\ddot{\eta}_1 + \omega_1^2 \eta_1 = 2 \left(\alpha_1 + \frac{1}{2} \xi_1^v \right) \dot{\eta}_1 + 2 \omega_1 \left(\theta_1 + \frac{1}{2 \omega_1} \xi_1 \right) \eta_1 + (F_1)^{\text{NL}} + \Xi_1$$

$$\ddot{\eta}_2 + \omega_2^2 \eta_2 = 2 \alpha_2 \dot{\eta}_2 + 2 \omega_2 \theta_2 \eta_2 + (F_2)^{\text{NL}}$$



5.1 REPRESENTING NOISE IN ANALYSIS OF THE GLOBAL DYNAMICS (cont'd)

- Results for probability density functions have been constructed using the Monte-Carlo method (Paparrizos, 1991; Burnley, 1996) applied to a Stratonovich form of the stochastic differential equations (Burnley, 1996).
- The following figures show a pressure trace and spectrum for one simulation.



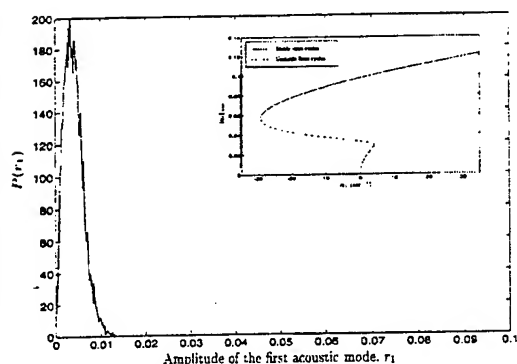
- Many simulations with initial conditions varied, and constructing probability distributions after the initial transients have decayed.



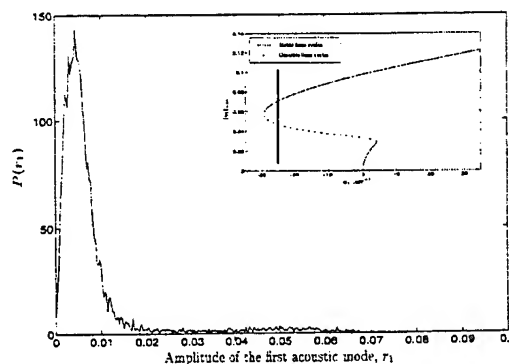
5.1 REPRESENTING NOISE IN ANALYSIS OF THE GLOBAL DYNAMICS (cont'd)

C. Solving the Stochastic Differential Equations (cont'd)

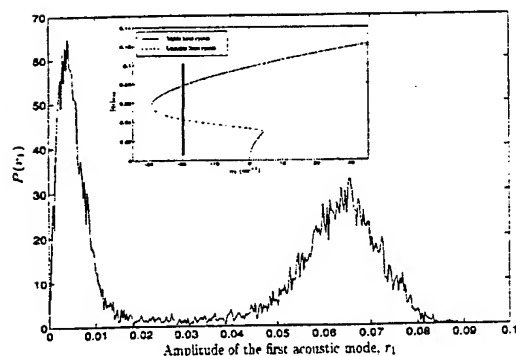
- A series of simulations have been carried out with the nonlinear combustion model described above, and the growth (decay) constant α , of the fundamental mode varied. The probability density functions are shown in the following figures.



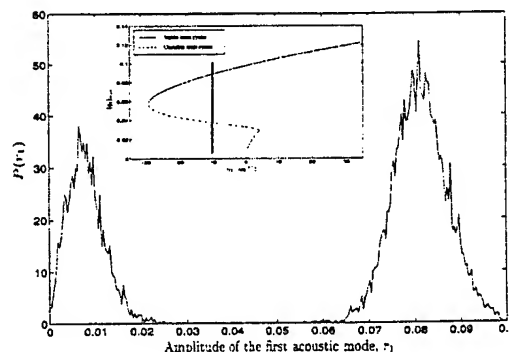
(a) $\alpha_1 = -35 \text{ sec}^{-1}$



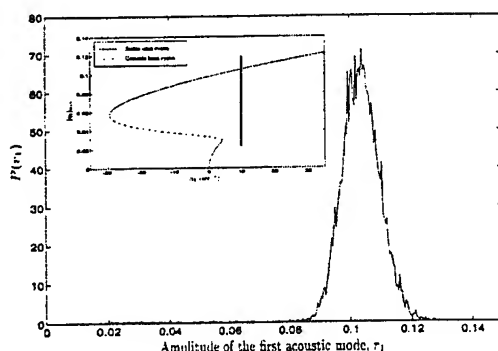
(b) $\alpha_1 = -25 \text{ sec}^{-1}$



(c) $\alpha_1 = -20 \text{ sec}^{-1}$



(d) $\alpha_1 = -10 \text{ sec}^{-1}$



(e) $\alpha_1 = +10 \text{ sec}^{-1}$



VI CONCLUDING REMARKS

- Indisputable theoretical and experimental evidence exists for the existence of various sorts of subcritical as well as supercritical bifurcations in combustors.
- A framework is available for investigating the consequences of global bifurcations in combustor dynamics.
- The consequences of many local subcritical bifurcations have not been examined.
- The proposal that hysteresis associated with recirculation zones and different stability of the associated steady combustion fields merits further investigation as a possible explanation for random occurrences of combustion instabilities.
- Numerical simulations of these problems remain in a primitive state.



**Some Aspects of Nonreproducibility of Self-Oscillation
Excitation**

in Combustion Chamber of Liquid Rocket Engine

K.P. Denisov*, V.N. Ivanov, V.P. Pikalov*****

Research Institute of Chemical Machine Building (NIICHIMMASH),

Sergiev-Posad, Russia

Abstract

Some aspects of low reproducibility of high-frequency self-oscillation excitation in combustion chamber of liquid rocket engine.

In the investigation of model combustion chambers it is shown that the observed effects of unreproducibility arise from:

- possibility of realization of combustion zone ambiguous (bistable) stationary states with invariant parameters of the propellant feeding system.;
- combustion zone nonlinear sensitivity to chamber natural acoustic field that results in the occurrence of self-oscillation unstable limit cycle of one or other mode.

* Vice-General Director.

** Senior Research Engineer.

*** Head, Research Division.

Nomenclature

- A_{rms} = root mean square of total pulsating signal
 F = frequency
 H = potential barrier
 P_c = static combustion chamber pressure
 P' = pulsating pressure component
 P'_{rms} = root mean square of pulsating pressure component
 P_{st} = stationary probability density function
 Q' = pulsating heat release component
 $\dot{P}' = P'$ complex amplitude
 $\dot{Q}' = Q'$ complex amplitude

 $R(\tau)$ = autocorrelation function
 SLC = stable limit cycle
 ULC = unstable limit cycle
 T = oscillation period
 V_0 = Oxygen velocity stream
 V_p = Propan velocity stream
 α = equivalence ratio (oxygen excess relative to the stoichiometric ratio)
 β = decay coefficient
 $\overline{\beta T}$ = effective oscillation decrement
 $\delta(\tau)$ = Dirac delta function
 λ = amplitude (envelope) of narrow-band signal
 λ_{SLC} = SLC amplitude
 λ_{ULC} = ULC amplitude
 $\xi(t)$ = normal delta-correlated (white) noise
 τ = temporal interval
 ϕ = oscillation phase
 ψ = potential function
 ω = oscillation angular frequency
 ω_0 = natural angular frequency

Introduction

Dynamic ambiguity of combustion regime in liquid rocket engine (LRE) chambers manifests itself in spontaneous transitions from a state of small random oscillation ("noises") to a state of regular self-oscillation of high amplitude with propellant supply condition and other monitored "external" factors being constant. A distinctive feature of those transitions is the fact that they occur occasionally, for no apparent reason. No observable disturbance (of pulse or explosive nature, for example) generally precedes the self-excitation event. Self-oscillation excitation is of "soft", smooth character. The self-oscillation termination occurs in a similar way. The random character of such spontaneous transitions causes us to speak of self-oscillation excitation nonreproducibility (such terms as "limited reproducibility", "random reproducibility" are also used).

At least two basic concepts exist of the nature of low reproducibility of acoustic self-oscillation excitation in combustion chambers.

One of the concepts is based on postulating a possibility of combustion zone space pattern bifurcations that are significant with respect to stability to small acoustic disturbance. This is equivalent to the stating that a stationary regime of propellant feeding to the chamber is not a factor that defines the flame pattern unambiguously.

Thus the given concept is based on the assumption that, in principle, generation of multiple combustion zone space patterns that differ in regimes of flame stabilization is possible at identical values of parameters defining the combustion chamber stationary mode. These combustion zone patterns may have different sensitivity to small acoustic disturbances.

In particular, the realization of one or other combustion zone space pattern may depend on a combination of random conditions that take place in the course of engine starting and operating in the specified regime. As a consequence

of the random character of one or other combustion zone space pattern realization, the self-oscillation excitation process acquires a statistic character also.

The second concept of nonreproducibility is based on the idea that a nonlinear ("hard") excitation of a potentially self-oscillating system occurs by the action of a stationary wide-band acoustic noise of turbulent combustion, or by the action of single random pressure disturbances of explosive nature that occur in combustion chamber sometimes. This model postulates the presence of unstable limit-cycle (ULC) self-oscillation that results from the fact that n , the effective index of interaction between oscillatory components Q' of heat release (or mass release) rate and oscillatory components P' of pressure is a nonlinear function of pressure oscillation amplitude $\lambda^{[1]}$:

$$n = \frac{\dot{Q}'}{\dot{P}'} = n(\lambda),$$

where \dot{Q}' and \dot{P}' are complex amplitude of Q' and P' , respectively.

The considered concepts of nonreproducibility are alternate in a sense because they lead to different scenarios of random beginning of self-oscillations. The adequacy of used diagnostic model is very important for successful application of methods and tools of diagnostics of combustion stability in LRE. In this connection the study of the nature of self-oscillation excitation low reproducibility, as well as the search of diagnostics methods and ways of predicting this phenomenon are of critical importance. Some results of the study of self-oscillation excitation low reproducibility in combustion chamber are presented. The data are based on experimental research work carried out at NIICHIMMASH's set-ups modeling oscillatory combustion.

1. External Symptoms of Spontaneous Combustion

Instability

A wide variety of external symptoms of spontaneous combustion instability are observed in engine tests of which the following two are most common:

a) instability is observed in a series of m identical tests of engines of the same type in $n > m$ cases immediately or in some random time t after the engine reaches the specified stationary operation regime (Fig.1a)

b) instability occurs in some time t_i after a certain engine reaches the specified operation regime and manifests itself as a single "spike" of self-oscillation (Fig. 1b) or as alternating 'noise' and self-oscillatory combustion regimes. (Fig.1c)

2. Model Combustion Chamber with a Single

Injection Element

Investigation was carried out in a model combustion chamber with a single coaxial injection element (Fig.2). Gaseous propane and gaseous oxygen were used as propellants. The combustion chamber is equipped with instruments for flame photographing and reaction zone oscillatory pressure measurement.

The following result was obtained. In the course of tests a distinct ambiguity of flame space pattern was recorded in a certain range of operating governing parameters: fuel flow rate and oxidizer flow rate. Depending on the ignition condition, flame stabilization regime (and flame space pattern, accordingly) could be in one of two stable stationary state (Fig.3). First of them corresponded to the flame stabilization inside the injection element in the vicinity of the fuel post edge (Scheme 1). The flame had an elongated form and radiated a relatively low level of noise (1...30 Pa in the 0...10 kHz range). The second stationary state corresponded to flame stabilization outside of the injection element at some distance from the oxidizer tube exit (Scheme 2). This state is characterized by a shorter smeared flame and a relatively high integral noise level (26... 90 Pa). The noise frequency contents were different in both cases. The mentioned ambiguity of stabilization mode (bistability) was observed in a wide range of the governing parameters (fuel flow velocity and oxidizer flow velocity).

A principally important effect was found in the tests: an acoustically stable 'noise' combustion corresponded to the flame stabilization Scheme 1

throughout the investigated range of the governing parameters (Fig 4a). In the case of flame stabilization according to Scheme 2, in the same range of the governing parameters there was a boundary beyond which strong self-oscillation of the first radial mode (of 2620 Hz , 320 Pa) excited. (Fig.4b).

This series of experiments showed that the bistability of combustion zone pattern could really give rise to dynamic ambiguity that manifests itself in the presence or absence of self-oscillation. With unmonitored ignition process (if it is unknown what particular flame stabilization regime is realized), the excitation of self-oscillation in an ensemble of similar tests becomes of a random, statistical nature. Thus it can be stated that the ambiguity of dynamic state of combustion may a consequence of a stochastic process of initial ignition and subsequent generation of one or another flame self-consistent spatial pattern.

It should be noted that in the given experiments, once the mixture was ignited and flame stabilization regime was established as per Scheme 1, an artificial transition from Scheme 1 to Scheme 2 was achieved by disturbing oxygen concentration in the reaction zone. Some air was injected in the oxygen feeding line for a short time for this purpose. (Fig.5). After the air injection was terminated, the system retained stabilization Scheme 2. In this case, after the system transition to the region of potential instability, self-oscillation excitation became a completely deterministic, reproducible phenomenon.

Thus in this example the self-oscillation excitation nonreproducibility is only apparent and is a result of the absence of information on flame stabilization regime on ignition. However the mere fact of recognizing a possibility of bifurcation of flame spatial pattern with subsequent self-oscillation excitation deserves attention.

3. Model Combustion Chamber with Gas-Liquid

Injection Elements

A combustion chamber of 104 mm in diameter was investigated (Fig.6). Propellants, liquid kerosene and gaseous (cold) oxygen were supplied from

cylinders. The chamber was equipped with an independent igniter, using methane and oxygen. A device for applying artificial pulse disturbances to the reaction zone and fuel feed cavity is mounted on the chamber.

The injection head includes four injection elements with radial input of liquid fuel into the flow of gaseous oxidizer.

The range of test regimes on coordinates: chamber static pressure, P_c – equivalence ratio (oxygen excess relative to the stoichiometric ratio), α , is shown in Fig. 7.

In the course of testing this injection head type the following dynamic state of combustion process were recorded;

- **noise stable state**, ($P_c \leq 0.4$ MPa), Fig.8;
- **chaotic alternation of noise and self-oscillatory states**. Each dynamic state occurrence instants and duration are random in the ensemble of realizations similar by P_c and α , ($P_c = 0.4$ MPa), Fig.9;
- **self-oscillatory combustion** ($f_{101} = 6300$ Hz, $P_c = 0.6 \dots 0.7$ MPa), Fig.10.

Thus it can be stated that in the $P = 0.4 \dots 0.6$ MPa, $\alpha = 0.65 \dots 0.75$ range the dynamic state of the combustion process is characterized by stochastic ambiguity and the ambiguity symptoms differ from those described in the previous section.

To understand the observed transition nature, let us consider a model of potentially self-oscillatory system being in the mode of hard excitation.

3.1. Model of potentially self-oscillatory system in the mode of hard excitation.

It should be noted that in the case under consideration the self-oscillation is excited at a frequency of combined first longitudinal mode –first tangential mode ($f_{101} = 6300$ Hz.). Therefore a simple one-mode approximation will be used in devising a model of dynamic transitions. In such approximation the combustion

chamber stochastic dynamics can be described by the following model of potentially self-oscillatory system ^[1,2]:

$$\frac{d^2 P'}{dt^2} + 2\beta(\lambda) \frac{dP'}{dt} + \omega_0^2 P' = \xi(t) \omega_0^2, \quad (1)$$

where: P' is oscillatory pressure;

t is time;

ω_0 is a circular frequency ;

$\beta(\lambda)$ is an effective coefficient of decay or generation, a nonlinear function of amplitude λ ;

$\xi(t)$ is a stationary normal delta-correlated (white) noise of turbulent combustion.

With the proviso that $\frac{\omega_0}{\beta(\lambda)} \gg 1$, the following evolutionary equation for pressure oscillation amplitude λ corresponds to equation (1)^[3]:

$$\frac{d\lambda}{dt} = -\beta(\lambda) \cdot \lambda + \omega_0^2 N_0 / 8\lambda + \zeta(t). \quad (2).$$

Here: N_0 is the spectral intensity of random noise $\xi(t)$;

$\zeta(t)$ is normal delta-correlated random function:

$$R(\tau) = \langle \zeta(t) \cdot \zeta(t + \tau) \rangle = \omega_0^2 \cdot N_0 \cdot \delta(\tau) / 4.$$

Within the framework of the self-oscillatory system with hard excitation a particular $\beta(\lambda)$ relationship is postulated which provides the existence of self-oscillation unstable limit cycle and stable limit cycle.

Evolutionary equation (2) describes one-dimension Markov process with coefficients of "drift" and "diffusion", equations (3) and (4), respectively:

$$a(\lambda) = -\beta(\lambda) \cdot \lambda + \omega_0^2 N_0 / 8\lambda, \quad (3)$$

$$b(\lambda) = \omega_0^2 N_0 / 4. \quad (4)$$

Equation (2) has the potential function in the following form:

$$\hat{O}(\lambda) = -\frac{1}{2} \int_0^\lambda \left(-\frac{\beta(\lambda) \cdot \lambda}{\beta_0} + \frac{\sigma^2}{\lambda} \right) d\lambda, \quad (5)$$

where:

$$\sigma^2 = \omega_0^2 \cdot N_0 / 8\beta_0, \quad (6)$$

$$\beta_0 = \beta(\lambda) \text{ at } \lambda \rightarrow 0, \quad (7)$$

and a stationary state probability density^[3,4]:

$$P_{st}(\lambda) = C_1 \exp[-2\hat{O}(\lambda)/\sigma^2] = C_1 \lambda \exp \left[-\frac{1}{\beta_0 \sigma^2} \int_0^\lambda \lambda \beta(\lambda) d\lambda \right]. \quad (8).$$

The C_1 constant is determined from the norming condition

$$\int_0^\infty P_{st}(\lambda) d\lambda = 1.$$

The calculated relations $\Phi(x)$ and P_{st} are shown in Fig 11 ($x = \lambda\sigma$).

As can be seen, $\Phi(x)$ potential has two minima that correspond to locally stable state of dynamic equilibrium: the left minimum corresponds to the noise state while the right one corresponds to the self-oscillatory state. Unstable dynamic equilibrium corresponds to the unstable limit cycle.

The distribution of state probability density $P(x)$ for a specific form of function $\beta = \beta(x)$ is bimodal and the maxima of probability density correspond to the minima of potential $\Phi(x)$. The probability density minimum corresponds to the maximum of potential $\Phi(x)$, i.e. to the unstable limit cycle.

The self-excitation of the dynamic system described by Eq. (1) is stochastic in principle, in the sense that it is impossible to know a priori the exact time instant when excitation will occur i. e. the time of system transition from noise to self-oscillatory state.

The mean expectation time of self-excitation event depends on the noise intensity N_0 and the potential barrier height h_1 . If the potential barrier is sufficiently high (which corresponds to a high amplitude of the unstable limit cycle compared to σ , Eq. (6)), and the noise intensity N_0 is small, the expectation

time can be very large, and self-oscillation excitation will be a very rare event, accordingly. And vice versa, with low potential barrier and high noise intensity, random transitions of "noise \longleftrightarrow self-oscillation" will occur. In this case pressure oscillogram for i-realization will look like alternating noise and self-oscillation regions, similar to those shown in Fig.9.

Thus within the limits of Model 1, the nonreproducibility of self-oscillation excitation, with 'external' conditions being constant, is attributed to the presence of unstable limit cycle and random wide-band noise $\xi(t)$.

3.2 System Identification

The task of identification of a potentially self-oscillatory system is stated in this case as follows: to what extent the initial uncertainty of the statistic model of the observed dynamic transitions can be reduced.

The model of potentially self-oscillatory system with hard excitation (Model 1) is taken as a base model. The following relationship connecting $\beta(\lambda)$ with the narrow-band noise amplitude probability density is obtained:

$$\frac{\beta(\lambda)}{\beta_0} = \sigma^2 \left\{ \frac{1}{\lambda^2} - \frac{\Psi(\lambda)}{\lambda} \right\}, \quad (9)$$

where

$$\Psi(\lambda) = \frac{d\{\ln P_{st}(\lambda)\}}{d\lambda}, \quad (10)$$

and $P_{st}(\lambda)$ is a function of amplitude probability density, estimated experimentally based on the realization of the random process $\lambda(t)$.

The realization of oscillatory process $P' = P'(t)$ filtered in the band $f=1000\dots10000$ Hz and the corresponding noise spectrogram for the region that precedes oscillation self-excitation ($t=4\dots5$ s) are shown in Fig.12 (a compressed oscillogram is presented). The narrow-band peak with decrement $\overline{\beta T} \approx 0.04$ observed in the vicinity of $f_{101} \approx 6150$ Hz corresponds to combined first tangential mode-first longitudinal mode of the chamber volume natural acoustical oscillations.

The estimate of probability density of envelope (amplitude) $\lambda(t)$ of narrow-band noise $P'(t) = \lambda(t) \cdot \cos(2\pi f_0 t + \varphi(t))$ in the region that precedes oscillation self-excitation is shown in Fig.13. The corresponding estimate of the decay coefficient $[\beta]$ - amplitude $[\lambda]$ relation. As can be seen in Fig.13, the reconstructed relation $\beta = \beta(\lambda)$ is of a falling character and predicts the existence of unstable limit cycle with amplitude $\lambda_{ULC} \approx 8\sigma$. The found fact of unstable limit cycle existence allows identifying the system being studied within the base model of a potentially self-oscillatory system with hard excitation of self-oscillation (Model 1).

It should be noted that for the case of dissipative system of the second order, $\beta(\lambda) = \beta_0 = \text{const}$, the distribution (8) changes to the known Rayleigh distribution for the amplitude (envelope) of linear narrow-band noise:

$$P_{st}(\lambda) = \frac{\lambda}{\sigma^2} e^{\frac{-\lambda^2}{2\sigma^2}}.$$

In the framework of Model 1, actually deterministic transition from a locally stable noise state into a self-oscillatory one can be performed by applying a pulse to the system (combustion zone). The pulse should be high sufficiently to overcome the potential barrier, (hard pulse excitation of the system). In this case oscillation with an amplitude of $\lambda > \lambda_{ULC}$ should develop in the system after the disturbance application.

In the same time, Model 1 assumes a possibility of a reverse transition from a self-oscillatory state to noise in case the pulse is applied as antiphase to the existent self-oscillation.

Such situation is shown in Fig 14 for the chamber under investigation. The pulse disturbance was applied to the chamber reaction zone by exploding an explosive charge.

It should be mentioned however that treatment of effects of self-oscillation excitation and termination under the action of artificial disturbance in the framework of Model 1 is not quite correct. There is reason to believe that, under the conditions of the described experiments, the artificial pulse disturbance,

apart from acoustic effect, produce a parametric effect on combustion (it changes the combustion zone pattern, possibly including change in the flame stabilization regime). This is suggested, in particular, by a specific character of the dynamic transition of "noise to self-oscillation": the decay of oscillatory response actually to the initial noise level, with a subsequent smooth transition to the stable limit cycle, Fig.15. A possibility of self-oscillation termination on application of a pulse to the fuel feed cavity is another evidence of parametric effects (Fig.16). The establishment of a new 'noise' stationary state on pulse application is also shown in Fig.16. This state differs in noise spectrum and level from the state that precedes oscillation self-excitation.

Thus the given series of experiments reveals a possibility of realization of combustion zone multiple stationary patterns, which is beyond the frames of the base Model 1.

The treatment presented shows that while devising diagnostic models of oscillatory combustion in LRE chambers it is necessary to consider, along with 'hard excitation' effects, a possibility of bifurcation of combustion stationary modes and dynamic state ambiguity resulted from the bifurcation..

Conclusion

From the conducted studies it is concluded that at least two aspects should be taken into consideration for devising adequate models of unstable combustion in LRE:

- possibility of realization of combustion zone ambiguous (bistable) stationary states with invariant parameters of the propellant feeding system.;
- combustion zone nonlinear sensitivity to chamber natural acoustic field that results in the occurrence of self-oscillation unstable limit cycle of one or other mode.

Both aspects of realization of flame self-consistent pattern may lead to the nonreproducibility of self-oscillation excitation in LRE combustion chamber.

References

1. Artamonov K.I. Thermodynamic Instability. M. Mashinistroyeniye, 1982. (Rus.)
2. Ilchenko M. A. and others. Operating Process Stability in Spacecraft. M. Mashinistroyeniye, 1995. (Rus.)
3. Stratonovich R. L., Landa P.S. Noise Action on a Hard-Excited Generator. IVUZ . Radiophysics, v.2, 1, 1959. (Rus.)
4. Horsthemke W., Lefever R. Noise-Induced Transitions. Berlin, Heidelberg, New-York, Tokyo: Springer Verlag, 1984 (Transl. to Rus.).

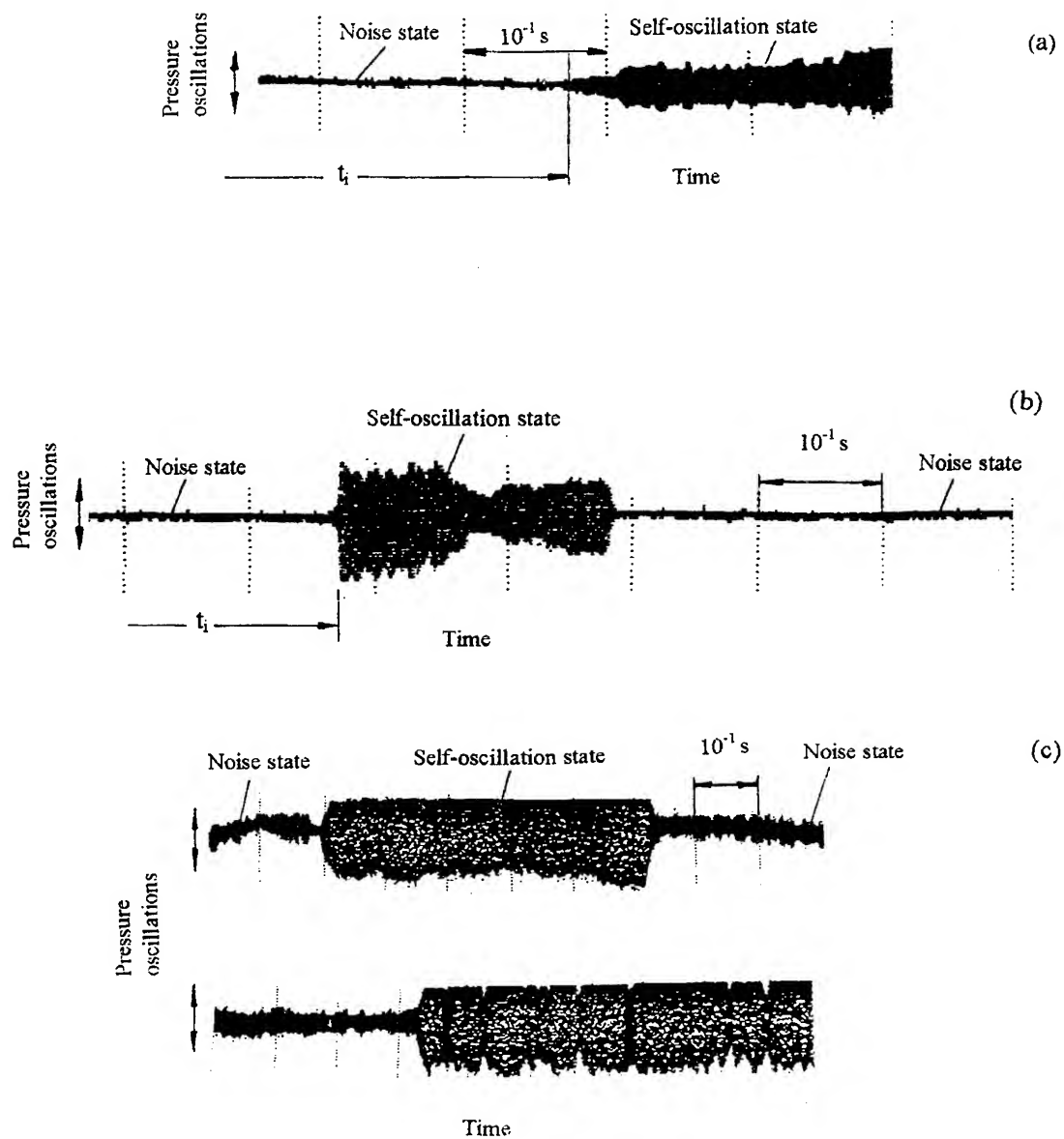


Fig. 1. Symptoms of spontaneous combustion instability (compressed displays of oscillatory processes).

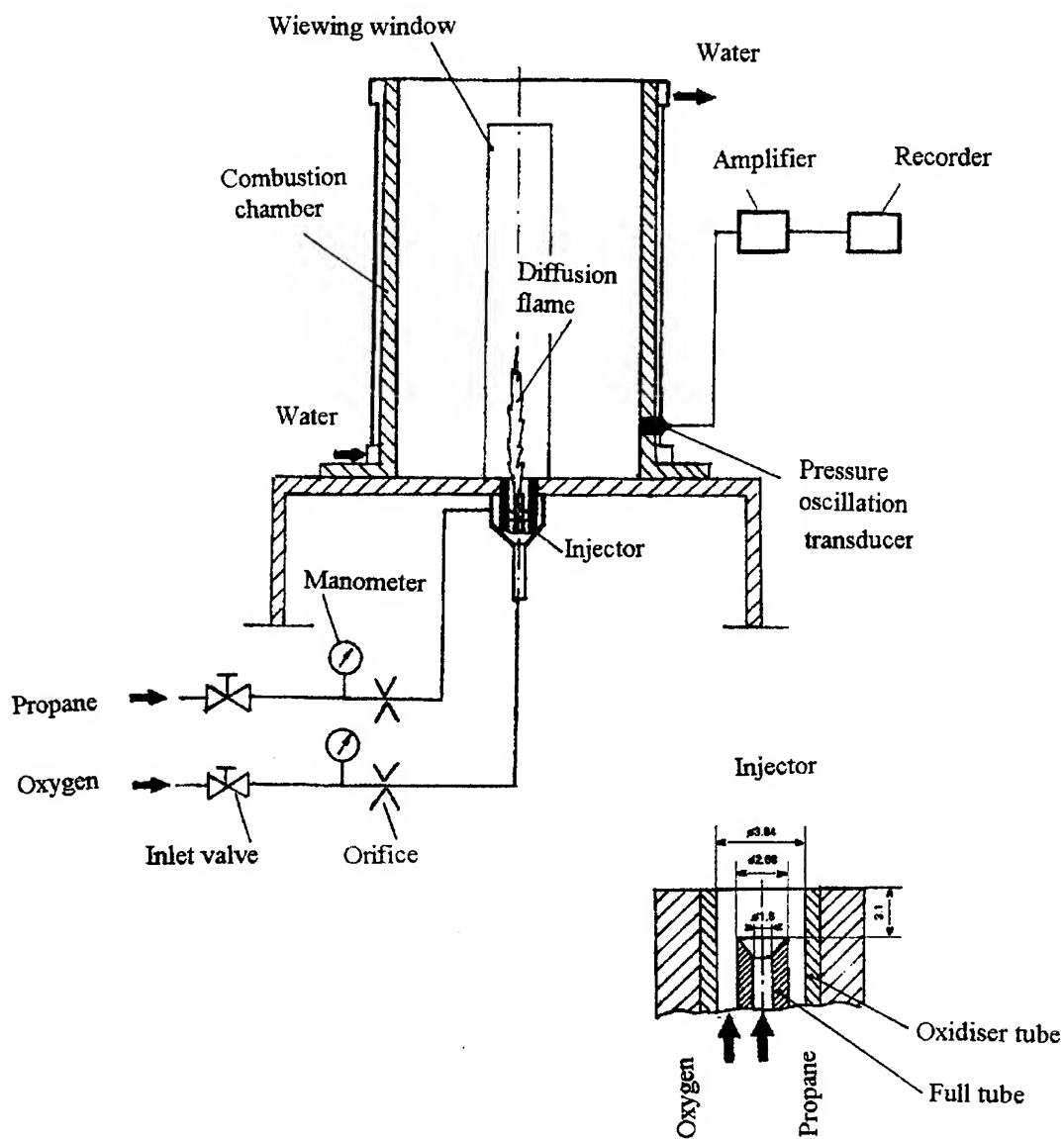


Fig. 2. Model combustion chamber with single coaxial injection element.

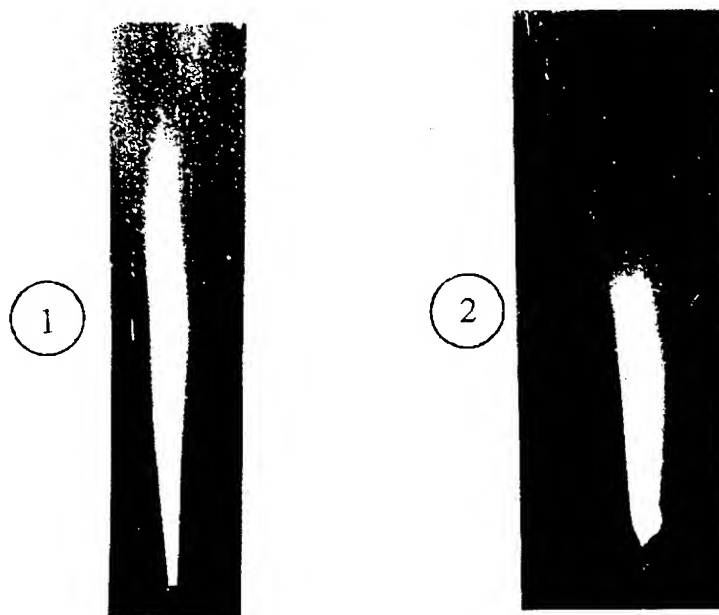


Fig. 3. Photograph of the diffusion flame.

1. Flame stabilization inside the injection element in the vicinity of the fuel post edge.
2. Flame stabilization outside of the injection element above the oxidizer tube.

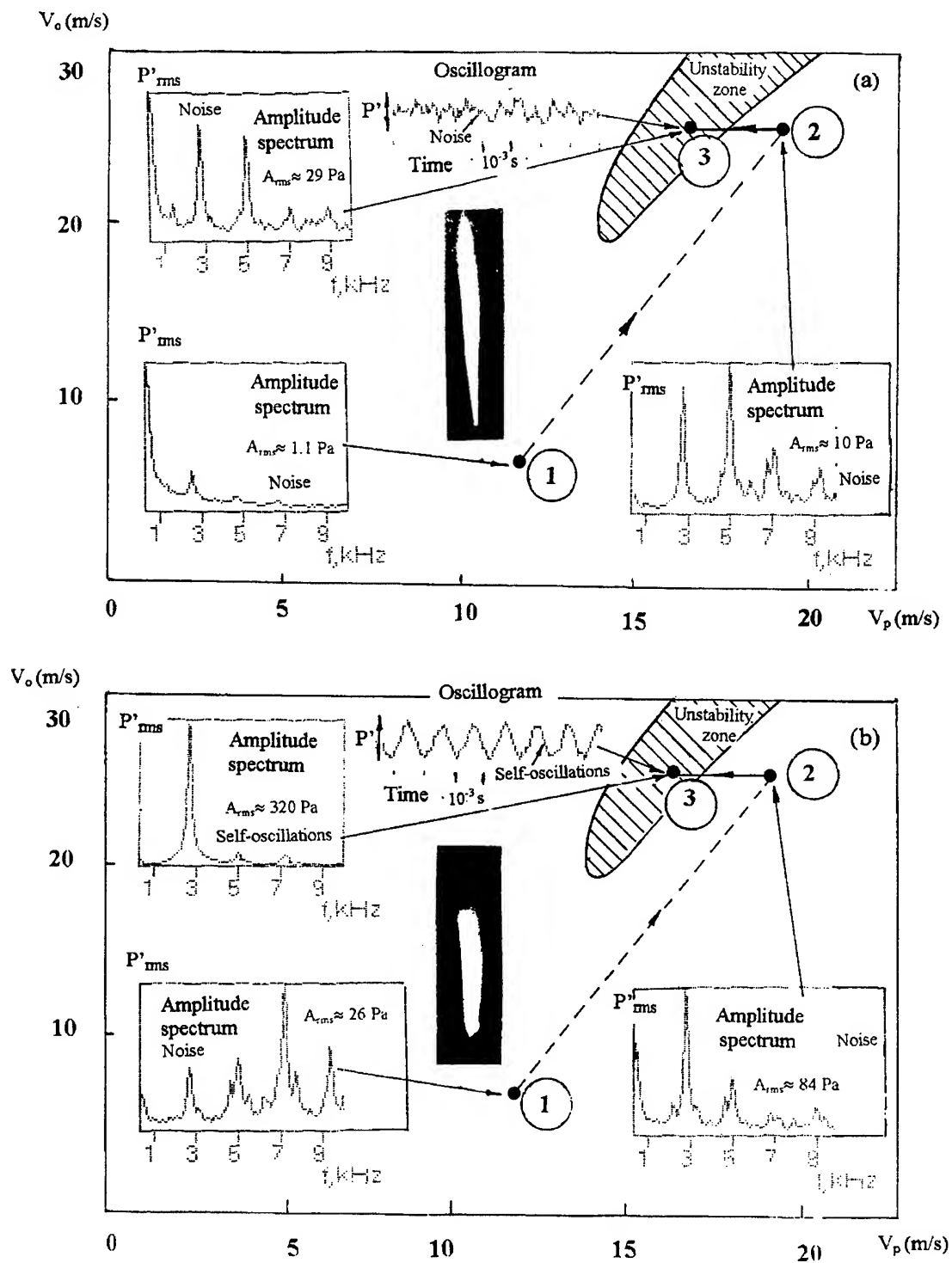


Fig. 4. Dynamic states and path of the system movement in the domain of governing parameters:
 a) flame stabilization as per Scheme 1;
 b) flame stabilization as per Scheme 2;
 (propellant feeding parameters, V_o and V_p , marked with similar figures are completely identical).

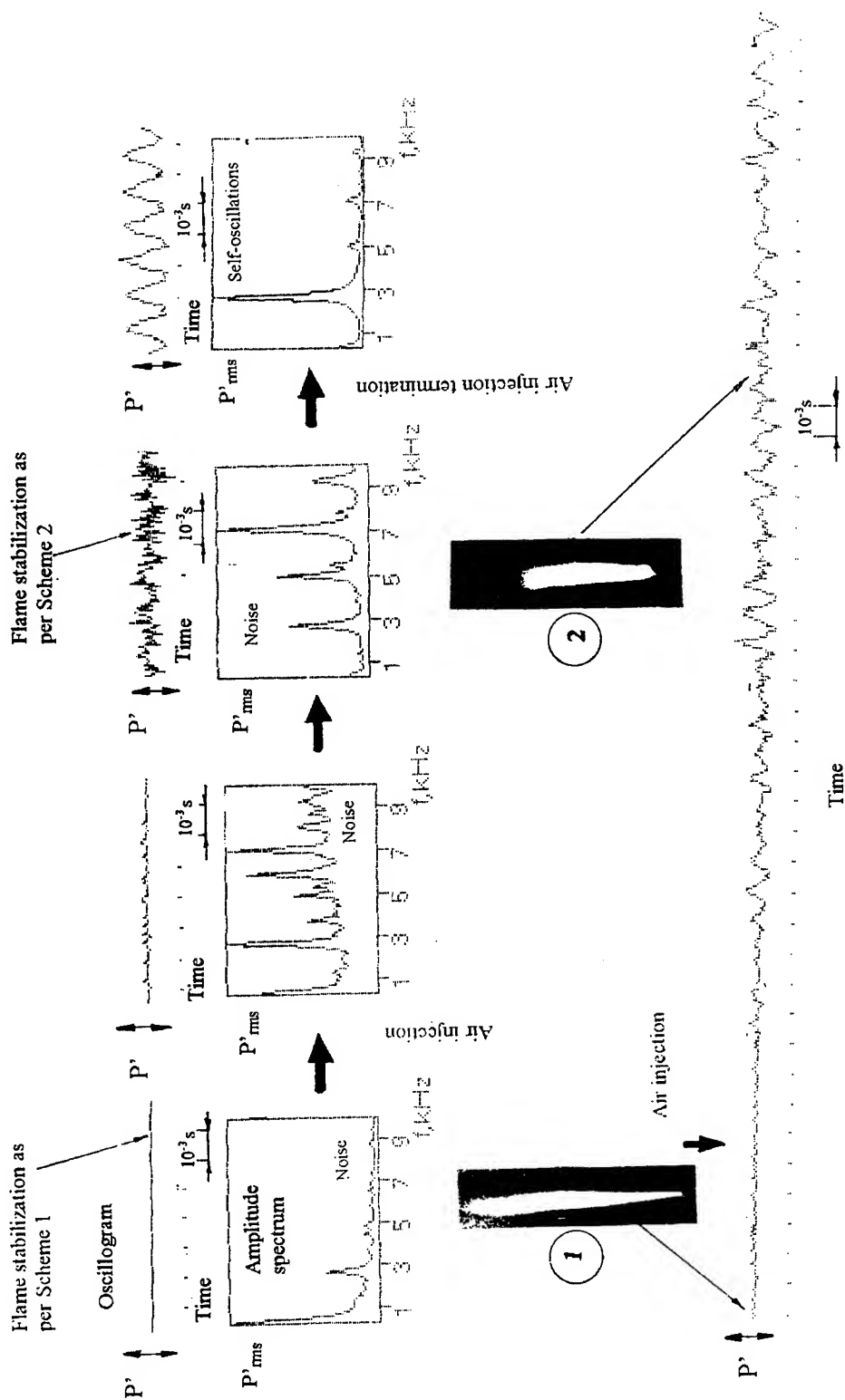


Fig. 5. Air injection induced transition from stabilization as per Scheme 1 to Scheme 2.

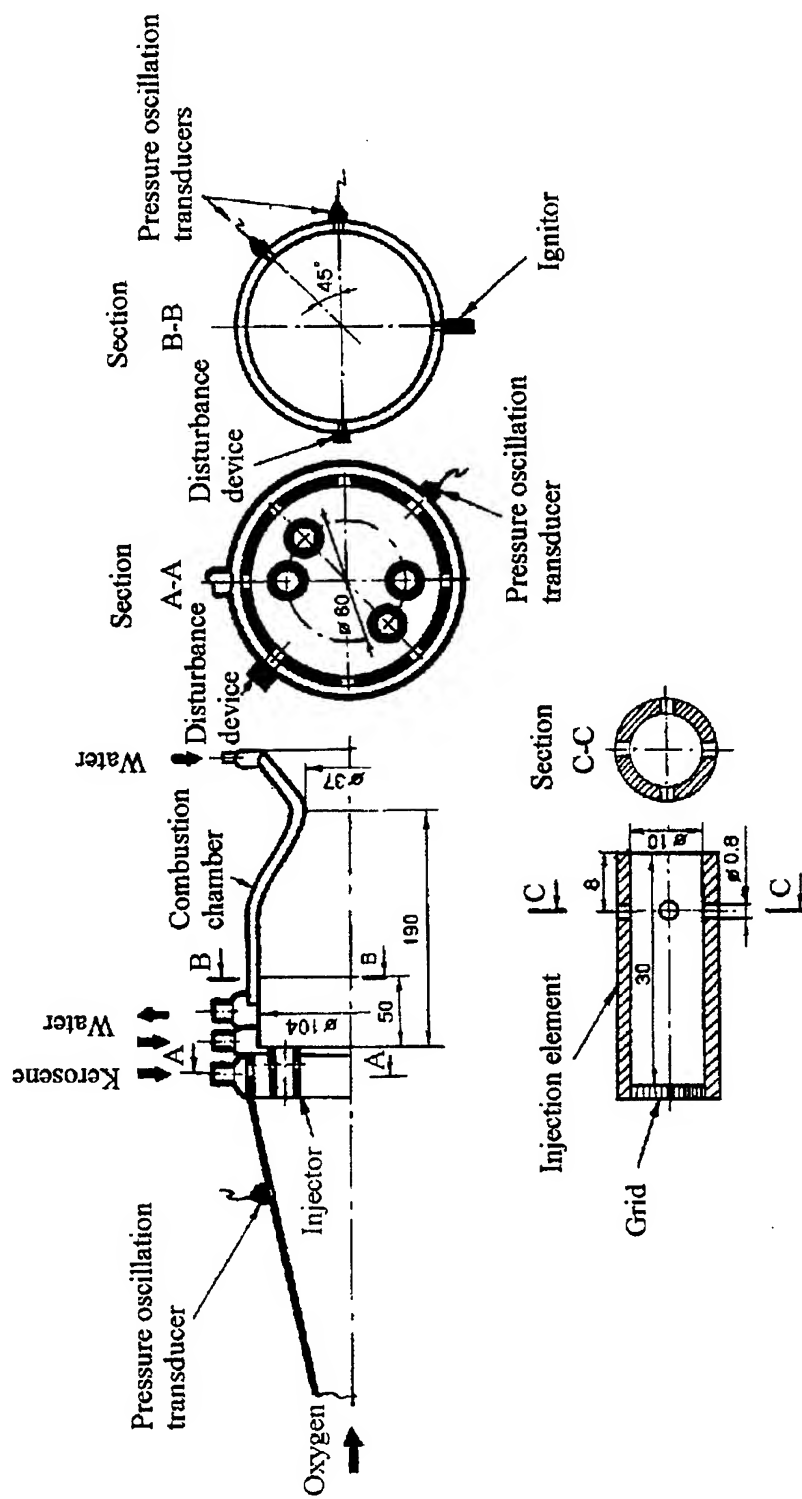


Fig. 6. Schematic of combustion instability study
(all dimensions are in millimeters)

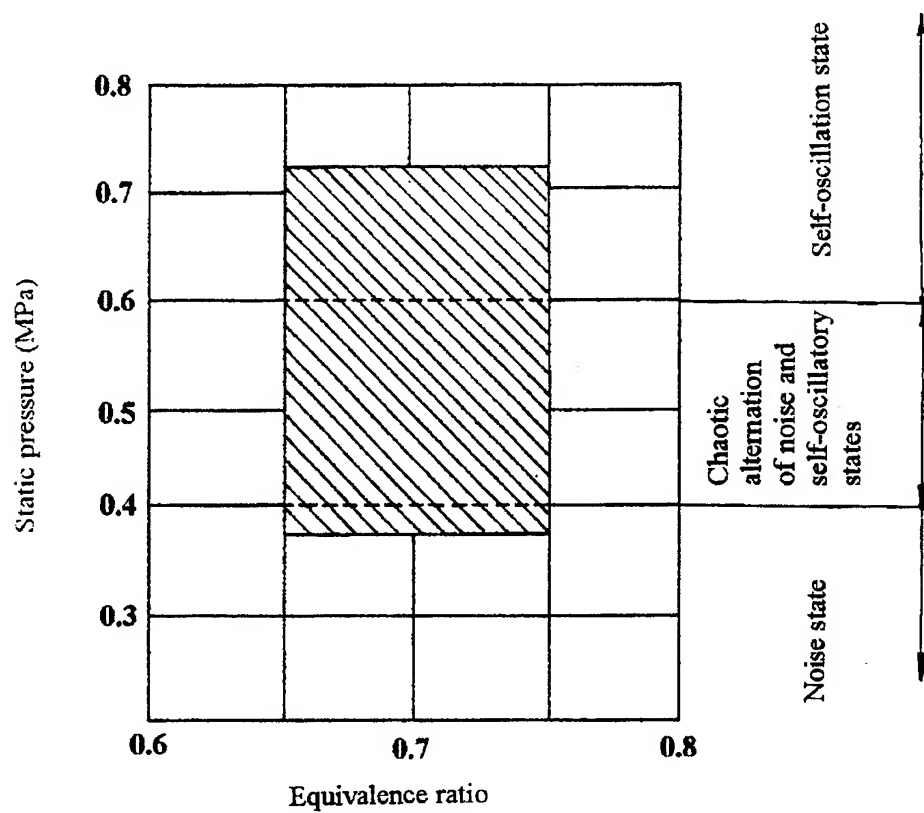


Fig. 7. Combustion chamber operation regimes.

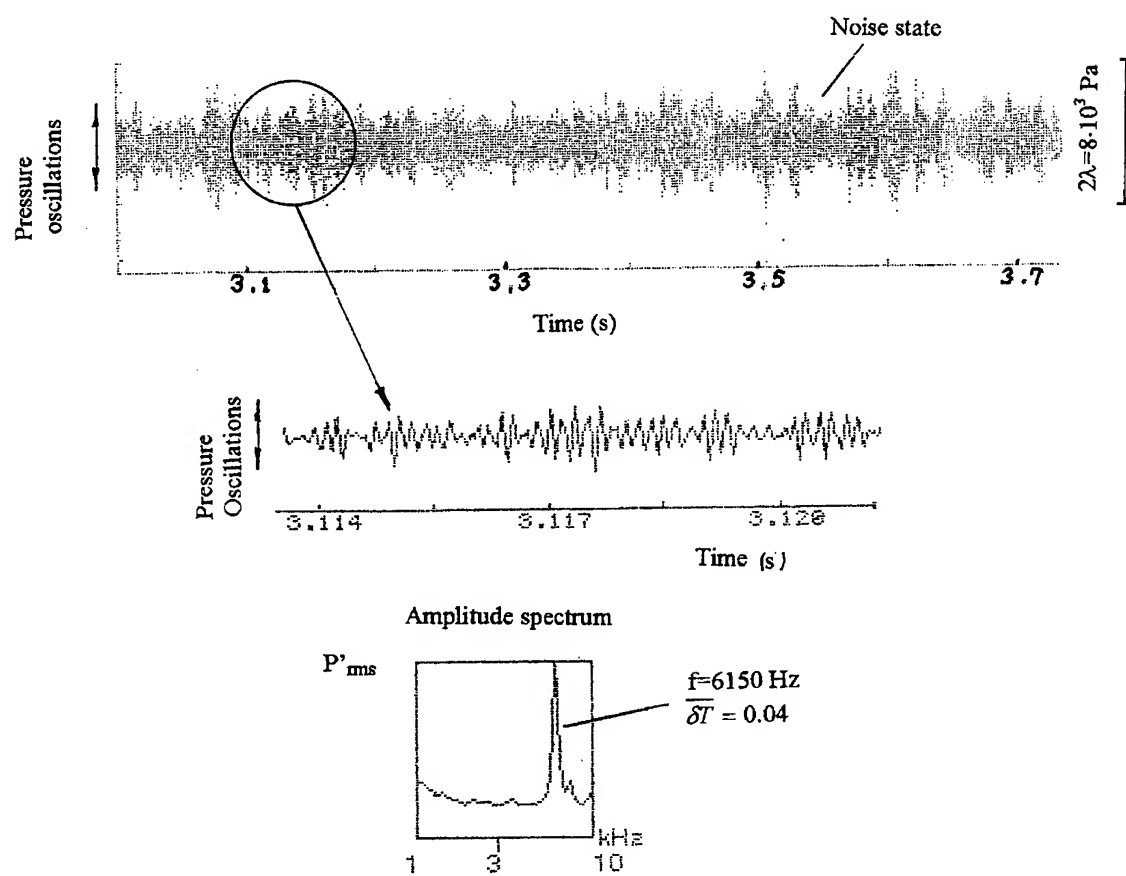


Fig. 8. Noise state of combustion process.

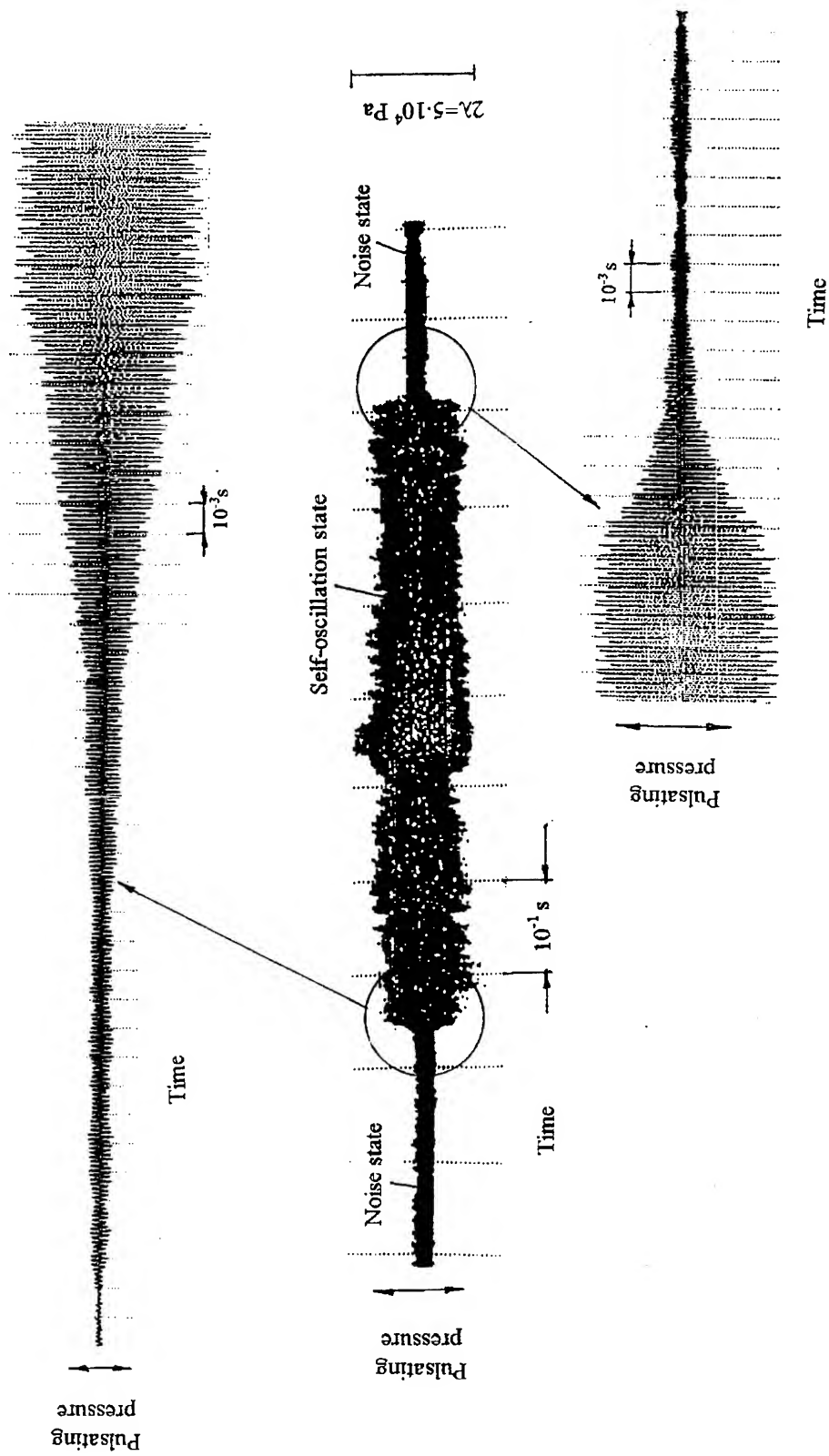


Fig. 9. Chaotic alternation of noise and self-oscillatory states.

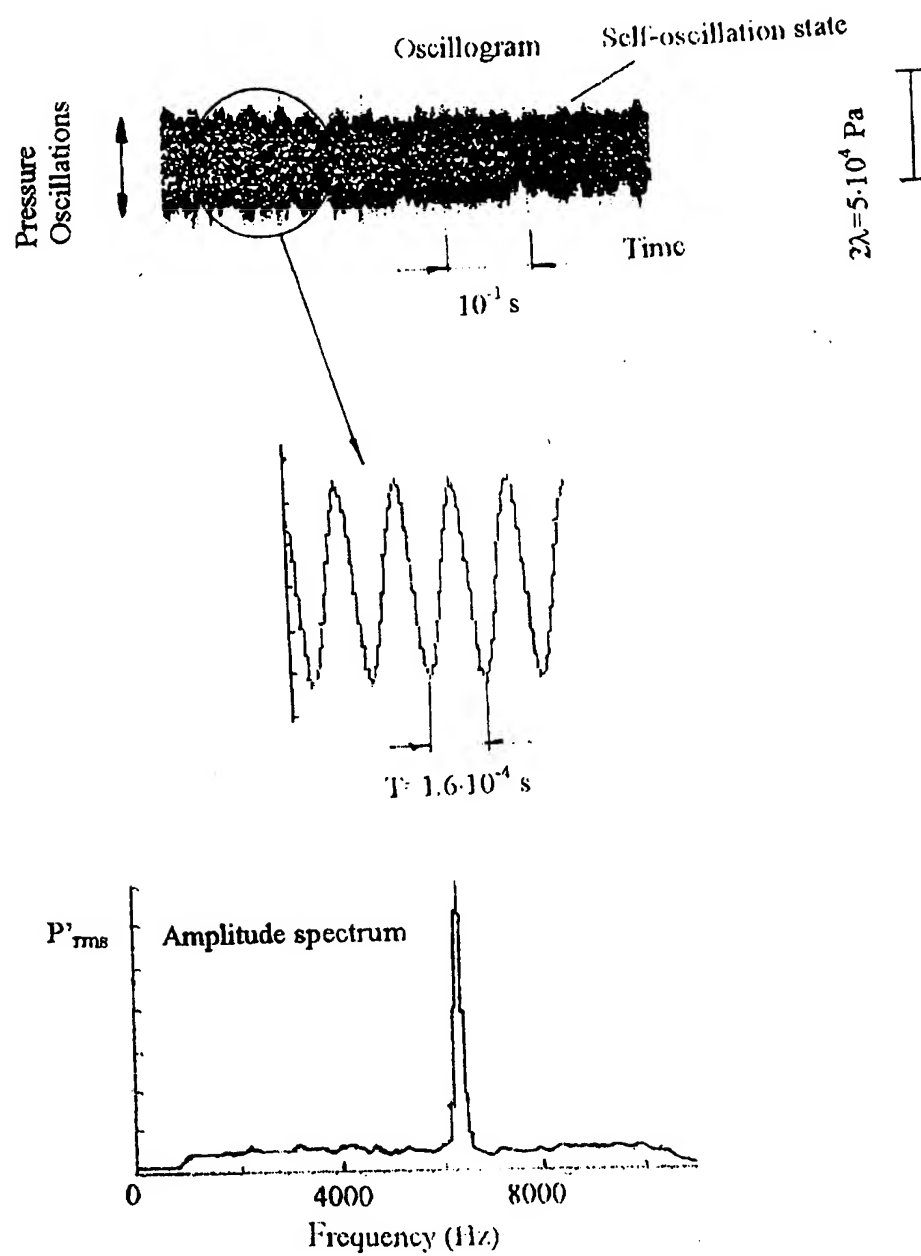


Fig. 10. Self-oscillatory combustion.

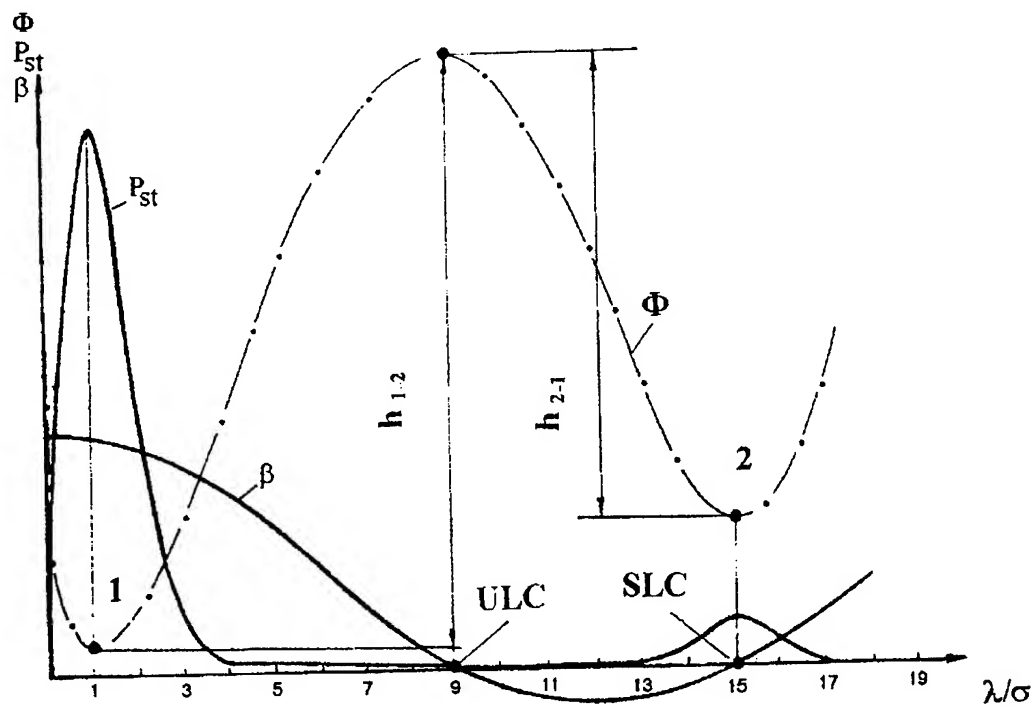


Fig. 11. Decay coefficient β , probability density P_{st} and potential Φ versus oscillation relative amplitude.

h_{1-2} – Potential barrier of the transition from state 1 to state 2

h_{2-1} – Potential barrier of the transition from state 2 to state 1

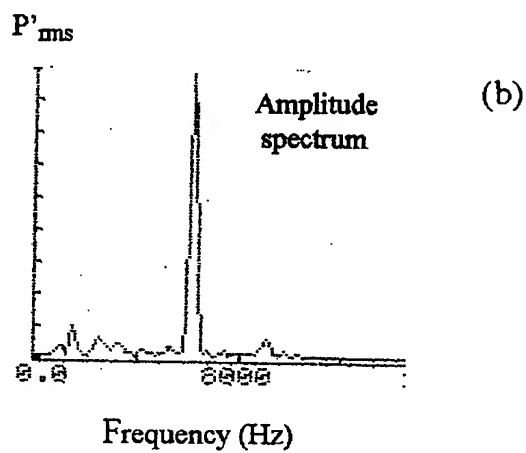
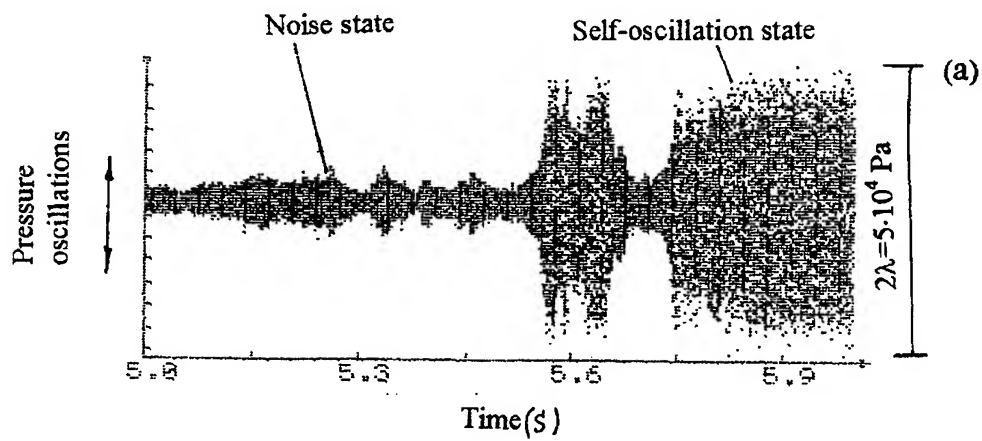


Fig. 12. Spontaneous dynamic transition "noise \rightarrow self-oscillation":

- a) compressed oscillogram;
- b) noise spectrum in the region preceding oscillation self excitation.

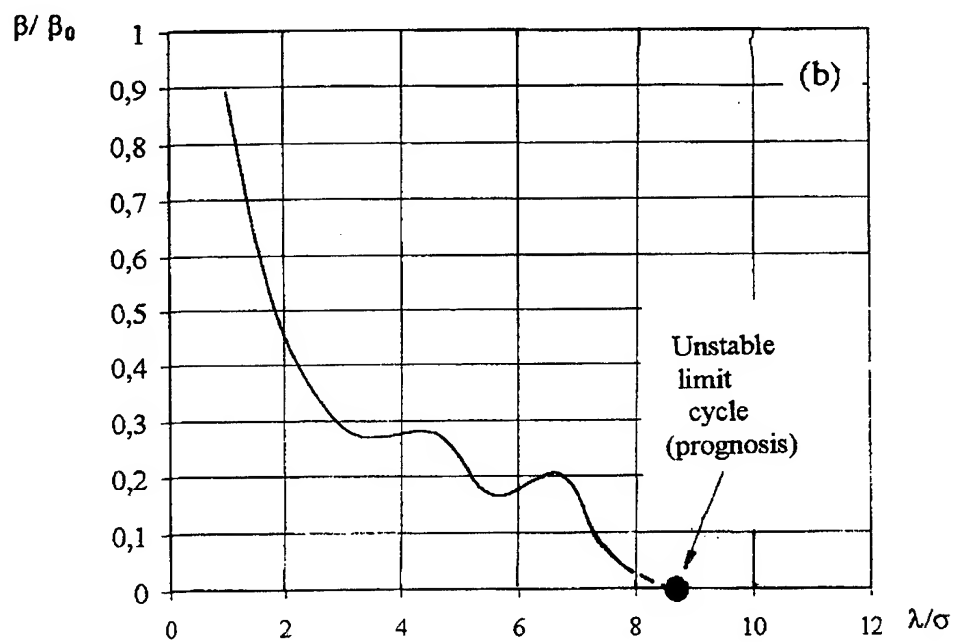
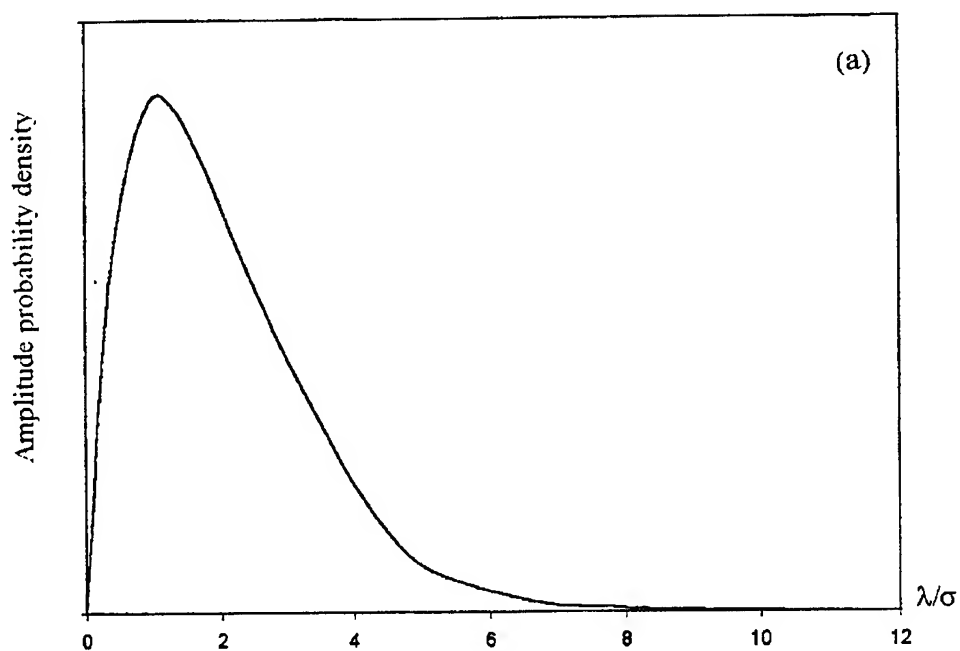


Fig. 13. Estimate of probability density of noise amplitude (a) and reconstructed relation "decay coefficient-amplitude" (b).

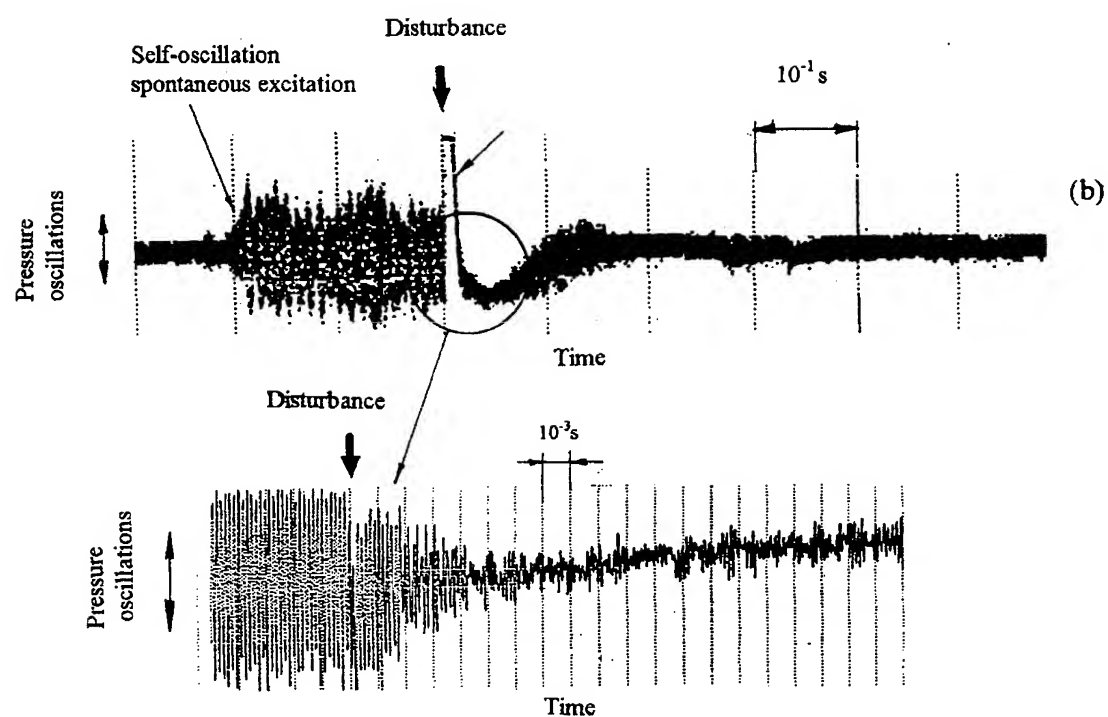
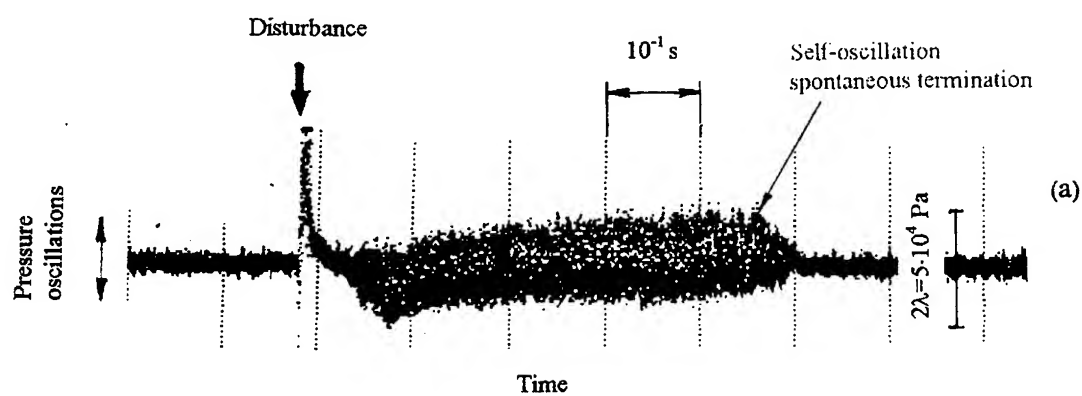


Fig. 14. Self-oscillation excitation (a) and termination (b) artificial disturbance (disturbance applied to the chamber reaction zone).

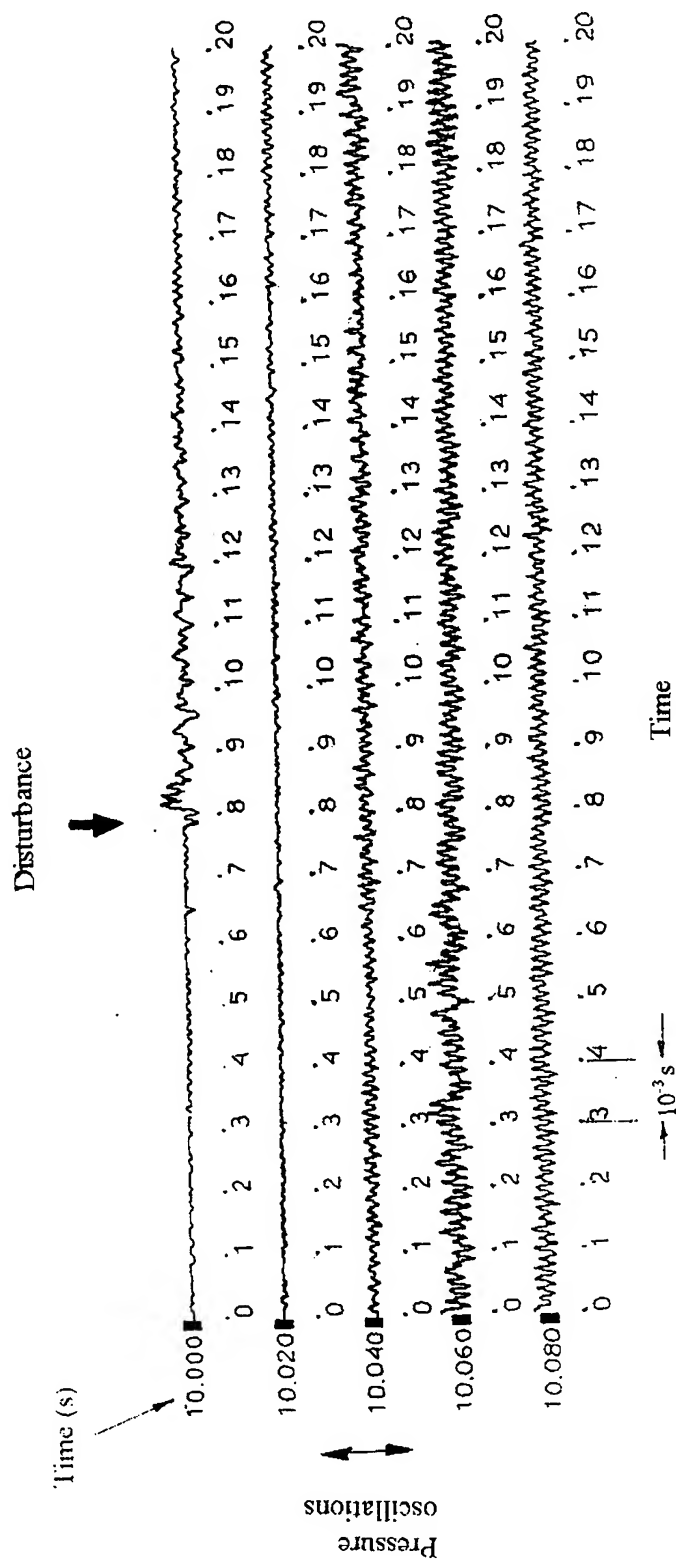


Fig. 15. Character of self-oscillation excitation artificial disturbance (disturbance applied to the chamber reaction zone).

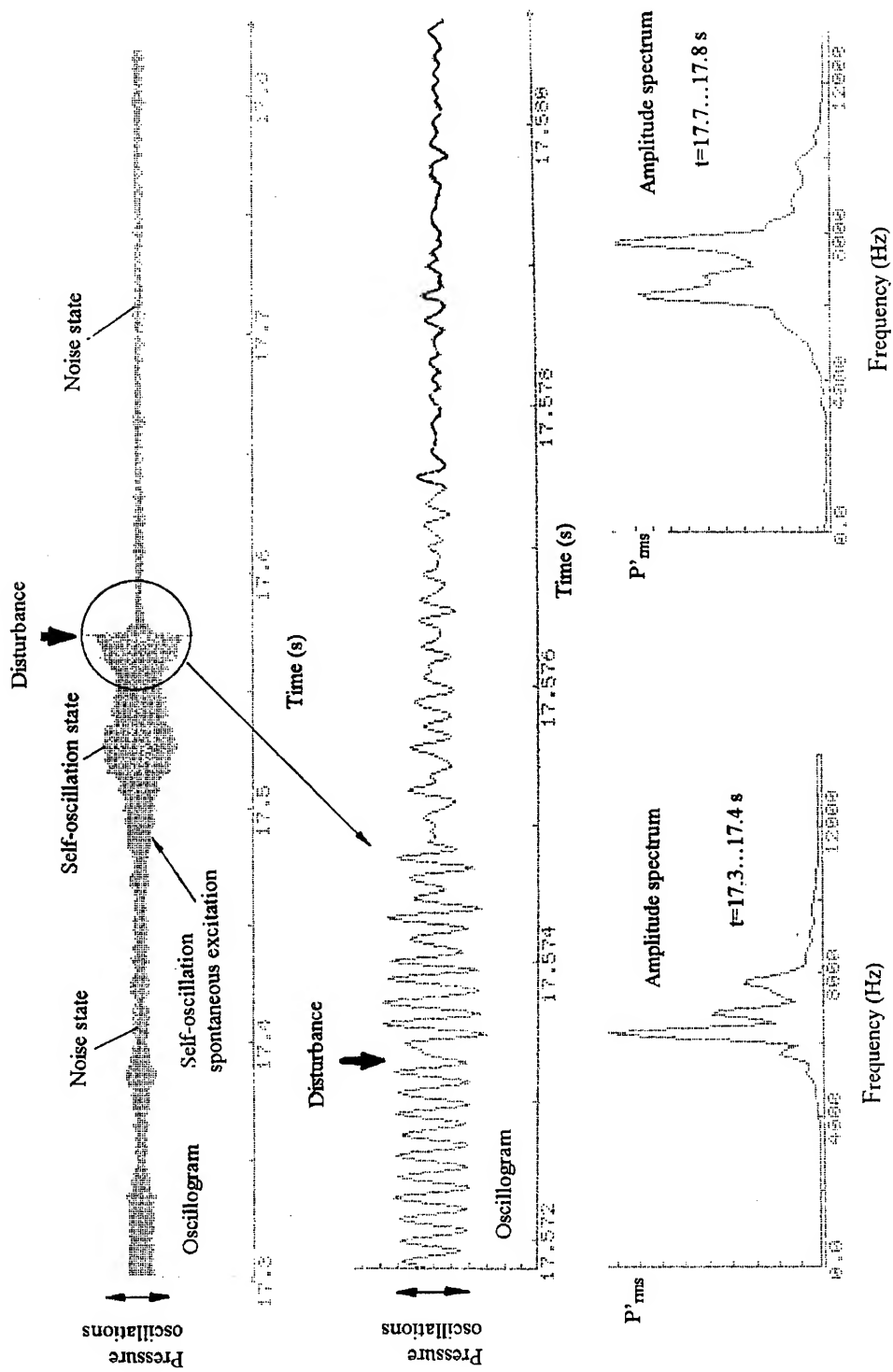


Fig. 16. Self-oscillation termination (disturbance applied to feed cavity).

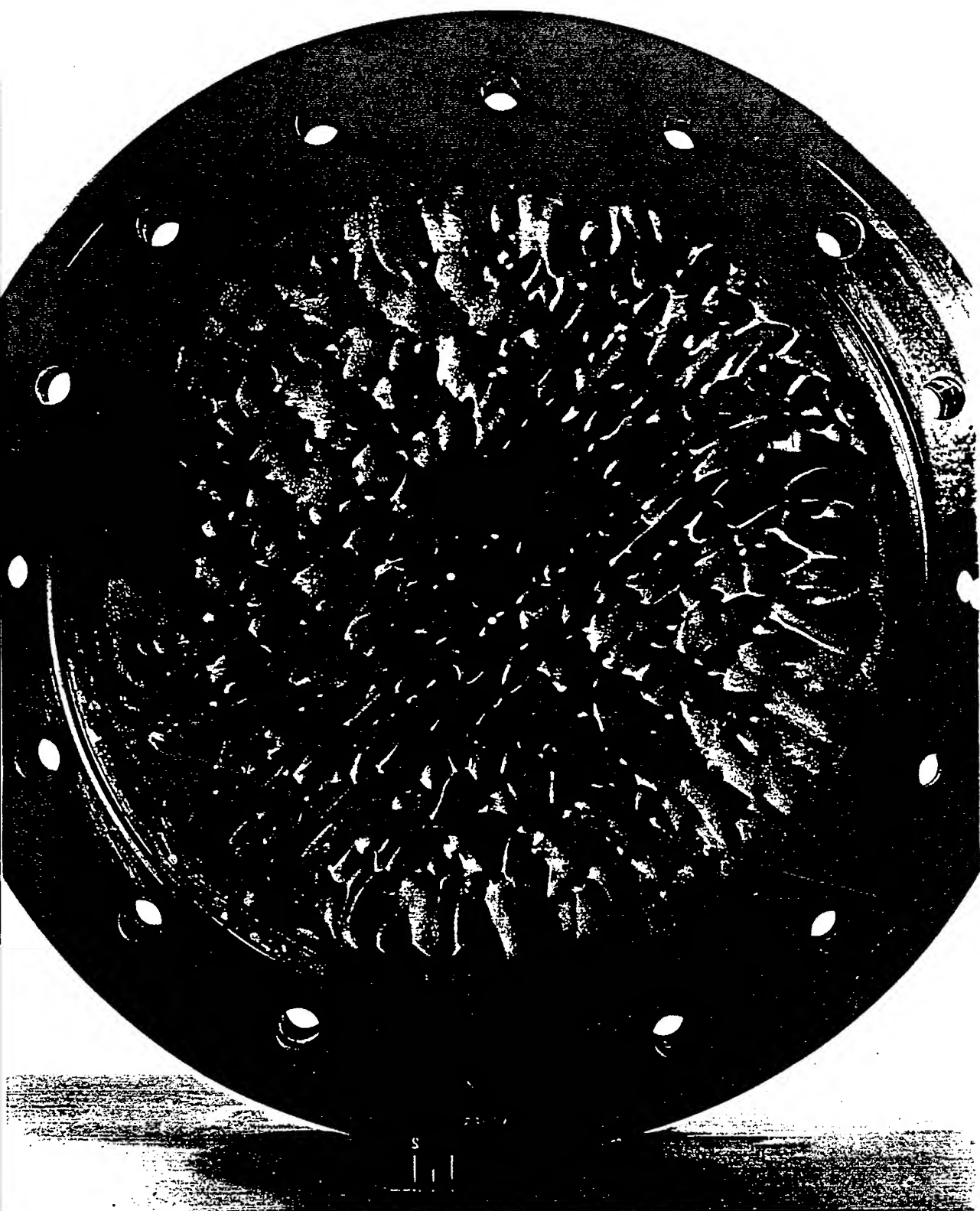
**Fundamental Combustion Instability Research
at Glenn Research Center in the 90's**

by

Kevin Breisacher

May 27-28 1999
Paris, France

GRC=LeRC



40K LOX/CH4 Stability testing

ROCCID

ROCCID LOX/RP-1 stability testing

HICCIP

PacAstro

FASTRAC

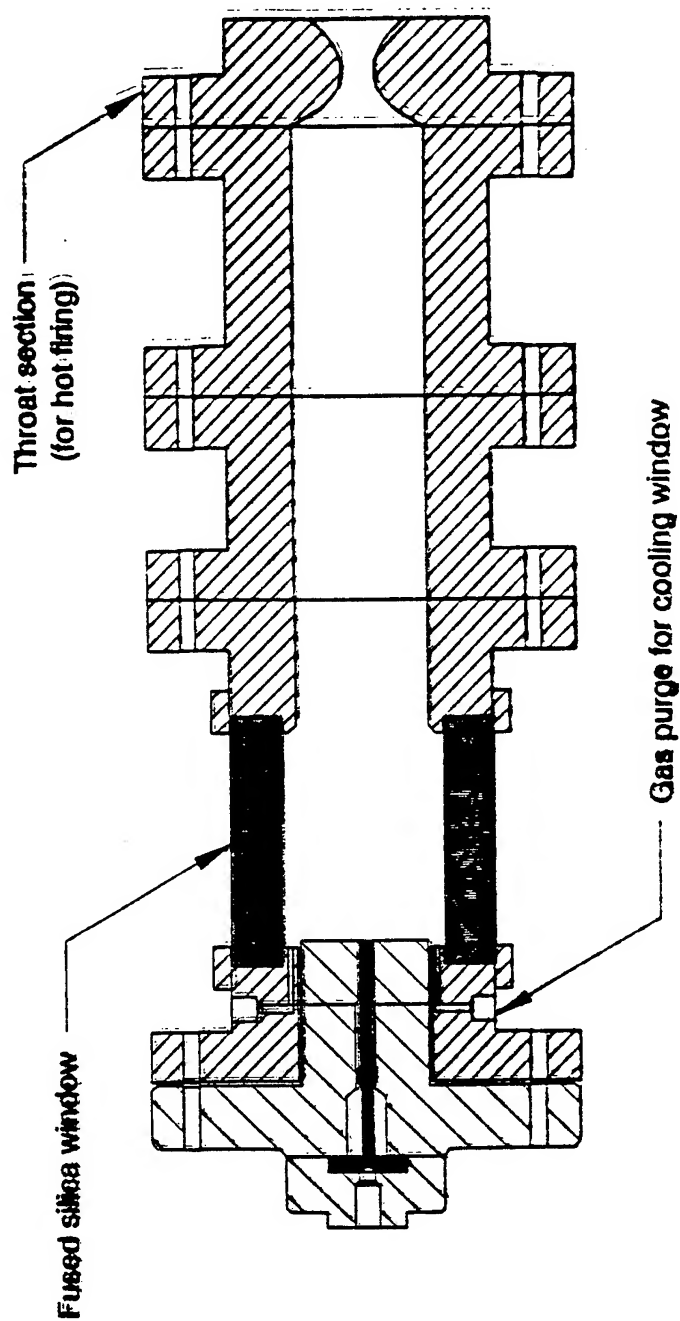
"Unique Combustion Stability Validation Database"

for "same" co-ax element

- air/H₂O simulants
- liquid/ gaseous nitrogen simulants
- hot fire Lox/H₂ PDPA data
- single element instability data

- "Coaxial Injector Spray Characterization Using Water/Air as Simulants", Michelle Zaller, Mark Klem, 28Th JANNAF Combustion Meeting, Volume 2, pp151-160, 1993.
- "LOX/Hydrogen Coaxial Injector Atomization Test Program", Michelle Zaller, 27th JANNAF Combustion Subcommittee Meeting, Volume 3, pp 229-237, 1990.
- "Coaxial Injector Reacting and Non-Reacting Cryogenic Spray Characterization", Mark Klem, 32nd JANNAF Combustion Subcommittee Meeting and Propulsion Engineering Research Center 7th Annual Symposium, Vol 2, 1995.
- "Axisymmetric Single Shear Element Combustion Instability Experiment", Kevin Breisacher, 29th Joint Propulsion Conference, AIAA 93-1953.

Cylindrical Chamber Design





Pr = 0.3

Gaseous and Liquid Nitrogen

No swirl

Gaseous Nitrogen: T = 55°F, .006 lb/s

Liquid Nitrogen: T = -270°F, .024 lb/s

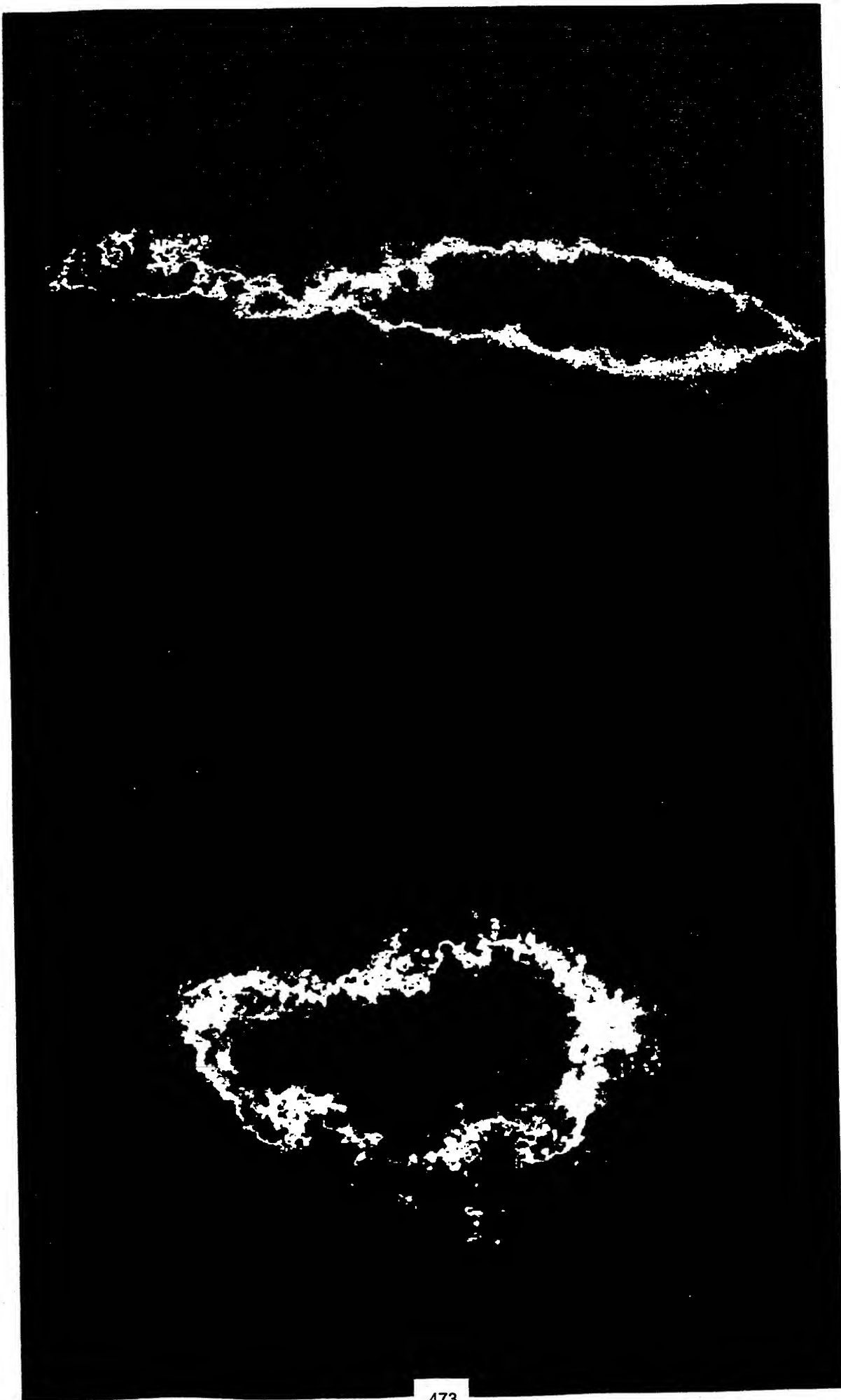
Pr = 1.2

Gaseous and Liquid Nitrogen

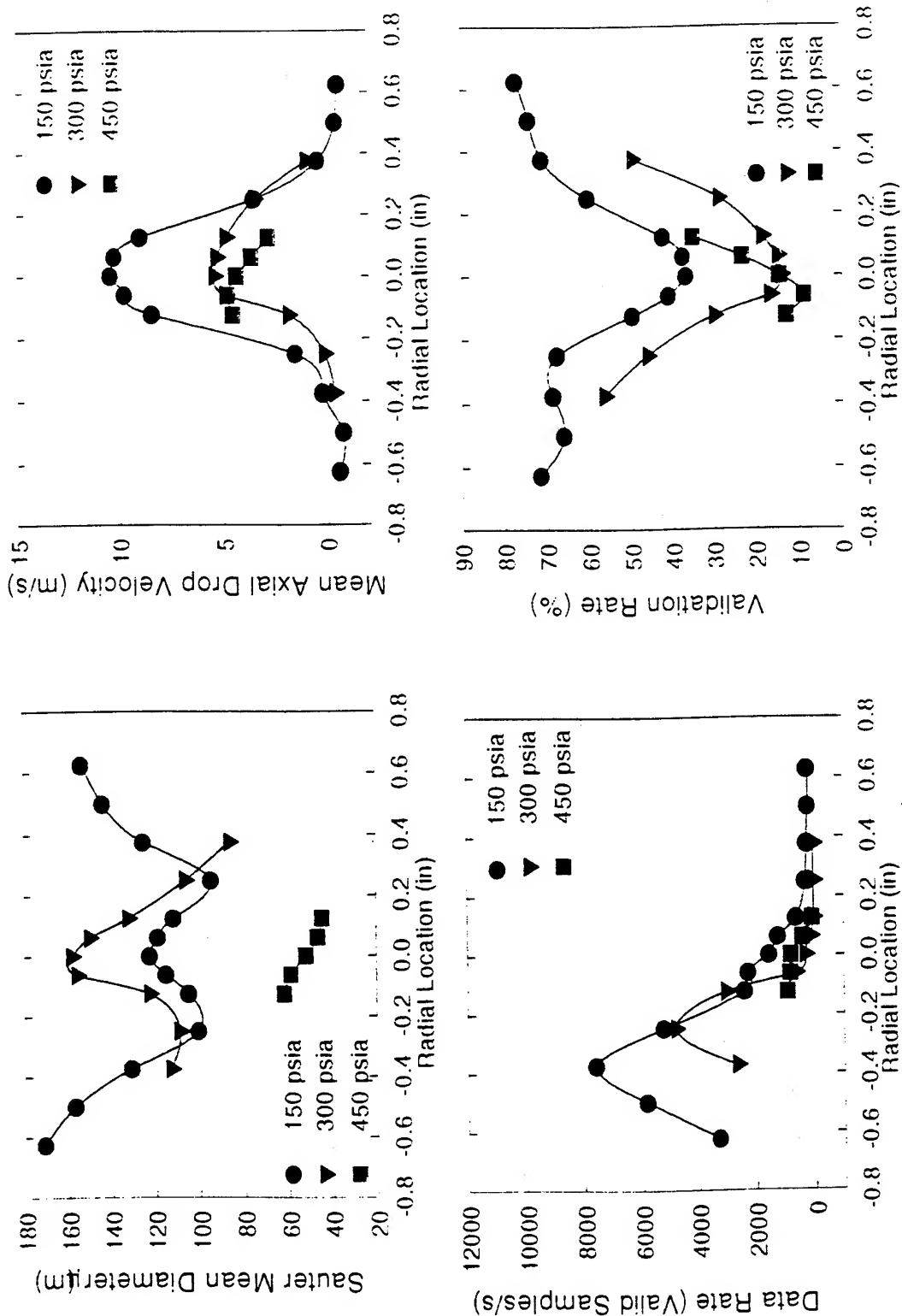
No swirl

Gaseous Nitrogen: T = 55°F, .006 lb/s

Liquid Nitrogen: T = -260°F, .024 lb/s

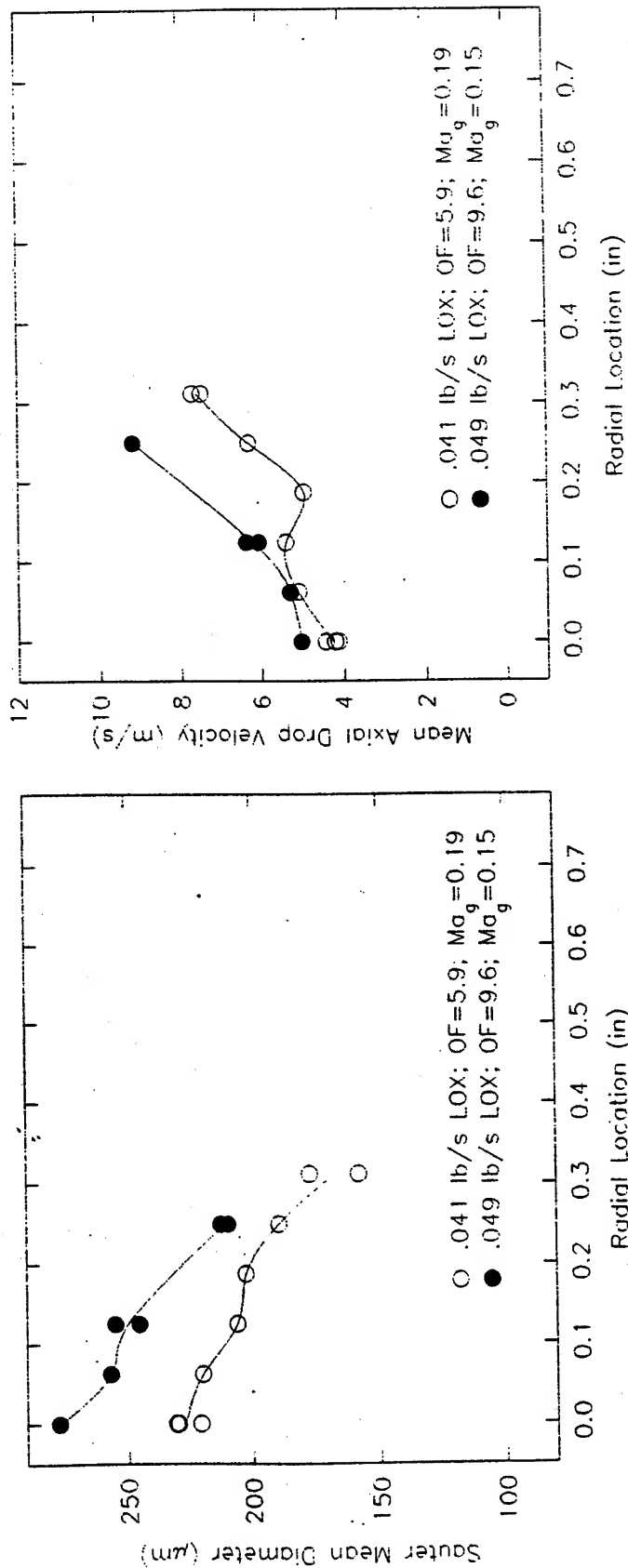


Vaporizing Liquid Nitrogen Spray Data for Varying Chamber Pressures



Liquid nitrogen flow rate .024 lb/s; gaseous nitrogen flow rate .012-.015 lb/s.

Mean Drop Size and Velocity Measurements in Liquid Oxygen/Gaseous Hydrogen Sprays



CHAMBER PRESSURE 160 PSIA ($P_r=0.2$)

$Re_L=60,000$

TEST PARAMETERS

FOR PHASE/DOPPLER DROP SIZE MEASUREMENTS

	Liquid/Gaseous Nitrogen	LOX/Gaseous Hydrogen
Pr	0.3	0.2
Tr	0.7	0.6
Re(L)	71,000	60,000
$\dot{m}(L)/\dot{m}(g)$	2,3	6,10
V(g) (ft/s)	78, 120	650, 820
Ma(g)	.07, .10	.15, .19

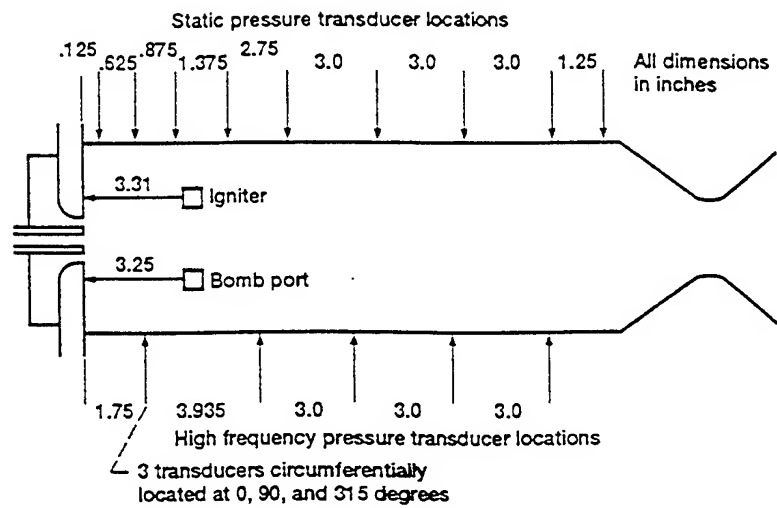


Figure 4.—Pressure transducer locations.

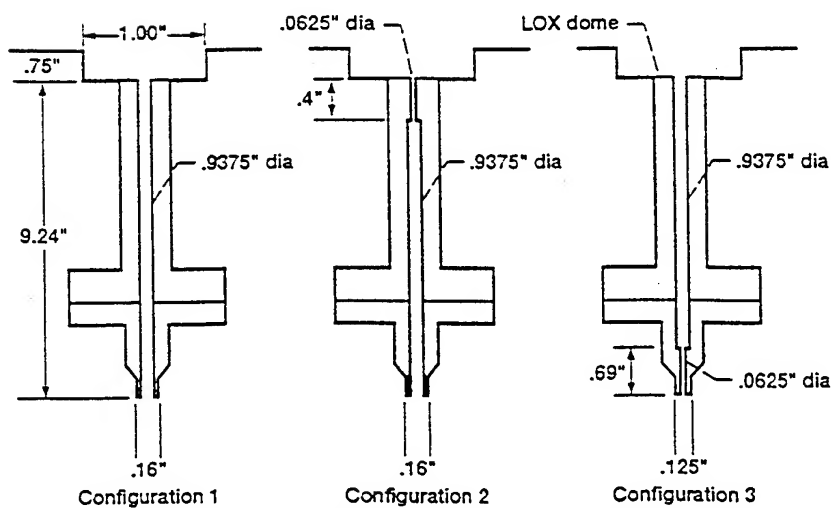


Figure 5.—Schematics of LOX post configurations.

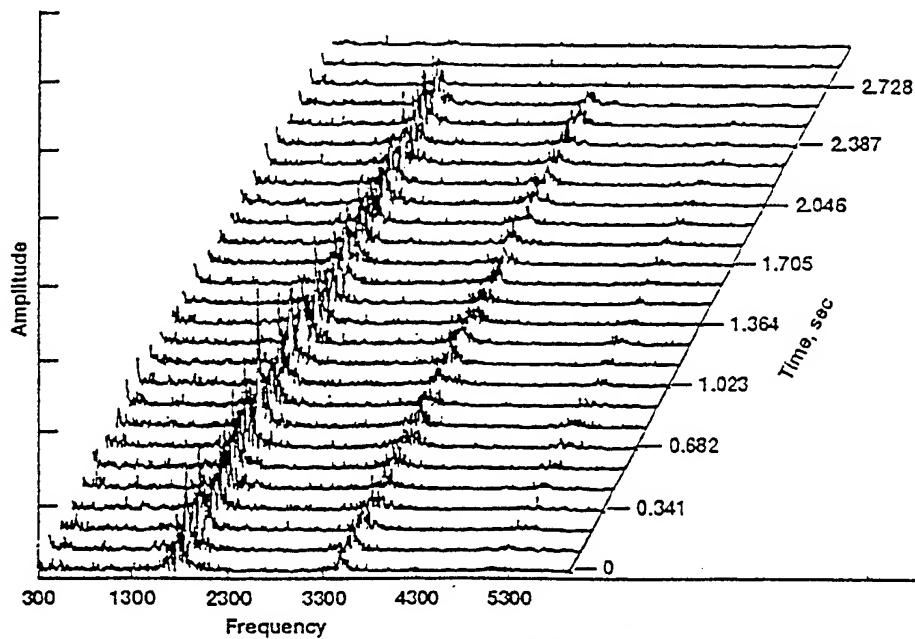


Figure 8.—Cascade plot of pressure for unstable test 292.

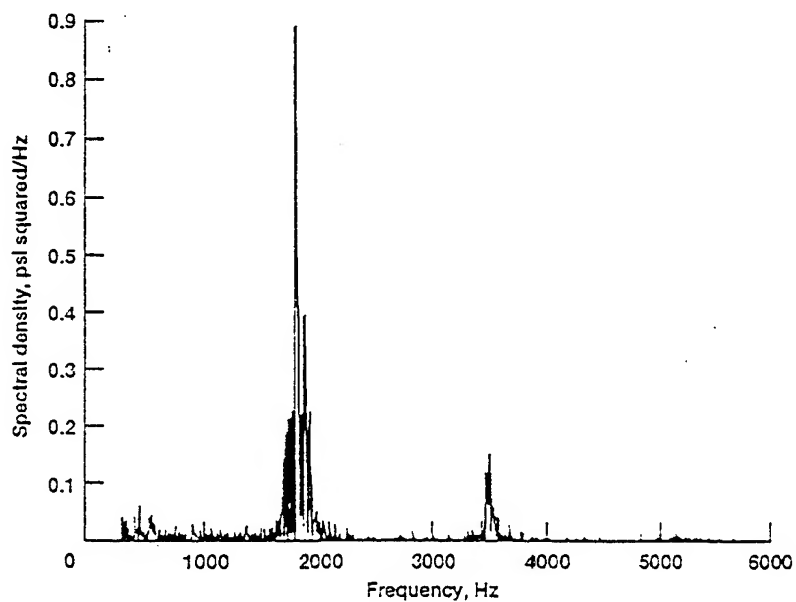


Figure 9.—Power spectral density plot for unstable test 292.

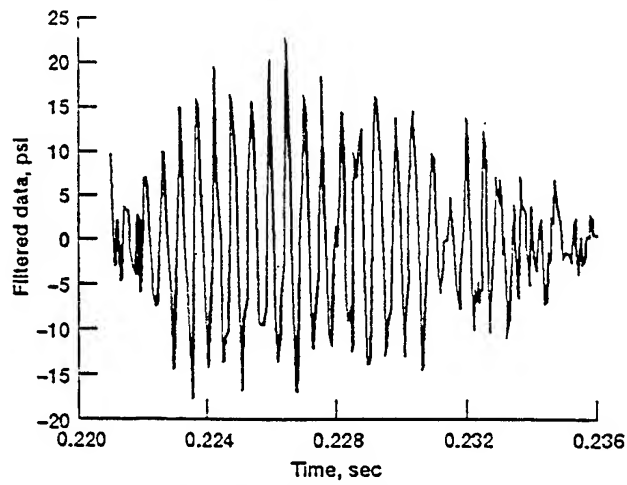


Figure 10.—Expanded digitized pressure trace for unstable test 286.

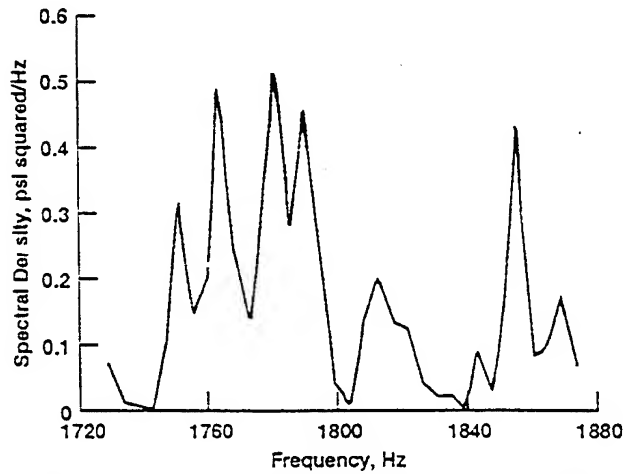


Figure 11.—Power spectral density plot for unstable test 286.

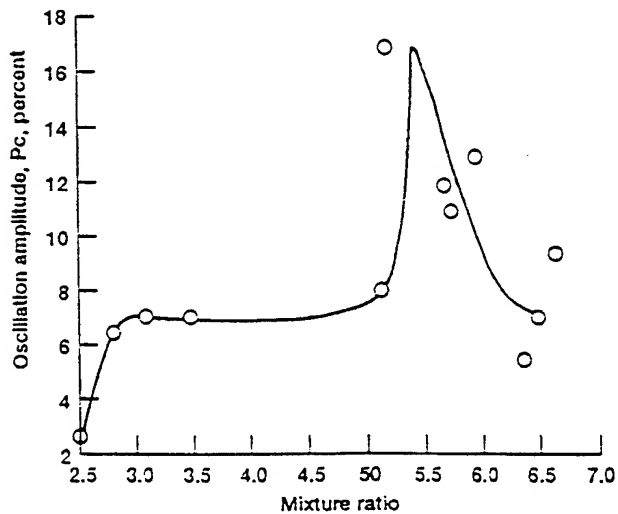


Figure 12.—Variation of oscillation amplitude with mixture ratio (configuration 3, $D_f = .235$).

High Energy Laser as a Stability Rating Device

Disclaimer: results presented are by no means
a thorough evaluation of the concept

Piggybacked at tail end of laser ignition test program

"High Energy Lasers as a Stability Rating Device"
Kevin Breisacher, Pennsylvania State Propulsion
Engineering Research Center, Volume 2, pp 148-152, 1995.

Bombs

ADVANTAGES

- may simulate "natural" engine disturbance
- database from experience
- can be positioned throughout the chamber

DISADVANTAGES

- may not create a resonance of sufficient amplitude to incite an instability
- chamber damage possible
- shrapnel damage possible
- thermal initiation: fizzling
- several bombs per test sometimes possible
- danger: unexploded bomb
ejecting a bomb

Laser Pulsing

ADVANTAGES

- clearer determination of stability margin
- multiple tests
(setup-oscillation, turn-off, etc.)
- no shrapnel
- aid in tuning stability aids
- potential HM device ("enhanced noise")

DISADVANTAGES

- optical access
ZnSe
Pcb
laser ignition
- sensitivity to location

Energy

1 grain RDX \longrightarrow 386 J
100 W CO₂ \longrightarrow 3.68 s

(of course want to couple to combustion process)

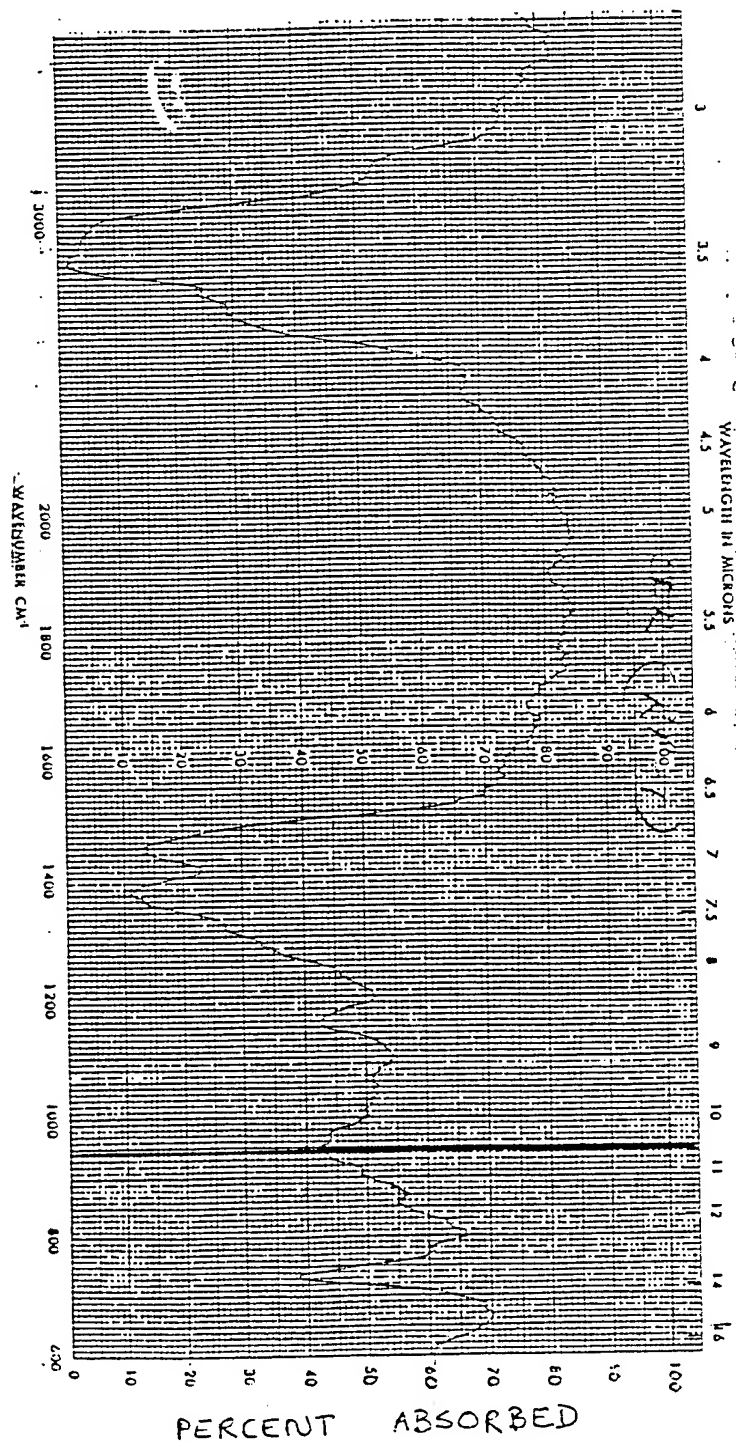
Power

100 W vs.

$$\frac{386 \text{ J}}{50 \text{ microseconds}} = 7.36 \text{ MW}$$

Why CO₂ ?

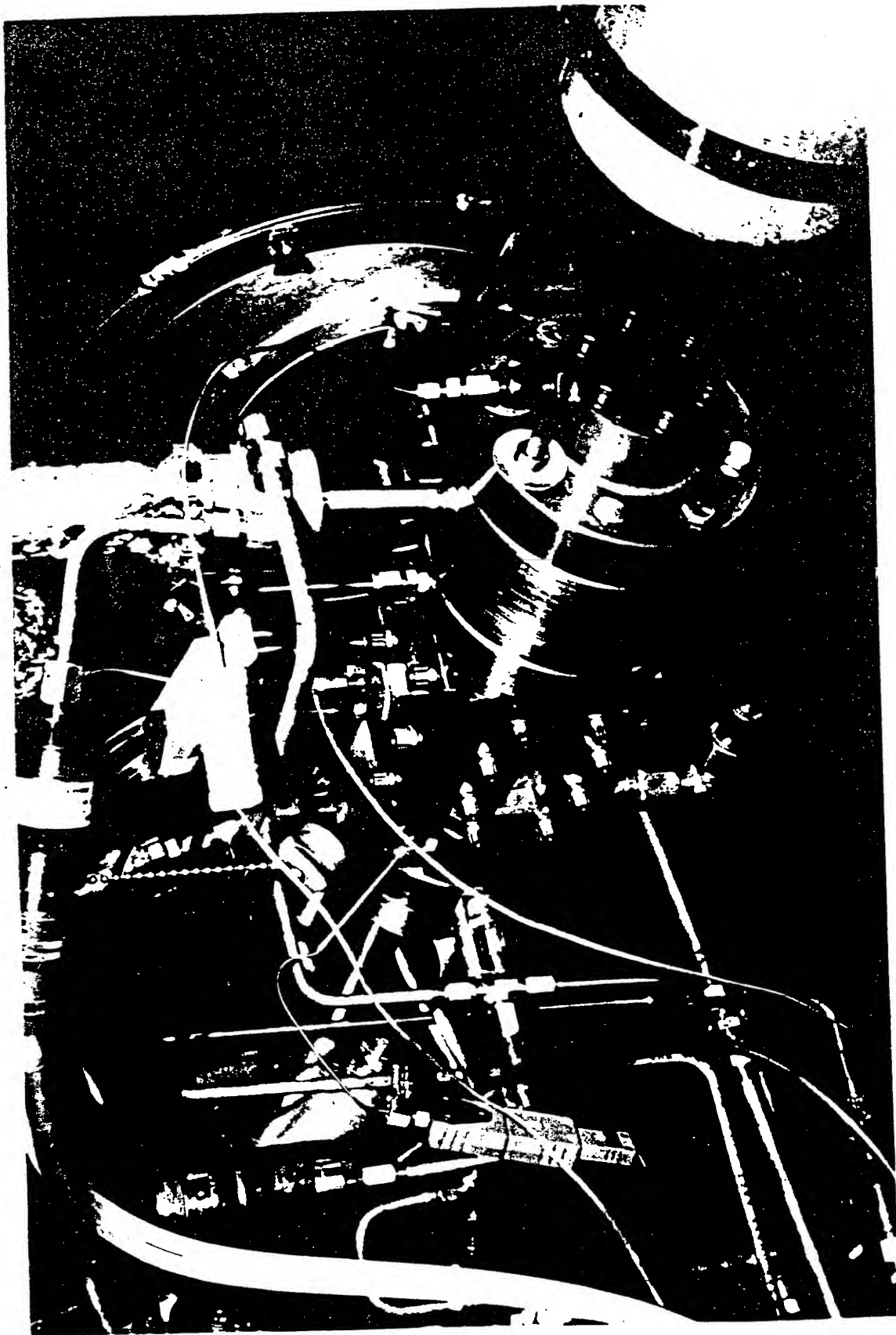
- cheap, reliable
\$15K / 100 W
- RP 1 fairly absorbent at 10.6
(optics too big and costly to create a laser spark at 10.6)

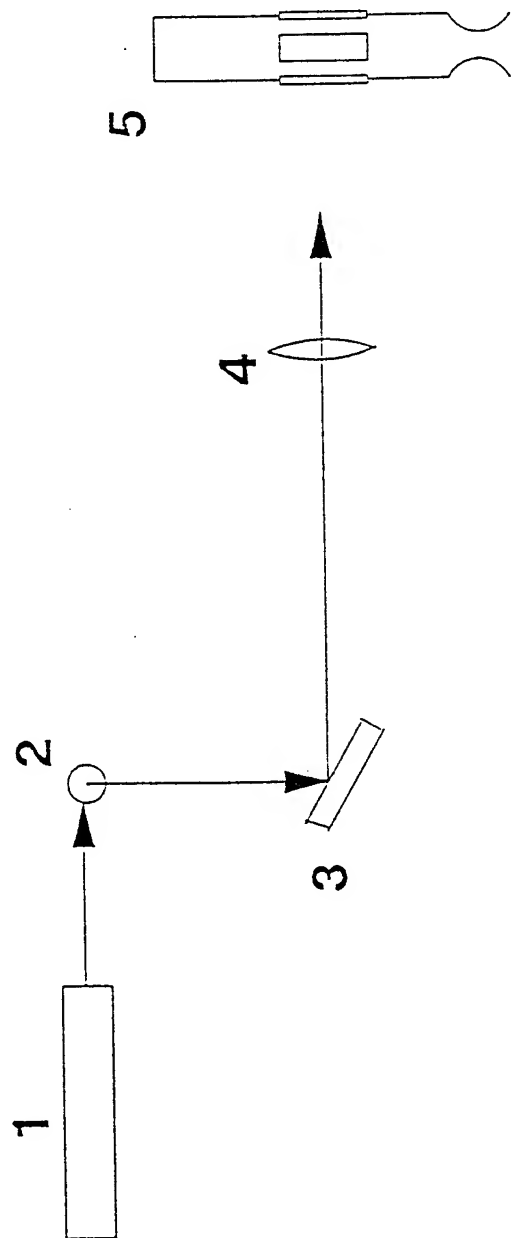


Test Engine

Length	8.88"
Diameter	2.06"
Pc	70 psi
MR	1.7 - 2.5

4 GOX/RP 1 triplets
nominal 1L 2622 Hz





1. CO2 Laser
2. Periscope
3. 45 - degree mirror
4. Focusing lens
5. Test combustor

CO2 Laser

Synrad 57-1 sealed gas, RF excitation

Power	100W
beam diameter	4 mm
wavelength	10.6 microns
pulse rate	2 - 10 kHz (at 50% duty cycle)
pulse energy	32 mJ - 17 mJ
	2 kHz 5 kHz

Attempts to drive at

2600 Hz, 3000 Hz, 5000 Hz, 5200 Hz

- no oscillations observed except when driving at 5000 Hz

Driving at 5000 Hz

oscillations ~ 3% of P_c
at 2380 Hz

beat frequency ~ 125 Hz

- power at 5000 Hz 35% > that at 2600 Hz or 5200 Hz
- closer to 1L frequency at half 5000 Hz

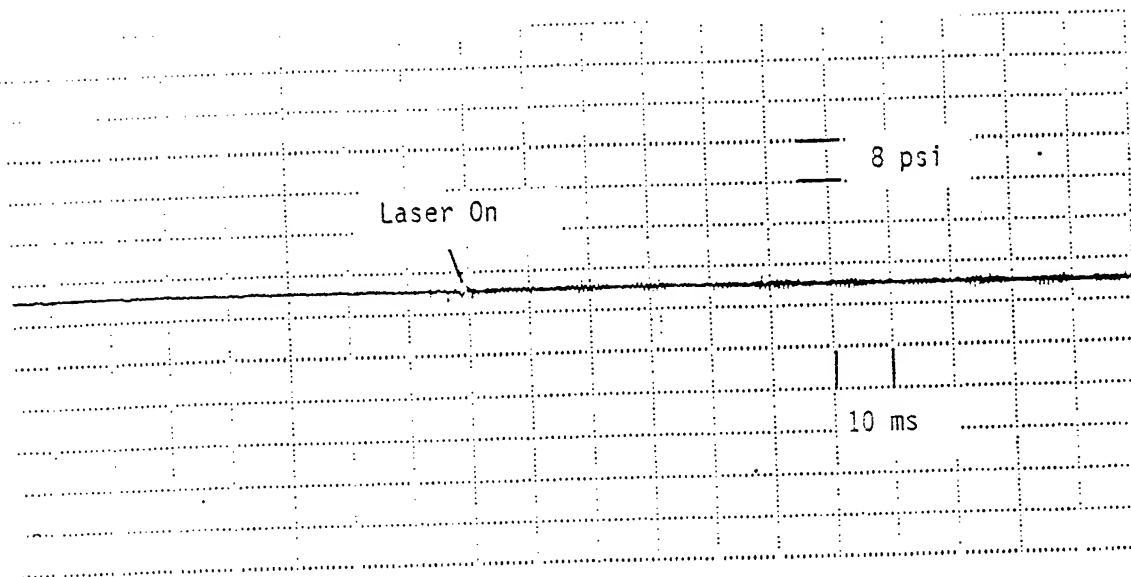


Figure 3a. - Pressure Trace

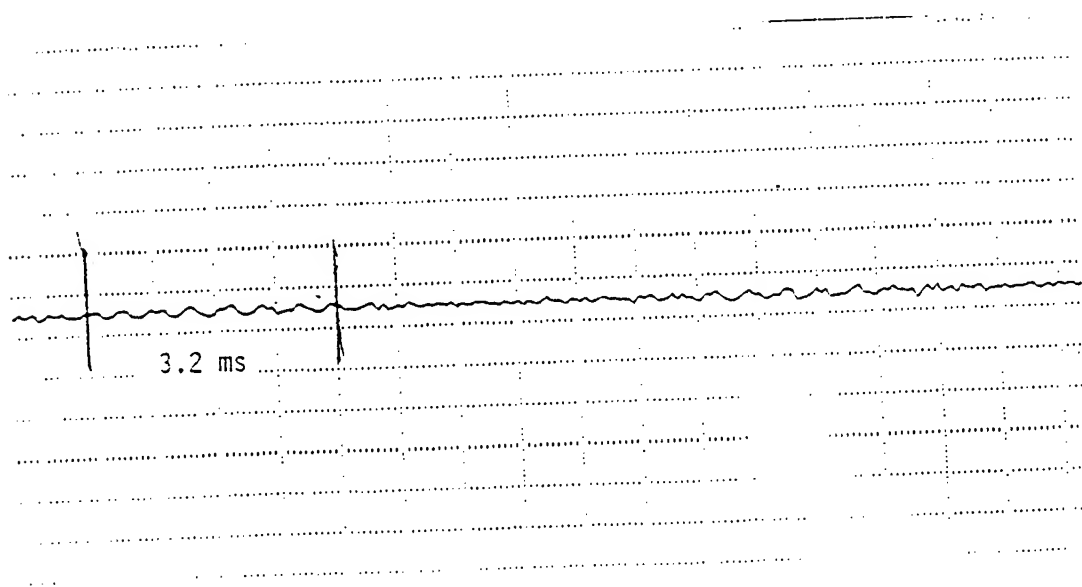
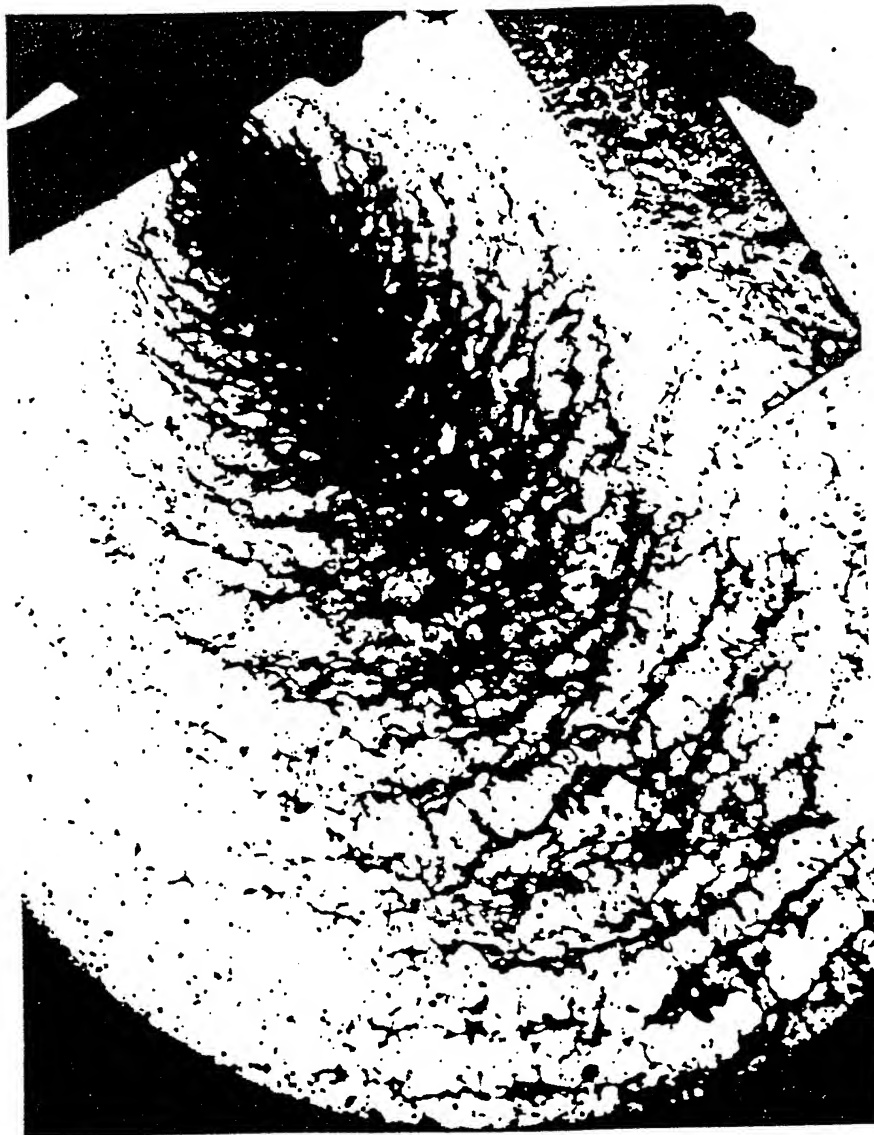


Figure 3b. - Expanded Pressure Trace

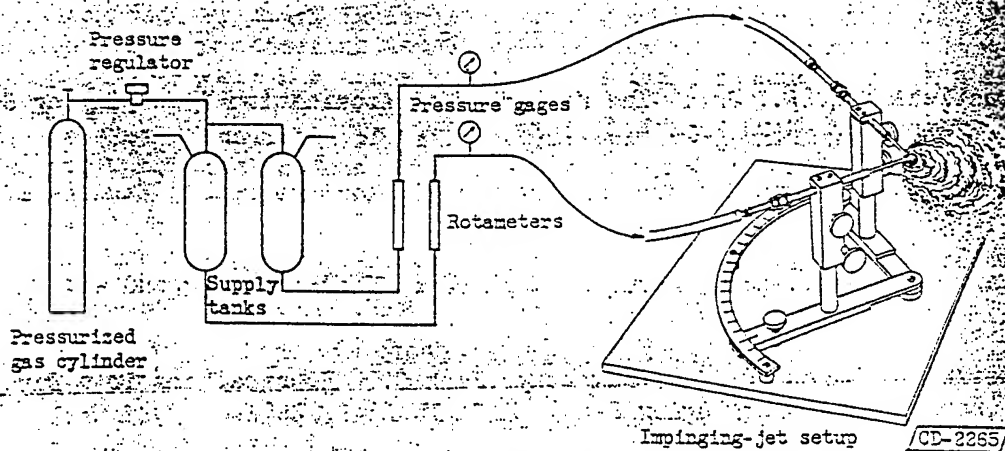
SUMMARY

Despite far from optimal conditions (unsteady combustion, inability to move the focal point) we were consistently able to drive very small amplitude oscillations with laser pulsing.

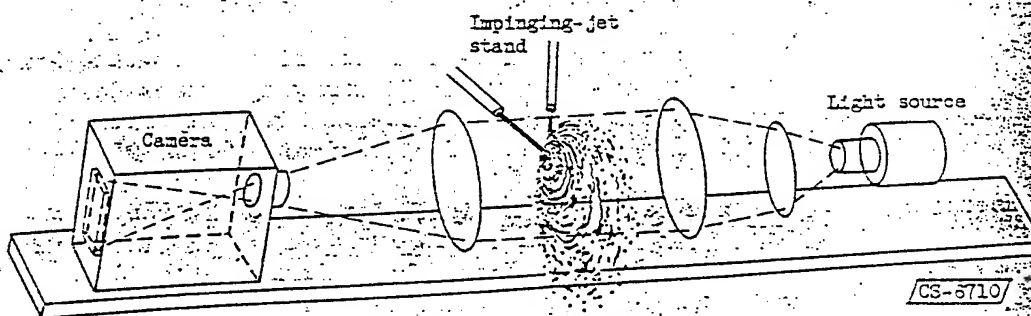
Atomization of an Impinging Jet Fan is Periodic ?



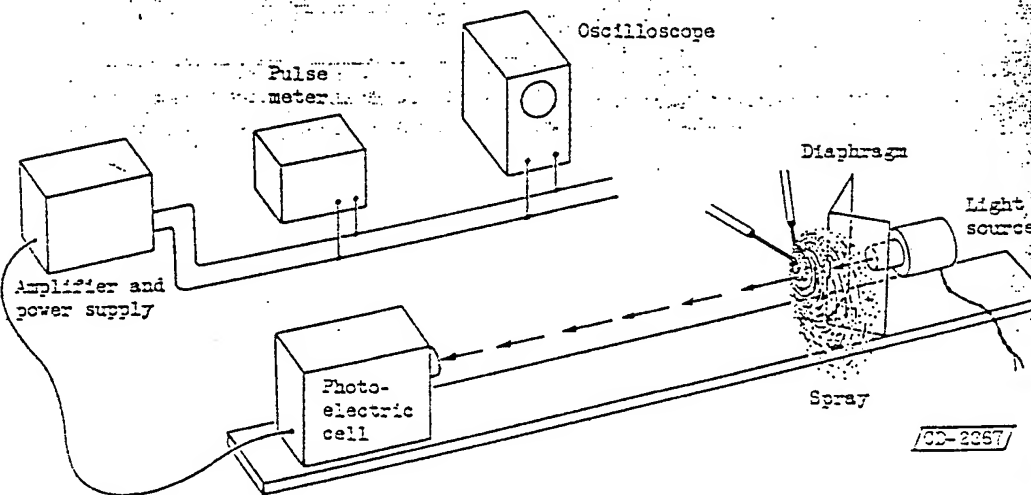
M16/D841q Rch1.3.0



(a) Flow apparatus.

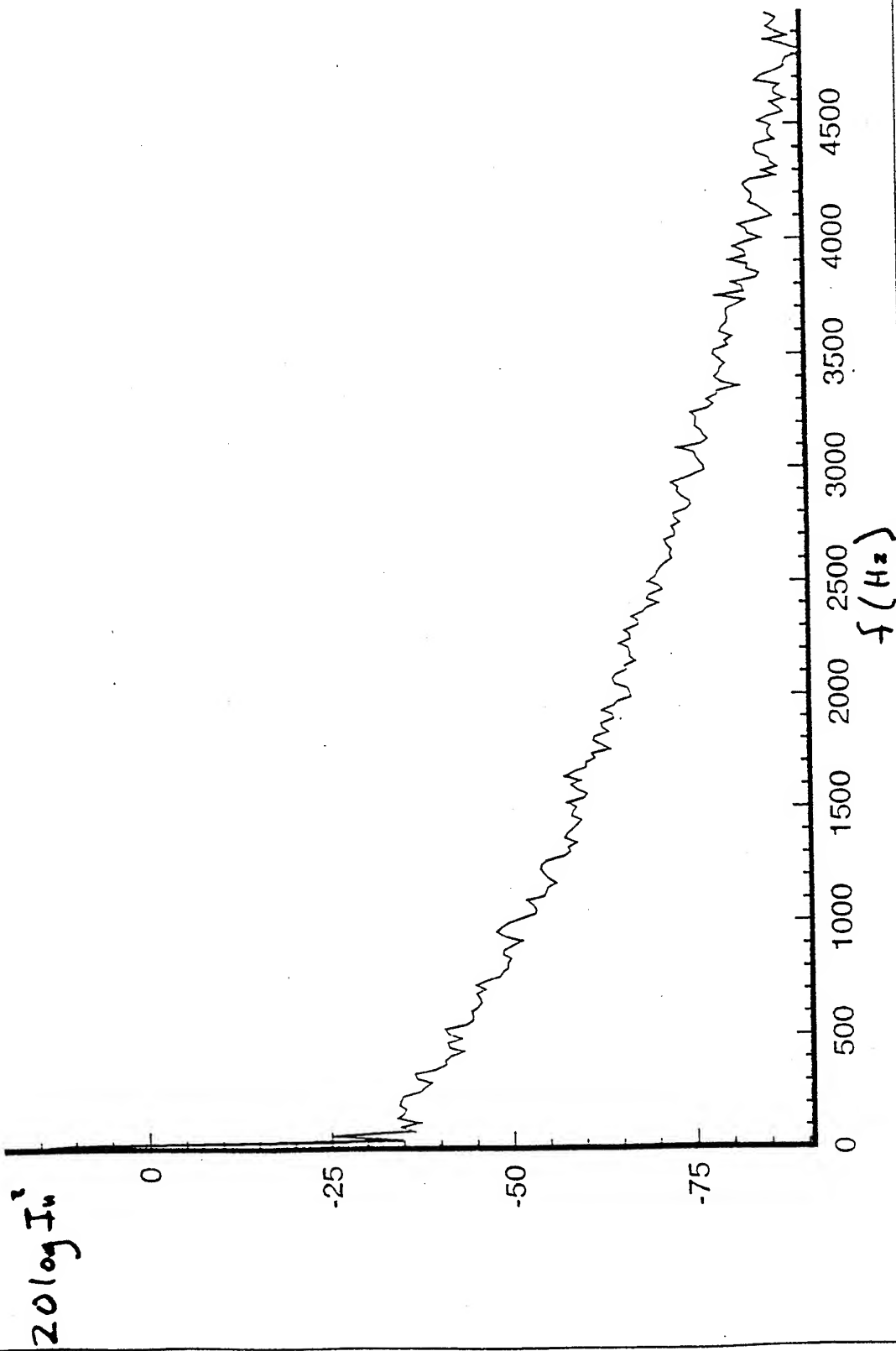


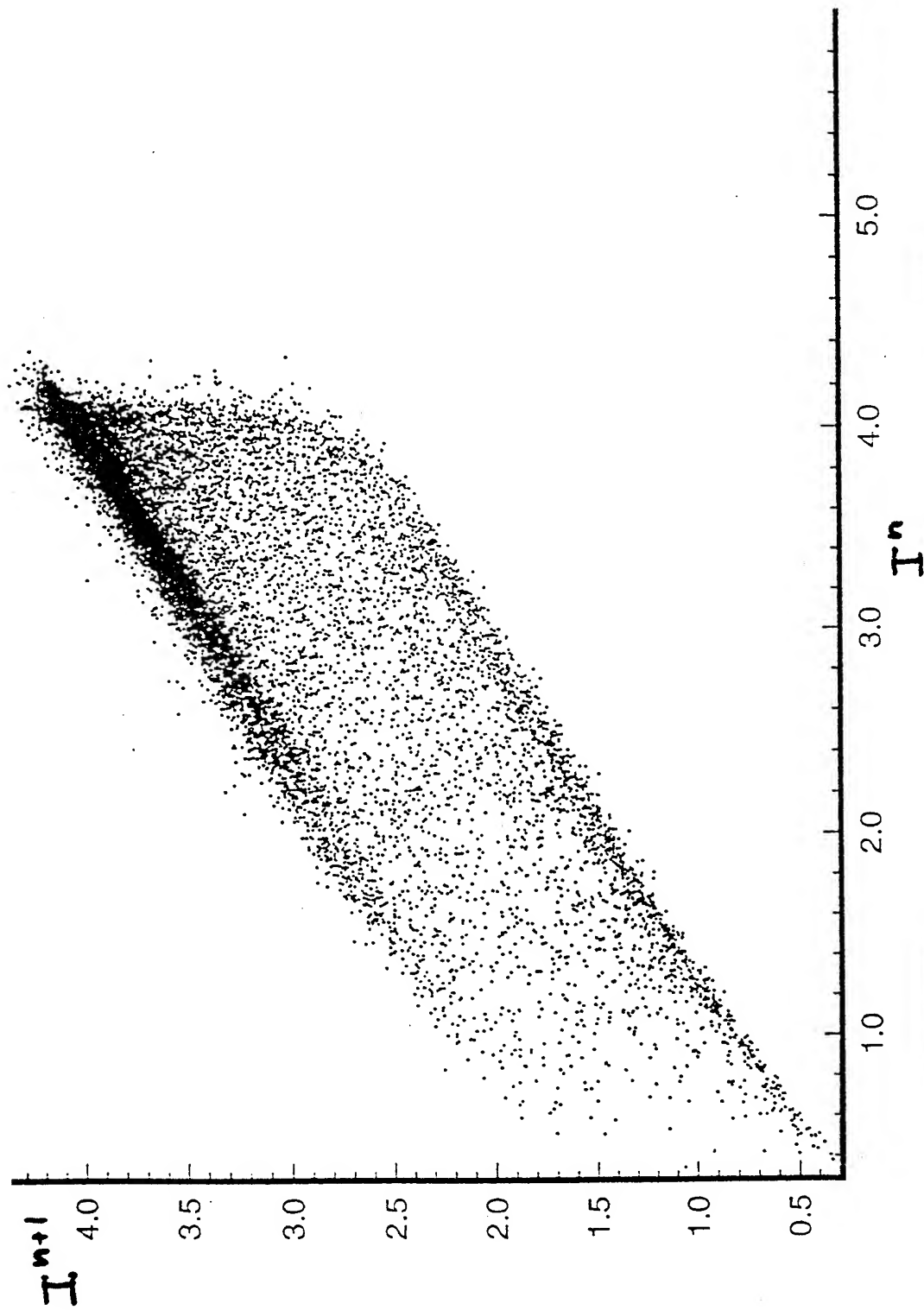
(b) Photographic apparatus.

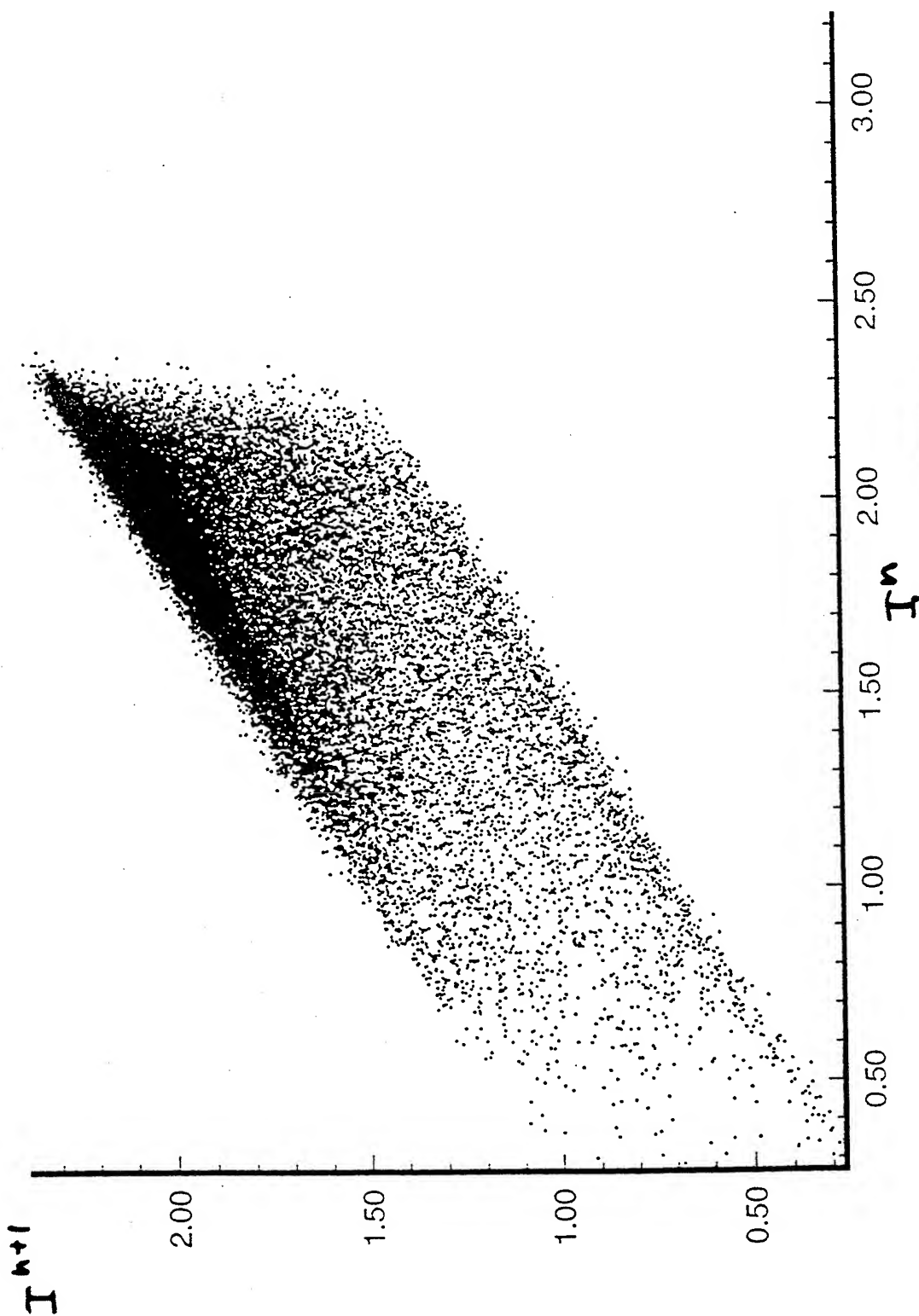


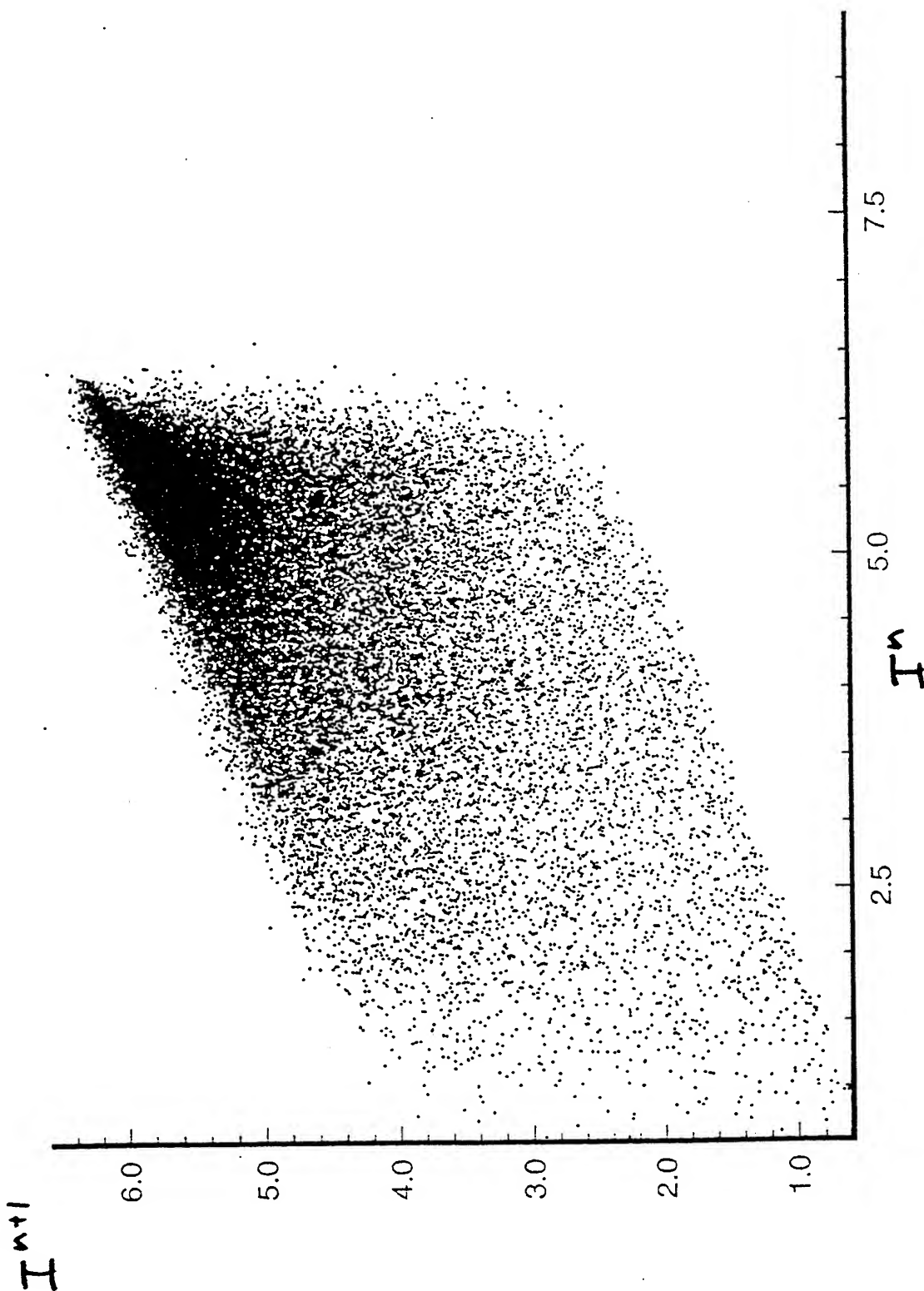
(c) Frequency measurement apparatus.

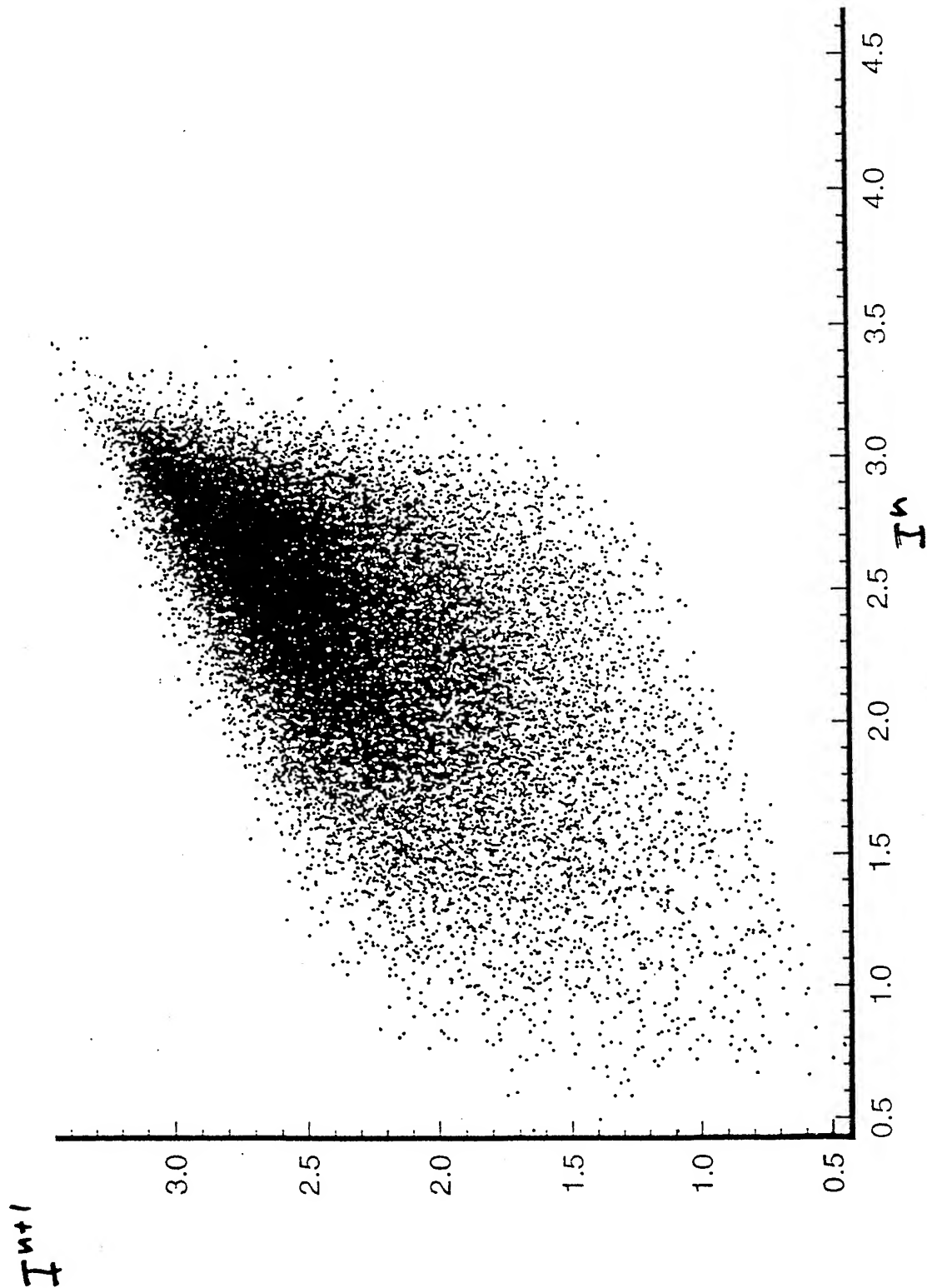
Figure 1. - Schematic diagram of impinging-jet apparatus and instrumentation.











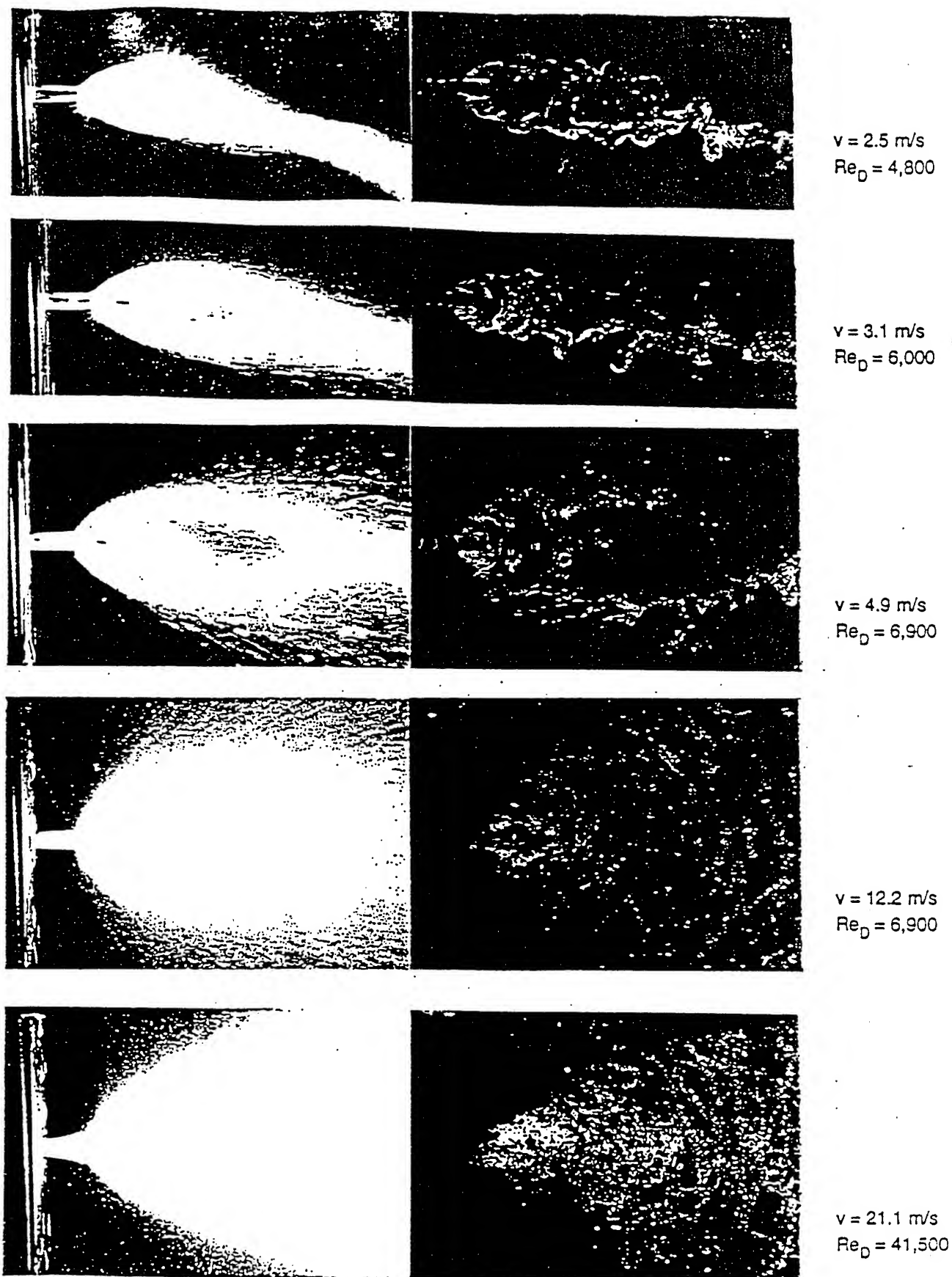
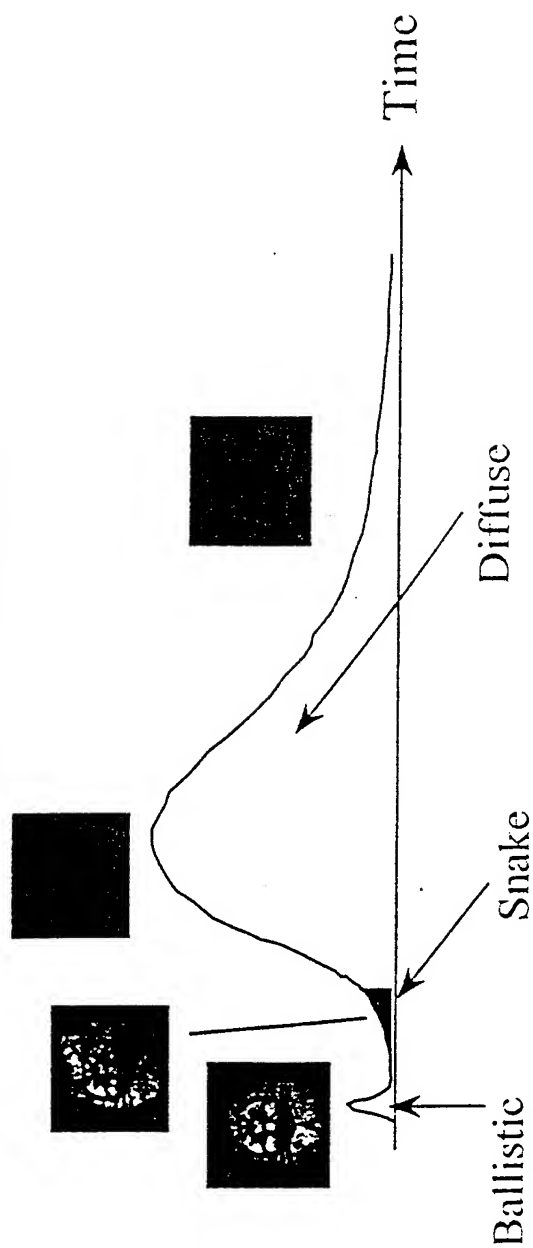
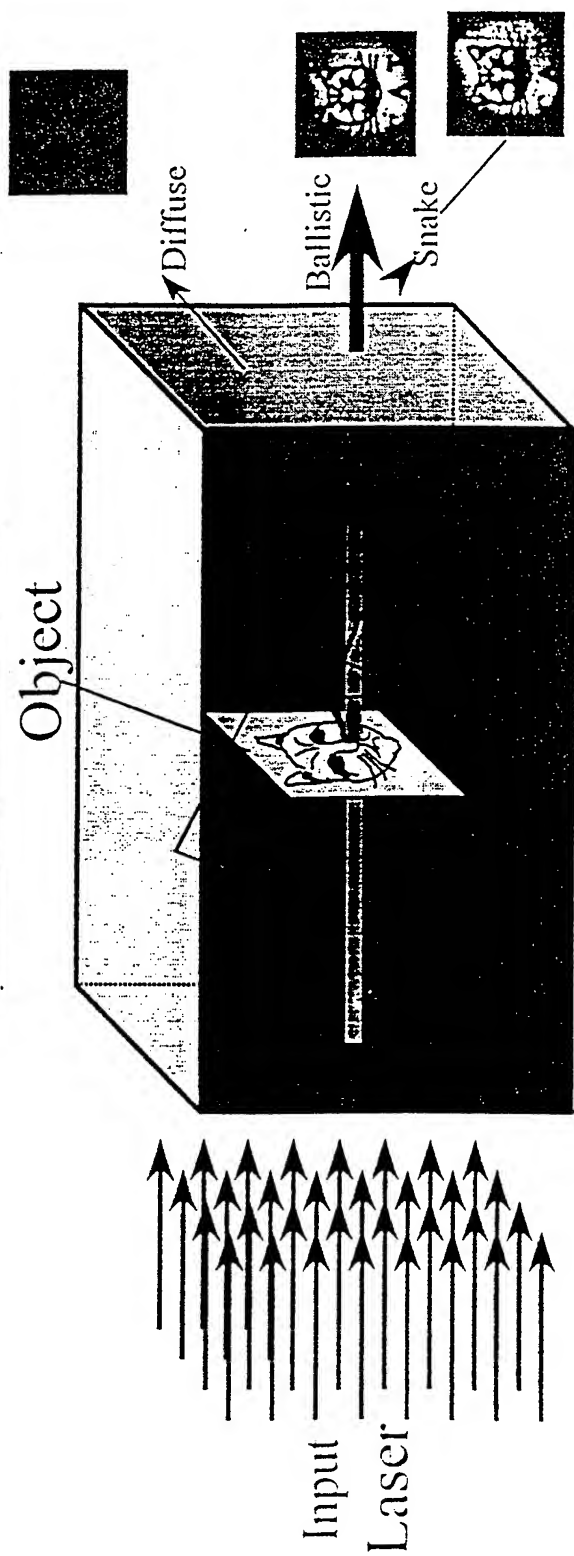


Figure 4 Comparison of multiple-exposure (time-averaged) with instantaneous photographs.

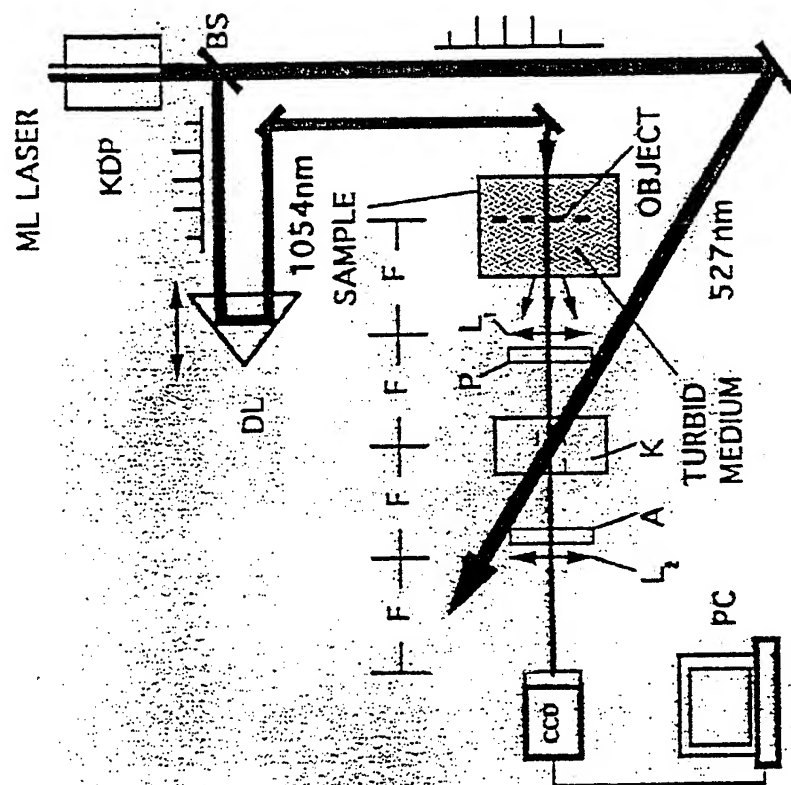
Ultrafast Imaging of Sprays

"Picosecond Imaging of Sprays", L. Wabg (CCNY), Kevin Breisacher, et al, Pennsylvania State University Propulsion Engineering Research Center, Volume 2, pp 221-225, 1995.

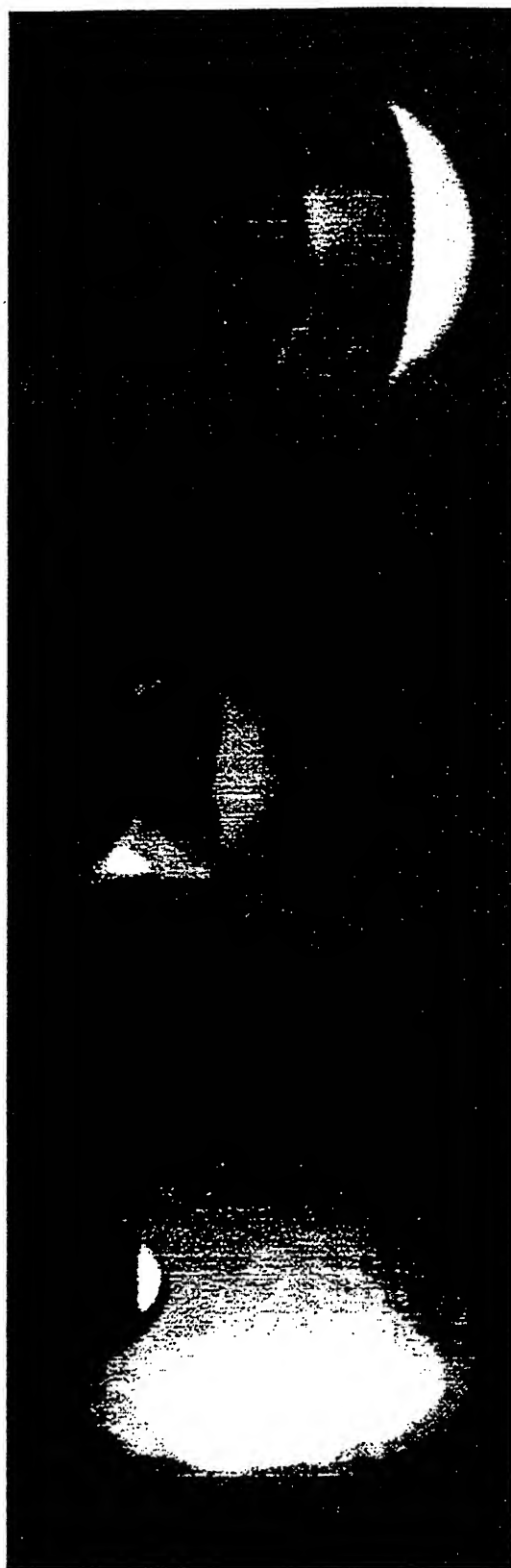
Optical Imaging



Time-Resolved Kerr-Fourier Imaging System



Results

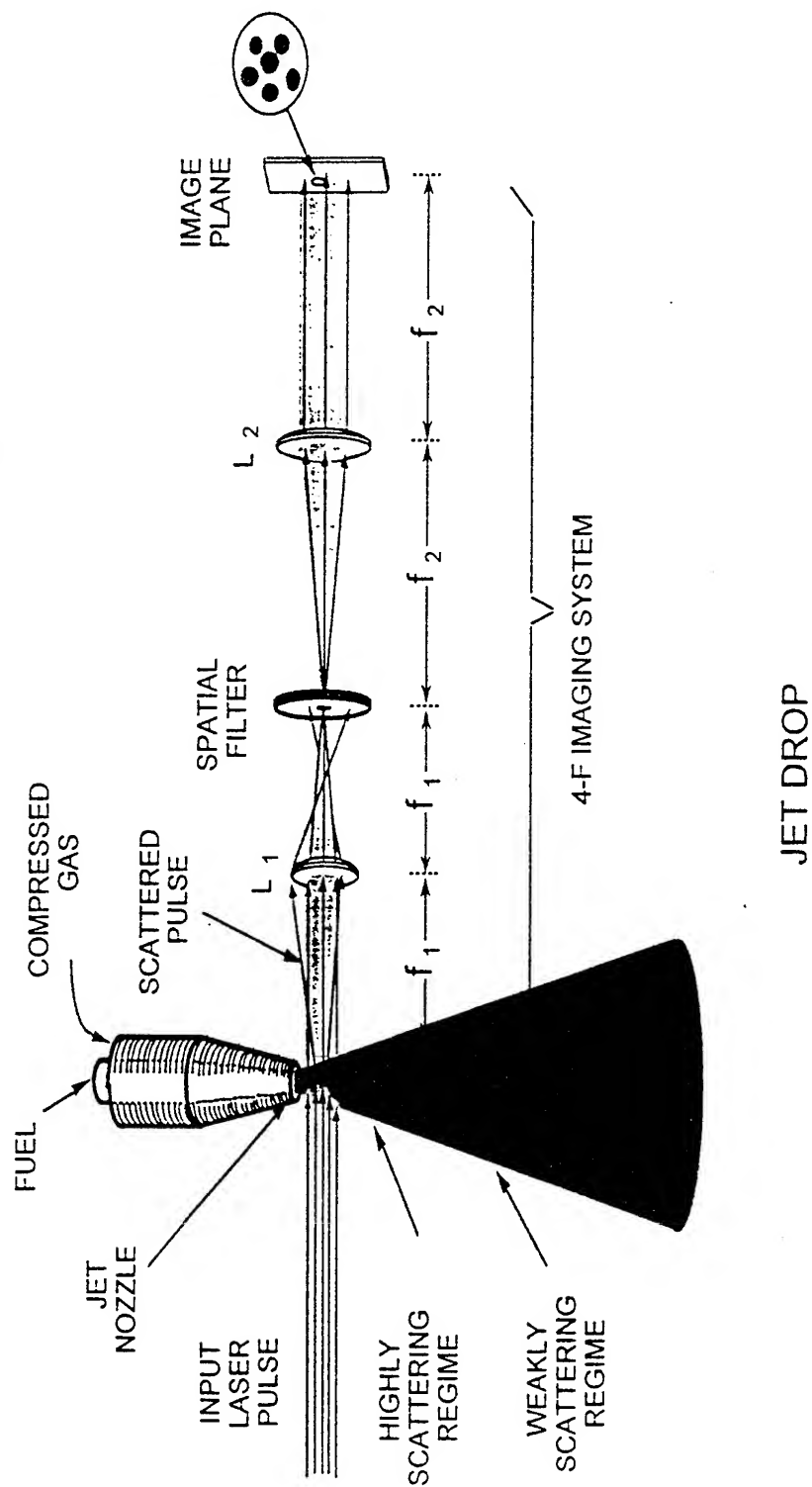


$T = 2 \text{ sec}$ $T = 5 \text{ sec}$ $T = 10 \text{ sec}$

Early time two-dimensional shadowgram image of water phantom droplet in a highly scattering host 50 mm thick of 2% diluted intralipid stok solution.

Probe beam : 1054 nm; Pump beam : 527 nm

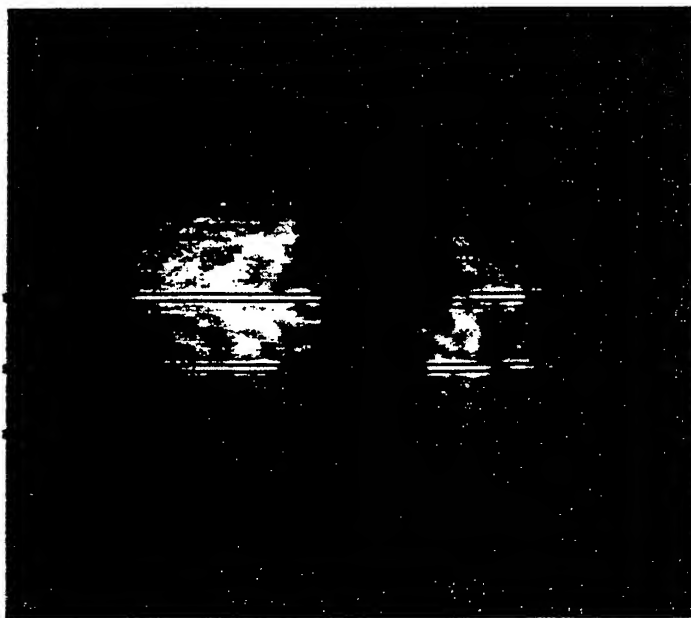
Experimental Setup



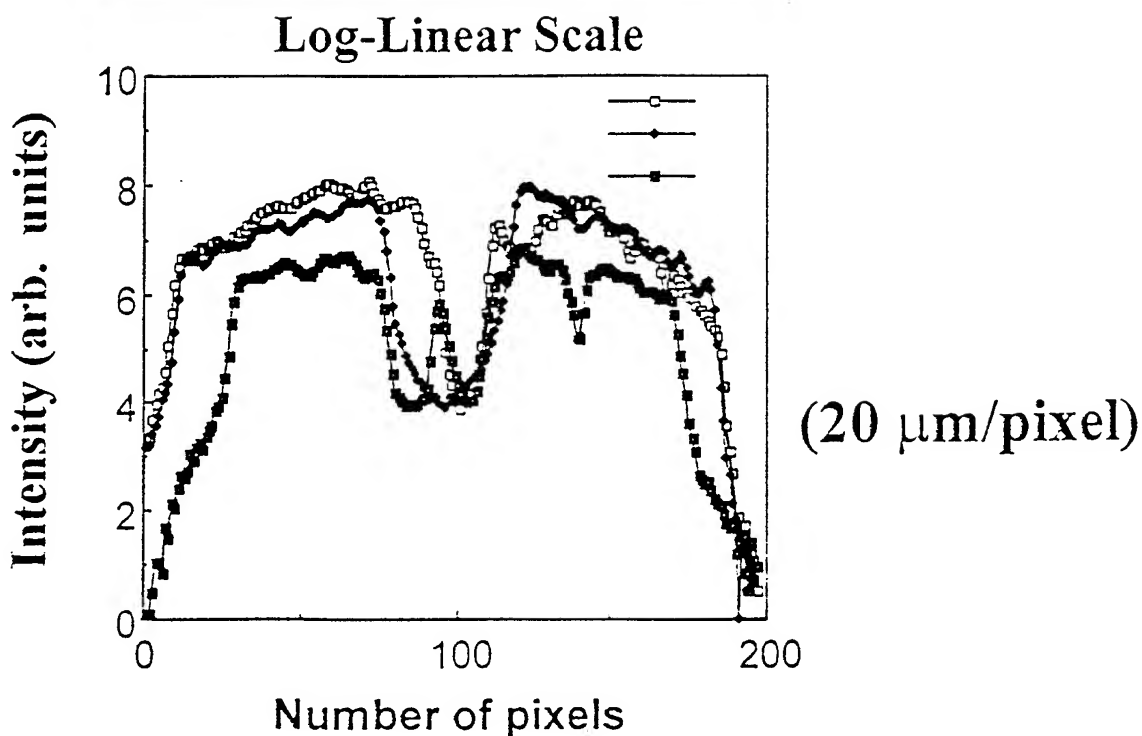
JET DROP

Results

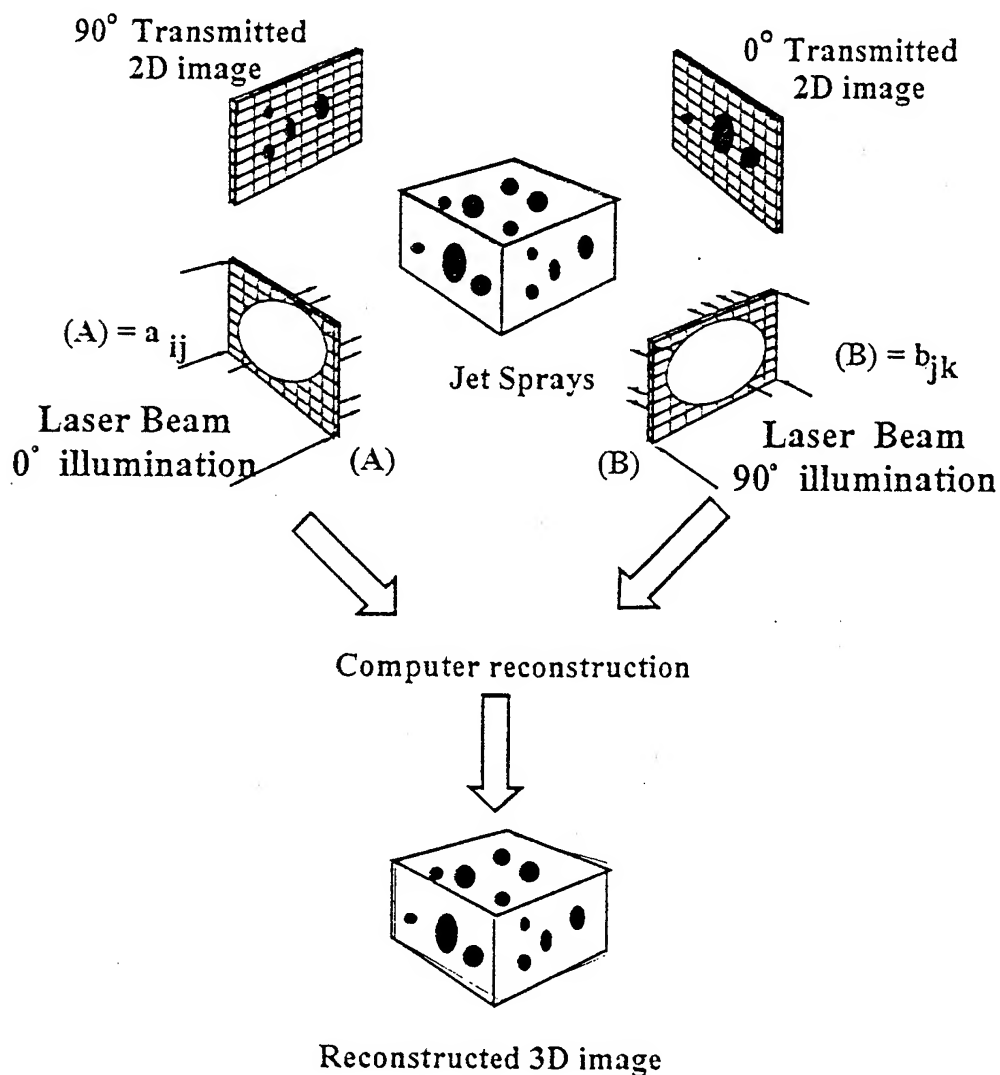
Time-Resolved Image of Jet-Fuel Spray



Area of
integration
 ~ 6 pixels
per channel



3D Jet Droplets Imaging



Summary

- Time-resolved imaging technique has been applied to jet stream: a simulated rocket engine injection element.
- Refinements to these techniques may enable drop size measurements in the highly scattering, optically dense region of multi-element rocket injectors.
- These types of measurements should greatly enhance the design of stable and higher performing rocket and automobile engines.

ISTANBUL TECHNICAL UNIVERSITY

1773

FACULTY OF MECHANICAL ENGINEERING

Prof. Dr. A. Nilufer EGRİCAN
Dean

URL: www.mkn.itu.edu.tr

E-Mail: egrican@mkn.itu.edu.tr

● **DIVISIONS**

- **Fluid Mechanics and Hydraulic Machinery**
- **Thermodynamics, Heat Transfer and Energy**
- **Design**
- **Materials and Manufacturing**
- **Theory of Machinery, System Dynamics and Control**
- **Mechanics**
- **Automotive**

Faculty

43 Professors

18 Associate Professors

26 Assistant Professors

7 Lecturers

Student Profile

1600 Undergraduate Students

350 Graduate Students

ABOUT ITS PAST

At ECOS' 95 July – 1995 Istanbul, closing session recommends establishing International Centre for Applied Thermodynamics.

In December 1997 official establishment started.

In July 1998 at ECOS' 98 in Nancy – France, first General Assembly met.

Approval of Statutes & By-Laws.

ELECTION:

Prof. Elias GYFTOPOULOS – U.S.A. as President, Prof. Richard GAGGIOLI – U.S.A. and Prof. Bjorn QVALE – Denmark as Vice Presidents, Prof. George TSATSARONIS as Chairman of the Executive Committee and Prof. A.Nilüfer EGRICAN as Secretary General of the Centre.

International Centre for Applied Thermodynamics (ICAT)



founded in 1997

**To promote and foster international
cooperation in the field of
Applied Thermodynamics and its applications**

OBJECTIVES

The general objective of the Centre is to promote and foster international cooperation in the field of Applied Thermodynamics and its applications.

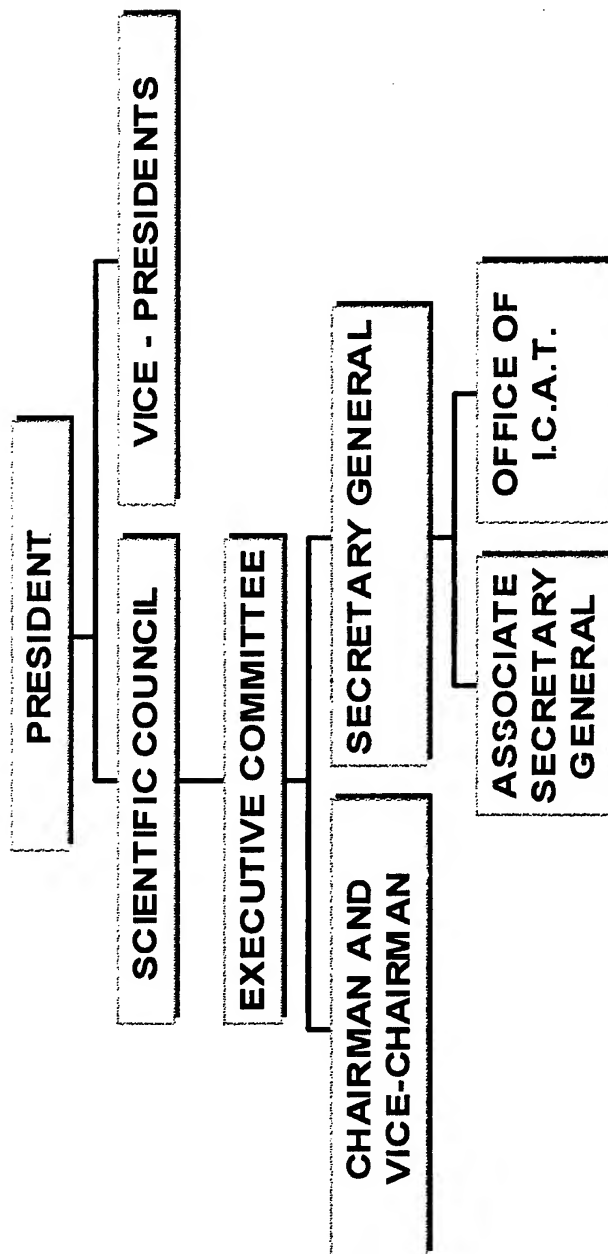
MAIN ACTIVITIES

- 9.1 Organizing conferences, symposia, seminars, forums, schools and courses on topics in the Field;**
- 9.2. Publishing material in the Field, such as proceedings, journals, reference books, directories, reports and data sheets;**
- 9.3. Collecting, evaluating and disseminating technical information in the Field;**
- 9.4. Promoting and assisting in the conduct of research in the Field;**
- 9.5. Promoting the exchange of personnel between organizations working in the field;**
- 9.6. Undertaking activities conducive to the general objectives of the Centre;**
- 9.7. Co-operating with international and national organizations having an interest in the Field.**

MEMBERSHIP

The membership of the Centre is composed of national, regional and international scientific and professional Institutions active in the Field.

ORGANIZATION



MEMBERS OF THE EXECUTIVE COMMITTEE

Prof. A. Özer Arnas
Prof. Adrian Bejan
Prof. Michel Feidt
Prof. Erich Hahne
Prof. G. Hirs
Prof. G. Manfrida
Prof. Phillip Mathieu
Prof. Björn Qvale
Prof. Gunnar Svedberg
Prof. Stanislaw Sieniutycz
Prof. Antonio Valero
Prof. George Tsatsaronis (Chairman)
Prof. Chiristos A. Frangopoulos
Prof. Michael J. Moran

MANAGING OFFICERS

**Vice-Chairman of the Executive Committee: Prof. Yalcin Gogus,
O.D.T.U. – Turkey**

Secretary General: Prof. A. Nilufer Egrican, I.T.U. – Turkey
Assistant Secretary General: Prof. Aksel Ozturk, I.T.U. – Turkey
Prof. Ediz Paykoc, O.D.T.U. – Turkey

PAST ACTIVITY

A Short Course on Thermoeconomics And Cogeneration

One of the goals of sustainable development is higher fuel efficiency at lower product cost for systems that use or produce power and heat. The course introduced a methodology that aims at this goal under the name *Thermoeconomics*. The methodology allows the intensive analysis of design concepts in order to reveal opportunities of fuel and cost savings.

The course was held at the Mechanical Engineering Faculty of Istanbul Technical University between 13-15 April 1999. Prior to lectures of Prof. El-Sayed, Prof. A. Yalcin Gogus and Prof. Taner Derbentli of Istanbul Technical University reviewed prerequisite thermal design models, economic calculations and basics of optimization. Yehia El-Sayed, emeritus Professor of Massachusetts Institute of Technology, is President of Advanced Energy Systems Analysis Inc..

PUBLICATIONS OF THE CENTRE

1-Proceedings of ECOS '95 (3 Volumes)

2- Proceedings of a work shop on Education of Applied Thermodynamics

3 -International Journal of Applied Thermodynamics

International Journal of Applied Thermodynamics

E-mail: ijat@mkn.itu.edu.tr

Honorary Editors

**A. Bejan
R.A. Gaggioli
E.P. Gyftopoulos
E.Hahne
J. Szargut**

Technical Editor-In-Chief

A.Ö. Arnas

Managing Editor

N. Egrican

VOLUME 1 NO.1-4

ISSN 1301-9724
JUNE 1998

International Journal of
Applied Thermodynamics

Honorary editors

A. Bejan
R. A. Gaggioli
E. P. Gyftopoulos
E. Hahne
J. Szargut

Technical Editor in Chief

A. Ö. Arinas



*International Centre for
Applied Thermodynamics*

e-mail : ijat@mko.itu.edu.tr

Editorial Board (European)

- N. EGRİCAN, Istanbul Technical University, TURKEY (Managing Editor)
- M. FEIDT, LEMTA, Universite Henri Poincare, FRANCE
- C. FRANGOPOULOS, National Technical University of Athens, GREECE
- Y. GÖÇÜŞ, Middle East Technical University, TURKEY (Associate Technical Editor-in-Chief)
- U. GROSS, Lehrstuhl für Technische Thermodynamik, GERMANY
- G. G. HIRS, Universiteit Twente, NETHERLANDS
- G. MANFRIDA, Universita Degli Studi di Firenze, ITALY
- P. MATHIEU, Universite de Liege, BELGIUM
- A. ÖZTÜRK, Istanbul technical University, TURKEY, (Publishing Editor)
- B. QVALE, Technical University of Denmark, DENMARK
- A. SHAVIT, Technion, Israel Institute of Technology, ISRAEL
- S. SIENIUTYCZ, Warsaw University of Technology, POLAND
- G. SVEDBERG, Royal Institute of Technology, SWEDEN
- G. TSATSARONIS, Technische Universitat Berlin, GERMANY
- A. VALERO, CIRCE-University of Zaragoza, SPAIN

PROJECTS

- **Analysis of Reactive Flow in Solid Rocket Motors
(NATO-CRG , Univ. of Colorado at Boulder,USA)**
- **Unsteady Flow in Centrifugal Compressors
(NATO-CRG, von Karman Institute, Belgium)**
- **Experimental Analysis of Louvered Fin Heat
Exchangers(Univ. of Illinois at Urbana,USA)**
- **Experimental and Numerical Analysis of Falling Film
Behavior(Univ. of Illinois at Urbana,USA)**
- **Thermoacoustic Refrigeration
(Johns Hopkins Univ.,USA)**

ANALYSIS OF REACTIVE FLOW IN SOLID ROCKET MOTORS

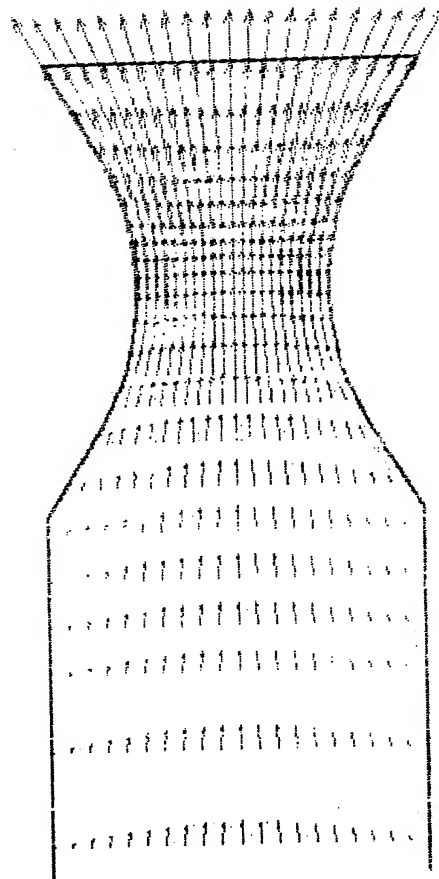
This study is concerned with modeling transient flow dynamics when there is interaction between propellant burning and the fluid dynamics in a solid propellant rocket motor chamber. The results will provide new perspectives about the physical processes occurring in the system. The application to the design processes should foster the development of more reliable motors with predictable performance.

E-mail:kadir@mkn.itu.edu.tr

FLOW IN A SOLID ROCKET MOTOR

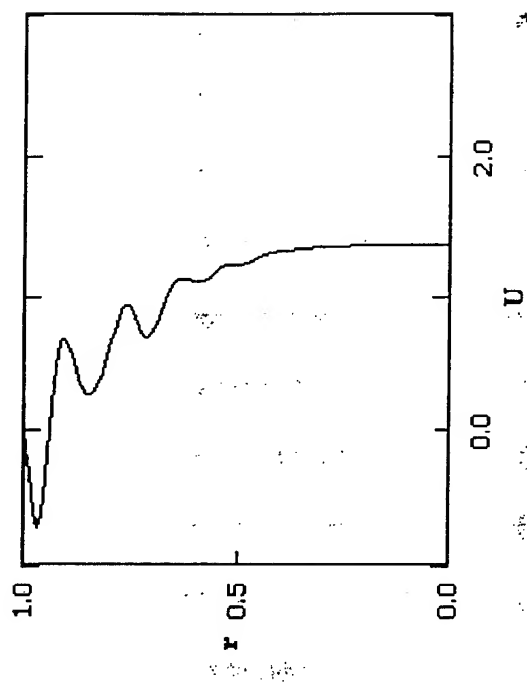
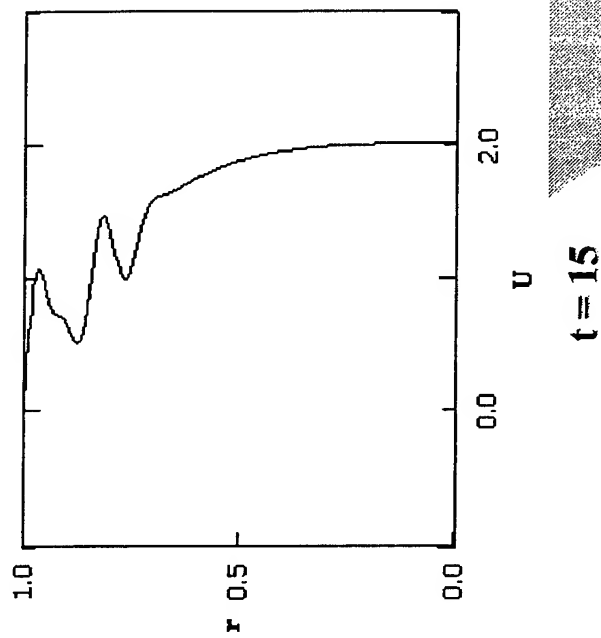
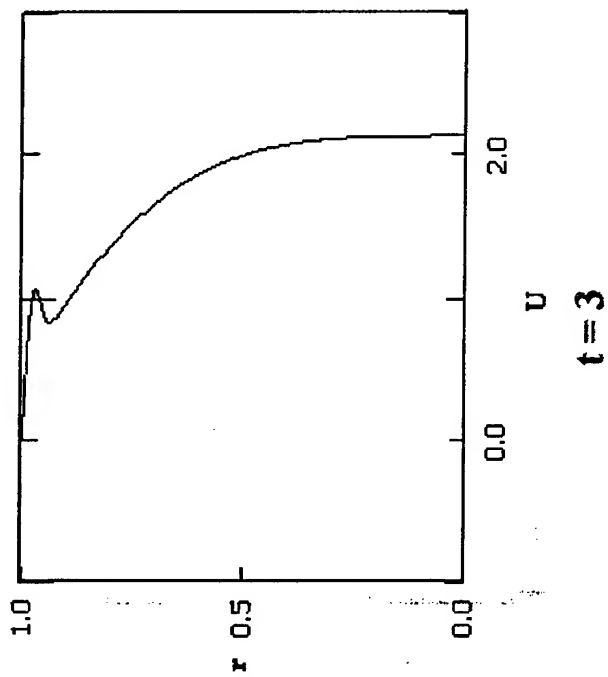


GRID STRUCTURE



VELOCITY PROFILES

Axial Velocity Profiles at Different Times

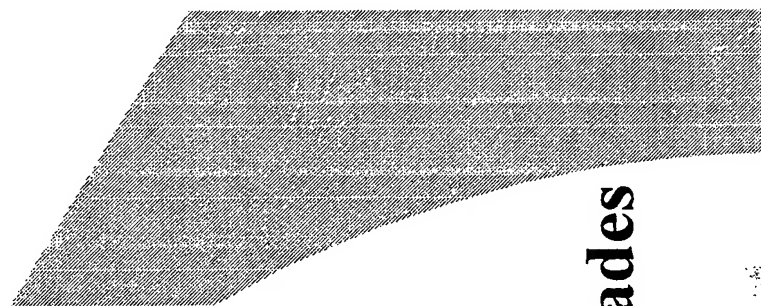
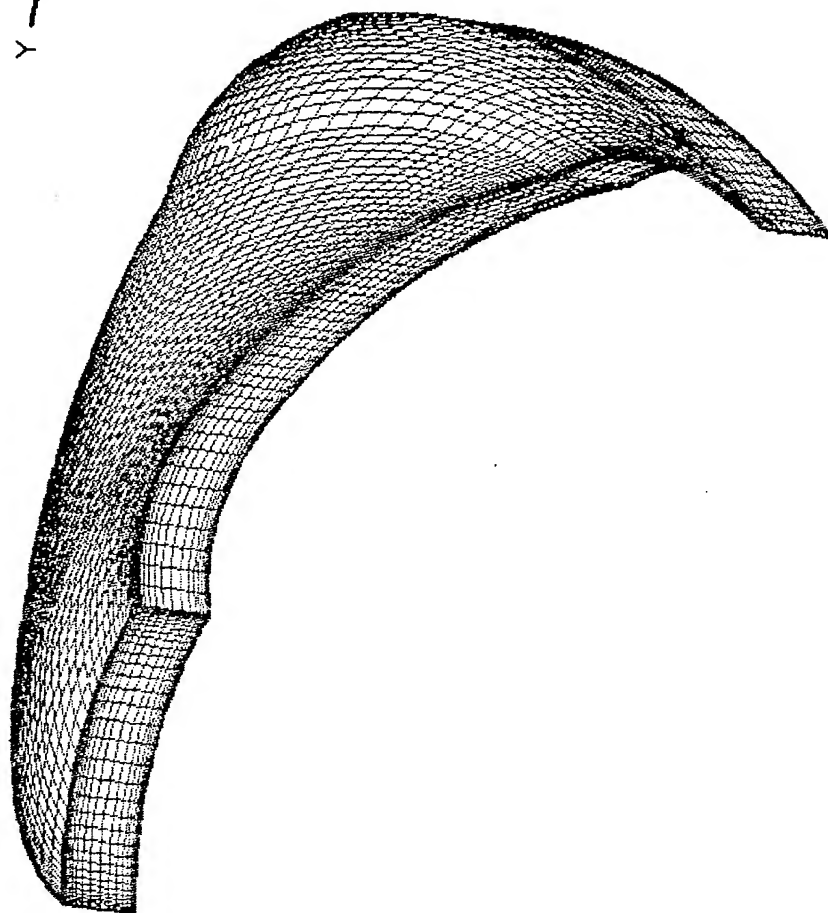


ANALYSIS OF THE FULL 3D FLOW IN CENTRIFUGAL IMPELLER

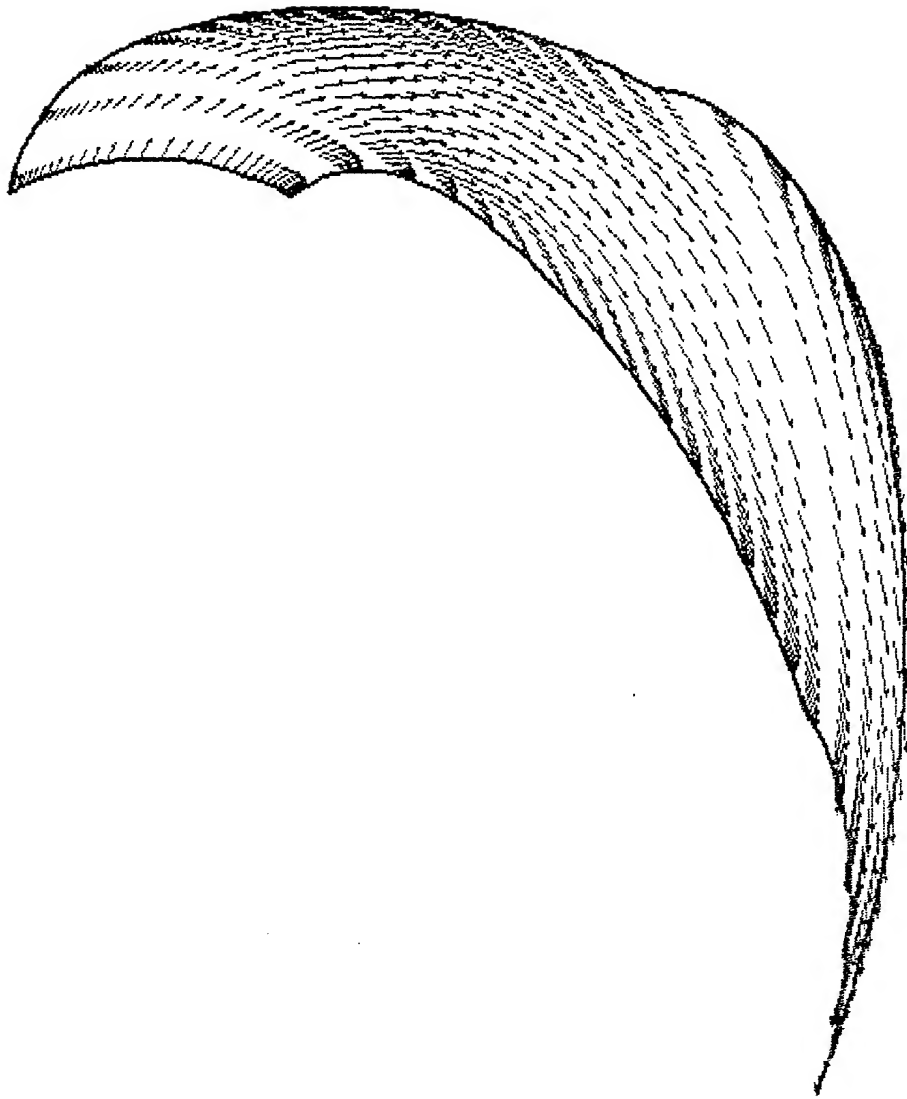
A flow solver, that allows the evaluation of the effects of different design parameters on the impeller performance, has been developed. Full 3D Navier - Stokes equations, including artificial compressibility approach for incompressible flows, are written in quasi-conservative form and are solved by using a finite volume method that employs Runge-Kutta time stepping. The solver is used to analyze the flow field inside different pump impellers for which experimental data is available. The comparison of the calculated and measured results reveals that the flow solver is capable of predicting impeller performances.

E-mail: erkan@mkn.itu.edu.tr

FLOW INSIDE IMPELLER BLADES

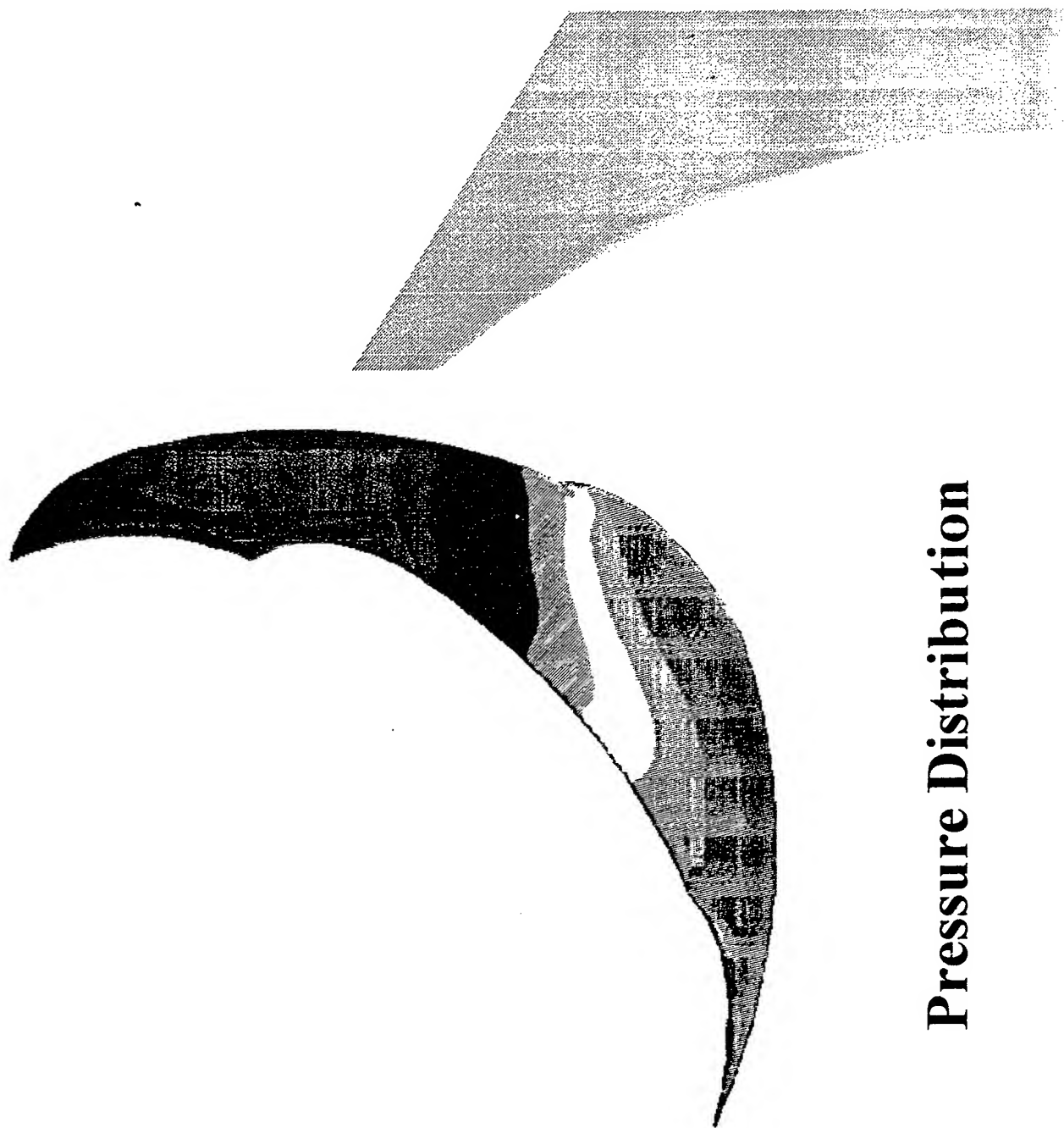


Grid Structure for Centrifugal Impeller Blades



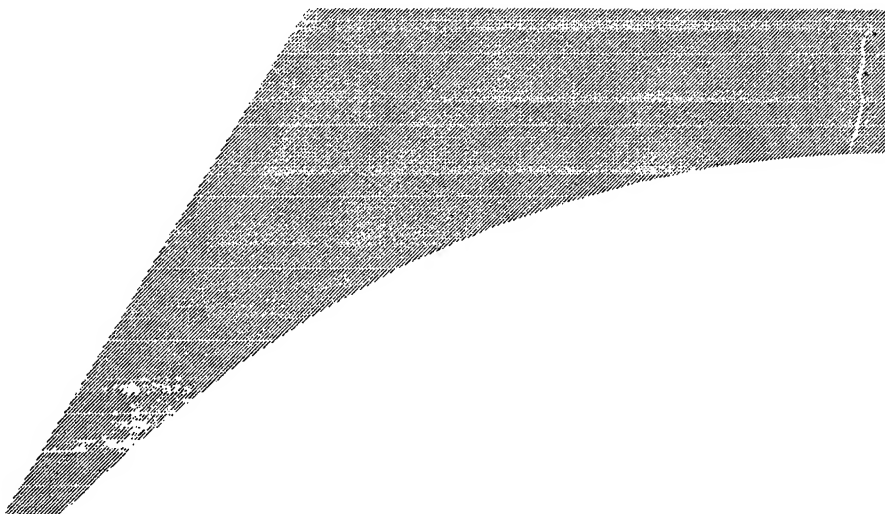
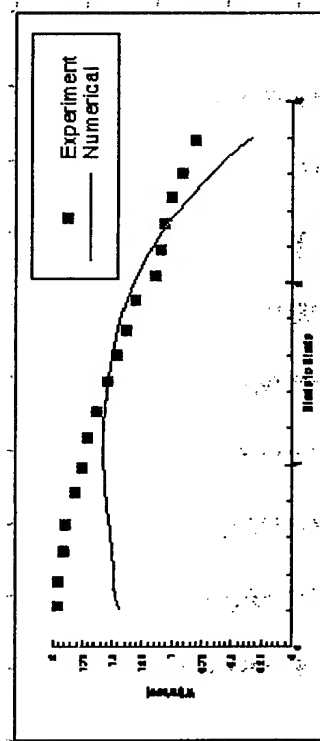
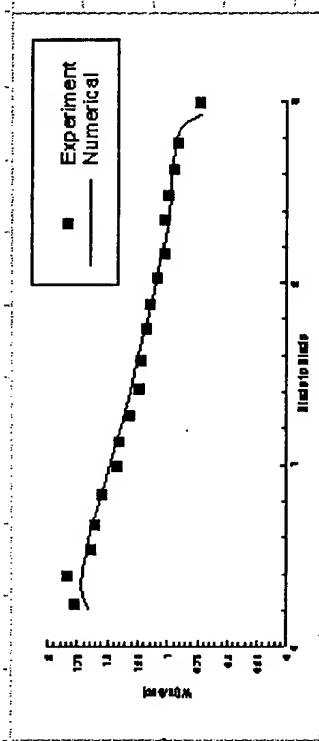
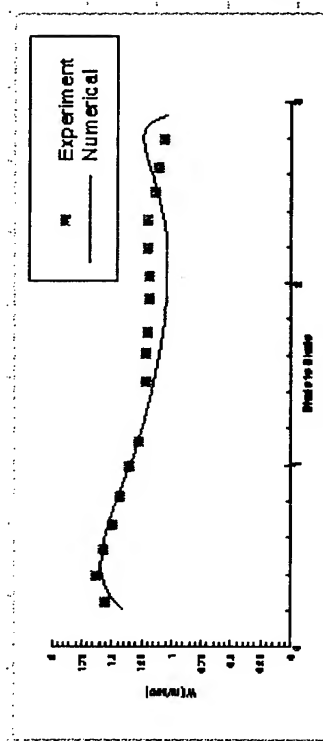
Velocity Field

Downloaded from ascelibrary.org by University of California, San Diego on 06/01/15. Copyright ASCE, For All Rights Reserved, No part of this document may be reproduced without written permission from ASCE.



Pressure Distribution

Comparison of Numerical and Experimental Velocity Distributions between Blades



EXPERIMENTAL AND NUMERICAL ANALYSIS OF FALLING FILM BEHAVIOR

The scope of the present study may be summarized as to analyse the inline-staggered jet modes and the jet instability and to simulate the jet. The new data will allow the effects of tube diameter and spacing to be ascertained. Tube diameter effects will be captured using the dimensionless Ohnesorge (Oh) number, and tube spacing effects are captured with s/D ..

The mentioned effects are being analysed numerically. The jet pattern are being simulated in three domains of the computation: the jet, the liquid film surrounding the tubes and the liquid bridge. The results will be compared to the experimental ones.

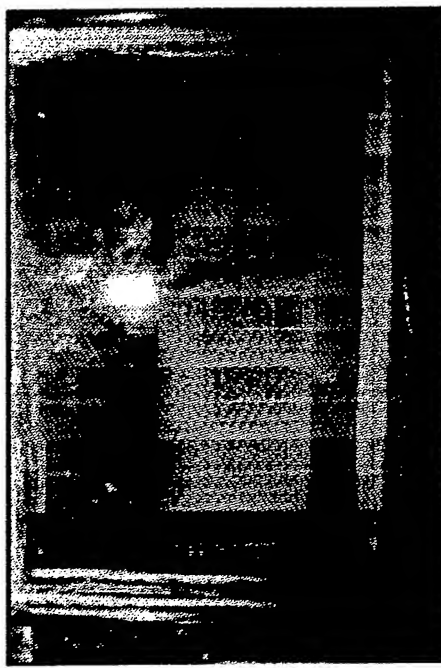
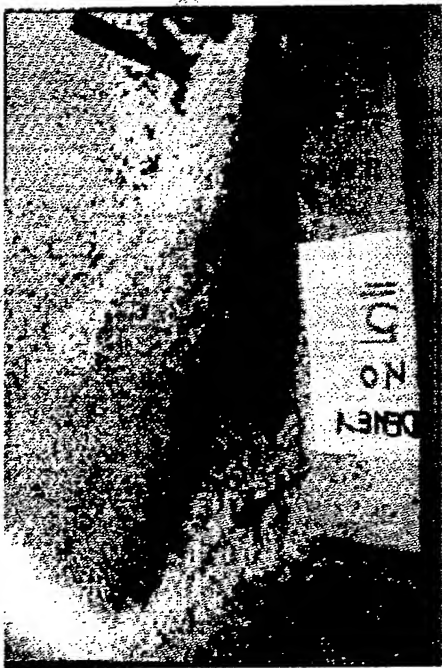
E-mail : seyhan@mkn.itu.edu.tr

EXPERIMENTAL ANALYSIS OF LOUVERED FIN HEAT EXCHANGERS PERFORMANCE

The main objective of this work is to provide a better understanding of the flow and the heat transfer phenomena in a louvered geometry. Therefore, previous to the experiments, an analytical work will be done for predicting the critical values of the geometric parameters such as , fin pitch, louver pitch, louver angel and fin thickness. Then , the manufactured specimens will be tested and the quantitative and qualitative data will be evaluated. The results will be a new input for a better design of higher performance.

E-mail: honbasi@mkn.itu.edu.tr

SMOLDERING COMBUSTION OF HORIZONTAL DUST LAYERS IN A FORCED AIR FLOW



E-mail: erhan@mkn.itu.edu.tr

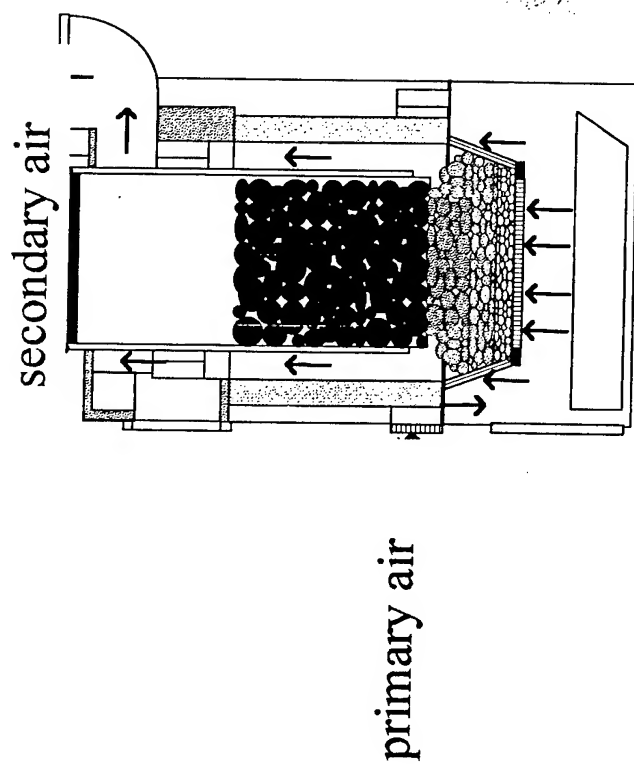
SMOLDERING COMBUSTION OF HORIZONTAL DUST LAYERS IN A FORCED AIR FLOW

In order to define the effects of these properties on the smoldering combustion propagation and on the flaming or extinguish, smoldering combustion of horizontal dust layers in a forced air flow was experimentally investigated. The experiments were carried out in a combustion box lined with ceramic fibrous and refractors with a thickness of 70 mm. The inside of this combustion box measured 150 x 200 x 500 mm. Wood dust and tobacco were used as experiment material. The air velocity supplied over the fuel bed was in the range of 1-4 m/s. The experiments were carried out for both forward and reverse smoldering combustion. The combustion wave propagation velocity parallel to the air supply direction was higher than the velocity of the wave perpendicular to the fuel bed. The resultant velocity increased with the increasing air velocity for both forward and reverse smoldering combustion. In the following pictures, the top view and the cross section of the combustion wave are seen.

E-mail: erhan@mkn.itu.edu.tr

EFFICIENCY ENHANCEMENT OF THE COAL FIRED DOMESTIC HEATERS AND STOVES

E-mail : uralcan @ mkn.itu.edu.tr



Domestic Downdraft Coal Burner

EFFICIENCY ENHANCEMENT OF THE COAL FIRED DOMESTIC HEATERS AND STOVES

The main objectives of this work were to obtain smokeless combustion and continuously coal feeding. The first group of experiments were carried out on the original hand fired furnace and later the furnace was reconstructed. The experiments were repeated on this new developed furnace. The results of the experiments were showed that the burning was taken under control, the excess air and CO emission were decreased and the efficiency raised to the value of %80.

E-mail: uralcan @ mkn.itu.edu.tr

UNDERFEED FIXED BED COAL COMBUSTION

E-mail : erhan@mkn.itu.edu.tr

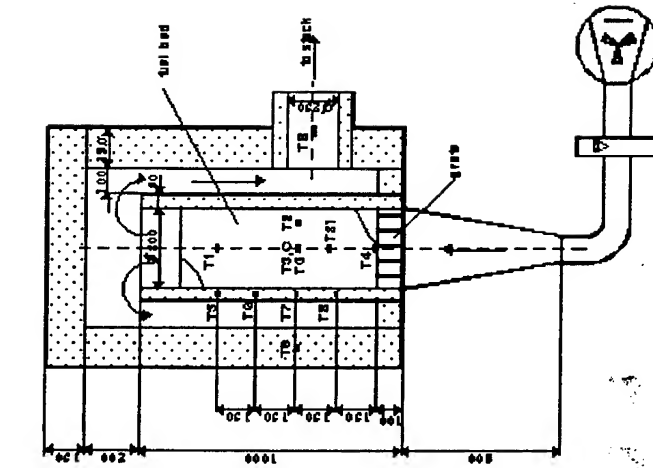
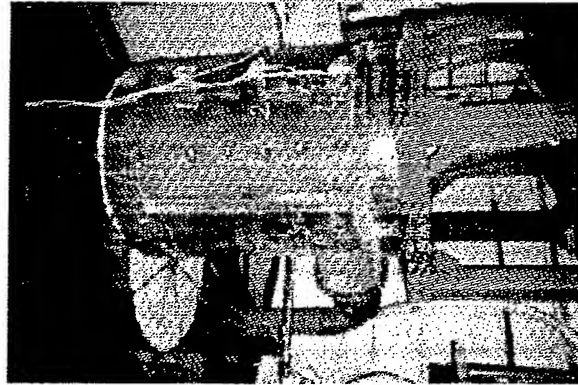


Figure 1. Combustion Bed



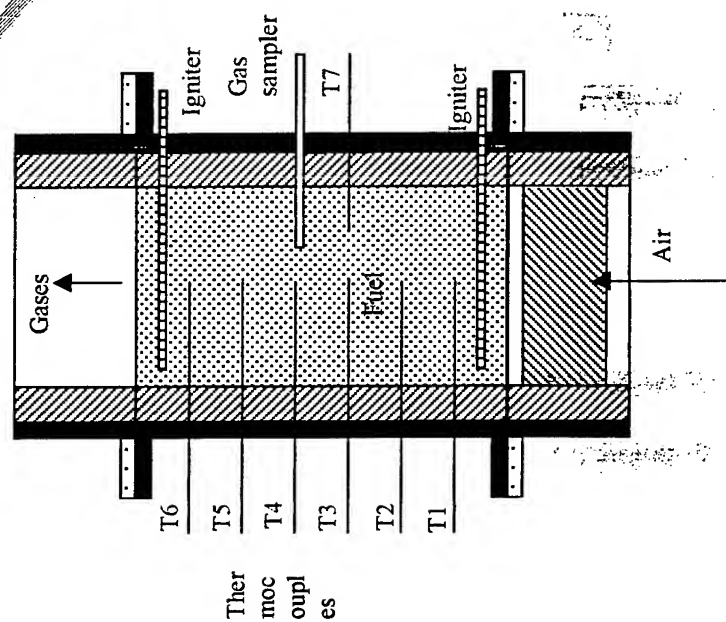
UNDERFEED FIXED BED COAL COMBUSTION

The object of this work is to develop a mathematical model of steady-state underfeed fixed bed coal combustion. In this combustion system the coal is fed from underneath the bed so that the reaction front is traveling down and the volatiles are carried up into the bed. Air is supplied through the tuyeres. The fixed bed coal combustion is described mathematically for a thin coal bed layer by means of energy, mass and species conservation equations. The model is supported with the computer codes obtaining reaction rates, physical properties and thermal conductivity. Using this computer simulation, combustion product concentrations, temperature and fixed carbon gradients can be predicted.

E-mail: erhan@mkn.itu.edu.tr

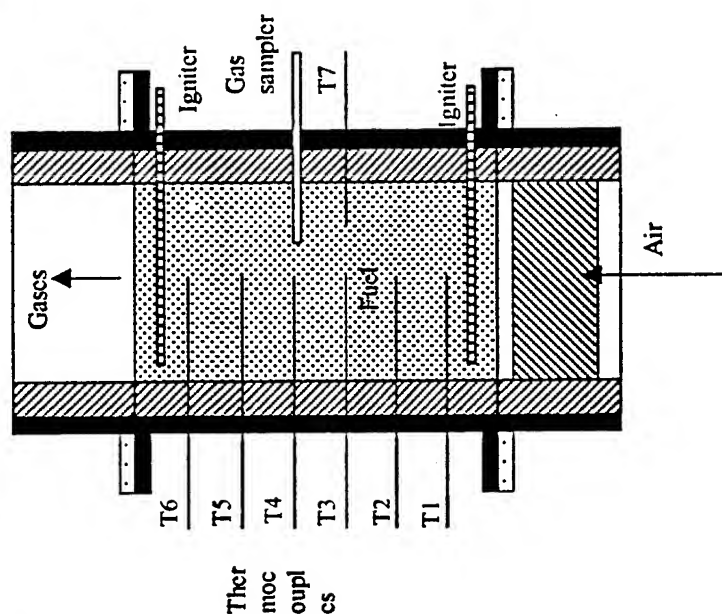
FORWARD AND BACKWARD SMOLDERING COMBUSTION

E-mail : erhan@mkn.itu.edu.tr



FORWARD AND BACKWARD SMOLDERING COMBUSTION

E-mail : erhan@mkn.itu.edu.tr



The main object of this work is to investigate one-dimensional smoldering combustion in dust layers. The experiments are carried out in a cylindrical combustion chamber with wood dust. The forward and backward smoldering combustion are investigated for various air supply velocities. The forward combustion appeared to be more steady.

• FLUIDIZED BED COMBUSTION OF LIGNITES AND COAL-BIOMASS MIXTURE

• COAL AND GAS DESULFURIZATION

• KINETICS OF COAL COMBUSTION AND CARBONIZATION

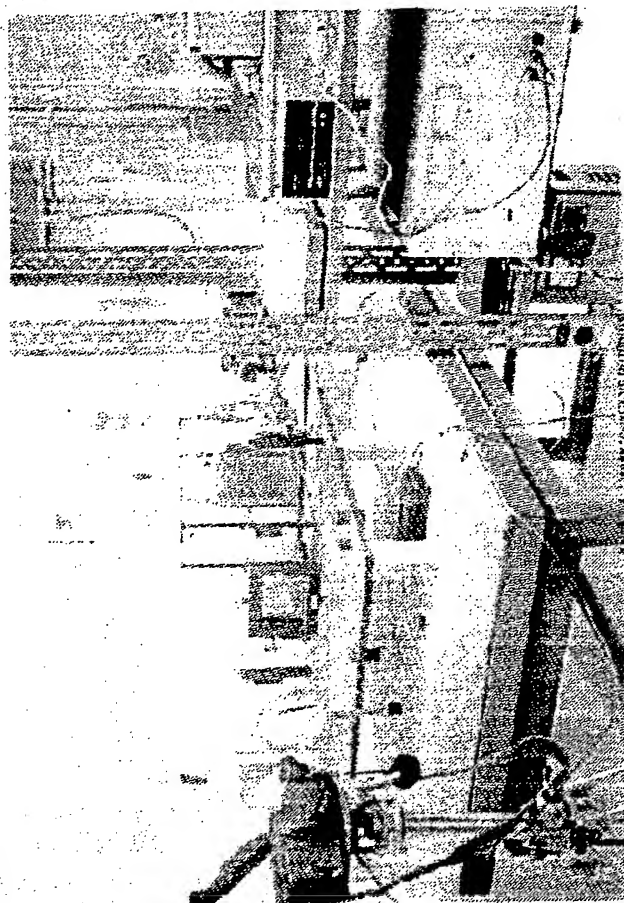
• BIOMASS AND ALTERNATIVE FUELS

• COAL-WATER SLURRY PREPARATION AND COMBUSTION

♦ PYROLYSIS OF COAL AND PRODUCT CHARACTERIZATION

INFLUENCE OF HORIZONTAL FINS WITH LOW THERMAL CONDUCTIVITY ON NATURAL CONVECTIVE HEAT TRANSFER FROM VERTICAL SURFACES

E- mail : turkmen@mkn.itu.edu.tr



INFLUENCE OF HORIZONTAL FINS WITH LOW THERMAL CONDUCTIVITY ON NATURAL CONVECTIVE HEAT TRANSFER FROM VERTICAL SURFACES

Natural convective heat transfer from a vertical plate with uniform base temperature and having transverse rectangular fins of low thermal conductivity has been investigated for a wide range of the spacing-to-fin height ratio. A holographic interferometer was employed as well, to visualise the temperature distribution in the boundary layer. Holographic images of thermal field were recorded using a video camera. These records were loaded on a PC using a frame grabber. A software for digital processing of these images has been developed and used for the analysis.

E-mail: turkmen@mkn.itu.edu.tr

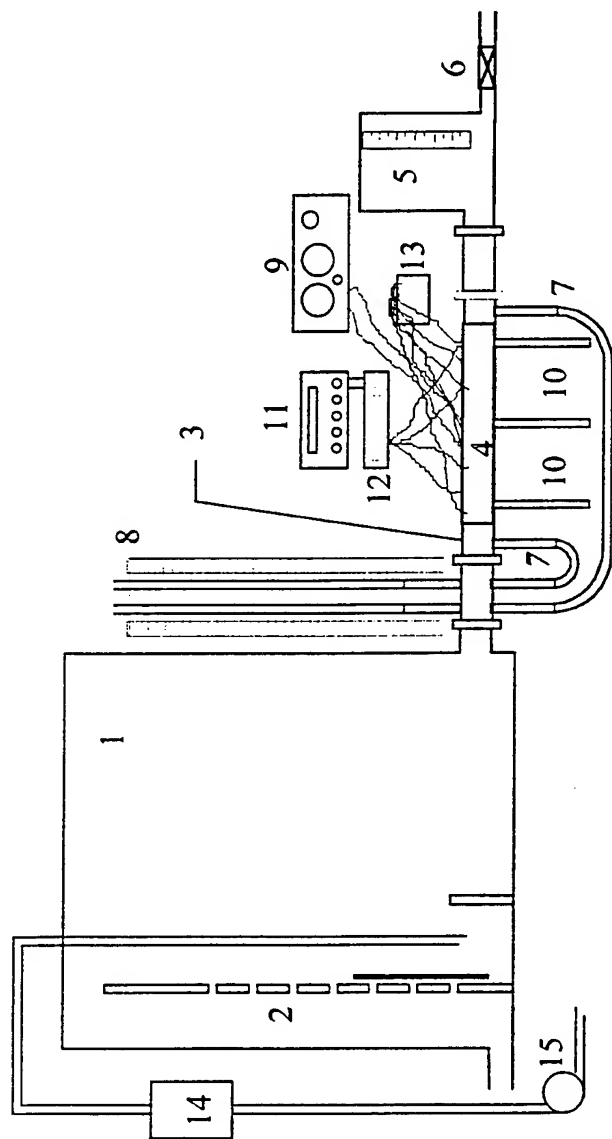
FORCED CONVECTIVE HEAT TRANSFER IN POROUS MEDIUM OF WIRE SCREEN MESHES

The hydrodynamic and heat transfer characteristics of a porous medium consisting of 20 wire screen meshes are examined theoretically and experimentally. The hydrodynamic experiments are conducted for the range of Reynolds number based on mean velocity and wire diameter from 1.5 to 12. The Ergun's constants and thermal dispersion coefficients are calculated in this range. Nusselt number variation is determined in both thermally developing and fully developed flows by the help of forced convection heat transfer experiments conducted for the uniform heat flux boundary condition. Correlation functions of Nusselt number in the range of fully developed and thermally developing, and of thermal entrance length are obtained from experimental data. Solutions of momentum and energy equations simulating the experimental model are obtained numerically with variable porosity and the anticipated thermal dispersion coefficients. The thermal dispersion coefficients well-adjusted to the experimental data are determined by numerical solution of the energy equation.

E- mail : mozdemir @ mkn.itu.edu.tr

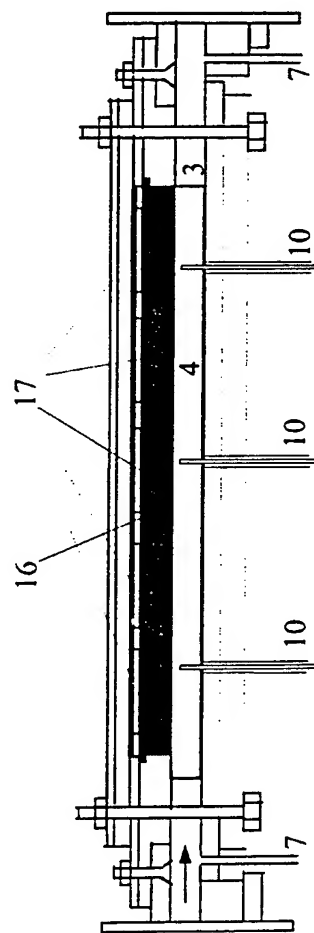
Experimental Apparatus

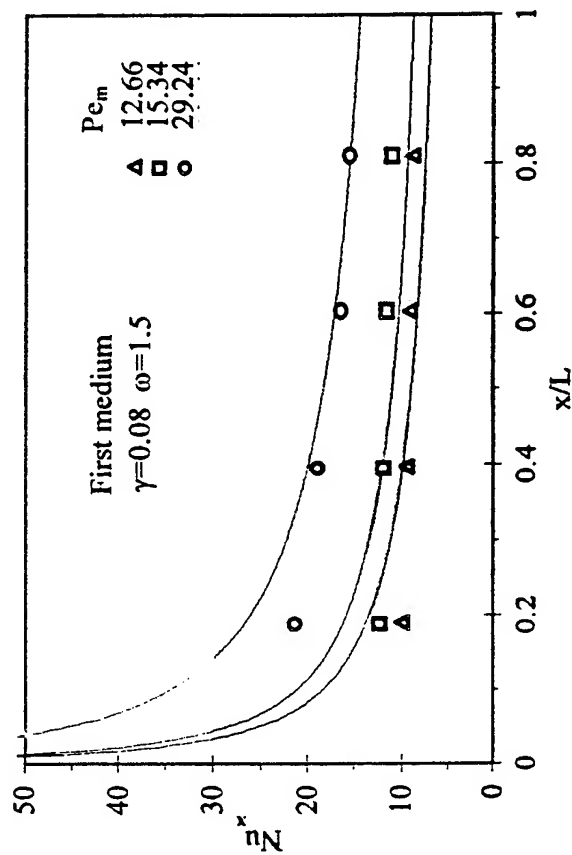
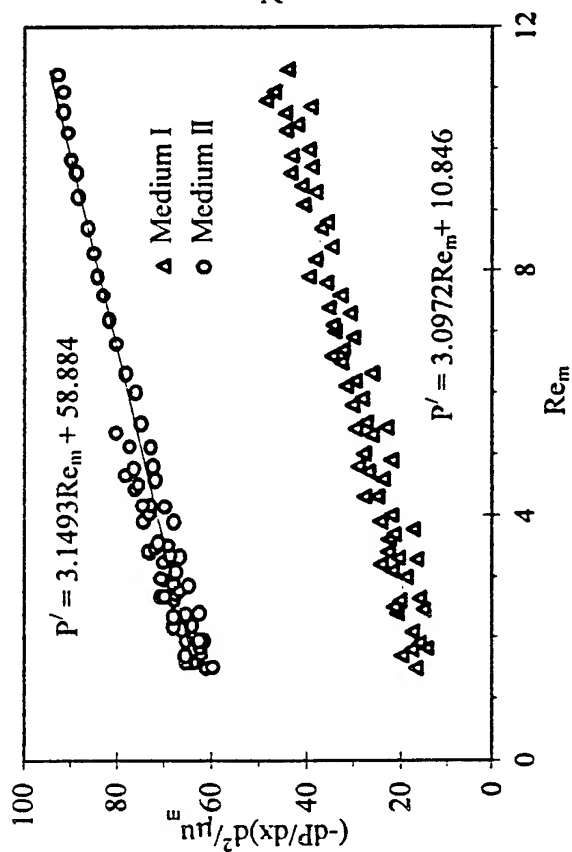
- 1) Upstream reservoir,
- 2) Dividers, 3) Test section, 4) Porous medium, 5) Downstream reservoir, 6) Valve,
- 7) Pressure taps,
- 8) Manometer, 9) Direct current source,
- 10) Temperature props,
- 11) Milivoltmeter,
- 12) Scanner, 13) Ice bath,
- 14) Water filter, 15) Pump



Test section and upper portion

- 3) Test section,
- 4) Porous medium,
- 7) Pressure taps,
- 10) Temperature probes,
- 16) Copper plate,
- 17) heaters

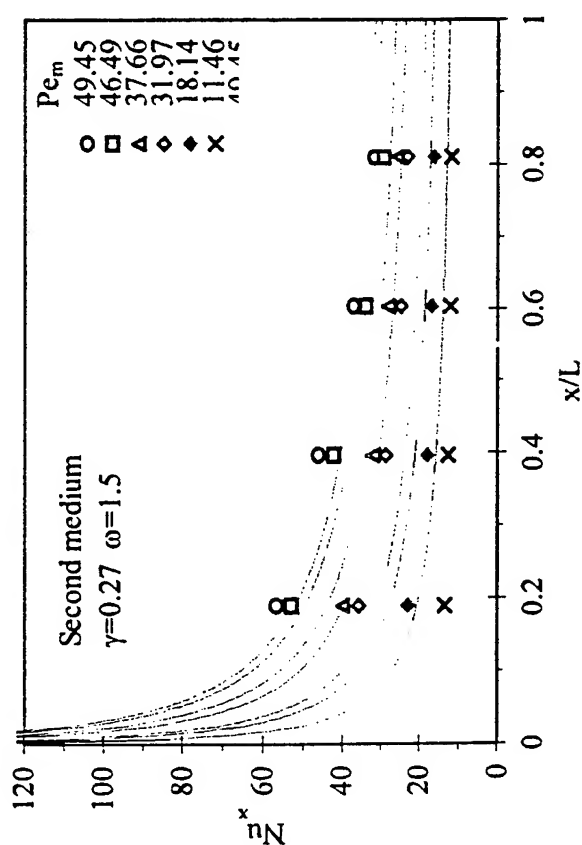


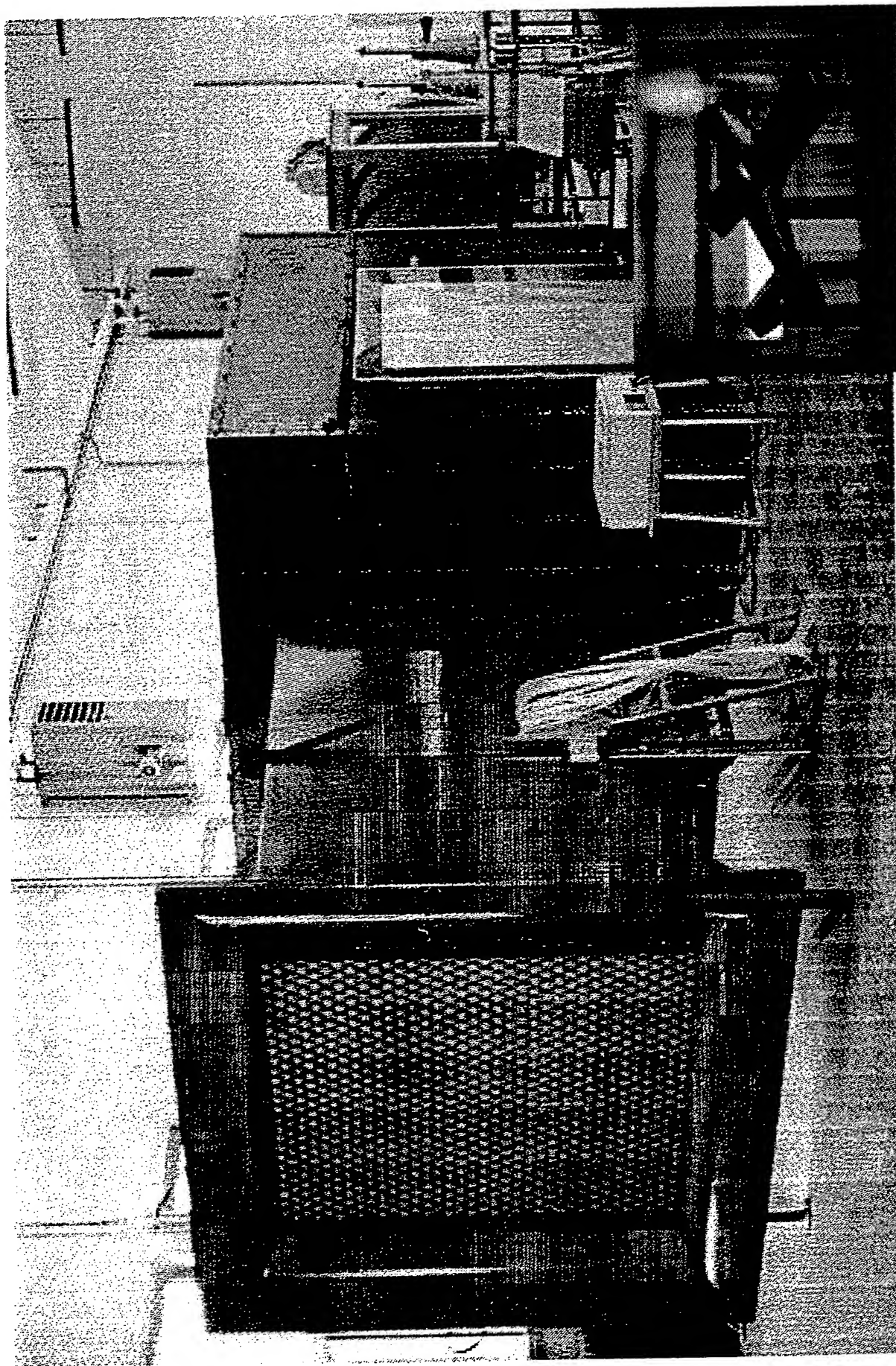


Variation of non-dimensional pressure gradient with respect to Reynolds Number.

Nu_x - x/L variation calculated by considering $\gamma=0.08$ and $\omega=1.5$ for the first medium.

Nu_x - x/L variation calculated by considering $\gamma=0.27$ and $\omega=1.5$ for the second medium.

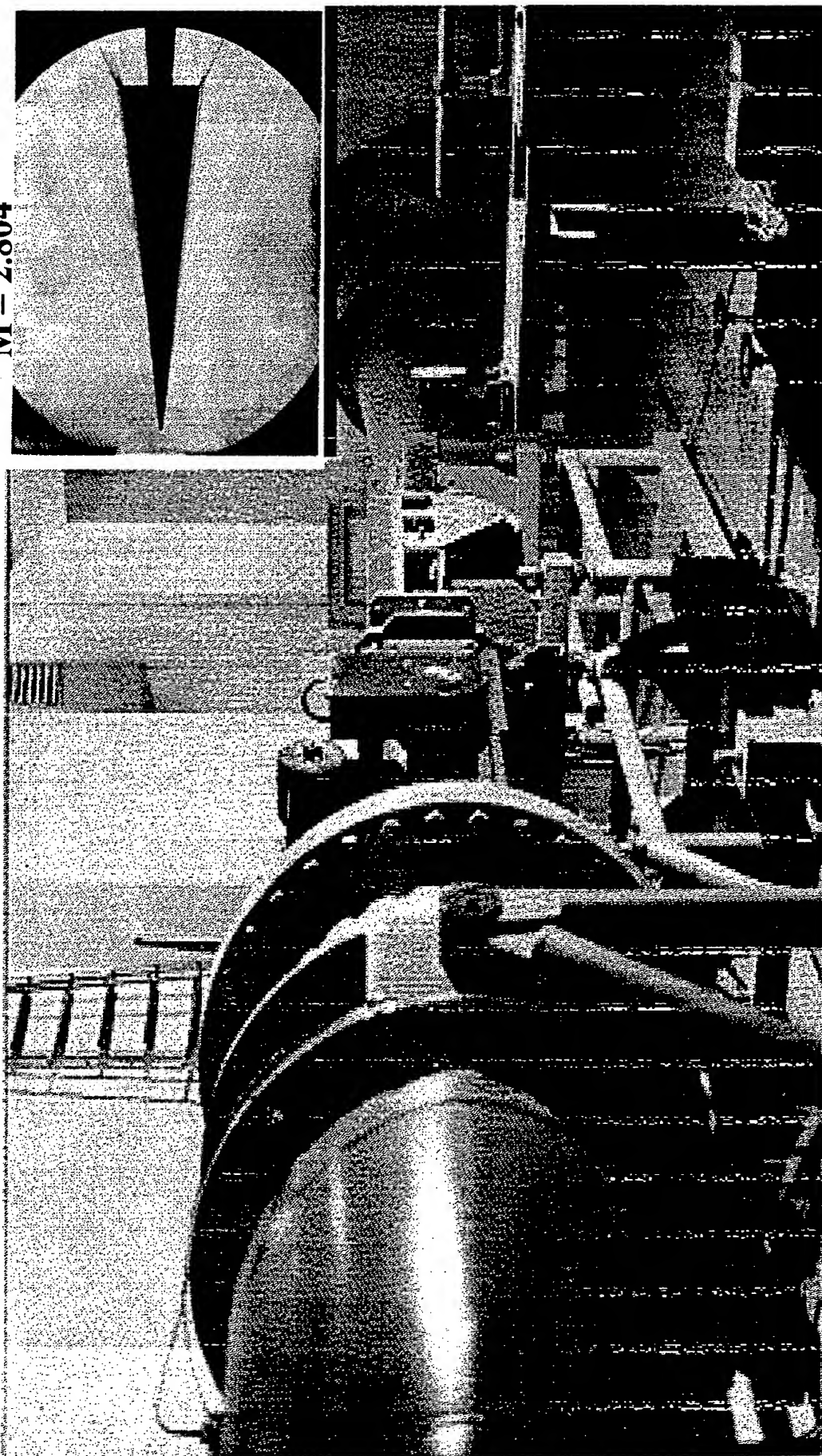




LOW-SPEED WIND TUNNEL
800 x 800 mm, 10 m/s < Velocity < 30 m/s

HIGH-SPEED WIND TUNNEL

Cone Flow and Mach Waves
 $M = 2.804$

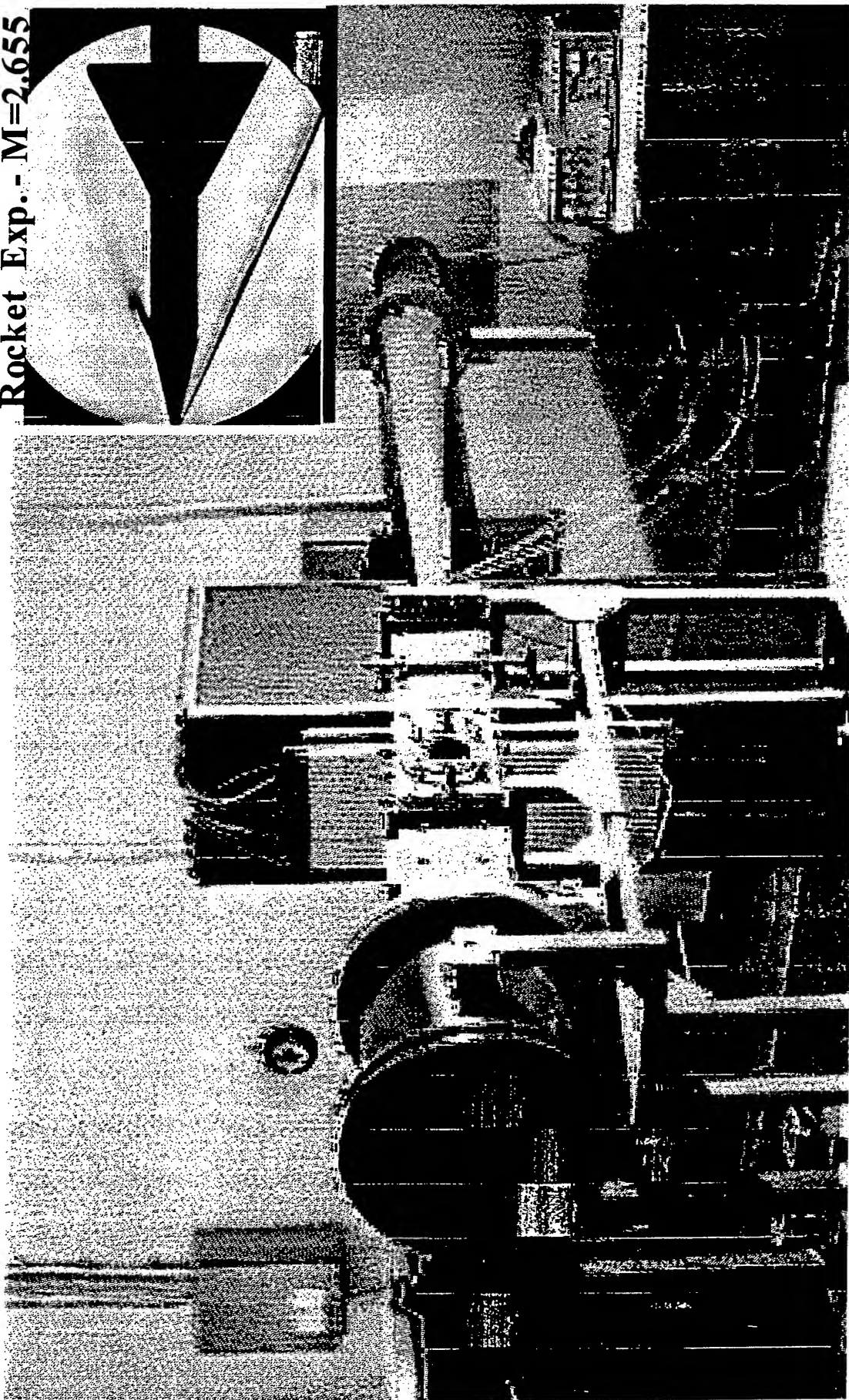


150 x 150 mm

$0.6 < \text{Mach} < 2.2$ and $2.3 < \text{Mach} < 4.0$

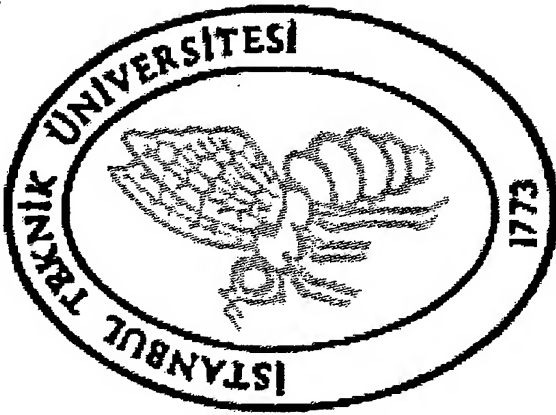
HIGH-SPEED WIND TUNNEL

Rocket Exp. - $M=2.655$



$30 \times 60 \text{ mm}$, $0.3 \leq \text{Mach} \leq 2.2$

Continuous Working



İSTANBUL TECHNICAL UNIVERSITY
Faculty of Mechanical Engineering
Mechanics Division

FLUIDS LABORATORIES

www.akis.itu.edu.tr

Dr. İ. Bedii Özdemir, Assoc. Professor

FLUIDS LABORATORIES

Subsonic Flows
Laboratory

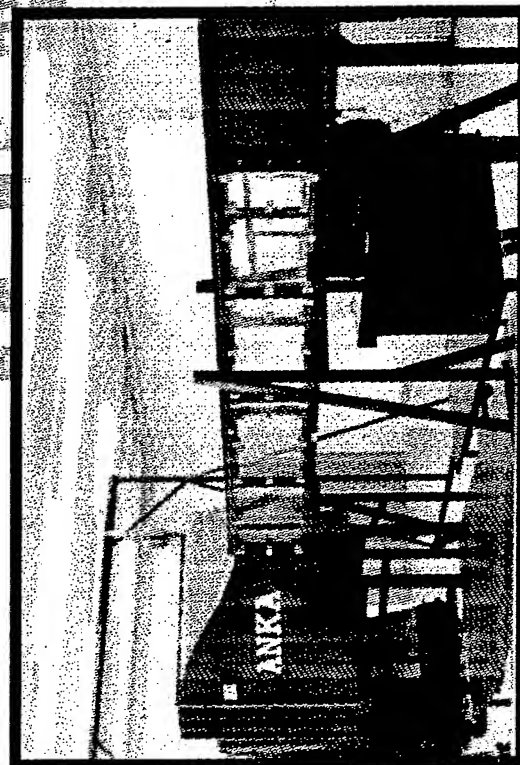
“ANKA”
Wind
Tunnel

Supersonic Flows
Laboratory

“TURNA”
Lateral Jet
Facility

“ISLIK”
Supersonic Jet
Facility

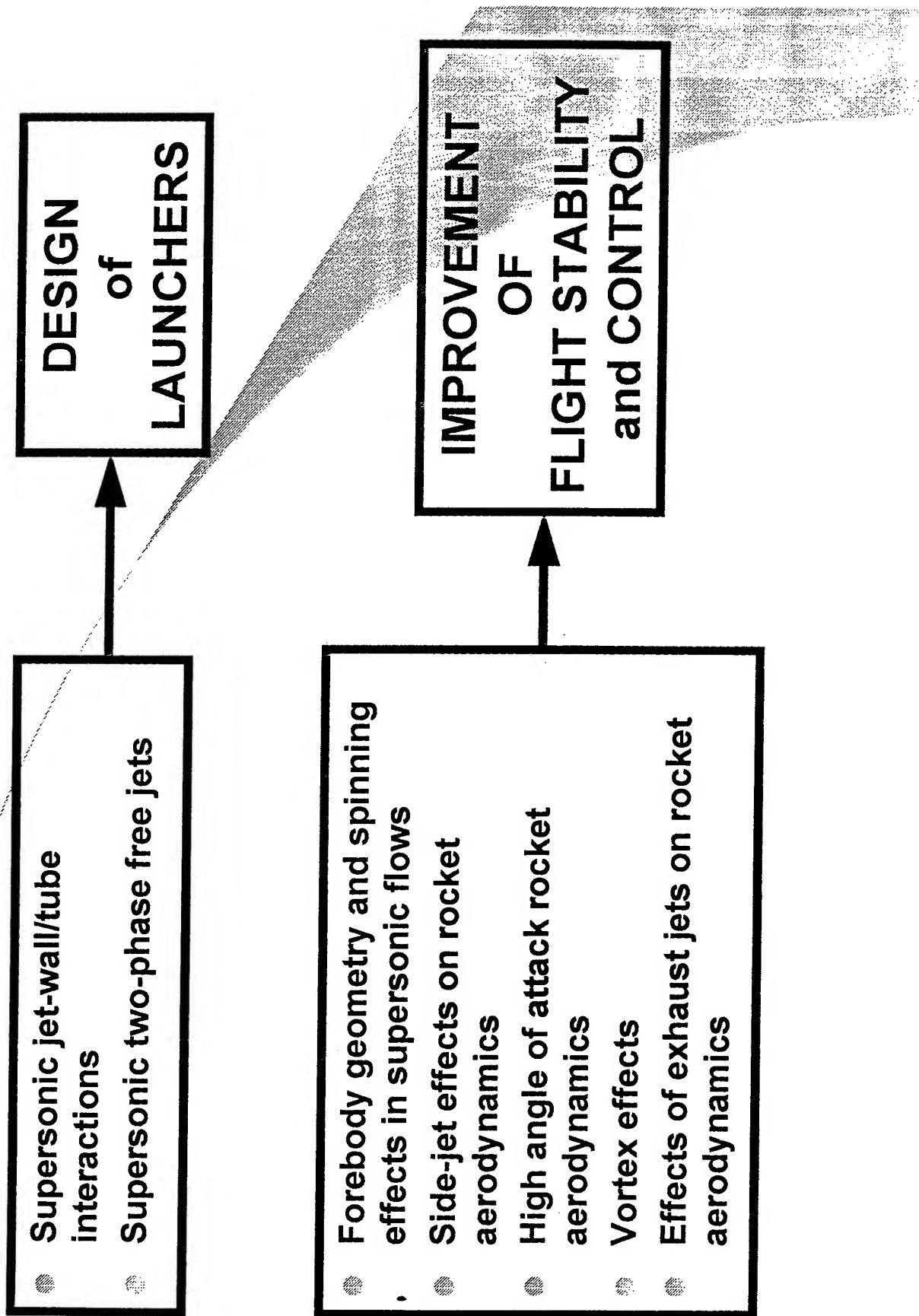
Combustion
Facility



Research on Aerodynamic Flows

Problems related to missile dispersion in ground proximity due to instabilities associated with dynamic loading on nearby surfaces by the impingement and deflection of rocket exhausts

- **High angle of attack and unsteady rocket aerodynamics**
- **Side-jet technology**



Research on Combustion

- **Combustion without flame**
- **Low-NO_x, high IFGR Combustor Design**
- **Applications on gas turbine technology**

CURRENT PROJECTS

- **Reduction of Missile Dispersion (Approved for grant)**
Sponsored by: *Ministry of Defense (MSB, Türkiye)*
- **High Pressure Low-NO_x Flameless Combustion System for Gas Turbines (Approved for grant)**
Sponsored by: *State Planning Organization (DPT, Türkiye)*
- **Unsteady Flow and Vorticity Interactions at High Angle of Attack (In progress)**
Sponsored by: *Defense Industries Research and Development Institute (SAGE, Türkiye)*
- **Vorticity Generated by Side Jets (In progress)**
Sponsored by: *Defense Industries Research and Development Institute (SAGE, Türkiye)*

COMPLETED PROJECTS

Reduction of Missile Dispersion (1996-98)

Sponsored by: *State Planning Organization (DPT, Türkiye)*

Study on Rocket Aerodynamics and Jet Effects on Model Geometries (1997-98)

Sponsored by: *Scientific and Technical Research Council of Turkey (TÜBİTAK, Türkiye)*

Reduction of Missile Dispersion and Improvement of Flight Stability (1996-98)

Sponsored by: *University Research Funds (İTÜ, Türkiye)*

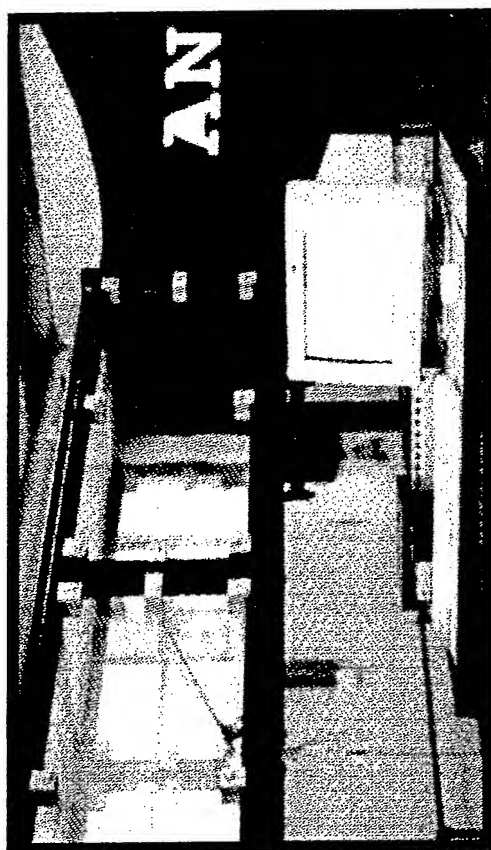
Supersonic Jet/Wall Interactions (1995-97)

Sponsored by: *Defense Industries Research and Development Institute (SAGE, Türkiye)*

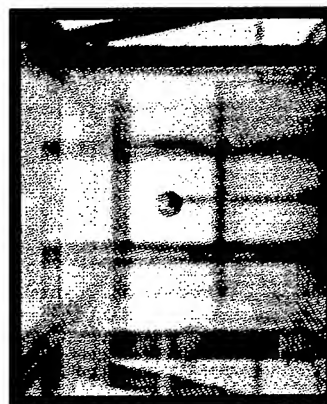
Aerodynamics of Crossflow with Side Jets (1995-97)

Sponsored by: *Defense Ids. Resch. and Dev. Ins. (SAGE, Türkiye)*

SUBSONIC FLOWS LABORATORY

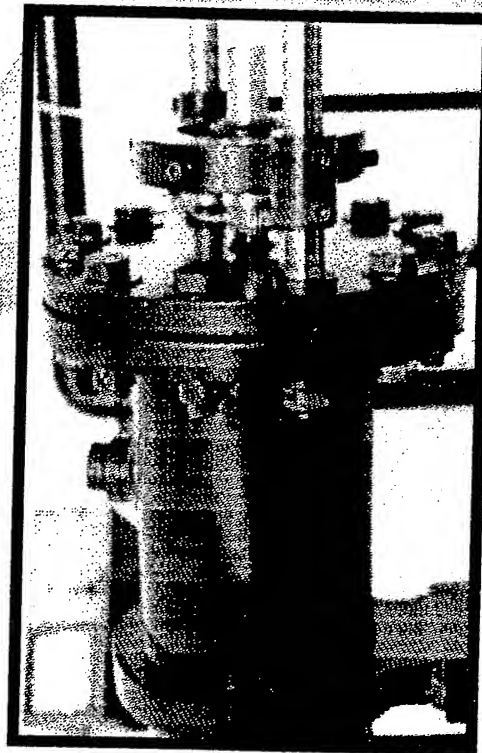
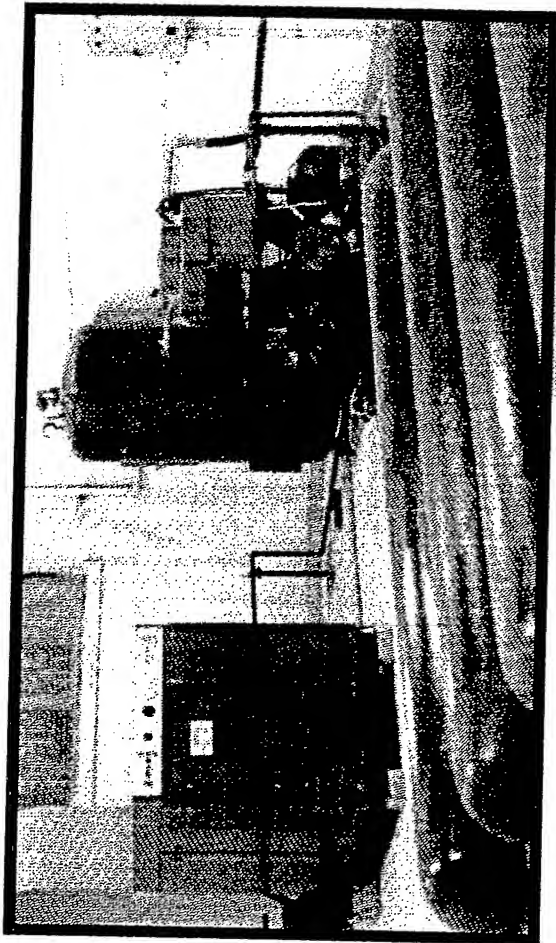


"ANKA" Wind Tunnel
 Type : Positive-pressured
 Driver : 45 kW AC motor
 Fan Type : Radial
 Test Sec. : 0.5x0.5 m², square
 Test Length: 2.5 m
 Max Spd. : 55 m/s
 Turbulence : 0.4%



"TURNA" Lateral Jet Facility
 Type : Radial fan with settling chamber
 Driver : 2.5 kW AC motor
 Jet Speed : 120 m/s
 Properties : Eqp. with nozzles of 30 and 52mm diameters

SUPERSONIC FLOWS LABORATORY



"ISLIK" Supersonic Jet Facility

- Type: Blow down (to ambient atmosphere)
- Mach number: 2.6
- Equip. with:
 - Stagnation chamber of $d=0.29$ m with nozzles $d=20$ mm, and 35 mm
 - High pressure facility:
 - Screw-type comp ($5.5 \text{ m}^3/\text{min} - 8 \text{ bar}$)
 - Receiver tank (1 m^3)
 - Piston-type comp ($0.4 \text{ m}^3/\text{min} - 50 \text{ bar}$)
 - High pressure air tanks ($2.5 \text{ m}^3 - 250 \text{ bar}$)

Instrumentation and Measurement Techniques

- **Hot-Wire Anemometry**

*3-D velocity measurements of subsonic turbulent flows;
velocity measurements with X-wire and miniature probes, 1-D
measurements of supersonic flows with film probes, surface
friction force and temperature measurements*

- **Thermocouples**

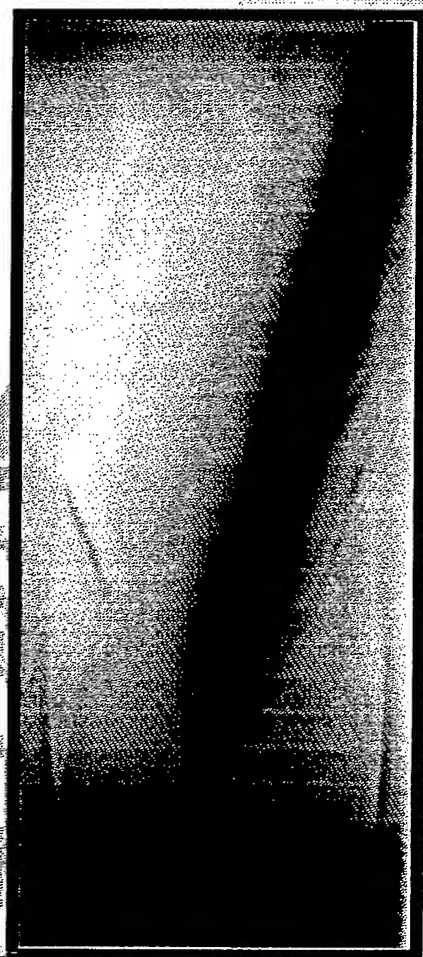
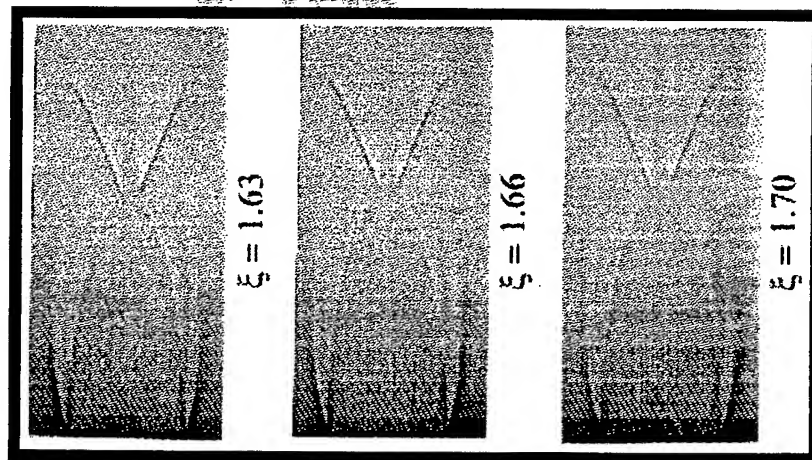
- **Fast Response Pressure Transducers**

- **Shadowgraph and Optical Systems**

- **Flow Visualization Set-up**

- **Pitot-tube and Pressure-based Instrumentations**

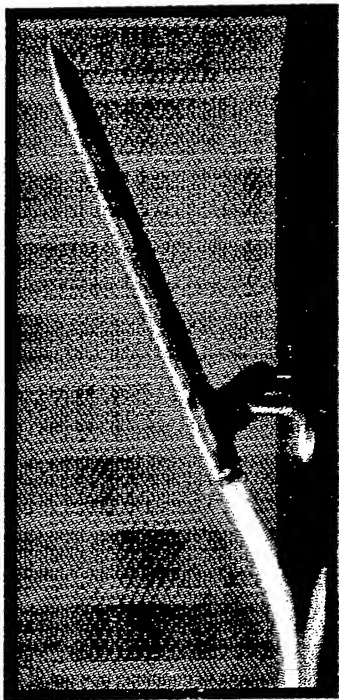
A short view of experiments



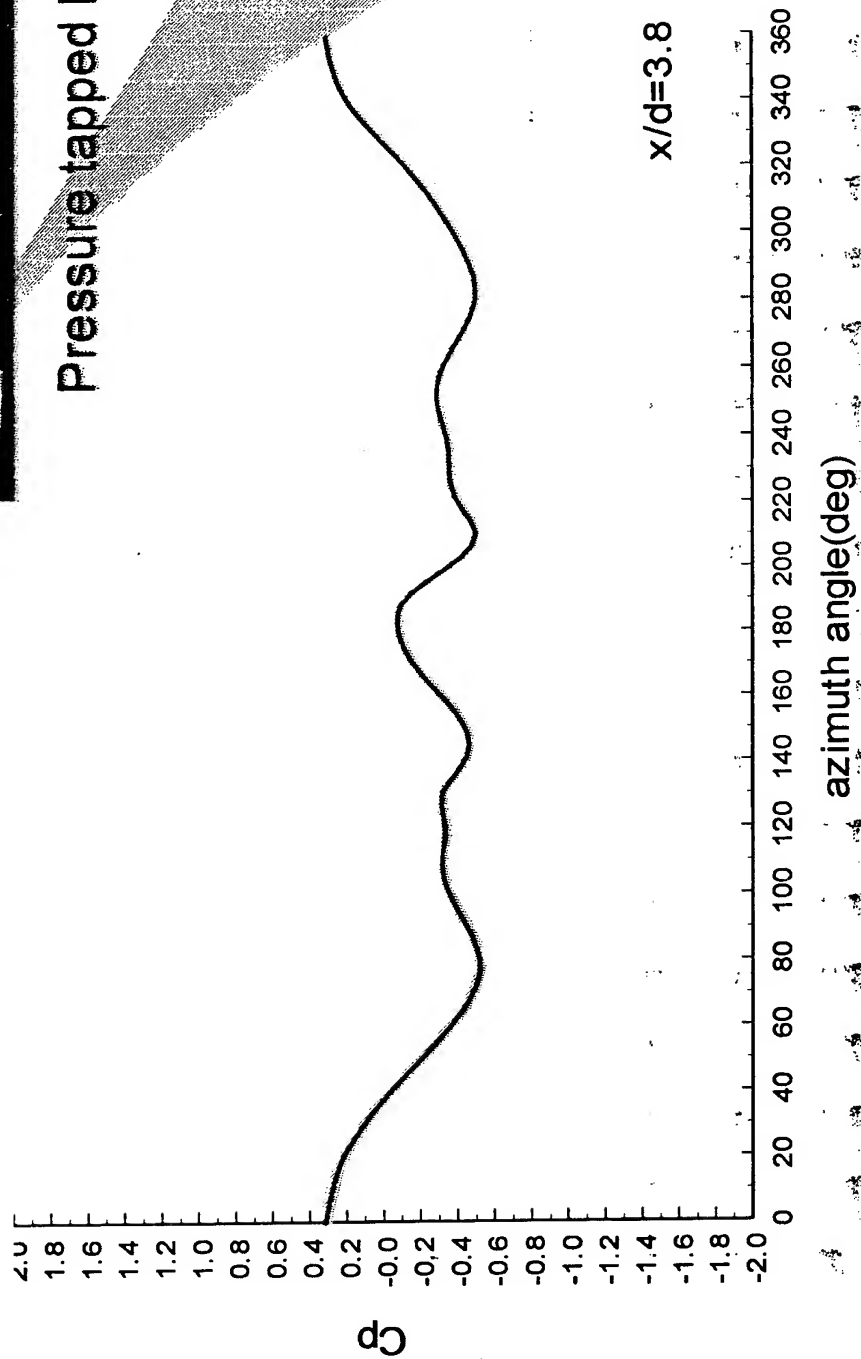
Supersonic flow over a bluff body

Photographs of supersonic free jets

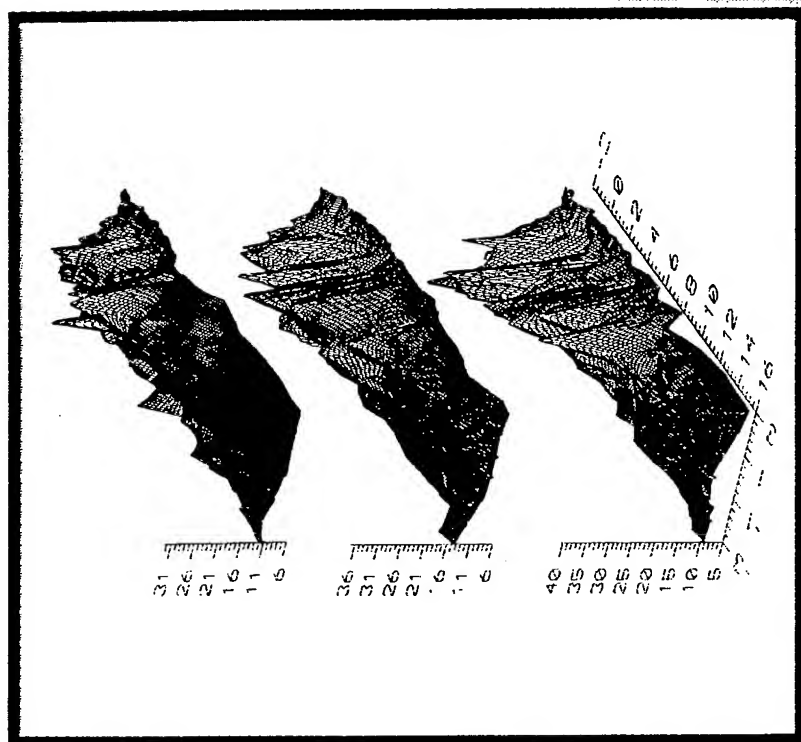
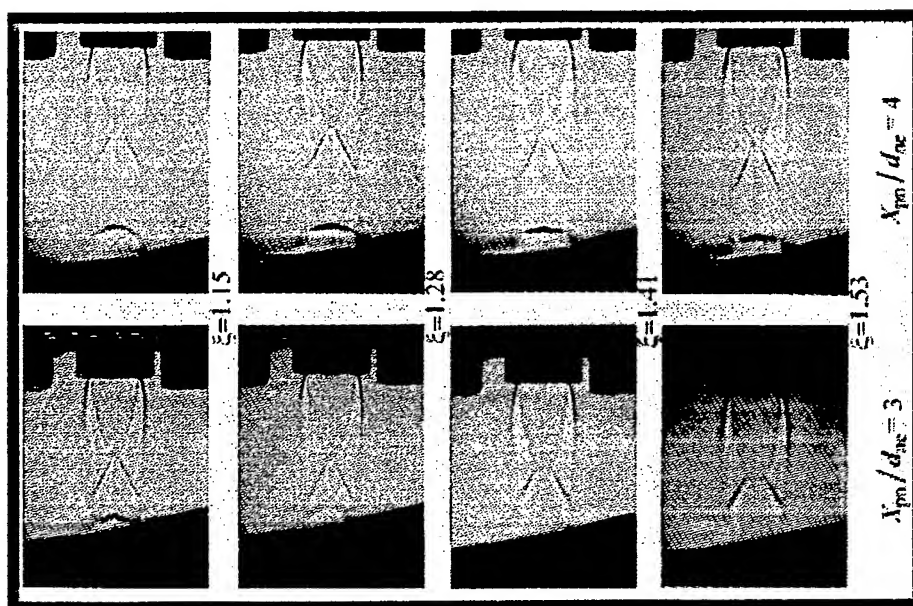
Pressure measurements on a tangent ogive forebody at 30 degree angle of attack



Pressure tapped body

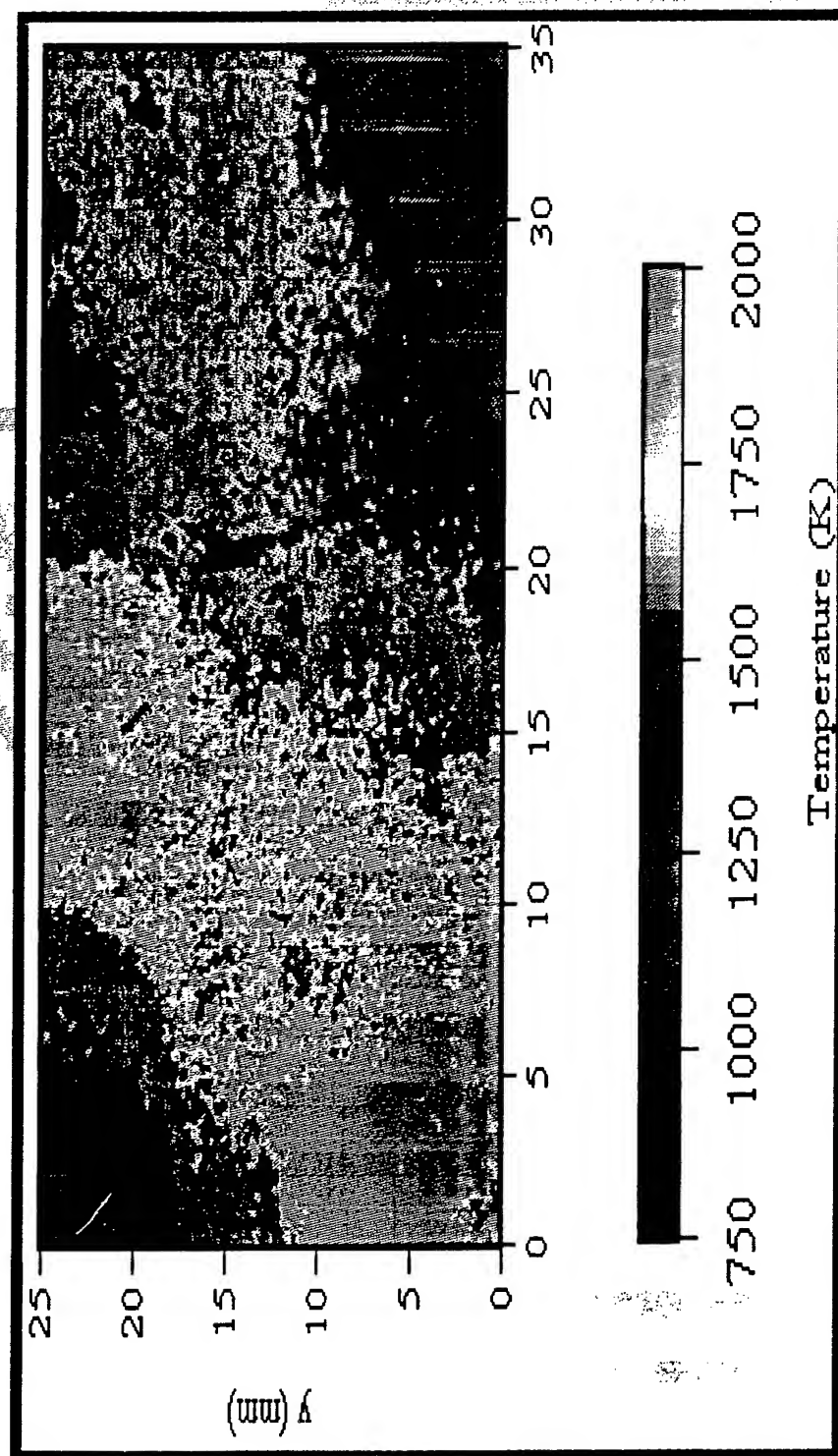


Shadowgraphs of a supersonic jet impingement with 10 degrees inclination

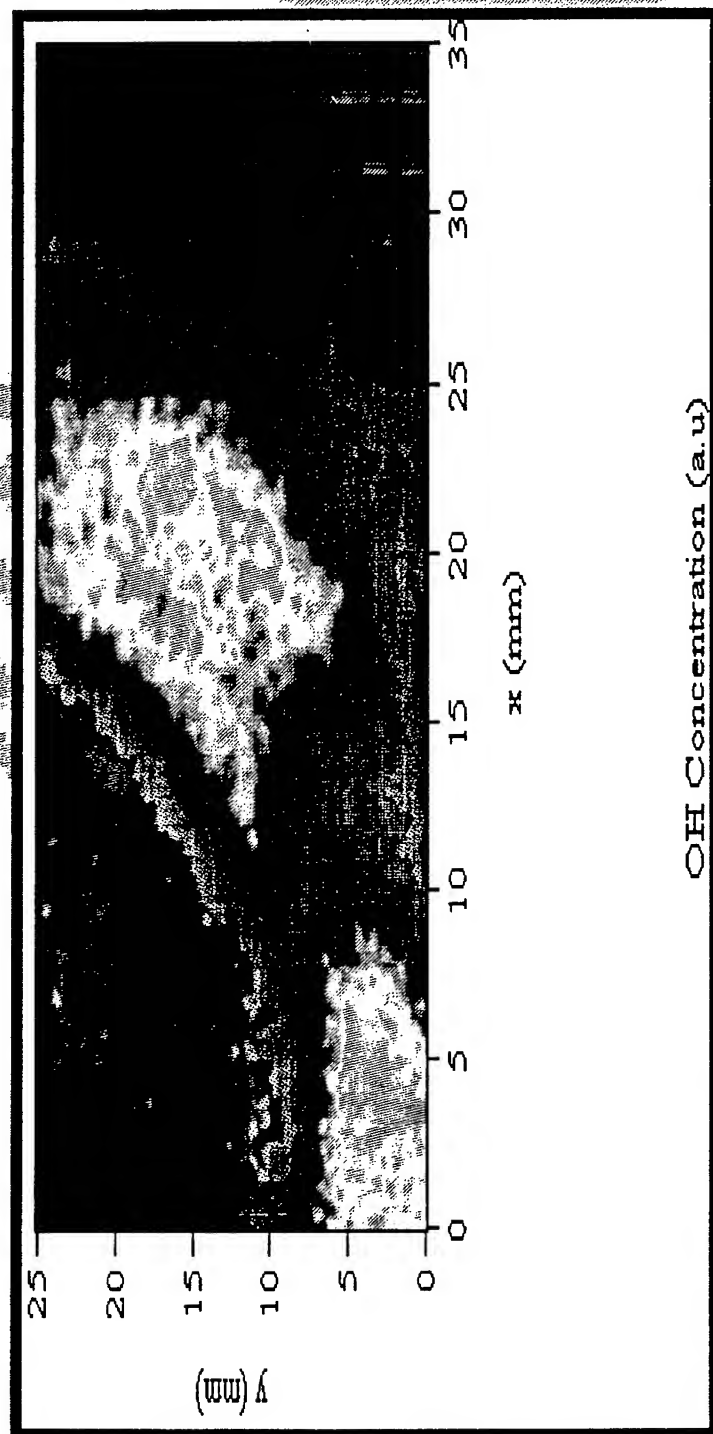


Wall pressure fluctuations
downstream
of a side jet in crossflow

Rayleigh measurement of temperature in the reaction zone of a combustion flow without flame



LIF measurement of OH concentration in the reaction zone of a combustion flow without flame



L-DV measurements of U and V velocity components in the reaction zone of a combustion flow without flame



AUTOMOTIVE LABORATORIES

E-mail : sorusbay @mkn.itu.edu.tr

Combustion Modelling

1. Modelling of combustion in Spark Ignition (SI) Engines

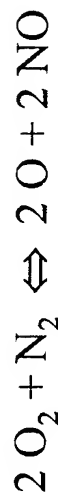
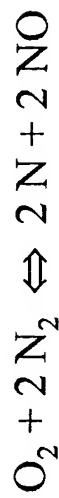
- * multi-dimensional gas flow in cylinder
- * single step reaction for fuel



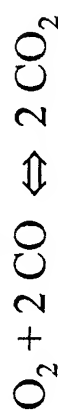
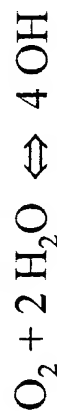
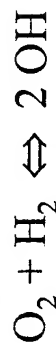
- * 3 kinetic reactions and 6 equilibrium reactions
- * effect of cylinder geometry, equivalence ratio etc has been investigated
- * effect of cylinder pressure on reaction rate is also investigated

Combustion Modelling

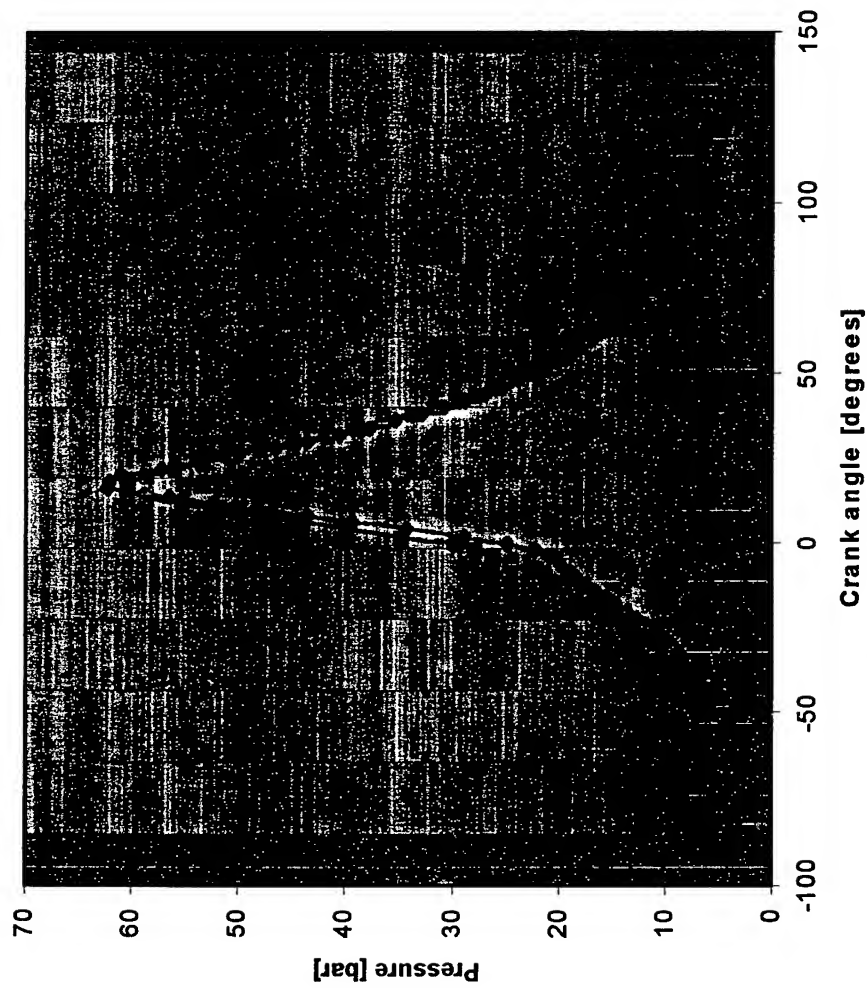
Kinetic reactions



Equilibrium reactions



Combustion Modelling



Comparison of
numerical
predictions with
experimental
data

Combustion Modelling

2. Modelling of combustion in Spark Ignition (SI) Engines

- * Multi-dimensional gas flow in cylinder
- * Reduced mechanism for combustion
- * Prediction of CO, NO_x, HC emissions

Combustion Modelling

3. Investigation of Knock in SI Engines (in progress)

- * Development of reduced mechanism for combustion of HC fuels

- * Low temperature reactions

Combustion Modelling

4. Chemical Kinetics of Methane Combustion (in progress)

- * Development of reduced mechanism for methane
- * Control of NO_x emissions in methane combustion systems - internal recirculation of combustion products (CFD application)

AUTOMATION TECHNOLOGIES DEVELOPMENT AND EDUCATION CENTER

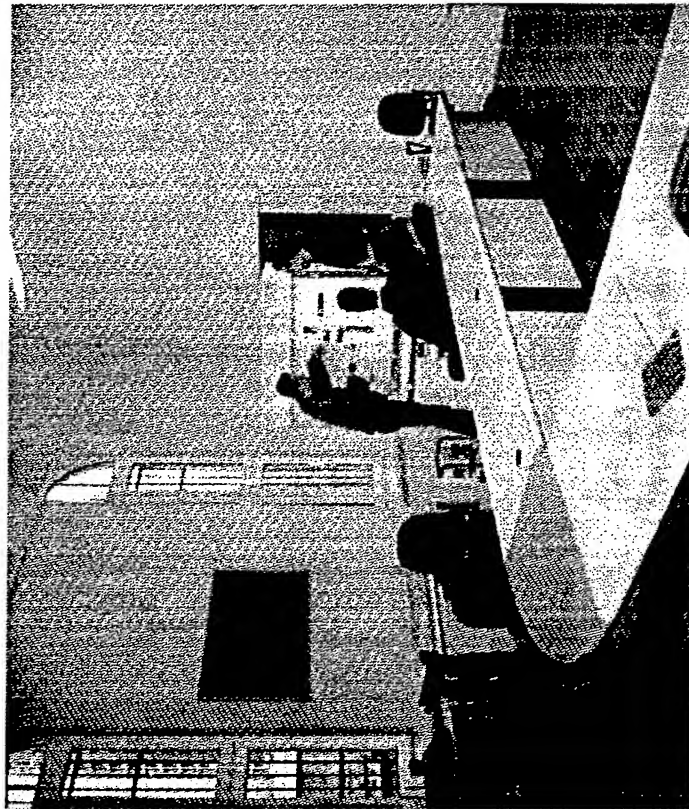
E-mail : guvenc@mkn.itu.edu.tr



- **Undergraduate and Graduate Level Education**
- **Research on Automation Technologies**
- **Projects through University - Industry Collaboration**



AUTOMATION TECHNOLOGIES



- **Engineering Calculations, Planning**
(*Engineering Software*)
- **Supervisory Control, SCADA systems**
- **Communication** (*Fieldbus, CAN*)
- **PC Based Data Acquisition and Control**
Control and Automation Using PLC's
- **Sensor Technology**
- **Electromechanical Systems and**
Electronics
- **Hydraulics/Electrohydraulics**
- **Pneumatics/Electropneumatics**

OUR CURRENT FACILITIES

- PC Based Computer System in a LAN Configuration
- PC Based Data Acquisition and Control Systems (5) and Graphical Programming Language
- PLC Systems
- Engineering Software (Simulation of Pneumatic Systems, Control, Analysis of Mechanical System Dynamics, Finite Element Analysis, Data Acquisition and Control)
- Pneumatic/Electropneumatic Education Sets
- Sensor Education Set
- Servopneumatic Positioning Systems
- AS-I Education Set
- Electronics Education Set
- Rapid Controller Prototyping/Hardware in the Loop Simulation Systems (2)
- Self Erecting Inverted Pendulum
- Various Measurement Devices etc. (Oscilloscopes, Multimeters, Digital Tachometers, Power Supplies, etc.)

